Spring 2022

Photophysics and Electronic Properties Of Photochromic Metal-Organic Frameworks

Corey R. Martin

PHOTOPHYSICS AND ELECTRONIC PROPERTIES OF PHOTOCHROMIC METAL-ORGANIC FRAMEWORKS

by

Corey R. Martin

Bachelor of Arts
Florida Gulf Coast University, 2017

Submitted in Partial Fulfillment of the Requirements

For the Degree of Doctorate of Philosophy in

Chemistry

College of Arts and Sciences

University of South Carolina

2022

Accepted by:

Natalia B. Shustova, Major Professor

Thomas Vogt, Committee Member

Andrew B. Greytak, Committee Member

Yanwen Wu, Committee Member

Tracey L. Weldon, Interim Vice Provost and Dean of the Graduate School

DEDICATION

This thesis is dedicated to my family. My mom, grandmother, grandfather, and brothers have been endlessly supportive during my Ph.D. journey. I would not be where I am without their constant guidance, love, and support.

ACKNOWLEDGEMENTS

I want to first thank my advisor, Natalia Shustova, for her endless and constant support during my Ph.D. journey. She has pushed me to develop into a motivated and compassionate scientist through her complete devotion to our success. Thank you for teaching me so much and giving me so many opportunities. I also want to thank my committee members, Dr. Greytak, Dr. Vogt, and Dr. Wu. You are always approachable and helpful, and I am grateful for your guidance and knowledge.

I want to thank my groupmates and friends in the Shustova lab, most notably Gabrielle Leith, Derek Williams, and Allison Rice who taught me everything I know, helped me academically and personally over several years, and are a constant support group. I want to also thank Kyoungchul Park, Preecha Kittikhunnatham, Otega Ejegbavwo, Brandon Yarbrough, Gina Wilson, and Grace Thaggard for being great friends and amazing coworkers.

ABSTRACT

Modulation of materials properties through light-based illumination has the capability to expand the technology sector due to stimuli-responsive dynamic behavior that cannot be achieved in traditional materials. For example, reversibly tuning photophysical profiles of such materials allows for switching between discrete states that is a key aspect for the developing logic gates, spatially- and temporally-resolved sensors, and on-demand drug delivery systems. My efforts have focused on employment of metal-organic frameworks (MOFs) as a versatile platform for the material development which contain photochromic moieties allowing for tailoring their electronic properties. Our group has expanded this direction to include heterometallic and actinide-containing metal nodes due to our recent findings on the electronic properties of actinide-containing MOFs. By combining heterometallic actinide-containing MOFs and photochromic molecules, we were able to develop a stepwise approach for tuning the electronic properties of MOFs through both "static" (i.e., irreversible modifications) and "dynamic" (i.e., reversible modifications) approaches. Overall, this work encompasses a growing field for tunable materials that will be a valuable addition to the ever-expanding technological landscape.

TABLE OF CONTENTS

LIST OF TABLES

LIST OF FIGURES

LIST OF SCHEMES

CHAPTER 1

LET THE LIGHT BE A GUIDE: CHROMOPHORE COMMUNICATION IN METAL-ORGANIC FRAMEWORKS

Martin, C. R.; Kittikhunnatham, P.; Leith, G. A.; Berseneva, A. A.; Park, K. C.; Greytak, A. B.; Shustova, N. B. *Nano Res.* **2020**, *14*, 338–354.

Chapter abstract. The photonic characteristics of chromophore-containing metal-organic frameworks (MOFs) have led to extensive photophysical studies in an effort to capitalize on the potency of precisely controlled chromophore ensembles. Several examples have laid the foundation that demonstrates how photophysical properties of chromophores can be manipulated by tuning their communications (interactions) through integration within a MOF matrix. Building upon this groundwork, utilization of a hybrid crystalline motif can induce preferential orientation of chromophores resulting in enhancement of their communication and access to tailoring their behavior compared to randomly oriented emissive molecules. In addition, integration within a framework is a vehicle to fuse chromophores into solid-state platforms, opening an avenue for chromophore utilization in applications such as portable electronics that require solids or thin films. For those reasons, the design of chromophore-containing MOFs with desirable properties that rely on the alignment and communication of hundreds of chromophores within a single platform is a pressing demand for the development of futuristic and efficient technologies. The main focus of this chapter is on harnessing the versatile MOF platform to accentuate the photophysical properties of integrated chromophores. In particular, studies based on periodic arrays of chromophores to enhance, alter, or tune photoluminescence response, produce upconverted emission, and invoke dynamic control of material properties using photochromic linkers will be discussed.

INTRODUCTION

The natural photosystem provides blueprints for replicating highly efficient chromophore organization and communication through employment of a modular platform[1–30] such as metal- or covalent-organic frameworks (MOFs or COFs).[31–36] A

particular interest in chromophores, i.e., organic molecules or molecular ensembles that absorb incident photons, revolves around their light-harvesting proficiency and the boundless possibilities of photonic energy utilization including solid-state lighting, photocatalysis, solar energy conversion, and optoelectronics.[37–40] The precise alignment of chromophores, observed in the natural photosystem and mirrored in engineered crystalline scaffolds, is one of the keys for addressing the growing demand for energy consumption that will be an ongoing challenge for generations to come.[41–45] In contrast to many amorphous systems, crystalline MOFs or COFs provide structural information about distances and angles between chromophores integrated in the matrices as well as their molecular conformations that can be applied to theoretical modeling and deliberate synthetic improvements of existing systems.[46,47] MOF modularity provides access to an exclusive toolbox containing an almost infinite combination of organic linkers and metal nodes.[48] In addition, a crystalline, porous motif offers several avenues for chromophore integration as: (1) pillars, (2) layers, (3) guest molecules within the scaffold pores, or (4) a combination of approaches 1–3 (Scheme 1.1). The nearly limitless combinations of organic and inorganic components within MOFs amplify their versatility and current examples are merely the dawn of understanding the possibilities that exist between MOF topology and the mutual orientation of chromophores.

Although a number of in-depth reports exist on the inclusion of chromophores within frameworks,[49–53] their current capabilities have, thus-far, fallen short of their extraordinary potential. The last several decades of research have delineated an extensive list of MOF advantages, especially in the area of hierarchical chromophore alignment. Reviews that describe energy transfer, photon upconversion, photocatalysis, and

photochromism can be found elsewhere;[42,54–57] this chapter focuses specifically on using tunable MOFs for chromophore alignment and communication, resulting in many cases of enhanced material properties. In particular, the topics covered in this chapter will be MOF-imposed photophysics (e.g., enhanced quantum yield (QY) as well as the appearance of fluorescence anisotropy and multichromatic luminescence), the photon upconversion phenomenon, and stimuli-responsive frameworks with incorporated and aligned photochromic moieties.[58–74]

MOF-BASED PHOTOLUMINESCENCE

A persistent challenge in designing luminescent MOFs is the balance between framework flexibility and overcoming the limited rigidity of organic linkers that can leave avenues for non-radiative relaxation.[75] These non-radiative pathways are dominated by low-energy vibrations, torsions, and rotations,[76] while excited state relaxation can also occur through emission of a photon (radiative decay). Control of radiative and non-radiative pathways can be achieved by topological tailoring (e.g., linker rigidification and linker "caging" within the framework pores)[77] and can significantly affect material performance as biomarkers, light-emitting diodes (LEDs), photovoltaics, and sensors.[78–82] As such, strategic design can result in control of chromophore organization and communication, i.e., intermolecular interactions of coupled chromophores, that is of the highest priority for developing the next generation of solid-state lighting materials based on MOFs. In this section, the effect of chromophore alignment on framework photophysical properties including multichromatic luminescence and anisotropic optical response will be discussed.

Chromophore Dynamics in Frameworks. The local environment and mutual orientation of chromophores embedded within frameworks, including their precise spatial orientations, molecular conformations, and inter- or intramolecular interactions, govern their physicochemical and photophysical properties. In this section, chromophore dynamics will be discussed as a variable for correlation of chromophore alignment in MOFs with the modulation of a photoluminescence response (Figure 1.1).[83] Many organic molecules that are highly fluorescent in dilute solutions become weakly emissive in the solid state or in highly concentrated solutions due to self-quenching.[84–88] This phenomenon, often referred to as aggregation-caused quenching (ACQ), is a persistent challenge in the field of organic-based solid-state lighting and sensing.[89–94] On the other hand, a unique class of chromophores (e.g., tetraphenylethylene (TPE) or hexaphenylsilole derivatives) exhibit aggregation-induced emission (AIE), i.e., non-radiative pathways are restricted by intermolecular interactions of chromophores in the solid state or highly concentrated solutions, resulting in photoluminescence with high quantum yields.[86–89,91,95–101]

A rigid MOF structure provides a platform for addressing ACQ through spatial chromophore separation and therefore, promoting chromophore behavior similar to that detected in dilute solutions.[102–107] For instance, 2,6-anthracenedicarboxylic acid molecules demonstrating ACQ can be integrated inside a Zr-based MOF as a linker and exhibit a similar emission profile compared to that of the non-coordinated ligand in *N*,*N*-dimethylformamide (DMF; λ_{em} = 423 nm, λ_{ex} = 390 nm).[108] At the same time, the MOF skeleton could restrict non-radiative pathways through framework rigidification and linker anchoring, leading to MOF-promoted AIE.[58,77,83,109–120] For instance, TPE-based derivatives exhibit high quantum yields in the solid state[121–124] due to suppression of low-

frequency phenyl torsional modes and C=C twisting modes through intermolecular interactions, resulting in bright emission.[4,58,77,91,97,99,110,121–126] In contrast, in dilute solutions, TPE-based molecules are usually non-emissive due to chromophore separation, promoting non-radiative decay pathways.[58,99,121] Nonetheless, MOFs could provide a route for organization and spatial separation of TPE-based chromophores while preserving their emission.[58] For instance, coordination of TPE molecules to d^{10} cations (Zn^{2+}) in Zn_2(TCPE-d_{16}), i.e., tethering, restricts the rotation of phenyl rings or twisting of the C=C bond in a TPE-linker (H_4TCPE = tetrakis(4-carboxyphenyl)ethylene).[77,97] The estimated activation barrier for the phenyl group rotation of the TPE linker within the MOF was found to be 43(6) kJ/mol (approximately 20 kJ/mol larger than non-coordinated TPE) using quadrupolar spin-echo solid-state ^{2}H nuclear magnetic resonance (NMR) spectroscopy.[77] In another study, the same MOF was applied towards development of a "turn-on" high-temperature TPE-based sensor for selective detection of gaseous ammonia.[62] Analyte sensing occurred through ammonia binding to the metal node resulting in changes of the materials photophysical response. Notably, at an elevated temperature of 100 °C, the TPE-based sensor revealed selectivity for ammonia binding.[62] Linker-centered emission in this case was maintained up to 300 °C in air. This type of system was followed up by other studies of high-performance TPE-based MOF sensors for the efficient detection of mycotoxins, benzenes, m-xylene, mesitylene, nitro explosives, and toxic metal ions.[127]

A prevailing strategy for developing white-light emission is the use of phosphor-converted white-light emitting diodes (PC-WLEDs) that are contingent on the availability of rare-earth metals.[37,118,128] Current commercial technologies for PC-WLEDs consist of a blue-emitting (InGaN) LED chip coated with cerium(III)-doped yttrium aluminum garnet

(Ce^{3+}:YAG) yellow phosphor to conjointly produce white-light emission.[129–131] To reduce the dependence on rare-earth metals, MOF-based photoluminescent materials with advanced chromophore alignment could provide an alternative pathway for developing yellow phosphors with high QYs. For instance, TPE-based linkers have been used for developing yellow-emitting frameworks. In one example, a naphthalene-decorated TPE-based linker (H_4TCNPE = 1,1,2,2-tetrakis(4-(6-carboxy-naphthalen-2-yl)phenyl)ethylene; λ_{em} = 524 nm, λ_{ex} = 455 nm) was prepared for coordinative immobilization inside a Zr-based framework, $Zr_6O_4(OH)_4(TCNPE)_2$ (LMOF-602)[132] The TCNPE-containing MOF possesses an emission maximum at 570 nm, and its QY was enhanced by 156% in comparison with the non-coordinated organic linker; specifically, QY = 18% for H_4TCNPE, λ_{ex} = 450 nm, while QY = 46% for LMOF-602, λ_{ex} = 455 nm. Moreover, the Commission International de I'Eclairage (CIE) coordinates for LMOF-602 were found to be (0.47, 0.51), and are similar to those of the commonly used YAG:Ce^{3+} yellow phosphor (0.41, 0.55).[131–134]

In an effort to suppress non-radiative pathways through coordinative immobilization in a rigid matrix, a benzylidene imidazolone (BI)-based chromophore was integrated as a linker in several Zn-based MOFs.[59,135–137] Interest in this particular class of molecules arises from the fact that they are primarily responsible for the strong emission of natural proteins.[138–145] In particular, 5-(4-hydroxybenzylidene)-3,5-dihydro-4*H*-imidazol-4-one (HBI) is highly emissive inside the *β*-barrel of a green fluorescent protein (GFP); however, outside of the protein barrel, phenyl ring rotation (e.g., tilting, twisting, and Hula twisting) can change the molecular conformation and cause relaxation of its excited state through non-radiative pathways.[136,146] Through several chromophore

organization routes, such as “fastened immobilization" (i.e., chromophore coordination to the framework skeleton through only one side by peptide bond formation), coordinative immobilization (i.e., chromophore anchoring to available metal centers leading to the formation of a MOF constructed by BI-based linkers), and guest incorporation, the emission maximum of MOF-incorporated chromophores belonging to the BI-family can be tuned over a wide spectral range from 440 to 649 nm.[50,59,67,135,137] For example, a BI-based derivative, 2-((1-(2-methoxy-2-oxoethyl)-2-methyl-5-oxo-1,5-dihydro-4*H*-imidazol-4-ylidene)methyl)-[1,1′-biphenyl]-4,4′-dicarboxylic acid (H_2BDC-HBI), that was almost non-emissive in an unrestricted environment,[144,147] became brightly emissive (λ_{em} = 516 nm, λ_{ex} = 365 nm) within the confined space of a crystalline matrix.[59]

In a similar vein, Lin and co-workers observed enhancement in chiral sensing through a cavity confinement effect promoted by the conformational rigidity exerted from the crystalline framework.[148] In particular, a 1,1'-bi-2-naphthol (BINOL)-based derivative, (*R*)-2,2'-dihydroxy-1,1'-binaphthyl-4,4',6,6'-tetrakis(4-benzoic acid) (H_4TCP-BINOL), was chosen as a fluorescent organic linker to construct a chiral porous MOF, Cd_2(TCP-BINOL). The strategic alignment of a BINOL-core simultaneously endows it with excellent enantioselectivity for amino alcohols as well as sensing capabilities through fluorescence quenching. Specifically, emission of Cd_2(TCP-BINOL) (λ_{em} = 440 nm, λ_{ex} = 350 nm) is quenched due to hydrogen bonding of the terminal hydroxy groups of the BINOL-core to amino alcohol analytes. The BINOL-containing MOF displayed enhanced enantioselectivity compared to other BINOL-based materials that was attributed to analyte confinement in the pores as well as conformational rigidity of the BINOL groups integrated in the lattice. Single-crystal X-ray diffraction reveals that the dihedral angle of the BINOL

moiety was fixed at 89.5°. This conformational rigidity allowed for a greater stereospecific formation of hydrogen-bonded complexes, thus allowing for higher selectivity overall.

So far in this section, we discussed how the confined space of a host affects physicochemical properties of a guest;[146] however, a guest can also affect the properties of the host.[66] For example, an array of aromatic volatile organic compounds (VOCs) were encapsulated in $Zn_2(BDC)_2(DPNDI)$ (H_2BDC = benzene-1,4-dicarboxylic acid; DPNDI = *N*,*N*′-di(4-pyridyl)-1,4,5,8-naphthalenediimide) causing a reversible structural transformation of the host that resulted in changes in emission that were detectable by the naked eye (Figure 1.2).[66] These emission features are enabled by dynamic structural transformations in the framework resulting in changes in alignment of guest molecules. Moreover, aromatic VOCs with different phenyl ring substituents embedded inside the framework pores caused reversible changes in emission profiles (Figure 1.2). In a similar vein, framework QYs can be tuned through guest-mediated rigidification (i.e., incorporation of an optically inactive guest).[149] As shown on the example of a non-emissive guest, *n*-pentane, embedded inside a Zn_2(TCBPE)(BPY) framework (LMOF-236; H_4TCBPE = 1,1,2,2-tetrakis(4-(4-carboxyphenyl)phenyl)ethene; BPY = 4,4'-bipyridine), guest-induced framework rigidification could be responsible for an enhancement in QY from 12% (LMOF-236) to 59% (*n*-pentane@LMOF-236).[149] Overall, further work in the field of confined space-imposed photophysics could significantly modify the material landscape of MOF-based sensors with an emphasis on alignment of chromophores as a part of the matrix or as a guest molecule.

Multichromatic Emission. By mimicking the design of multichip white-light emitting diodes (MC-WLEDs), in which the independent components (i.e., red, green, and

blue LEDs) are made to act in unison, MOF-based white-light phosphors can be developed. MOFs can behave as a platform for mutual chromophore communication where each type of chromophore contributes to multichromatic emission.[150] As mentioned previously in Scheme 1.1, distinct chromophore functionalities can be integrated in different parts of the framework.[151] For instance, chromophores can form layers (e.g., tetratopic porphyrin-based linkers),[152] while other chromophores with a different photophysical profile can be inserted as pillars, and therefore, can result in orthogonal mutual chromophore orientation of two types of emissive linkers working in harmony.[50,135] However, the most common and less synthetically challenging avenue of chromophore integration inside a MOF matrix to date still relies on preparation of guest@host materials.[153,154] For instance, it was demonstrated that a white-light emitting MOF could be fabricated through encapsulation of a dye (e.g., rhodamine B (RhB), basic red 2 (BR-2), or Astrazon pink FG (APFG)) into a MOF with emissive TPE linkers (LIFM-WZ-6; Zn_2(TATZTPE)(BPY); H_4TATZTPE = 4,4',4'',4'''-(4,4',4'',4'''-(ethene-1,1,2,2-tetrayltetrakis(benzene-4,1-diyl))-tetrakis(1*H*-1,2,3-triazole-4,1-diyl))tetra-benzoic acid).[155] Three white-light emitting MOFs (RhB@LIFM-WZ-6, BR-2@LIFM-WZ-6, and APFG@LIFM-WZ-6) were developed by optimizing the amount of each encapsulated dye inside the MOF (e.g., 0.1 wt% for RhB@LIFM-WZ-6, 2.0 wt% for BR-2@LIFM-WZ-6, and 0.1 wt% for APFG@LIFM-WZ-6). At 365-nm excitation, RhB@LIFM-WZ-6, BR-2@LIFM-WZ-6, and APFG@LIFM-WZ-6 phosphors exhibited CIE coordinates of (0.33, 0.35), (0.33, 0.36), and (0.34, 0.36), respectively, and are very similar to those of desirable white-light emitting materials with CIE coordinates of (0.33, 0.33). Interestingly, white-light emission from each dye@LIFM-WZ-6 was not the result of superposition of emission profiles (guest and

MOF). Instead, energy transfer (EnT) from LIFM-WZ-6 to RhB in RhB@LIFM-WZ-6 was confirmed by time-resolved experiments that demonstrated a reduced fluorescence lifetime of the MOF from 4.5 ns to 2.3 ns after RhB encapsulation.

Another approach to achieve white-light emission is based on core-shell MOF growth, i.e., one type of MOF can be used as a seed crystal for overgrowth of a second structure around the parent framework.[156] For instance, by using cubic crystals of a RhB-loaded cyclodextrin-MOF (RhB@CD-MOF; CD-MOF = (KOH)*2*(γ-CD); γ-CD = γ-cyclodextrin), it was found that additional shells of dye@CD-MOF could be formed with variable guests embedded (e.g., first a RhB@CD-MOF core is produced, then overgrown with a FL@CD-MOF shell (FL = fluorescein)).[156] Spatial organization of chromophores within a single MOF using this method provides the opportunity for bright solid-state emission that would otherwise be reduced in the solid-state via ACQ.[86,90,157] Several shells, i.e., FL@CD-MOF and 7-HCm@CD-MOF (7-HCm = 7-hydroxycoumarin), could also be consecutively grown on one RhB@CD-MOF core.[156] Under 365-nm irradiation, CIE coordinates measured for a core:shell:shell MOF (where RhB@CD-MOF = core, FL@CD-MOF = first shell, and 7-HCm@CD-MOF = second shell) were found to be (0.35, 0.32), that is close to the desired coordinates (0.33, 0.33) for white-light emitters.[156,157]

White-light emitting MOFs can also be obtained by incorporating multiple emissive dyes into the pores of a non-emissive MOF.[156,158] This strategy was demonstrated on the example of three dyes, RhB, FL, and 7-amino-4-(trifluoromethyl)coumarin (C-151), incorporated inside ZIF-8 using three different encapsulation approaches.[158] In the first approach (model 1, Figure 1.3), a white-light phosphor was made from a mixture of dye@ZIF-8 crystallites: RhB@ZIF-8, FL@ZIF-8, and C-151@ZIF-8. Each dye@ZIF-8

sample was prepared through a two-step procedure. First, incorporation of the dye was achieved during MOF formation, i.e., the solution used for MOF synthesis contains both the MOF precursors and the selected dye. Second, a ZIF-8 shell was grown over the core (dye@ZIF-8) to exclude the effect of the surface-adsorbed dyes on the composite emission. Prepared RhB@ZIF-8, FL@ZIF-8, and C-151@ZIF-8 exhibited red (QY = 60%), green (QY = 63%), and blue emission (QY = 42%), respectively. The solid-state mixture consisting of these three dye@ZIF-8 samples was found to possess CIE coordinates of (0.32, 0.34) under 365-nm excitation.[158] In the second method (model 2, Figure 1.3), a white-light emitting MOF was produced by simultaneously encapsulating RhB, FL, and C-151, within a single-phase of ZIF-8 (i.e., several dye molecules in one MOF crystal) with spatially separated chromophores occupying discrete pores of the framework. In particular, a white-light phosphor with CIE coordinates of (0.34, 0.34) under 365-nm excitation was prepared by concurrent heating of MOF precursors at millimolar dye concentrations, followed by growth of a pure ZIF-8 shell over the core.[158] Lastly, in the third method (model 3, Figure 1.3), a white-light emitting MOF was fabricated by encapsulating RhB, FL, and C-151 sequentially into a single ZIF-8 crystal via shell-by-shell overgrowth. In other words, each layer of dye@ZIF-8 is alternated by a ZIF-8 shell, thus separating the dye@ZIF-8 layers from one another and preventing Förster resonance energy transfer (FRET) between different dyes. For example, a multishell dyes@ZIF-8 nanocomposite possessing white-light emission was prepared by consecutive growth of: first, a solid ZIF-8 shell over C-151@ZIF-8, then FL@ZIF-8 followed by another solid ZIF-8 shell, and lastly a layer of RB@ZIF-8 followed by the final ZIF-8 shell (model 3, Figure 1.3). At optimized dye concentrations, the multishell dyes@ZIF-8 nanocomposite exhibited white-

light emission with CIE coordinates of (0.32, 0.34) under 365-nm excitation.[158] Therefore, these examples portend MOF-based devices as a versatile platform for developing white-light emitting materials as a result of chromophore communication through meticulous crystal engineering.

Apart from developing white-light LEDs, incorporation of multiple chromophores in tunable MOFs can also be applied for improving the performance of MOF-based devices, in particular MOF-based sensors. In order to safeguard the accuracy of a sensor that is susceptible to environmental factors (e.g., concentration gradients, excitation power fluctuations, and environment-induced non-radiative relaxation), MOF-based multichromatic sensors with self-referencing capabilities were designed.[159,160] For example, efficient colorimetric luminescent pH sensing was observed in a mixed-lanthanide bimetallic MOF, $Eu_{0.20}Tb_{0.80}$(HDPDA) (H_4DPDA = 4-(3,5-dicarboxyphenyl)pyridine-2,6-dicarboxylic acid).[161] In this framework, the emission intensity of Tb^{3+} (λ_{em} = 543 nm, λ_{ex} = 320 nm) varies, while the emission of Eu^{3+} (λ_{em} = 616 nm, λ_{ex} = 320 nm) remains constant in a pH range of 3.90 to 7.50. Therefore, the ratio of the emission intensity of the band centered at 616 nm (IEu^{3+}) to that of the band centered at 543 nm (ITb^{3+}) was determined to evaluate the pH of a solution. The pH-dependent fluorescence intensity of the Tb^{3+} component was explained using DFT calculations. Theoretical modeling indicated that the deprotonation of uncoordinated carboxylic acid groups from HDPDA, caused by an increase in pH, enhanced EnT from the triplet excited state of the linker to the excited state of Tb^{3+}, corresponding to the emission band at 543 nm. Therefore, this self-referencing system could be used to determine the pH based on (IEu^{3+})/(ITb^{3+}), paving the way for MOFs to emerge as a class of self-referencing

luminescent sensors by combining multiple emitters in one well-defined ensemble. In addition to improving sensing performance of MOF-based sensors, this strategy can be utilized to mimic the design of MC-WLEDs to achieve MOF-based white-light phosphors.

Anisotropic Photoluminescence. When excited by unpolarized light, an ensemble of randomly-oriented fluorescent chromophores (observed in solution) can exhibit unpolarized emission. Polarized emission (fluorescence anisotropy) can only be achieved through excitation photoselection with polarized light and in the absence of rapid rotational diffusion. Larger anisotropy values, and emission polarization even for unpolarized excitation, can be achieved by strategically aligning chromophores, and hence, transition dipole moments (Figure 1.4).[162] Alignment can readily be achieved through incorporation of chromophores into a MOF matrix. Such material development is driven by the demands in areas such as spatially-resolved sensors, nanophotonic circuits, or laser components,[163–168] as such, placing chromophores in frameworks possessing periodic structures could help to address industrial needs.[169–174] For instance, the $Zn_2(TDC)_2$(NP-P4VB) MOF (H_2TDC = 9,10-triptycenedicarboxylic acid; NP-P4VB = bis(4-pyridyl)dineopentoxyl-*p*-phenylenedivinylene), exhibiting strongly polarized fluorescence, was constructed by connecting $Zn_2(TDC)_2$ layers through axially-coordinated NP-P4VB linkers as pillars.[169] In contrast to randomly oriented NP-P4VB chromophores in solution, their integration in a MOF matrix resulted in polarized fluorescence (λ_{em} = 513 nm, λ_{ex} = 405 nm) that is nearly perpendicular (~80–90°) to the normal plane of the platelet MOF crystals, confirming that the NP-P4VB (chromophore) pillars are highly aligned in the MOF crystal. The degree of polarized fluorescence (A; $A = (I_{\parallel} - I_{\perp})/(I_{\parallel} + 2I_{\perp})$; $I_{\parallel}$ and $I_{\perp}$ represent the fluorescence

intensities measured parallel and perpendicular to the platelet surface normal, respectively) was estimated to vary from 0.7 to 0.8 for $Zn_2(TDC)_2$(NP-P4VB).

Another example of a MOF demonstrating an anisotropic fluorescence response could be prepared by encapsulating a fluorescent chromophore into the MOF channels as a guest.[170] In this example, a fluorescent dye, DMASM ($DMASM_+$ = 4-[*p*-(dimethylamino)styryl]-1-methylpyridinium), was encapsulated into the one-dimensional (1D) channel along the *c*-axis of ZJU-68 ($H_2[Zn_3O(CPQC)_3]$; H_2CPQC = 7-(4-carboxyphenyl)quinoline-3-carboxylic acid) with an average pore size of 6.0 Å via an in situ self-assembly method (i.e., DMASM was added to a precursor solution of ZJU-68 followed by solvothermal synthesis). DMASM@ZJU-68 exhibited a strong emission with large anisotropy when it was excited parallel to the 1D crystal channels, i.e., along the *c*-axis, at λ_{ex} = 1380 nm. When the MOF was excited at the same wavelength perpendicular to the *c*-axis, no detectable emission was observed, indicating excitation polarization. This observation shows that the chromophores are highly oriented along the crystal channels. Interestingly, the large fluorescence anisotropy was not observed when the same dye was encapsulated in a MOF with larger 1D channels, such as bio-MOF-1 ($(Me_2NH_2)_2[Zn_8(AD)_4(BPDC)_6O]$; AD^- = adeninate; H_2BPDC = 4,4′-biphenyldicarboxylic acid).[175] The absence of anisotropic emission in DMASM@bio-MOF-1 compared to DMASM@ZJU-68 was attributed to the larger pore size of bio-MOF-1 (~10 Å), promoting a greater range of orientations for chromophore guest molecules.[170,175] These findings portend the future directions of MOFs as a powerful platform for anisotropic polarization of aligned emissive dye molecules.

PHOTON UPCONVERSION IN MOFS

The combination of inorganic and organic moieties has proven a successful approach for improving the efficiency of photon upconversion: the emission of photons at higher energies (shorter wavelengths) upon excitation with lower-energy photons.[176] MOFs could be considered as an ideal vehicle for honing this process due to the strategic innate alignment of chromophores. In general, the photon upconversion process is advantageous since it harnesses incident lower-energy photons to generate higher-energy visible and ultraviolet excitations. The shift in energy is in the opposite direction of the Stokes shift observed in typical fluorescence processes, and as such can result in light emission against a very low background.[176,177] Materials capable of efficient photon upconversion are in great demand for applications in full-color displays, light-triggered nanomedicine, minimally-invasive bioimaging, photodynamic therapy, high-density data storage, and microfabrication.[170,178–182] MOFs offer several pathways for photon upconversion to occur. Sensitized triplet-triplet annihilation (*s*TTA), energy transfer upconversion (ETU), excited-state absorption (ESA), multi-photon absorption (MPA), and second-harmonic generation (SHG) are discussed herein.

Upconversion via *s*TTA. Upconversion through *s*TTA typically occurs in systems containing strongly light absorbing (sensitizer) and emitting (annihilator) organic chromophores or metal nodes.[183] In the *s*TTA process (Figure 1.5), a high-energy photon is emitted by an excited singlet annihilator that is the product of combining two triplet annihilators generated from two lower energy photons. Specifically, photoexcitation of a sensitizer (chromophore 1) generates an excited singlet state sensitizer that can convert to its triplet state via intersystem crossing (ISC). Next, the triplet-state sensitizer transfers its

energy to an annihilator (chromophore 2) through triplet-triplet energy transfer, forming a triplet-state annihilator. Finally, a pair of triplet-state annihilators recombine (triplet-triplet annihilation or TTA) to form an excited singlet annihilator that emits a photon of higher energy than that of the two initial excitation photons.[184] Due to the complexity of the *s*TTA process, chromophore organization (sensitizer and annihilator mutual orientation) in the scaffold can drastically affect the sTTA efficiency.[183,184] The key figures-of-merit used to evaluate the performance of *s*TTA systems are: maximum upconversion quantum yield (Φ_{UC}) that is equal to the number of photons generated from the upconversion process divided by the number of incident photons and threshold excitation intensity (I_{th}) that indicates the excitation intensity above which a maximum Φ_{UC} can be achieved.[184] A theoretical maximum for Φ_{UC} is 50% since an upconverted photon is generated from two incident photons.

In a prototypical benchmark example of *s*TTA upconversion in the solid state, a sensitizer (PtOEP; Pt(II) octaethylporphyrin) and an annihilator (DPA = 9,10-diphenylanthracene) are embedded in a rubbery and viscous polymeric medium (e.g., ethyleneoxide/epichlorohydrin copolymer,[185,186] polyurethane,[187] or poly(butyl acrylate)).[188] Upconversion in this system depends on the residual movement of the triplet annihilators and is limited by the polymeric medium due to a low triplet exciton diffusion length (L_T) [185–188]. Consequently, low L_T usually coincides with a high excitation power density (typically greater than one solar irradiance)[186–188] to enable upconversion and is undesirable for many biological applications such as in vivo bioimaging.[189,190] One approach to increase L_T is based on annihilator alignment in a periodic crystal.[69–71] Indeed, many studies have utilized the hierarchy of MOF motifs to their advantage by organizing

sensitizer and annihilator chromophores in the crystalline matrices, that can in turn increase L_T and reduce the excitation power density required for photon upconversion.[69,70,191] The first report of *s*TTA upconversion in MOFs was demonstrated on the example of Zn(ADB) (H_2ADB = 4,4′-(anthracene-9,10-diyl)dibenzoic acid, annihilator).[69] The surface of the MOF nanocrystals were modified with a carboxylate-containing sensitizer (Pd(II) mesoporphyrin IX), and then the nanocrystals were embedded in poly(methyl methacrylate) (PMMA). This elegant system showed notably low I_{th} of 0.049 mW cm^{-2}, that is 30-fold lower than the solar irradiance value at the same excitation wavelength (1.6 mW cm^{-2} at 532 ± 5 nm). Moreover, considerably high Φ_{UC} of 1.9% using low laser power density of ~ 5 mW cm^{-2} was achieved, which is unprecedented since the low laser power does not exceed the solar irradiance value.[69] By employing the strategy to increase L_T based on annihilator alignment, integration of H_2ADB (annihilator) into Zn(ADB) yielded an organized system with a L_T of 4 μm.[69] Notably, the reported L_T of Zn(ADB) is significantly larger than that found for the anthracene core of ADB^{2-} itself arranged as nanoaggregates (L_T = 7.3 nm),[192] likely due to the periodic nature and chromophore organization in the MOF.

In addition to annihilator organization, the effect of a MOF crystal size on threshold excitation intensity, I_{th}, was investigated by Monguzzi and co-workers.[70] They developed a kinetic model for describing the upconversion dynamics in a nanocrystal and were able to determine I_{th} values required to reach the maximum upconversion QY. The micron-scale L_T in a MOF matrix (1D L_T can be up to 6.3 × 10^{-6} m)[69] suggests 100% TTA yield (Φ_{TTA}) in MOF crystals with nanoscale sizes (~1 × 10^{-9} m), i.e., when exciton diffusion length is appreciably larger than the maximum distance between two triplets generated in the MOF

crystal, regardless of excitation density. This strategy implies that all generated triplet states in a MOF nanocrystal would annihilate rather than be involved in recombination, hence resulting in 100% annihilation efficiency (100% Φ_{TTA}). Their model proposed that the threshold excitation intensity could be minimized by optimizing the size of MOF nanocrystals (e.g., I_{th} below one solar radiance can be obtained from a MOF nanocrystal with a size ranging from 20 to 60 nm). The prepared matrix of Zn(ADB) MOF, ADB^{2-} acting as the annihilator, poly(butyl acrylate) as the polymeric medium, and PtOEP as a sensitizer, exhibited a low I_{th} of ~2×10^{-1} mW cm^{-2} and a maximum Φ_{UC} of ~6%, validating their model.[70]

Besides MOF crystal size, distribution of sensitizers within MOF-based *s*TTA-upconversion systems is also an important factor for controlling upconversion efficiency. For instance, the performance of MOF-based *s*TTA-upconversion can be improved through alignment of sensitizer molecules in MOF structures by coordination to unsaturated metal nodes (i.e., nodes possessing open sites for coordination of additional linkers; such as $Zr_6O_8(OH)_8$ nodes with less than 12 organic linkers per node).[71] In this case, a sensitizer, Pd(II)-meso-tetrakis(4-carboxyphenyl)porphyrin (H_4Pd-TCPP), was introduced into a Zr-based MOF constructed of annihilator chromophores (H_2DCDPA = 4,4′-(9,10-anthracenediyl)dibenzoic acid) by coordination to the metal node, i.e., the sensitizer was coordinated to unsaturated Zr-metal nodes[192–194] as shown in Figure 1.5. Theoretical studies estimated the diffusion length, L_T, in such systems to be 1.6 μm. Since the average nearest-neighbor distance between two sensitizers was calculated to be 26.5 nm, the calculated long-range triplet diffusion length of 1.6 μm is large enough to cover the average distance between two neighbors, enabling efficient triplet energy migration. A low I_{th} value of 2.5

mW cm^{-2} and a high maximum Φ_{UC} (up to 1.28%) in aqueous media allowed for in vivo imaging of lymph nodes in a live mouse through *s*TTA-upconversion with a lower power density (5 mW cm^{-2}). Upconversion imaging was performed *in vivo* (λ_{ex} = 532 nm) using MOF crystals of approximately 55 nm in size, resulting in high imaging contrast.[71] Furthermore, this work foreshadows the use of MOFs with strategically aligned chromophores as a bioimaging material with upconversion occurring at red or near-infrared excitation where living tissues are more transparent.

Upconverting devices using *s*TTA can be fabricated via layer-by-layer techniques constructed from surface-anchored MOFs (SURMOFs).[195] In one case, a SURMOF was constructed from a sensitizer, Pd(II) 5,15-diphenyl-10,20-di(4-carboxyphenyl) porphyrin (Pd-H_2DCP), and an annihilator, ADB^{2-}, connected by Zn nodes.[195] Several configurations of SURMOFs, constructed from alternation of (A) Zn-ADB and (B) Zn-(Pd-DCP) layers, were assessed to determine the role of layer thickness on photon upconversion and thus, optimizing I_{th} of the SURMOF-based *s*TTA upconverting device. By controlling the thickness of each layer, I_{th} of the SURMOF-based *s*TTA upconverting device was optimized. Remarkably, I_{th} of ~0.8 mW cm^{-2} was observed for the SURMOF-based device by tuning the thicknesses of the layers to 110 and 30 nm, for sensitizer (B) and annihilator (A) layers, respectively. Furthermore, *s*TTA-upconversion was utilized for improving the solar energy conversion performance of SURMOF-based devices.[196,197] Sun and co-workers reported that *s*TTA-upconversion enhanced the generated photocurrent of a standard electrochemical cell.[196] In this example, a working electrode was fabricated by growing a Zn(PLDC) SURMOF (H_2PLDC = 3,9-perylenedicarboxylic acid) on mesoporous TiO_2 using a liquid phase epitaxial method via alternating deposition of an

annihilator, H_2PLDC, and zinc acetate. A standard electrochemical cell consisting of a working electrode and a sensitizer, PtOEP, suspended in an acetonitrile solution of [Co(tris-BPY)$_3$]$^{2+/3+}$ (cobalt(II/III) tris(2,2'-bipyridine)) was shown to generate a photocurrent when irradiated at 530-nm irradiation, that was notably 10-fold larger than that of the system constructed from only the annihilator or the sensitizer. A correlation between the excitation power density and photocurrent density of the device (fabricated from both the annihilator and the sensitizer) was used to confirm that sTTA-upconversion caused the photocurrent enhancement. In another example reported by the same group, a dye sensitized solar cell (DSSC) was fabricated from a Zn(PLDC) SURMOF as an annihilator and a boron-dipyrromethene (BODIPY) dye as a metal-free sensitizer embedded in PMMA.[197] As a first step, the Zn(PLDC) SURMOF was prepared on a layer of TiO_2. Then, the exposed carboxylic acid groups from the SURMOF were modified via a photochemical reaction between BODIPY and PMMA, thus forming a glassy film of BODIPY/PMMA on top of TiO_2-Zn(PLDC). As a result, the constructed DSSC exhibited a five-fold increased photocurrent upon irradiation at 532-nm compared to a DSSC constructed from the Zn(PLDC) SURMOF without the sensitizer layer (i.e., the absence of BODIPY within the polymer matrix).[197]

Upconversion via ESA and ETU. In contrast to *s*TTA-upconversion systems that are based primarily on organic chromophores as the active components for upconversion (Figure 1.5), metal ions (traditionally rare-earth elements) play a crucial role in the development of upconversion systems based on the excited state absorption or energy transfer upconversion processes as shown in Figures 1.6a and 1.6b, respectively.[179] These systems are commonly based on metal oxide or metal fluoride crystals doped with one or

more type(s) of rare-earth metal ions (e.g., Er^{3+}, Nd^{3+}, Tm^{3+}, or Yb^{3+}) acting as emissive centers.[179] The ESA and ETU processes both involve sequential absorption of two or more photons, but they possess different upconversion mechanisms (Figures 1.6a and 1.6b). In the case of upconversion via ESA, the first photon absorption populates a metastable excited state of the metal ion, and then absorption of a second photon promotes the metal ion from the metastable excited state to an upper excited state, followed by upconversion emission as shown in Figure 1.6a.[198,199] In most cases of upconversion via ETU, a populated excited state on one metal ion decays through non-radiative EnT to a nearby second metal ion that is already in a meta-stable excited state, yielding upconverted emission as it subsequently transitions to the ground state.[199] Similar to metal oxide or metal fluoride crystals, integration of an additional metal or metals into the lattice of a MOF can result in upconverted emission through ESA or ETU processes. In this section, on the examples of heterometallic MOFs exhibiting upconversion via ESA or ETU, the control of upconversion emission through the communication of emitting metal cations will be discussed.

In particular, the upconversion process on the example of trimetallic rare-earth-based frameworks containing Y^{3+}, Er^{3+}, and Yb^{3+} in the metal nodes, can be attributed to ETU.[200–202] In one report, Jin and colleagues reported upconversion via ETU in a trimetallic MOF ($(Y_{0.95}Er_{0.03}Yb_{0.02})_3(BDC)_{3.5}(OH)_2$) containing a combination of rare-earth metals.[200] Under 980-nm laser excitation, the MOF exhibited four distinct emission bands, including one red emission band centered at 654 nm, two green emission bands centered at 545 and 524 nm, and one indigo emission band centered at 455 nm. According to the proposed ETU mechanism, the 545 and 524 nm green emission bands were attributed to absorption of two

photons, while the 455 nm indigo emission band was ascribed to a three-photon process. In the follow-up report, $Y_{0.91}Er_{0.04}Yb_{0.05}(PZA)(OH)$ (H_2PZA = 2,3-pyrazinedicarboxylic acid) also exhibited upconverted emission via ETU.[201] This MOF showed two-photon upconversion emission bands at 520–550 nm and 650–660 nm, both of which were evident under 975-nm laser excitation. The same group also demonstrated that organic linkers could be used as a variable to tune emission via ETU in MOFs.[202] The effect of the linker was probed through differences in upconverted emission profiles of $Y_{0.91}Er_{0.04}Yb_{0.05}(PZA)(OH)$ and an OBA-based analog, $Y_{0.94}Er_{0.03}Yb_{0.03}(OBA)(OX)_{0.5}$ (H_2OBA = 4,4'-oxybis(benzoic acid); H_2OX = oxalic acid).[202] The OBA-based MOF exhibited upconversion emission bands corresponding to two-photon excitation centered at 653, 542, and 520 nm, as well as an emission band centered at 407 nm corresponding to three-photon excitation. On the other hand, the PZA-based MOF only exhibited upconversion emission bands corresponding to two-photon excitation, as described above. The absence of emission in the blue region in the emission profile of $Y_{0.91}Er_{0.04}Yb_{0.05}(PZA)(OH)$ in comparison with that of $Y_{0.94}Er_{0.03}Yb_{0.03}(OBA)(OX)_{0.5}$ was attributed to the presence of PZA^{2-} in the former.[202]

Recent studies by Ma and co-workers demonstrated that a bimetallic $Y_{1-X}Er_X(BTC)$ (H_3BTC = 1,3,5-benzenetricarboxylic acid) framework prepared by solvothermal synthesis exhibited upconversion via ESA.[203] Under 980-nm laser excitation, this MOF showed upconversion emission bands centered at 520, 540, and 651 nm. One key advantage for using MOFs for producing upconverted photons, in contrast to other rare-earth-doped materials,[199] is their inherent tunability and ease of varying the mole fraction of incorporated metals without significantly changing the overall geometry, as well as

multiple strategies to incorporate metals with acute synthetic control.[194,204] For instance, emission intensity was tuned as a function of Er^{3+} mole fraction in $Y_{1-X}Er_X(BTC)$, ranging from 2% to 100% of incorporated Er^{3+}.[203] The maximum quantum yield, 0.13%, was observed for the MOF with Er^{3+} mole fraction fixed at 6%. At higher mole fractions of Er^{3+}, a quenching effect arises from the excitation energy migrating among Er^{3+} cations, resulting in a decreased quantum yield. Furthermore, in order to distinguish between ETU and ESA upconversion mechanisms, Yb^{3+} (promoting ETU) was added to the MOF matrix and three trimetallic MOFs ($Y_{0.60}Yb_{0.30}Er_{0.10}(BTC)$, $Y_{0.30}Yb_{0.60}Er_{0.10}(BTC)$, and $Yb_{0.90}Er_{0.10}(BTC)$) were studied by monitoring changes in their emission profiles.[203] In these experiments, the mole fraction of Er^{3+} in the MOFs was fixed at 10%, while the mole fractions of Y^{3+} and Yb^{3+} varied. All prepared MOFs exhibited the same emission intensity regardless of the Yb^{3+} percentage. The results of those studies revealed that Y^{3+} and Yb^{3+} are not active centers responsible for the upconversion process, suggesting that the upconversion was governed by an ESA process where both photon absorption and upconversion take place within the same metal ion (Er^{3+}). The described experimental findings highlight MOFs as a versatile platform for promoting ETU or ESA tunability through precise mutual orientation of several metals incorporated within the same framework.

Upconversion via MPA and SHG. Some nonlinear optical (NLO) chromophores exhibit efficient upconversion via MPA or SHG. Unlike ETU or ESA, involving sequential absorption of two or more photons through a series of real excited states (Figure 1.6), upconversion via SHG and MPA in NLO materials involves a single elementary process (Figure 1.7). In SHG (a special case of sum frequency generation) two photons of the same

frequency are annihilated, generating a single scattered photon at twice the frequency. In MPA, the simultaneous absorption of two or more photons leads to population of a real excited state (Figure 1.7). Both processes require high instantaneous power densities that are typically accomplished with pulsed lasers. Integration of NLO chromophores in MOFs allows for the realization of a novel class of chromophore-directed light-controlling solid-state materials [205,206]. This section will focus on the effect of chromophore alignment in MOFs on fostering upconversion via MPA and SHG.

The brightness of a chromophore under MPA depends on its action cross-section: the product of the photoluminescence quantum yield (η) and the appropriate MPA absorption cross-section value, σ_n, where n = number of photons absorbed (i.e., σ_2 = a two-photon absorption cross-section or σ_3 = a three-photon absorption cross-section) [205]. While utilization of MPA of NLO chromophores have been realized thus far in solutions and doped solid matrices (e.g., epoxy and composite glass), MOFs have recently emerged as a novel NLO solid-state materials class.[205,207,208] As discussed earlier, MOFs can modulate η via the structure and local environment of a chromophore, and likewise, present an opportunity to fine-tune σ_n. Although nonlinear absorption is directly proportional to chromophore concentration, low concentrations of chromophores (0.01−0.10 M) are typically employed to prevent undesirable chromophore aggregation that could jeopardize chromophore quantum yield.[205] However, recent studies have demonstrated that organization of NLO chromophores through their integration into a MOF matrix can overcome concentration limitations as well as enhance the MPA action cross-section of chromophores.[4,72,209] For instance, in the case of a TPE-based MOF, $Zr_6O_4(OH)_4(TCPE)_3$, that exhibited MPA-based upconversion,[72] the two-photon action cross-section, $\eta\sigma_2$, of the

H_4TCPE linker was enhanced from 55 to 1035 Goeppert-Mayer units (GM = 10^{-50} cm^4 × s × $photon^{-1}$) upon integration in a rigid Zr-based MOF. The choice of metal can also affect the action cross-section. For instance, for the hafnium containing analog, $Hf_6O_4(OH)_4(TCPE)_3$, a drastic decrease of $\eta\sigma_2$ from 1035 GM determined for $Zr_6O_4(OH)_4(TCPE)_3$ to 292 GM was detected.[72]

Another factor that can enhance the MPA action cross-section is the spatial arrangement of chromophores within a MOF structure.[4,210,211] Fischer and co-workers reported a significant difference in the MPA action cross-section of two MOFs constructed from the same chromophore but with different concentrations on the example of Cd_2(TPBD) (tppd-Cd; H_4TPBD = tetrakis(1,1'-biphenyl-4-carboxylic acid)-1,4-benzenediamine) and Zn_2(TPBD) (tppd-Zn).[4] The authors hypothesized that the Cd-based MOF, possessing an interchromophore distance of 11.5 and 10.9 Å (center to center distance of the *p*-phenylenediamine cores), has a twenty-fold enhancement in MPA action cross-section[206,212] compared to the Zn-based MOF with an interchromophore distance of 10.0 and 15.1 Å, likely due to higher chromophore density (1.19 M for tppd-Cd and 1.00 M for tppd-Zn) in the former, and therefore, stronger excitonic interactions (Figure 1.7).

The effect of chromophore spatial arrangement in MOFs on the MPA action cross-section was further surveyed by investigating structurally similar Zn-MOFs.[210] In particular, $Zn_2(SDC)_2(An_2Py)$ and $Zn_2(BPDC)_2(An_2Py)$ (An_2Py = trans,trans-9,10-bis(4-pyridylethenyl) anthracene; H_2SDC = 4,4'-stilbenedicarboxylic acid) were prepared using the same chromophore, an anthracene-based linker, but with a different photoinactive linker, SDC^{2-} versus $BPDC^{2-}$. The lengths of the photoinactive linkers are 17.25 Å and 15.15 Å for SDC^{2-} and $BPDC^{2-}$, respectively. Employment of different-size linkers led to

different $\eta\sigma_2$ values of 0.96 GM ($Zn_2(BPDC)_2(An_2Py)$) and 1.95 GM ($Zn_2(SDC)_2(An_2Py)$), emphasizing the importance of spatial chromophore arrangement in modular scaffolds for facile optimization of MPA.

Proximity of NLO chromophores (linkers) to guest molecules with a high quantum yield can promote EnT between these moieties, leading to another approach for enhancement of the MPA action cross-section.[209] For instance, encapsulation of anthracene inside $Zn_2(SDC)_2(An_2Py)$ resulted in enhancement of the $\eta\sigma_2$ value by approximately one order-of-magnitude compared to the MOF itself. This enhancement is attributed to FRET occurring between the host MOF and the guest molecule.[209]

Unlike MPA, SHG combines two photons with the same frequency and coherently generates one photon with twice the frequency. This process is traditionally observed in crystals belonging to non-centrosymmetric space groups (e.g., KH_2PO_4, $LiNdO_3$, and α-quartz). Recently, several reports highlighted the possibility of utilizing non-centrosymmetric MOFs for production of upconverted photons via SHG, in particular, MOFs with diamondoid topologies.[63,73,213–218] For example, Vittal and co-workers showed that Zn- and Cu-based MOFs, $Zn(PVB)_2$ and $Cu(PVB)_2$ (HPVB = trans-2-(4-pyridyl)-4-vinylbenzoic acid), possessing a seven-fold interpenetrated diamondoid topology and belonging to the non-centrosymmetric space group, *Cc*, demonstrated SHG activity with effective second-order nonlinearity (d_{eff}) of 1.3 and 4.0 pm V^{-1}, respectively.[73] Interestingly, the non-DMF solvated form of the Zn-based MOF with an eight-fold interpenetrated diamondoid topology had an increased d_{eff} of 14.4 pm V^{-1}. This enhancement could be attributed to stronger π–π interactions between the individual diamondoid networks in the eight-fold interpenetrated diamondoid network. Enhanced

linker interactions and an increased oscillator strength of the linker resulted in an enhanced transition dipole moment magnitude of the chromophore in the eight-fold interpenetrated network.[73]

SHG-active MOFs could also be realized through incorporation of a chromophore with large hyperpolarizability as a guest inside the scaffold.[63] For instance, a pyridinium hemicyanine cationic chromophore, 4-(4-(diphenylamino)styryl)-1-dodecylpyridinium (DPASD) can be embedded into 1D channels of ZJU-28 ($(Me_2NH_2)_3[In_3(BTB)_4]$; H_3BTB = 4,4′,4″-benzene-1,3,5-triyl-tribenzoic acid)), and as a result, photon upconversion can be achieved. The observed SHG activity was attributed to restriction of chromophore rotation, twisting, and bending inside the channels of ZJU-28. This hypothesis was confirmed based on control experiments performed on guest-embedded frameworks possessing larger apertures in which no upconversion was detected.[63] Thus, precise chromophore organization in MOFs provides a fresh glance on MPA and SHG processes for their further utilization in multi-photon microscopy, laser technologies, and bioimaging.

SCAFFOLD-DIRECTED PHOTOCHROMIC PROPERTIES

Crystalline, hybrid architectures that undergo changes in their physical and chemical properties under exposure to external stimuli such as light, pressure, or pH create a myriad of technological opportunities. For example, photochromic molecules capable of switching between two discrete states upon light irradiation open an avenue for dynamic control over materials properties as a function of excitation wavelength. Studies of photochromic MOFs provide a starting point for consideration of their utilization as "smart" sensors, lenses, and optical materials.[219–223] A detailed description of photochromic scaffolds (Figure 1.8) can be found in a recent review.[57] This section will summarize recent

advances in the photochromic unit organization through their integration into a MOF scaffold. For instance, Gao and co-workers studied the photochromic properties of the extended viologen linker, 2,5-bis(pyridinium-4-yl)thiazolo[5,4-d]thiazole tetracarboxylic acid ($[H_4TTVTC]^{2+}$), through its incorporation in a Cd-based MOF, $[Cd_2(TTVTC)]Cl_2$.[65] Interestingly, the non-coordinated linker does not exhibit any photochromic properties, suggesting that the photoinduced electron transfer (PET), and consequently photochromism, arise from other factors, e.g., chromophore alignment, metal coordination, framework interpenetration, and molecular packing. In this case, the photochromic behavior is attributed to the MOFs interpenetrated structure affording an interframework donor-acceptor interaction. In particular, PET occurs between the carboxylate oxygen and the thiazolo[5,4-*d*]thiazole (TT)-core of the linker according to X-ray photoelectron spectroscopy analysis of the N(1s) and O(1s) peaks. As a continuation of this work, the same research team also designed a Zn-based MOF constructed from the $[TTVTC]^{2-}$ extended viologen linkers for sensing applications.[224] The two-dimensional MOF, Zn(TTVTC), was found to be highly fluorescent and stable in solvent and aqueous media, but was able to selectively detect Cr(VI) anions such as CrO_4^{2-} and $Cr_2O_7^{2-}$ in an aqueous solution. Sensing was attributed to a competing absorption mechanism of excitation light between MOF and analyte, thus dimming fluorescence. The selectivity of this MOF sensor for Cr(VI) anions in aqueous media was tested against other anions, such as ClO_4^-, NO_3^-, SO_4^{2-}, I^-, Br^-, Cl^-, F^-, and SCN^-. It was found that the quenching efficiencies were significantly lower ($\leq 3\%$) for several studied anions (e.g., ClO_4^-, NO_3^-, SO_4^{2-}, I^-, Br^-, Cl^-, F^-, and SCN^-) compared to the almost complete quenching effect in the presence of Cr(VI) anions (quenching efficiencies of $\geq 94\%$ at 1 mM of CrO_4^- in an aqueous solution).

A photochromic probe for detecting *N*-methyl-2-pyrrolidone (NMP) and DMF molecules was developed on the basis of a naphthalene diimide (NDI) containing-MOF ($ZnSiF_6(DPNDI)_2$) loaded with naphthalene guest molecules.[60] The electron-donating naphthalene guest molecules were immobilized in the pores through intermolecular interactions between the donor naphthalene guest and the electron-deficient scaffold acting as an acceptor. Soaking naphthalene@[$ZnSiF_6(DPNDI)_2$] in NMP, an electron-donating solvent, followed by UV-light irradiation, produced a drastic color change from yellow to brown. UV-irradiation resulted in the formation of a radical NDI species, according to electron spin resonance spectroscopic studies. In this case, the NDI-based backbone of the framework can accept electrons from the NMP molecules upon UV-irradiation without generating the charge transfer state between naphthalene guest molecules and DPNDI. Overall, unification of precise chromophore alignment with photochromic properties has only recently come to light, making photoswitchable chromophores one parameter for tuning optical behavior in MOF-based devices.

In addition to sensing capabilities, integration of a photochromic unit as a backbone linker (i.e., photoisomerization proceeds through the framework skeleton) or as a linker side group (i.e., photoisomerization occurs within the pores of the framework) in a MOF can modulate photoisomerization rates over several orders-of-magnitude as a function of MOF topology and rigidity.[225] Cycloreversion kinetics were studied on the examples of spiropyran- and diarylethene-containing Zn- and Zr-based MOFs.[225] For example, for spiropyran derivatives incorporated inside $Zn_2(DBTD)(TNDS)$ (H_4DBTD = 3',6'-dibromo-4',5'-bis(4-carboxyphenyl)-1[1,1':2',1'-tetraphenyl]-4,4'-dicarboxylic acid; TNDS = 1',3',3'-trimethyl-6-nitro-4',7'-di(pyridin-4-yl)spiro[chromene-2,2'-indoline]), the

cycloreversion rate was found to be 1.6×10^{-1} s^{-1} that is comparable to that of the non-coordinated linker, TNDS, in solution (1.2×10^{-1} s^{-1} (3 mM in DMF)). This tunability of photoisomerization rates was applied towards mapping changes of material properties.[225] For instance, photoresponsive linkers allowed for monitoring material degradation over time or under harsh conditions (e.g., exposure to vapors of hydrochloric acid). Integration of photochromic units into MOFs could also be applied as a tool for modifying ensemble electronic properties such as conductivity.[226] For example, the band gap of $Zn_2(BPDC)_2(BPMTC)$ (BPMTC = bis(5-pyridyl-2-methyl-3-thienyl)cyclopentane) was reduced from 1.87 eV to 1.73 eV upon UV-irradiation (365 nm), while its conductivity was enhanced.[226] Notably, both optical band gap and conductivity changes could also be reversed upon visible light (590 nm) irradiation.[226] Overall, changes in the absorption profile can be correlated with changes in conductivity as a function of an excitation wavelength. These examples illustrate the potential for aligned photochromic chromophores in a MOF matrix for evolving the technological and energy landscapes.

SUMMARY

Control of chromophore communication and alignment through utilization of a MOF matrix has only recently come to the forefront, and there is a plethora of knowledge to unearth. The modularity of the MOF platform enables unparalleled manipulation of chromophore alignment through tailoring geometries, distances, and modification of topology. As shown on the examples above, improvement in chromophore communication could lead to an enhancement of quantum yields in solid-state lighting devices, induction of fluorescence anisotropy, and improving of selectivity and detection limits of sensing devices. Therefore, this chapter strives to bridge the gap between tunable chromophore

structures and geometries (which can be achieved through recent advances in organic synthesis) and chromophore alignment (which can be altered through the topological versatility of the MOF platform). However, there are still major challenges that have to be overcome in chromophore-containing frameworks that hinder their practical application. In particular, mechanistic studies and theoretical reports on extended crystalline motifs predicting chromophore behavior in such complex assemblies are very limited despite the fact that they are imperative for gaining fundamental understanding necessary for tuning chromophore alignment and communication in MOFs. Another avenue that could be pursued is the further development of approaches for suppression of non-radiative decay pathways of a chromophore in scaffolds. This direction could be addressed from a theoretical point of view and confirmed spectroscopically through estimation of energy barriers for suppression of non-radiative relaxations such as low-energy vibrations, torsions, and rotations. Two more facets regarding the development of MOFs for lighting applications that also requires attention include prolonged photostability and mechanistic investigations of the photobleaching phenomenon. In particular, MOF photostability needs to be improved since organic chromophores often undergo photobleaching after extended periods of exposure to external stimuli.

From a synthetic perspective, a majority of existing reports on chromophore-based MOFs focuses on chromophores as symmetric dye molecules that can be functionalized with terminal carboxyl and pyridyl groups for MOF integration; however, reports on bulky asymmetric dye molecules are largely unexplored. From another vantage point, it could be fruitful to expand upon “conventional” chromophore-based MOFs that primarily utilize the properties of a single type of chromophore (e.g., photon upconversion, stimuli-responsive

technologies, or luminescence-based sensing), thus limiting their potential for advanced applications, by employing multiple types of chromophores in a common MOF motif. Therefore, there is an unfulfilled opportunity to develop a novel class of chromophore-based frameworks with unique properties by combining the properties of asymmetric dye molecules or multiple chromophores into MOFs for enhanced chromophore communication.

Chromophore-containing MOFs have shown great potential as solid-state photon upconversion materials; however, enhancement of their efficiency is still an avenue for careful examination. In particular, there is a lack of systematic studies on tuning the efficiency of the elementary steps of photon upconversion via *s*TTA. Through scrupulous framework design, that should include optimization of chromophore molecular conformation and alignment, significant enhancement of quantum yields could be achieved. Consideration of these steps could potentially result in a lower excitation power density for generation of detectable upconverted photons that would also make MOF-based materials more biocompatible. Investigations of MOF biocompatibility and cellular selectivity are imperative to achieve further advancements in biological imaging. To date, there are a very few reports on ESA and ETU in MOFs, leaving this area open for future investigations since all reports presented in this chapter are based on very few examples of rare earth-containing frameworks that could be considered as just the tip of the iceberg.

In terms of processability, several obstacles need to be addressed for the development of MOFs with increased compatibility toward device fabrication. Since MOFs are traditionally grown as single crystals or polycrystalline powders, thin films of chromophore-integrated MOFs should be prepared and tested. Growth of crystals of an

appreciable size with preferentially oriented chromophores for their use in non-linear optics or optoelectronics could also be a rewarding route to pursue. Although the ability to integrate a chromophore adorned MOF into a device is a difficult feat itself, a multidisciplinary approach toward materials development could drive progress forward.

Ultimately, there are numerous opportunities for improving chromophore communication in MOF matrices, promising a strategy to realize novel classes of solid-state materials that possess properties essential for development of light-managing applications, such as solid-state lighting phosphors, anisotropic laser components, bioimaging media, solar cell components, optoelectronic devices, or chemical sensors. The continued exploration of aligned chromophores in MOFs must be pursued in order to place MOFs at the pinnacle of the rapidly expanding technological materials landscape.

REFERENCES

[1] Goswami, S.; Miller, C. E.; Logsdon, J. L.; Buru, C. T.; Wu, Y.-L.; Bowman, D. N.; Islamoglu, T.; Asiri, A. M.; Cramer, C. J.; Wasielewski, M. R. et al. *ACS Appl. Mater. Interfaces* **2017**, *9*, 19535–19540.

[2] Goswami, S.; Chen, M.; Wasielewski, M. R.; Farha, O. K.; Hupp, J. T. *ACS Appl. Mater. Interfaces* **2018**, *10*, 34409–34417.

[3] Champsaur, A. M.; Yu, J.; Roy, X.; Paley, D. W.; Steigerwald, M. L.; Nuckolls, C.; Bejger, C. M. *ACS Cent. Sci.* **2017**, *3*, 1050–1055.

[4] Mayer, D. C.; Manzi, A.; Medishetty, R.; Winkler, B.; Schneider, C.; Kieslich, G.; Pöthig, A.; Feldmann, J.; Fischer, R. A. *J. Am. Chem. Soc.* **2019**, *141*, 11594–11602.

[5] Qiao, X.-Q.; Zhang, Z.-W.; Li, Q.-H.; Hou, D.; Zhang, Q.; Zhang, J.; Li, D.-S.; Feng, P.; Bu, X. *J. Mater. Chem. A* **2018**, *6*, 22580–22589.

[6] Park, H. J.; So, M. C.; Gosztola, D.; Wiederrecht, G. P.; Emery, J. D.; Martinson, A. B. F.; Er, S.; Wilmer, C. E.; Vermeulen, N. A.; Aspuru-Guzik, A. et al. *ACS Appl. Mater. Interfaces* **2016**, *8*, 24983–24988.

[7] Rudd, N. D.; Liu, Y.; Tan, K.; Chen, F.; Chabal, Y. J.; Li, J. *ACS Sustain. Chem.*

Eng. **2019**, *7*, 6561–6568.

[8] Chen, X.; Bu, X.; Lin, Q.; Mao, C.; Zhai, Q.-G.; Wang, Y.; Feng, P. *Chem. Eur. J.* **2017**, *23*, 11913–11919.

[9] Zhang, Y.; Yuan, S.; Day, G.; Wang, X.; Yang, X.; Zhou, H.-C. *Coord. Chem. Rev.* **2018**, *354*, 28–45.

[10] Marin, D. M.; Payerpaj, S.; Collier, G. S.; Ortiz, A. L.; Singh, G.; Jones, M.; Walter, M. G. *Phys. Chem. Chem. Phys.* **2015**, *17*, 29090–29096.

[11] Medishetty, R.; Nalla, V.; Nemec, L.; Henke, S.; Mayer, D.; Sun, H.; Reuter, K.; Fischer, R. A. *Adv. Mater.* **2017**, *29*, 1605637.

[12] Nocera, D. G. *Acc. Chem. Res.* **2012**, *45*, 767–776.

[13] Lustig, W. P.; Shen, Z.; Teat, S. J.; Javed, N.; Velasco, E.; O'Carroll, D. M.; Li, J. *Chem. Sci.* **2020**, *11*, 1814–1824.

[14] Gust, D.; Moore, T. A.; Moore, A. L. *Acc. Chem. Res.* **2009**, *42*, 1890–1898.

[15] Imahori, H.; Mori, Y.; Matano, Y. *J. Photochem. Photobiol. C Photochem. Rev.* **2003**, *4*, 51–83.

[16] Alstrum-Acevedo, J. H.; Brennaman, M. K.; Meyer, T. J. *Inorg. Chem.* **2005**, *44*, 6802–6827.

[17] Berardi, S.; Drouet, S.; Francàs, L.; Gimbert-Suriñach, C.; Guttentag, M.; Richmond, C.; Stoll, T.; Llobet, A. *Chem. Soc. Rev.* **2014**, *43*, 7501–7519.

[18] Tachibana, Y.; Vayssieres, L.; Durrant, J. R. *Nat. Photonics* **2012**, *6*, 511–518.

[19] Kärkäs, M. D.; Verho, O.; Johnston, E. V.; Åkermark, B*Chem. Rev.* **2014**, *114*, 11863–12001.

[20] Liu, C.; Colón, B. C.; Ziesack, M.; Silver, P. A.; Nocera, D. G. *Science* **2016**, *352*, 1210–1213.

[21] Whang, D. R.; Apaydin, D. H. *ChemPhotoChem* **2018**, *2*, 148–160.

[22] Xu, H.-Q.; Yang, S.; Ma, X.; Huang, J.; Jiang, H.-L. *ACS Catal.* **2018**, *8*, 11615–11621.

[23] Zhou, Y.; Hu, W.; Yang, S.; Huang, J. *Phys. Chem. Chem. Phys.* **2020**, *22*, 3849–

3854.

[24] Jiao, W.; Zhu, J.; Ling, Y.; Deng, M.; Zhou, Y.; Feng, P. *Nanoscale* **2018**, *10*, 20339–20346.

[25] Liu, X.-Y.; Zhang, F.; Goh, T.-W.; Li, Y.; Shao, Y.-C.; Luo, L.; Huang, W.; Long, Y.-T.; Chou, L.-Y.; Tsung, C.-K. *Angew. Chem. Int. Ed.* **2018**, *57*, 2110–2114.

[26] Shao, B.; Aprahamian, I. *ChemPhotoChem* **2019**, *3*, 361–364.

[27] Gerkman, M. A.; Gibson, R. S. L.; Calbo, J.; Shi, Y.; Fuchter, M. J.; Han, G. G. D. *J. Am. Chem. Soc.* **2020**, *142*, 8688–8695.

[28] Zhang, Y.; Pang, J.; Li, J.; Yang, X.; Feng, M.; Cai, P.; Zhou, H.-C. *Chem. Sci.* **2019**, *10*, 8455–8460.

[29] Baudron, S. A. *CrystEngComm* **2016**, *18*, 4671–4680.

[30] Khatun, A.; Panda, D. K.; Sayresmith, N.; Walter, M. G.; Saha, S. *Inorg. Chem.* **2019**, *58*, 12707–12715.

[31] Kim, Y.; Lee, J. H.; Ha, H.; Im, S. W.; Nam, K. T. *Nano Converg.* **2016**, *3*, 19.

[32] Heidary, N.; Harris, T. G. A. A.; Ly, K. H.; Kornienko, N. *Physiol. Plant.* **2019**, *166*, 460–471.

[33] Nguyen, A. I.; Van Allsburg, K. M.; Terban, M. W.; Bajdich, M.; Oktawiec, J.; Amtawong, J.; Ziegler, M. S.; Dombrowski, J. P.; Lakshmi, K. V.; Drisdell, W. S. et al. *Proc. Natl. Acad. Sci.* **2019**, *116*, 11630–11639.

[34] Paille, G.; Gomez-Mingot, M.; Roch-Marchal, C.; Lassalle-Kaiser, B.; Mialane, P.; Fontecave, M.; Mellot-Draznieks, C.; Dolbecq, A. *J. Am. Chem. Soc.* **2018**, *140*, 3613–3618.

[35] Luo, Y.-C.; Chu, K.-L.; Shi, J.-Y.; Wu, D.-J.; Wang, X.-D.; Mayor, M.; Su, C.-Y. *J. Am. Chem. Soc.* **2019**, *141*, 13057–13065.

[36] Zhang, S.; Wang, S.; Guo, L.; Chen, H.; Tan, B.; Jin, S. *J. Mater. Chem. C* **2020**, *8*, 192–200.

[37] Lustig, W. P.; Wang, F.; Teat, S. J.; Hu, Z.; Gong, Q.; Li, J. *Inorg. Chem.* **2016**, *55*, 7250–7256.

[38] Zhu, J.; Maza, W. A.; Morris, A. J. *J. Photochem. Photobiol. A Chem.* **2017**, *344*,

64–77.

[39] Wang, Q.; Gao, Q.; Al-Enizi, A. M.; Nafady, A.; Ma, S. *Inorg. Chem. Front.* **2020**, *7*, 300–339.

[40] Li, Y.; Pang, A.; Wang, C.; Wei, M. *J. Mater. Chem.* **2011**, *21*, 17259–17264.

[41] Lee, C. Y.; Farha, O. K.; Hong, B. J.; Sarjeant, A. A.; Nguyen, S. T.; Hupp, J. T. *J. Am. Chem. Soc.* **2011**, *133*, 15858–15861.

[42] So, M. C.; Wiederrecht, G. P.; Mondloch, J. E.; Hupp, J. T.; Farha, O. K. *Chem. Commun.* **2015**, *51*, 3501–3510.

[43] Williams, D. E.; Rietman, J. A.; Maier, J. M.; Tan, R.; Greytak, A. B.; Smith, M. D.; Krause, J. A.; Shustova, N. B. *J. Am. Chem. Soc.* **2014**, *136*, 11886–11889.

[44] Goswami, S.; Ma, L.; Martinson, A. B. F.; Wasielewski, M. R.; Farha, O. K.; Hupp, J. T. *ACS Appl. Mater. Interfaces* **2016**, *8*, 30863–30870.

[45] Cho, J.; Park, J. H.; Kim, J. K.; Schubert, E. F. *Laser Photon. Rev.* **2017**, *11*, 1600147.

[46] Williams, D. E.; Shustova, N. B. *Chem. Eur. J.* **2015**, *21*, 15474–15479.

[47] Wilbraham, L.; Coudert, F. X.; Ciofini, I. *Phys. Chem. Chem. Phys.* **2016**, *18*, 25176–25182.

[48] Xu, L.-J.; Xu, G.-T.; Chen, Z.-N. *Coord. Chem. Rev.* **2014**, *273–274*, 47–62.

[49] Sikdar, N.; Jayaramulu, K.; Kiran, V.; Rao, K. V.; Sampath, S.; George, S. J.; Maji, T. K. *Chem. Eur. J.* **2015**, *21*, 11701–11706.

[50] Dolgopolova, E. A.; Williams, D. E.; Greytak, A. B.; Rice, A. M.; Smith, M. D.; Krause, J. A.; Shustova, N. B. *Angew. Chem. Int. Ed.* **2015**, *54*, 13639–13643.

[51] Son, H. J.; Jin, S.; Patwardhan, S.; Wezenberg, S. J.; Jeong, N. C.; So, M.; Wilmer, C. E.; Sarjeant, A. A.; Schatz, G. C.; Snurr, R. Q. et al. *J. Am. Chem. Soc.* **2013**, *135*, 862–869.

[52] Yang, N.-N.; Fang, J.-J.; Sui, Q.; Gao, E.-Q. *ACS Appl. Mater. Interfaces* **2018**, *10*, 2735–2744.

[53] Jones, C. L.; Tansell, A. J.; Easun, T. L. *J. Mater. Chem. A* **2016**, *4*, 6714–6723.

[54] Dolgopolova, E. A.; Rice, A. M.; Martin, C. R.; Shustova, N. B. *Chem. Soc. Rev.* **2018**, *47*, 4710–4728.

[55] Yanai, N.; Kimizuka, N. *Chem. Commun.* **2016**, *52*, 5354–5370.

[56] Dhakshinamoorthy, A.; Asiri, A. M.; García, H. *Angew. Chem. Int. Ed.* **2016**, *55*, 5414–5445.

[57] Rice, A. M.; Martin, C. R.; Galitskiy, V. A.; Berseneva, A. A.; Leith, G. A.; Shustova, N. B. *Chem. Rev.*, **2020**, *120*, 8790–8813.

[58] Shustova, N. B.; McCarthy, B. D.; Dincă, M. *J. Am. Chem. Soc.* **2011**, *133*, 20126–20129.

[59] Williams, D. E.; Dolgopolova, E. A.; Pellechia, P. J.; Palukoshka, A.; Wilson, T. J.; Tan, R.; Maier, J. M.; Greytak, A. B.; Smith, M. D.; Krause, J. A. et al. *J. Am. Chem. Soc.* **2015**, *137*, 2223–2226.

[60] Liu, J.-J.; Shan, Y.-B; Fan, C.-R.; Lin, M.-J.; Huang, C.-C.; Dai, W.-X. *Inorg. Chem.* **2016**, *55*, 3680–3684.

[61] Yan, D.; Tang, Y.; Lin, H.; Wang, D. *Sci. Rep.* **2015**, *4*, 4337.

[62] Shustova, N. B.; Cozzolino, A. F.; Reineke, S.; Baldo, M.; Dincă, M. *J. Am. Chem. Soc.* **2013**, *135*, 13326–13329.

[63] Yu, J.; Cui, Y.; Wu, C.; Yang, Y.; Wang, Z.; O'Keeffe, M.; Chen, B.; Qian, G. *Angew. Chem. Int. Ed.* **2012**, *51*, 10542–10545.

[64] Jiao, J.; Kang, J.-X.; Ma, Y.; Zhao, Q.; Li, H.; Zhang, J.; Chen, X. *Front. Chem.* **2019**, *7*, 768.

[65] Li, P.; Guo, M.-Y.; Yin, X.-M.; Gao, L.-L.; Yang, S.-L.; Bu, R.; Gong, T.; Gao, E.-Q. *Inorg. Chem.* **2019**, *58*, 14167–14174.

[66] Takashima, Y.; Martínez, V. M.; Furukawa, S.; Kondo, M.; Shimomura, S.; Uehara, H.; Nakahama, M.; Sugimoto, K.; Kitagawa, S. *Nat. Commun.* **2011**, *2*, 168.

[67] Dolgopolova, E. A.; Moore, T. M.; Fellows, W. B.; Smith, M. D.; Shustova, N. B. *Dalt. Trans.* **2016**, *45*, 9884–9891.

[68] Pan, M.; Zhu, Y.-X.; Wu, K.; Chen, L.; Hou, Y.-J.; Yin, S.-Y.; Wang, H.-P.; Fan, Y.-N.; Su, C.-Y. *Angew. Chem. Int. Ed.* **2017**, *56*, 14582–14586.

[69] Mahato, P.; Monguzzi, A.; Yanai, N.; Yamada, T.; Kimizuka, N. *Nat. Mater.* **2015**, *14*, 924–930.

[70] Meinardi, F.; Ballabio, M.; Yanai, N.; Kimizuka, N.; Bianchi, A.; Mauri, M.; Simonutti, R.; Ronchi, A.; Campione, M.; Monguzzi, A. *Nano Lett.* **2019**, *19*, 2169–2177.

[71] Park, J.; Xu, M.; Li, F.; Zhou, H.-C. *J. Am. Chem. Soc.* **2018**, *140*, 5493–5499.

[72] Medishetty, R.; Nemec, L.; Nalla, V.; Henke, S.; Samoć, M.; Reuter, K.; Fischer, R. A. *Angew. Chem. Int. Ed.* **2017**, *56*, 14743–14748.

[73] Chen, Z.; Gallo, G.; Sawant, V. A.; Zhang, T.; Zhu, M.; Liang, L.; Chanthapally, A.; Bolla, G.; Quah, H. S.; Liu, X. et al. *Angew. Chem. Int. Ed.* **2020**, *59*, 833–838.

[74] Wang, M.-L.; Fu, C.; Li, L.; Zhang, H. *Inorg. Chem. Commun.* **2018**, *94*, 142–145.

[75] Kreno, L. E.; Leong, K.; Farha, O. K.; Allendorf, M.; Van Duyne, R. P.; Hupp, J. T. *Chem. Rev.* **2012**, *112*, 1105–1125.

[76] Peng, Q.; Niu, Y.; Deng, C.; Shuai, Z. *Chem. Phys.* **2010**, *370*, 215–222.

[77] Shustova, N. B.; Ong, T.-C.; Cozzolino, A. F.; Michaelis, V. K.; Griffin, R. G.; Dincă, M. *J. Am. Chem. Soc.* **2012**, *134*, 15061–15070.

[78] Yang, C.; Chen, K.; Chen, M.; Hu, X.; Huan, S. Y.; Chen, L.; Song, G.; Zhang, X. B. *Anal. Chem.* **2019**, *91*, 2727–2733.

[79] Wang, Z.; Wang, Z.; Lin, B.; Hu, X.; Wei, Y.; Zhang, C.; An, B.; Wang, C.; Lin, W. *ACS Appl. Mater. Interfaces* **2017**, *9*, 35253–35259.

[80] Liu, J.; Zhou, W.; Liu, J.; Fujimori, Y.; Higashino, T.; Imahori, H.; Jiang, X.; Zhao, J.; Sakurai, T.; Hattori, Y. et al. *J. Mater. Chem. A* **2016**, *4*, 12739–12747.

[81] Wang, F.; Liu, W.; Teat, S. J.; Xu, F.; Wang, H.; Wang, X.; An, L.; Li, J. *Chem. Commun.* **2016**, *52*, 10249–10252.

[82] Cui, Y.; Yue, Y.; Qian, G.; Chen, B. *Chem. Rev.* **2012**, *112*, 1126–1162.

[83] Haldar, R.; Mazel, A.; Krstić, M.; Zhang, Q.; Jakoby, M.; Howard, I. A.; Richards, B. S.; Jung, N.; Jacquemin, D.; Diring, S. et al. *Nat. Commun.* **2019**, *10*, 2048.

[84] Fakis, M.; Anestopoulos, D.; Giannetas, V.; Persephonis, P. *J. Phys. Chem. B* **2006**, *110*, 24897–24902.

[85] Amrutha, S. R.; Jayakannan, M. *J. Phys. Chem. B* **2008**, *112*, 1119–1129.

[86] Ma, X.; Sun, R.; Cheng, J.; Liu, J.; Gou, F.; Xiang, H.; Zhou, X. *J. Chem. Educ.* **2016**, *93*, 345–350.

[87] Yuan, W. Z.; Lu, P.; Chen, S.; Lam, J. W. Y.; Wang, Z.; Liu, Y.; Kwok, H. S.; Ma, Y.; Tang, B. Z. *Adv. Mater.* **2010**, *22*, 2159–2163.

[88] Huang, M.; Yu, R.; Xu, K.; Ye, S.; Kuang, S.; Zhu, X.; Wan, Y. *Chem. Sci.* **2016**, *7*, 4485–4491.

[89] Li, Z.; Qin, A. *Natl. Sci. Rev.* **2014**, *1*, 22–24.

[90] Huang, Y.; Xing, J.; Gong, Q.; Chen, L.-C.; Liu, G.; Yao, C.; Wang, Z.; Zhang, H.-L.; Chen, Z.; Zhang, Q. *Nat. Commun.* **2019**, *10*, 169.

[91] Mei, J.; Leung, N. L. C.; Kwok, R. T. K.; Lam, J. W. Y.; Tang, B. Z. *Chem. Rev.* **2015**, *115*, 11718–11940.

[92] Yamada, H.; Xu, C.; Fukazawa, A.; Wakamiya, A.; Yamaguchi, S. *Macromol. Chem. Phys.* **2009**, *210*, 904–916.

[93] Wang, C.; Li, Z. *Mater. Chem. Front.* **2017**, *1*, 2174–2194.

[94] Yamaguchi, M.; Ito, S.; Hirose, A.; Tanaka, K.; Chujo, Y. *Mater. Chem. Front.* **2017**, *1*, 1573–1579.

[95] Luo, J.; Xie, Z.; Xie, Z.; Lam, J. W. Y.; Cheng, L.; Chen, H.; Qiu, C.; Kwok, H. S.; Zhan, X.; Liu, Y. et al. *Chem. Commun.* **2001**, *18*, 1740–1741.

[96] Gao, M.; Tang, B. Z. *ACS Sensors* **2017**, *2*, 1382–1399.

[97] Hong, Y.; Lam, J. W. Y.; Tang, B. Z. *Chem. Soc. Rev.* **2011**, *40*, 5361–5388.

[98] Zhao, Z.; Zhang, H.; Lam, J. W. Y.; Tang, B. Z. *Angew. Chem. Int. Ed.* **2020**, *59*, 9888-9907.

[99] Chen, Y.; Lam, J. W. Y.; Kwok, R. T. K.; Liu, B.; Tang, B. Z. *Mater. Horiz.* **2019**, *6*, 428–433.

[100] Wang, H.; Zhao, E.; Lam, J. W. Y.; Tang, B. Z. *Mater. Today* **2015**, *18*, 365–377.

[101] Ding, D.; Li, K.; Liu, B.; Tang, B. Z. *Acc. Chem. Res.* **2013**, *46*, 2441–2453.

[102] Schrimpf, W.; Jiang, J.; Ji, Z.; Hirschle, P.; Lamb, D. C.; Yaghi, O. M.; Wuttke, S.

Nat. Commun. **2018**, *9*, 1647.

[103] Zhang, N.; Zhang, D.; Zhao, J.; Xia, Z. *Dalt. Trans.* **2019**, *48*, 6794–6799.

[104] Ryu, U.; Yoo, J.; Kwon, W.; Choi, K. M. *Inorg. Chem.* **2017**, *56*, 12859–12865.

[105] Maity, K.; Mukherjee, D.; Sen, M.; Biradha, K. *ACS Appl. Nano Mater.* **2019**, *2*, 1614–1620.

[106] Tehrani, M. S.; Zare-Dorabei, R. *RSC Adv.* **2016**, *6*, 27416–27425.

[107] Hassanzadeh, J.; Al Lawati, H. A. J.; Al Lawati, I. *Anal. Chem.* **2019**, *91*, 10631–10639.

[108] Rowe, J. M.; Soderstrom, E. M.; Zhu, J.; Usov, P. M.; Morris, A. J. *Can. J. Chem.* **2018**, *96*, 875–880.

[109] Wu, X.-H.; Luo, P.; Wei, Z.; Li, Y.-Y.; Huang, R.-W.; Dong, X.-Y.; Li, K.; Zang, S.-Q.; Tang, B. Z. *Adv. Sci.* **2019**, *6*, 1801304.

[110] Wei, Z.; Gu, Z.-Y.; Arvapally, R. K.; Chen, Y.-P.; McDougald, R. N.; Ivy, J. F.; Yakovenko, A. A.; Feng, D.; Omary, M. A.; Zhou, H.-C. *J. Am. Chem. Soc.* **2014**, *136*, 8269–8276.

[111] Yu, L.; Chen, H.; Yue, J.; Chen, X.; Sun, M.; Tan, H.; Asiri, A. M.; Alamry, K. A.; Wang, X.; Wang, S. *Anal. Chem.* **2019**, *91*, 5913–5921.

[112] Rouhani, F.; Morsali, A.; Retailleau, P. *ACS Appl. Mater. Interfaces* **2018**, *10*, 36259–36266.

[113] Wang, A.; Fan, R.; Wang, P.; Fang, R.; Hao, S.; Zhou, X.; Zheng, X.; Yang, Y. *Inorg. Chem.* **2017**, *56*, 12881–12892.

[114] Du, T.; Jiang, H.; Wang, X. *Inorg. Chem. Commun.* **2019**, *107*, 107452.

[115] Zhang, M.; Feng, G.; Song, Z.; Zhou, Y.-P.; Chao, H.-Y.; Yuan, D.; Tan, T. T. Y.; Guo, Z.; Hu, Z.; Tang, B. Z. et al. *J. Am. Chem. Soc.* **2014**, *136*, 7241–7244.

[116] Choi, S.; Lee, H.-E.; Ryu, C. H.; Lee, J.; Lee, J.; Yoon, M.; Kim, Y.; Park, M. H.; Lee, K. M.; Kim, M. *Chem. Commun.* **2019**, *55*, 11844–11847.

[117] Wang, F.-M.; Zhou, L.; Lustig, W. P.; Hu, Z.; Li, J.-F.; Hu, B.-X.; Chen, L.-Z.; Li, J. *Cryst. Growth Des.* **2018**, *18*, 5166–5173.

[118] Hu, Z.; Huang, G.; Lustig, W. P.; Wang, F.; Wang, H.; Teat, S. J.; Banerjee, D.; Zhang, D.; Li, J. *Chem. Commun.* **2015**, *51*, 3045–3048.

[119] Xiong, J.; Qian, X.; Zhao, L.; Xu, J. *Inorg. Chem. Commun.* **2019**, *105*, 20–25.

[120] Yin, H.-Q.; Wang, X.-Y.; Yin, X.-B. *J. Am. Chem. Soc.* **2019**, *141*, 15166–15173.

[121] Cai, Y.; Du, L.; Samedov, K.; Gu, X.; Qi, F.; Sung, H. H. Y.; Patrick, B. O.; Yan, Z.; Jiang, X.; Zhang, H. et al. *Chem. Sci.* **2018**, *9*, 4662–4670.

[122] Baysec, S.; Preis, E.; Allard, S.; Scherf, U. *Macromol. Rapid Commun.* **2016**, *37*, 1802–1806.

[123] Iasilli, G.; Battisti, A.; Tantussi, F.; Fuso, F.; Allegrini, M.; Ruggeri, G.; Pucci, A. *Macromol. Chem. Phys.* **2014**, *215*, 499–506.

[124] Dong, W.; Ma, Z.; Chen, P.; Duan, Q. *Mater. Lett.* **2019**, *236*, 480–482.

[125] Xu, K.; Yu, B.; Li, Y.; Su, H.; Wang, B.; Sun, K.; Liu, Y.; Peng, Q.; Hou, H.; Li, K. *Chem. Commun.* **2018**, *54*, 12942–12945.

[126] Wu, X.-X.; Fu, H.-R.; Han, M.-L.; Zhou, Z.; Ma, L.-F. *Cryst. Growth Des.* **2017**, *17*, 6041–6048.

[127] Ma, L.; Feng, X.; Wang, S.; Wang, B. *Mater. Chem. Front.* **2017**, *1*, 2474–2486.

[128] Liu, X.-Y.; Li, Y.; Tsung, C.-K.; Li, J. *Chem. Commun.* **2019**, *55*, 10669–10672.

[129] Xing, G.; Feng, Y.; Gao, Z.; Tao, M.; Wang, H.; Wei, Y.; Molokeev, M. S.; Li, G. *CrystEngComm* **2019**, *21*, 3605–3612.

[130] Fu, Y.; Wang, X.; Peng, M. *J. Mater. Chem. C* **2020**, *8*, 6079–6085.

[131] Li, G.; Tian, Y.; Zhao, Y.; Lin, J. *Chem. Soc. Rev.* **2015**, *44*, 8688–8713.

[132] Yu, L.; Wang, H.; Liu, W.; Teat, S. J.; Li, J. *Cryst. Growth Des.* **2019**, *19*, 6850–6854.

[133] Shen, C.; Zhong, C.; Ming, J. *J. Exp. Nanosci.* **2013**, *8*, 54–60.

[134] Zhao, Y.; Xu, H.; Zhang, X.; Zhu, G.; Yan, D.; Yu, *J. Eur. Ceram. Soc.* **2015**, *35*, 3761–3764.

[135] Dolgopolova, E. A.; Rice, A. M.; Smith, M. D.; Shustova, N. B. *Inorg. Chem.* **2016**, *55*, 7257–7264.

[136] Follenius-Wund, A.; Bourotte, M.; Schmitt, M.; Iyice, F.; Lami, H.; Bourguignon, J.-J.; Haiech, J.; Pigault, C. *Biophys. J.* **2003**, *85*, 1839–1850.

[137] Dolgopolova, E. A.; Moore, T. M.; Ejegbavwo, O. A.; Pellechia, P. J.; Smith, M. D.; Shustova, N. B. *Chem. Commun.* **2017**, *53*, 7361–7364.

[138] Meech, S. R. *Chem. Soc. Rev.* **2009**, *38*, 2922–2934.

[139] Jancsó, A.; Kovács, E.; Cseri, L.; Rózsa, B. J.; Galbács, G.; Csizmadia, I. G.; Mucsi, Z. *Spectrochim. Acta. A. Mol. Biomol. Spectrosc.* **2019**, *218*, 161–170.

[140] Petkova, I.; Dobrikov, G.; Banerji, N.; Duvanel, G.; Perez, R.; Dimitrov, V.; Nikolov, P.; Vauthey, E. *J. Phys. Chem. A* **2010**, *114*, 10–20.

[141] Gutiérrez, S.; Martínez-López, D.; Morón, M.; Sucunza, D.; Sampedro, D.; Domingo, A.; Salgado, A.; Vaquero, J. J. *Chem. Eur. J.* **2015**, *21*, 18758–18763.

[142] Conyard, J.; Heisler, I. A.; Chan, Y.; Bulman Page, P. C.; Meech, S. R.; Blancafort, L. *Chem. Sci.* **2018**, *9*, 1803–1812.

[143] Bourotte, M.; Schmitt, M.; Follenius-Wund, A.; Pigault, C.; Haiech, J.; Bourguignon, J.-J. *Tetrahedron Lett.* **2004**, *45*, 6343–6348.

[144] Niwa, H.; Inouye, S.; Hirano, T.; Matsuno, T.; Kojima, S.; Kubota, M.; Ohashi, M.; Tsuji, F. I. *Proc. Natl. Acad. Sci.* **1996**, *93*, 13617–13622.

[145] Nielsen, M. B.; Andersen, L. H.; Rocha-Rinza, T. *Monatsh. Chem.* **2011**, *142*, 709–715.

[146] Dolgopolova, E. A.; Berseneva, A. A.; Faillace, M. S.; Ejegbavwo, O. A.; Leith, G. A.; Choi, S. W.; Gregory, H. N.; Rice, A. M.; Smith, M. D.; Chruszcz, M. et al. *J. Am. Chem. Soc.* **2020**, *142*, 4769–4783.

[147] McCapra, F.; Razavi, Z.; Neary, A. P. *J. Chem. Soc. Chem. Commun.* **1988**, 790–791.

[148] Wanderley, M. M.; Wang, C.; Wu, C.-D.; Lin, W. *J. Am. Chem. Soc.* **2012**, *134*, 9050–9053.

[149] Lustig, W. P.; Teat, S. J.; Li, J. *J. Mater. Chem. C* **2019**, *7*, 14739–14744.

[150] Pan, M.; Liao, W.-M.; Yin, S.-Y.; Sun, S.-S.; Su, C.-Y. *Chem. Rev.* **2018**, *118*, 8889–8935.

[151] Sun, C.-Y.; Wang, X.-L.; Zhang, X.; Qin, C.; Li, P.; Su, Z.-M.; Zhu, D.-X.; Shan, G.-G.; Shao, K.-Z.; Wu, H. et al. *Nat. Commun.* **2013**, *4*, 2717.

[152] Huh, S.; Kim, S.-J.; Kim, Y. *CrystEngComm* **2016**, *18*, 345–368.

[153] Hao, Y.; Chen, S.; Zhou, Y.; Zhang, Y.; Xu, M. *Nanomaterials* **2019**, *9*, 974.

[154] Liu, Y.; Dong, H.; Wang, K.; Gao, Z.; Zhang, C.; Liu, X.; Zhao, Y.S.; Hu, F. *ACS Appl. Mater. Interfaces* **2018**, *10*, 35455–35461.

[155] Wang, Z.; Zhu, C.-Y.; Mo, J.-T.; Fu, P.-Y.; Zhao, Y.-W.; Yin, S.-Y.; Jiang, J.-J.; Pan, M.; Su, C.-Y. *Angew. Chem. Int. Ed.* **2019**, *58*, 9752-9757.

[156] Chen, Y.; Yu, B.; Cui, Y.; Xu, S.; Gong, J. *Chem. Mater.* **2019**, *31*, 1289–1295.

[157] Nie, H.; Hu, K.; Cai, Y.; Peng, Q.; Zhao, Z.; Hu, R.; Chen, J.; Su, S.-J.; Qin, A.; Tang, B. Z. *Mater. Chem. Front.* **2017**, *1*, 1125–1129.

[158] Liu, X.-Y.; Xing, K.; Li, Y.; Tsung, C.-K.; Li, J. *J. Am. Chem. Soc.* **2019**, *141*, 14807–14813.

[159] Ji, G.; Wang, J.; Gao, X.; Liu, J.; Guan, W.; Liu, H.; Liu, Z. *Eur. J. Inorg. Chem.* **2018**, *2018*, 1998–2003.

[160] Hu, X.-L.; Qin, C.; Wang, X.-L.; Shao, K.-Z.; Su, Z.-M. *Chem. Commun.* **2015**, *51*, 17521–17524.

[161] Xia, T.; Cui, Y.; Yang, Y.; Qian, G. *ChemNanoMat* **2017**, *3*, 51–57.

[162] Jameson, D. M.; Ross, J. A. *Chem. Rev.* **2010**, *110*, 2685–2708.

[163] Gijsbers, A.; Nishigaki, T.; Sánchez-Puig, N. *J. Vis. Exp.* **2016**, *116*, 54640.

[164] Swonger, K. N.; Robinson, A. S. *Curr. Protoc. Protein Sci.* **2018**, *93*, e63.

[165] Clayton, A. H. A.; Hanley, Q. S.; Arndt-Jovin, D. J.; Subramaniam, V.; Jovin, T. M. *Biophys. J.* **2002**, *83*, 1631–1649.

[166] Vinegoni, C.; Dubach, J. M.; Feruglio, P. F.; Weissleder, R. *IEEE J. Sel. Top. Quantum Electron.* **2016**, *22*, 6801607.

[167] Chen, J.; Liu, J.; Chen, X.; Qiu, H. *Chin. Chem. Lett.* **2019**, *30*, 1575–1580.

[168] Bur, A. J.; Roth, S. C.; Thomas, C. L. *Rev. Sci. Instrum.* **2000**, *71*, 1516–1523.

[169] Wang, H.; Vagin, S. I.; Lane, S.; Lin, W.; Shyta, V.; Heinz, W. R.; Dyck, C. V.; Bergren, A. J.; Gardner, K.; Rieger, B. et al. *Chem. Mater.* **2019**, *31*, 5816–5823.

[170] He, H.; Ma, E.; Cui, Y.; Yu, J.; Yang, Y.; Song, T.; Wu, C.-D.; Chen, X.; Chen, B.; Qian, G. *Nat. Commun.* **2016**, *7*, 11087.

[171] Guo, J. F.; Li, C. M.; Hu, X. L.; Huang, C. Z.; Li, Y. F. *RSC Adv.* **2014**, *4*, 9379–9382.

[172] Yan, D.; Gao, R.; Wei, M.; Li, S.; Lu, J.; Evans, D. G.; Duan, X. *J. Mater. Chem. C* **2013**, *1*, 997–1004.

[173] Chen, C.-X.; Wei, Z.-W.; Fan, Y.-N.; Su, P.-Y.; Ai, Y.-Y.; Qiu, Q.-F.; Wu, K.; Yin, S.-Y.; Pan, M.; Su, C.-Y. *Chem* **2018**, *4*, 2658–2669.

[174] Yan, D.; Lloyd, G. O.; Delori, A.; Jones, W.; Duan, X. *ChemPlusChem* **2012**, *77*, 1112–1118.

[175] Yu, J.; Cui, Y.; Xu, H.; Yang, Y.; Wang, Z.; Chen, B.; Qian, G. *Nat. Commun.* **2013**, *4*, 2719.

[176] Wen, S.; Zhou, J.; Schuck, P. J.; Suh, Y. D.; Schmidt, T. W.; Jin, D. *Nat. Photonics* **2019**, *13*, 828–838.

[177] Zhou, J.; Liu, Z.; Li, F. *Chem. Soc. Rev.* **2012**, *41*, 1323–1349.

[178] Yu, J.; Cui, Y.; Wu, C.-D.; Yang, Y.; Chen, B.; Qian, G. *J. Am. Chem. Soc.* **2015**, *137*, 4026–4029.

[179] Zhou, J.; Liu, Q.; Feng, W.; Sun, Y.; Li, F. *Chem. Rev.* **2015**, *115*, 395–465.

[180] Sun, Q.-C.; Ding, Y. C.; Sagar, D. M.; Nagpal, P. *Prog. Surf. Sci.* **2017**, *92*, 281–316.

[181] Hou, Z.; Deng, K.; Li, C.; Deng, X.; Lian, H.; Cheng, Z.; Jin, D.; Lin, J. *Biomaterials* **2016**, *101*, 32–46.

[182] Deng, R.; Qin, F.; Chen, R.; Huang, W.; Hong, M.; Liu, X. *Nat. Nanotechnol.* **2015**, *10*, 237–242.

[183] Monguzzi, A.; Tubino, R.; Meinardi, F. *Phys. Rev. B* **2008**, *77*, 155122.

[184] Monguzzi, A.; Tubino, R.; Hoseinkhani, S.; Campione, M.; Meinardi, F. *Phys. Chem. Chem. Phys.* **2012**, *14*, 4322–4332.

[185] Singh-Rachford, T. N.; Lott, J.; Weder, C.; Castellano, F. N. *J. Am. Chem. Soc.* **2009**, *131*, 12007–12014.

[186] Islangulov, R. R.; Lott, J.; Weder, C.; Castellano, F. N. *J. Am. Chem. Soc.* **2007**, *129*, 12652–12653.

[187] Kim, J.-H.; Deng, F.; Castellano, F. N.; Kim, J.-H. *Chem. Mater.* **2012**, *24*, 2250–2252.

[188] Monguzzi, A.; Bianchi, F.; Bianchi, A.; Mauri, M.; Simonutti, R.; Ruffo, R.; Tubino, R.; Meinardi, F. *Adv. Energy Mater.* **2013**, *3*, 680–686.

[189] Galli, R.; Uckermann, O.; Andresen, E. F.; Geiger, K. D.; Koch, E.; Schackert, G.; Steiner, G.; Kirsch, M. *PLoS One* **2014**, *9*, e110295.

[190] Wilmink, G. J.; Opalenik, S. R.; Beckham, J. T.; Davidson, J. M.; Jansen, E. D. *J. Biomed. Opt.* **2006**, *11*, 041114.

[191] Rowe, J. M.; Zhu, J.; Soderstrom, E. M.; Xu, W.; Yakovenko, A.; Morris, A. J. *Chem. Commun.* **2018**, *54*, 7798–7801.

[192] Nandi, A.; Manna, B.; Ghosh, R. *Phys. Chem. Chem. Phys.* **2019**, *21*, 11193–11202.

[193] Yuan, S.; Lu, W.; Chen, Y.-P.; Zhang, Q.; Liu, T.-F.; Feng, D.; Wang, X.; Qin, J.; Zhou, H.-C. *J. Am. Chem. Soc.* **2015**, *137*, 3177–3180.

[194] Ejegbavwo, O. A.; Martin, C. R.; Olorunfemi, O. A.; Leith, G. A.; Ly, R. T.; Rice, A. M.; Dolgopolova, E. A.; Smith, M. D.; Karakalos, S. G.; Birkner, N. et al. *J. Am. Chem. Soc.* **2019**, *141*, 11628–11640.

[195] Oldenburg, M.; Turshatov, A.; Busko, D.; Wollgarten, S.; Adams, M.; Baroni, N.; Welle, A.; Redel, E.; Wöll, C.; Richards, B. S. et al. *Adv. Mater.* **2016**, *28*, 8477–8482.

[196] Ahmad, S.; Liu, J.; Gong, C.; Zhao, J.; Sun, L. *ACS Appl. Energy Mater.* **2018**, *1*, 249–253.

[197] Ahmad, S.; Liu, J.; Ji, W.; Sun, L. *Materials* **2018**, *11*, 1868.

[198] Li, M.; Gul, S.; Tian, D.; Zhou, E.; Wang, Y.; Han, Y.; Yin, L.; Huang, L. *Dalton Trans.* **2018**, *47*, 12868–12872.

[199] Dong, H.; Sun, L.-D.; Yan, C.-H. *Chem. Soc. Rev.* **2015**, *44*, 1608–1634.

[200] Weng, D.; Zheng, X.; Jin, L. *Eur. J. Inorg. Chem.* **2006**, *2006*, 4184–4190.

[201] Weng, D.; Zheng, X.; Chen, X.; Li, L.; Jin, L. *Eur. J. Inorg. Chem.* **2007**, *2007*, 3410–3415.

[202] Sun, C.-Y.; Zheng, X.-J.; Chen, X.-B.; Li, L.-C.; Jin, L.-P. *Inorg. Chim. Acta* **2009**, *362*, 325–330.

[203] Zhang, X.; Li, B.; Ma, H.; Zhang, L.; Zhao, H. *ACS Appl. Mater. Interfaces* **2016**, *8*, 17389–17394.

[204] Dolgopolova, E. A.; Brandt, A. J.; Ejegbavwo, O. A.; Duke, A. S.; Maddumapatabandi, T. D.; Galhenage, R. P.; Larson, B. W.; Reid, O. G.; Ammal, S. C.; Heyden, A. et al. *J. Am. Chem. Soc.* **2017**, *139*, 5201–5209.

[205] He, G. S.; Tan, L.-S.; Zheng, Q.; Prasad, P. N. *Chem. Rev.* **2008**, *108*, 1245–1330.

[206] Medishetty, R.; Zaręba, J. K.; Mayer, D.; Samoć, M.; Fischer, R. A. *Chem. Soc. Rev.* **2017**, *46*, 4976–5004.

[207] Nathan, V.; Guenther, A. H.; Mitra, S. S. *J. Opt. Soc. Am. B* **1985**, *2*, 294–316.

[208] Bhawalkar, J. D.; He, G. S.; Prasad, P. N. *Rep. Prog. Phys.* **1996**, *59*, 1041–1070.

[209] Quah, H. S.; Chen, W.; Schreyer, M. K.; Yang, H.; Wong, M. W.; Ji, W.; Vittal, J. J. *Nat. Commun.* **2015**, *6*, 7954.

[210] Quah, H. S.; Nalla, V.; Zheng, K.; Lee, C. A.; Liu, X.; Vittal, J. J. *Chem. Mater.* **2017**, *29*, 7424–7430.

[211] Gupta, M.; Kottilil, D.; Tomar, K.; Lu, S.; Vijayan, C.; Ji, W.; Bharadwaj, P. K. *ACS Appl. Nano Mater.* **2018**, *1*, 5408–5413.

[212] Xu, C.; Webb, W. W. *J. Opt. Soc. Am. B* **1996**, *13*, 481–491.

[213] Zhang, Y.-X.; Li, B.-X.; Lin, H.; Ma, Z.; Wu, X.-T.; Zhu, Q.-L. *J. Mater. Chem. C* **2019**, *7*, 6217–6221.

[214] Huang, X.; Li, Q.; Xiao, X.; Jia, S.; Li, Y.; Duan, Z.; Bai, L.; Yuan, Z.; Li, L.; Lin, Z. et al. *Inorg. Chem.* **2018**, *57*, 6210–6213.

[215] Song, T.; Yu, J.; Cui, Y.; Yang, Y.; Qian, G. *Dalton Trans.* **2016**, *45*, 4218–4223.

[216] Guo, J.-S.; Xu, G.; Jiang, X.-M.; Zhang, M.-J.; Liu, B.-W.; Guo, G.-C. *Inorg. Chem.*

2014, *53*, 4278–4280.

[217] Yang, H.; Sang, R.-L.; Xu, X.; Xu, L. *Chem. Commun.* **2013**, *49*, 2909–2911.

[218] Prasad, S. S.; Sudarsanakumar, M. R.; Dhanya, V. S.; Suma, S.; Kurup, M. R. P. *J. Mol. Struct.* **2018**, *1167*, 134–141.

[219] Garai, B.; Mallick, A.; Banerjee, R. *Chem. Sci.* **2016**, *7*, 2195–2200.

[220] Kawata, S.; Kawata, Y. *Chem. Rev.* **2000**, *100*, 1777–1788.

[221] Qin, M.; Huang, Y.; Li, F.; Song, Y. *J. Mater. Chem. C* **2015**, *3*, 9265–9275.

[222] Irie, M.; Fukaminato, T.; Matsuda, K.; Kobatake, S. *Chem. Rev.* **2014**, *114*, 12174–12277.

[223] Schwartz, H. A.; Ruschewitz, U.; Heinke, L. *Photochem. Photobiol. Sci.* **2018**, *17*, 864–873.

[224] Li, P.; Yin, X.-M.; Gao, L.-L.; Yang, S.-L.; Sui, Q.; Gong, T.; Gao, E.-Q. *ACS Appl. Nano Mater.* **2019**, *2*, 4646–4654.

[225] Williams, D. E.; Martin, C. R.; Dolgopolova, E. A.; Swifton, A.; Godfrey, D. C.; Ejegbavwo, O. A.; Pellechia, P. J.; Smith, M. D.; Shustova, N. B. *J. Am. Chem. Soc.* **2018**, *140*, 7611–7622.

[226] Dolgopolova, E. A.; Galitskiy, V. A.; Martin, C. R.; Gregory, H. N.; Yarbrough, B. J.; Rice, A. M.; Berseneva, A. A.; Ejegbavwo, O. A.; Stephenson, K. S.; Kittikhunnatham, P. et al. *J. Am. Chem. Soc.* **2019**, *141*, 5350–5358.

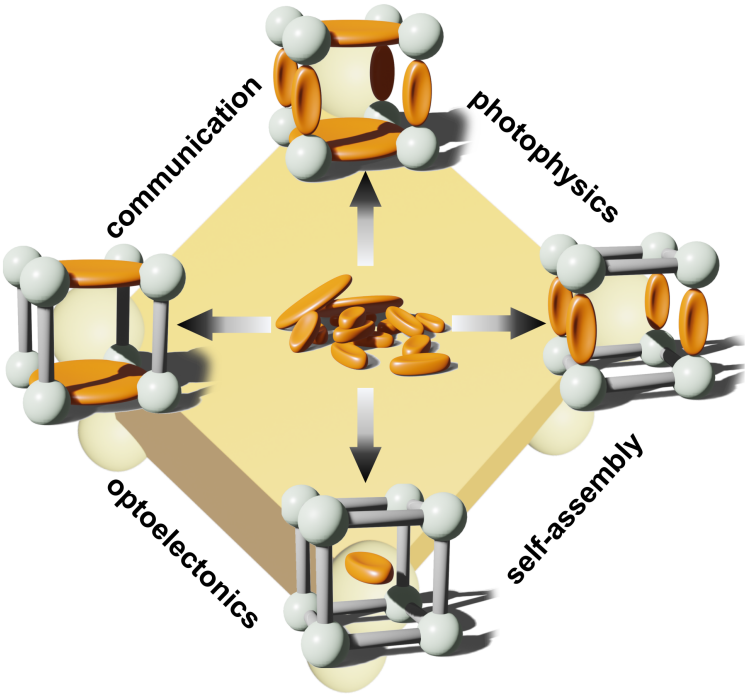

Scheme 1.1. MOF-imposed chromophore organization.

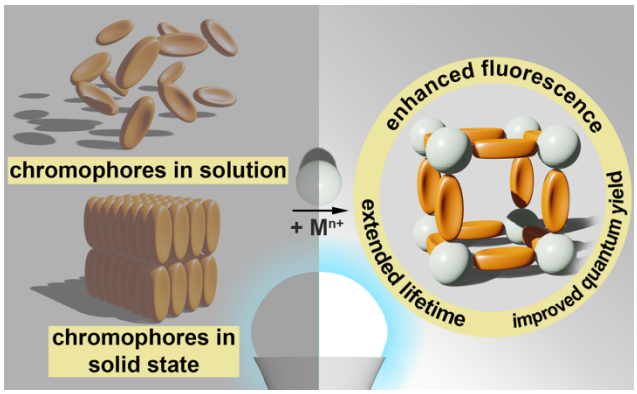

Figure 1.1. (*left*) From aggregation in the solid state and random orientation in solution towards (*right*) precise organization, separation, and molecular conformation through a MOF scaffold. Reproduced with permission from Ref. [37], © American Chemical Society 2016.

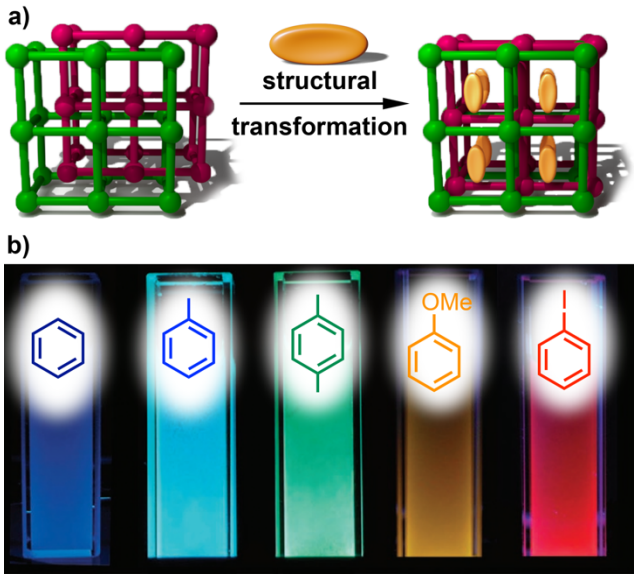

Figure 1.2. (a) Sensing of analytes via structural transformation in an interpenetrated MOF. (b) MOF powders suspended in aromatic solvents (analytes) under 365-nm irradiation. Reproduced with permission from Ref. [66], © Springer Nature 2011.

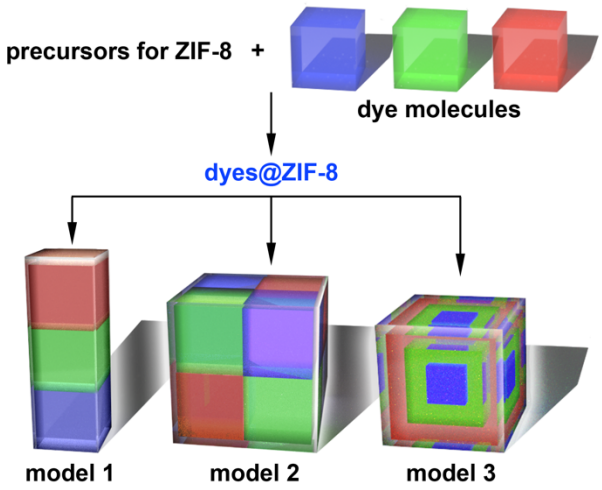

Figure 1.3. Approaches for preparing white-light emitting MOFs through chromophore integration: multi-phase single shell dye@ZIF-8 (model 1), single-phase single-shell dyes@ZIF-8 (model 2), and single-phase multi-shell dyes@ZIF-8 (model 3). Reproduced with permission from Ref. [158], © American Chemical Society 2019.

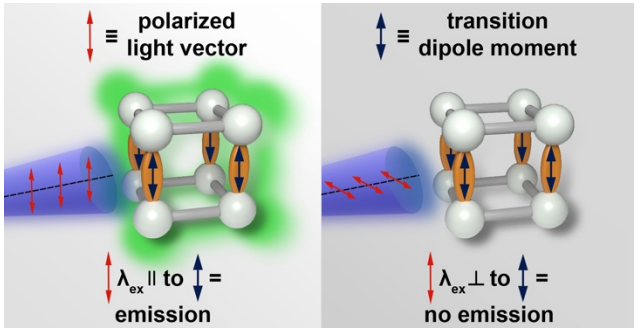

Figure 1.4. Schematic representation of fluorescence anisotropy in MOFs where (*left*) the vector of polarized light is parallel to the transition dipole moment of chromophores resulting in framework emission, and where (*right*) the vector of polarized light is perpendicular to the chromophores transition dipole moment, resulting in no framework emission.

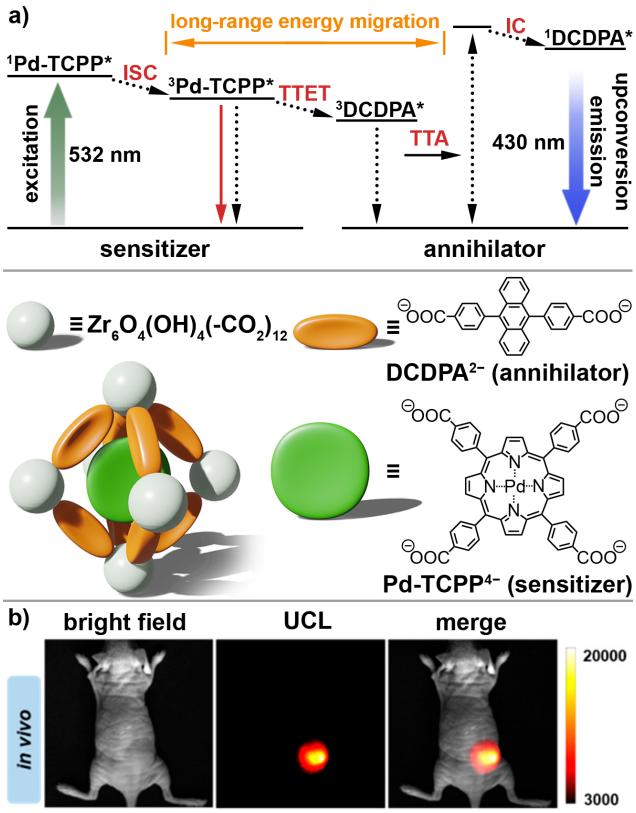

Figure 1.5. (a) Simplified diagram representing sensitized triplet-triplet annihilation in a Zr-MOF constructed from anthracene (orange ellipsoid) and porphyrin (green disc) linkers. (b) *In vivo* imaging of a Zr-MOF within mouse tumors. (*left to right*) bright field, triplet-triplet annihilation upconversion (UCL) spectra, and merged images of bright field and UCL spectra. Reproduced with permission from Ref. [71], © American Chemical Society 2018.

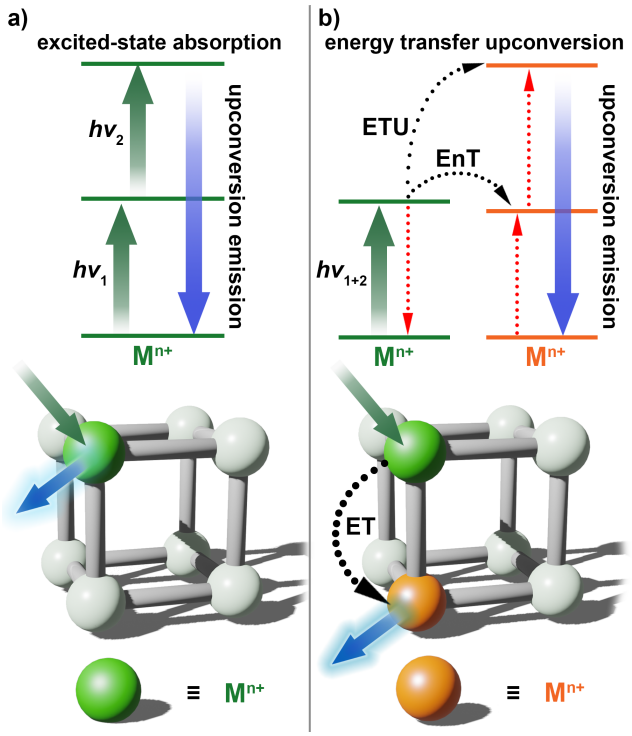

Figure 1.6. (*top*) Simplified diagrams of (a) photon upconversion via excited-state absorption (ESA) and (b) energy-transfer upconversion (ETU). Bold green arrows represent photon absorption, black dotted arrows represent excited state EnT, red dotted arrows represent possible excited state non-radiative decay pathways, and bold blue arrows represent upconverted emission. (*bottom*) Schematic representation of ESA and ETU in MOFs.

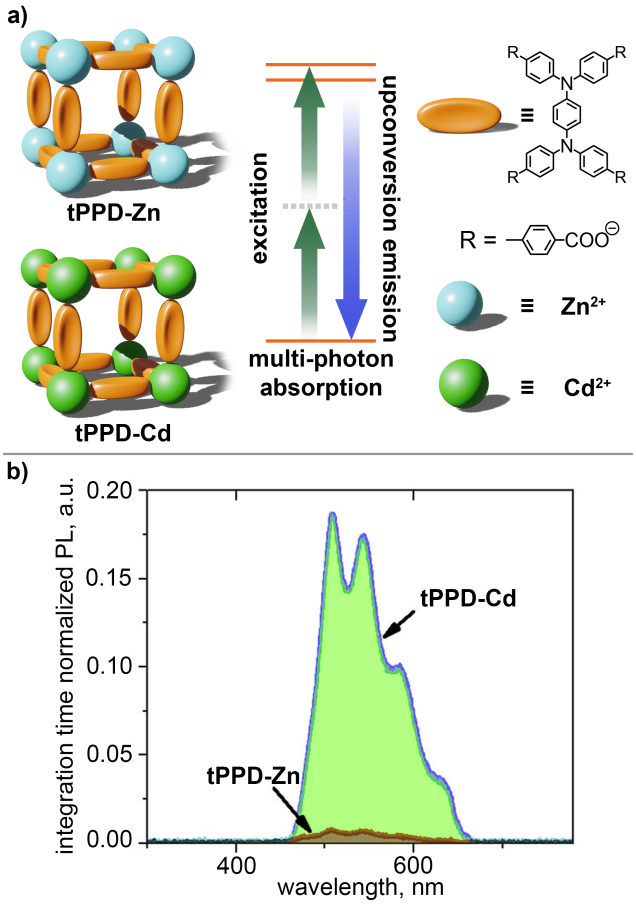

Figure 1.7. (a) Simplified diagram representing upconversion through multi-photon absorption in zinc- and cadmium-based MOFs. (b) Two-photon excited fluorescence spectra of tPPD-Cd and tPPD-Zn. Reproduced with permission from Ref. [4], © American Chemical Society 2019.

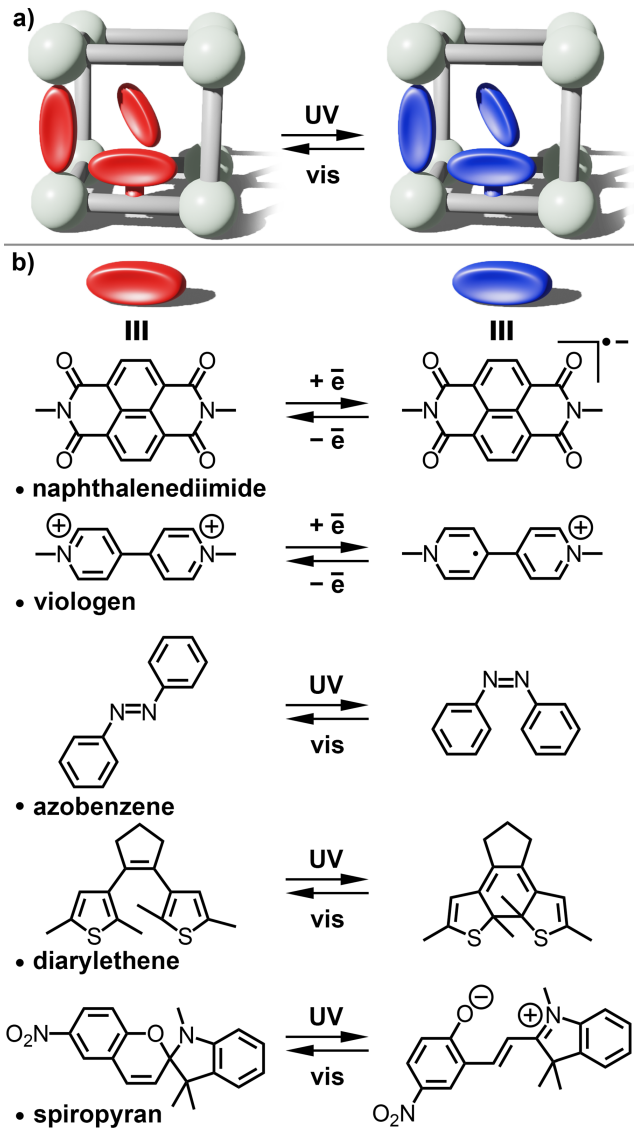

Figure 1.8. (a) Schematic representation of photoisomerization of photochromic molecules integrated as a framework backbone, side group, or guest. (b) Examples of photochromic units that have been included in MOF scaffolds. Reproduced from Ref. [57], © American Chemical Society 2019.

CHAPTER 2

FLIPPING THE SWITCH: FAST PHOTOISOMERIZATION IN A CONFINED ENVIRONMENT

Williams, D. E.;† Martin, C. R.;† Dolgopolova, E. A.;† Swifton, A.; Godfrey, D. C.; Ejegbavwo, O. A.; Pellechia, P. J.; Smith, M. D.; Shustova, N. B. *J. Am. Chem. Soc.* **2018**, *140*, 7611–7622.

Chapter abstract. Stimuli-responsive materials are vital for addressing emerging demands in the advanced technology sector as well as current industrial challenges. Here, we report for the first time that coordinative integration of photoresponsive building blocks possessing photochromic spiropyran and diarylethene moieties within a rigid scaffold of metal−organic frameworks (MOFs) could control photophysics, in particular, cycloreversion kinetics, with a level of control that is not accessible in the solid state or solution. On the series of photoactive materials, we demonstrated for the first time that photoisomerization rates of photochromic compounds could be tuned within almost 2 orders of magnitude. Moreover, cycloreversion rates of photoresponsive derivatives could be modulated as a function of the framework structure. Furthermore, through MOF engineering we were able to achieve complete isomerization for coordinatively immobilized spiropyran derivatives, typically exhibiting limited photoswitching behavior in the solid state. For instance, spectroscopic analysis revealed that the novel monosubstituted spiropyran derivative grafted to the backbone of the MOF pillar exhibits a remarkable photoisomerization rate of 0.16 s^{-1}, typical for cycloreversion in solution. We also applied the acquired fundamental principles toward mapping of changes in material properties, which could provide a pathway for monitoring material aging or structural deterioration.

INTRODUCTION

Photochromic building blocks capable of switching between two discrete states upon external stimuli are vital for applications such as “smart” windows, transition lenses, optical switches, or controlled drug delivery systems mainly due to the drastic difference in the photoisomer properties.[1−14] For instance, upon changing excitation wavelength,

temperature, pressure, or pH, a material absorption/emission profile, dielectric constant, or reduction potential could be drastically modulated.[15–21]

Due to the tunability and multifaceted modularity of metal-organic frameworks (MOFs),[22–44] photochromic derivatives could be embedded into a framework through different pathways: inside the pores or as linkers (or a part of a linker).[45–53] In this work, we developed a novel synthetic methodology in combination with recent advances in the MOF field[54–80] to probe photophysics of photochromic compounds in a confined environment defined by framework topology (Scheme 2.1). We attempted for the first time to gain fundamental knowledge of cycloreversion kinetics (i.e., transition between two states upon radiation with visible light) of two distinct classes of photochromic compounds with spiropyran and diarylethene cores in the solid state, in solution, and coordinatively immobilized inside the rigid matrix. For that, we prepared novel spiropyran derivatives with anchors for metal coordination, which resulted in the first example of a spiropyran-based MOF with a photochromic unit as a side group on the linker backbone. Such coordinative immobilization of photochromic derivatives inside a scaffold allowed us to study the possibility of tuning photoisomerization rates as a function of framework topology with a level of control that is not accessible in the solid state or solution. We have investigated five systems, which provide us different pathways for anchoring of photochromic compounds to allow for tunability of rigidity and photoswitching capacity. In our studies, we were also able to investigate the effect of steric hindrance on photoswitching ability. As a result, the acquired fundamental principles were applied toward mapping the changes of material properties, which provide a pathway for utilization of the introduced concept toward development of stimuli-responsive markers.

RESULTS AND DISCUSSION

This section includes the following subsections: (1) synthesis and study of photochromic compounds (also including characterization of diastereoisomer equilibration kinetics for one of the novel ligands bearing two photoswitchable units); (2) design and preparation of frameworks for integration of synthesized photochromic compounds, highlighting benefits of framework structural tunability (Scheme 2.1) including structural analysis; (3) photoisomerization kinetics of photochromic molecules in the solid state and solution as well as after their incorporation inside a rigid scaffold; (4) mapping changes of material properties through utilization of a prepared photochromic scaffold.

Comprehensive analysis of the frameworks and their precursors includes single-crystal and powder X-ray diffraction (PXRD), solid-state and solution nuclear magnetic resonance (NMR), Fourier transform infrared (FTIR), steady-state fluorescence, diffuse reflectance, UV−vis spectroscopies, and mass spectrometry, which will be discussed for each respective system.

Synthesis of Photochromic Linkers. To build novel stimuli-responsive frameworks with coordinatively immobilized photoswitchable units, we prepared four different photochromic molecules belonging to two distinct classes (Figures 2.1−2.3). Photochromic linkers with a diarylethene core were chosen due to their fatigue-resistant photochromic performance, thermal stability, and rapid response in the solid state (Figure 2.1).[78−81] For coordinative immobilization inside the framework, the photoswitchable core was modified with pyridyl groups or carboxylic acid arms to facilitate coordination to metal centers. The diarylethene derivatives, 1,2-bis(2-methyl-5-(pyridin-4-yl)thiophen-3-

yl)cyclopent-1-ene (BPMTC) and 4,4′-(cyclopent-1-ene-1,2-diyl)bis(5-methylthiophene-2-carboxylic acid) (H_2BCMTC) are shown in Figure 2.3.[82,83]

As the second class of photochromic linkers, we chose spiropyran derivatives due to the different pathway of the photoinduced cyclization reaction in comparison with diarylethene derivatives (Figure 2.1). In contrast to diarylethenes, for which isomerization could be described by covalent bond formation between the methylthiophene groups,[84] spiropyran-based compounds undergo relatively large structural changes centered on the sp^3 "spiro"-carbon, rotating from orthogonal to planar geometry (Figure 2.1).[3,85,86] Moreover, spiropyran is hydrophobic and uncharged, whereas its colored isomer, merocyanine, is a hydrophilic zwitterion (Figure 2.1).[87] Furthermore, diarylethene-based compounds are capable of 100% reversible photoisomerization in the solid state,[88] while spiropyran derivatives do not typically lead to solid-state reversible photoisomerization due to the necessary large structural reorganization.[89] In general, solid-state spiropyran photoisomerization has been explored for derivatives tethered to solid supports.[90] Therefore, there is a demand to systematically create solid-state spiropyran-based materials to harness the full potential of spiropyran derivatives in advanced technologies.

To overcome such steric hindrance observed for spiropyran groups in the solid state, we synthesized two novel photochromic linkers with spiropyran groups attached to the ligand backbone (Figure 2.1 and Scheme 2.2). Such derivatization of photochromic units will allow for their integration inside the rigid core of a porous framework, where spiropyran photoisomerization could occur within the pore aperture. With this in mind, we prepared 1′,3′,3′-trimethyl-6-nitro-4′,7′-di(pyridin-4-yl)spiro[chromene-2,2′-indoline] (TNDS, Scheme 2.3), and 1′,1‴,3′,3′,3‴,3‴-hexamethyl-6,6″-dinitro-4′,4‴ di(pyridin-4-yl)-

7′,7‴-bispiro[chromene-2,2′-indoline] (HDDB, Scheme 2.4) via a multistep synthetic procedure as shown in Scheme 2.2 (six steps for TNDS and seven steps for HDDB, Schemes 2.3 and 2.4, respectively). These linkers with one- and two photoresponsive moieties on one backbone can be also used as a model compound to probe the influence of steric hindrance on spiropyran isomerization.

All the prepared photochromic linkers and their precursors underwent comprehensive analysis by ^{1}H and ^{13}C NMR, FTIR spectroscopies, single-crystal X-ray diffraction, and mass spectrometry. Detailed description can be found in the experimental section below (Figures 2.9−2.14). The compound, HDDB (Schemes 2.2 and 2.4), containing two spiropyran groups attached to the linker skeleton, is of a particular interest to study the enantiomerization process of spiropyran units due to resolvable diastereoisomers. As it was previously shown on the example of its precursor,[91] the HDDB linker can exist in three unique diastereomers: $HDDB_{in-in}$, $HDDB_{in-out}$, and $HDDB_{out-out}$ (Figures 2.1 and 2.13). We studied the thermal equilibration process of HDDB in solution to estimate the effect of steric hindrance of spiropyran groups on the possibility of isomerization.

The thermal equilibration of the system was studied using a similar procedure utilized by Klajn and co-workers.[94] A thermal equilibration process among the three isomers, HDDBin−in, HDDBin−out, and HDDBout−out was represented as a cyclic reversible reaction involving three components with six first order reactions described by six rate constants (where k = rate constant, C = concentration).

$$\partial C_{in-in}/\partial t = -k_1 C_{in-in} - k_{-3} C_{in-in} + k_{-1} C_{in-out} + k_3 C_{out-out}$$

$$\partial C_{in-out}/\partial t = -k_1 C_{in-out} - k_2 C_{in-out} + k_1 C_{in-in} + k_{-2} C_{out-out}$$

$$\partial C_{out-out}/\partial t = -k_3 C_{in} C_{out-out} - k_{-2} C_{out-out} + k_{-3} C_{in-in} + k_2 C_{in-out}$$

To reduce the number of unknown variables, the steady state[95] was described with following equations:

$$k_{-1} = k_1 (C_{in-in,eq}/C_{in-out,eq})$$

$$k_{-2} = k_2 (C_{in-out,eq}/C_{out-out,eq})$$

$$k_{-3} = k_3 (C_{out-out,eq}/C_{in-in,eq})$$

To be able to monitor thermal isomerization process, we isolated two pure diastereoisomers, $HDDB_{in–in}$ and $HDDB_{in–out}$ (see the SI), to track changes of chemical shifts in the NMR spectra for *N*-bound methyl group protons (Scheme 2.2 and Figure 2.2), which allow us to distinguish among the three diastereoisomers. In order to estimate equilibration kinetics between diastereoisomers in solution, $HDDB_{in–in}$ was dissolved in dichloromethane-d_2, and its spectra were monitored by ^{1}H NMR spectroscopy. As shown in Figure 2.2, the equilibration among the three isomers was reached after 3 days. We solved the rate equations numerically (see the experimental section for more details) and obtained six rate constants (k_1 = 0.214, $k_{–1}$ = 0.122, k_2 = 0.228, $k_{–2}$ = 0.402, k_3 = 0.481, $k_{–3}$ = 0.481), which were used to model the concentration profiles. A good agreement was achieved between the experimental and calculated results. The obtained rate constant values were similar to those of the HDDB precursor (VII′, Scheme 2.4). Therefore, we can hypothesize that the extension of ligand backbone containing spiropyran moieties with pyridyl group does not significantly affect isomerization rates.

Synthesis of Photoresponsive 1, 2, 3, 3′, and 4 MOFs. The prepared linkers were used for coordinative immobilization inside the porous scaffolds. We used two distinct approaches for linker incorporation. One approach relies on coordination of linkers

containing pyridyl groups to unsaturated metal sites of a framework. Three photochromic ligands, TNDS, HDDB, and BPMTC (Figure 2.3), contain terminal pyridyl groups, which make them suitable for incorporation between two-dimensional (2D) MOF layers. For instance, BPMTC has been previously utilized as pillars in a MOF, in which 2D layers consist of a tetracarboxylate linker, $DBTD^{4-}$ (H_4DBTD = 3′,6′-dibromo-4′,5′-bis(4-carboxyphenyl)-1[1,1′:2′,1″-tetraphenyl]-4,4″-dicarboxylic acid, Figure 2.3).[29] We anticipated that our novel spiropyran pillars could also bind axially to the zinc paddle wheel secondary building units (SBUs). Indeed, integration of TNDS and HDDB were performed between 2D layers, consisting of $DBTD^{4-}$ connected by $Zn_2(O_2C-)_4$, and resulted in formation of Zn_2(DBTD)(TNDS) (1), Zn_2(DBTD)(HDDB) (2), and Zn_2(DBTD)(BPMTC) (**3**, Figures 2.3 and 2.15–2.22, see experimental details in the experimental section).

As discussed above, the structures consist of stacked layers of $DBTD^{4-}$ connected in the equatorial planes of planar zinc paddle wheel SBUs (Figure 2.3). Both **1** and **2** consist of a pillar backbone with three and four six-membered rings, respectively, which are anchored to the axial positions of the SBUs with 2-fold disorder (for more details see the crystallographic section of the SI, Table 2.5). The bulk samples of **1** and **2** were also characterized using PXRD, and the acquired data are in agreement with their simulated patterns (Figure 2.4). The ^1H NMR spectroscopic studies of digested **1** (i.e., destroyed in the presence of hydrochloric acid) also confirm the presence of the photochromic pillars (Figure 2.17). The $^{13}C\{^1H\}$ CP-MAS NMR spectroscopic analysis confirmed integration of photochromic moieties in **2** (Figure 2.20). The FTIR spectra of **1** and **2** are shown in Figures 2.16 and 2.19, respectively.

MOF **3** contains the BPMTC linker coordinatively anchored between the axial zinc paddle wheel SBUs and the 2D layers of $DBTD^{4-}$, as it was previously reported (Figure 2.3).[29] The powder pattern of the bulk sample of **3** is in good agreement with the simulated pattern (Figure 2.21). The ^{1}H NMR spectrum of the digested sample shows the presence of both BPMTC and H_4DBTD (Figure 2.22). The structure **3′** consists of the same BPMTC linker integrated between 2D sheets composed of the Zn-based paddle wheel connected by $BPDC^{2-}$ linkers (Table 2.5, Figures 2.23–2.25). Single-crystal X-ray diffraction showed the presence of 2-fold interpenetrated frameworks (Figure 2.23 and Table 2.5).

In the case of **4**, we applied a different method for coordinative immobilization of H_2BCMTC inside the porous scaffold. We integrated a photochromic compound as a capping linker in an already synthesized framework using a previously developed synthetic methodology.96 For that, we used a Zr-based framework, $Zr_6(Me_2BPDC)_4$,[77] consisting of 2,2′-dimethylbiphenyl-4,4′-dicarboxylate, Me_2BPDC^{2-}, linkers coordinated to $Zr_6O_4(OH)_8(H_2O)_4^{8+}$ metal nodes (Figure 2.3). The H_2BCMTC integration occurred through replacement of the terminal OH− and H_2O groups in the SBU. The schematic representation of such installation is shown in Figure 2.3, and more details about suitable linkers for such coordination as well as calculation of the appropriate linker size can be found elsewhere.[97] However, it is important to note that $Zr_6(Me_2BPDC)_4$ is flexible enough to accommodate structural changes associated with capping linker insertion. The powder pattern of prepared $Zr_6(Me_2BPDC)_4$ was also in good agreement with the simulated pattern,[77] and framework crystallinity was retained after incorporation of $BCMTC^{2-}$ (Figure 2.26). To remove any traces of residual (noncoordinated) linkers, we applied an extensive washing procedure using a Soxhlet apparatus. After that, the installation of

$BCMTC^{2-}$ into **4** was confirmed by ^{1}H NMR spectroscopy of digested **4** (Figure 2.25). In combination with experimental spectroscopic studies, the geometrical constraints placed by the linker size and pocket dimension of the framework suggest that the capping linker can occupy both axial and equatorial positions of Zr-nodes, *ca*. 50% occupancy of available sites.

Photophysics of Photochromic Compounds. The photoswitching behaviors of photochromic molecules with spiropyran and diarylethene cores are vastly distinct mainly due to the nature of structural changes associated with photoinduced isomerization. The expansion of the photoswitch from the spiropyran form to the merocyanine form is accompanied by significant structural changes and, therefore, can severely impact the photoisomerization rate.[4,98–100] In general, spiropyran derivatives consist of two moieties: indoline and chromene linked together through a single sp^3 "spiro" chiral carbon. Once the photoswitch is irradiated with UV light (λ_{ex} < 400 nm), the photoswitch undergoes a cyclization reaction and generates a highly colored zwitterionic form (merocyanine), shown in Figure 2.1.[85]

Diarylethene photoswitches also have two isomeric forms, colorless ("open") and colored ("closed", Figure 2.1). The colorless "open" form of diarylethene can be irradiated with UV light, which causes formation of a bond between the two heterocyclic thiophene moieties, generating the colored diarylethene form (Figure 2.1).[80] However, the diarylethene photoswitch, unlike spiropyran, is thermally stable in either form and does not undergo such a drastic structural change during isomerization. In fact, relatively little movement of diarylethene "arms" within the same plane is necessary to achieve rapid photoisomerization, particularly in the solid state. To probe photoisomerization kinetics of

the prepared spiropyran and diarylethene derivatives for the first time, we performed photophysical measurements in solution and in the solid state. For solution studies, a 3 mM solution of the photoswitch was loaded into a 8 mm × 1 mm front-facing quartz sample cell. For solid-state studies, 4 μmol of photoswitch was mixed with 100 mg of potassium bromide, which was then pressed into the same 8 mm sample cell.

Spiropyran Derivatives in the Solid State, in Solution, and Coordinatively Immobilized in Scaffolds 1 and 2. The photochromic cycloreversion kinetics of both the TNDS and HDDB linker were investigated in the solid state, in solution, and coordinatively inside scaffolds (Figures 2.3, 2.4, and 2.15–2.20). Figure 2.5 shows photoisomerization of TNDS in the solid state and solution with an excitation wavelength of 365 nm. As expected, the TNDS powder was not fully reversible due to the necessity of significant structural changes required for the photoisomerization process. As a result, the TNDS derivative displayed limited photoconversion to the colorless form in the solid state, whereas in solution, complete photoinduced reversion was successfully achieved. The photophysical studies of TNDS in *N*,*N*-dimethylformamide (DMF) showed a linear correlation of ln(A) versus time of irradiation, which is in line with the data previously reported for other spiropyran derivatives in solution.[90,101−103] The rate constant, k, was found to be 0.12 s^{-1}. Cycloreversion plots and experimentally determined rates are shown in Figure 2.6 and Table 2.1, respectively.

In comparison with TNDS, HDDB also showed limited photoisomerization in the solid state, while demonstrating 100% photoconversion in solution. However, measurements of photoisomerization rates in solution were complicated by the presence of three isomers, $HDDB_{in-in}$, $HDDB_{in-out}$, and $HDDB_{out-out}$ (Figure 2.1), each of which possess

a different photoisomerization rate. For the isolated $HDDB_{in-in}$ isomer, *k*, was found to be 0.20 s^{-1} in DMF, which decreases up to 0.06 s^{-1} during conversion of $HDDB_{in-in}$ to $HDDB_{in-out}$ and $HDDB_{out-out}$. Coordinative immobilization of TNDS and formation of **1** significantly affects its photophysics. Indeed, once TNDS was integrated into a rigid scaffold, it demonstrated solution-like photoisomerization behavior, even in the solid state. Integrated TNDS (**1**) showed 100% conversion from merocyanine to spiropyran with a rate of 0.16 s^{-1} (Figures 2.5 and 2.7, Table 2.1). Therefore, a framework provides a pathway for photoswitch isomerization in the solid state through the spatial separation of photochromic linkers in contrast to the close packing observed for free ligand in the solid state.

Based on the results observed for **1**, we integrated the bulkier HDDB inside the rigid scaffold resulting in preparation of **2**. However, HDDB does not exhibit photophysical behavior similar to TNDS. In contrast, HDDB exhibits limited photoisomerization more typical for the solid state, rather than that in solution. Such difference between integrated HDDB and TNDS could be attributed to the presence of two photoswitchable moieties and their close proximity in a framework, which impede the complete cycloreversion process. Thus, comparison of integrated TNDS versus coordinatively embedded HDDB possessing the same photoresponsive moieties but dissimilar in their amount (**1** vs **2**, respectively) allowed us to demonstrate the crucial role of steric hindrance in the photoisomerization process.

Diarylethene Derivatives in the Solid State, in Solution, and Coordinatively Immobilized in 3, 3′, and 4 Scaffolds. In the case of diarylethene photoswitches, we found that both BPMTC and H_2BCMTC were fully reversible in the solid state and solution

(λ_{ex}(cyclization) = 365 nm, λ_{ex}(cycloreversion) ≥ 400 nm, Figure 2.1). In solution, the rate constants, *k*, for the BPMTC cycloreversion reaction varied in a narrow range from 0.01 to 0.03 s^{-1} (Figures 2.5−7, Tables 2.1 and 2.2). The obtained *k* values for BPMTC are in line with literature data reported for other diarylethene derivatives and support the previous hypothesis that solvent polarity does not exhibit a significant effect on the cycloreversion process due to irrelevance of ring-opening process to changes in a molecular conformation.[79,104−108] The photoisomerization rate for H_2BCMTC in methanol (2.6×10^{-2} s^{-1}) was also comparable with the rate of BPMTC in the same solvent (1.8×10^{-2} s^{-1}, Figure 2.6, Tables 2.1 and 2.2). However, in contrast to spiropyran derivatives, diarylethene photoswitches underwent fast cycloreversion in the solid state, which could be explained by the accommodation of strain energy generated by the geometrical structure change during the cyclization reaction as well as the low activation energy of ring-opening process.[105−107] For instance, photoinduced isomerization of BPMTC occurs with a rate of *k* = 0.20 s^{-1}. However, this tendency was not observed for coordinatively immobilized BPMTC inside a rigid framework.

In **3**, where the BPMTC linker is coordinatively immobilized as a pillar between $DBTD^{4-}$-containing layers (Figure 2.3), the recovery of the open-form isomer was found to be 0.0028 s^{-1}, which is ∼70 times slower in comparison with the "free" compound in the solid state. Such a drastic rate decrease could be associated with the fact that the BPMTC pyridyl arms are tethered between the two-dimensional layers of $DBTD^{4-}$, which impede the possibility of pillar photoisomerization since photoinduced transformations should occur through the linker skeleton. By changing framework topology, we were able to enhance the photoisomerization rate by almost four times. Thus, BPMTC in framework

3′, connected to the skeleton of Zn-BPDC units, consisting of more flexible dicarboxylic units, $BPDC^{2-}$, photoisomerizes with the rate $k = 0.01\ s^{-1}$. Remarkably, the obtained k value for **3′** correlates with behavior of the linker in solution (Tables 2.1 and 2.22, Figure 2.25) and could be attributed to a high degree of framework flexibility in **3′** in comparison with **3**. Notably, both **3** and **3′** frameworks were able to accommodate structural changes associated with the photoisomerization process of BPMTC coordinatively immobilized between metal nodes, which was confirmed by PXRD. Thus, a rigid framework allowed us to tune the photoisomerization rate mimicking solution or solid-state behavior as a function of its topology.

In the case of H_2BCMTC, the rate constant in the solid state was found to be 4.8 × 10−2 s^{-1}, which is four times slower in comparison with BPMTC (Figures 2.5 and 2.7, Table 2.1) as well as other diarylethene derivatives.[79,104−108] Such difference could be explained by the fact that H_2BCMTC could result in formation of a "hydrogen-bonding" framework with behavior similar to a MOF matrix (Figure 2.31). We hypothesize that hydrogen-bonding interactions in the solid state could restrict molecular dynamics in a similar fashion as a MOF and potentially be a reason for the similar rate constants (4.1 × 10^{-2} s^{-1} (**4**) and 4.8 × 10^{-2} s^{-1} (solid state, Table 2.1).

To summarize this subsection, we showed the effect of a rigid scaffold on photoisomerization kinetics for two distinct classes of photochromic molecules. Based on the comparison of spiropyran- and diarylethene-based linkers possessing different photoisomerization pathways, we promoted photoinduced isomerization of spiropyran derivatives in the solid state through their integration inside a porous matrix. Moreover, coordinatively immobilized spiropyran derivatives can mimic solution-like photophysical

behavior. However, steric hindrance still could impede photoisomerization dynamics as it was shown on the example of the photochromic linker possessing two spiropyran moieties located in close proximity to each other. On the example of diarylethene-based frameworks with different topologies and structural flexibilities, we showed the possibility to tune and control the photoisomerization rate of incorporated photochromic linkers with a level of control that cannot be achieved in the solid state or solution. To the best of our knowledge, the presented studies are the first example of extensive photophysical studies demonstrating tunability of photoisomerization rates within 2 orders of magnitude for the same organic linker (Figure 2.6). We hypothesize that such drastic difference in behavior could be potentially tuned as a function of framework topology, which provides a pathway for development of new "smart" photoswitchable materials with a controllable photoresponse.

Photochromic Compounds to Map Changes in Material Properties. The concept of photoisomerization inside a confined environment discussed above could be potentially translated toward mapping of changes in a profile of a material. We tested the hypothesis that prepared photochromic porous scaffolds, overcoming steric hindrance for photoisomerization processes, can be utilized as a marker for material degradation. The advantage of a porous framework is that it promoted photoisomerization under irradiation (or daylight exposure), and the changes in the photophysical profile of a material became "invisible" due to a relatively rapid photoisomerization when the scaffold is intact, that is, its integrity is maintained.

In our studies, we used the TNDS-containing MOF (1), which was mixed with potassium bromide, leading to formation of the slightly colored homogeneous mixture

(Figure 2.8 and 2.32). After deposition of the obtained mixture on filter paper, nitrogen gas was bubbled through a 6 M HCl solution. Notably, exposure to just nitrogen did not lead to any surface changes. Hydrochloric acid vapors were released through a narrow tip (i.d. = 4 mm) to localize their effect. As shown in Figure 2.8, such treatment resulted in local framework degradation, which is accompanied by linker release, that is, formation of noncoordinated photochromic TNDS. Surface changes were monitored by photoluminescence spectroscopy and structural ones by PXRD. Figure 2.8 demonstrates that before acid vapor exposure, the emission profile has a maximum of λ_{max} = 680 nm (λ_{ex} = 350 nm) but framework degradation causes a hypsochromic shift of more than 100 nm, and therefore the emission maximum became similar to that of a "free" photochromic linker. These drastic changes in emission (from purple to green) allowed detection of scaffold degradation by the naked eye. Moreover, these changes were local, that is, occurred only at the exposed area. As a control experiment, the noncoordinated linker, TNDS, was exposed to HCl vapors under similar conditions (Figure 2.28). In that case, we observed similar emission with λ_{max} = 550 nm (λ_{ex} = 345 nm) to that of the "exposed" framework. The same protonation of TNDS was observed in solution by bubbling HCl vapors (Figure 2.29). Furthermore, due to framework degradation (monitored by PXRD studies), the "released" photochromic TNDS highlighted the corroded areas permanently, which provided a pathway to use such changes as a good indicator for necessary material treatment or replacement. To summarize, the presented concept could be applied toward invasive monitoring of material surfaces with a good spatial resolution. These studies could potentially provide an avenue to monitor material aging or structural deterioration, which

are key points for a number of industrial processes or applications including tests of aircraft reliability or steel corrosion.

SUMMARY

The presented studies focus on photoisomerization kinetics of two distinct classes of photochromic derivatives with spiropyran and diarylethene cores in the solid state, in solution, and coordinatively immobilized inside the rigid scaffold. To study such dependence as well as the possible effect of steric hindrance, we prepared two novel spiropyran compounds, TNDS and HDDB, with one and two photoswitching moieties, which resulted in preparation of the first examples of MOFs (**1** and **2**) with spiropyran moieties embedded as a part of the organic linker. Due to the presence of different HDDB isomers ($HDDB_{in-in}$, $HDDB_{in-out}$, and $HDDB_{out-out}$), we were also able to study thermal equilibration process of HDDB in solution to estimate the effect of steric hindrance of spiropyran groups on isomerization.

For the first time, through utilization of five distinct frameworks (**1**, **2**, **3**, **3′**, and **4**), we also showed that (i) the solid-state spiropyran metal−organic materials with capability of reversible photoinduced isomerization could be prepared; (ii) a photochromic linker could be integrated as not only pillars but also postsynthetically installed capping linkers; (iii) the photoisomerization rate could be tuned as a function of framework structure; (iv) coordinatively immobilized spiropyran derivatives inside a MOF could possess a high isomerization rate mimicking solution behavior; and (v) the acquired fundamental principles could be translated toward mapping changes in material properties to develop stimuli-responsive markers.

To conclude, the presented studies not only address some aspects of photophysics of photochromic compounds integrated in a confined environment but also provide a pathway for development of a new generation of photoactive materials.

EXPERIMENTAL SECTION

Materials. Zinc(II) nitrate hexahydrate (technical grade, Ward's Science), tin(II) chloride anhydrous (98%, Beantown Chemicals), copper(I) chloride anhydrous (97%, Strem Chemicals), bis(triphenylphosphine)palladium(II) dichloride (96%, Oakwood Chemical), copper powder (99.9%, Alfa Aesar), sodium carbonate (ACS grade, Ameresco), magnesium sulfate anhydrous (USP, Chem-Implex, International Inc.), sodium sulfate anhydrous (99.5%, Oakwood Chemical), sodium hydroxide (ACS, Oakwood Chemical), 2,5-dibromonitrobenzene (99%, Oakwood Chemical), sodium nitrite (98%, Oakwood Chemical), 3-methyl-2-butanone (98%, Beantown Chemicals), methyl trifluoromethanesulfonate (97%, Matrix Scientific), 2-hydroxy-5-nitrobenzaldehyde (98%, Oakwood Chemical), pyridine-4-boronic acid (95%, Matrix Scientific), hexabromobenzene (>99%, TCI America), *p*-tolylmagnesium bromide (0.5 M in diethyl ether, Acros Organics), hydrochloric acid (ACS, Fisher Chemical), sulfuric acid (ACS grade, Fisher Chemical), nitric acid (ACS reagent, Sigma-Aldrich), fluoroboric acid (48%, Oakwood Chemical), ethanol (200 proof, Decon Laboratories, Inc.), methanol (ACS grade, Fisher Scientific), methylene chloride (99.9%, Fisher Chemical), acetone (ACS grade, Sigma-Aldrich), ethyl acetate (99.9%, Fisher Chemical), chloroform (99.9%, Fisher Chemical), diethyl ether (ACS grade, J. T. Baker Chemicals), hexanes (ACS, BDH), *N*,*N*-dimethylformamide (ACS grade, Oakwood Chemical), piperidine (99%, Sigma-Aldrich), carbon tetrachloride (99.9%, Sigma-Aldrich), bromine (99.8%, Acros-Organic),

tetrahydrofuran (HPLC grade, Beantown Chemicals), chloroform-*d* (Cambridge Isotopes), acetone-d_6 (Cambridge Isotopes), methylene chloride-d_2 (Cambridge Isotopes), and dimethyl sulfoxide-d_6 (Cambridge Isotopes) were used as received.

The compounds 2,5-dibromoaniline (**II**, Scheme 2.3),[92] (2,5-dibromophenyl)hydrazine (**III**, Scheme 2.3),[93] 4,7-dibromo-2,3,3-trimethyl-3*H*-indole (IV, Scheme 2.3),[93] 4,4′-dibromo-2,2′-dinitro-1,1′-biphenyl (**II′**, Scheme 2.4),[91] 4,4′-dibromo-[1,1′-biphenyl]-2,2′-diamine (**III′**, Scheme 2.4),[91] (4,4′-dibromo-[1,1′-biphenyl]-2,2′-diyl)-bis(hydrazine) (**IV′**, Scheme 2.4),[91] 4,4′dibromo-2,2′,3,3,3′,3′-hexam-ethyl-3*H*,3′*H*-7,7′-biindole (**V′**, Scheme 2.4),[91] 3′,6′-dibromo-4′,5′-bis(4-carboxyphenyl)-1[1,1′:2′,1″-tetraphenyl]-4,4″-dicarboxylic acid (H_4DBTD, Figure 2.3),[109] 1,2-bis(2-methyl-5-(pyridin-4-yl)thiphen-3-yl)cyclopent-1-ene (BPMTC, Figures 2.1 and 2.3),[82] 4,4′-(cyclopent-1-ene-1,2-diyl)bis(5-methylthiophene-2-carboxylic acid) (H_2BCMTC, Figures 2.1 and 2.3),[83] 2,2′-dimethylbiphenyl-4,4′-dicarboxylic acid (H_2Me_2BPDC),[110] and $Zr_6(Me_2BPDC)_4$[77] were prepared according to the reported procedures.

Preparation of [4,7-Dibromo-1,2,3,3-tetramethyl-3*H*-indol-1-ium][trifluoromethanesulfonate] ($[C_{12}H_{14}Br_2N]^+[CF_3O_3S]^-$, V, Scheme 2.3). Compound V (Scheme 2.3) was prepared based on a modified literature procedure.[91] Methyl trifluoromethanesulfonate (4.13 g, 25.2 mmol) was added to synthesized **IV** (Scheme 2.3) (2.00 g, 6.31 mmol) in 120 mL of diethyl ether and 80 mL of hexanes. After the resulting mixture was stirred vigorously for 8 hours at room temperature, a pale pink powder was collected by filtration and washed with diethyl ether (3 × 10 mL). After drying under vacuum, **V** (Scheme 2.3) (2.70 g, 5.61 mmol) was isolated in 89% yield and used without further purification.

Preparation of 4′,7′-dibromo-1′,3′,3′-trimethyl-6-nitrospiro-[chromene-2,2′-indoline] ($C_{19}H_{16}Br_2N_2O_3$, VI, Scheme 2.3). Under a nitrogen atmosphere, piperidine (1.41 g, 16.6 mmol) was added to a solution of **V** (2.00 g, 4.15 mmol, Scheme 2.3) and 2-hydroxy-5-nitrobenzaldehyde (1.25 g, 7.47 mmol) in 80 mL of ethanol and heated at reflux for 8 hours. After cooling to 0 °C, the resulting light-yellow precipitate was filtered and washed with cold ethanol. After drying under vacuum, **VI** (0.971 g, 2.02 mmol, Scheme 2.3) was isolated in 48% yield. Crystals of **VI** (Scheme 2.3) were obtained upon cooling of the crude reaction mixture in ethanol at 0 °C over several days. The detailed description for the crystallographic data collection and refinement details are given in the experimental section (Table 2.3). The determined structure of **VI** (Scheme 2.3) is shown in Figure 2.9. ^{1}H NMR (acetone-*d*, 300 MHz): δ = 1.27 (3H, s), 1.49 (3H, s), 3.17 (3H, s), 6.00−6.04 (1H, d, J = 10.4 Hz), 6.92−6.95 (1H, d, J = 8.55 Hz), 6.96−6.99 (1H, d, J = 9.00), 7.26−7.29 (1H, d, J = 8.62 Hz), 7.30−7.33 (1H, d, J = 10.4 Hz), 8.09−8.13 (1H, dd, J = 2.83, 8.96 Hz) ppm (Figure 2.10). ^{13}C NMR (acetone-d_6, 400 MHz): δ = 20.61, 22.46, 32.91, 54.59, 101.15, 108.00, 116.27, 118.15, 119.48, 121.36, 123.81, 126.69, 126.75, 130.59, 135. 93, 136.86, 142.31, 147.37, 160.18 ppm (Figure 2.10). FTIR (neat, cm^{-1}): 3076, 2968, 2934, 2868, 2545, 2162, 2041, 1980, 1910, 1736, 1654, 1614, 1577, 1510, 1478, 1466, 1443, 1396, 1379, 1361, 1331, 1272, 1255, 1228, 1175, 1145, 1127, 1088, 1061, 1017, 955, 927, 915, 904, 877, 834, 811, 792, 771, 745, 717, 703, 666. HRMS (ESI, *m*/*z*) calculated for $C_{19}H_{16}Br_2N_2O_3$ $[M + H]^+$ 478.9601, found 478.9600.

Preparation of 1′,3′,3′-trimethyl-6-nitro-4′,7′-di(pyridin-4-yl)-spiro[chromene-2,2′-indoline] ($C_{29}H_{24}N_4O_3$, TNDS, Scheme 2.3). Using a Schlenk technique, 25 mL of dry DMF was transferred into a flask containing **VI** (300 mg, 0.624

mmol, Scheme 2.3), Na_2CO_3 (240 mg, 2.26 mmol), $PdCl_2(PPh_3)_2$ (88.0 mg, 0.125 mmol), CuCl (134 mg, 1.35 mmol), and pyridine-4-boronic acid (460 mg, 3.74 mmol). The obtained mixture was stirred for 3 days at 120 °C. After cooling to room temperature, the reaction mixture was transferred into a 250 mL separatory funnel, following dilution with deionized water (75 mL). The product was then extracted with ethyl acetate (3 × 50 mL). The organic layers were combined, washed with brine (50 mL), and dried over sodium sulfate, followed by filtration and solvent removal under vacuum. The resulting red/brown oil underwent several recrystallizations in ethyl acetate and hexanes. The obtained orange powder was dissolved in ethyl acetate (20 mL) and hexanes (30 mL), and the solvent was removed under vacuum until a suspension formed. The suspension was filtered to collect a light-yellow powder. After drying on vacuum, TNDS (44.0 mg, 93.8 μmol) was isolated in 17% yield. Single crystals of TNDS were obtained by slow evaporation of saturated acetone solution at 0 °C. The detailed description for the crystallographic data collection and refinement details are given in the experimental section (Table 2.4).

The X-ray structure of TNDS is shown in Figure 2.11. ^{1}H NMR acetone-d_6, 400 MHz): δ = 0.81 (3H, s), 1.33 (3H, s), 2.43 (3H, s), 6.00−6.03 (1H, d, J = 10.5 Hz), 6.69−6.71 (1H, d, J = 7.9 Hz), 6.85− 6.88 (1H, d, J = 9.0 Hz), 7.12−7.14 (1H, d, J = 7.9 Hz), 7.18−7.22 (1H, d, J = 10.6 Hz), 7.39−7.45 (1H, m), 8.01−8.05 (1H, dd, J = 2.8 and 9.0 Hz), 8.08 (1H, d, J = 2.8 Hz), 8.64 (4H, m) ppm (Figure 2.12). ^{13}C NMR (acetone-d_6 400 MHz): δ = 20.61, 22.46, 32.91, 54.59, 101.14, 108.00, 116.27, 118.15, 119.49, 121.36, 123.81, 126.74, 130.59, 135.93, 136.86, 142.31, 147.37, 160.18 ppm (Figure 2.12). FTIR (neat, cm^{-1}): 3746, 2965, 2344, 2163, 2049, 1981, 1596, 1543, 1522, 1494, 1464, 1438, 1392, 1363, 1337, 1286, 1253, 1216, 1145, 1129, 1072, 1055, 1011, 980, 939, 905, 873,

827, 803, 749, 729, 681 (Figure 2.16). HRMS (ESI, *m*/*z*) calculated for $C_{29}H_{24}N_4O_3$ $[M + H]^+$ 477.1918, found 477.1921.

Preparation of [4,4′-dibromo-1,1′,2,2′,3,3,3′,3′-octamethyl-3*H*,3′*H*-[7,7′-biindole]-1,1′-diium]bis-[trifluoromethane-sulfonate] ($[C_{24}H_{28}Br_2N_2]^{2+}[(CF_3O_3S)_2]^{2-}$, VI′, Scheme 2.4). Compound VI′ (Scheme 2.4) was prepared based on a modified literature procedure.[91] Methyl trifluoromethanesulfonate (1.50 g, 10.1 mmol) was added to synthesized **V′** (Scheme 2.4) (1.00 g, 2.11 mmol) in 90 mL of diethyl ether and 60 mL of hexanes. After the resulting mixture was stirred vigorously for 8 hours at room temperature, a pale pink powder was collected by filtration and washed with diethyl ether (3 × 10 mL). After drying under vacuum, **VI′** (1.57g, 1.96 mmol, Scheme 2.4) was isolated in 93% yield and used without further purification.

Preparation of 4′4,‴-dibromo-1′,1‴,3′,3‴-hexamethyl-6,6″-dinitro-7′,7‴-bispiro[chromene-2,2′-indoline] ($C_{38}H_{32}Br_2N_4O_6$, VII′, Scheme 2.4). Compound **VII′** (Scheme 2.4) was prepared based on a modified literature procedure.[91] Using a Schlenk technique, piperidine (713 mg, 8.37 mmol) was added to a solution of **VI′** (Scheme 2.4) (1.50 g, 1.87 mmol) and 2-hydroxy-5-nitrobenzaldehyde (706 mg, 4.38 mmol) in 60 mL of ethanol and heated at reflux for 8 hours. After cooling to 0 °C, the resulting light-yellow precipitate was filtered and washed with cold ethanol. After drying under vacuum, VII′ (761 mg, 948 μmol, Scheme 2.4) was isolated in 51% yield. ^{1}H NMR (acetone-d_6, 400 MHz): δ = 1.30 (6H, s), 1.43 (6H, s), 2.59 (6H, s), 5.96−5.99 (2H, d, J = 10.4 Hz), 6.34−6.37 (2H, d, J = 9.00 Hz), 6.87− 6.90 (2H, d, J = 8.18 Hz), 6.97−7.00 (2H, d, J = 8.25 Hz), 7.24−7.28 (2H, d, J = 10.4 Hz), 7.59−7.54 (2H, dd, J = 2.77 and 9.01), 8.10 (2H, d, J = 2.73 Hz). FTIR (neat, cm^{-1}): 3556, 3076, 2976, 2934, 2873, 2258, 2162, 2040, 1980,

1895, 1654, 1614, 1572, 1513, 1473, 1447, 1435, 1397, 1363, 1336, 1274, 1255, 1232, 1179, 1148, 1126, 1088, 1062, 1022, 1001, 950, 923, 905, 863, 823, 799, 766, 747, 709, 697.

Preparation of 1′,1‴,3′,3′,3‴,3‴-hexamethyl-6,6″-dinitro-4′,4‴- di(pyridin-4-yl)-7′,7‴-bispiro[chromene-2,2′-indoline] ($C_{48}H_{40}N_6O_6$, HDDB, Scheme 2.4). Using a Schlenk technique, 20 mL of dry DMF was transferred to a flask containing **VII′** (336 mg, 420 μmol, Scheme 2.4), Na_2CO_3 (84.0 mg, 793 μmol), $PdCl_2(PPh_3)_2$ (47.0 mg, 670 μmol), CuCl (168 mg, 1.69 mmol), and pyridine-4-boronic acid (206 mg, 1.68 mmol). The resulting mixture was stirred for 2 days at 120 °C. After cooling to room temperature, the reaction mixture was transferred in a 250 mL separatory funnel, following dilution with deionized water (75 mL). The product was then extracted with ethyl acetate (3 × 50 mL). The organic layers were combined, washed with brine (50 mL), and dried over sodium sulfate, followed by filtration and solvent removal under vacuum. The obtained red/brown oil was recrystallized several times using ethyl acetate and hexanes. The resulting orange powder was dissolved in ethyl acetate (20 mL) and hexanes (30 mL), and the solvent was removed under vacuum until a suspension formed. The suspension was filtered to collect a light-tan powder. After drying on vacuum, HDDB (50.0 mg, 625 μmol) was isolated in 15% yield. In order to obtain crystals of a specific diastereomer of HDDB, it was subjected to preparatory TLC using a 5:95 (v/v) methanol/dichloromethane, in which the product was extracted with acetone followed by slow evaporation of the solvent overnight, and crystals of $HDDB_{in-in}$ were isolated. Single crystals of $HDDB_{in-out}$ were obtained from a solution of HDDB in 50:50 (v/v) ethyl acetate/hexanes that had been cooled to 0 °C for several days. The detailed description for the crystallographic data collection and refinement

details are given in the experimental section (Table 2.4). The determined structure of $HDDB_{in-out}$ and $HDDB_{in-in}$ are shown in Figure 2.13. ^{1}H NMR (dichloromethane-d_2, 400 MHz): δ = 0.74 (1H, s), 1.24 (6H, s), 2.58 (6H, s), 5.79−5.83 (2H, d, J = 10.5 Hz), 6.23−6.26 (2H, d, J = 9.06 Hz), 6.55−6.58 (2H, d, J = 7.81 Hz), 6.93−6.96 (2H, d, J = 10.7 Hz), 7.05−7.08 (2H, d, J = 7.91 Hz), 7.29−7.31 (4H, d, J = 5.81 Hz), 7.52−7.57 (2H, dd, J = 2.70, 8.99 Hz), 7.94−7.95 (2H, d, J = 2.69 Hz), 8.58−8.60 (2H, d, J = 5.23 Hz) ppm (Figure 2.14). ^{13}C NMR (acetone-d_6, 400 MHz): δ = 21.00, 25.65, 31.66, 52.51, 108.23, 114.92, 118.80, 120.65, 120.89, 121.17, 122.99, 125.13, 125.64, 129.69, 131.38, 132.90, 136,40, 141.08, 145.72, 149.54, 160.00 ppm (Figure 2.14). FTIR (neat, cm^{-1}): 3327, 2972, 2934, 2364, 2343, 2288, 2191, 2150, 2043, 1984, 1920, 1648, 1613, 1594, 1576, 1519, 1467, 1386, 1340, 1282, 1230, 1180, 1149, 1125, 1090, 1074, 1059, 1020, 951, 928, 906, 833, 803, 747, 706, 682, 661 (Figure 2.19). HRMS (ESI, m/z) calculated for $C_{48}H_{40}N_6O_6$ $[M + H]^+$ 797.3088, found 797.3094.

Preparation of 1 ($Zn_2C_{63}H_{40}N_4O_{11}Br_2$, Zn_2(DBTD)(TNDS)). MOF **1** was prepared using a slightly modified literature procedure.[109] In a one-dram vial, $Zn(NO_3)_2 \cdot 6H_2O$ (18 mg, 59 μmol), H_4DBTD (5.4 mg, 7.5 μmol), and TNDS (5.0 mg, 10.5 μmol) were dissolved in 0.8 mL of DMF with 0.1 μL of HCl, followed by sonication. The resulting solution was placed in a preheated oven at 80 °C for 24 hours, then cooled down to room temperature over 2 hours. Red almond-shaped crystals of **1** (13.1 mg, 9.4 μmol) were isolated in 90% yield. The detailed description for the crystallographic data collection and refinement details are given in the experimental section (Table 2.5). The determined structure of **1** is shown in Figure 2.15. FTIR (neat, cm^{-1}): 3445, 3069, 2931, 2880, 1642, 1609, 1558, 1495, 1460, 1435, 1385, 1338, 1275, 1255, 1220, 1178, 1151, 1092 (Figure

2.16). The PXRD pattern of **1** is shown in Figure 2.16. The ^{1}H NMR spectra and mass-spectrometry data of digested **1** are shown in Figure 2.17. The experimental procedure utilized for MOF digestion can be found in the SI.

Preparation of 2 ($Zn_2C_{82}H_{56}N_6O_{14}Br_2$, Zn_2(DBTD)(HDDB)). MOF **2** was prepared using a slightly modified literature procedure.[29] In a one-dram vial, $Zn(NO_3)_2 \cdot 6H_2O$ (8.8 mg, 30 μmol), H_4DBTD (2.5 mg, 3.5 μmol), and HDDB (4.8 mg, 6.0 μmol) were dissolved in 1 mL of DMF and 0.2 μL of HBF_4, followed by sonication. The resulting solution was placed in a preheated oven at 85 °C for 18 hours, then cooled down to room temperature over 2 hours. Deep red oval plate crystals of **2** (9.6 mg, 5.8 μmol) were isolated in 97% yield. The detailed description for the crystallographic data collection and refinement details are given below (Table 2.5). The determined structure of **2** is shown in Figure 2.18. FTIR (neat, cm^{-1}): 3450, 2934, 2870, 1660, 1558, 1463, 1436, 1385, 1337, 1316, 1274, 1255, 1221, 1178, 1152, 1090 (Figure 2.19). PXRD pattern and $^{13}C\{^{1}H\}$ CP-MAS NMR spectrum of **2** are shown in Figures 2.19 and 2.20, respectively.

Preparation of 3 ($Zn_2C_{59}H_{44}N_2O_8Br_2$, Zn_2(DBTD)(BPMTC)). MOF **3** was prepared using a slightly modified literature procedure.[29] In a one- dram vial, $Zn(NO_3)_2 \cdot 6H_2O$ (35.0 mg, 120 μmol), H_4DBTD (10.0 mg, 13.9 μmol), and BPMTC (9.0 mg, 22 μmol) were dissolved in a solution of 2 mL of DMF and one drop of HBF_4, followed by sonication. The resulting solution was placed in a preheated oven at 85 °C for 18 hours, then cooled down to room temperature over 2 hours. Colorless plate crystals of **3** (13 mg, 10 μmol) were isolated in 75% yield. FTIR (neat, cm^{-1}): 3485, 3067, 2925, 2870, 1665, 1639, 1610, 1556, 1502, 1435, 1385, 1255, 1222, 1177, 1150, 1091 The PXRD pattern of

3 is shown in Figure 2.21. The ^{1}H NMR spectra and mass spectrometry data of digested **3** are shown in Figure 2.22.

Preparation of 3′ ($Zn_2C_{53}H_{30}N_2O_4S_2$, $Zn_2(BPDC)_2(BPMTC)$). In a 20 mL vial, $Zn(NO_3)_2{\cdot}6H_2O$ (7.0 mg, 24 μmol), H_2BPDC (6.0 mg, 25 μmol), and BPMTC (10 mg, 24 μmol) were dissolved in a solution of 2 mL of DMF, followed by sonication. The resulting solution was heated at 110 °C in an isothermal oven. After 24 hours, the reaction mixture was cooled down to room temperature over 2 hours. Light brown rectangular block crystals of **3′** (9.2 mg, 8.9 μmol) were isolated in 74% yield. The detailed description for the crystallographic data collection and refinement details are given below (Table 2.5). The determined structure of **3′** is shown in Figure 2.23. FTIR (neat, cm^{-1}): 3410, 3080, 2932, 2866, 1660, 1604, 1545, 1500, 1384, 1253, 1176, 1140, 1095, 1080, 1022, 1005, 859, 840, 800, 770, 704, 681, 660 (Figure 2.24). The PXRD pattern of **3′** is shown in Figure 2.24.

Preparation of 4 ($Zr_6C_{81}H_{78}O_{34}S_2$, $Zr_6(Me_2BPDC)_4(BCMTC)_{0.5}$). MOF **4** was prepared using a modified synthetic route.[96] Crystals of $Zr_6(Me_2BPDC)_4$ (30 mg, 16 μmol) were added to solution of H_2BCMTC (42 mg, 0.12 mmol) in 4 mL of DMF in a one-dram vial. The vial was placed in a preheated oven at 75 °C for 24 hours, then cooled to room temperature over 2 hours. Light tan crystals of **4** (35 mg, 14 μmol) were isolated in 64% yield. FTIR (neat, cm^{-1}): 3450, 2935, 2855, 1657, 1586, 1544, 149,5 1411, 1384, 1255, 1208, 1139, 1091. The PXRD pattern of **4** is shown in Figure 2.26. The ^{1}H NMR spectra of digested **4** is shown in Figure 2.27.

UV-vis, diffuse reflectance, and fluorescence spectroscopies. Steady-state emission spectra were acquired on an Edinburgh FS5 fluorescence spectrometer equipped with a 150 W continuous wave xenon lamp source for excitation. Emission measurements

on solid samples were collected on the powders of the appropriate materials placed inside a 0.5 mm quartz sample holder using the front- facing module. The Ocean Optics JAZ spectrometer was also used for absorbance and diffuse reflectance measurements. An Ocean Optics ISP-REF integrating sphere was connected to the spectrometer using a 450 μm SMA fiber optic cable. A 400 nm long pass filter was placed between an 8.0 mm quartz sample cell with cover and the integrating sphere to filter any UV light from the internal tungsten−halogen lamp. An Ocean Optics WS-1 Spectralon® reflectance standard was placed on the sample cell throughout the measurements. A mounted high- powered LED (M365L2, Thorlabs), λ = 365 nm, was used for in situ irradiation of the samples. Before time-resolved UV−vis and diffuse reflectance measurements, the sample background was subtracted to obtain the spectra corresponding to photophysical behavior of the photochromic derivatives.

^{13}C CP-MAS NMR spectroscopy. Solid-state NMR spectra (^{13}C CP-MAS) were collected on a Bruker Avance III-HD 500 MHz spectrometer fitted with a 1.9 mm MAS probe. ^{13}C{^{1}H} CP-MAS NMR spectra (125.79 MHz) were collected at ambient temperature with a sample rotation rate of 20 kHz. For cross-polarization, 2.0 ms contact time with linear ramping on the ^{1}H channel and 62.5 kHz field on the ^{13}C channel were used. ^{1}H dipolar decoupling was performed with SPINAL64 modulation and 147 kHz field strength. Free induction decays (2048−5000 transients) were collected with a 27 ms acquisition time over a 400 ppm spectra width with a relaxation delay of 2.0 s.

Other physical measurements. FTIR spectra were obtained on a PerkinElmer Spectrum 100. NMR spectra were collected on Bruker Avance III-HD 300 and Bruker Avance III 400 MHz NMR spectrometers. ^{13}C and ^{1}H NMR spectra were referenced to

natural abundance ^{13}C peaks and residual ^{1}H peaks of deuterated solvents, respectively. Powder X-ray diffraction patterns were recorded on a Rigaku Miniflex II diffractometer with accelerating voltage and current of 30 kV and 15 mA, respectively. The Waters QTOF-I quadrupole time-of-flight and Thermo Scientific Orbitrap Velos Pro mass spectrometers were used to record the mass spectra of the prepared compounds.

X-ray crystal structure determination for VI ($C_{19}H_{16}Br_2N_2O_3$, Scheme 2.3). X-ray intensity data from a pale-yellow parallelogram-shaped plate were collected at 100(2) K using a Bruker D8 QUEST diffractometer equipped with a PHOTON-100 CMOS area detector and an Incoatec microfocus source (Mo Kα radiation, λ = 0.71073 Å). The raw area detector data frames were reduced and corrected for absorption effects using the Bruker APEX3, SAINT+ and SADABS programs.[111,112] Final unit cell parameters were determined by least-squares refinement of 9121 reflections taken from the data set. The structure was solved with SHELXT.[113] Subsequent difference Fourier calculations and full-matrix least-squares refinement against F^2 were performed with SHELXL-2016[113] using OLEX2.[114]

The compound crystallizes in the monoclinic system. The pattern of systematic absences in the intensity data was consistent with the space group $P2_1/c$. The structure solution revealed two apparent crystallographically independent, chemically similar molecules in the asymmetric unit. One is fully ordered and refines normally. This molecule was given atom label suffixes "A". The second independent molecule shows similar geometry, but if refined with a single position shows highly elongated anisotropic displacement parameters and large residual electron density peaks among the atoms. This second molecule exhibits whole-molecule disorder. Obtaining a satisfactory disorder

model was difficult owing to the large number of atoms which appear nearly superimposed and only a relative few which are not. Eventually a disorder model consisting of three discrete components was successfully refined. The components were given atom label suffixes B, C, and D. The total site population was constrained to sum to 100%, and the disorder populations fractions refined to B/C/D = 0.366(3)/0.276(3)/0.358(3). A large array of geometric restraints was necessary for stability and chemical reasonableness. The 1,2- and 1,3-distances of all three disorder components were restrained to be similar to those of molecule "A" using SHELX SAME restraints. The planar parts of the molecule were further restrained with FLAT instructions (C3–C8 and N2/C12–C19). The anisotropic displacement parameters of atoms which are nearly superimposed in the asymmetric unit (*e.g.*, C1 B–D) were held equal, and some triplets of atoms were further restrained with isotropic approximation restraints (SHELX ISOR instructions, atoms C19 B/C/D and C3C/C8B/C8D). All non-hydrogen atoms were refined with anisotropic displacement parameters. Hydrogen atoms bonded to carbon were located in Fourier difference maps before being placed in geometrically idealized positions and included as riding atoms with d(C–H) = 0.95 Å and U_{iso}(H) = 1.2U_{eq}(C) for aromatic hydrogen atoms and d(C–H) = 0.98 Å and U_{iso}(H) = 1.5U_{eq}(C) for methyl hydrogens. The methyl hydrogens were allowed to rotate as a rigid group to the orientation of maximum observed electron density. The largest residual electron density peak in the final difference map is 0.66 e/Å^3, located 0.73 Å from Br2A. Trial refinement models in alternative space groups such as $P2_1$, Pc, $P2/c$ and also in $P1$ also showed similar whole-molecule disorder, and it is therefore concluded that the crystal is best described as having a disordered structure in space group $P2_1/c$ as described above. The refinement data are given in Table 2.3.

X-ray crystal structure determination for TNDS ($C_{29}H_{24}N_4O_3$). X-ray intensity data from a colorless plate were collected at 100(2) K using a Bruker D8 QUEST diffractometer equipped with a PHOTON-100 CMOS area detector and an Incoatec microfocus source (Mo Kα radiation, λ = 0.71073 Å). The raw area detector data frames were reduced and corrected for absorption effects using the Bruker APEX3, SAINT+ and SADABS programs.[111,112] Final unit cell parameters were determined by least-squares refinement of 9170 reflections taken from the data set. The structure was solved with SHELXT.[113] Subsequent difference Fourier calculations and full-matrix least-squares refinement against F^2 were performed with SHELXL-2016[113] using OLEX2.[114]

The compound crystallizes in the triclinic system. The space group *P*-1 was confirmed by structure solution. The asymmetric unit consists of one molecule. All non-hydrogen atoms were refined with anisotropic displacement parameters. Hydrogen atoms bonded to carbon were located in Fourier difference maps before being placed in geometrically idealized positions and included as riding atoms with d(C-H) = 0.95 Å and U_{iso}(H) = 1.2U_{eq}(C) for aromatic hydrogen atoms and d(C–H) = 0.98 Å and U_{iso}(H) = 1.5U_{eq}(C) for methyl hydrogens. The methyl hydrogens were allowed to rotate as a rigid group to the orientation of maximum observed electron density. The largest residual electron density peak in the final difference map is 0.28 e/Å^3, located 0.78 Å from C14. The refinement data are given in Table 2.3.

X-ray crystal structure determination for VII' ($C_{38}H_{32}Br_2N_4O_6$, Scheme 2.4). X-ray intensity data from a colorless block were collected at 100(2) K using a Bruker D8 QUEST diffractometer equipped with a PHOTON 100 CMOS area detector and an Incoatec microfocus source (Mo Kα radiation, λ = 0.71073 Å).[111] The raw area detector

data frames were reduced and corrected for absorption effects using the SAINT+ and SADABS programs.[111] Final unit cell parameters were determined by least-squares refinement of 9985 reflections taken from the data set. The structure was solved by direct methods with SHELXT.[112] Subsequent difference Fourier calculations and full-matrix least-squares refinement against F^2 were performed with SHELXL-2014[113] using OLEX2.[114]

The compound crystallizes in the monoclinic system. The pattern of systematic absences in the intensity data was consistent with the space group $P2_1/c$, which was confirmed by structure solution. The asymmetric unit consists of one $C_{38}H_{32}Br_2N_4O_6$ molecule and a region of heavily disordered solvent species. All non-hydrogen atoms of the $C_{38}H_{32}Br_2N_4O_6$ molecule were refined with anisotropic displacement parameters. Hydrogen atoms were located in Fourier difference maps before being placed in geometrically idealized positions and included as riding atoms with d(C–H) = 1.00 Å and U_{iso}(H) = 1.2U_{eq}(C) for methine hydrogen atoms and U_{iso}(H) = 1.5U_{eq}(C) for methyl hydrogens. The methyl hydrogens were allowed to rotate as a rigid group to the orientation of maximum observed electron density. After identification of the $C_{38}H_{32}Br_2N_4O_6$ molecule, many large residual electron density peaks remained in a volume centered at (0,0,½). These arise from severely disordered solvent molecules. No stable and reasonable disorder model could be achieved despite much effort. From the disorder modeling efforts, the solvent species are likely a mixture of hexane and methylene chloride. The contribution of these diffusely scattering species to the structure factors was therefore accounted for with the Squeeze program.[114] Squeeze calculated a solvent-accessible volume of 809 Å^3 (21% of the total unit cell volume), corresponding to 230 electrons per unit cell. The

reported F.W. and *d*(calc) are computed from known unit cell contents only. The largest residual electron density peak in the final difference map is 1.18 e/Å^3, located 0.93 Å from H10B. The refinement data are given in Table 2.4.

X-ray crystal structure determination for HDDB$_{in–in}$, ($C_{48}H_{40}N_6O_6$). X-ray intensity data from a pale green tablet were collected at 100(2) K using a Bruker D8 QUEST diffractometer equipped with a PHOTON-100 CMOS area detector and an Incoatec microfocus source (Mo Kα radiation, λ = 0.71073 Å). The raw area detector data frames were reduced and corrected for absorption effects using the Bruker APEX3, SAINT+ and SADABS programs.[111,112] Final unit cell parameters were determined by least-squares refinement of 9008 reflections taken from the data set. The structure was solved with SHELXT.[113] Subsequent difference Fourier calculations and full-matrix least-squares refinement against F^2 were performed with SHELXL-2016[113] using OLEX2.[114]

The compound crystallizes in the monoclinic system. The pattern of systematic absences in the intensity data was consistent with the space group $P2_1/c$, which was confirmed by structure solution. The asymmetric unit consists of one molecule. All non-hydrogen atoms were refined with anisotropic displacement parameters. Hydrogen atoms bonded to carbon were located in Fourier difference maps before being placed in geometrically idealized positions and included as isotropically refined riding atoms with *d*(C–H) = 0.95 Å for aromatic and *d*(C–H) = 0.98 Å for methyl hydrogens. The methyl hydrogens were allowed to rotate as a rigid group to the orientation of maximum observed electron density. The largest residual electron density peak in the final difference map is 0.27 e/Å^3, located 0.76 Å from C22. The refinement data are given in Table 2.4.

X-ray crystal structure determination for $HDDB_{in–out}$ ($C_{48}H_{40}N_6O_6$). Crystals of the compound grew as densely intergrown light brown aggregations. Difficulty was encountered in cleaving apart a predominantly single domain of suitable size for intensity measurements. Eventually a fragment giving a diffraction pattern largely free of multiple maxima and diffuse streaking was found. X-ray intensity data were collected at 100(2) K using a Bruker D8 QUEST diffractometer equipped with a PHOTON-100 CMOS area detector and an Incoatec microfocus source (Mo Kα radiation, λ = 0.71073 Å). Strong low-angle peaks were observed, but reflection intensity decreased rapidly with θ. No appreciable scattering was observed above $2\theta_{max}$ of ~46°. Longer scan times (>60s/°) simply increased the number of low-angle reflections which were beyond the measurement range of the area detector and thereby required a higher speed re- scan. Analysis of the intensity statistics using the Bruker XPREP program showed the mean reflection $I/\sigma(I)$ fell below 2.0 in the d = 0.90–0.88 Å shell, where also the $R(\sigma)$ value rose to greater than 0.50 ($R(\sigma) = \Sigma[\sigma(F_{obs}^2)]/\Sigma[F_{obs}^2]$). Data were truncated at 2θ = 0.90 Å ($2\theta_{max}$ = 46.5°) for this reason. The raw area detector data frames were reduced and corrected for absorption effects using the Bruker APEX3, SAINT+ and SADABS programs.[111,112] Final unit cell parameters were determined by least-squares refinement of 9672 reflections taken from the data set. The structure was solved with SHELXT.[113] Subsequent difference Fourier calculations and full-matrix least-squares refinement against F^2 were performed with SHELXL-2016[113] using OLEX2.[114]

The compound crystallizes in the monoclinic system. The pattern of systematic absences in the intensity data was consistent with the space group $P2_1/c$, which was verified by structure solution. The asymmetric unit consists of two crystallographically independent

$C_{48}H_{40}N_6O_6$ molecules, one ethyl acetate molecule and a region of disordered and unidentified solvent peaks. The two $C_{48}H_{40}N_6O_6$ molecules were numbered identically except for label suffixes A or B. Efforts to model the solvent disorder were unsuccessful. Some solvents peaks are relatively isolated, suggesting a mixture of water molecules and ethyl acetate. The Squeeze program in PLATON was used to account for these species. solvent-accessible volume was calculated to be 398 $Å^3$ per unit cell (5% of the total cell volume), containing the equivalent of 80 electrons per unit cell. The scattering contribution of this electron density was added to the structure factors computed from the known part of the structure during refinement. For comparison, the residual factors were R_1/wR_2 = 0.085/0.245 for the best disorder model, and R_1/wR_2 = 0.0813/0.2322 after Squeeze. The reported crystal density and *F.W*. are calculated from the known part of the structure only. All non-hydrogen atoms were refined with anisotropic displacement parameters. Hydrogen atoms bonded to carbon were located in Fourier difference maps before being placed in geometrically idealized positions and included as riding atoms with *d*(C–H) = 0.95 Å and *U*iso(H) = 1.2*U*eq(C) for aromatic hydrogen atoms, *d*(C–H) = 0.99 Å and *U*iso(H) = 1.2*U*eq(C) for methylene hydrogen atoms, and *d*(C–H) = 0.98 Å and *U*iso(H) = 1.5*U*eq(C) for methyl hydrogens. The methyl hydrogens were allowed to rotate as a rigid group to the orientation of maximum observed electron density. The largest residual electron density peak in the final difference map is 0.68 e/$Å^3$, located 0.62 Å from H4SB, near the ethyl acetate molecule. The refinement data are given in Table 2.4.

X-ray crystal structure determination for MOF 1, Zn_2(DBTD)(TNDS) ($C_{50}H_{24}Br_2N_2O_8Zn_2$). X-ray intensity data from a red almond- shaped plate were collected at 220(2) K using a Bruker D8 QUEST diffractometer equipped with a PHOTON-100

CMOS area detector and an Incoatec microfocus source (Mo Kα radiation, $\lambda = 0.71073$ Å). The crystals develop cracks and lose crystallinity in air and under oil. Diffraction pattern quality at 100 K was inferior to those at higher temperatures, showing broader maxima and stronger diffuse streaking. Diffraction intensities fell off rapidly with θ. The dataset was truncated at $d = 0.98$ Å, at which point the mean reflection $I/\sigma(I)$ was less than 2.0. The raw area detector data frames were reduced and corrected for absorption effects using the Bruker APEX3, SAINT+ and SADABS programs.[111,112] Final unit cell parameters were determined by least-squares refinement of 2965 reflections taken from the data set. The structure was solved with SHELXT.[113,117] Subsequent difference Fourier calculations and full-matrix least-squares refinement against F_2 were performed with SHELXL-2017[113] using OLEX2.[114]

The compound crystallizes in the space group *Pmmm* of the orthorhombic system. It is structurally similar to previously reported compounds.[118] The asymmetric unit consists of ¼ of a Zn atom, ¼ of one $C_{34}H_{16}Br_2O_8$ cross-linking ligand, ¼ of one $C_{29}H_{24}N_4O_3$ pillar ligand and a large volume of unidentified disordered solvent guest molecules. The unique pyridyl ring and the central phenyl ring of the $C_{29}H_{24}N_4O_3$ pillar are disordered across mirror planes. The -$C_{13}H_{14}N_2O_3$ substituent of the central phenyl ring of the pillar could not be crystallographically located. It is presumably bonded to C15/C15* and is therefore disordered over four symmetry-equivalent positions and contributes too weakly to the structure factors to be reasonably located. The largest electron density peak in this region was 0.43 e/Å^3, located 1.97 Å from C15, and could not be modeled as part of the -$C_{13}H_{14}N_2O_3$ substituent. For the final refinement cycles, C15 was left 'naked', with no substituent. Enhanced rigid-bond restraints were applied to the U_{ij} values of all atoms

(SHELX RIGU). Additional spherical restraints (ISOR) were applied to the displacement ellipsoids of atoms C6 and C7. The disordered interstitial solvent species could not be reasonably modeled. Their contribution to the structure factors was accounted for using the Squeeze technique. The contribution of the unlocated -$C_{13}H_{14}N_2O_3$ substituent atoms was also accounted for with Squeeze.[5,6] The solvent-accessible volume was calculated to be 2394 Å^3 (73% of the total unit cell volume), containing the scattering equivalent of 420 electrons per unit cell. The reported formula and *F.W.* reflect the expected framework atoms with the complete $C_{29}H_{24}N_4O_3$ pillar but not the unknown solvent content. All non-hydrogen atoms were refined with anisotropic displacement parameters. Hydrogen atoms bonded to carbon were placed in geometrically idealized positions and included as riding atoms with d(C-H) = 0.9 Å and U_{iso}(H) = 1.2U_{eq}(C). The largest residual electron density peak in the final difference map is 0.73 e/Å^3, located 1.20 Å from Zn1. The refinement data are given in Table 2.5.

X-ray crystal structure determination for MOF 2, Zn_2(DBTD)(HDDB), ($C_{82}H_{56}N_6O_{14}Zn_2Br_2$). X-ray intensity data from a deep red oval plate were collected at 220(2) K using a Bruker D8 QUEST diffractometer equipped with a PHOTON-100 CMOS area detector and an Incoatec microfocus source (Mo Kα radiation, λ = 0.71073 Å). The raw area detector data frames were reduced and corrected for absorption effects using the Bruker APEX3, SAINT+ and SADABS programs.[1,2] The diffraction pattern was characterized by broad maxima and pronounced diffuse streaking. Diffraction intensities fell off rapidly with θ. The dataset was truncated at d = 0.98 Å, at which point the mean reflection $I/\sigma(I)$ was less than 1.7. Final unit cell parameters were determined by least-squares refinement of 5853 reflections taken from the data set. The structure was solved

with SHELXT.[3,7] Subsequent difference Fourier calculations and full-matrix least-squares refinement against F^2 were performed with SHELXL-20173 using OLEX2.[4]

The compound crystallizes in the space group *Pmmm* of the orthorhombic system. It is structurally similar to previously reported compounds.[9] The asymmetric unit consists of ¼ of a Zn atom, ¼ of one $C_{34}H_{16}Br_2O_8$ cross-linking ligand, ¼ of one $C_{48}H_{40}N_6O_6$ pillar ligand and a large volume of unidentified disordered solvent guest molecules. The unique pyridyl ring and the central phenyl ring of the $C_{48}H_{40}N_6O_6$ pillar are disordered across mirror planes. The two -$C_{13}H_{14}N_2O_3$ substituents of the two central phenyl rings of the pillar could not be crystallographically located. They are presumably attached at carbon atom sites C15/C16 and are therefore each disordered over four symmetry-equivalent positions. The substituents apparently contribute too weakly to the structure factors to be reasonably located. The largest electron density peak in this region was 0.25 e/Å^3, located > 2 Å from C16, and could not be modeled as part of a -$C_{13}H_{14}N_2O_3$ substituent. For the final refinement cycles, C15 and C16 were left 'naked', with no substituent. Appropriate C–C and C–N distance (DFIX) restraints were applied to the disordered groups. The independent parts of the disordered pyridyl and phenyl rings were restrained with a FLAT instruction. Disordered carbon atoms were refined isotropically. All other non-hydrogen atoms were refined with anisotropic displacement parameters. Spherical restraints (ISOR) were applied to the displacement ellipsoids of atoms C5, C6, and C7. The disordered interstitial solvent species could not be reasonably modeled. The contribution of these diffusely scattering species to the structure factors was accounted for using the Squeeze technique.[5,6] The contribution of the two unlocated -$C_{13}H_{14}N_2O_3$ substituent groups was also accounted for with Squeeze. The solvent-accessible volume was calculated to be 3031

Å^3 (76% of the total unit cell volume), containing the scattering equivalent of 453 electrons per unit cell. The reported formula and *F.W.* reflect the expected framework atoms with the complete di-substituted $C_{48}H_{40}N_6O_6$ pillar but not the unknown solvent content. Hydrogen atoms were placed in geometrically idealized positions and included as riding atoms d(C–H) = 0.95 Å and U_{iso}(H) = 1.2U_{eq}(C). The largest residual electron density peak in the final difference map is 1.12 e/Å^3, located 1.24 Å from Zn1. The refinement data are given in Table 2.5.

X-ray crystal structure determination for MOF 3', $Zn_2(BPDC)_2(BPMTC)$, ($C_{53}H_{30}N_2O_4S_2Zn_2$). X-ray intensity data from a light brown rectangular block were collected at 100(2) K using a Bruker D8 QUEST diffractometer equipped with a PHOTON-100 CMOS area detector and an Incoatec microfocus source (Mo Kα radiation, λ = 0.71073 Å). The raw area detector data frames were reduced and corrected for absorption effects using the Bruker APEX3, SAINT+, and SADABS programs.[1,2] Final unit cell parameters were determined by least-squares refinement of 9798 reflections taken from the data set. The structure was solved with SHELXT.[3] Subsequent difference Fourier calculations and full-matrix least-squares refinement against F^2 were performed with SHELXL-2017[3] using OLEX2.[4]

The compound crystallizes in the monoclinic system. The pattern of systematic absences in the intensity data was consistent with the space groups *C*2, *C*m and *C*2/*m*. The solution program SHELXT identified *C*2 as the correct space group, which was confirmed by obtaining a stable and sensible refinement. The final model was checked with the ADDSYM program, which found no missed symmetry elements.[5] The asymmetric unit in *C*2 consists of two independent [$Zn_2(C_{14}H_8O_4)_2(C_{25}H_{22}N_2S_2)$] networks and a large

interstitial volume of disordered solvent species. One of the two networks consists of two independent zinc atoms (Zn1/Zn2), one $C_{25}H_{22}N_2S_2$ ligand and two independent $C_{14}H_8O_4$ ligands. The second network consists of one zinc atom (Zn3), half of one $C_{25}H_{22}N_2S_2$ ligand and one $C_{14}H_8O_4$ ligand. The Zn3/Zn3* dimer and the half-$C_{25}H_{22}N_2S_2$ ligand are located on two-fold axes of rotation. Atom C38 of the five-membered ring of this ligand (C36/C37/C38/C37*/C36*) is disordered about the two-fold and was refined with half-occupancy. Anisotropic displacement parameter restraints (DELU and ISOR) were applied to atoms C36, C37, and C38. The C-C distances in this ring were restrained to be similar to like bonds in the ordered ring C11–C15 (SHELX SADI) or were restrained to d(C–C) = 1.54(1) Å (DFIX). No satisfactory disorder model could be achieved for the interstitial species. Trial modeling attempts suggest a mixture of DMF and other unknown solvents, likely water. The Squeeze program in PLATON was used to account for these species.[6] The solvent-accessible volume was calculated to be 4064 $Å^3$ per unit cell (40.7% of the total cell volume), containing the equivalent of 846 electrons per unit cell. The scattering contribution of this diffuse electron density was added to the structure factors computed from the known part of the structure during refinement. The reported crystal density and *F.W.* are calculated from the known part of the structure only. All non-hydrogen atoms were refined with anisotropic displacement parameters. Hydrogen atoms bonded to carbon were located in Fourier difference maps before being placed in geometrically idealized positions and included as riding atoms with d(C–H) = 0.95 Å and U_{iso}(H) = 1.2U_{eq}(C) for aromatic hydrogen atoms and d(C–H) = 0.99 Å and U_{iso}(H) = 1.2U_{eq}(C) for methylene hydrogen atoms. The largest residual electron density peak in the final difference map is 0.28 e/$Å^3$, located 0.83 Å from O12. The absolute structure (Flack) parameter was 0.20(1),

indicating the crystal was an inversion twin. An inversion matrix was included in the final refinement cycles with the Flack parameter as the minor twin volume fraction. The refinement data are given in Table 2.5.

General digestion procedure. In order to study the prepared MOFs by ^{1}H NMR spectroscopy and mass-spectrometry, a solution of 500 μL of DMSO-d_6 and 3 μL of concentrated HCl (or DCl for **1**) was added to 5 mg of material, followed by sonication and heating until complete sample dissolution. In the case of **4**, the percent linker installation was calculated based on linker ratios found in the ^{1}H NMR spectra of the digested samples. The amount of linker installation can be calculated from geometrical analysis of the parent MOF structure and length of the installed linker as shown by Zhou and co-workers.[10] Thus, in combination with experimental spectroscopic studies, the geometrical constraints placing by the linker size and pocket dimension of the framework suggest that the capping linker can occupy both axial and equatorial positions of Zr-nodes, ca. 50% occupancy of available sites.

General procedure for photophysical measurements. For solution studies, a 3 mM solution of a photoswitch was loaded into a 8 mm × 1 mm front-facing quartz sample cell. For solid-state studies, 4 μmol of photoswitch was mixed with 100 mg potassium bromide, which was then pressed into the same 8-mm sample cell. The materials were irradiated with a high-powered LED (λ = 365 nm), without moving the sample cell until a sufficient absorption was measured (0.05 a.u). For consistency, upon reaching an absorption of = 0.05 a.u., the LED was shut off, and then the sample was irradiated with visible light from a tungsten-halogen lamp incorporated inside the ISP-REF Ocean Optics

integrating sphere (the corresponding filters were applied). Absorption data was collected as a function of time.

Derivation of rate constants from the NMR data. The thermal equilibration of three diastereomers of HDDB in solution was studied according to the reversible cyclic reaction scheme involving six first-order reactions with rate constants k_1, k_{-1}, k_2, k_{-2}, k_3, and k_{-3}.[11,12] Changes in concentrations of different isomers are governed by the three differential equations (see the main text) with six parameters (k_1, k_2, k_3, k_{-1}, k_{-2}, and k_{-3}). The exact solution of the equation for any particular set of values k_1, k_2, k_3, k_{-1}, k_{-2}, k_{-3} is found by the MATLAB function "*ode45*." Then function "*fminsearch*" was used to minimize the mean sum of squares of distances between the experimental dataset and the corresponding values of the exact solution. We also employed the following method to reduce dimensionality of the problem (see the main text). Without the dimensionality reduction, the differential equation yields to the same solutions on certain subspaces of the six-dimensional space of parameters k_1, k_2, k_3, k_{-1}, k_{-2}, and k_{-3}. Therefore, the chosen loss function (mean sum of squares of distances) has the same value on these subspaces, which makes it impossible to obtain the correct values of the parameters by minimizing the loss function. After this step is taken we found that the function "*fminsearch*" with the initial values of k_1, k_2, and k_3 that are between 0 and 1 and are not close to zero and tends to yield to approximately the same final values of the parameters (the values of the corresponding parameters coincide up to the third decimal place).

The obtained rate constants are in $CDCl_3$ were $k_1 = 0.214$, $k_{-1} = 0.122$, $k_2 = 0.228$, $k_{-2} = 0.402$, $k_3 = 0.481$, and $k_{-3} = 0.481$.

REFERENCES

[1] Brown, J. W.; Henderson, B. L.; Kiesz, M. D.; Whalley, A. C.; Morris, W.; Grunder, S.; Deng, H.; Furukawa, H.; Zink, J. I.; Stoddart, J. F.; Yaghi, O. M. *Chem. Sci.* **2013**, *4*, 2858−2864.

[2] Yanai, N.; Uemura, T.; Inoue, M.; Matsuda, R.; Fukushima, T.; Tsujimoto, M.; Isoda, S.; Kitagawa, S. *J. Am. Chem. Soc.* **2012**, *134*, 4501−4504.

[3] Tian, Z.; Wu, W.; Wan, W.; Li, A. D. Q. *J. Am. Chem. Soc.* **2011**, *133*, 16092−16100.

[4] Simeth, N. A.; Crespi, S.; Fagnoni, M.; König, B. *J. Am. Chem. Soc.* **2018**, *140*, 2940−2946.

[5] Kashihara, R.; Morimoto, M.; Ito, S.; Miyasaka, H.; Irie, M. *J. Am. Chem. Soc.* **2017**, *139*, 16498−16501.

[6] Liu, Z.; Wang, H. I.; Narita, A.; Chen, Q.; Mics, Z.; Turchinovich, D.; Klaüi, M.; Bonn, M.; Müllen, K. *J. Am. Chem. Soc.* **2017**, *139*, 9443−9446.

[7] Potisek, S. L.; Davis, D. A.; Sottos, N. R.; White, S. R.; Moore, J. S. *J. Am. Chem. Soc.* **2007**, *129*, 13808−13809.

[8] Xing, Q. J.; Li, N. J.; Chen, D. Y.; Sha, W. W.; Jiao, Y.; Qi, X. X.; Xu, Q. F.; Lu, J. M. *J. Mater. Chem. B* **2014**, *2*, 1182−1189.

[9] Cotí, K. K.; Belowich, M. E.; Liong, M.; Ambrogio, M. W.; Lau, Y. A.; Khatib, H. A.; Zink, J. I.; Khashab, N. M.; Stoddart, J. F. *Nanoscale* **2009**, *1*, 16−39.

[10] Bajpai, A. K.; Shukla, S. K.; Bhanu, S.; Kankane, S. Prog. *Polym. Sci.* **2008**, *33*, 1088−1118.

[11] Wilkinson, M.; Kafizas, A.; Bawaked, S. M.; Obaid, A. Y.; Al-Thabaiti, S. A.; Basahel, S. N.; Carmalt, C. J.; Parkin, I. P. *ACS Comb. Sci.* **2013**, *15*, 309−319.

[12] Liou, J.-C.; Teng, M.-C.; Tsai, Y.-S.; Lin, E.-C.; Chen, B.-Y. *Mol. Vis.* **2015**, *21*, 846−856.

[13] Sumi, T.; Takagi, Y.; Yagi, A.; Morimoto, M.; Irie, M. *Chem. Commun.* **2014**, *50*, 3928−3930.

[14] Szaciłowski, K. *Chem. Rev.* **2008**, *108*, 3481−3548.

[15] Wagner, K.; Byrne, R.; Zanoni, M.; Gambhir, S.; Dennany, L.; Breukers, R.; Higgins, M.; Wagner, P.; Diamond, D.; Wallace, G. G.; Officer, D. L. *J. Am. Chem. Soc.* **2011**, *133*, 5453−5462.

[16] Kumar, S.; Van Herpt, J. T.; Gengler, R. Y. N.; Feringa, B. L.; Rudolf, P.; Chiechi, R. C. *J. Am. Chem. Soc.* **2016**, *138*, 12519−12526.

[17] Zhu, L.; Zhu, M. Q.; Hurst, J. K.; Li, A. D. Q. *J. Am. Chem. Soc.* **2005**, *127*, 8968−8970.

[18] Williams, D. E.; Rietman, J. A.; Maier, J. M.; Tan, R.; Greytak, A. B.; Smith, M. D.; Krause, J. A.; Shustova, N. B. *J. Am. Chem. Soc.* **2014**, *136*, 11886−11889.

[19] Patel, D. G.; Walton, I. M.; Cox, J. M.; Gleason, C. J.; Butzer, D. R.; Benedict, J. B. *Chem. Commun.* **2014**, *50*, 2653−2656.

[20] Schulz-Senft, M.; Gates, P. J.; Sönnichsen, F. D.; Staubitz, A. *Dyes Pigm.* **2017**, *136*, 292−301.

[21] Irie, M. *Photochem. Photobiol. Sci.* **2010**, *9*, 1535−1542.

[22] Yaghi, O. M.; O'Keeffe, M.; Ockwig, N. W.; Chae, H. K.; Eddaoudi, M.; Kim, J. *Nature* **2003**, *423*, 705−714.

[23] Flaig, R. W.; Osborn Popp, T. M.; Fracaroli, A. M.; Kapustin, E. A.; Kalmutzki, M. J.; Altamimi, R. M.; Fathieh, F.; Reimer, J. A.; Yaghi, O. M. *J. Am. Chem. Soc.* **2017**, *139*, 12125−12128.

[24] Helal, A.; Yamani, Z. H.; Cordova, K. E.; Yaghi, O. M. *Natl. Sci. Rev.* **2017**, *4*, 296−298.

[25] Parent, L. R.; Pham, C. H.; Patterson, J. P.; Denny, M. S.; Cohen, S. M.; Gianneschi, N. C.; Paesani, F. *J. Am. Chem. Soc.* **2017**, *139*, 13973−13976.

[26] Rieth, A. J.; Dincă, M. *J. Am. Chem. Soc.* **2018**, *140*, 3461−3466.

[27] Ji, P.; Feng, X.; Veroneau, S. S.; Song, Y.; Lin, W. *J. Am. Chem. Soc.* **2017**, *139*, 15600−15603.

[28] Vogelsberg, C. S.; Uribe-Romo, F. J.; Lipton, A. S.; Yang, S.; Houk, K. N.; Brown, S.; Garcia-Garibay, M. A. *Proc. Natl. Acad. Sci. U. S. A.* **2017**, *114*, 13613−13618.

[29] Park, J.; Feng, D.; Yuan, S.; Zhou, H. C. *Angew. Chem., Int. Ed.* **2015**, *54*, 430−435.

[30] Liu, C.; Luo, T.-Y.; Feura, E. S.; Zhang, C.; Rosi, N. L. *J. Am. Chem. Soc.* **2015**, *137*, 10508−10511.

[31] Usov, P. M.; Huffman, B.; Epley, C. C.; Kessinger, M. C.; Zhu, J.; Maza, W. A.; Morris, A. J. *ACS Appl. Mater. Interfaces* **2017**, *9*, 33539−33543.

[32] Alsbaiee, A.; Smith, B. J.; Xiao, L.; Ling, Y.; Helbling, D. E.; Dichtel, W. R. *Nature* **2016**, *529*, 190−194.

[33] Whittemore, T. J.; White, T. A.; Turro, C. J. Am. Chem. Soc. 2018, 140, 229−234.

[34] Feng, L.; Yuan, S.; Zhang, L.-L.; Tan, K.; Li, J.-L.; Kirchon, A.; Liu, L.-M.; Zhang, P.; Han, Y.; Chabal, Y. J.; Zhou, H.-C. *J. Am. Chem. Soc.* **2018**, *140*, 2363−2372.

[35] Zhu, J.; Usov, P. M.; Xu, W.; Celis-Salazar, P. J.; Lin, S.; Kessinger, M. C.; Landaverde-Alvarado, C.; Cai, M.; May, A. M.; Slebodnick, C.; Zhu, D.; Senanayake, S. D.; Morris, A. J. *J. Am. Chem. Soc.* **2018**, *140*, 993−1003.

[36] Smith, M. K.; Jensen, K. E.; Pivak, P. A.; Mirica, K. A. *Chem. Mater.* **2016**, *28*, 5264−5268.

[37] Kim, H.; Yang, S.; Rao, S. R.; Narayanan, S.; Kapustin, E. A.; Furukawa, H.; Umans, A. S.; Yaghi, O. M.; Wang, E. N. *Science* **2017**, *356*, 430−434.

[38] Zhao, Y.; Lee, S. Y.; Becknell, N.; Yaghi, O. M.; Angell, C. A. *J. Am. Chem. Soc.* **2016**, *138*, 10818−10821.

[39] Li, B.; Cui, X.; O'Nolan, D.; Wen, H.-M.; Jiang, M.; Krishna, R.; Wu, H.; Lin, R.-B.; Chen, Y.-S.; Yuan, D.; Xing, H.; Zhou, W.; Ren, Q.; Qian, G.; Zaworotko, M.; Chen, B. *Adv. Mater.* **2017**, *29*, 1704210.

[40] Lin, Z.; Thacker, N. C.; Sawano, T.; Drake, T.; Ji, P.; Lan, G.; Cao, L.; Liu, S.; Wang, C.; Lin, W. *Chem. Sci.* **2018**, *9*, 143−151.

[41] Yuan, S.; Feng, L.; Wang, K.; Pang, J.; Bosch, M.; Lollar, C.; Sun, Y.; Qin, J.; Yang, X.; Zhang, P.; Wang, Q.; Zou, L.; Zhang, Y.; Zhang, L.; Fang, Y.; Li, J.; Zhou, H. C. *Adv. Mater.* **2018**, 1704303.

[42] Spore, A. B.; Rosi, N. L. *CrystEngComm* **2017**, *19*, 5417−5421.

[43] Milner, P. J.; Martell, J. D.; Siegelman, R. L.; Gygi, D.; Weston, S. C.; Long, J. R. ***Chem. Sci.*** 2018, *9*, 160−174.

[44] Plonka, A. M.; Banerjee, D.; Woerner, W. R.; Zhang, Z.; Nijem, N.; Chabal, Y. J.;

Li, J.; Parise, J. B. *Angew. Chem., Int. Ed.* **2013**, *52*, 1692−1695.

[45] Walton, I. M.; Cox, J. M.; Coppin, J. A.; Linderman, C. M.; Patel, D. G.; Benedict, J. B. *Chem. Commun.* **2013**, *49*, 8012−8014.

[46] Park, J.; Yuan, D.; Pham, K. T.; Li, J. R.; Yakovenko, A.; Zhou, H. C. *J. Am. Chem. Soc.* **2012**, *134*, 99−102.

[47] Walton, I. M.; Cox, J. M.; Mitchell, T. B.; Bizier, N. P.; Benedict, J. B. *CrystEngComm* **2016**, *18*, 7972−7977.

[48] Gong, L. L.; Yao, W. T.; Liu, Z. Q.; Zheng, A. M.; Li, J. Q.; Feng, X. F.; Ma, L. F.; Yan, C. S.; Luo, M. B.; Luo, F. *J. Mater. Chem. A* **2017**, *5*, 7961−7967.

[49] Lyndon, R.; Konstas, K.; Ladewig, B. P.; Southon, P. D.; Kepert, P. C. J.; Hill, M. R. *Angew. Chem., Int. Ed.* **2013**, *52*, 3695−3698.

[50] Fu, W.-Q.; Liu, M.; Gu, Z.-G.; Chen, S.-M.; Zhang, J. *Cryst. Growth Des.* **2016**, *16*, 5487−5492.

[51] Healey, K.; Liang, W.; Southon, P. D.; Church, T. L.; D'Alessandro, D. M. *J. Mater. Chem. A* **2016**, *4*, 10816−10819.

[52] Zhang, F.; Zou, X.; Feng, W.; Zhao, X.; Jing, X.; Sun, F.; Ren, H.; Zhu, G. *J. Mater. Chem.* **2012**, *22*, 25019−25026.

[53] Schwartz, H. A.; Olthof, S.; Schaniel, D.; Meerholz, K.; Ruschewitz, U. *Inorg. Chem.* **2017**, *56*, 13100−13110.

[54] Yaghi, O. M. *J. Am. Chem. Soc.* **2016**, *138*, 15507−15509.

[55] Schoedel, A.; Li, M.; Li, D.; O'Keeffe, M.; Yaghi, O. M. *Chem. Rev.* **2016**, *116*, 12466−12535.

[56] Schukraft, G. E. M.; Ayala, S.; Dick, B. L.; Cohen, S. M. *Chem. Commun.* **2017**, *53*, 10684−10687.

[57] Gong, X.; Young, R. M.; Hartlieb, K. J.; Miller, C.; Wu, Y.; Xiao, H.; Li, P.; Hafezi, N.; Zhou, J.; Ma, L.; Cheng, T.; Goddard, W.; Farha, O. K.; Hupp, J. T.; Wasielewski, M. R.; Stoddart, J. F. *J. Am. Chem. Soc.* **2017**, *139*, 4107−4116.

[58] Rieth, A. J.; Yang, S.; Wang, E. N.; Dincă, M. *ACS Cent. Sci.* **2017**, *3*, 668−672.

[59] Campbell, M.; Dincă, M. *Sensors* **2017**, *17*, 1108.

[60] Gonzalez, M. I.; Kapelewski, M. T.; Bloch, E. D.; Milner, P. J.; Reed, D. A.; Hudson, M. R.; Mason, J. A.; Barin, G.; Brown, C. M.; Long, J. R. *J. Am. Chem. Soc.* **2018**, *140*, 3412−3422.

[61] Milner, P. J.; Siegelman, R. L.; Forse, A. C.; Gonzalez, M. I.; Runcěvski, T.; Martell, J. D.; Reimer, J. A.; Long, J. R. *J. Am. Chem. Soc.* **2017**, *139*, 13541−13553.

[62] Hu, Z.; Deibert, B. J.; Li, J. *Chem. Soc. Rev.* **2014**, *43*, 5815−5840.

[63] Epley, C. C.; Roth, K. L.; Lin, S.; Ahrenholtz, S. R.; Grove, T. Z.; Morris, A. J. *Dalt. Trans.* **2017**, *46*, 4917−4922.

[64] Chen, X.; Bu, X.; Lin, Q.; Mao, C.; Zhai, Q.-G.; Wang, Y.; Feng, P. *Chem. - Eur. J.* **2017**, *23*, 11913−11919.

[65] Jagadesan, P.; Whittemore, T.; Beirl, T.; Turro, C.; McGrier, P. L. *Chem. - Eur. J.* **2017**, *23*, 917−925.

[66] Ling, Y.; Klemes, M. J.; Xiao, L.; Alsbaiee, A.; Dichtel, W. R.; Helbling, D. E. *Environ. Sci. Technol.* **2017**, *51*, 7590−7598.

[67] Jiang, J.; Furukawa, H.; Zhang, Y. B.; Yaghi, O. M. *J. Am. Chem. Soc.* **2016**, *138*, 10244−10251.

[68] Fracaroli, A. M.; Siman, P.; Nagib, D. A.; Suzuki, M.; Furukawa, H.; Toste, F. D.; Yaghi, O. M. *J. Am. Chem. Soc.* **2016**, *138*, 8352−8355.

[69] Ko, M.; Aykanat, A.; Smith, M.; Mirica, K. *Sensors* **2017**, *17*, 2192.

[70] Yu, X.; Wang, L.; Cohen, S. M. *CrystEngComm* **2017**, *19*, 4126− 4136.

[71] Haikal, R. R.; Hua, C.; Perry, J. J.; O'Nolan, D.; Syed, I.; Kumar, A.; Chester, A. H.; Zaworotko, M. J.; Yacoub, M. H.; Alkordi, M. H. *ACS Appl. Mater. Interfaces* **2017**, *9*, 43520−43528.

[72] Bobbitt, N. S.; Mendonca, M. L.; Howarth, A. J.; Islamoglu, T.; Hupp, J. T.; Farha, O. K.; Snurr, R. Q. *Chem. Soc. Rev.* **2017**, *46*, 3357−3385.

[73] Ji, P.; Solomon, J. B.; Lin, Z.; Johnson, A.; Jordan, R. F.; Lin, W. *J. Am. Chem. Soc.* **2017**, *139*, 11325−11328.

[74] Huang, N.; Yuan, S.; Drake, H.; Yang, X.; Pang, J.; Qin, J.; Li, J.; Zhang, Y.; Wang, Q.; Jiang, D.; Zhou, H.-C. *J. Am. Chem. Soc.* **2017**, *139*, 18590−18597.

[75] Luo, T.-Y.; Liu, C.; Eliseeva, S. V.; Muldoon, P. F.; Petoud, S.; Rosi, N. L. *J. Am. Chem. Soc.* **2017**, *139*, 9333−9340.

[76] Semino, R.; Moreton, J. C.; Ramsahye, N. A.; Cohen, S. M.; Maurin, G. *Chem. Sci.* **2018**, *9*, 315−324.

[77] Yuan, S.; Lu, W.; Chen, Y.-P.; Zhang, Q.; Liu, T.-F.; Feng, D.; Wang, X.; Qin, J.; Zhou, H.-C. *J. Am. Chem. Soc.* **2015**, *137*, 3177−3180.

[78] Kobatake, S.; Shibata, K.; Uchida, K.; Irie, M. *J. Am. Chem. Soc.* **2000**, *122*, 12135−12141.

[79] Irie, M.; Lifka, T.; Kobatake, S.; Kato, N. *J. Am. Chem. Soc.* **2000**, *122*, 4871−4876.

[80] Irie, M.; Fukaminato, T.; Matsuda, K.; Kobatake, S. *Chem. Rev.* **2014**, *114*, 12174−12277.

[81] Kitagawa, D.; Tsujioka, H.; Tong, F.; Dong, X.; Bardeen, C. J.; Kobatake, S. *J. Am. Chem. Soc.* **2018**, *140*, 4208−4212.

[82] Tam, E. S.; Parks, J. J.; Shum, W. W.; Zhong, Y. W.; Santiago- Berríos, M. B.; Zheng, X.; Yang, W.; Chan, G. K. L.; Abruña, H. D.; Ralph, D. C. *ACS Nano* **2011**, *5*, 5115−5123.

[83] Lucas, L. N.; Jong, J. J.; Esch, J. H.; Kellogg, R. M.; Feringa, B. L. *Eur. J. Org. Chem.* **2003**, *2003*, 155−166.

[84] Kobatake, S.; Uchida, K.; Tsuchida, E.; Irie, M. *Chem. Commun.* **2002**, 2804−2805.

[85] Klajn, R. *Chem. Soc. Rev.* **2014**, *43*, 148−184.

[86] Krysanov, S. A.; Alfimov, M. V. *Chem. Phys. Lett.* **1982**, *91*, 77−80.

[87] Swansburg, S.; Buncel, E.; Lemieux, R. P. *J. Am. Chem. Soc.* **2000**, *122*, 6594−6600.

[88] Kobatake, S.; Takami, S.; Muto, H.; Ishikawa, T.; Irie, M. *Nature* **2007**, *446*, 778−781.

[89] Wojtyk, J. T. C.; Wasey, A.; Kazmaier, P. M.; Hoz, S.; Buncel, E. *J. Phys. Chem. A* **2000**, *104*, 9046−9055.

[90] Udayabhaskararao, T.; Kundu, P. K.; Ahrens, J.; Klajn, R. *ChemPhysC*hem **2016**, *17*, 1805−1809.

[91] Kundu, P. K.; Olsen, G. L.; Kiss, V.; Klajn, R. *Nat. Commun.* **2014**, *5*, 3588.

[92] Maya, F.; Tour, J. M. *Tetrahedron* **2004**, *60*, 81−92.

[93] Benniston, A. C.; Harriman, A.; Howell, S. L.; Li, P.; Lydon, D. P. *J. Org. Chem.* **2007**, *72*, 888−897.

[94] Kundu, P. K.; Lerner, A.; Kucănda, K.; Leitus, G.; Klajn, R. *J. Am. Chem. Soc.* **2014**, *136*, 11276−11279.

[95] Starzak, M. E. Mathematical Methods in Chemistry and Physics; Springer US: Boston, MA, **1989**.

[96] Dolgopolova, E. A.; Ejegbavwo, O. A.; Martin, C. R.; Smith, M. D.; Setyawan, W.; Karakalos, S. G.; Henager, C. H.; Zur Loye, H. C.; Shustova, N. B. *J. Am. Chem. Soc.* **2017**, *139*, 16852−16861.

[97] Yuan, S.; Chen, Y. P.; Qin, J. S.; Lu, W.; Zou, L.; Zhang, Q.; Wang, X.; Sun, X.; Zhou, H. C. *J. Am. Chem. Soc.* **2016**, *138*, 8912− 8919.

[98] Harada, J.; Kawazoe, Y.; Ogawa, K. *Chem. Commun.* **2010**, *46*, 2593−2595.

[99] Gentili, P. L.; Nocchetti, M.; Miliani, C.; Favaro, G. *New J. Chem.* **2004**, *28*, 379−386.

[100] Beńard, S.; Yu, P. *Adv. Mater.* **2000**, *12*, 48−50.

[101] Whelan, J.; Abdallah, D.; Wojtyk, J.; Buncel, E. *J. Mater. Chem.* **2010**, *20*, 5727−5735.

[102] Florea, L.; McKeon, A.; Diamond, D.; Benito-Lopez, F. *Langmuir* **2013**, *29*, 2790−2797.

[103] Breslin, V. M.; Garcia-Garibay, M. A. *Cryst. Growth Des.* **2017**, *17*, 637−642.

[104] Shoji, H.; Kitagawa, D.; Kobatake, S. New J. Chem. 2014, 38, 933−941.

[105] Miyasaka, H.; Nobuto, T.; Itaya, A.; Tamai, N.; Irie, M. *Chem. Phys. Lett.* **1997**, *269*, 281−285.

[106] Irie, M.; Lifka, T.; Uchida, K.; Kobatake, S.; Shindo, Y. *Chem. Commun.* **1999**, 747−750.

[107] Tani, K.; Ishibashi, Y.; Miyasaka, H.; Kobatake, S.; Irie, M. *J. Phys. Chem. C* **2008**,

112, 11150−11157.

[108] Irie, M.; Sayo, K. *J. Phys. Chem.* **1992**, *96*, 7671−7674.

[109] Farha, O. K.; Malliakas, C. D.; Kanatzidis, M. G.; Hupp, J. T. *J. Am. Chem. Soc.* **2010**, *132*, 950−952.

[110] Burrows, A. D.; Frost, C. G.; Mahon, M. F.; Richardson, C. *Chem. Commun.* **2009**, 4218−4220.

[111] APEX3 Version 2016.5-0 and SAINT+ Version 8.37A. Bruker AXS, Inc., Madison, Wisconsin, USA, **2016**.

[112] SADABS-2016: Krausa, L., Herbst-Irmer, R., Sheldrick G.M., S. D. *J. Appl. Crystallogr.* **2015**, *48*, 3–10.

[113] Sheldrick, G. M. *Acta Crystallogr.* **2015**, *71*, 3–8.

[114] Dolomanov, O. V.; Bourhis, L. J.; Gildea, R. J.; Howard, J. A. K.; Puschmann, H. *J. Appl. Crystallogr.* **2009**, *42*, 339–341.

[115] van der Sluis, P.; Spek, A. L. *Acta Crystallogr.* **1990**, *46A*, 194–201.

[116] PLATON SQUEEZE: Spek, A. L. *Acta Crystallogr. Sect.* **2015**, C71, 9–18.

[117] Sheldrick, G. M. *Acta Crystallogr. A*. **2008**, *64*, 112–122.

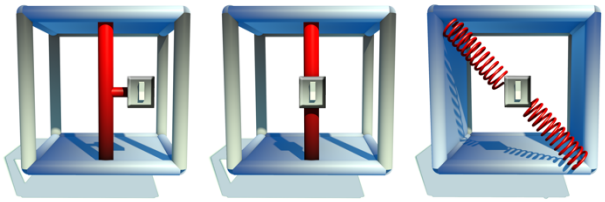

Scheme 2.1. Schematic representation of coordinatively immobilized photochromic derivatives inside the metal-organic rigid scaffold. The photochromic moiety integrated (*left*) as a side group on the organic linker, (*middle*) as a framework backbone, and (*right*) as a capping linker[77] with a size similar to the framework pocket. A grey "photoswitch" symbol indicates the position of a photochromic unit.

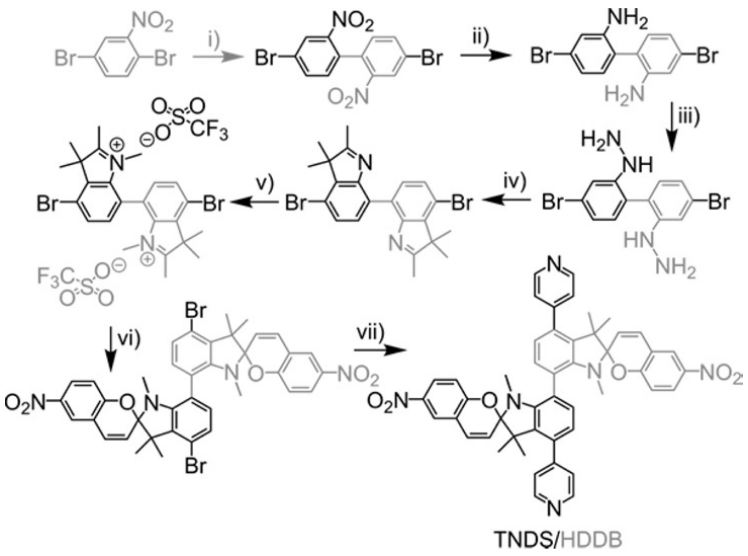

Scheme 2.2. Reaction scheme for the synthesis of TNDS (black) and HDDB (grey). Reagents and conditions: (i) Cu powder, DMF, 120 °C 4 h; (ii) $SnCl_2$, HCl, EtOH, reflux 12 h; (iii) $NaNO_2$, HCl, 0 °C 1 h/$CO(NH_2)_2$, 0 °C 10 min/$SnCl_2$, 0 °C, 4 h; (iv) 3-methyl-2-butanone, reflux 3 h/H_2SO_4, EtOH, reflux 3 h; (v) Et_2O, hexanes, methyl trifluoromethanesulfonate, room temperature, 8 h; (vi) 2-hydroxy-5-nitrobenzaldahyde, EtOH, piperidine, reflux 8 h; (vii) pyridine-4-boronic acid, $PdCl_2(PPh_3)_2$, CuCl, Na_2CO_3, DMF, 120 °C, 48 h.[91–93]

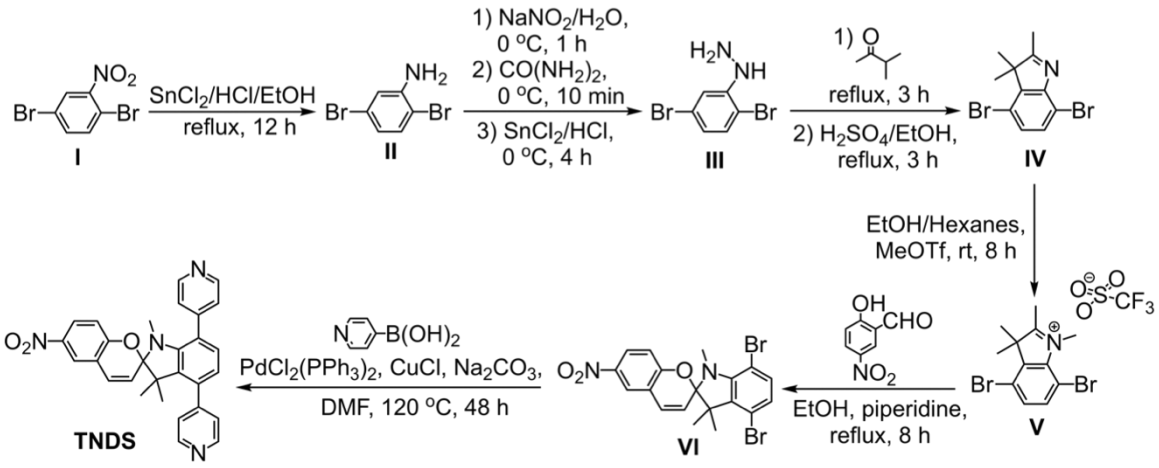

Scheme 2.3. Synthesis of TNDS.

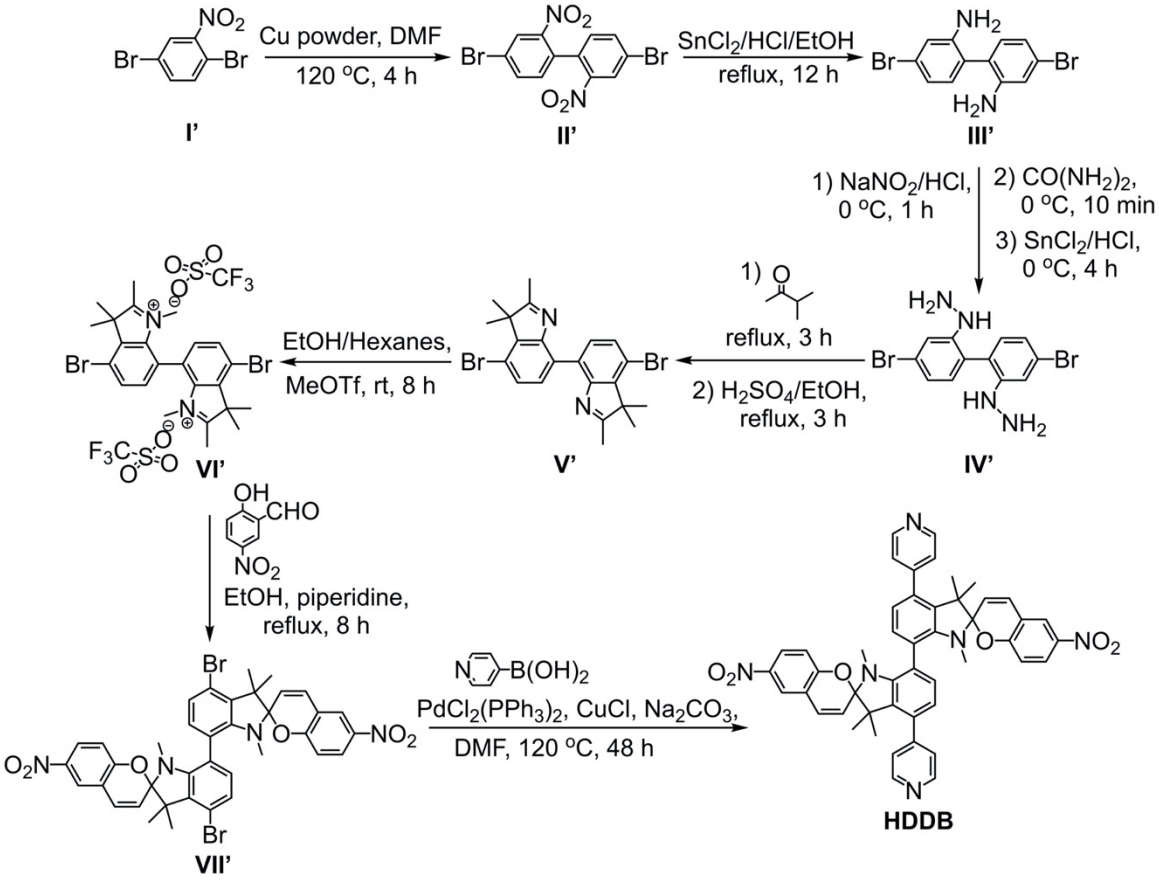

Scheme 2.4. Synthesis of HDDB.

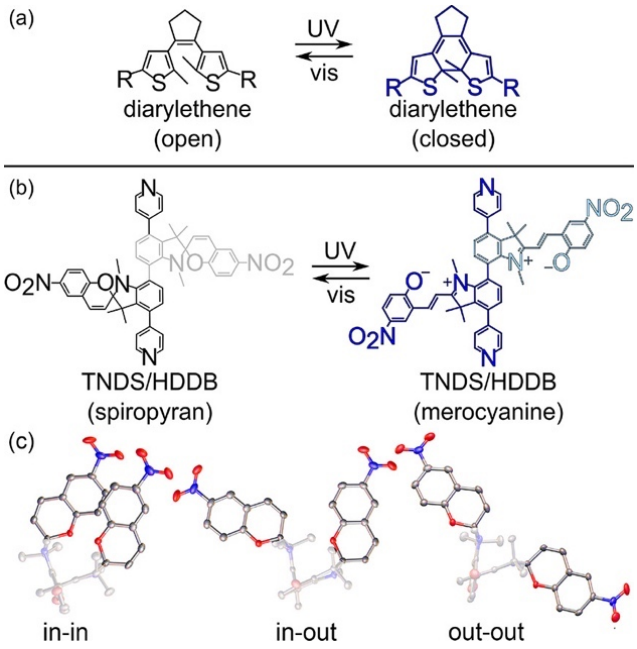

Figure 2.1. Photoisomerization of the (a) diarylethene-based and (b) spiropyran derivatives. (c) For simplicity, structural differences of "in−in", "in−out", and "out−out" diastereoisomers are shown on the example of the brominated precursor (Scheme 2.2)[91] of HDDB. Displacement ellipsoids drawn at the 60% probability level. Gray, blue, and red spheres represent C, N, and O atoms, respectively.

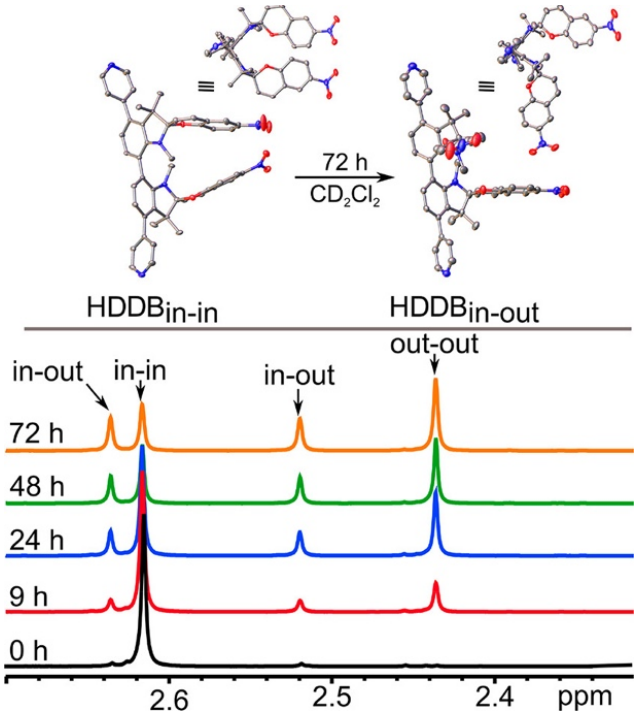

Figure 2.2. (*top*) Single crystal X-ray structures of HDDBin−in and HDDBin−out. Two orientations of each diastereoisomer are shown. Displacement ellipsoids drawn at the 60% probability level. Gray, blue, and red spheres represent C, N, and O atoms, respectively. (*bottom*) A region of the ^{1}H NMR spectra for thermal equilibration of $HDDB_{in-in}$ to $HDDB_{in-out}$ and $HDDB_{out-out}$ in CD_2Cl_2 is shown at t = 0, 9, 24, 48, and 72 h. The full spectra for the $HDDB_{in-in}$ conversion are shown in Figure 2.30.

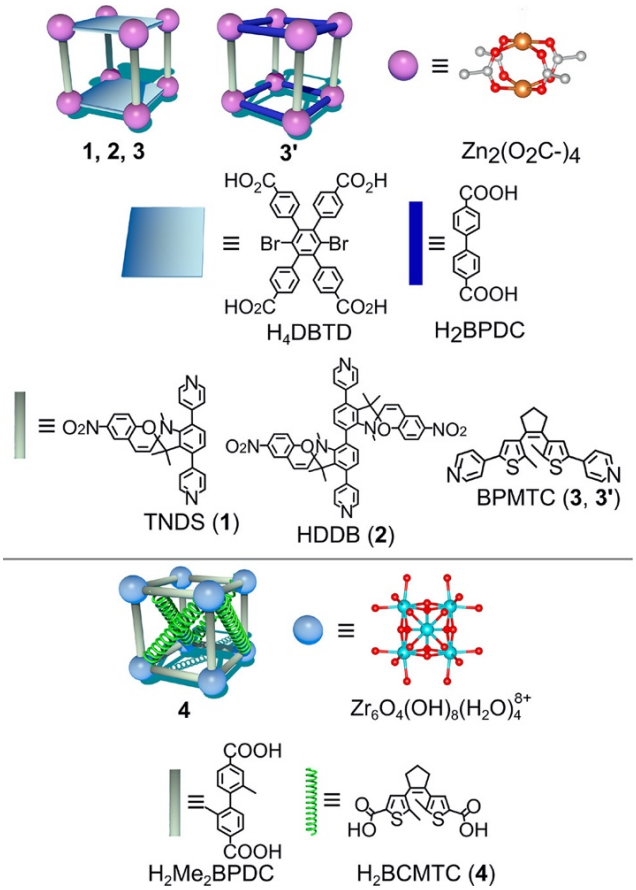

Figure 2.3. (*top*) TNDS, HDDB, and BPMTC linkers were used to synthesize **1**, **2**, and **3** (**3′**), respectively, in the presence of H_4DBTD (H_2BPDC). (*bottom*) The linker, H_2BCMTC, was installed as a capping linker into an existing MOF framework, $Zr_6(Me_2BPDC)_4$,[77] to make **4**. Orange, red, teal, and gray spheres correspond to zinc, oxygen, zirconium, and carbon atoms, respectively.

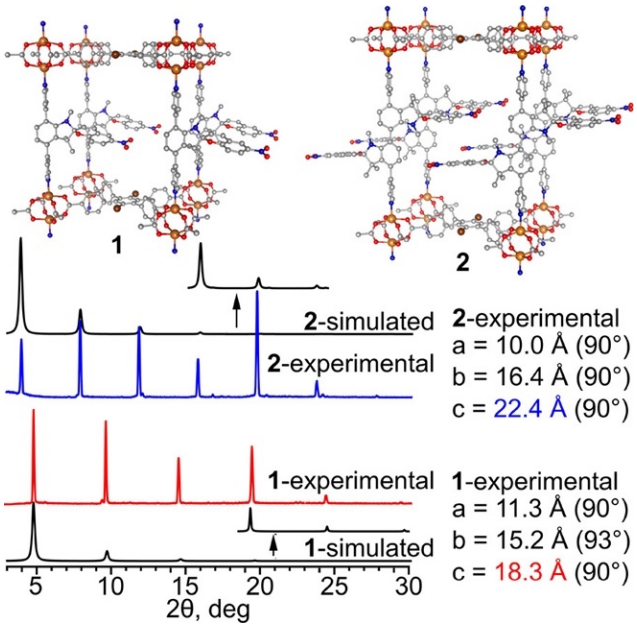

Figure 2.4. (*top*) Single-crystal structures of **1** and **2** with simulated spiropyran moiety located in the pores. (*bottom*) The simulated and experimental PXRD patterns of MOFs **1** (red) and **2** (blue). The colored text shows the increase of interlayer distance for each MOF, which is in agreement with the sizes of the installed photochromic linkers.

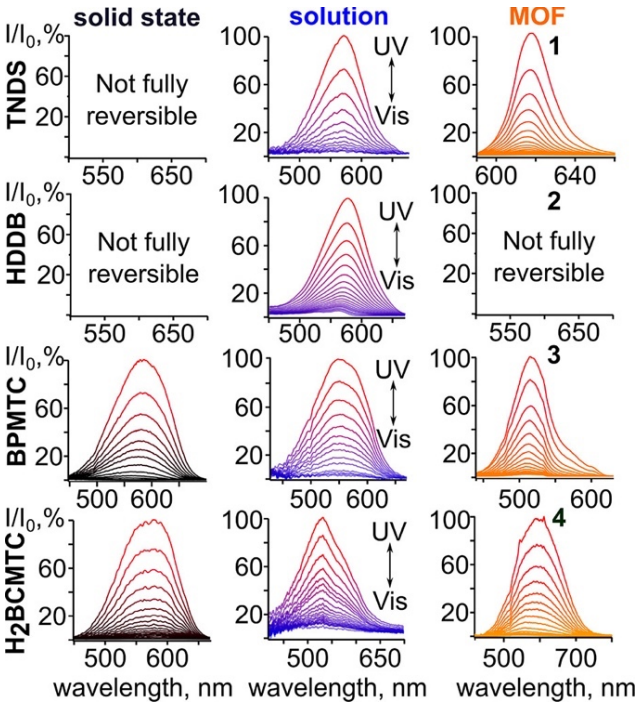

Figure 2.5. Normalized absorption plots of TNDS, HDDB, BPMTC, and H_2BCMTC in the solid state, in solution, and coordinatively immobilized inside a MOF upon irradiation with UV and visible light.

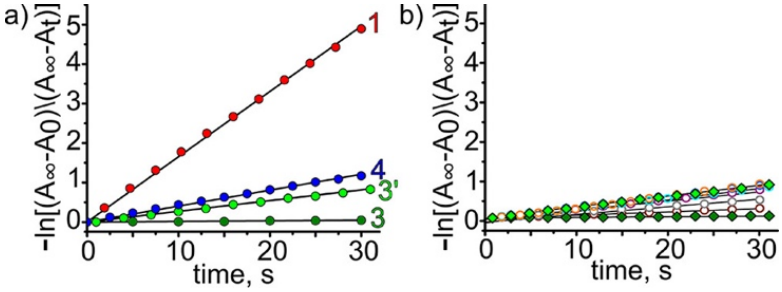

Figure 2.6. (a) Cycloreversion kinetics of photochromic MOFs upon irradiation with visible light. (b) Cycloreversion kinetics plots for BPMTC linker in solution (circles: brown, ethanol; gray, methanol; purple, acetonitrile; light blue, tetrahydrofuran; blue, toluene; orange, chloroform) and coordinatively immobilized inside MOFs **3** (dark green diamonds) and **3′** (light green diamonds).

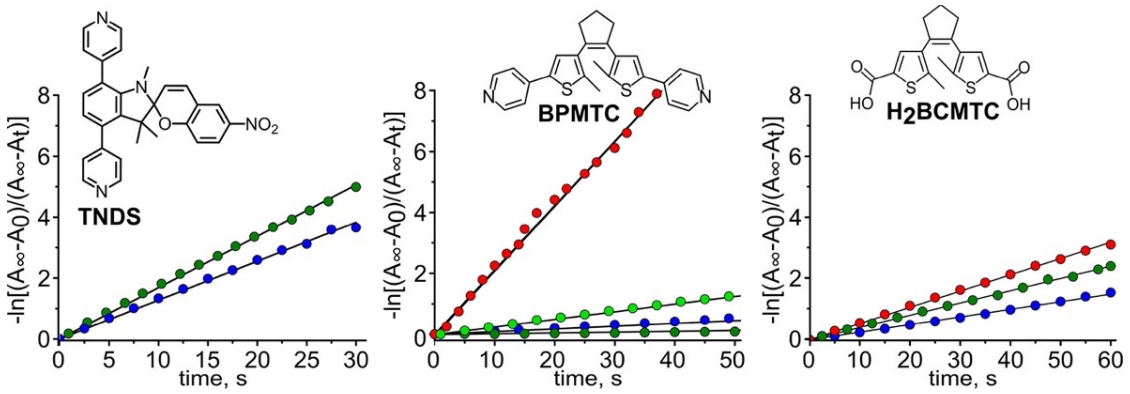

Figure 2.7. Cycloreversion kinetics of TNDS, BPMTC, and H_2BCMTC as a solid (red), in solution (blue, TNDS and BPMTC in DMF and H_2BCMTC in methanol; the solvent was chosen according to solubility and photochromic behavior), and immobilized in a MOF (green) upon irradiation with visible light.

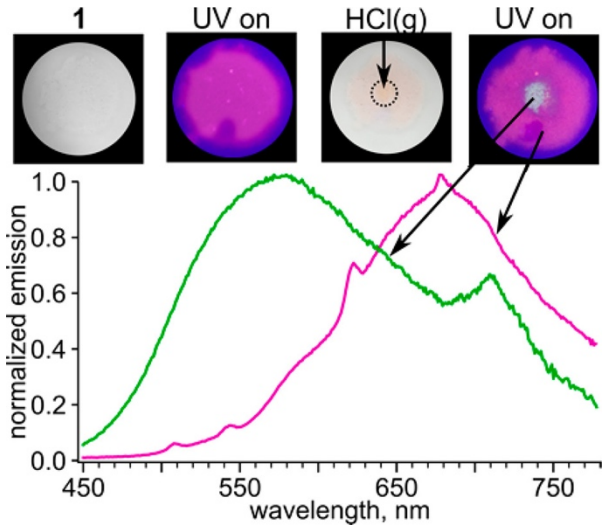

Figure 2.8. (*top*) The surface of **1** was subjected to HCl vapors and shows evidence of MOF degradation at the point of contact. (bottom) The fluorescence spectra of **1** before (purple) and after (green) exposure to HCl vapors.

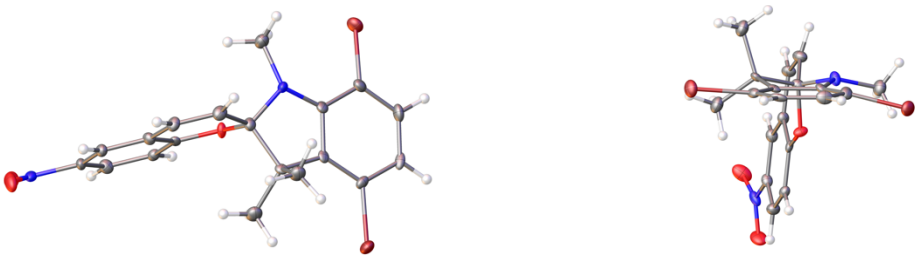

Figure 2.9. The X-ray crystal structure of **VI**. Displacement ellipsoids are drawn at the 50% probability level. Blue, brown, red, gray, and white spheres represent N, Br, O, C, and H atoms, respectively.

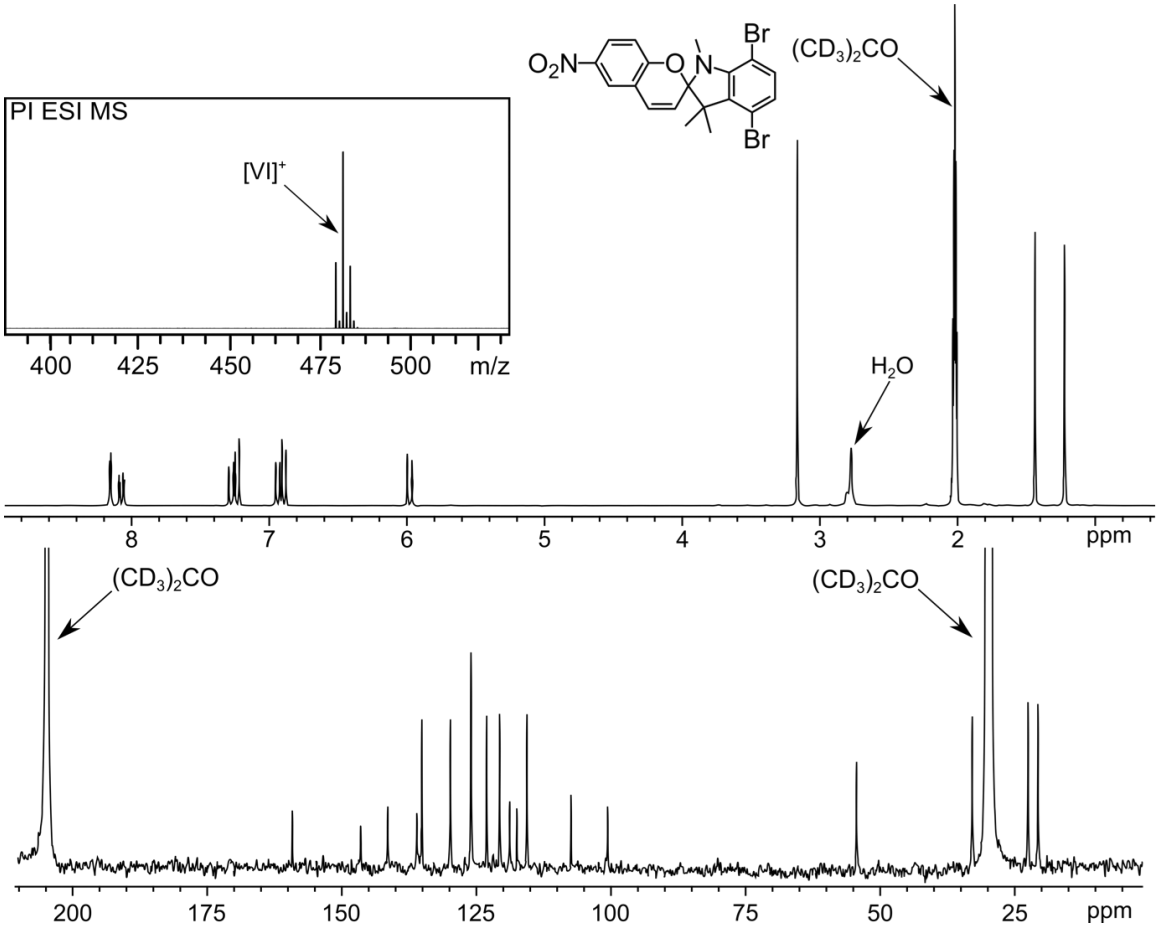

Figure 2.10. ^{1}H NMR (*top*) and ^{13}C NMR (*bottom*) spectra of **VI** in acetone-d_6. The inset shows the positive ion electrospray mass-spectrum of **VI**.

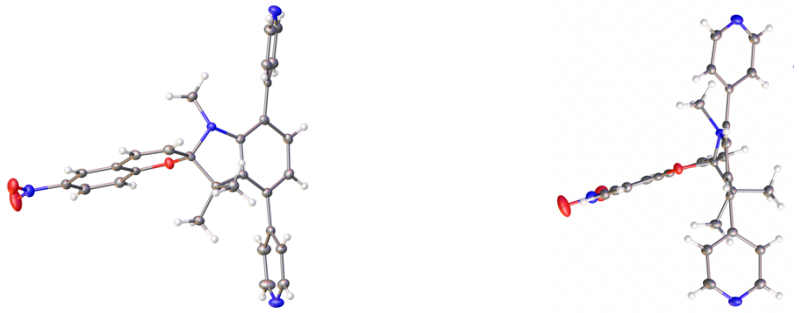

Figure 2.11. The single crystal X-ray structure of TNDS. Displacement ellipsoids are drawn at the 50% probability level. Blue, red, gray, and white spheres represent N, O, C, and H atoms, respectively.

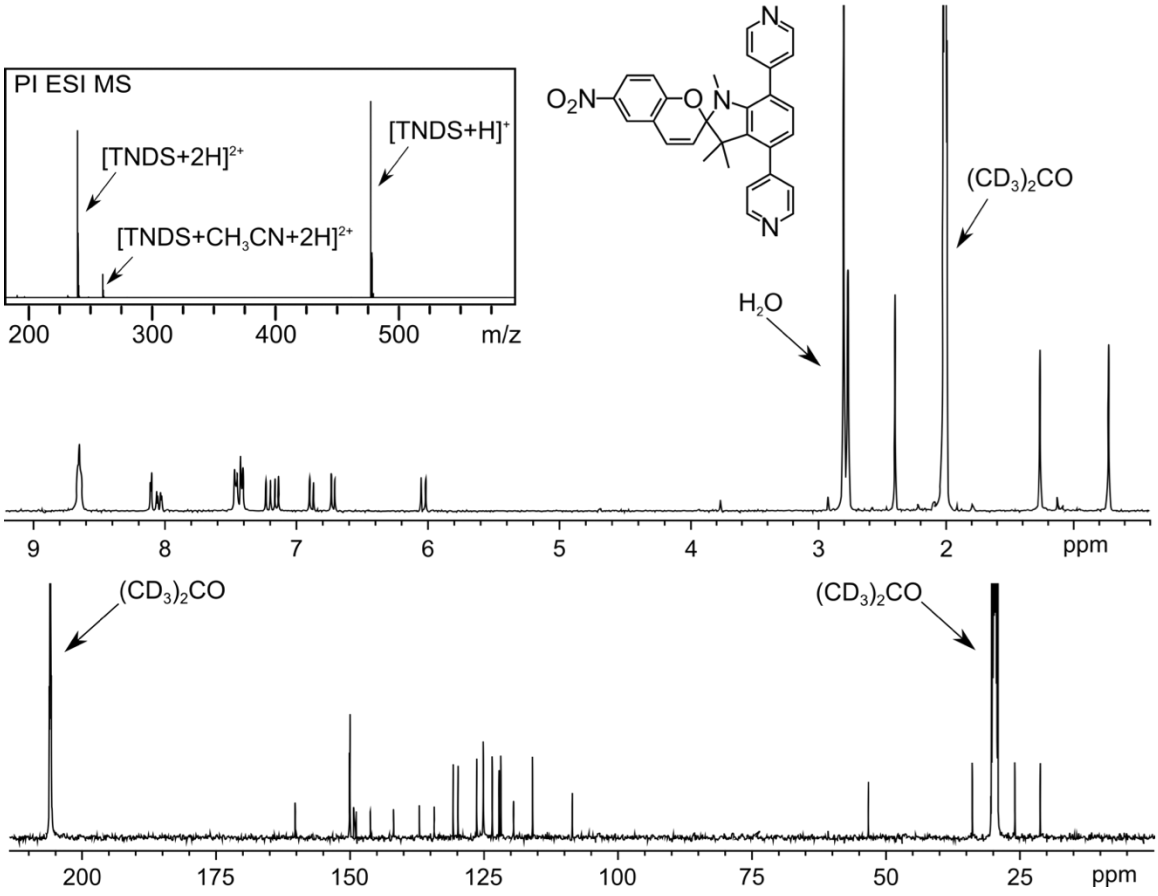

Figure 2.12. ^{1}H NMR (*top*) and ^{13}C NMR (*bottom*) spectra of TNDS in acetone-d_6. The inset shows the positive ion electrospray mass-spectrum of TNDS.

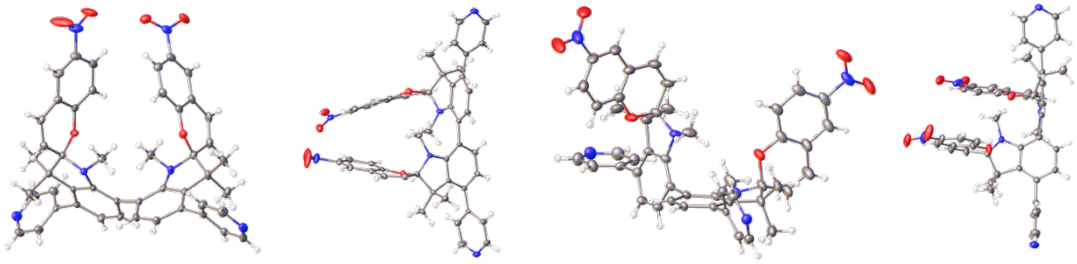

Figure 2.13. (*left*). The single-crystal structure of $HDDB_{in–in}$. Displacement ellipsoids are drawn at the 50% probability level. (*right*) The single-crystal structure of $HDDB_{in–out}$. Displacement ellipsoids are drawn at the 30% probability level. Blue, red, gray, and white spheres represent N, O, C, and H atoms, respectively.

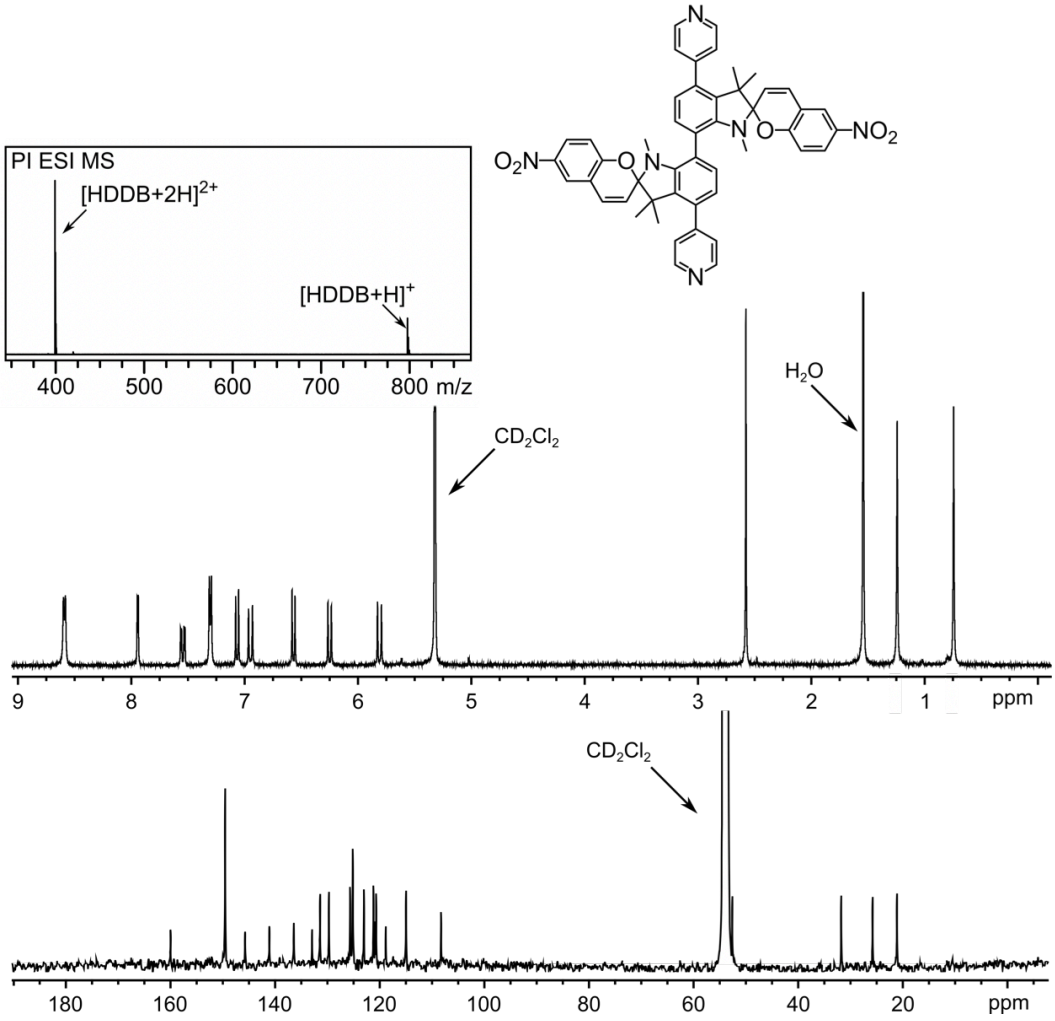

Figure 2.14. ^{1}H NMR (*top*) and ^{13}C NMR (*bottom*) spectra of $HDDB_{in–in}$ in dichloromethane-d_2. The inset shows the positive ion electrospray mass-spectrum of HDDB.

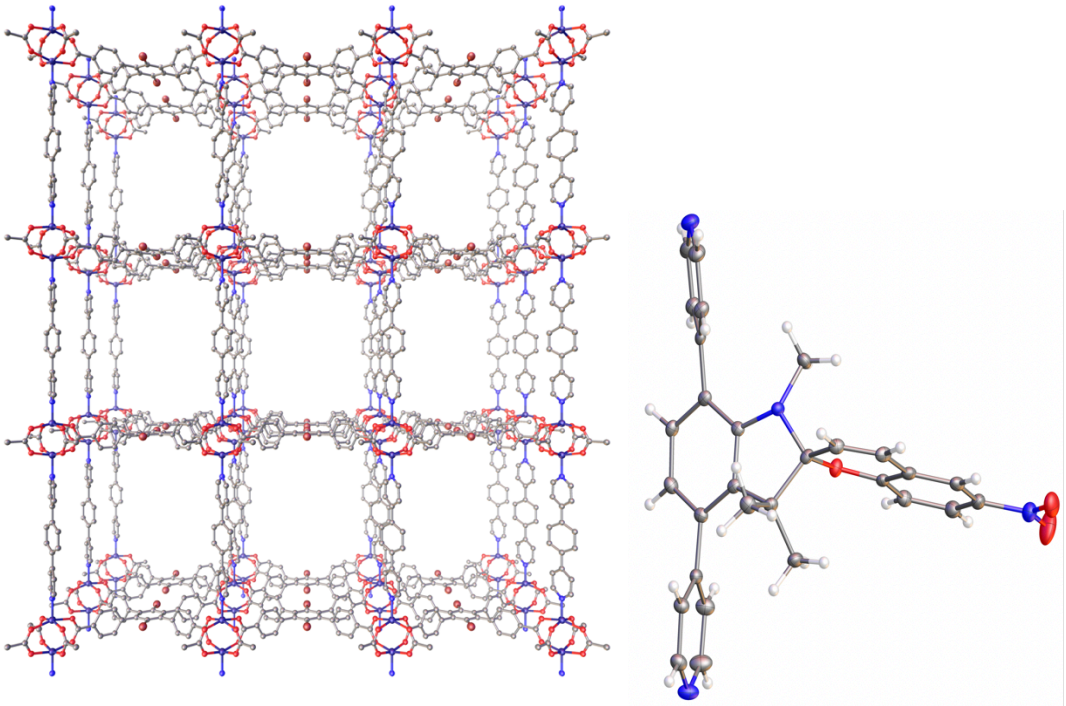

Figure 2.15. (*left*) The X-ray crystal structure of **1**. Solvent molecules, hydrogen atoms, and the disordered part of the molecules are omitted for clarity. (*right*) The X-ray crystal structure of TNDS. Thermal ellipsoids are drawn at the 50% probability level. Blue, brown, red, purple, gray, and white spheres represent N, Br, O, Zn, C, and H atoms, respectively.

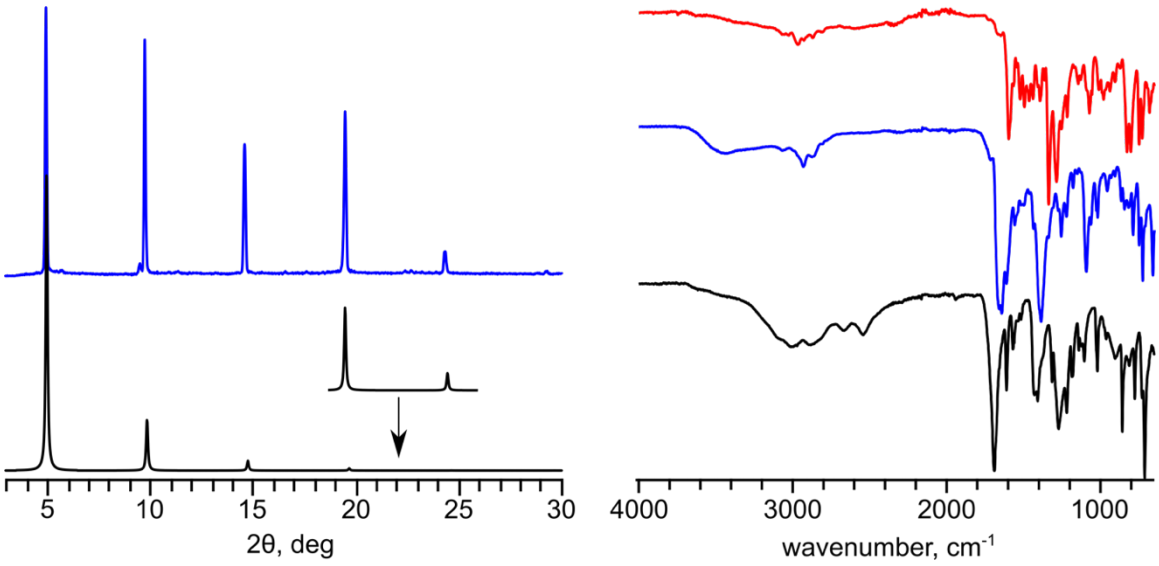

Figure 2.16. (*left*) PXRD patterns of **1**: simulated (black) and as-synthesized (blue). (*right*) FTIR spectra of TNDS (red), 1 (blue), and H_4DBTD (black).

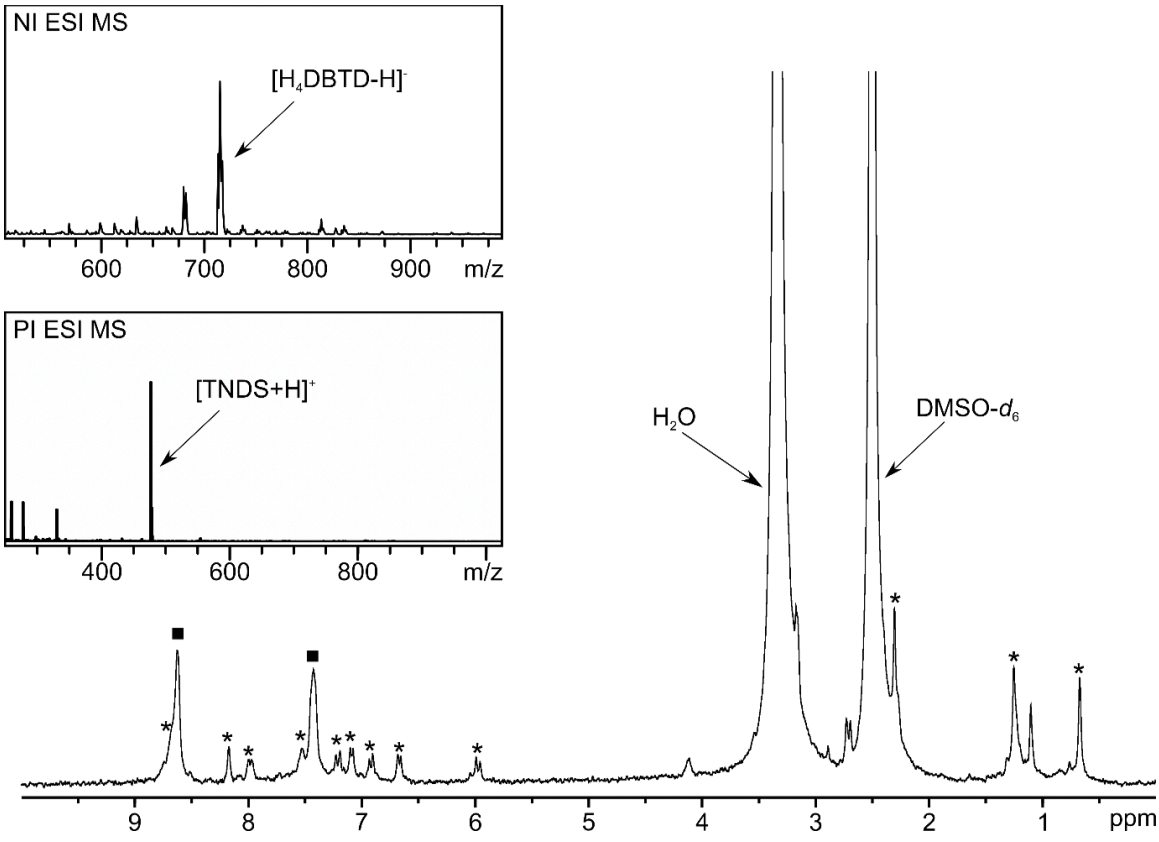

Figure 2.17. H NMR spectrum of digested 1 in DMSO-d6. The peaks corresponding to H_4DBTD (■) and TNDS (∗) are labeled. The insets (*top*) show the negative ion electrospray mass-spectrum and (*bottom*) the positive ion electrospray mass-spectrum of digested **1**.

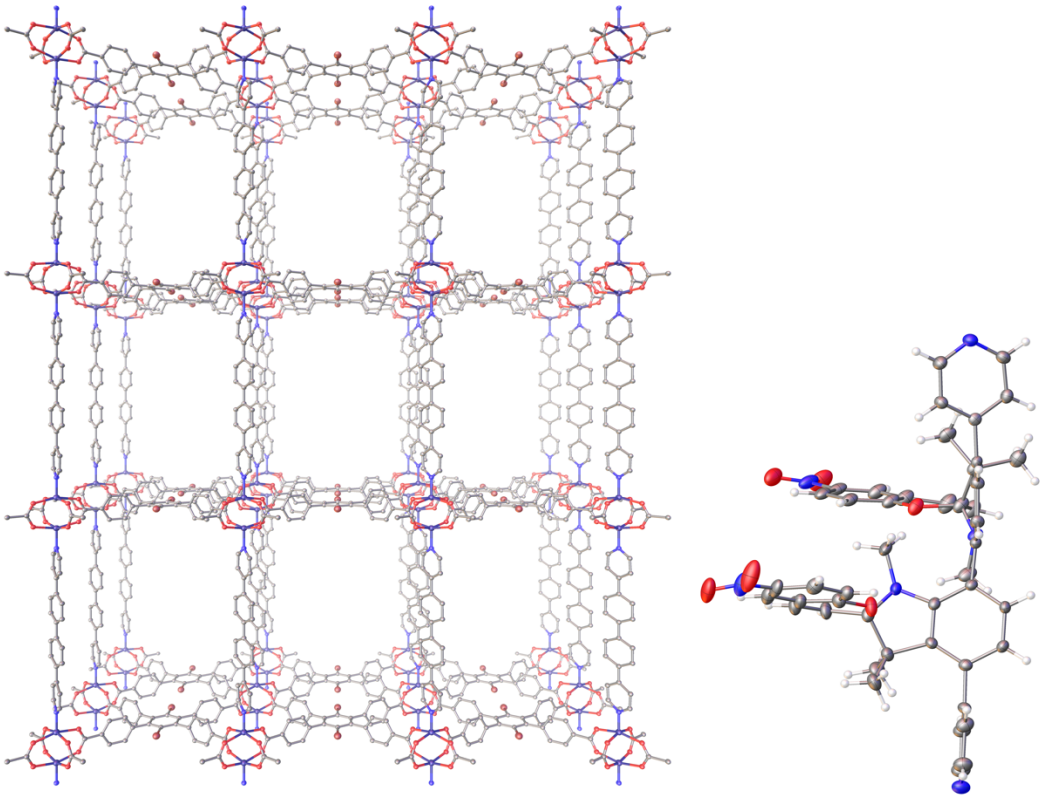

Figure 2.18. (*left*) The X-ray crystal structure of **2**. Solvent molecules, hydrogens atoms, and the disordered part of the molecules are omitted for clarity. (*right*) The X-ray crystal structure of $HDDB_{in-out}$. Thermal ellipsoids are drawn at the 30% probability level. Blue, brown, red, purple, gray, and white spheres represent N, Br, O, Zn, C, and H atoms, respectively.

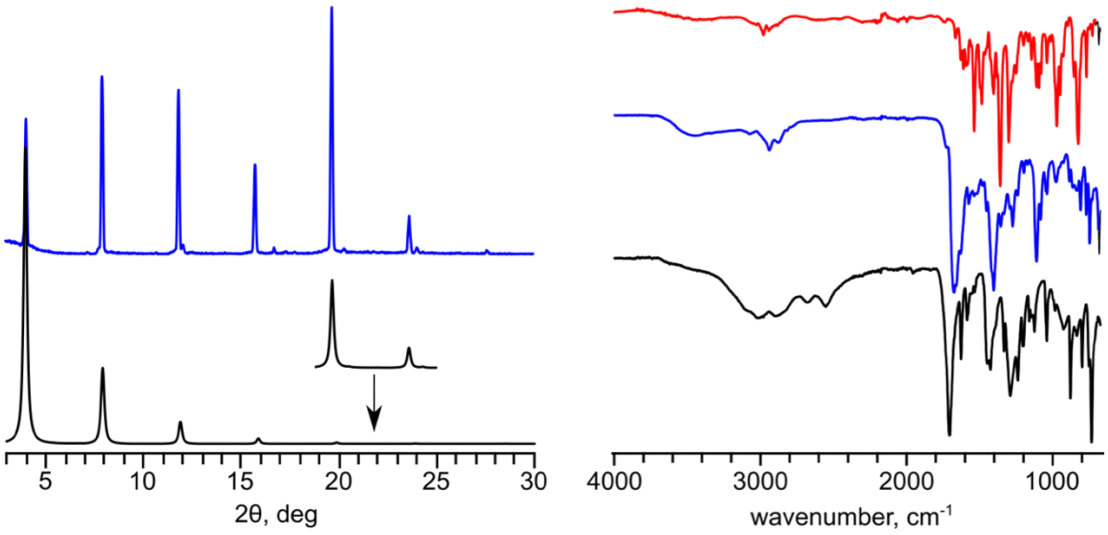

Figure 2.19. (*left*) PXRD patterns of **2**: simulated (black) and as-synthesized (blue). (*right*) FTIR spectra of HDDB (red), **2** (blue), and H_4DBTD (black).

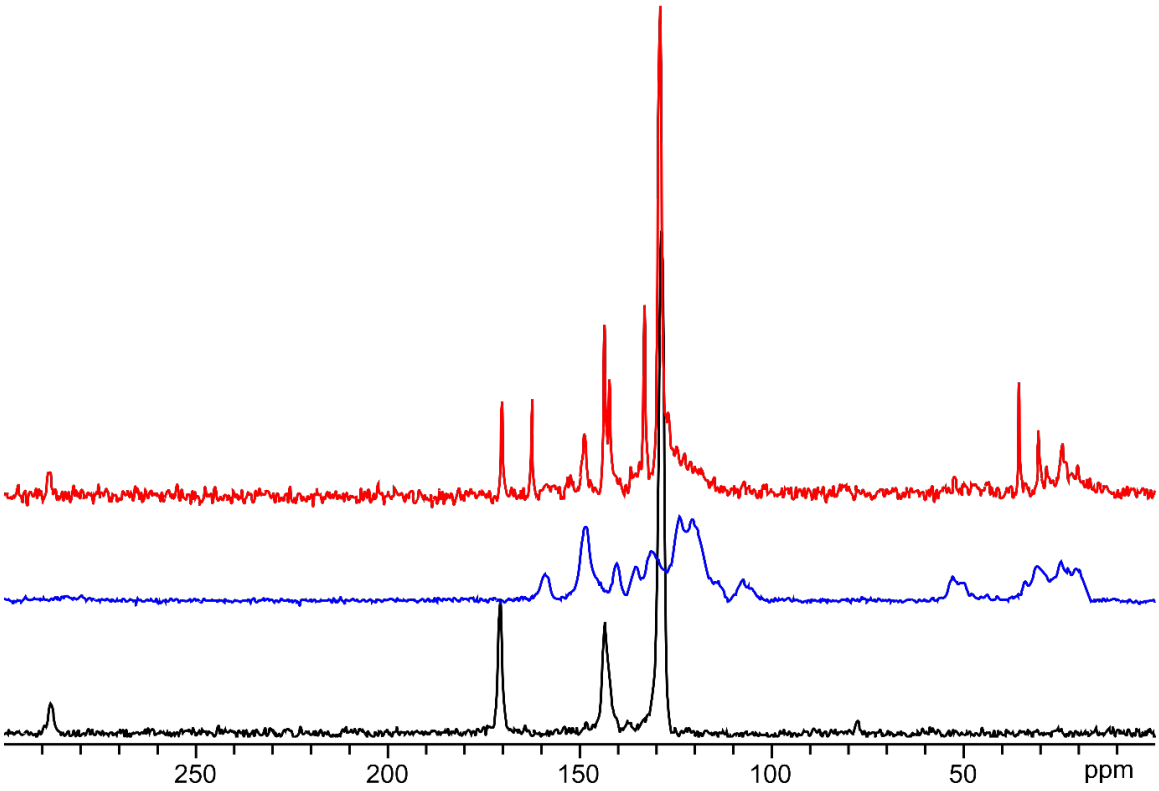

Figure 2.20. $^{13}C\{^{1}H\}$ CP-MAS NMR spectra of **2** (red), HDDB (blue), and H_4DBTD (black).

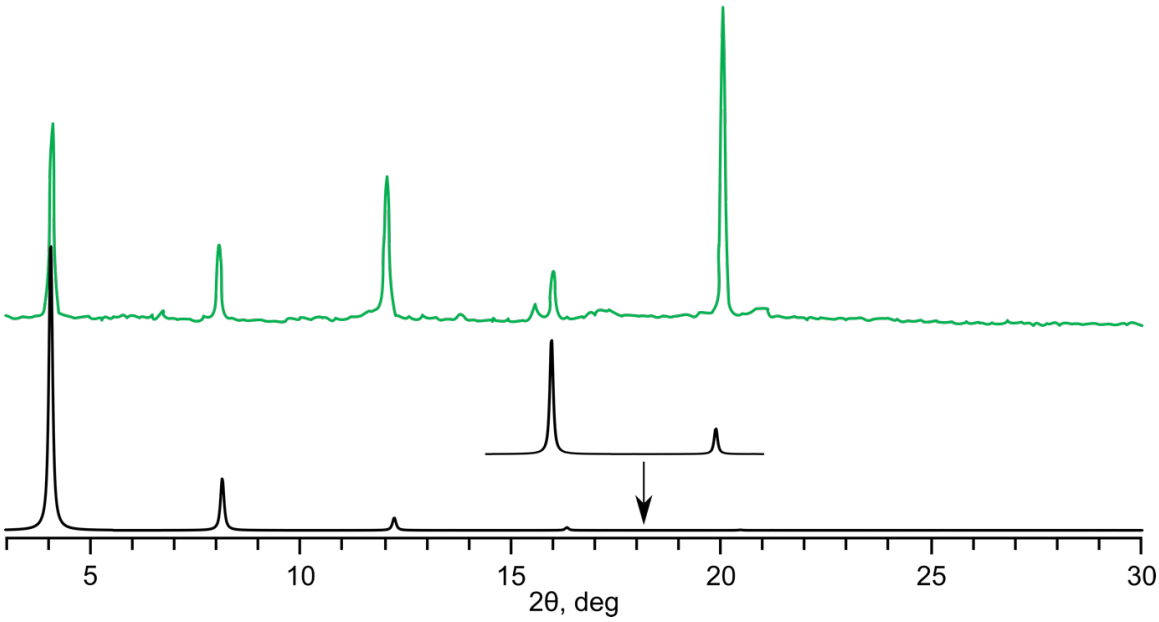

Figure 2.21. PXRD patterns of **3**: simulated (black)[13] and as-synthesized (green).

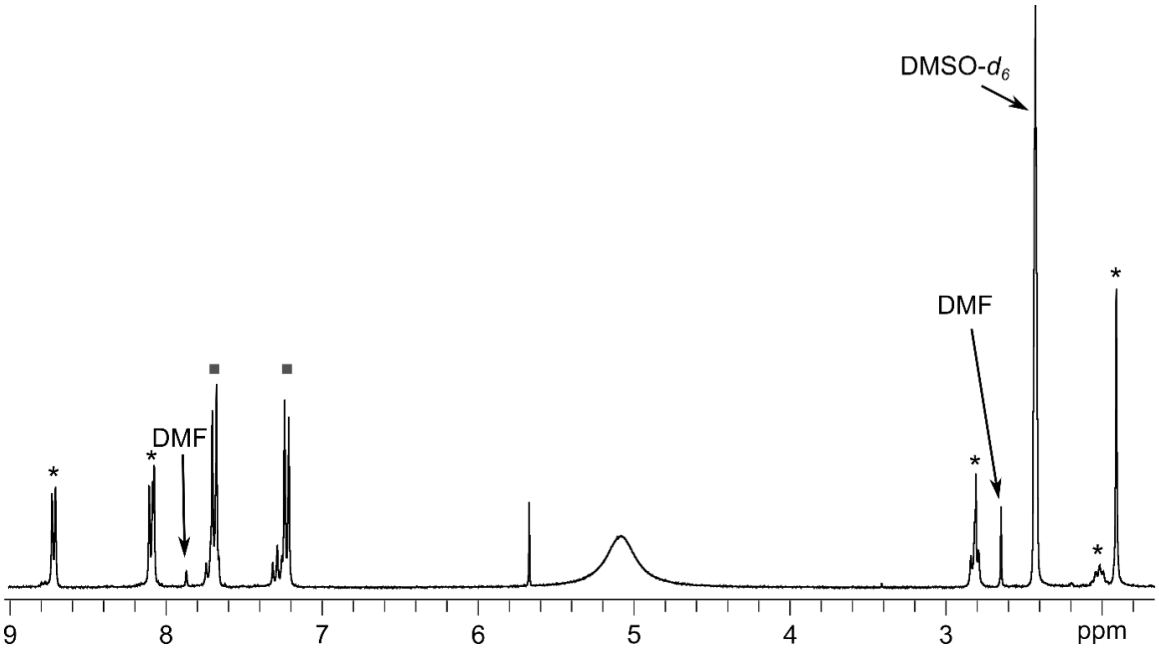

Figure 2.22. ^{1}H NMR spectrum of digested **3**. The peaks corresponding to H_4DBTD (■) and BPMTC (∗) are labeled.

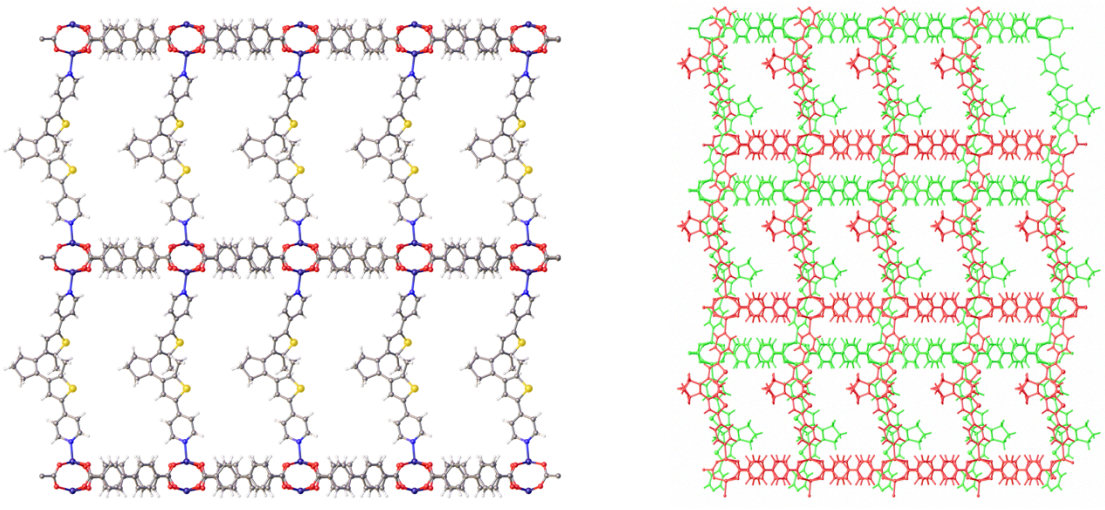

Figure 2.23. (*left*) The X-ray crystal structure of one non-interpenetrated component of **3'**. (*right*) The X-ray crystal structure of **3'** showing both interpenetrated frameworks. Solvent molecules are omitted for clarity. Blue yellow, red, purple, gray, and white spheres represent N, S, O, Zn, C, and H atoms, respectively.

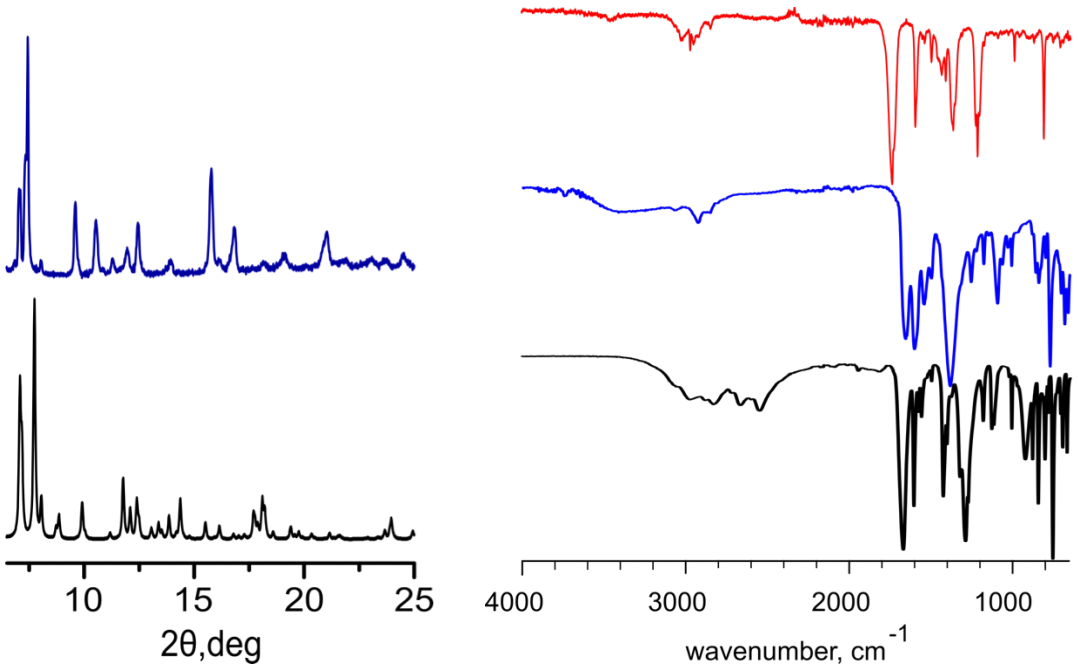

Figure 2.24. (*left*) PXRD patterns of **3'**: simulated (black) and as-synthesized (blue). (*right*) FTIR spectra of BPMTC (red), **3'** (blue), and H_2BPDC (black).

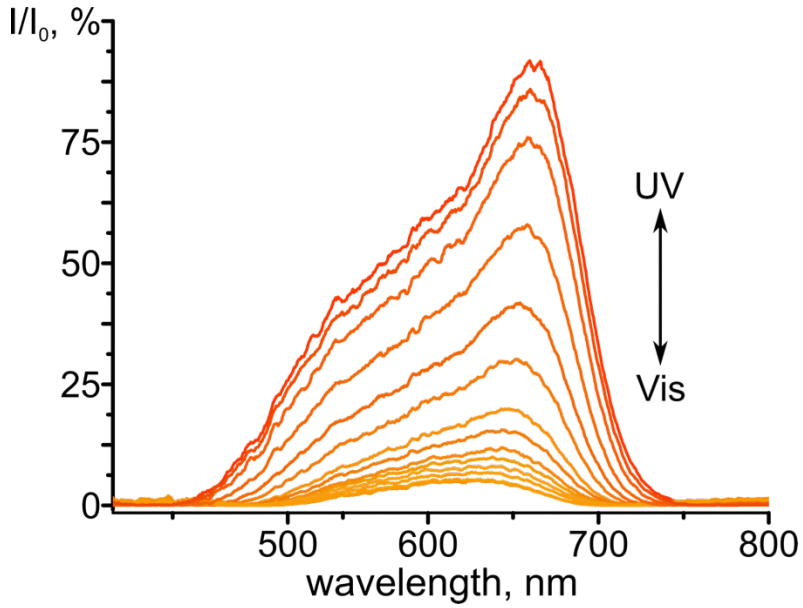

Figure 2.25. Normalized absorption spectra of **3'** upon irradiation with UV and visible light.

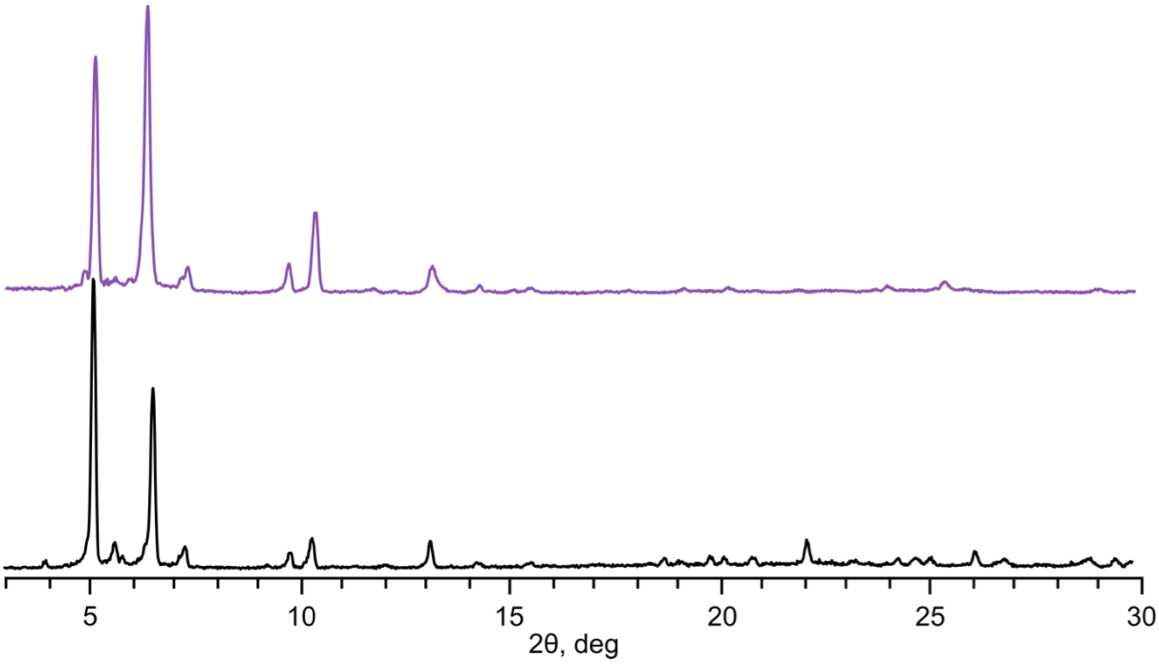

Figure 2.26. PXRD patterns of as-synthesized $Zr_6(Me_2BPDC)_4$ (black)[14] and **4** (purple).

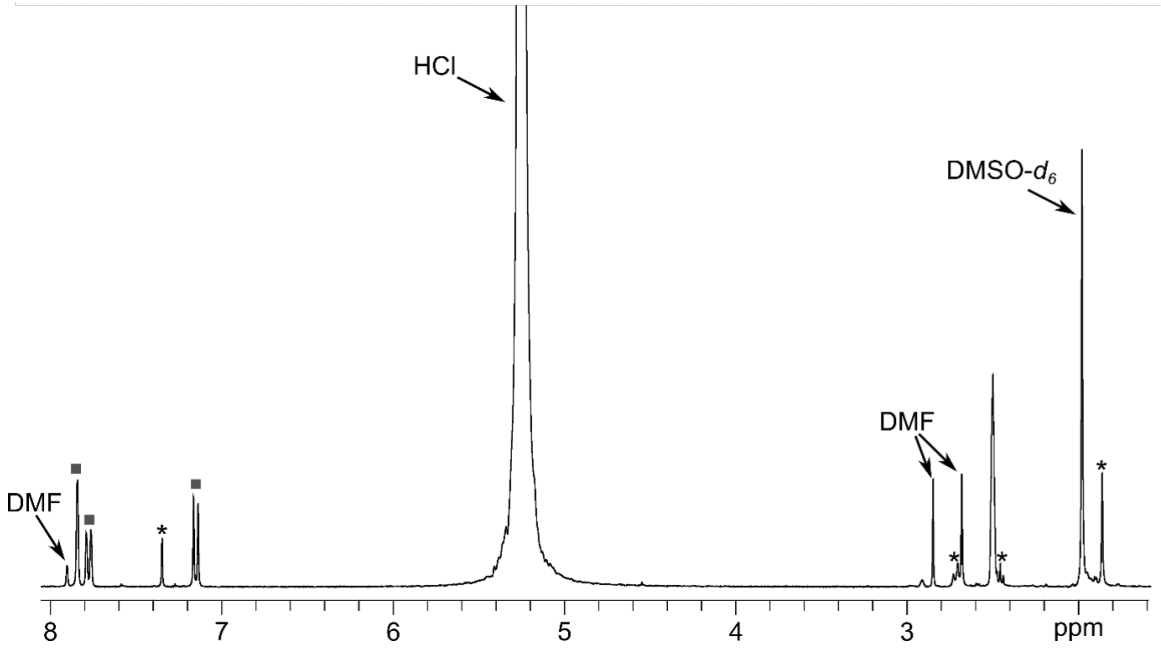

Figure 2.27. ^{1}H NMR spectrum of digested **4**. The peaks corresponding to H_2Me_2BPDC (■) and H_2BCMTC (∗) are labeled.

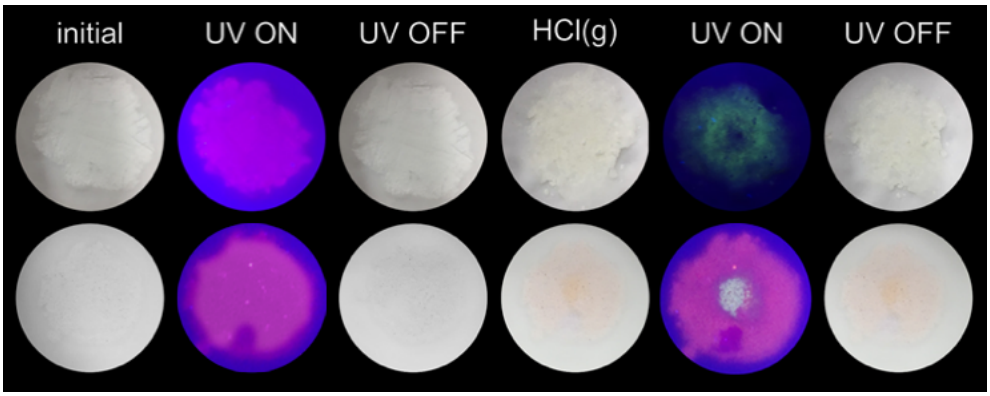

Figure 2.28. TNDS in the solid state (*top*) and coordinatively immobilized in **1**. Both samples were mixed with potassium bromide and then they were exposed to vapors of hydrochloric acid obtained by bubbling of the nitrogen gas through the 6 M HCl solution.

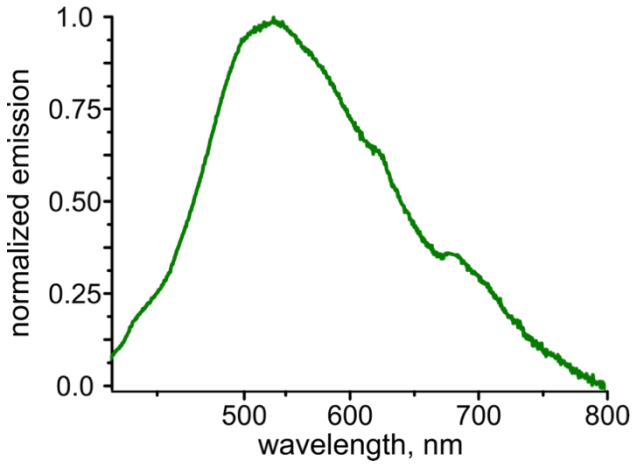

Figure 2.29. Normalized emission spectrum of TNDS powder obtained after exposure to gaseous hydrochloric acid in solution (λ_{max}= 540 nm, λ_{ex} = 360 nm).

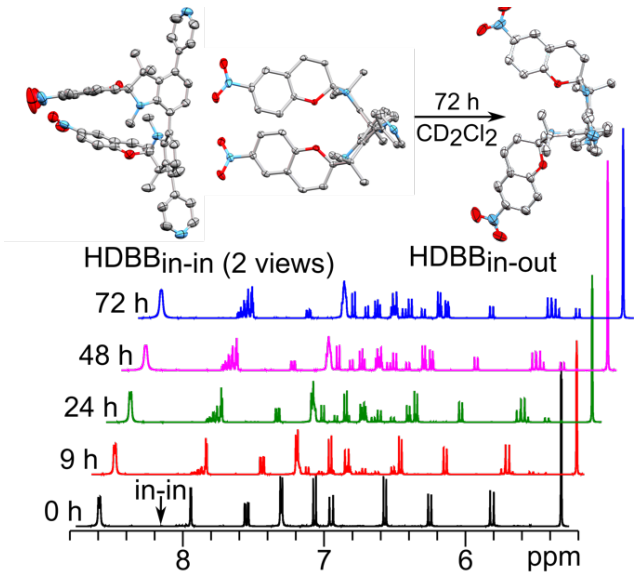

Figure 2.30. (*top*) Single crystal X-ray structures of $HDDB_{in–in}$ and $HDDB_{in–out}$. (*bottom*) The ^1H NMR spectra showing the conversion of $HDDB_{in–in}$ to the other isomers, $HDDB_{in–out}$ and $HDDB_{out–out}$ during 3 days.

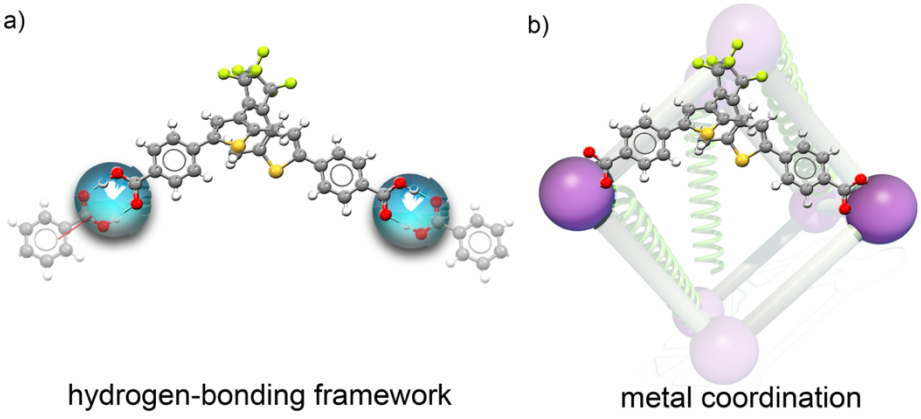

Figure 2.31. Two different types of BCMTC-based frameworks formed through hydrogen bonding and metal coordination.

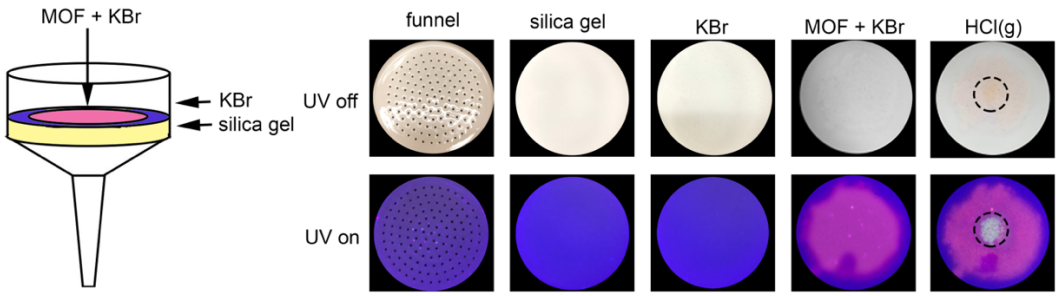

Figure 2.32. (*left*) Schematic representation of the experimental setup. (*right*) Photographs demonstrating changes in the emission and absorption profiles during interaction of the HCl vapors with photoactive MOF surface.

Table 2.1. Rate constants of cycloreversion process (k, s^{-1}) of TNDS, HDDB, BPMTC, and H_2BCMTC in the solid state, in solution, and coordinatively immobilized in a MOF.

	solid state	solution	MOF
TNDS	*a*	1.2×10^{-1} *b*	1.6×10^{-1} (**1**)
HDDB	*a*	$(6.0–20) \times 10^{-2}$ *b*	*a* (**2**)
BPMTC	2.0×10^{-1}	1.0×10^{-2} *b*	2.8×10^{-3} (**3**) 2.0×10^{-2} (**3'**)
H_2BCMTC	4.8×10^{-2}	2.6×10^{-2} *c*	4.1×10^{-2} (**4**)

[a]Photoisomerization was not fully reversible. [b]C = 3 mM in DMF. [c]C = 3 mM in MeOH

Table 2.2. Rate constants of cycloreversion process of BPMTC in different solvents (concentration = 3 mM).

solvent	$k \times 10^{-2}$, s^{-1}
N,*N*-dimethylformamide	1.0
toluene	2.8
tetrahydrofuran	2.7
chloroform	2.9
dichloromethane	2.4
acetonitrile	2.4
ethanol	1.0
methanol	1.9

Table 2.3. X-ray structure refinement data for compound **VI**[a] and TNDS.[a]

compound	**VI**	TNDS
formula	$C_{19}H_{16}N_2O_3Br_2$[b]	$C_{29}H_{24}N_4O_3$[b]
FW	480.16	476.52
T, K	100(2)	100(2)
crystal system	monoclinic	triclinic
space group	$P2_1/c$	*P*-1
Z	8	2
a, Å	9.3937(3)	8.9034(3)
b, Å	33.5488(13)	10.0040(4)
c, Å	11.4358(4)	15.0137(6)

α, °	90	92.4060(10)
β, °	92.7950(10)	105.7170(10)
γ, °	90	113.9040(10)
V, Å^3	3599.7(2)	1159.22(8)
d_{calc} g/cm^3	1.772	1.365
μ, mm^{-1}	1.008	0.090
F(000)	1904.0	500.0
crystal size, mm^3	0.26 × 0.2 × 0.15	0.18 × 0.08 × 0.05
theta range	4.314 to 60.424	4.522 to 52.85
index ranges	−13 ≤ h ≤ 13 −47 ≤ k ≤ 47 −16 ≤ l ≤ 16	−11 ≤ h ≤ 11 −12 ≤ k ≤ 12 −18 ≤ l ≤ 18
refl. collected	177181	33010
data/restraints/parameters	10644/516/653	4759/0/329
GOF on F^2	1.329	1.005
largest peak/hole e/Å^3	0.67/−1.01	0.28/−0.20
R_1 (wR_2), %, [$I \geq 2$sigma(I)][c]	5.53 (11.17)	4.30 (8.94)

[a]Mo-Kα (λ = 0.71073 Å) radiation

[b]Formula is given based on single-crystal X-ray data and does not include disordered solvent molecules

[c]$R_1 = \Sigma||F_o| - |F_c||/ \Sigma |F_o|$, $wR_2 = \{\Sigma [w(F_o^2 - F_c^2)^2]/ \Sigma [w(F_o^2)^2]\}^{1/2}$

Table 2.4. X-ray structure refinement data for compound **VII'**,[a] $HDDB_{in–in}$,[a] and $HDDB_{in–out}$.[a]

compound	**VII'**	$HDDB_{in–in}$	$HDDB_{in–out}$
formula	$C_{38}H_{32}N_4O_6Br_2$[b]	$C_{48}H_{40}N_6O_6$[b]	$C_{50}H_{44}N_6O_7$[b]
FW	800.49	796.86	840.91
T, K	100(2)	100(2)	100(2)
crystal system	monoclinic	monoclinic	monoclinic
space group	$P2_1/c$	$P2_1/c$	$P2_1/c$
Z	4	4	8
a, Å	12.9265(8)	17.2113(8)	15.7656(10)
b, Å	27.1065(17)	9.6042(4)	22.9720(15)
c, Å	11.5966(6)	25.5421(12)	23.9458(15)
α, °	90	90	90
β, °	105.835(2)	109.466(2)	94.083(2)
γ, °	90	90	90
V, Å^3	3909.2(4)	3980.8(3)	8650.4(10)
d_{calc} g/cm^3	1.360	1.330	1.291
μ, mm^{-1}	2.121	0.089	0.088
F(000)	1624.0	1672.0	3536.0
crystal size, mm^3	0.46 × 0.4 × 0.34	0.22 × 0.14 × 0.06	0.36 × 0.18 × 0.16
theta range	4.446 to 55.638	4.566 to 52.742	4.392 to 46.706

index ranges	$-16 \le h \le 16$ $-35 \le k \le 35$ $-15 \le l \le 15$	$-21 \le h \le 21$ $-12 \le k \le 12$ $-31 \le l \le 31$	$-17 \le h \le 17$ $-25 \le k \le 25$ $-26 \le l \le 26$
refl. collected	190319	154012	237374
data/restraints/ parameters	9241/0/457	8112/0/587	12536/0/1150
GOF on F^2	1.032	1.051	1.058
largest peak/hole e/Å^3	1.18/−1.40	0.27/−0.26	0.68/−0.68
R_1 (wR_2), %, $[I \ge 2\text{sigma}(I)]$[c]	4.32 (10.72)	4.51 (9.52)	8.13 (21.15)

[a]Mo-Kα (λ = 0.71073 Å) radiation

[b]Formula is given based on single-crystal X-ray data and does not include disordered solvent molecules

[c]$R_1 = \Sigma||F_o| - |F_c||/ \Sigma |F_o|$, $wR_2 = \{\Sigma [w(F_o^2 - F_c^2)^2]/ \Sigma [w(F_o^2)^2]\}^{1/2}$

Table 2.5. X-ray structure refinement data for compound **1**,[a] **2**,[a] and **3'**.[a]

compound	**1**	**2**	**3**
formula	$C_{63}H_{40}N_4O_{11}Zn_2Br_2$[b]	$C_{82}H_{56}N_6O_{14}Zn_2Br_2$[b]	$C_{53}H_{38}N_2O_8S_2Zn_2$[b]
FW	1319.55	1639.88	1035.71
T, K	220(2)	220(2)	100(2)
crystal system	orthorhombic	orthorhombic	monoclinic
space group	*Pmmm*	*Pmmm*	*C*2
Z	1	4	6
a, Å	11.291(4)	11.149(2)	19.9556(11)
b, Å	15.799(5)	15.869(3)	22.8307(14)
c, Å	18.292(6)	22.608(5)	21.9438(12)
α, °	90	90	90
β, °	90	90	91.054(2)
γ, °	90	90	90
V, Å^3	3263.0(18)	4000.1(13)	9995.9(10)
d_{calc} g/cm^3	0.672	2.723	1.022
μ, mm^{-1}	1.008	3.327	0.823
F(000)	664.0	3328.0	3156
crystal size, mm^3	0.46 × 0.2 × 0.18	0.4 × 0.36 × 0.2	0.14 × 0.1 × 0.1
theta range	4.434 to 42.596	4.424 to 42.52	4.454 to 53.46
index ranges	$-11 \le h \le 11$ $-14 \le k \le 16$ $-18 \le l \le 18$	$-11 \le h \le 11$ $-16 \le k \le 16$ $-23 \le l \le 23$	$-25 \le h \le 25$ $-28 \le k \le 28$ $-27 \le l \le 27$

refl. collected	12712	23134	153458
data/restraints/ parameters	2089/84/103	2555/28/90	21209/30/915
GOF on F^2	1.027	1.039	1.021
largest peak/hole e/Å^3	0.76/−0.53	1.12/−0.94	0.28/−0.34
R_1 (wR_2), %, [$I \geq 2\text{sigma}(I)$][c]	5.71 (14.31)	6.97 (19.34)	4.20 (8.52)

[a]Mo-Kα (λ = 0.71073 Å) radiation

[b]Formula is given based on single-crystal X-ray data and does not include disordered solvent molecules

[c]$R_1 = \Sigma||F_o| - |F_c||/ \Sigma |F_o|$, $wR_2 = \{\Sigma [w(F_o^2 - F_c^2)^2]/ \Sigma [w(F_o^2)^2]\}^{1/2}$

CHAPTER 3

PHOTORESPONSIVE FRAMEWORKS: ENERGY TRANSFER IN THE SPOTLIGHT

Martin, C. R.; Park, K. C.; Corkill, R. E.; Kittikhunnatham, P.; Leith, G. A.; Mathur, A.; Abiodun, S. L.; Greytak, A. B.; Shustova, N. B. *Faraday Discuss.* **2021**, *231*, 266–280.

Chapter abstract. In this chapter, spiropyran-containing metal- and covalent-organic frameworks (MOFs and COFs, respectively) are probed as platforms for fostering photochromic behavior in solid-state materials, while simultaneously promoting directional energy transfer (ET). In particular, Förster resonance energy transfer (FRET) between spiropyran and porphyrin derivatives integrated as linkers in the framework matrix is discussed. The photochromic spiropyran derivatives allow for control over material optoelectronic properties through alternation of excitation wavelengths. Photoinduced changes in the material electronic profile have also been probed through conductivity measurements. Time-resolved photoluminescence studies were employed to evaluate the effect of photochromic linkers on material photophysics. Furthermore, "forward" and "reverse" FRET processes occurring between two distinct chromophores were modeled, and the Förster critical radii and ET rates were estimated to support the experimentally observed changes in material photoluminescence.

INTRODUCTION

Mimics of the natural photosystem, that rely on the spatial organization of hundreds of thousands of porphyrinoid derivatives (capable of, for example, oxygen transport in hemoglobin or detoxification of anthropogenics via cytochrome P450), have been central to research due to their proven and unrivalled potentials.[1–3] Crystalline metal- or covalent-organic frameworks (MOFs and COFs, respectively) could promote hierarchical organization of organic linkers that can be assembled around metal centers,[4–25] opening a pathway for scaffold-imposed photocatalysis. Such chromophore organization through COFs or MOFs presents an opportunity to study and model energy transfer (ET) processes for the realization of directional ET in frameworks.[26–28] There are a number of studies

focused on ET processes in MOFs[27–35] and COFs[36,37] that describe different mechanisms and methods to achieve efficient ET. Herein, we consider the possibility to modulate the ET processes, in particular Förster resonance energy transfer (FRET), through spiropyran-based photochromic units embedded in the rigid matrix of a framework as either a side group or a guest (Scheme 3.1). The prepared materials were studied by powder and single-crystal X-ray diffraction (PXRD and SC-XRD, respectively), ^{1}H nuclear magnetic resonance (NMR) spectroscopy, mass-spectrometry (MS), and conductivity measurements as well as diffuse reflectance, steady-state, and time-resolved photoluminescence (PL) spectroscopy; the latter spectroscopic techniques were employed to study the possibility of directing excited-state decay pathways through photoisomerization of a spiropyran moiety integrated inside a rigid framework.

RESULTS AND DISCUSSION

Spiropyran and its derivatives exhibit rapid photoinduced spiropyran-to-merocyanine isomerization in solution;[38–40] however, in the solid-state, similar transformations are hindered due to significant structural rearrangements accompanied with photoisomer conversion.[40] Recent progress in the field of spiropyran-based materials has demonstrated that MOFs can serve as a platform to promote such transformations in the solid state by providing framework voids for spiropyran photoisomerization to occur.[41–44] Remarkably, it was demonstrated that such MOF-promoted photoisomerization can occur with rates comparable to those in solution.[42] In contrast to the previously reported diarylethene-based MOFs, another common class of photochromic molecule[45,46] that has been integrated as a part of a framework skeleton (i.e., coordinated to the metal from both sides of a diarylethene core),[31,32,47–49] spiropyran photoisomerization occurs inside of the

framework pores. Consequently, the rearrangement of a photochromic unit is less sterically hindered, as reflected by the photoisomerization rates.[42]

For integration within a MOF, we synthesized a photochromic spiropyran- based derivative, 1',3',3'-trimethyl-6-nitro-4',7'-di(pyridin-4-yl)spiro[chromene-2,2'-indoline] (TNDS), functionalized with two pyridyl arms for coordination to a metal center.[42] The framework for TNDS integration was selected based on two criteria: the presence of metal sites available for coordination of the photochromic linker and appropriate spectral overlap of the donor (D) emission and acceptor (A) absorption spectra that is required for FRET to take place.[27,28] Both of these criteria are satisfied by the two-dimensional (2D) framework, Zn_2(ZnTCPP) (H_4TCPP = tetrakis(4-carboxyphenyl)-porphyrin).[50] This framework is composed of 2D layers consisting of paddlewheel $Zn_2(O_2C)_4^-$ secondary-building units (SBUs), bridged together by $ZnTCPP^{4-}$ ligands (Figure 3.1).[50]

In the paddlewheel-based SBUs of Zn_2(ZnTCPP), Zn atoms are axially coordinated with labile solvent molecules that can be replaced by TNDS, resulting in the coordinative integration of photochromic pillars between porphyrin-based layers and the construction of a three-dimensional (3D) photoresponsive framework (Figure 3.1).[51,52] In Figure 3.1, it is shown that the porphyrin-containing 2D framework emits at $\lambda_{em(max)}$ = 660 nm (λ_{ex} = 350 nm), and its emission spectrum overlaps with the TNDS absorption profile. Due to the spectral overlap and photoinduced control of the TNDS absorption profile, we hypothesized that TNDS photoisomerization could result in changes of the MOF emission profile and modulate resonance ET efficiency. However, TNDS emission ($\lambda_{em(max)}$ = 690 nm; λ_{ex} = 350 nm) also overlaps with the absorption of Zn_2(ZnTCPP) (Figure 3.6), and therefore, the “reverse” process of transferring energy from TNDS to Zn_2(ZnTCPP) could

also take place. Therefore, there could be two pathways for FRET to occur: from Zn_2(ZnTCPP) (D) to TNDS (A), that will be referred to from now on as a "forward" FRET process and from TNDS (D) to Zn_2(ZnTCPP) (A; "reverse" FRET).

Heating of TNDS in the presence of $Zn(NO_3)_2 \cdot 6H_2O$ and H_4TCPP in a *N*,*N*-diethylformamide/ethanol/nitric acid mixture at 80 °C for 14 hours led to the formation of dark-red crystals of Zn_2(ZnTCPP)(TNDS). According to PXRD data, novel Zn_2(ZnTCPP)(TNDS) is isostructural to Zn_2(DBTD)(TNDS) (H_4DBTD = 3',6'- dibromo-4',5'-bis(4-carboxyphenyl)-[1,1':2',1"-terphenyl]-4,4"-dicarboxylic acid), also containing photochromic TNDS (Figure 3.7).[42] Similar to Zn_2(DBTD)(TNDS),[42] the 2D layers of Zn_2(ZnTCPP) are connected by TNDS pillars. These structural similarities are reflected by the resemblance in PXRD patterns of Zn_2(ZnTCPP)(TNDS) and Zn_2(DBTD)(TNDS)[42] as shown in Figure 3.7. Crystals of Zn_2(ZnTCPP)(TNDS) were sufficient to perform SC-XRD analysis; however, due to significant crystallographic disorder (likely occurring due to the rotational and photoresponsive nature of the coordinated TNDS linker), anisotropic refinement could not be performed for all atoms in the structure, even upon utilization of synchrotron radiation. This challenge is common for porphyrin-based photochromic frameworks,[31,32] and the situation becomes even more complex due to the presence of the photochromic unit isomerizing under irradiation.[53,54] The collected unit cell parameters of Zn_2(ZnTCPP)(TNDS), a = b = 16.642 Å, and c = 34.002 Å ($\alpha = \beta = \gamma = 90°$), are distinct from those of 2D Zn_2(ZnTCPP) by the unit cell parameter, c. This parameter indicates a change of the interlayer distance from 34 Å (Zn_2(ZnTCPP)(TNDS)) to 19 Å[50] (Zn_2(ZnTCPP)). This interlayer expansion is consistent with the length of TNDS (11.416 Å, measured as the N···N distance between pyridyl arms of TNDS). Comparison of the

PXRD patterns of Zn_2(ZnTCPP)(TNDS) and Zn_2(ZnTCPP)[42,50] revealed a peak shift from higher 2θ to lower angles, that is also associated with the interlayer expansion observed in Zn_2(ZnTCPP)(TNDS) (e.g., from $2\theta = 9.6°$ (002) in the Zn_2(ZnTCPP) pattern to $\theta = 4.9°$ (002) in the Zn_2(ZnTCPP)(TNDS) pattern). Integration of TNDS between 2D porphyrin-based layers was also confirmed by Fourier-transform infrared (FTIR) spectroscopy through the appearance of the ν(C–O–C) stretch associated with the presence of the benzopyran group in the TNDS linker (its absence was also confirmed in Zn_2(ZnTCPP), Figure 3.7).[55] According to ^{1}H NMR spectroscopy and MS of the digested Zn_2(ZnTCPP)(TNDS) sample (Figure 3.8), H_4TCPP and TNDS are present in a ratio of 1:0.98, indicating almost complete installation of photochromic TNDS between the Zn_2(ZnTCPP) layers.

To confirm that embedded TNDS preserves its photochromic behavior upon immobilization inside a MOF's rigid matrix, the spectroscopic properties of Zn_2(ZnTCPP)(TNDS) were studied under irradiation with UV and visible light. The changes in absorption profile were monitored by time-resolved diffuse reflectance spectroscopy (Figure 3.2). The attenuation rate for the TNDS cyclization reaction (merocyanine-to-spiropyran) immobilized in Zn_2(ZnTCPP)(TNDS) was estimated under visible-light irradiation (a 400 nm longpass filter was used to remove UV light from a white halogen lamp) and was found to be 1.5×10^{-1} s^{-1}, which is in line with the previously reported value for Zn_2(DBTD)(TNDS) (1.6×10^{-1} s^{-1}).[42] Therefore, TNDS integrated in the matrix of the porphyrin-based MOF still exhibited photochromic behavior. Moreover, the estimated cyclization rate of Zn_2(ZnTCPP)(TNDS) is comparable with the photoisomerization rate of TNDS in a 3 mM *N*,*N*-dimethylformamide (DMF) solution (1.2

$\times 10^{-1}$ s^{-1}).[42] A detailed description of the photophysical experiments is given in the Experimental section below.

As previously described, switching of spiropyran from its "closed" form to its zwitterionic photoisomer (merocyanine) induces a change in conjugation and charge distribution.[40,45,56–60] The difference in electronic structure of photoisomers gives rise to the possibility of current cycling (i.e., changes in current values with a steady applied bias (500 mV)) upon irradiation alternation (i.e., switching between 365 nm and 590 nm excitation) as shown in Figure 3.2. Furthermore, the time-resolved changes observed optically in the diffuse reflectance profile closely match the changes in the electronic properties (Figure 3.2). To demonstrate that the observed changes were exclusively associated with the installed photochromic linker, TNDS, control experiments using non- photochromic Zn_2(ZnTCPP) were carried out. Indeed, no optical or current cycling was observed for non-photochromic Zn_2(ZnTCPP), as shown in Figure 3.2.

Moreover, changes in the absorption edge of Zn_2(ZnTCPP)(TNDS) upon UV-light excitation are consistent with a reduction in band gap (Figure 3.10).[43,60–62] The possibility of the "forward" FRET process between Zn_2(ZnTCPP) (D) and TNDS (A) was evaluated through steady-state and time-resolved PL studies. The Zn_2(ZnTCPP) framework (Figure 3.1) possesses a broad emission in the range of 600–750 nm with λ_{max} = 650 nm (λ_{ex} = 350 nm). If only the "forward" FRET process took place (in the absence of "reverse" FRET), changes in the absorption profile associated with spiropyran-to-merocyanine conversion would result in a dramatic alteration of the PL spectrum due to quenching of the Zn_2(ZnTCPP) emission (and enhancement of TNDS emission), as the D–A distance is well below the Förster critical transfer radius (*vide infra*). Indeed, Figure 3.3 clearly shows

changes in the emission profile of Zn_2(ZnTCPP)(TNDS), resulting in an overall decrease in intensity after 90 seconds of in situ irradiation with UV light (λ_{ex} = 330–385 nm) by 47%. Restoration of the Zn_2(ZnTCPP)(TNDS) emission was observed upon sample irradiation with 590 nm light (or, over time in the dark). Control experiments performed on non-photochromic Zn_2(ZnTCPP) demonstrated the absence of emission alternation (Figure 3.3), providing further confirmation that optical cycling was observed due to the presence of photoresponsive linkers.

Time-resolved PL data indicated a shorter decay lifetime for Zn_2(ZnTCPP)(TNDS) compared to that of Zn_2(ZnTCPP) (Figure 3.11). Analysis of the obtained curves revealed multi- exponential decay in each case (supporting fits are described in Table 3.1). As a result of the analysis, shortening of the amplitude-averaged lifetime (τ) from 0.893 ns (Zn_2(ZnTCPP)) to 0.502 ns (Zn_2(ZnTCPP)(TNDS)) was observed, and in the absence of the "reverse" FRET process, the corresponding "forward" FRET efficiency and ET rate would be 44% and 0.872 ns^{-1}, respectively. It is important to note, however, that the "reverse" FRET process should be considered as well. To examine the rates of "forward" and "reverse" FRET processes, we calculated the spectral overlap functions, (J), between donor and acceptor (Figure 3.4), based on the normalized emission spectrum, approximate quantum yield, and approximate molar extinction spectrum for each species (more details can be found in the ESI). Our calculations determined that $J_{forward} = 2.21 \times 10^{-14}$ M^{-1} cm^3 and $J_{reverse} = 11.2 \times 10^{-14}$ M^{-1} cm^3. The corresponding Förster critical radii (R_o) were found to be 27.3 Å ($R_{o\ forward}$) and 24.4 Å ($R_{o\ reverse}$), both of which are far greater than the D–A distance approximated from the structural data (~12 Å). Therefore, both "forward" and "reverse" FRET processes are expected to occur in our system. To predict the relative

decrease in emission intensity upon UV excitation for Zn_2(ZnTCPP)(TNDS), we considered the radiative decay rate, k_r, non-radiative decay rate, k_{nr}, and ET rate, $k_{ET} = (B \times J)/r_6)k_r$, (for the Zn_2(ZnTCPP) and TNDS components; B = a constant related to the refractive index and mutual orientation of chromophores, r = the distance between chromophores (estimated as 12 Å), and k_r and k_{nr} are estimated from the amplitude-average lifetime and estimated quantum yield (QY = 10% for Zn_2(ZnTCPP) and 1% for Zn_2(TNDS)(DBTD)) see the experimental section for more details). As a result of the performed analysis, k_{ET} forward was estimated to be 156 ns^{-1} while k_{ET} reverse was calculated to be 66 ns^{-1}. The kinetic model predicts limited quenching of the donor in this case, with donor emission continuing to dominate the emission spectrum due to the low radiative rate and QY of the acceptor, TNDS (in the merocyanine form, Figure 3.3).

For comparison with our findings in MOFs, we probed the photochromic behavior of spiropyran integrated inside the COF as an alternative platform.[63–65] We prepared a COF (herein referred to as COF**1**) through a condensation reaction of 1,3,5-tri-(4-aminophenyl)benzene (TAPB), 2,5-dimethoxyterephthalaldehyde (DMTA), and 2,5-bis(2-propynyloxy)terephthalaldehyde (BPTA),[66,67] as shown in Figure 3.5. The alkyne-functionalized COF was chosen due to its broad emission profile that leads to sufficient spectral overlap with spiropyran (Figure 3.5). The PXRD pattern and FTIR spectrum of COF**1** can be found in Figures 3.12 and 3.13, respectively. Synthesized COF**1** exhibited emission in the 500–800 nm range with $\lambda_{em(max)}$ = 680 nm (λ_{ex} = 350 nm), similar to that of Zn_2(ZnTCPP) (Figures 3.1 and 3.5). As a next step, we incorporated spiropyran, 1',3'-dihydro-1',3',3'-trimethyl-6-nitrospiro[2*H*-1-ben-zopyran-2,2'-(2*H*)-indole] (SP, Scheme 3.1) as a guest within the pores of COF**1** via 72 hours of soaking in a tetrahydrofuran (THF)

solution at 40 °C, resulting in SP@COF**1** (more details are given in the Experimental section below). The amount of SP integrated into SP@COF**1** was confirmed through ^{1}H NMR spectroscopy of the digested sample (Figure 3.14, see the Experimental section for more details). The absorption spectrum of SP is shown in Figure 3.5, along with the emission spectrum of COF**1**. Through analysis of the ^{1}H NMR spectrum (Figure 3.14), we determined that there is an average of one SP molecule per two COF pores. In a similar vein to the aforementioned studies on MOFs, we monitored changes in the emission profile of SP@COF**1** through epifluorescence measurements and, similar to Zn_2(ZnTCPP)(TNDS), emission decreased upon UV excitation (λ_{ex} = 330–385 nm, Figure 3.15). As expected, the control experiment performed on the parent COF**1** sample did not demonstrate changes in its emission profile (Figure 3.15). Therefore, we attribute the changes in SP@COF**1** to the integrated SP moiety. Furthermore, time-resolved PL measurements revealed a shortened amplitude-averaged lifetime for SP@COF**1** (0.479 ns) compared to COF**1** (0.649 ns, Figure 3.16). As a result, it is plausible to suggest that COFs, similar to MOFs, could be used as a platform to promote FRET processes that involve SP derivatives. A more detailed analysis of multiple-chromophore photophysics is underway.

SUMMARY

The aforementioned results demonstrate that spiropyran and its derivatives integrated inside porous matrices such as COFs and MOFs maintain a photochromic response that can address the challenge for preparation of spiropyran- containing solid-state materials that has previously been encountered. Along these lines, the observed cyclization rate of synthesized TNDS is comparable with that of spiropyran derivatives in solution, which has only recently been achieved.[42] The photochromic behavior of TNDS

was used to control the optoelectronic properties of the material through alternation of excitation wavelengths. Furthermore, “forward” and “reverse” FRET processes occurring between two types of chromophores were modeled with an estimation of Förster critical radii and energy transfer rates, confirming the experimentally observed changes in material emission intensity. The presented studies bring energy transfer of porous materials into the spotlight for developing a new generation of stimuli- responsive devices.

EXPERIMENTAL SECTION

Materials. Tin(II) chloride anhydrous (98%, BeanTown Chemical), copper(I) chloride anhy- drous (97%, Strem Chemicals), bis(triphenylphosphine)palladium(II) dichloride (96%, Oakwood Chemical), sodium carbonate (ACS grade, Ameresco), magnesium sulfate anhydrous (99.4%, Chem-Impex International Inc.), sodium sulfate anhydrous (99.5%, Oakwood Chemical), sodium chloride (ACS grade, Fisher Chemical), sodium hydroxide (ACS, Oakwood Chemical), potassium hydroxide (ACS grade, Fisher Chemical), potassium carbonate (99.8%, Mallinckrodt), sodium nitrite (98%, Oakwood Chemical), silica gel (60 nm, Macron), 1,3,3-tri- methylindolino-60-nitrobenzopyrylospiran (98%, TCI), 2,5-dibromonitrobenzene (99%, Oakwood Chemical), 3-methyl-2-butanone (>99%, TCI), methyl tri- □uoromethanesulfonate (97%, Matrix Scienti□c), 2-hydroxy-5-nitrobenzaldehyde (98%, Oakwood Chemical), 1,3,5-tribromobenzene (98%, Sigma-Aldrich), 1,4- dimethoxybenzene (99%, Oakwood Chemical), 4-aminophenylboronic acid hydrochloride (99%, Chem-Impex International, Inc.), Aliquat 336 (reagent grade, BeanTown Chemical), boron tribromide (reagent grade, Sigma-Aldrich), prop- argyl bromide (80 wt% in toluene, reagent grade, Oakwood Chemical), n-butyl- lithium (reagent grade, Sigma-Aldrich), hydrochloric acid (ACS,

Fisher Chemical), sulfuric acid (ACS grade, Fisher Chemical), nitric acid (ACS reagent, Sigma- Aldrich), □uoroboric acid (48%, Oakwood Chemical), acetic acid (ACS grade, Fisher Chemical), ethanol (200 proof, Decon Laboratories, Inc.), methanol (ACS grade, Fisher Chemical), acetone (ACS grade, Sigma-Aldrich), ethyl acetate (99.9%, Fisher Chemical), chloroform (99.9%, Fisher Chemical), dichloro- methane (ACS grade, Macron), diethyl ether (ACS grade, J. T. Baker® Chemicals), hexanes (ACS grade, BDH), acetonitrile (ACS grade, Fisher Chemical), N,N- dimethylformamide (ACS grade, Oakwood Chemical), N,N-diethylformamide (>99%, TCI), piperidine (99%, Sigma-Aldrich), carbon tetrachloride (99.9%, Sigma-Aldrich), bromine (99.8%, Acros Organics), tetrahydrofuran (HPLC grade, BeanTown Chemical), 1-butanol (99.4%, Oakwood Chemical), 1,2-dichloroben- zene (98%, Alfa Aesar), 1,4-dioxane (99+%, Alfa Aesar), chloroform-d (Cambridge Isotope Laboratories, Inc.), deuterium chloride (Sigma-Aldrich), and dimethyl sulfoxide-d6 (Cambridge Isotope Laboratories, Inc.) were used as received.

The MOF and COF linkers, 1',3',3'-trimethyl-6-nitro-4',7'-di(pyridin-4-yl)spiro [chromene-2,2'-indoline] (TNDS),[42] 3',6'-dibromo-40,50-bis(4-carboxyphenyl)- [1,1':2',1'-terphenyl]-4,4'-dicarboxylic acid (H_4DBTD),[68] 2,5-dimethoxyterephthalaldehyde (DMTA),[69] 1,3,5-tri-(4-aminophenyl)benzene (TAPB),[70] and 2,5-bis(2-propynyloxy)terephthalaldehyde (BPTA),[71] were synthesized based on modified literature procedures. The MOFs, Zn_2(ZnTCPP)[50] and Zn_2(DBTD)(TNDS),[42] were synthesized based on modified literature procedures. The COFs, COF**1**[66,67] and SP@COF**1**,[44] were synthesized based on modified literature procedures.

Preparation of Zn_2(ZnTCPP)(TNDS). The MOF, Zn_2(ZnTCPP)(TNDS), was prepared using a modified literature procedure.[50] In a one-dram vial, $Zn(NO_3)_2 \cdot 6H_2O$ (17

mg, 57 mmol) and H_4TCPP (7.9 mg, 0.010 mmol) were dissolved in 2.1/0.5 mL DEF/EtOH followed by sonication for 10 minutes. To the solution, TNDS (7.2 mg, 0.015 mmol) in 0.16 mL DEF (*N*,*N*-diethylformamide) and 30 mL of HNO_3 (1.0 M in ethanol (EtOH)) were added. The resulting solution was sonicated for 10 minutes and then heated at 80 °C for 14 hours in an isothermal oven. After heating for 14 hours, the reaction mixture was cooled down to room temperature over 2 hours. Dark red plate-like crystals of Zn_2(ZnTCPP)(TNDS) (15 mg, 9.2 mmol) were isolated in 92% yield. FTIR (neat, cm^{-1}): 660, 665, 701, 713, 718, 735, 747, 775, 794, 838, 872, 888, 996, 1010, 1022, 1063, 1100, 1143, 1175, 1204, 1255, 1277, 1338, 1387, 1398, 1492, 1504, 1550, 1603, 1618, 1649, 1656, and 2927 (Figure 3.8). The PXRD pattern of Zn_2(ZnTCPP)(TNDS) is shown in Figure 3.7. The ^{1}H NMR spectrum and MS data of digested Zn_2(ZnTCPP)(TNDS) are shown in Figure 3.9. The experimental procedure utilized for MOF digestion can be found below.

Preparation of SP@COF1. The COF, SP@COF1, was prepared using a modified literature procedure. In a one-dram vial, COF**1** (18.0 mg) and 1,3,3-trimethylindolino-6'-nitro- benzopyrylospiran (SP; 64.0 mg, 0.198 mmol) were added, followed by the addition of THF (0.400 mL) and heated at 40 °C. After 72 h, the precipitate was collected and washed with THF (5 mL) and acetonitrile (5 mL) to remove any excess SP from the surface of the COF. As a result, a yellow powder (16 mg) was collected. FTIR (neat, cm^{-1}): 662, 694, 739, 828, 879, 1014, 1038, 1095, 1144, 1180, 1210, 1289, 1340, 1409, 1443, 1464, 1489, 1504, 1591, 1611, 1673, 1717, 1727, 2044, 2854, 2924, and 2960 (Figure 3.13). The PXRD pattern of SP@COF**1** is shown in Figure 3.13. The ^{1}H NMR spectrum of digested SP@COF**1** is shown in Figure 3.9. It was determined to have 0.46 SP

per three –OMe units (i.e., 0.46 SP per COF pore). The experimental procedure utilized for COF digestion can be found below.

General digestion procedure. In order to study the prepared MOFs and COFs by ^{1}H NMR spectroscopy, a solution of 500 mL of DMSO-d_6 and 5.0 mL of deuterium chloride were added to 5.0 mg of washed material, followed by sonication for 5 minutes and heating at 75 °C (MOFs) or 100 °C (COFs) for 24 hours. The percentage of each component were calculated based on proton ratios obtained through integration of signals in the ^{1}H NMR spectra of digested samples (Figure 3.9 and 3.14).

Diffuse reflectance and photoluminescence spectroscopy. Diffuse reflectance spectra were collected on an Ocean Optics JAZ spectrometer. An Ocean Optics ISP-REF integrating sphere was connected to the spectrometer using a 450 mm SMA fiber optic cable. Samples were loaded in a 4.0 mm quartz sample cell, which was referenced to an Ocean Optics WS-1 Spectralon® standard. A mounted high-powered LED (M365L2, Thorlabs, λ_{ex} = 365 nm, distance = 1 cm, LEDD1B power supply set at 700 mA) was used for in situ irradiation of the samples.

Steady-state emission spectra were acquired on an Edinburgh FS5 fluorescence spectrometer equipped with a 150 W Continuous Wave Xenon Lamp source for excitation. Emission measurements on solid samples were collected on the powders of the desired materials placed inside a 0.5 mm quartz sample holder using the front-facing module.

Emission via epifluorescence microscopy was measured using an Olympus BX51 microscope equipped with a UV filter cube that allows for excitation between 330–385 nm and emission from >420 nm (Olympus U-MWU2). A 120 W mercury vapor short arc lamp was used as an excitation light source. Samples were measured under simultaneous

irradiation until no changes in emission were observed for 30 seconds. For measurements over time, spectra were recorded on an Ocean Optics USB4000 spectrometer under continuous UV-irradiation (λ_{ex} = 330– 385 nm) and the epifluorescence microscopic images of samples before and after UV-irradiation were collected with a color digital CMOS camera (Canon EOS REBEL T3/1100D). The integration time was set to 100 ms with 10 scans averaged per spectrum and a boxcar width of 5.

Fluorescence decay lifetimes were measured using a DeltaFlex TCSCP Lifetime Fluorometer from Horiba Instruments equipped with a 373 nm pulsed-laser diode. First, a small spot of type-NVH immersion oil (Cargille Labs) was placed onto the polished side of a cut silicon wafer and then the sample was mixed with the immersion oil. The silicon wafer was then placed on the front-facing module. Prior to reaching the photon counter, light passed through a monochromator that was set to 660 nm to filter stray light. MOFs were irradiated for 5 minutes (10 minutes for COFs) with UV light prior to sample measurement to ensure conversion to merocyanine.

Optical cycling. Optical cycling of photochromic MOFs and COFs was carried out using an Ocean Optics JAZ spectrometer. An Ocean Optics ICPREF integration sphere was connected to the spectrometer using a 450 mm SMA fiber optic cable. Prior to time-resolved DR measurements, the sample background spectrum was subtracted to remove the region that does not correspond to photophysical behavior of the photochromic moieties integrated into the framework. A sample was placed inside a 4.0 mm quartz sample holder and a 400 nm longpass glass filter (Thorlabs, FGCL400) was placed between the quartz sample cell with a quartz cover slide and the integrating sphere to filter any UV light from the internal tungsten- halogen lamp. The quartz sample holder with a quartz cover slide

and longpass filter were attached to the top of the integrating sphere with electrical tape to prevent sample displacement. A mounted high-powered LED (M365L2, Thorlabs, λ_{ex} = 365 nm, distance = 2 cm, and LEDD1B power supply set to 245 mA) was used for in situ irradiation of the sample for 1 minute, then the sample was allowed to undergo photoinduced reversion on the top of the integration sphere for 15 seconds while a spectrum was collected every 200 ms. This procedure was repeated for three consecutive irradiation cycles (Figure 3.2).

Conductivity measurements. A two-point method was employed to measure the conductivity, σ (S cm^{-1}), of the pressed pellets according to the following equation:

$$\sigma = Il/VA$$

Where I = current, l = thickness of the pellets, V = voltage, and A = surface area of the prepared pellets.

The electrical conductance in the prepared materials followed Ohm's law and was measured by fitting a linear current (I)–voltage (V) curve. An "in-house" two- contact probe pressed pellet setup (2C3PS)[60,72,73] made it possible to fabricate the pressed pellets and perform measurements in situ while also allowing for simultaneous MOF irradiation and monitoring changes in electrical current flow under the applied voltage. The MOF powder (10 mg), pre-dried for 20 minutes in air (unless otherwise noted), was pressed between two stainless steel rods inside an insulating quartz tube. The diameter of the resulting pellet was the same as the inner diameter of the quartz tube (d = 2 mm). The thickness of the pellets was kept consistent (l = 1 mm) using the same amount of material. After forming a small pellet, the stainless-steel rods were connected to a sourcemeter (Keithley Instruments GmbH, Germering, Germany, model 2636A) using a 3-slot triax-to-alligator clip cable to

perform conductivity measurements. For all measurements, the number of power line cycles (NPLC) was set to 5 with a delay of 1 ms.

To measure the electrical conductivity for photochromic MOFs before and after irradiation with UV light, the samples were first dried in air for 20 minutes and then placed into the 2C3PS. The samples were measured in the dark initially and then again after irradiation with a mounted high-powered LED (M365L2, Thorlabs, λ_{ex} = 365 nm, distance = 6 cm, LEDD1B power supply set at 700 mA) for 5 minutes. The measurements were performed using the 2C3PS connected to a sourcemeter (Keithley Instruments GmbH, Germering, Germany, model 2636A). The *I–V* curves were collected by supplying a voltage in the range 1 V to +1 V. The electrical conductance in the prepared materials follows Ohm's law and was estimated by fitting the obtained linear I–V curves.

Conductance cycling. Dependence of the current values on UV- and visible-light excitation wavelength for Zn_2(ZnTCPP)(TNDS) was measured in the previously discussed 2C3PS that was connected to a sourcemeter (Keithley Instruments GmbH, Germering, Germany, model 2636A; Figure 3.2). A constant voltage (500 mV) was applied while current was measured every 100 ms (NPLC = 5 with a delay of 1 ms). Before data collection, an equilibration time (t = 90 s) was applied in the dark. Then, the sample was irradiated (t = 15 s) using a high-powered LED (M365L2, Thorlabs λ_{ex} 365 nm, the LED-sample distance = 2 cm, LEDD1B power supply set to 700 mA), followed by thermal relaxation in the dark (t = 15 seconds). The procedure was repeated for three consecutive irradiation cycles. PXRD studies were used to confirm the integrity of the MOFs and COFs after optical cycling (Figure 3.17–3.19).

Other physical measurements. FTIR spectra were obtained on a Perkin-Elmer Spectrum 100. H NMR spectra were collected on a Bruker Avance III-HD 400 MHz NMR spectrometer. ^{1}H NMR spectra were referenced to residual ^{1}H peaks of deuterated solvents. PXRD patterns of MOFs were recorded on a Rigaku Miniflex 6G diffractometer at a scan rate of 10° minute^{-1} with accelerating voltage and current of 40 kV and 15 mA, respectively. PXRD patterns of COFs were recorded on a Rigaku Miniflex 6G diffractometer at a scan rate of 5° minute^{-1} with accelerating voltage and current of 40 kV and 15 mA, respectively. The Water QTOF-I quadrupole time-of-flight and Thermo Scientific Orbitrap Velos Pro mass spectrometers were used to record the mass spectra of the prepared compounds.

Fitting of fluorescence decays. The fluorescence decays for Zn_2(ZnTCPP), Zn_2(ZnTCPP)(TNDS), Zn_2(DBTD)(TNDS), COF**1**, and SP@COF**1** were fit with the multi exponential function:[74,75]

$$I(t) = \int_{\infty}^{t} IRF(t') \sum_{i=1}^{n} B_i e^{\left[-\frac{t-t'}{\tau_i}\right]} dt' \qquad (Eq.S1)$$

Where τ and B are lifetime and amplitude, respectively.

For triexponential functions, the amplitude-weighted average fluorescence lifetimes (τ_{avg}) were calculated based on the following equation:

$$\tau_{avg} = \frac{B_1\tau_1 + B_2\tau_2 + B_3\tau_3}{B_1 + B_2 + B_3} \qquad (Eq.S2)$$

For biexponential functions, the amplitude-weighted average fluorescence lifetimes (τ_{avg}) were calculated based on the following equation:

$$\tau_{avg} = \frac{B_1\tau_1 + B_2\tau_2}{B_1 + B_2} \qquad (Eq.S3)$$

Spectral overlap function and Förster radius. The spectral overlap function, *J*, was calculated from the experimental donor emission and acceptor absorption using the following equation:

$$J = \int f(\lambda)d\lambda, f(\lambda) = F_D(\lambda)\varepsilon_A(\lambda)\lambda^4 \qquad (Eq.S4)$$

Where $F_D(\lambda)$ is the donor emission spectrum normalized to unit area and $\varepsilon_A(\lambda)$ is the molar extinction spectrum of the acceptor (Figure 3.4). The calculated overlap function has been used for estimation of the corresponding Förster critical radius, R_o, i.e., the distance at which energy transfer efficiency is 50%:

$$R_o(cm) = (8.79 \times 10^{-25} \times \kappa^2 n^{-4} Q_d J)^{\frac{1}{6}} \qquad (Eq.S5)$$

Where $Q_d = k_r \times \tau_D$ (k_r = donor radiative rate), κ is an orientation factor (taken to be κ^2=2/3 corresponding to randomized orientations, and n is the effective refractive index taken to be n=1.33). The function, $f(\lambda)$, is plotted in Figure 3.4.

REFERENCES

[1] Hod, I.; Sampson, M. D.; Deria, P.; Kupiak, C. P.; Farh,a O. K.; Hupp, J. T. *ACS Catal.* **2015**, *5*, 6302–6309.

[2] Diercks, C. S.; Lin, S.; Kornienko, N.; Kapustin, E. A.; Nichols, E. M.; Zhu, C.; Zhao, Y.; Chang, C. J.; Yaghi, O. M. *J. Am. Chem. Soc.* **2018**, *140*, 1116–1122.

[3] Kornienko, N.; Zhao, Y.; Kley, C. S.; Zhu, C.; Kim, D.; Lin, S.; Chang, C. J.; Yaghi, O. M.; Yang, P. *J. Am. Chem. Soc.* **2015**, *137*, 14129–14135.

[4] Simon-Yarza, T.; Mielcarek, A.; Couvreur, P.; Serre, C. *Adv. Mater.* **2018**, *30*, 1707365.

[5] Das, A.; D'Alessandro, D. M. *Dalton Trans.* **2016**, *45*, 6824–6829.

[6] Takashima, Y.; Martínez, V. M.; Furukawa, S.; Kondo, M.; Shimomura, S.; Uehara, H.; Nakahama, M.; Sugimoto, K.; Kitagawa, S. *Nat. Commun.* **2011**, *2*, 168.

[7] Zhang, S.-Y.; Shi, W.; Cheng, P.; Zaworotko, M. J. *J. Am. Chem. Soc.* **2015**, *137*,

12203–12206.

[8] Coudert, F.-X.; Fuchs, A. H. *Coord. Chem. Rev.* **2016**, *307*, 211–236.

[9] Orellana-Tavra, C.; Mercado, S. A. and Fairen-Jimenez, D. *Adv. Healthcare Mater.* **2016**, *5*, 2261–2270.

[10] Choi, K. M.; Kim, D.; Rungtaweevoranit, B.; Trickett, C. A.; Barmanbek, J. T. D.; Alshammari, A. S.; Yang, P.; Yaghi, O. M. *J. Am. Chem. Soc.* **2017**, *139*, 356–362.

[11] Zhou, H.-C.; Kitagawa, S. *Chem. Soc. Rev.* **2014**, *43*, 5415–5418.

[12] Kang, X.; Wu, X.; Han, X.; Yuan, C.; Liu. Y.; Cui, Y. *Chem. Sci.* **2020**, *11*, 1494–1502.

[13] Rojas, S.; Arenas-Vivo, A.; Horcajada, P. *Coord. Chem. Rev.* **2019**, *388*, 202–226.

[14] Zhang, Y.; Pang, J.; Li, J.; Yang, X.; Feng, M.; Cai P.; Zhou, H.-C. *Chem. Sci.* **2019**, *10*, 8455–8460.

[15] Hu, W.; Yang, F.; Pietraszak, N.; Gu J.; Huang, J.; *Phys. Chem. Chem. Phys.* **2020**, *22*, 25445–25449.

[16] Gerkman, M. A.; Gibson, R. S. L.; Calbo, J.; Shi, Y.; Fuchter, M. J.; Han, G. G. D.; *J. Am. Chem. Soc.* **2020**, *142*, 8688–8695.

[17] Rudd, N. D.; Liu, Y.; Tan, K.; Chen, F.; Chabal, Y. J.; Li, J. *ACS Sustainable Chem. Eng.* **2019**, *7*, 6561–6568.

[18] Chen, Y.; Li, P.; Zhou, J.; Buru, C. T.; ĐorCević, L.; Li, P.; Zhang, X.; Cetin, M. M.; Stoddart, J. F.; Stupp, S. I.; Wasielewski, M. R.; Farha, O. K. *J. Am. Chem. Soc.* **2020**, *142*, 1768–1773.

[19] Jiao, W.; Zhu, J.; Ling, Y.; Deng, M.; Zhou Y.; Feng, P. *Nanoscale*, **2018**, *10*, 20339–20346.

[20] Kalaj, M.; Cohen, S. M. *ACS Cent. Sci.*, **2020**, *6*, 1046–1057.

[21] Zhou, W.; Huang, D.-D.; Wu, Y.-P.; Zhao, J.; Wu, T.; Zhang, J.; Li, D.-S.; Sun, C.; Feng, P.; Bu, X. *Angew. Chem., Int. Ed.* **2019**, *58*, 4227–4231.

[22] Majewski, M. B.; Peters, A. W.; Wasielewski, M. R.; Hupp, J. T.; Farha, O. K. *ACS Cent. Sci.* **2018**, *3*, 598–611.

[23] Bigdeli, F.; Lollar, C. T.; Morsali, A.; Zhou, H.-C. *Angew. Chem., Int. Ed.* **2020**, *59*, 4652–4669.

[24] Xia, Z.; Li, F.; Xu, L.; Feng, P. *Dalton Trans.* **2020**, *49*, 11157–11162.

[25] Liu, X.-Y.; Lustig, W. P.; Li, J. *ACS Cent. Sci.* **2020**, *5*, 2671–2680.

[26] Silva, R. C.; Silva, L. O.; Andrade-Bartolomeu, A.; Brocksom, T. J.; Oliveira, K. T. *Beilstein J. Org. Chem.* **2020**, *16*, 917–955.

[27] Williams, D. E.; Shustova, N. B. *Chem. –Eur. J.* **2015**, *21*, 15474–15479.

[28] So, M. C.; Wiederrecht, G. P.; Mondloch, J. E.; Hupp, J. T.; Farha, O. K. *Chem. Commun.* **2015**, *51*, 3501–3510.

[29] Dolgopolova, E. A.; Rice, A. M.; Smith, M. D.; Shustova, N. B. *Inorg. Chem.* **2016**, *55*, 7257–7264.

[30] Dolgopolova, E. A.; Williams, D. E.; Greytak, A. B.; Rice, A. M.; Smith, M. D.; Krause, J. A.; Shustova, N. B. *Angew. Chem., Int. Ed.* **2015**, *54*, 13639–13643.

[31] Park, J.; Feng, D.; Yuan, S.; Zhou, H.-C. *Angew. Chem., Int. Ed.* **2015**, *54*, 430–435.

[32] Williams, D. E.; Rietman, J. A.; Maier, J. M.; Tan, R.; Greytak, A. B.; Smith, M. D.; Krause, J. A.; Shustova, N. B. *J. Am. Chem. Soc.* **2014**, *136*, 11886–11889.

[33] Lee, C. Y.; Farha, O. K.; Hong, B. J.; Sarjeant, A. A.; Nguyen, S. T.; Hupp, J. T. *J. Am. Chem. Soc.* **2011**, *133*, 15858–15861.

[34] Park, K. C.; Seo, C.; Gupta, G.; Kim, J.; Lee, C. Y. *ACS Appl. Mater. Interfaces* **2017**, *9*, 38670–38677.

[35] Zhang, Q.; Zhang, C.; Cao, L.; Wang, Z.; An, B.; Lin, Z.; Huang, R.; Zhang, Z.; Wang, C.; Lin, W. *J. Am. Chem. Soc.* **2016**, *138*, 5308–5315.

[36] Ding, S.-Y.; Wang, P.-L.; Yin, G.-L.; Zhang, X.; Lu, G. *Int. J. Hydrogen Energy* **2019**, *44*, 11872–11876.

[37] Yao, L.; Zhang, Y.; Wang, H.-X.; Guo, Y.; Zhuang, Z.-M.; Wen, W.; Zhang X.; Wang, S. *J. Mater. Chem. A*, **2020**, *8*, 8518–8526.

[38] Rice, A. M.; Martin, C. R.; Galitskiy, V. A.; Berseneva, A. A.; Leith, G. A.; Shustova, N. B. *Chem. Rev.* **2020**, *120*, 8790–8813.

[39] Gonzalez, A.; Kengmana, E. S.; Fonseca, M. V.; Han, G. G. D. *Materials Today Advances* **2020**, *6*, 100058.

[40] Klajn, R. *Chem. Soc. Rev.* **2014**, *43*, 148–184.

[41] Healey, K.; Liang, W.; Southon, P. D.; Church, T. L.; D'Alessandro, D. M. *J. Mater. Chem. A*, **2016**, *4*, 10816–10819.

[42] Williams, D. E.; Martin, C. R.; Dolgopolova, E. A.; Swifton, A.; Godfrey, D. C.; Ejegbavwo, O. A.; Pellechia, P. J.; Smith, M. D.; Shustova, N. B. *J. Am. Chem. Soc.* **2018**, *140*, 7611–7622.

[43] Martin, C. R.; Leith, G. A.; Kittikhunnatham, P.; Park, K. C.; Ejegbavwo, O. A.; Mathur, A.; Callahan, C. R.; Desmond, S. L.; Keener, M. R.; Ahmed, F.; Pandey, S.; Smith, M. D.; Phillpot, S. R.; Greytak, A. B.; Shustova, N. B. *Angew. Chem., Int. Ed.* **2021**, *133*, 8152–8160.

[44] Garg, S.; Schwartz, H.; Kozlowska, M.; Kanj, A. B.; Müller, K.; Wenzel, W.; Ruschewitz, U.; Heinke, L. *Angew. Chem., Int. Ed.* **2019**, *58*, 1193–1197.

[45] M. Irie, T. Fukaminato, K. Matsuda and S. Kobatake, *Chem. Rev.*, **2014**, *114*, 12174–12277.

[46] Irie, M. *Chem. Rev.,* **2000**, *100*, 1685–1716.

[47] Patel, D. G.; Walton, I. M.; Cox, J. M.; Gleason, C. J.; Butzer, D. R.; Benedict, J. B. *Chem. Commun.* **2014**, *50*, 2653–2656.

[48] Walton, I. M.; Cox, J. M.; Mitchell, T. B.; Bizier, N. P.; Benedict, J. B. *CrystEngComm* **2016**, *18*, 7972–7977.

[49] Walton, I. M.; Cox, J. M.; Benson, C. A.; Patel, D. G.; Chen, Y.-S.; Benedict, J. B. *New J. Chem.* **2016**, *40*, 101–106.

[50] Choi, E.-Y.; Wray, C. A.; Hu, C.; Choe, W. *CrystEngComm*, **2009**, *11*, 553–555.

[51] Burnett, B. J.; Choe, W. *CrystEngComm*, **2012**, *14*, 6129–6131.

[52] Burnett, B. J.; Barron, P. M.; Hu, C.; Choe, W. *J. Am. Chem. Soc.*, **2011**, *133*, 9984–9987.

[53] Kruttwig, K.; Yankelevich, D. R.; Brueggemann, C.; Tu, C.; L'Etoile, N.; Knoesen,

A.; Louie, A. Y. *Molecules* **2012**, *17*, 6605–6624.

[54] Scarmagnani, S.; Walsh, Z.; Slater, C.; Alhashimy, N.; Paull, B.; Macka, M.; Diamond, D. *J. Mater. Chem.*, **2008**, *18*, 5063–5071.

[55] Barroso-Bogeat, A.; Alexandre-Franco, M.; Fernández-González, C.; Gómez-Serrano, V. *Energy Fuels* **2014**, *28*, 4096–4103.

[56] Buback, J.; Nuernberger, P.; Kullmann, M.; Langhojer, F.; Schmidt, R.; Würthner, F.; Brixner, T. *J. Phys. Chem. A* **2011**, *115*, 3924–3935.

[57] Dolgopolova, E. A.; Rice, A. M.; Martin, C. R.; Shustova, N. B. *Chem. Soc. Rev.* **2018**, *47*, 4710–4728.

[58] Kim, D.; Zhang, Z.; Xu, K. *J. Am. Chem. Soc.* **2017**, *139*, 9447–9450.

[59] Sanchez-Lozano, M.; Estévez, C. M.; Hermida-Ramón, J.; Serrano-Andres, L. *J. Phys. Chem. A* **2011**, *115*, 9128–9138.

[60] Dolgopolova, E. A.; Galitskiy, V. A.; Martin, C. R.; Gregory, H. N.; Yarbrough, B. J.; Rice, A. M.; Berseneva, A. A.; Ejegbavwo, O. A.; Stephenson, K. S.; Kittikhunnatham, P.; Karakalos, S. G.; Smith, M. D.; Greytak, A. B.; Garashchuk, S.; Shustova, N. B. *J. Am. Chem. Soc.* **2019**, *141*, 5350–5358.

[61] Leong, C. F.; Wang, C.-H.; Ling, C. D.; D'Alessandro, D. M. *Polyhedron* **2018**, *154*, 334–342.

[62] Nguyen, H. L.; Vu, T. T.; Le, D.; Doan, T. L. H.; Nguyen, V. Q.; Phan, N. T. S. *ACS Catal.* **2017**, *7*, 338–342.

[63] Geng, K.; He, T.; Liu, R.; Dalapati, S.; Tan, K. T.; Li, Z.; Tao, S.; Gong, Y.; Jiang, Q.; Jiang, D. *Chem. Rev.* **2020**, *120*, 8814–8933.

[64] Lohse, M. S.; Bein, T. *Adv. Funct. Mater.* **2018**, *28*, 1705553.

[65] Leith, G. A.; Berseneva, A. A.; Mathur, A.; Park, K. C.; Shustova, N. B. *Trends Chem.*, **2020**, *2*, 367–382.

[66] Xu, H.; Gao, J.; Jiang, D. *Nat. Chem.* **2015**, *7*, 905–912.

[67] Rice, A. M.; Dolgopolova, E. A.; Yarbrough, B. J.; Leith, G. A.; Martin, C. R.; Stephenson, K. S.; Heugh, R. A.; Brandt, A. J.; Chen, D. A.; Karakalos, S. G.; Smith, M. D.; Hatzell, K. B.; Pellechia, P. J.; Garashchuk, S.; Shustova, N. B. *Angew. Chem., Int. Ed.* **2018**, *57*, 11310–11315.

[68] Farha, O. K.; Malliakas, C. D.; Kanatzidis, M. G.; Hupp, J. T. *J. Am. Chem. Soc.* **2010**, *132*, 950–952.

[69] Kadokawa, J.-I.; Tanaka, Y.; Yamashita, Y.; Yamamoto, K. *Eur. Polym. J.*, **2012**, *48*, 549–559.

[70] Schwab, M. G.; Hamburger, M.; Feng, X.; Shu, J.; Spiess, H. W.; Wang, X.; Antonietti, M.; Müllen, K. *Chem. Commun.* **2010**, *46*, 8932–8934.

[71] Jeon, S.; Park, S.; Nam, J.; Kang, Y.; Kim, J.-M. *ACS Appl. Mater. Interfaces* **2016**, *8*, 1813–1818.

[72] Sun, L.; Park, S. S.; Sheberla, D.; Dincă, M. *J. Am. Chem. Soc.* **2016**, *138*, 14772–14782.

[73] Wudl, F.; Bryce, M. R. *J. Chem. Educ.* **1990**, *67*, 717–718.

[74] Williams, D. E.; Rietman, J. A.; Maier, J. M.; Tan, R.; Greytak, A. B.; Smith, M. D.; Krause, J. A.; Shustova, N. B. *J. Am. Chem. Soc.* **2014**, *136*, 11886–11889.

[75] Lakowicz, J. R. Principles of Fluorescence Spectroscopy, Springer, New York, **2007**.

[76] Williams, D. E.; Martin, C. R.; Dolgopolova, E. A.; Swifton, A.; Godfrey, D. C.; Ejegbavwo, O. A.; Pellechia, P. J.; Smith, M. D.; Shustova, N. B. *J. Am. Chem. Soc.* **2018**, *140*, 7611–7622.

[77] Xu, H.; Gao, J.; Jiang, D. *Nat. Chem.* **2015**, *7*, 905–912.

[78] Rice, A. M.; Dolgopolova, E. A.; Yarbrough, B. J.; Leith, G. A.; Martin, C. R.; Stephenson, K. S.; Heugh, R. A.; Brandt, A. J.; Chen, D. A.; Karakalos, S. G.; Smith, M. D.; Hatzell, K. B.; Pellechia, P. J.; Garashchuk, S.; Shustova, N. B. *Angew. Chem. Int. Ed.* **2018**, *57*, 11310–11315.

[79] Barroso-Bogeat, A.; Alexandre-Franco, M.; Fernández-González, C.; Gómez-Serrano, V. *Energy Fuels* **2014**, *28*, 4096–4103.

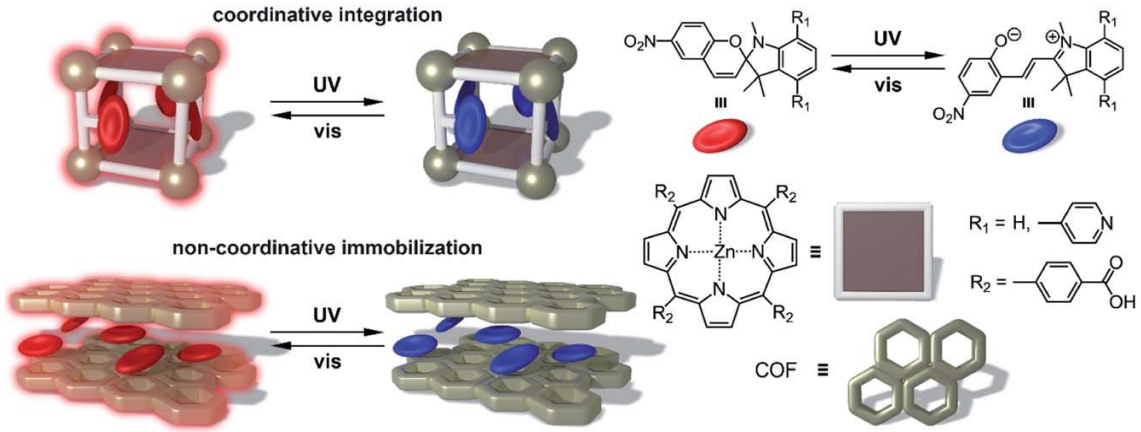

Scheme 3.1. (*top left*) Schematic representation of photoresponsive MOFs containing photochromic spiropyran moieties coordinatively immobilized inside a framework. (*bottom left*) Spiropyran derivatives integrated as guests inside a COF through non-coordinative immobilization. (*right*) The components for MOF and COF preparation including the photoisomerization of the spiropyran core under UV and visible excitations.

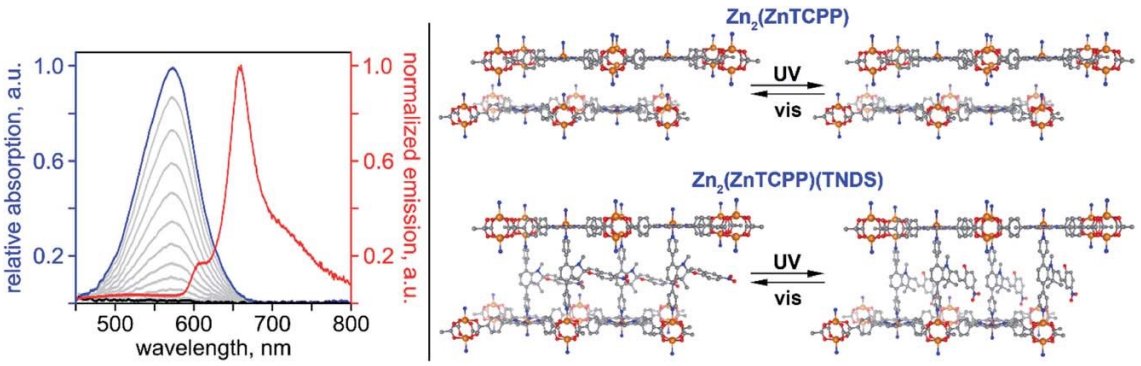

Figure 3.1. (*left*) Normalized absorption spectra of TNDS (63 mM in DMF) in the open (blue trace) and closed (black trace) forms. The gray lines correspond to the absorption spectra of TNDS collected during conversion from the open to closed forms. The red trace shows the normalized solid-state emission spectrum of Zn_2(ZnTCPP) (λ_{ex} = 350 nm). (*right*) Structures of (*top*) Zn_2(ZnTCPP) and (*bottom*) Zn_2(ZnTCPP)(TNDS).

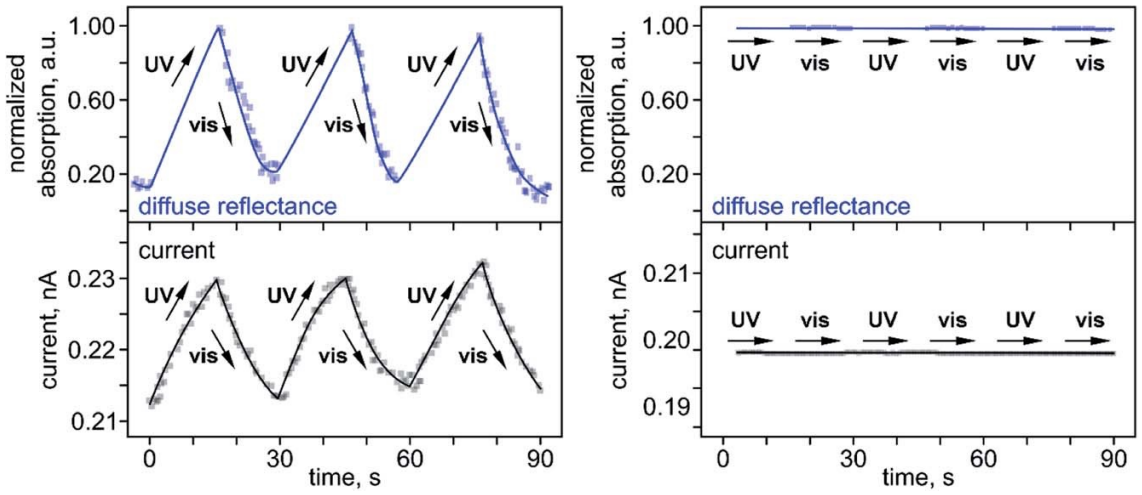

Figure 3.2. (*left*) Normalized optical and current cycling of photochromic Zn_2(ZnTCPP)(TNDS) through alternation of UV (λ_{ex} = 365 nm) and visible (λ_{ex} = 590 nm) light irradiation. (*right*) Control experiments performed for Zn_2(ZnTCPP) under alternation of UV (λ_{ex} = 365 nm) and visible (λ_{ex} = 590 nm) light irradiation. Absorption of the UV-irradiated sample is normalized to a value of 1.0 at 665 nm, and all subsequent values are scaled according to this value.

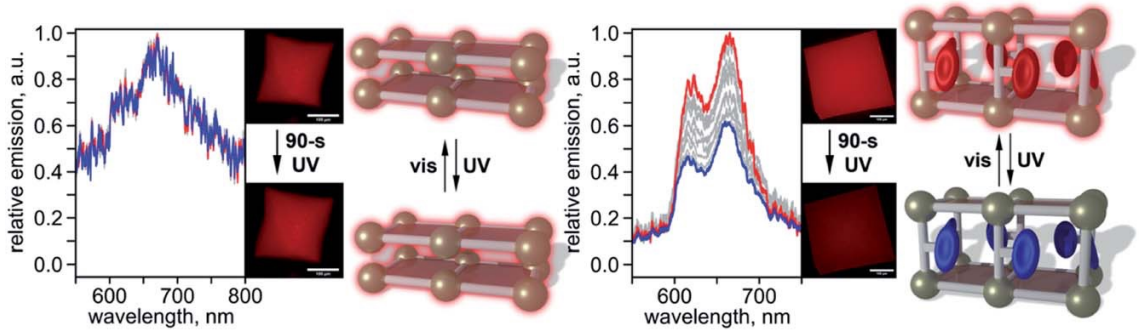

Figure 3.3. Emission photoswitch attenuation via epifluorescence microscopy for (*left*) Zn_2(ZnTCPP) and (*right*) Zn_2(ZnTCPP)(TNDS). Emission data of the pre-UV-irradiated samples (red) are normalized to a value of 1.0 at 665 nm and all subsequent values are scaled according to these values. The images near each plot show the epifluorescence images of single-crystals before and after 90 seconds UV irradiation (λ_{ex} = 330–385 nm). Schematic representation and structures of (*left*) Zn_2(ZnTCPP) and (*right*) Zn_2(ZnTCPP)(TNDS).

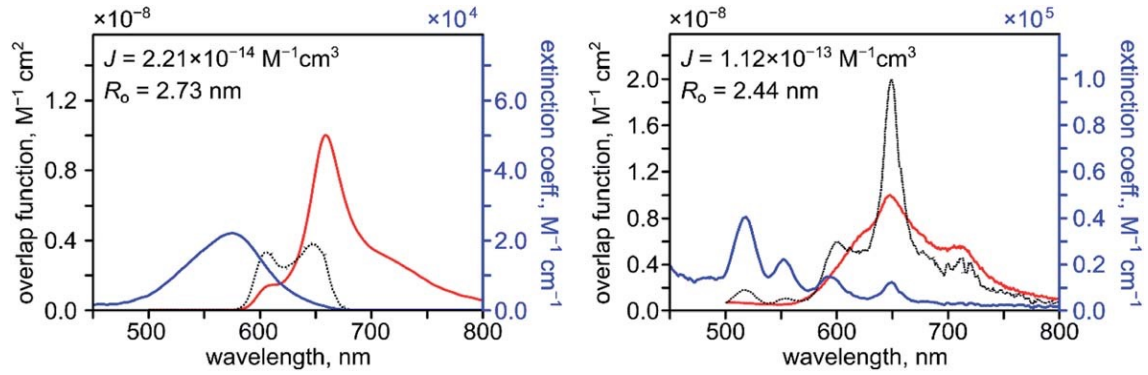

Figure 3.4. (*left*) Förster analysis for the "forward" ET process illustrating the spectral overlap function (dashed black line, left vertical axis) calculated for the measured emission spectrum of Zn_2(ZnTCPP) (red line, arbitrary scale), and the molar extinction spectrum of TNDS in DMF (63 mM, blue line, right vertical axis). (*right*) Förster analysis for the "reverse" ET process illustrating the spectral overlap function (dashed black line, left vertical axis) calculated for the measured emission spectrum of TNDS in DMF (63 mM, red line, arbitrary scale), and the molar extinction spectrum of H_4TCPP in DMF (7.8 mM, blue line, right vertical axis).

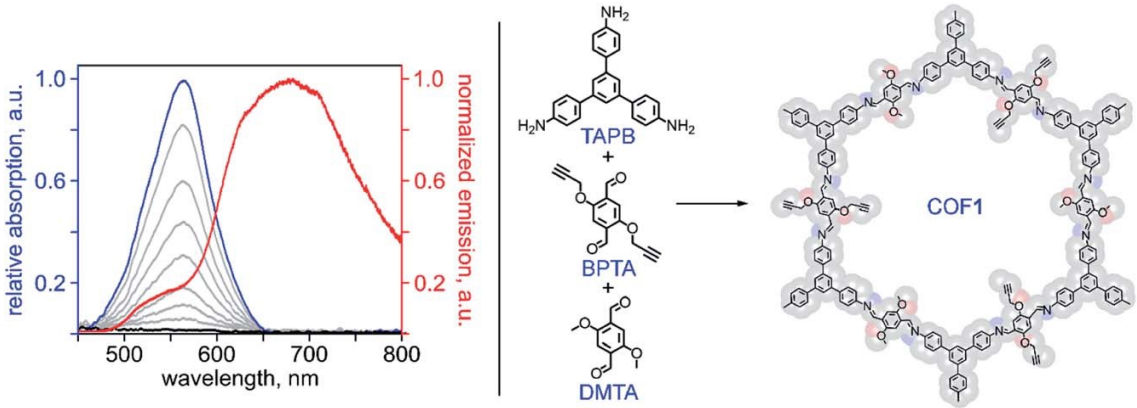

Figure 3.5. (*left*) Absorption spectra of SP (63 mM in DMF) in the open (blue trace) and closed (black trace) forms. The gray lines correspond to absorption spectra of SP collected during conversion from open to closed forms. The red trace shows the normalized solid-state emission spectrum of COF**1** (λ_{ex} = 350 nm). (*right*) Synthetic scheme for COF**1** and a schematic representation of its structure.

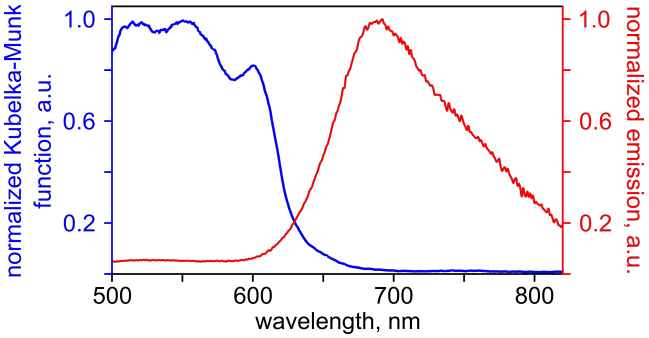

Figure 3.6. Emission spectrum of TNDS (red, 63 μM in DMF, λ_{ex} = 350 nm) and absorption spectrum of Zn_2(ZnTCPP) (blue).

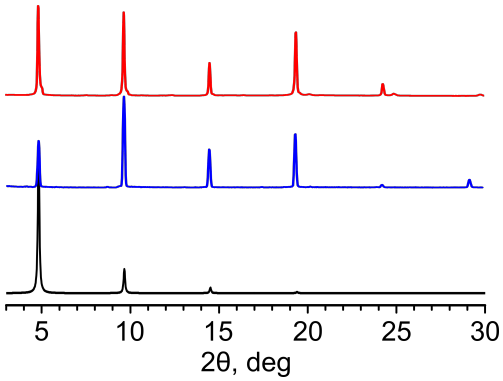

Figure 3.7. PXRD patterns of simulated Zn_2(DBTD)(TNDS)[76] (black), experimental Zn_2(DBTD)(TNDS) (blue), and experimental Zn_2(ZnTCPP)(TNDS) (red).

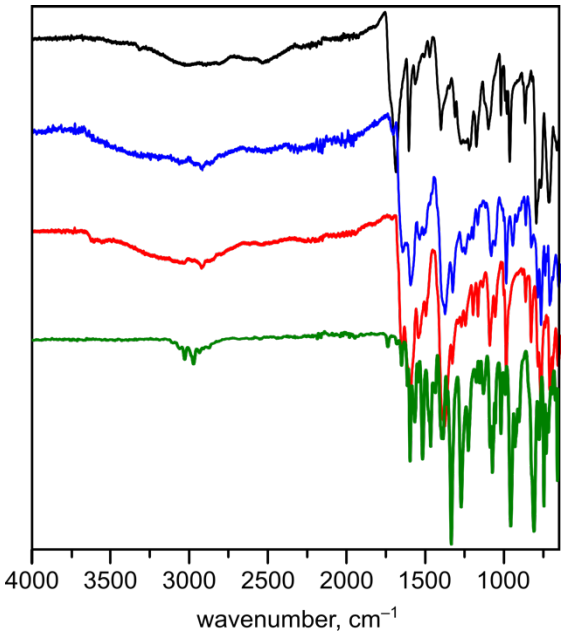

Figure 3.8. FTIR spectra of H_4TCPP (black), Zn_2(ZnTCPP) (blue), Zn_2(ZnTCPP)(TNDS) (red), and TNDS (green).

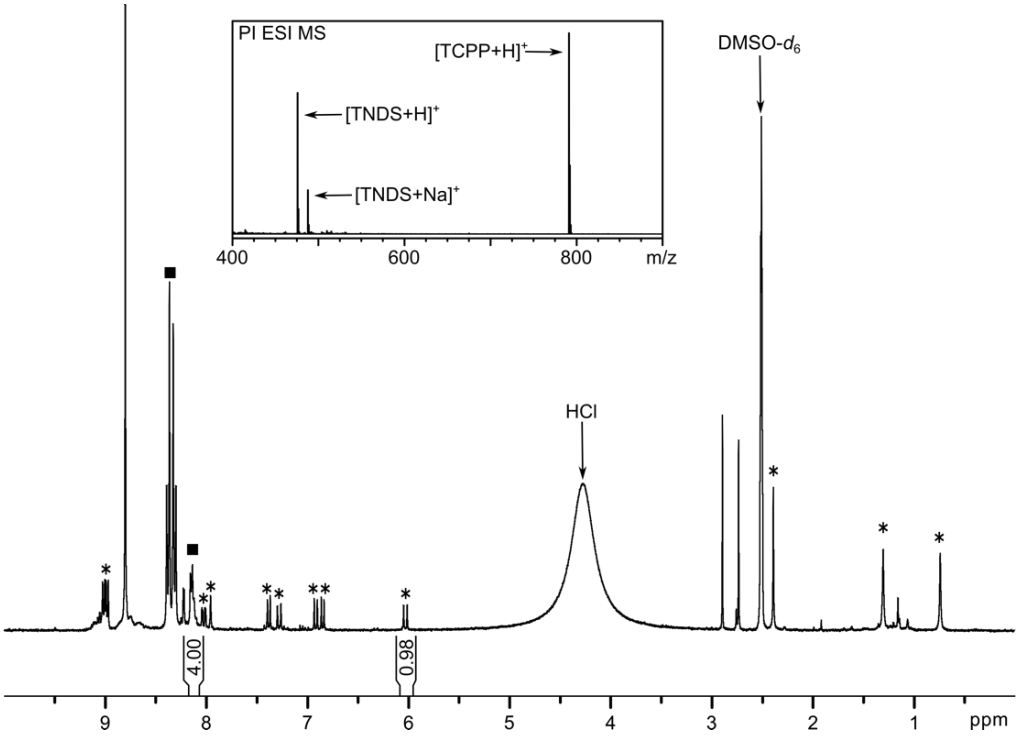

Figure 3.9. ^{1}H NMR spectrum of digested Zn_2(ZnTCPP)(TNDS). The peaks corresponding to H_4TCPP (■) and TNDS (∗) are labeled. The inset shows the positive ion electrospray ionization mass-spectrum of digested Zn_2(ZnTCPP)(TNDS).

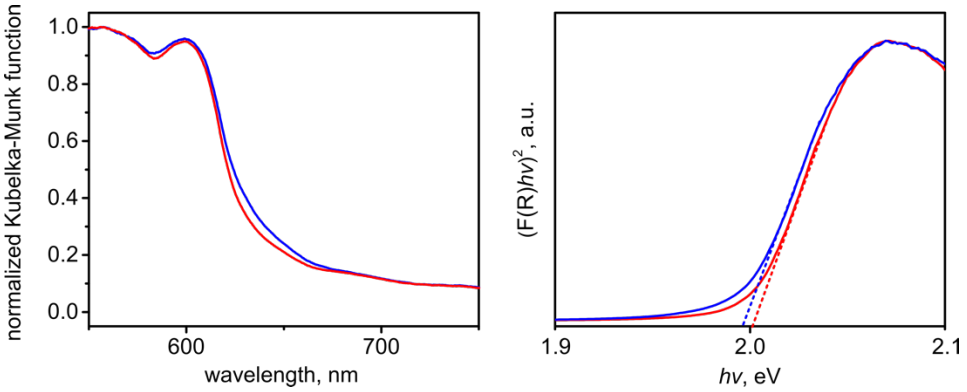

Figure 3.10. (*left*) Normalized diffuse reflectance spectra and (*right*) Tauc plots ($[F(R) \times h\nu]^2$ vs $h\nu$) of Zn_2(ZnTCPP)(TNDS) before (red) and after (blue) UV-irradiation (λ_{ex} = 365 nm, t = 1 minute).

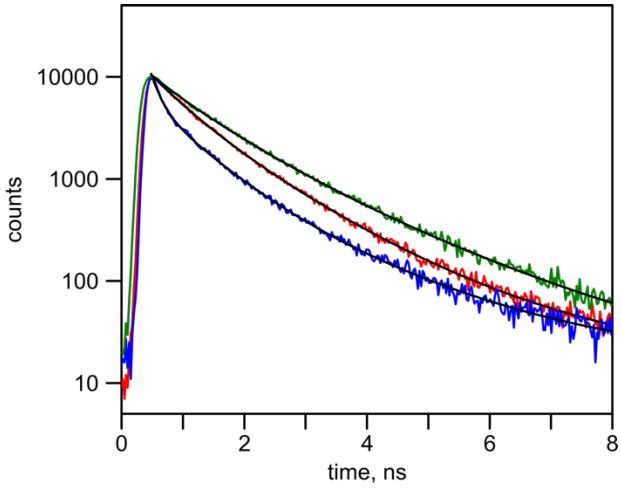

Figure 3.11. Fluorescence decays of Zn_2(DBTD)(TNDS) (green), Zn_2(ZnTCPP) (red), and Zn_2(ZnTCPP)(TNDS) (blue). The black solid lines are fits of the decays according to equation S1.

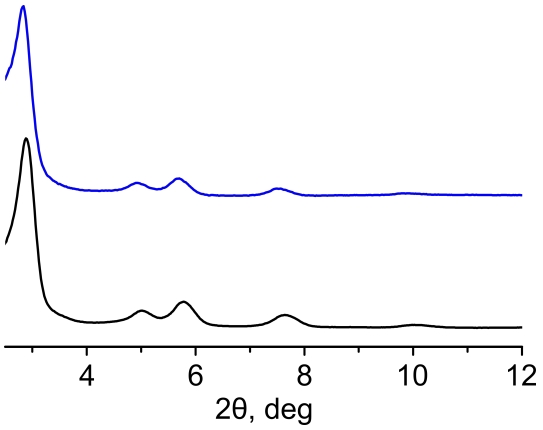

Figure 3.12. PXRD patterns of COF**1**[77,78] (black) and SP@COF**1** (blue).

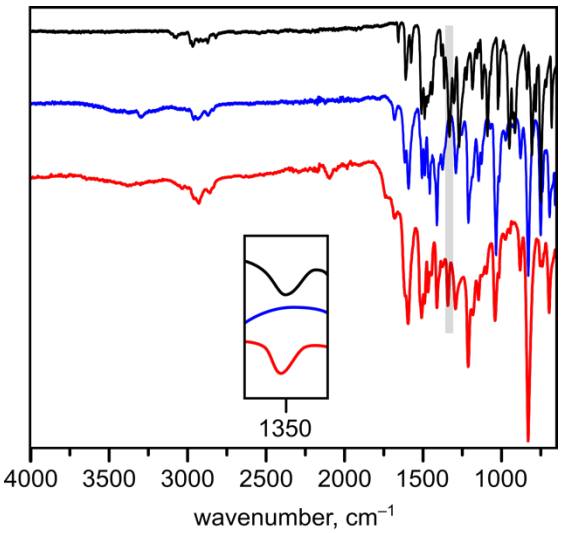

Figure 3.13. FTIR spectra of SP (black), COF**1** (blue), and SP@COF**1** (red). The gray area highlights the appearance of the *ν*(C–O–C) band at 1350 cm^{-1} in SP@COF**1** corresponding to SP.[79]

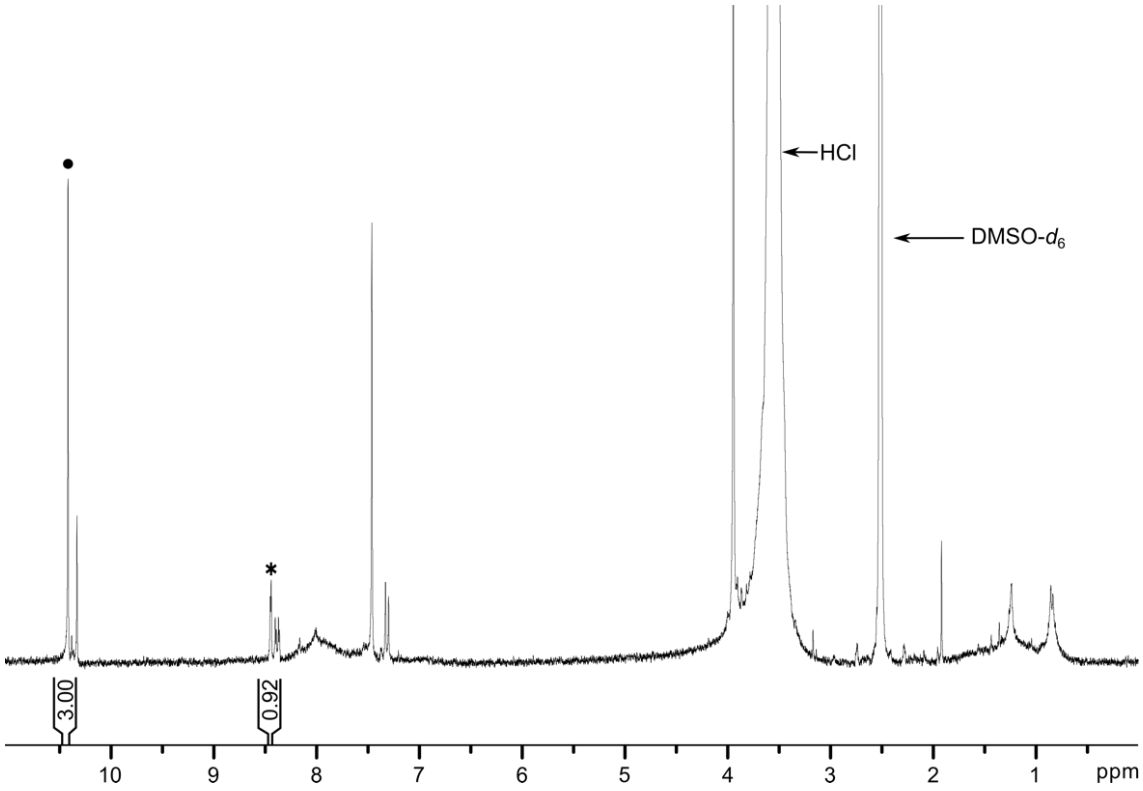

Figure 3.14. ^{1}H NMR spectrum of digested SP@COF**1**. The peaks corresponding to 2,5-dimethoxyterephthalaldehyde (●) and SP (∗) are labeled.

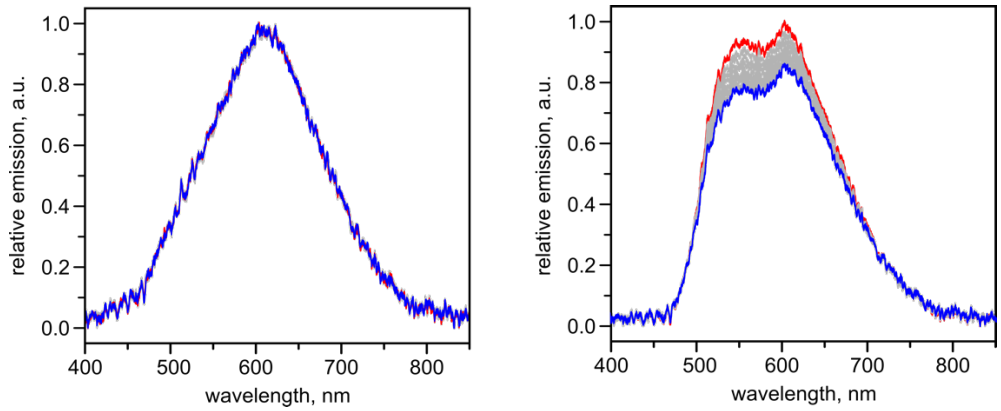

Figure 3.15. Emission attenuation via epifluorescence microscopy for COF**1** (*left*) and SP@COF**1** (*right*; λ_{ex} = 330–385 nm). Emission data are normalized relative to the maximum intensity of the initial sample without disturbing the sample during UV-irradiation (i.e., in situ irradiation): $(I-I_{min})/(I_{max}-I_{min})$ where I is the emission intensity, I_{min} is the minimum value for the corresponding spectrum, and I_{max} is the maximum emission intensity of the initial spectrum.

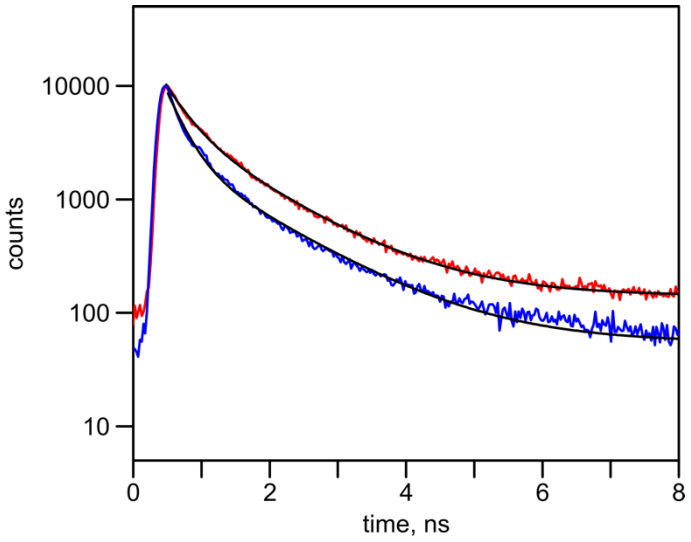

Figure 3.16. Fluorescence decays of COF**1** (red) and SP@COF**1** (blue). The black solid lines are fits of the decays according to equation S1.

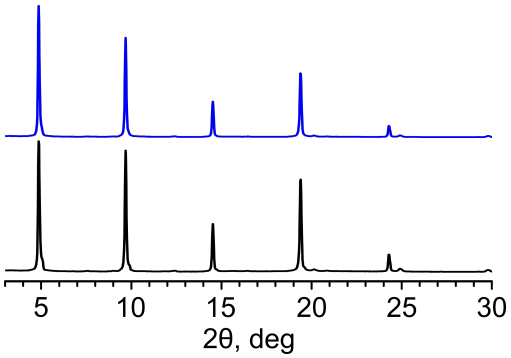

Figure 3.17. PXRD patterns of Zn_2(ZnTCPP)(TNDS) before (black) and after (blue) UV-irradiation (λex = 365 nm, t = 5 minutes).

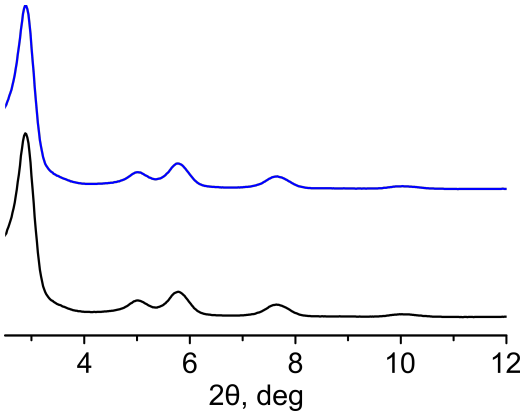

Figure 3.18. PXRD patterns of COF**1** before (black) and after (blue) UV-irradiation (λ_{ex} = 365 nm, t = 5 minutes).

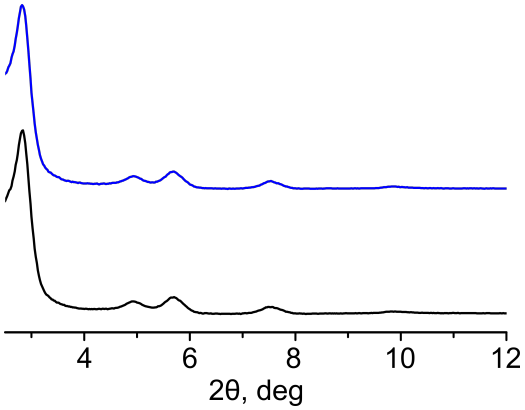

Figure 3.19. PXRD patterns of SP@COF**1** before (black) and after (blue) UV-irradiation (λ_{ex} = 365 nm, t = 5 minutes).

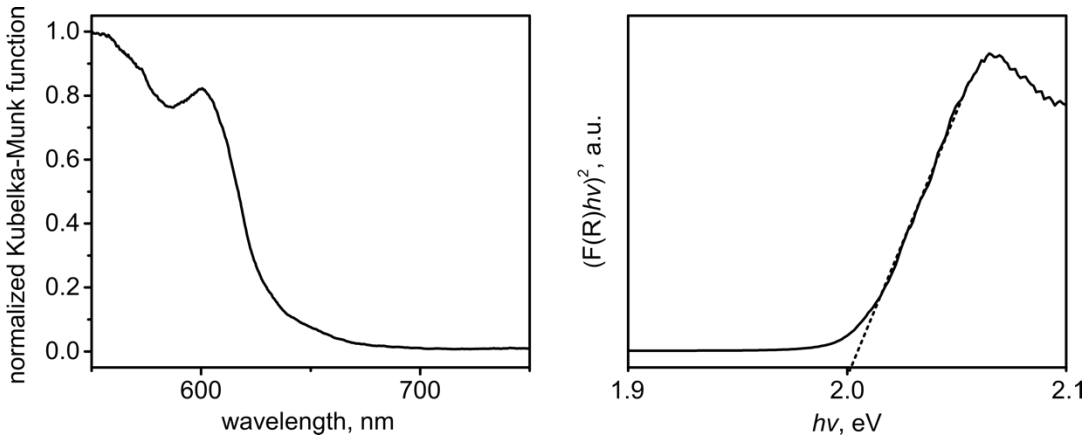

Figure 3.20. (*left*) Normalized diffuse reflectance spectrum and (*right*) Tauc plot ($[F(R) \times h\nu]^2$ vs $h\nu$) of Zn_2(ZnTCPP).

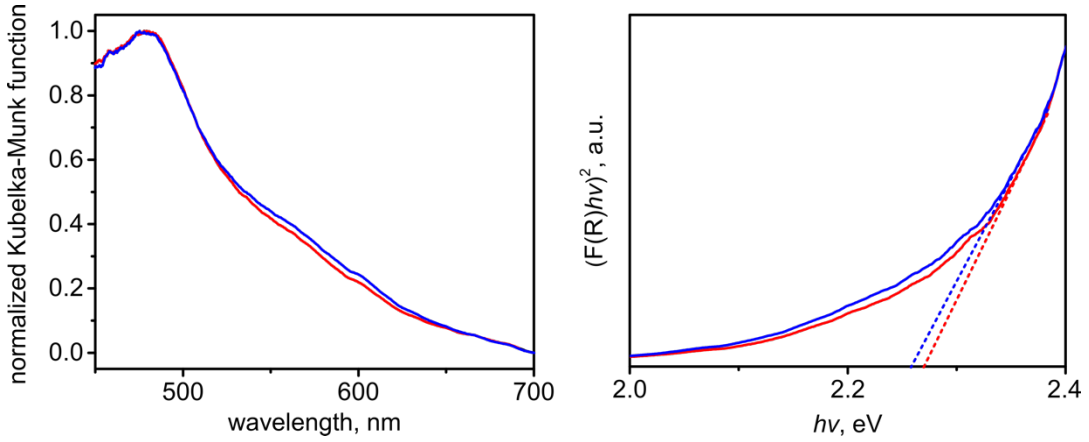

Figure 3.21. (*left*) Normalized diffuse reflectance spectra and (*right*) Tauc plots ($[F(R) \times h\nu]^2$ vs $h\nu$) of SP@COF**1** before (red) and after (blue) UV-irradiation (λ_{ex} = 365 nm, t = 1 minute).

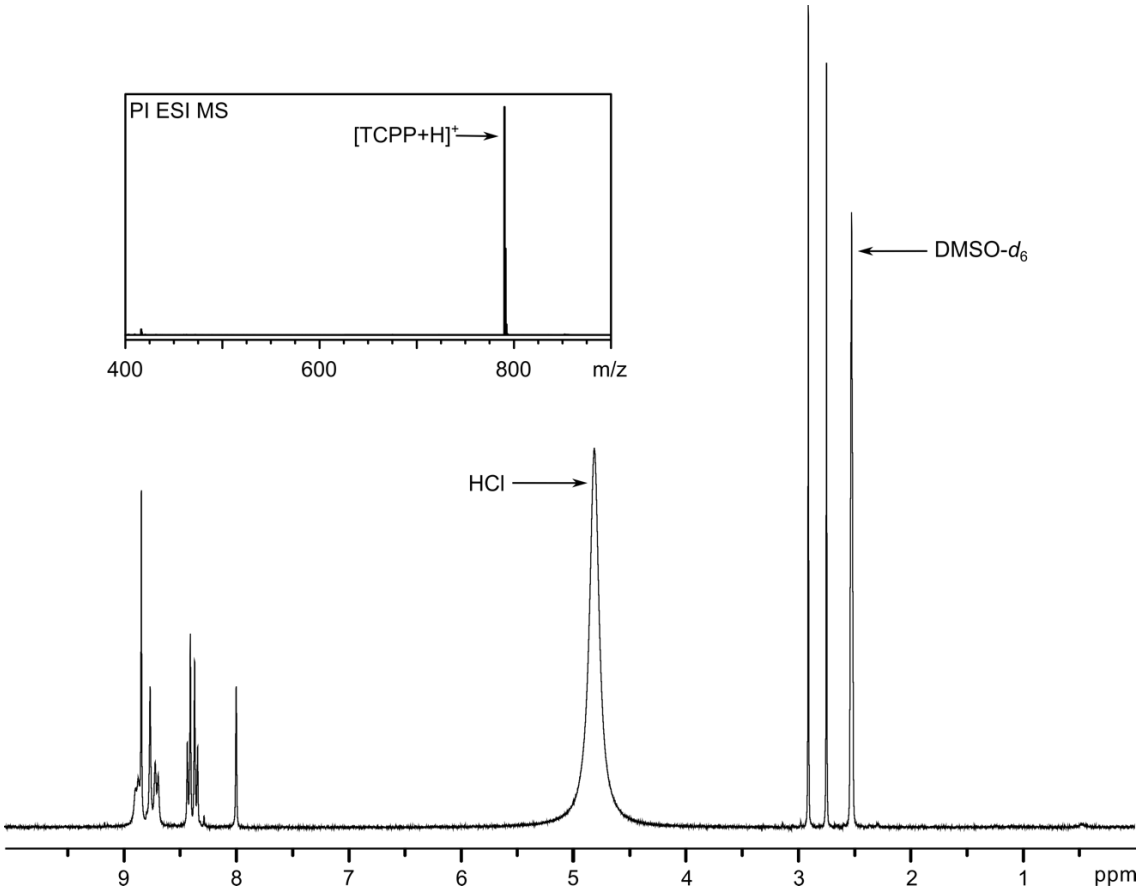

Figure 3.22. ^{1}H NMR spectrum of digested Zn_2(ZnTCPP). The inset shows the positive ion electrospray ionization mass-spectrum of digested Zn_2(ZnTCPP).

Table 3.1. Fluorescence decay lifetimes for Zn_2(ZnTCPP), Zn_2(ZnTCPP)(TNDS), Zn_2(DBTD)(TNDS), COF**1**, and SP@COF**1**.

	type of fitting	χ^2	τ_{avg}, ns
Zn_2(ZnTCPP)	triexponential	1.29	0.893
Zn_2(ZnTCPP)(TNDS)	triexponential	1.26	0.502
Zn_2(DBTD)(TNDS)	triexponential	1.03	1.09
COF**1**	biexponential	1.77	0.649
SP@COF**1**	biexponential	2.65	0.479

CHAPTER 4

STIMULI-MODULATED METAL OXIDATION STATES IN MOFS

Martin, C. R.; Park, K. C.; Leith, G. A.; Yu, J.; Mathur, A.; Wilson, G. R.; Gange, G. B.; Barth, E. L.; Ly, R. T.; Manley, O. M.; Forrester, K. L.; Karakalos, S. G.; Smith, M. D.; Makris, T. M.; Vannucci, A. K.; Peryshkov, D. V.; Shustova, N. B. *J. Am. Chem. Soc.* **2022**, DOI: 10.1021/jacs.1c11984

Chapter abstract. Tuning metal oxidation states in metal-organic framework (MOF) nodes by switching between two discrete linker photoisomers via an external stimulus was probed for the first time. On the examples of three novel photochromic copper-based frameworks, we demonstrated the capability of switching between +2 and +1 oxidation states, on demand. In addition to crystallographic methods used for material characterization, the role of the photochromic moieties for tuning the oxidation state was probed via conductivity measurements, cyclic voltammetry, electron paramagnetic resonance, X-ray photoelectron, and diffuse reflectance spectroscopies. We confirmed the reversible photoswitching activity including photoisomerization rate determination of spiropyran- and diarylethene-containing linkers in extended frameworks, resulting in changes in metal oxidation states as a function of alternating excitation wavelengths. To elucidate the switching process between two states, the photoisomerization quantum yield of photochromic MOFs was determined for the first time. Overall, the introduced non-invasive concept of metal oxidation state modulation on the examples of stimuli-responsive MOFs foreshadows a new pathway for alternation of material properties towards targeted applications

INTRODUCTION

Metal oxidation state modulation is paramount for tailoring and tuning the properties of materials (e.g., catalytic activity, stability, or charge/energy transport), and therefore, defines their practical implementation.[1–11] For example, transition metal-based catalysis almost exclusively relies on changes in the metal oxidation states during their catalytic cycles.[12–15] In a similar vein, mixed-valance metals determine the electronic properties of countless semiconducting materials.[16–26] Reversible tuning of metal oxidation

states allows for switching between discrete states and is a key aspect for developing logic gates, spatially- and temporally-resolved sensors, and on-demand drug delivery systems.[27–30] These cutting-edge concepts could be realized, for instance, using an external stimulus (e.g., temperature, pressure, light, or pH).[31–38]

In the presented studies, we offer the realization of non-invasive oxidation state modulation through the integration of photoresponsive moieties inside novel copper-containing metal-organic frameworks (MOFs).[39–42] This approach provides an opportunity to control metal oxidation states as a function of an excitation wavelength (Scheme 4.1). In particular, we demonstrate the first example of metal oxidation state reversibility in novel two- and three-dimensional copper-based photochromic MOFs through light-induced transformations of two distinct classes of photoresponsive molecules. Fundamental insights into the frameworks photophysical profiles and electronic structures are discussed extensively, including determination of photoisomerization rates ($k_{forward}$ and $k_{reverse}$) for novel copper-based photochromic MOFs. Cycling of optical and electronic response as a function of an excitation wavelength in photoresponsive frameworks was probed through diffuse reflectance (DR) spectroscopy and conductivity measurements. Electron-paramagnetic resonance (EPR) and X-ray photoelectron spectroscopies (XPS) were used to monitor the photoinduced changes in oxidation states in the prepared MOFs under *in situ* and *ex situ* UV irradiation (λ_{ex} = 365 nm). Material structure and integrity was studied after linker photoisomerization in the MOFs by single-crystal and powder X-ray diffraction (PXRD), respectively. Finally, to shed light on the possible mechanism of modulating metal oxidation states, we estimated the photoisomerization quantum yield of photoresponsive moieties integrated within a rigid MOF matrix for the first time.

RESULTS AND DISCUSSION

As a "knob" for tuning metal oxidation states in MOFs, we chose two classes of distinct photochromic compounds, diarylethene and spiropyran derivatives, based on the following aspects: (i) the possibility of linker integration inside an extended structure with preservation of the linker photochromic behavior;[41] (ii) the opportunity to probe the effect of the presence of a radical upon photoexcitation as a result of charge transfer;[42] and (iii) a wide range of photoisomerization rates due to distinct photoisomerization mechanisms.[45]

MOF Synthesis and Characterization. Spiropyran-containing compounds exhibit relatively fast photoisomerization in solution or in porous media[45] in comparison with diarylethene derivatives.[45] In the case of spiropyran derivatives, photoisomerization occurs due to an excited state heterocyclic bond cleavage of benzopyran to a metastable *cis*-merocyanine isomer, and a subsequent *cis*-to-*trans* isomerization to form the zwitterionic merocyanine photoisomer (Figure 4.1).[31] In contrast, diarylethene and its derivatives undergo fast photoisomerization in the solid-state due to minimal geometric reorganization required for switching between two photoisomers (Figure 4.1).[45–47] In particular, diarylethene undergoes a 6π-electron electrocyclic rearrangement, resulting in bond formation between the two methyl thiophene groups and extension of π-electron conjugation along the backbone, forming the colored photoisomer.[48]

For coordinative immobilization inside a framework, we prepared two diarylethene-based derivatives, 1,2-bis(2-methyl-5-(pyridin-4-yl)thiophen-3-yl)cyclopent-1-ene (BPMTC, Figure 4.1) and 4,4'-(cyclopent-1-ene-1,2-diyl)bis(5-methylthiophene-2-carboxylic acid) (H_2BCMTC, Figure 4.1),[49,50] as well as a spiropyran-based derivative, 1',3',3'-trimethyl-6-nitro-4',7'-di(pyridin-4-yl)spiro[chromene-2,2'-indoline] (TNDS,

Figure 4.1).[45] For control experiments, we selected 2,5-di(pyridin-4-yl)benzaldehyde (DPB-CHO, Figure 4.8)[51] as a non-photochromic analog due to its applicability for preparation of isostructural MOFs for direct comparison of the structures containing photoresponsive diarylethene and spiropyran units.

The metal choice for MOF preparation was determined by several factors: (i) the possibility to prepare a framework with photochromic linkers installed as pillars; (ii) tendency for reduction (comparable with the redox potentials of the chosen photochromic units in their excited states),[52–56] and (iii) the possibility to detect changes in oxidation states *in situ*. As a result, copper(II) was selected for photoresponsive MOF preparation. The copper-based frameworks have been synthesized through a transmetallation procedure,[57–59] and the d^9-paramagnetic nature of the copper(II) species allowed for probing changes in metal oxidation states *in situ* via EPR spectroscopy since Cu(II)↔Cu(I) switching would result in changes in the EPR signal.[60] Moreover, copper(II) species are relatively easy to reduce in comparison with, for instance, Co(II) or Ni(II) species.[61–64] As precursors, we synthesized the zinc-based MOFs: $Zn_{2.0}$(TNDS)(DBTD), $Zn_{2.0}$(BPMTC)(DBTD), and $Zn_{2.0}$(DPB-CHO)(DBTD) (Figure 4.1; H_4DBTD = 3',6'-dibromo-4',5'-bis(4-carboxyphenyl)-[1,1':2',1"-terphenyl]-4,4"-dicarboxylic acid).[45,65] Material characterization of Zn-MOFs by PXRD and FTIR spectroscopy is provided in the experimental section (Figures 4.9–4.14). Framework transmetallation was carried out in a DMF solution of copper(II) nitrate over seven days (see the experimental section for more details). After cation exchange, the resulting samples were extensively washed using a Soxhlet extraction procedure to remove residual copper species from the pores prior to MOF characterization. PXRD studies of the prepared frameworks demonstrated that

transmetallated MOFs are isostructural to the zinc-based analogs (Figures 4.9–4.11),[45,65] confirming preservation of framework integrity during the cation exchange process. The FTIR spectra can be found in Figures 4.12–15. To estimate the degree of transmetallation, inductively coupled plasma mass spectrometry (ICP-MS) was employed. As a result, complete zinc-to-copper transmetallation was observed for $Cu_{2.0}$(BPMTC)(DBTD). In the case of $Cu_{1.9}Zn_{0.1}$(TNDS)(DBTD) and $Cu_{1.2}Zn_{0.8}$(DPB-CHO)(DBTD), 95% and 60% of zinc cations were replaced by copper. Preparation of Cu(BCMTC)(MeOH) was carried out through direct synthesis by heating copper(II) chloride in the presence of H_2BCMTC in methanol at 60 °C for 30 minutes using water as a medium, followed by the addition of an aqueous solution of ethylenediamine (see the experimental section for more details).

A schematic representation of all prepared frameworks, $Cu_{2.0}$(BPMTC)(DBTD), $Cu_{1.9}Zn_{0.1}$(TNDS)(DBTD), and Cu(BCMTC)(MeOH), is shown in Figure 4.1. The single-crystal X-ray data are provided in Figures 4.17 ($Cu_{1.9}Zn_{0.1}$(TNDS)(DBTD)), 4.8 ($Cu_{1.2}Zn_{0.8}$(DPB-CHO)(DBTD)), and 4.18 (Cu(BCMTC)(MeOH)). The $Cu_{2.0}$(BPMTC)(DBTD), $Cu_{1.9}Zn_{0.1}$(TNDS)(DBTD), and $Cu_{1.2}Zn_{0.8}$(DPB-CHO)(DBTD) structures are constructed from two-dimensional (2D) layers in which the tetradentate linkers, $DBTD^{4-}$, are connected by paddlewheel-based metal nodes in their equatorial positions (Figures 4.1, 4.8, 4.17, and 4.18). The $DBTD^{4-}$-based 2D layers are connected with the corresponding pillars, such as TNDS, BPMTC, or DPB-CHO, coordinated to the axial positions of the paddlewheel metal nodes. The selected framework topology (i.e., photochromic linkers integrated as pillars between 2D layers) is essential for promoting TNDS linker photoisomerization, that is accompanied by a large structural rearrangement (Figure 4.1).[31–33,45] The Cu(BCMTC)(MeOH) structure also consists of 2D layers;

however, the layers contain photochromic $BCMTC^{2-}$ units bound to the equatorial positions of a copper paddlewheel, while axial metal node sites are occupied by coordinated methanol molecules (Figure 4.18). In other words, the Cu(BCMTC)(MeOH) framework is two-dimensional with no interlayer coordination. Notably, the proximity of the copper paddlewheel units in Cu(BCMTC)(MeOH) is closer (shortest inter-paddlewheel metal-to-metal (M−M) distance = 5.52 Å) than in $Cu_{1.9}Zn_{0.1}$(TNDS)(DBTD) (shortest inter-paddlewheel M−M distance = 11.5 Å).

Photophysical Studies. DR spectroscopic studies were used as a first step to evaluate the absorption profiles and photoisomerization rates of the prepared photoresponsive frameworks. In comparison with zinc-based MOFs, integration of copper cations complicated the DR spectra of the MOFs (Figures 4.19 and 4.20). For instance, in the spiropyran-based MOF, $Cu_{1.9}Zn_{0.1}$(TNDS)(DBTD), the appearance of an additional absorption band centered at 480 nm was detected (Figure 4.19). Notably, during the copper-to-zinc transmetallation procedure, copper cations can integrate not only inside the metal nodes, but can also coordinate to the linker, as shown in Figure 4.2.[66] To investigate this effect further, we stored a mixture of (1',3'-dihydro-1',3',3'-trimethyl-6-nitrospiro[2*H*-1-benzopyran-2,2'-(2*H*)-indole]; SP) and $Cu(NO_3)_2$ in tetrahydrofuran (THF) in the dark for three days after the measurements of the absorption profile were performed. As a result, a strong absorption band at 480 nm was detected (Figure 4.21), corresponding to chelation of Cu^{2+} to merocyanine, that is in line with the literature reports.[66–69] In addition, the intensity of this band changed upon altering the SP-to-$Cu(NO_3)_2$ ratio. We also found that the release of coordinated Cu(II) can be achieved through photoisomerization from the merocyanine to spiropyran isomer under 590 nm irradiation, resulting in the disappearance

of the 480 band (Figure 4.21), that is in line with the literature reports demonstrating the release of M(II) cations upon visible irradiation (M = Cu and Zn; Figure 4.2).[66–71] We applied the aforementioned strategy of copper(II) release for treating the $Cu_{1.9}Zn_{0.1}$(TNDS)(DBTD) sample, before any spectroscopic measurements, to remove any complexity associated with the presence of copper cations chelated to the organic linker. We accomplished the release of copper(II) species through irradiation of the prepared MOF with 590 nm light, as indicated by the disappearance of the band at 480 nm (Figure 4.21). This treatment allowed us to deconvolute the effect of TNDS versus chelated copper cations monitored through the changes in the absorption profile.

The photochromic behavior of the synthesized frameworks was evaluated using DR spectroscopy through monitoring the attenuation of photoswitch isomerization (Figures 4.3, 4.22, and 4.23).[45] The MOF samples were exposed to UV irradiation (λ_{ex} = 365 nm) to convert the photochromic moieties into their respective colored forms, and the corresponding spectra of the photoswitch attenuation were collected over time (see more details in the SI). Diarylethene-based MOFs, ($Cu_{2.0}$(BPMTC)(DBTD) and Cu(BCMTC)(MeOH)), exhibited absorption bands centered at 540 nm and 580 nm, respectively, corresponding to the presence of photochromic units that attenuated over time with a reverse rate, $k_{reverse}$, of 3.2×10^{-3} s^{-1} and 2.0×10^{-2} s^{-1}, respectively (Figures 4.3 and 4.22). The determined $k_{reverse}$ for $Cu_{2.0}$(BPMTC)(DBTD) is similar to that of a previously reported diarylethene-based MOF (e.g., $Zn_{2.0}$(BPMTC)(DBTD); 2.8×10^{-3} s^{-1}).[45] For the 2D layered structure, Cu(BCMTC)(MeOH), incomplete attenuation was observed over time, i.e., the absorption profile did not change after two minutes of attenuation (Figure

4.22). Thus, the rate, $k_{reverse}$, for Cu(BCMTC)(MeOH) attenuation was determined from the first 30 seconds of attenuation.

The estimated photoisomerization rate of BPMTC-integrated MOFs was slower in comparison with that observed for integrated TNDS moieties. In the case of $Cu_{1.9}Zn_{0.1}$(TNDS)(DBTD), the rate, $k_{reverse}$, was determined to be 1.0×10^{-1} s^{-1}, that is similar to that of the Zn-based analog (1.6×10^{-1} s^{-1}; Figure 4.23).[45] Such behavior can be explained by the fact that in the diarylethene-based MOFs, the photoisomerization process affects the MOF skeleton since the photoswitch coordinates to metal nodes from both sides of the molecule,[45] while photoisomerization of the TNDS linker occurs within the pores.[45,65,72]

A photophysics-electronic property correlation was established through comparison of time-resolved DR and conductivity measurement data. We utilized a home-built *in situ* two-contact probe pressed-pellet set-up[65,73,74] that allowed for monitoring the prepared MOFs electronic response as a function of an excitation wavelength (more details in the SI). Initially, we monitored the changes in current, I, under a steady applied voltage, V, under alternating 15-second cycles of UV (λ_{ex} = 365 nm) and visible (λ_{ex} = 590 nm) irradiation. Current cycling for $Cu_{2.0}$(BPMTC)(DBTD) and $Cu_{1.9}Zn_{0.1}$(TNDS)(DBTD) is shown in Figures 4.3 and 4.24, respectively. As a control experiment, we performed the same measurements for non-photochromic $Cu_{1.2}Zn_{0.8}$(DPB-CHO)(DBTD), and no significant changes in the current were detected upon exposure to either 365 or 590 nm irradiation (Figure 4.25). As shown in Figures 4.3 and 4.24, observed current cycling correlates with the changes in the MOFs absorption profile (Figures 4.19 and 4.20). These observations are in line with the changes in density of states near the Fermi edge detected

via XPS (Figure 4.26). Thus, the integration of photochromic moieties inside frameworks allowed us to dynamically control the electronic behavior of MOFs as a function of an excitation wavelength.

EPR studies. Following electronic and optical measurements, we chose EPR spectroscopy to probe possible changes in the oxidation state of copper within the MOF metal nodes. If linker photoisomerization upon irradiation results, for instance, in reduction of copper from Cu(II) (d^9) to Cu(I) (d^{10}), it should be reflected through changes in the EPR signal.[60] Solid-state continuous-wave (CW) EPR spectroscopic studies were carried out on the MOF samples under UV (365 nm) and visible (590 nm) light.

For sample irradiation, two approaches were employed. In the first approach, the samples were irradiated *in situ*, i.e., the photochromic MOFs were irradiated inside the EPR tubes using a mounted light-emitting diode (LED; λ_{ex} = 365 or 590 nm) and a fiber optic (see the experimental section for more details). As a control, prior to and between measurements, the fiber optic-loaded empty EPR tube was tested to ensure no chemical contaminations between the experiments. The *in situ* method of irradiation allowed us to study photochromic frameworks that possess rapid photoisomerization kinetics, such as $Cu_{1.9}Zn_{0.1}$(TNDS)(DBTD) ($k_{reverse}$ = 1.0 × 10^{-1} s^{-1}, as determined above). For photochromic samples with slower photoisomerization kinetics, such as $Cu_{2.0}$(BPMTC)(DBTD) (3.2 × 10^{-3} s^{-1}), *ex situ* sample irradiation can also be performed as an alternative approach (i.e., UV irradiation can occur outside of the EPR cavity) since the photoswitch attenuation (even in the presence of visible light) occurs during several hours.[45] To accomplish *ex situ* irradiation, the sample was carefully removed from the EPR

cavity and exposed to 365 nm excitation wavelength (see the experimental details in the SI).

For $Cu_{2.0}$(BPMTC)(DBTD), containing the diarylethene-based photoswitch, we performed both *in situ* and *ex situ* irradiation experiments, while monitoring the X-band frequency (9.382 GHz) in the EPR spectrum, and therefore, the possible conversion of paramagnetic (Cu(II)) to diamagnetic (Cu(I)) centers. In the dark, an axial signal (i.e., $g_x = g_y \neq g_z$)) was observed at a *g*-value of 2.062 for $Cu_{2.0}$(BPMTC)(DBTD) (Figure 4.4) that could be assigned to monomeric Cu(II) or thermally populated antiferromagnetically coupled Cu(II).[75–79] The relative decrease in the EPR response was analyzed by double integration of the EPR spectra collected in the dark and under UV irradiation, then relative signal reduction (%) was estimated (see the experimental section for more details). Upon UV irradiation using the *in situ* approach for $Cu_{2.0}$(BPMTC)(DBTD), the Cu(II) signal (260–335 mT)[80–82] decreased by 11%, that we attributed to photoswitch-induced Cu(II) reduction (Figure 4.27).

To promote a more dramatic change in the EPR signal upon UV irradiation, we explored the *ex situ* irradiation method, as it would allow for a shorter LED-to-sample distance (i.e., higher photon flux) as well as access to a larger irradiation area (Figure 4.28). Indeed, the EPR signal of $Cu_{2.0}$(BPMTC)(DBTD) was reduced by 32% upon only 30 minutes of *ex situ* UV exposure as opposed to three hours for *in situ* irradiation leading to an 11% reduction (λ_{ex} = 365 nm for *ex situ* and *in situ* irradiation methods; Figures 4.4 and 4.27). For confirmation that the observed EPR signal attenuation was caused by Cu(II) reduction via photochromic units, we performed control experiments on an isostructural, non-photochromic, Cu-based MOF, $Cu_{1.2}Zn_{0.8}$(DPB-CHO)(DBTD). As clearly shown in

Figure 4.29, there are no changes in the EPR profile of $Cu_{1.2}Zn_{0.8}$(DPB-CHO)(DBTD) upon UV irradiation using either *in situ* or *ex situ* irradiation methods (λ_{ex} = 365 nm). Furthermore, two non-photochromic MOFs containing Cu(II) paddlewheel metal nodes, $Zn_{1.40}Cu_{1.60}(BTC)_2$ and $Zn_{1.95}Cu_{1.05}(BTC)_2$, ($H_3BTC$ = 1,3,5-benzenetricarboxylic acid, Figures 4.30 and 4.31) were prepared and analyzed.[57,83] These samples also possessed similar hyperfine coupling resonances and a similar *g*-value (2.061) to that of $Cu_{2.0}$(BPMTC)(DBTD) (2.062). As expected, no changes in the intensity of the EPR signal were observed upon extensive UV exposure (Figure 4.32), confirming that the stimuli-responsive units were responsible for the observed changes in the Cu(II) signal reduction in photochromic MOFs. In addition, several Cu(II) and Cu(I) salts were analyzed under UV irradiation to further investigate the possible effect of UV excitation (Figures 4.33–4.35). As expected, no changes in the EPR signal intensity were detected even after prolonged exposure to UV light using both *in situ* and *ex situ* methods (Figures 4.33–4.35).

To correlate the sample area that underwent UV irradiation with the observed changes in the EPR signal, we compared the experimental and theoretical signal decrease based on irradiation area. For that, we constructed a simplified model to approximate the amount of sample influenced by UV light under our set-up (Figure 4.28). In the *ex situ* approach, the sample was only irradiated from one side of the EPR tube to minimize sample disturbance upon removal from the EPR spectrometer cavity. The volume of the MOF sample in the irradiation area was estimated to be 14 mm^3 based on an approximation of UV light penetration depth (~0.8 mm) measured with vernier calipers (further details in the SI). The total sample in the tube was approximated as a cylinder of volume 35 mm^3, and thus, 40% of the sample was exposed to UV irradiation. As a result, the reduction of the

EPR signal in the $Cu_{2.0}$(BPMTC)(DBTD) sample was found to be 32%, compared to the theoretical maximum of 40% estimated through irradiation area calculations (the *ex situ* approach; Figure 4.28). Using the *in situ* approach, the top (UV irradiated) and bottom (kept in the dark, Figure 4.28) portion of the cylinder were approximated using volumes of 5.6 mm^3 and 29.4 mm^3, respectively. Therefore, 16% of the sample is in the irradiation area in the case of the *in situ* irradiation, that is in line with the observed changes in the Cu(II) EPR signal (11%; Figure 4.27).

To support our conclusions based on changes in the EPR spectra, we utilized XPS for *in situ* monitoring of changes in metal oxidation states.[84–87] Scanning the Cu(2p) region of $Cu_{2.0}$(BPMTC)(DBTD) in the dark, we observed a strong signal corresponding to Cu(II) and a small peak corresponding to Cu(I), that was determined previously to be due to a charging effect for Cu(II) paddlewheel-based MOFs (Figure 4.4).[86] After *in situ* UV irradiation for 18 hours, we observed a significant decrease in the Cu(II) signal and enhancement of the Cu(I) signal. In fact, the change observed in the EPR spectrum (*ex situ* for $Cu_{2.0}$(BPMTC)(DBTD) = 32%) closely matched the observed changes detected in the XPS data (31%). Moreover, we also observed a 30% change in the intensity of the S(2p) electron binding energy (Figure 4.4) that corresponds to changes between the "closed" and "open" forms of the diarylethene linker (consistent with previous reports).[65] Therefore, both EPR and XPS studies demonstrated a correlation between the changes in the oxidation states and photoisomer conversion that coincide with optical property changes detected using DR spectroscopy. In the EPR spectrum collected for Cu(BCMTC)(MeOH), we observed a rhombic Cu(II)-centered signal (*g*-value = 2.061; Figure 4.36). Notably, the EPR signal from the Cu(BCMTC)(MeOH) sample was much broader in comparison with

$Cu_{2.0}$(BPMTC)(DBTD). Due to irreversible photochromic behavior (vide infra), we limited further studies performed for Cu(BCMTC)(MeOH). However, despite structural differences, we observed similar changes from the other two frameworks in the EPR spectrum upon UV irradiation, indicating that photochromic units can control the MOFs paramagnetic behavior.

In the case of $Cu_{1.9}Zn_{0.1}$(TNDS)(DBTD), that rapidly photoisomerizes,[45] only the *in situ* irradiation method was suitable for performing EPR measurements (vide supra). It is important to note that prior to EPR experiments, the $Cu_{1.9}Zn_{0.1}$(TNDS)(DBTD) sample was irradiated with 590 nm light, followed by extensive washing with DMF to remove any copper cations possibly coordinated to the merocyanine photoisomer, as discussed above. In the dark, prior to UV irradiation, the axial Cu(II) signal at a *g*-value of 2.061 (Figures 4.5 and 4.37) appeared nearly identical to that of $Cu_{2.0}$(BPMTC)(DBTD) (Figure 4.4). Upon 30 minutes of *in situ* UV exposure, the signal was reduced by 8%, based on integrating the area under the curve of the EPR absorption spectrum. The observed changes in the copper oxidation state were also supported by XPS measurements. Scanning the Cu(2p) region before and after 18 hours of UV exposure revealed a 24% increase in the Cu(I) signal (based on area by integration of the XPS spectrum) that was over three times larger than the *in situ* UV irradiation EPR experiments (8%; Figure 4.5). We attributed the observed difference in EPR and XPS results to a limited area of the sample that underwent irradiation during the EPR spectroscopic experiments (only the top section of the EPR tube) compared to UV exposure of the entire sampling area during XPS measurements (that is more similar to *ex situ* irradiation experiments). It is important to note that all detected changes in the EPR spectra were reversible. For instance, *in situ* irradiation of a fresh

sample of $Cu_{1.9}Zn_{0.1}$(TNDS)(DBTD) with 365 nm light for 30 minutes reduced Cu(II) by 8%, while 590 nm irradiation for 30 minutes resulted in a 94% restoration of the EPR signal (Figure 4.38).

To study the correlation between the observed changes in the EPR spectra and reversibility of changes in metal oxidation states upon irradiation, we also probed chemical (irreversible) reduction of MOF copper centers. After the addition of 10 μL of a 1.0 M hydrazine THF solution to $Cu_{2.0}$(BPMTC)(DBTD), we monitored changes in the EPR signal at the X-band frequency. As expected, we observed a partial decrease of the EPR signal associated with Cu(II) reduction (Figure 4.39). Further addition of a more concentrated hydrazine solution to the MOF sample resulted in the formation of an EPR silent sample, indicative of the complete reduction of Cu(II) metal centers. The PXRD pattern of the hydrazine-reduced sample also showed substantially diminished crystallinity (Figure 4.40).

To further shed light on the mechanism of Cu(II) reduction in the presence of MOF photochromic linkers, we employed cyclic voltammetry (CV) studies with the support of literature reports.[24,62] As a first step, we performed CV measurements on BPMTC and TNDS in the dark and under constant UV irradiation (λ_{ex} = 365 nm). For photochromic BPMTC (5.0 mM in acetonitrile (ACN), vs. SCE, Figure 4.41), we observed no redox behavior in the dark; however, under UV irradiation, an irreversible oxidation wave at E_{ox} = 0.63 V was evident. An irreversible oxidation wave for TNDS (5.0 mM in ACN, vs. SCE) was also observed (E_{ox} = 1.24 V) under UV irradiation (Figure 4.41). With this data in conjunction with the overlays of the absorption and emission spectra, we calculated the excited state potential using the following equation (eq. 1):[63,64]

$$E_{ox}^{*} = E_{ox} - E_{0-0}$$

Where E_{ox}^{*} is the excited state oxidation potential, E_{ox} is the measured oxidation potential of the ground state, and E_{0-0} is the energy of the lowest energy excited state transition, estimated as the intercept of absorption and emission energy (Figure 4.42). Using this relationship, the calculated E_{ox}^{*} values for TNDS and BPMTC are −0.80 V and −1.29 V vs. SCE, respectively. The literature value for the Cu(II/I) couple was observed at −0.31 V[65] suggesting that the reduction of Cu(II) to Cu(I) is feasible through oxidation of BPMTC and TNDS excited states.[63,64]

There are several literature reports that support the formation of a radical cation of spiropyran- and diarylethene-based compounds upon photoirradiation,[52–56] and this process could potentially affect the observed photoinduced charge transfer. To further study this observation, we performed EPR measurements involving the addition of a radical trap, 5,5-dimethyl-1-pyrroline-N-oxide (DMPO) to the sample.[92–94] In the case of the diarylethene-based linker, an EPR spectrum of a THF solution of BPMTC (80 mM) and DMPO (40 mM) was first collected in the dark and after UV irradiation (more experimental details in the SI). As shown in Figure 4.6, we observed the appearance of a radical signal from the BPMTC–DMPO adduct with a *g*-value of 2.009 (Figure 4.6), that is in line with literature reports.[95,96] In the case of SP, we observed the appearance of a radical signal after UV irradiation of a THF solution of SP (80 mM) and DMPO (40 mM, Figure 4.6). The *g*-value was found to be 2.009 (Figure 4.6).[97–100] As a control experiment, a solution of DMPO in THF (in the absence of photochromic molecules) was irradiated with UV light, and no new EPR signal was observed (Figure 4.43).

To summarize, these results are consistent with the hypothesis that radical-mediated charge transfer (that was observed previously for diarylethene-containing molecular donor-

acceptor pairs and complexes)[53,101] can promote the reduction of Cu(II) to Cu(I) in MOFs containing photochromic spiropyran- or diarylethene-based moieties.

Photoisomerization Quantum Yield Measurements. As a part of our studies performed on photochromic MOFs, it is important to probe photoisomerization quantum yield (φ_{PI}) of photochromic MOFs. The φ_{PI} value is a fundamental photophysical property that has been overlooked in photoresponsive MOFs,[32,34] despite being imperative for their practical implementation. In our case, we define φ_{PI} for the first time for the forward photoisomerization process (i.e., upon irradiation with UV light).[102–105]

In the case of diarylethene derivatives integrated inside a rigid MOF matrix, φ_{PI} could be greatly enhanced by aligning the chromophores in an antiparallel confirmation (as opposed to parallel; Figure 4.7).[106–110] In solution, parallel and antiparallel conformers of diarylethene and its derivatives are typically present in nearly equal proportions.[111,112] However, confinement-restricted diarylethene compounds could exhibit high φ_{PI} due to elimination of the parallel confirmation, as previously shown on the example of cyclodextrin cavities[113,114] or organic crystalline lattices.[106,115,116] In contrast, spiropyran and its derivatives undergo a rapid internal conversion (from the S_1 to S_2 states of spiropyran),[117,118] limiting φ_{PI} to 10% for spiropyran derivatives. Thus, we anticipate a much more pronounced effect on diarylethene-integrated linkers compared to spiropyran-based ones.

For the determination of φ_{PI}, we first prepared Aberchrome 670 films of known thickness and φ_{PI} of 27% using an established literature procedure.[102] The photoisomerization quantum yield was determined using the following relationship (eq. 2):[102]

$$\frac{\varphi_{A670}\varepsilon_{A670}(1-T_{A670})}{k_{forward(A_{670})}} = \frac{\varphi_{crystal}\varepsilon_{crystal}(1-T_{crystal})}{k_{forward(crystal)}}$$

Where T is the transmission at an excitation wavelength (λ_{ex} = 365 nm), ε is the molar extinction coefficient of the chromophore at the monitoring wavelength (e.g., $\lambda_{(abs)max}$ = 601 nm for TNDS), and $k_{forward}$ is the rate of the forward process.[102] The increase in absorption (decrease in transmission) was recorded over time and fit with a first-order rate equation to estimate the forward reaction rate.[31,35,119–123] More experimental details and the procedure implemented can be found in the SI. A summary of the acquired results is illustrated in Figure 4.7. Thus, φ_{PI} for $Cu_{2.0}$(BPMTC)(DBTD) was found to be as high as 79% in the MOF, compared to, for instance, 21–40% observed for molecular arrays of diarylethene oligomers[115] and 21–50% detected for diarylethene derivatives in solution (3,3'-(perfluorocyclopent-1-ene-1,2-diyl)bis(2,4-dimethylthiophene) and 3,3'-(perfluorocyclopent-1-ene-1,2-diyl)bis(2-methyl-5-phenylthiophene)).[115,116] In fact, φ_{PI} for diarylethene-derivatives in solution cannot exceed 50% due to a nearly equal ratio of parallel and antiparallel conformations.[116]

As expected, a MOF matrix imposes conformational restriction on the BPMTC linker through elimination of the parallel confirmation and therefore, enhancement of φ_{PI} was detected. In contrast to the diarylethene-based MOF, we found φ_{PI} of TNDS photoisomerization to be 8% in $Cu_{1.9}Zn_{0.1}$(TNDS)(DBTD), demonstrating a solution-like behavior. Specifically, the value of φ_{PI} for $Cu_{1.9}Zn_{0.1}$(TNDS)(DBTD) is similar to that reported for spiropyran in solutions (e.g., 5–9%),[124–126] likely due to rapid internal conversion and large geometric reorganization.[117,118] The experimentally observed 79% and 8% values of φ_{PI} are the first reports in the area of photochromic MOFs demonstrating the advantages of a framework rigid matrix: (i) selective elimination of the parallel

confirmation and φ_{PI} enhancement for coordinatively immobilized diarylethene derivatives and (ii) possibility to overcome challenges associated with limited photoisomerization of spiropyran derivatives in the solid state.[31,35,45]

SUMMARY

We report a novel concept of reversible modulation of metal oxidation states in metal-organic frameworks through integration of photochromic moieties as a function of an excitation wavelength. On the example of three novel copper-based diarylethene- and spiropyran-containing frameworks, we observed switching between Cu(II) and Cu(I) states upon UV and visible light alternation. We monitored the changes in material properties through a combination of powder and single-crystal X-ray diffraction, conductivity measurements, cyclic voltammetry, electron paramagnetic resonance, X-ray photoelectron, and diffuse reflectance spectroscopies. Photochromic behavior and the corresponding changes in the frameworks electronic properties were also demonstrated, including determination of the forward and reverse rates for the photoisomerization processes. Finally, photoisomerization quantum yields of photochromic moieties coordinatively immobilized within a porous matrix were determined for the first time. To summarize, the surface of tuning photoswitchable molecules oxidation states has only been scratched, and we believe that a thrust of research in this direction is imminent and will greatly impact the expanding materials landscape.

EXPERIMENTAL SECTION

Materials. Copper(II) nitrate hemi(pentahydrate) (98.3%, Mallinckrodt AR), copper(II) chloride dihydrate (98+%, Alfa Aesar), zinc(II) nitrate hexahydrate (lab grade, Ward's Science), tetrakis(triphenylphosphine)palladium(0) (98%, Matrix Scientific),

tin(II) chloride anhydrous (98%, BeanTown Chemical), copper(I) chloride anhydrous (97%, Strem Chemicals), titanium(IV) tetrachloride (99%, Alfa Aesar), zinc dust (95%, Macron), sodium carbonate (ACS grade, Ameresco), magnesium sulfate anhydrous (USP, Chem-Impex, International Inc.), sodium sulfate anhydrous (99.5%, Oakwood Chemical), sodium hydroxide (ACS grade, Oakwood Chemical), potassium hydroxide (ACS grade, Fisher Chemical), 1′,3′-dihydro-1′,3′,3′-trimethyl-6-nitrospiro[2*H*-1-benzopyran-2,2′-(2*H*)-indole] (>98%, TCI America), 2,5-dibromonitrobezene (99%, Oakwood Chemical), sodium nitrite (98%, Oakwood Chemical), 3-methyl-2-butanone (98%, BeanTown Chemical), methyl trifluoromethanesulfonate (97%, Matrix Scientific), 2-hydroxy-5-nitrobenzaldehyde (98%, Oakwood Chemical), 2-methylthiophene (98%, Matrix Scientific), *N*-chlorosuccinimide (98%, Sigma-Aldrich), glutaryl dichloride (97%, Acros Organics), 4-bromopyridine hydrochloride (98%, Matrix Scientific), 1,3,5-benzenetricarboxylic acid (98%, Alfa Aesar), tributyl borate (98%, Strem Chemicals), urea (98+%, Alfa Aesar), hexabromobenzene (>99%, TCI America), *p*-tolylmagnesium bromide (0.5 M in diethyl ether, Acros Organic), ethylenediamine (99%, Oakwood Chemical), hydrochloric acid (ACS grade, Fisher Chemical), sulfuric acid (ACS grade, Fisher Chemical), nitric acid (ACS reagent, Sigma-Aldrich), fluoroboric acid (48%, Oakwood Chemical), glacial acetic acid (ACS grade, BDH), ethanol (200 proof, Decon Laboratories, Inc.), methanol (ACS grade, Fisher Scientific), methylene chloride (99.9%, Fisher Chemical), acetone (ACS grade, Sigma-Aldrich), ethyl acetate (99.9%, Fisher Chemical), chloroform (99.9%, Fisher Chemical), diethyl ether (ACS grade, J. T. Baker Chemicals), hexanes (ACS grade, BDH), *N*,*N*-dimethylformamide (ACS grade, Oakwood Chemical), piperidine (99%, Sigma-Aldrich), carbon tetrachloride (99.9%, Sigma-

Aldrich), bromine (99.8%, Acros Organics), tetrahydrofuran (HPLC grade, BeanTown Chemical), *n*-butyllithium solution (2.5 M in hexanes, Sigma-Aldrich), benzene (ACS grade, Fischer Scientific), carbon disulfide (99.9%, Sigma-Aldrich), ethylene glycol (HPLC grade, Amresco), acetonitrile (99.5%, Sigma-Aldrich), tetrabutylammonium hexafluorophosphate (98%, TCI America), hydrazine monohydrate (98%, BeanTown Chemical), chloroform-*d* (99.8%, Cambridge Isotope Laboratories, Inc.), acetone-d_6 (99.9%, Cambridge Isotope Laboratories, Inc.), and dimethyl sulfoxide-d_6 (99.9%, Cambridge Isotope Laboratories, Inc.) were used as received.

The compounds 1′,3′,3′-trimethyl-6-nitro-4′,7′-di(pyridin-4-yl)spiro[chromene-2,2′-indoline] (TNDS),[128] 1,2-bis(2-methyl-5-(pyridin-4-yl)thiophen-3-yl)cyclopent-1-ene (BPMTC),[129] 4,4'-(cyclopetn-1-ene-1,2-diyl)bis(5-methylthiophene-2-carboxylic acid) (H_2BCMTC),[130] 3′,6′-dibromo4′,5′-bis(4-carboxyphenyl)-1[1,1′:2′,1″-tetraphenyl]-4,4″-dicarboxylic acid (H_4DBTD),[131] 2,5-di(pyridin-4-yl)benzaldehyde (DPB-CHO),[132] $Zn_3(BTC)_2$ (H_3BTC = 1,3,5-benzenetricarboxylic acid),[133] $Zn_{2.0}$(TNDS)(DBTD),[128] $Zn_{2.0}$(BPMTC)(DBTD),[134] and $Zn_{2.0}$(DPB-CHO)(DBTD)[135] were synthesized based on literature procedures.

Preparation of $Cu_{1.9}Zn_{0.1}$(TNDS)(DBTD). In a 1-dram vial, crystals of $Zn_{2.0}$(TNDS)(DBTD) (13.1 mg, 9.93 μmol) were immersed in a *N*,*N*-dimethylformamide (DMF) solution of $Cu(NO_3)_2$ (40.0 mM, 1.00 mL) for seven days at room temperature. The dark red $Cu_{1.9}Zn_{0.1}$(TNDS)(DBTD) crystals were collected by filtration and washed with DMF (2 × 2.00 mL). The yield was determined to be 92% (12.0 mg, 9.12 μmol) after drying in air for 30 minutes. Before further characterization of the prepared crystals, a washing procedure was performed. Crystals of the MOF were filtered, immersed in fresh DMF (2.00

mL) for 48 hours, and DMF was refreshed three times each day. The structure of $Cu_{1.9}Zn_{0.1}$(TNDS)(DBTD) was determined by single-crystal X-ray diffraction (Figure 4.17). Structural refinement data can be found in Table 4.2. The crystallinity of $Cu_{1.9}Zn_{0.1}$(TNDS)(DBTD) was confirmed by powder X-ray diffraction (PXRD; Figure 4.10). The Fourier-transform infrared (FTIR) spectra of H_4DBTD, $Zn_{2.0}$(TNDS)(DBTD), $Cu_{1.9}Zn_{0.1}$(TNDS)(DBTD), and TNDS are shown in Figure 4.13. A Soxhlet extraction procedure was performed for 72 hours with a DMF and ethanol (9:1 v/v) solvent mixture prior to inductively coupled plasma mass spectrometry (ICP-MS) analysis to remove residual copper and zinc cations. A transmetallation of 93% was determined by ICP-MS.

Preparation of $Cu_{2.0}$(BPMTC)(DBTD). In a 1-dram vial, crystals of $Zn_{2.0}$(BPMTC)(DBTD) (12.8 mg, 10.2 μmol) were immersed in a DMF solution of $Cu(NO_3)_2$ (40.0 mM, 1.00 mL) for seven days at room temperature. The green $Cu_{2.0}$(BPMTC)(DBTD) crystals were collected by filtration and washed with DMF (2 × 2.00 mL). The yield was determined to be 89% (11.4 mg, 9.09 μmol) after drying the MOF in air for 30 minutes. Before further characterization of the prepared crystals, a washing procedure was performed. Crystals of the MOF were filtered, immersed in DMF (2.00 mL) for 48 hours, and DMF was refreshed three times each day. The structure and crystallinity of $Cu_{2.0}$(BPMTC)(DBTD) was confirmed by PXRD (Figure 4.9). The FTIR spectra of H_4DBTD, $Zn_{2.0}$(BPMTC)(DBTD), $Cu_{2.0}$(BPMTC)(DBTD), and BPMTC are shown in Figure 4.12. A Soxhlet extraction procedure was performed for 72 hours with a DMF and ethanol (9:1 v/v) solvent mixture prior to ICP-MS analysis to remove residual copper and zinc cations. A transmetallation of 100% was determined by ICP-MS.

Preparation of $Cu_{1.2}Zn_{0.8}$(DPB-CHO)(DBTD). In a 1-dram vial, crystals of $Zn_{2.0}$(DPB-CHO)(DBTD) (4.70 mg, 4.26 μmol) were immersed in a DMF solution of $Cu(NO_3)_2$ (30.0 mM, 1.00 mL) for seven days at room temperature. The blue-green $Cu_{1.2}Zn_{0.8}$(DPB-CHO)(DBTD) crystals were collected by filtration and washed with DMF (2 × 2.00 mL). The yield was determined to be 91% (4.28 mg, 3.89 μmol) after drying the MOF in air for 30 minutes. Before further characterization of the prepared crystals, a washing procedure was performed. Crystals of the MOF were filtered, immersed in DMF (2.00 mL) for 48 hours, and DMF was refreshed three times each day. The structure of $Cu_{1.2}Zn_{0.8}$(DPB-CHO)(DBTD) was determined by single-crystal X-ray diffraction (Figure 4.8). Structural refinement data can be found in Table 4.2. The crystallinity of $Cu_{1.2}Zn_{0.8}$(DPB-CHO)(DBTD) was confirmed by PXRD (Figure 4.11). The FTIR spectra of H_4DBTD, $Zn_{2.0}$(DPB-CHO)(DBTD), $Cu_{1.2}Zn_{0.8}$(DPB-CHO)(DBTD), and DPB-CHO are shown in Figure 4.14. A Soxhlet extraction procedure was performed for 72 hours with a DMF and ethanol (9:1 v/v) solvent mixture prior to ICP-MS analysis to remove residual copper and zinc cations. A transmetallation of 59% was determined by ICP-MS.

Preparation of Cu(BCMTC)(MeOH) [$(Cu_2(BCMTC)_2(MeOH)_2 \cdot 0.77MeOH \cdot 1.21H_2O)$]. To a 20-mL vial containing 17.0 mg (36.5 μmol) of $CuCl_2 \cdot 2H_2O$ and 0.100 mL H_2O, a 4.00 mL MeOH solution of H_2BCMTC (35.0 mg, 0.100 mmol) was added dropwise while stirring. The vial was then heated to 60 °C and 10.0 μL of 0.100 M NaOH was added and the mixture was stirred for 30 minutes. Next, a solution of ethylenediamine (94.0 μL H_2O and 6.00 μL en) was added dropwise while stirring at 60 °C. The mixture was stirred for 30 minutes, filtered, placed into a new 20-mL vial, that was left uncapped in the dark for seven days. Blue crystals were collected

by filtration and washed with MeOH (2 × 2.00 mL). The yield was determined to be 18% (8.21 mg, 6.57 μmol) after drying the MOF in air for 30 minutes. The structure of Cu(BCMTC)(MeOH) was determined by single-crystal X-ray diffraction (Figure 4.18). Structural refinement data can be found in Table 4.1. The crystallinity of Cu(BCMTC)(MeOH) was confirmed by PXRD (Figure 4.16). The FTIR spectra of Cu(BCMTC)(MeOH) and H_2BCMTC are shown in Figure 4.15.

Preparation of $Zn_3(BTC)_2$. The $Zn_3(BTC)_2$ framework was synthesized based on a modified literature procedure.[133] To a 250-mL pressure flask, $Zn(NO_3)_2 \cdot 6H_2O$ (5.00 g, 16.8 mmol), 1,3,5-benzenetricarboxylic acid (3.53 g, 16.8 mmol), and DMF (0.100 L) were added, and the resulting mixture was sonicated for 10 minutes until the reagents were fully dissolved. The flask was then heated at 70 °C for four days in an isothermal oven. After cooling to room temperature, the colorless crystals were collected by vacuum filtration, washed with DMF (3 × 20 mL), and then stored in DMF for further use. Colorless crystals of $Zn_3(BTC)_2$ were collected in 80% yield after drying the MOF in air for one hour. The crystallinity of $Zn_3(BTC)_2$ was confirmed by PXRD (Figure 4.30), and the PXRD pattern of as-synthesized $Zn_3(BTC)_2$ matched the simulated pattern of the MOF.[7]

Preparation of $Zn_{1.40}Cu_{1.60}(BTC)_2$. In a 20-mL vial, crystals of $Zn_3(BTC)_2$ (0.380 g, 0.623 mmol) were immersed in an ethanol solution of $Cu(NO_3)_2$ (1.01 M, 5.00 mL) for 24 hours at room temperature. The yield of $Zn_{1.40}Cu_{1.60}(BTC)_2$ blue crystals was determined to be 80% after drying the MOF in air for one hour. Before further characterization of the prepared crystals, a washing procedure was performed. Crystals of the MOF were filtered, immersed in ethanol for three days, and ethanol was refreshed twice each day. The crystallinity of $Zn_{1.40}Cu_{1.60}(BTC)_2$ was confirmed by PXRD (Figure 4.30),

and the PXRD pattern of as-synthesized $Zn_{1.40}Cu_{1.60}(BTC)_2$ matched the simulated pattern of $Zn_3(BTC)_2$.[133] The sample composition was confirmed by ICP-MS.

Preparation of $Zn_{1.95}Cu_{1.05}(BTC)_2$. In a 20-mL vial, crystals of $Zn_3(BTC)_2$ (100 mg, 0.164 mmol) were soaked in an ethanol solution of $Cu(NO_3)_2$ (1.01 M, 2.00 mL) for nine hours at room temperature. The yield of $Zn_{1.95}Cu_{1.05}(BTC)_2$ blue crystals was determined to be 82% after drying in air for one hour. Before further characterization of the prepared crystals, a washing procedure was performed. Crystals of the MOF were filtered, immersed in ethanol for three days, and ethanol was refreshed twice each day. The crystallinity of $Zn_{1.95}Cu_{1.05}(BTC)_2$ was confirmed by PXRD (Figure 4.30), and the PXRD pattern of as-synthesized $Zn_{1.95}Cu_{1.05}(BTC)_2$ matched the simulated pattern of $Zn_3(BTC)_2$.[133] The sample composition was confirmed by ICP-MS.

Diffuse reflectance spectroscopy. Diffuse reflectance spectra were collected on an Ocean Optics JAZ spectrometer. An Ocean Optics ISP-REF integrating sphere was connected to the spectrometer using a 450-μm SMA fiber optic cable. Samples were loaded in a 4.0-mm quartz sample cell, that was referenced to an Ocean Optics WS-1 Spectralon® standard. A mounted high-powered LED (M365L2, Thorlabs, λ_{ex} = 365 nm, distance = 1 cm, and LEDD1B power supply set at 700 mA) was used for *in situ* irradiation of the samples.

Optical cycling. Optical cycling of photochromic MOFs was carried out using an Ocean Optics JAZ spectrometer. An Ocean Optics ICPREF integrating sphere was connected to the spectrometer using a 450-μm SMA fiber optic cable. Prior to time-resolved DR measurements, the sample background was subtracted to remove the region that does not correspond to photophysical behavior of the photochromic moieties integrated

into the framework. A sample was placed inside a 4.0-mm quartz sample holder and a 400-nm longpass glass filter (Thorlabs, FGL400) was placed between the quartz sample cell with cover and the integrating sphere to filter any UV light from the internal tungsten-halogen lamp. The quartz sample holder and longpass filter were attached to the top of the integrating sphere with electrical tape to prevent sample displacement. A mounted high-powered LED (M365L2, Thorlabs, λ_{ex} = 365 nm, distance = 2 cm, and LEDD1B power supply set at 245 mA) was used for *in situ* irradiation of the sample for 15 seconds, then the sample was allowed to undergo photoinduced reversion on the top of the integration sphere for 15 seconds while a spectrum was collected every 0.5 seconds.

Photoluminescence spectroscopy. Steady-state emission spectra were acquired on an Edinburgh FS5 fluorescence spectrometer equipped with a 150 W Continuous Wave Xenon Lamp source for excitation. Emission measurements on solid samples were collected from the powders of the desired materials placed inside a 0.5-mm quartz sample holder using the front-facing module.

Electronic structure as a function of external stimuli. A two-point method was employed to measure the current response of pressed pellets A home-built two-contact probe pressed pellet set-up (2C3PS)[135,139,140] made it possible to fabricate the pressed pellets and perform measurements *in situ*, while also allowing for simultaneous MOF irradiation and monitoring of changes in electrical current flow under the applied voltage. The MOF crystalline powder (10 mg), that was pre-dried for 20 minutes in air, was pressed between two stainless-steel rods inside an insulating quartz tube. The diameter of the resulting pellet is the same as the inner diameter of the quartz tube (d = 2 mm). The thickness of the pellets was kept consistent (l = 1 mm) by using the same amount of

material. After forming a small pellet, the stainless-steel rods were connected to a Keithley 2636A sourcemeter using a 3-slot Triax to alligator clip (Keithley 237-ALG-2 Triax cable) to perform conductivity measurements. For all measurements, the number of power line cycles (NPLC) was set to 5. A constant voltage (1 V) was applied while current was measured every two seconds. Before data collection, an equilibration time (t = 90 seconds) was applied in the dark. Then, the sample was irradiated (t = 15 seconds) using a 365 nm high-powered LED (M365L2, Thorlabs, λ_{ex} = 365 nm, distance = 6 cm, and LEDD1B power supply set at 700 mA), followed by relaxation by irradiating with a 590 nm high-powered LED (M590L3, Thorlabs, λ_{ex} = 590 nm, distance = 6 cm, and LEDD1B power supply set at 500 mA; Figures 4.3, 4.24 and 4.25).

Cyclic voltammetry. Cyclic voltammetry (CV) measurements were carried out in anhydrous acetonitrile (ACN) using a Pine WaveNowXV Potentiostat combined with the Aftermath software. All sample preparation occurred in a controlled atmosphere N_2 glovebox. For measurements of TNDS and BPMTC, all solutions contained 0.1 M tetrabutylammonium hexafluorophosphate and 5.0 mM analyte. Measurements were performed in a glass solution reservoir equipped with saturated calomel electrode (SCE) reference, platinum wire counter, and glassy carbon working electrodes. CV scans were collected at 100 mV s^{-1}. CV scans were initially collected of the samples in the dark, followed by exposure to 365 nm irradiation for five minutes and simultaneous voltammogram acquisition (Figure 4.41).

Excited state potentials of TNDS and BPMTC. The excited state oxidation potentials (E_{ox}^*) of BPMTC and TNDS were calculated using the following equation:[141,142]

$$E_{ox}^{*} = E_{ox} - E_{0-0}$$

Where E_{ox} is the oxidation potential measured from CV, and E_{0-0} is the energy of the lowest vibrational transition that was determined as the intercept of the normalized absorption and emission spectra (Figure 4.42).[141,142]

Electron paramagnetic resonance. X-Band electron paramagnetic resonance (EPR) spectra were recorded on an X-band Bruker EMXplus with the following settings: microwave frequency = 9.384109 GHz, modulation frequency = 100 kHz, modulation amplitude = 1.0 G, conversion time = 6 ms, and time constant = 10 μs. The sweep time, sweep range, and microwave power are reported under each spectrum. Solid samples were loaded into tared quartz tubes and sample masses were recorded. Photochromic samples were measured under applied 365 nm irradiation by two methods: "*ex situ*" irradiation and "*in situ*" irradiation. For *ex situ* irradiation, the quartz tube containing the sample was flushed with argon and subsequently sealed with PTFE tape, a PTFE cap, and then taped with electrical tape. The sample was then loaded into the magnet chamber and an initial spectrum was recorded (t = 0). Next, the quartz tube was carefully removed from the chamber and irradiated with 365 nm light using a mounted high-powered LED (M365L2, Thorlabs, λ_{ex} = 365 nm, distance = 1 cm, and LEDD1B power supply set at 700 mA). Following sample irradiation, the quartz tube was carefully returned to the sample chamber and spectra were recorded. This process was repeated for several irradiation cycles. For *in situ* sample irradiation, the quartz tube containing the sample was flushed with argon and a custom Thorlabs fiber optic (FT1000UMT; Ø1000 μm core TECS-clad multimode optical fiber, 0.39 NA, SMA connector) was lowered into the tube under a stream of argon. Next, the fiber optic was wrapped with PTFE tape to tightly fit inside of the quartz tube and was then fixed to the tube with electrical tape. The fiber optic was connected to a fiber-

coupled LED (M365F1, Thorlabs, λ_{ex} = 365 nm, and LEDD1B power supply set at 700 mA). The sample was then loaded into the magnet chamber and an initial spectrum was recorded (t = 0). Next, samples were measured over time under constant applied 365 nm irradiation without disturbing the sample. The decrease in signal intensity (signifying Cu(II) reduction) was shown to be reversible under 590 nm irradiation using a high-powered LED (M590L3, Thorlabs, λ_{ex} = 590 nm, and LEDD1B power supply set at 500 mA) placed on the SMA end of the custom Thorlabs fiber optic. The relative changes in the EPR spectra were quantified by doubly integrating the differential curve (after UV irradiation), compared to the double integration of the signal area prior to irradiation. Spectra were simulated using the "pepper" function in EasySpin version 5.2.30.[143] $Cu_{2.0}$(BPMTC)(DBTD) was simulated as an axial spectrum with g values = [2.062, 2.350]. Line broadening was modeled with gStrain = [0.033, 0.055]. $Cu_{1.9}Zn_{0.1}$(TNDS)(DBTD) was simulated as an axial spectrum with g values = [2.061, 2.345]. Line broadening was modeled with gStrain = [0.033, 0.030]. $Cu_{1.2}Zn_{0.8}$(DPB-CHO)(DBTD) was simulated as a rhombic spectrum with g values = [2.062, 2.072, 2.347]. Line broadening was modeled with gStrain = [0.002, 0.077, 0.027].

Chemical reduction of $Cu_{2.0}$(BPMTC)(DBTD). A control experiment for the chemical reduction of $Cu_{2.0}$(BPMTC)(DBTD) was performed by adding hydrazine monohydrate as a reducing agent and monitoring the reduction of the Cu(II) signal via EPR spectroscopy. First, a spectrum of pristine $Cu_{2.0}$(BPMTC)(DBTD) in the solid state was collected, then 20 μL (1.0 M) of hydrazine monohydrate in tetrahydrofuran was added to the sample (Figure 4.39). Specifically, the hydrazine monohydrate solution was added directly into the EPR tube containing $Cu_{2.0}$(BPMTC)(DBTD). A significant signal

reduction was observed, that suggests the reduction of Cu(II); however, some Cu(II) was still present according to the EPR spectrum (Figure 4.39). Another chemical reduction experiment was performed in order to determine how the complete reduction of Cu(II) affects the EPR signal. The spectrum of pristine $Cu_{2.0}$(BPMTC)(DBTD) in the solid state was initially collected, and then 20 μL of 99% hydrazine monohydrate (Figure 4.39) was added directly into the quartz tube. Complete signal reduction was observed as shown in Figure 4.38. The collected PXRD pattern contains no defined signals after the addition of hydrazine to $Cu_{2.0}$(BPMTC)(DBTD) (Figure 4.40).

Photoisomerization quantum yield. The photoisomerization quantum yield of MOF single crystals was measured based on the literature procedure.[144,145] To prepare polystyrene for thin films, inhibitor-free styrene (5.50 mL, 48.0 mmol), 4-cyano-4-(phenylcarbonothioylthio)pentanoic acid (1.30 mg, 4.80 μmol), and tetrahydrofuran (5.50 mL) were combined in a 25-mL Schlenk tube. A solution of 10.0 mM azobisisobutyronitrile in tetrahydrofuran (96.0 μL, 0.960 μmol) was added to the Schlenk tube. The solution was degassed with argon for 15 minutes, and the reaction mixture was heated at 90 °C for 20 hours. The mixture was allowed to cool to room temperature and then added to hexanes (0.100 L) and centrifuged at 6500 rpm for five minutes. The supernatant was decanted off, and the solid was dried in a vacuum oven for 18 hours. Gas-phase chromatography analysis was performed against a polystyrene standard. A number-average molar mass of 14.6 kg/mol with dispersity of 1.7 was observed. Films of Aberchrome 670 were prepared by spin-coating (3000 rpm, SCS 6800 Spin Coater Series) a chloroform solution of Aberchrome 670 (6.5 mg/mL) and polystyrene (63 mg/mL).[145]

The following relationship was used to determine the quantum yield of cyclization for photochromic MOF single crystals:[144,145]

$$\frac{\Phi_{film}\varepsilon_{film}(1-T_{film})}{k_{forward}{}_{film}} = \frac{\Phi_{crystal}\varepsilon_{crystal}(1-T_{crystal})}{k_{forward}{}_{crystal}}$$

Where Φ, ε, $k_{forward}$, and T represent the quantum yield of photoisomerization, the absorption coefficient at the monitoring wavelength, the photoisomerization rate, and the transmittance at 365 nm, respectively.

The photoisomerization quantum yield of Aberchrome 670 was previously reported as 27% in an identically prepared thin film.[145] Transmittance was measured on a Horiba iHR320 spectrometer (Horiba Scientific) connected to an Olympus microscope in transmission mode. The absorption coefficients for photochromic molecules were measured in their respective solutions after 1 minute of 365 nm irradiation. The slope was determined by monitoring the transmission at 590 nm while irradiating the film with a custom Thorlabs fiber optic (FT1000UMT; Ø1000 μm core TECS-clad multimode optical fiber, 0.39 NA, SMA connector) connected to a fiber-coupled LED (M365F1, Thorlabs, λ_{ex} = 365 nm, and LEDD1B power supply set at 700 mA). Single crystals of MOFs were measured under identical conditions. In order to maintain an identical photon flux and irradiation area, the samples were measured under 20-times magnification and the LED-coupled fiber optic set-up was not disturbed between measurements. The penetration depth of UV light in the MOF crystals was probed by using transmission measurements. For instance, the transmission of $Cu_{1.9}Zn_{0.1}$(TNDS)(DBTD) was determined to be 27 ± 0.3% at 365 nm for a crystal with a thickness of 80 μm. Thus, the penetration depth of UV light can be approximated as 90–110 μm at λ = 365. This value correlates well with the estimated 32% conversion based on *ex situ* EPR irradiation.

X-ray photoelectron spectroscopy. The X-ray photoelectron spectroscopy (XPS) studies on MOF samples were carried out using a Kratos AXIS Ultra DLD system equipped with a monochromatic Al Kα source operated at 15 keV and 150 W, a hemispherical analyzer, charge neutralizer, and a load lock chamber for rapid introduction of samples without breaking vacuum. The base pressure in the XPS analysis chamber was 2×10^{-9} Torr before sample introduction and $\leq 2 \times 10^{-8}$ Torr during experiments. XPS data were collected with a step size of 0.06 eV and a dwell time of one second. A charge neutralizer was used to compensate for sample charging by bombarding the sample with low-energy electrons.[146] Employing a charge neutralizer is a known strategy applied for insulating copper-containing MOFs.[146] Electrons are generated by a hot filament, and the trajectories of the electrons toward the sample were controlled by electric and magnetic fields. The samples were measured before and after 18 hours of UV irradiation. The prolonged period for irradiation in XPS measurements was due to a large LED-to-sample distance, resulting in a lower power irradiation. For example, irradiation by the mounted high-power LED (M365F1, Thorlabs, λ_{ex} = 365 nm, and LEDD1B power supply set at 700 mA) at 1 cm results in a power density of 40 mW/cm^2 whereas the power density is 0.2 mW/cm^2 at 20 cm through a similar thickness glass window. Survey scans were acquired to establish that there were no contaminants introduced during the sample preparation. The survey scans were collected with a step size of 0.8 eV and dwell times of 0.3 seconds. The curve fitting procedure was carried out using the XPS Peak 41 software and the peak approximation was carried out by a combination of Gaussian and Lorentzian functions, with a Shirley-type background simulation for core level peaks, except for the Cu(2p) peak which a Tougaard

type background was used. The samples were referenced to the adventitious C(1s) peak at 284.6 eV.

Other physical measurements. FTIR spectra were obtained on a Perkin-Elmer Spectrum 100. ^{1}H NMR spectra were collected on a Bruker Avance III-HD 400 MHz NMR spectrometer. ^{1}H NMR spectra were referenced to residual ^{1}H peaks of deuterated solvents, respectively. PXRD patterns were recorded on a Rigaku Miniflex II diffractometer at a scan rate of 1 °/minute with accelerating voltage and current of 30 kV and 15 mA, respectively. ICP-MS analysis was conducted using a Finnigan ELEMENT XR double focusing magnetic sector field inductively coupled plasma mass spectrometer with Ir, Rh, or both as internal standards. A Micromist U-series nebulizer (0.2 mL/min, GE, Australia), quartz torch, and injector (Thermo Fisher Scientific, USA) were used for sample introduction. Sample gas flow was 1.08 mL/minute and the forwarding power was 1250 W. The samples were digested in Teflon vessels with nitric and hydrochloric acids and then heated at 180 °C for 4 hours. The Water QTOF-I quadrupole time-of-flight and Thermo Scientific Orbitrap Velos Pro mass spectrometers were used to record the mass spectra of the prepared compounds.

X-ray crystal structure determination for $Cu_2(BCMTC)_2(MeOH)_2 \cdot 0.77MeOH \cdot 1.21H_2O$. [Cu(BCMTC)(MeOH)]. X-ray intensity data from a blue-green block were collected at 100(2) K using a Bruker D8 QUEST diffractometer equipped with a PHOTON-II area detector and an Incoatec microfocus source (Mo Kα radiation, λ = 0.71073 Å). The raw area detector data frames were reduced, scaled, and corrected for absorption effects using the Bruker APEX3, SAINT+ and SADABS programs.[147,148] The structure was solved with SHELXT.[149,150]

Subsequent difference Fourier calculations and full-matrix least-squares refinement against F^2 were performed with SHELXL-2018[149,150] using OLEX2.[151]

The compound crystallizes in the monoclinic system. The pattern of systematic absences in the intensity data was consistent with the space group $P2_1/n$, which was confirmed by structure solution. The asymmetric unit consists of two unique copper atoms, $C_{17}H_{14}O_4S_2$ ligands, methanol ligands and a region of disordered solvent electron density. The solvated compound was resolved as $Cu_2(BCMTC)_2(MeOH)_2 \cdot 0.77MeOH \cdot 1.21H_2O$. Methyl group of one methanol is disordered over two positions (C36A/C36B) with a major component occupancy of 0.82(2). The disordered solvent guests were modeled as a mixture of variably occupied methanol molecules and oxygen atoms of water molecules. For the solvent guest model, two methanol molecules (C1S/O1S, C2S/O2S) were identified and refined isotropically with *d*(C–O) = 1.45(2) distance restraints. Four additional significant electron density peaks could not be reasonably fit to methanol and were modeled as water oxygen atoms O3S–O6S. Refined occupancies for both species were in the range 0.21(1)–0.47(2). All non-hydrogen atoms were refined with anisotropic displacement parameters with the exception of the guest solvent atoms (isotropic). Hydrogen atoms bonded to carbon were placed in geometrically idealized positions and included as riding atoms with *d*(C−H) = 0.95 Å and *U*iso(H) = 1.2*U*eq(C) for arene hydrogen atoms, *d*(C−H) = 0.99 Å and *U*iso(H) = 1.2*U*eq(C) for methylene hydrogen atoms, and *d*(C–H) = 0.98 Å and *U*iso(H) = 1.5*U*eq(C) for methyl hydrogens. The methyl hydrogens were allowed to rotate as a rigid group to the orientation of maximum observed electron density. The two unique coordinated methanol oxygen hydrogen atoms were located and refined isotropically with *d*(O−H) = 0.85(2) Å distance restraints. No hydrogen atoms were located or calculated for

any of the solvent guest species. The largest residual electron density peak in the final difference map is 1.19 e/Å^3, located 0.83 Å from Cu1.

X-ray crystal structure determination for $Cu_{1.9}Zn_{0.1}$(TNDS)(DBTD). X-ray intensity data from a red plate were collected at 220(2) K using a Bruker D8 QUEST diffractometer equipped with a PHOTON-II area detector and an Incoatec microfocus source (Mo K_α radiation, λ = 0.71073 Å). The raw area detector data frames were reduced and corrected for absorption effects using the Bruker APEX3, SAINT+ and SADABS programs.[147,148] The structure was solved with SHELXT.[149,150] Subsequent difference Fourier calculations and full-matrix least-squares refinement against *F*2 were performed with SHELXL-2018[149,150] using OLEX2.[151]

The compound crystallizes in the space group *Pmmm* of the orthorhombic system. The asymmetric unit consists of ¼ of a mixed Zn/Cu site atom, ¼ of one $C_{34}H_{16}Br_2O_8$ cross-linking ligand, ¼ of one $C_{29}H_{24}N_4O_3$ pillar ligand and a large volume of unidentified disordered solvent guest molecules. Occupancies of the mixed Zn/Cu site could not be resolved crystallographically but were manually fixed at 95% Cu / 5% Zn in accordance with elemental analysis (ICP-MS) results. The unique pyridyl ring and the central phenyl ring of the pillar are disordered across mirror planes. The -$C_{13}H_{14}N_2O_3$ substituent attached to the central phenyl ring of the pillar could not be crystallographically located. It is presumably bonded to C15/C15* and is therefore disordered over four symmetry-equivalent positions. It contributes too weakly to the structure factors to be plausibly located. The largest electron density peak in this region was 0.45 e/Å^3, located *ca*. 2.1 Å from C15, which could not be modeled as part of the -$C_{13}H_{14}N_2O_3$ substituent. For the final refinement cycles, C15 was left 'naked', with no substituent. Enhanced rigid-bond

restraints were applied to the U_{ij} values of all atoms (SHELX RIGU). Additional spherical restraints (ISOR) were applied to the displacement ellipsoids of atoms C6 and C7. The disordered interstitial solvent species could not be reasonably modeled. Their contribution to the structure factors was accounted for using the Squeeze technique. The contribution of the unlocated -$C_{13}H_{14}N_2O_3$ substituent atoms was also accounted for with Squeeze.[5] The solvent-accessible volume was calculated to be 2410 Å^3 (73% of the total unit cell volume), containing the scattering equivalent of 332 electrons per unit cell. The reported formula and F.W. reflect the known framework atoms only. All non-hydrogen atoms were refined with anisotropic displacement parameters. Hydrogen atoms bonded to carbon were placed in geometrically idealized positions and included as riding atoms with d(C–H) = 0.95 Å and Uiso(H) = 1.2Ueq(C). The largest residual electron density peak in the final difference map is 0.50 e/Å^3, located 1.53 Å from Br1.

X-ray crystal structure determination for $Cu_{1.2}Zn_{0.8}$(DPB-CHO)(DBTD). X-ray intensity data from a green almond-shaped plate were collected at 100(2) K using a Bruker D8 QUEST diffractometer equipped with a PHOTON-100 CMOS area detector and an Incoatec microfocus source (Mo K_α radiation, λ = 0.71073 Å). The raw area detector data frames were reduced and corrected for absorption effects using the Bruker APEX3, SAINT+, and SADABS programs.[147,148] The structure was solved with SHELXT.[149,150] Subsequent difference Fourier calculations and full-matrix least-squares refinement against F^2 were performed with SHELXL-2018[149,150] using OLEX2.[151]

The compound crystallizes in the space group *Pmmm* of the orthorhombic system. The asymmetric unit consists of ¼ of a mixed Zn/Cu site atom, ¼ of one $C_{34}H_{16}Br_2O_8$ cross-linking ligand, ¼ of one $C_{17}H_{12}N_2O$ pillar ligand and a large volume of unidentified

disordered solvent guest molecules. Occupancies of the mixed Zn/Cu site could not be resolved crystallographically but were fixed at 60% Cu / 40% Zn based on ICP-MS results. The unique pyridyl ring and the central phenyl ring of the $C_{17}H_{12}N_2O$ pillar are disordered across mirror planes. The −CHO substituent of the central phenyl ring of the pillar could not be crystallographically located. It is presumably bonded to C15/C16 and their symmetry-equivalents and is therefore disordered over eight symmetry-equivalent positions and contributes too weakly to the structure factors to be reasonably located. The largest electron density peak in this region was 0.38 e/Å^3, located > 1.8 Å from C15, and could not be modeled as part of the −CHO substituent. For the final refinement cycles, C15 was left 'naked', with no substituent. Enhanced rigid-bond restraints were applied to the U_{ij} values of all atoms (SHELX RIGU). Additional spherical restraints (ISOR) were applied to the displacement ellipsoids of atoms C6 and C7. The disordered interstitial solvent species could not be reasonably modeled. Their contribution to the structure factors was accounted for using the Squeeze technique. The contribution of the unlocated −CHO substituent atoms was also accounted for with Squeeze.[152] The solvent-accessible volume was calculated to be 2319 Å^3 (73% of the total unit cell volume), containing the scattering equivalent of 486 electrons per unit cell. The reported formula and F.W. reflect the expected framework atoms with the complete $C_{17}H_{12}N_2O$ pillar but not the unknown solvent content. All non-hydrogen atoms were refined with anisotropic displacement parameters. Hydrogen atoms bonded to carbon were placed in geometrically idealized positions and included as riding atoms with d(C−H) = 0.95 Å and Uiso(H) = 1.2Ueq(C). The largest residual electron density peak in the final difference map is 1.13 e/Å^3, located 0.90 Å from the mixed Zn/Cu site.

REFERENCES

[1] Chen, Y.; Zhang, X.; Wang, X.; Drout, R. J.; Mian, M. R.; Cao, R.; Ma, K.; Xia, Q.; Li, Z.; Farha, O. K. *J. Am. Chem. Soc.* **2021**, *143*, 4302–4310.

[2] Fang, Y.; Powell, J. A.; Li, E.; Wang, Q.; Perry, Z.; Kirchon, A.; Yang, X.; Xiao, Z.; Zhu, C.; Zhang, L.; Huang, F.; Zhou, H.-C. *Chem. Soc. Rev.* **2019**, *48*, 4707–4730.

[3] Zhao, S. Y.; Zhang, B.; Su, H.; Zhang, J. J.; Li, X. H.; Wang, K. X.; Chen, J. S.; Wei, X.; Feng, P. *J. Mater. Chem. A* **2018**, *6*, 4331–4336.

[4] Karges, J.; Stokes, R. W.; Cohen, S. M. *Trends Chem.* **2021**, *3*, 523–534.

[5] Liu, W.; Fang, Y.; Li, J. *Adv. Funct. Mater.* **2018**, *28*, 1705593.

[6] Li, S.; Gao, Y.; Li, N.; Ge, L.; Bu, X.; Feng, P. *Energy Environ. Sci.* **2021**, *14*, 1897–1927.

[7] Gerkman, M. A.; Gibson, R. S. L.; Calbo, J.; Shi, Y.; Fuchter, M. J.; Han, G. G. D. *J. Am. Chem. Soc.* **2020**, *142*, 8688–8695.

[8] Zhou, W.; Huang, D.; Wu, Y.; Zhao, J.; Wu, T.; Zhang, J.; Li, D.; Sun, C.; Feng, P.; Bu, X. *Angew. Chem. Int. Ed.* **2019**, *131*, 4271–4275.

[9] Yang, Y.; Zhang, X.; Kanchanakungwankul, S.; Lu, Z.; Noh, H.; Syed, Z. H.; Farha, O. K.; Truhlar, D. G.; Hupp, J. T. *J. Am. Chem. Soc.* **2020**, *142*, 21169–21177.

[10] Cadiau, A.; Kolobov, N.; Srinivasan, S.; Goesten, M. G.; Haspel, H.; Bavykina, A. V.; Tchalala, M. R.; Maity, P.; Goryachev, A.; Poryvaev, A. S.; Eddaoudi, M.; Fedin, M. V.; Mohammed, O. F.; Gascon, J.; *Angew. Chem. Int. Ed.* **2020**, *132*, 13570–13574.

[11] Park, J.; Jiang, Q.; Feng, D.; Zhou, H. *Angew. Chem. Int. Ed.* **2016**, *128*, 7304–7309.

[12] Liu, X.; Kirlikovali, K. O.; Chen, Z.; Ma, K.; Idrees, K. B.; Cao, R.; Zhang, X.; Islamoglu, T.; Liu, Y.; Farha, O. K. *Chem. Mater.* **2021**, *33*, 1444–1454.

[13] Wang, X. N.; Zhao, Y.; Li, J. L.; Pang, J. D.; Wang, Q.; Li, B.; Zhou, H. C. *Dalt. Trans.* **2021**, *50*, 3854–3861.

[14] Kalaj, M.; Cohen, S. M. *ACS Cent. Sci.* **2020**, *6*, 1046–1057.

[15] Yang, S.; Hu, W.; Nyakuchena, J.; Fiankor, C.; Liu, C.; Kinigstein, E. D.; Zhang, J.;

Zhang, X.; Huang, J. *Chem. Commun.* **2020**, *56*, 13971–13974.

[16] Murase, R.; Leong, C. F.; D'Alessandro, D. M. *Inorg. Chem.* **2017**, *56*, 14373–14382.

[17] Park, J. G.; Aubrey, M. L.; Oktawiec, J.; Chakarawet, K.; Darago, L. E.; Grandjean, F.; Long, G. J.; Long, J. R. *J. Am. Chem. Soc.* **2018**, *140*, 8526–8534.

[18] Xie, L. S.; Sun, L.; Wan, R.; Park, S. S.; Degayner, J. A.; Hendon, C. H.; Dincă, M. *J. Am. Chem. Soc.* **2018**, *140*, 7411–7414.

[19] Hei, X.; Teat, S. J.; Liu, W.; Li, J. Eco-Friendly, *J. Mater. Chem. C* **2020**, *8*, 16790–16797.

[20] Sabury, S.; Adams, T. J.; Kocherga, M.; Kilbey, S. M.; Walter, M. G. *Polym. Chem.* **2020**, *11*, 5735–5749.

[21] Zhou, Z.; Mukherjee, S.; Hou, S.; Li, W.; Elsner, M.; Fischer, R. A. *Angew. Chem. Int. Ed.* **2021**, *60*, 20551–20557.

[22] Noh, H.; Jeon, N.; Martinson, A. B. F.; Hupp, J. T. *ACS Appl. Energy Mater.* **2020**, *3*, 5095–5100.

[23] Owens-Baird, B.; Wang, J.; Wang, S. G.; Chen, Y. S.; Lee, S.; Donadio, D.; Kovnir, K. III-V *J. Am. Chem. Soc.* **2020**, *142*, 2031–2041.

[24] Batool, S. S.; Gilani, S. R.; Tahir, M. N.; Siddique, A.; Harrison, W. T. A. *J. Struct. Chem.* **2016**, *57*, 1176–1181.

[25] Gonçalves, B. F.; Lagrow, A. P.; Pyrlin, S.; Owens-Baird, B.; Botelho, G.; Marques, L. S. A.; Ramos, M. M. D.; Kovnir, K.; Lanceros-Mendez, S.; Kolen'ko, Y. V. *Nanomaterials* **2021**, *11*, 1148.

[26] Li, C.; Wang, K.; Li, J.; Zhang, Q. *ACS Materials Lett.* **2020**, *2*, 779–797.

[27] Zhang, H.; Cheng, H-M.; Ye, P. *Chem. Soc. Rev.* **2018**, *47*, 6009–6012.

[28] De Ruiter, G.; Tartakovsky, E.; Oded, N.; Van Der Boom, M. E. *Angew. Chem. Int. Ed.* **2010**, *49*, 169–172.

[29] Pal, S.; Sen, B.; Lohar, S.; Mukherjee, M.; Banerjee, S.; Chattopadhyay, P. *Dalt. Trans.* **2014**, *44*, 1761–1768.

[30] Blunden, B. M.; Stenzel, M. H. *J. Chem. Technol. Biotechnol.* **2015**, *90*, 1177–1195.

[31] Klajn, R. *Chem. Soc. Rev.* **2013**, *43*, 148–184.

[32] Rice, A. M.; Martin, C. R.; Galitskiy, V. A.; Berseneva, A. A.; Leith, G. A.; Shustova, N. B. *Chem. Rev.* **2019**, *120*, 8790–8813.

[33] Leith, G. A.; Martin, C. R.; Mathur, A.; Kittikhunnatham, P.; Park, K. C.; Shustova, N. B. *Adv. Energy Mater.* **2021**, 2100441.

[34] Castellanos, S.; Kapteijn, F.; Gascon, J. *CrystEngComm* **2016**, *18*, 4006–4012.

[35] Morimoto, M.; Irie, M. *Chem. Commun.* **2005**, 3895–3905.

[36] Dolgopolova, E. A.; Rice, A. M.; Martin, C. R.; Shustova, N. B. *Chem. Soc. Rev.* **2018**, *47*, 4710–4728.

[37] Chi, Z.; Zhang, X.; Xu, B.; Zhou, X.; Ma, C.; Zhang, Y.; Liu, S.; Xu, J. *Chem. Soc. Rev.* **2012**, *41*, 3878–3896.

[38] Andrzejewski, M.; Katrusiak, A. *J. Phys. Chem. Lett.* **2017**, *8*, 279–284.

[39] Zhang, Y.; Hu, W.; Wang, D.; Reinhart, B. J.; Huang, J. *J. Mater. Chem. A* **2021**, *9*, 6180–6187.

[40] Small, L. J.; Schindelholz, M. E.; Nenoff, T. M. *Ind. Eng. Chem. Res.* **2021**, *60*, 7998–8006.

[41] Fan, Z.; Wang, Z.; Cokoja, M.; Fischer, R. A. *Catal. Sci. Technol.* **2021**, *11*, 2396–2402.

[42] He, Y.; Yang, S.; Fu, Y.; Wang, F.; Ma, J.; Wang, G.; Chen, G.; Wang, M.; Dong, R.; Zhang, P.; Feng, X. *Small Struct.* **2021**, *2*, 2000095.

[43] Liu, J. J.; Guan, Y. F.; Li, L.; Chen, Y.; Dai, W. X.; Huang, C. C.; Lin, M. J. *Chem. Commun.* **2017**, *53*, 4481–4484.

[44] Jhang, P. C.; Chuang, N. T.; Wang, S. L. *Angew. Chem. Int. Ed.* **2010**, *49*, 4200–4204.

[45] Williams, D. E.; Martin, C. R.; Dolgopolova, E. A.; Swifton, A.; Godfrey, D. C.; Ejegbavwo, O. A.; Pellechia, P. J.; Smith, M. D.; Shustova, N. B. *J. Am. Chem. Soc.* **2018**, *140*, 7611–7622.

[46] Irie, M.; Lifka, T.; Uchida, K.; Kobatake, S.; Shindo, Y. *Chem. Commun.* **1999**, 747–750.

[47] Tani, K.; Ishibashi, Y.; Miyasaka, H.; Kobatake, S.; Irie, M. *J. Phys. Chem. C* **2008**, *112*, 11150–11157.

[48] Irie, M.; Fukaminato, T.; Matsuda, K.; Kobatake, S. *Chem. Rev.* **2014**, *114*, 12174–12277.

[49] Tam, E. S.; Parks, J. J.; Shum, W. W.; Zhong, Y. W.; Santiago-Berríos, M. B.; Zheng, X.; Yang, W.; Chan, G. K. L.; Abruña, H. D.; Ralph, D. C. *ACS Nano* **2011**, *5*, 5115–5123.

[50] Williams, D. E.; Rietman, J. A.; Maier, J. M.; Tan, R.; Greytak, A. B.; Smith, M. D.; Krause, J. A.; Shustova, N. B. *J. Am. Chem. Soc.* **2014**, *136*, 11886–11889.

[51] Dolgopolova, E. A.; Williams, D. E.; Greytak, A. B.; Rice, A. M.; Smith, M. D.; Krause, J. A.; Shustova, N. B. *Angew. Chem. Int. Ed.* **2015**, *54*, 13639–13643.

[52] Steen, J. D.; Duijnstee, D. R.; Sardjan, A. S.; Martinelli, J.; Kortekaas, L.; Jacquemin, D.; Browne, W. R. *J. Phys. Chem. A* **2021**, *125*, 3355–3361.

[53] Morimoto, M.; Kobatake, S.; Irie, M. *Chem. Commun.* **2006**, 2656–2658.

[54] Healey, K.; Liang, W.; Southon, P. D.; Church, T. L.; D'Alessandro, D. M. *J. Mater. Chem. A* **2016**, *4*, 10816–10819.

[55] Moriyama, Y.; Matsuda, K.; Tanifuji, N.; Irie, S.; Irie, M. *Org. Lett.* **2005**, *7*, 3315–3318.

[56] Hakouk, K.; Oms, O.; Dolbecq, A.; Marrot, J.; Saad, A.; Mialane, P.; El Bekkachi, H.; Jobic, S.; Deniard, P.; Dessapt, R. *J. Mater. Chem. C* **2014**, *2*, 1628–1641.

[57] Ejegbavwo, O. A.; Berseneva, A. A.; Martin, C. R.; Leith, G. A.; Pandey, S.; Brandt, A. J.; Park, K. C.; Mathur, A.; Farzandh, S.; Klepov, V. V.; Heiser, B. J.; Chandrashekhar, M.; Karakalos, S. G.; Smith, M. D.; Phillpot, S. R.; Garashchuk, S.; Chen, D. A.; Shustova, N. B. *Chem. Sci.* **2020**, *11*, 7379–7389.

[58] Metavarayuth, K.; Ejegbavwo, O.; McCarver, G.; Myrick, M. L.; Makris, T. M.; Vogiatzis, K. D.; Senanayake, S. D.; Manley, O. M.; Ebrahim, A. M.; Frenkel, A. I.; Hwang, S.; Rajeshkumar, T.; Jimenez, J. D.; Chen, K.; Shustova, N. B.; Chen, D. A. *J. Phys. Chem. Lett.* **2020**, *11*, 8138–8144.

[59] Zhang, S.; Cheng, P. *CrystEngComm* **2015**, *17*, 4250–4271.

[60] Godiksen, A.; Stappen, F. N.; Vennestrøm, P. N. R.; Giordanino, F.; Rasmussen, S. B.; Lundegaard, L. F.; Mossin, S. *J. Phys. Chem. C* **2014**, *118*, 23126–23138.

[61] Hush, N. S.; Woolsey, I. S. *J. Am. Chem. Soc.* **1972**, *94*, 4107–4114.

[62] Xiao, Z.; Natarajan, M.; Zhong, W.; Liu, X. *Electrochim. Acta* **2020**, *340*, 135998.

[63] Comba, P.; Löhr, A. M.; Pfaff, F.; Ray, K. *Isr. J. Chem.* **2020**, *60*, 957–962.

[64] Ershova, I. V.; Smolyaninov, I. V.; Bogomyakov, A. S.; Fedin, M. V.; Starikov, A. G.; Cherkasov, A. V.; Fukin, G. K.; Piskunov, A. V. *Dalt. Trans.* **2019**, *48*, 10723–10732.

[65] Dolgopolova, E. A.; Galitskiy, V. A.; Martin, C. R.; Gregory, H. N.; Yarbrough, B. J.; Rice, A. M.; Berseneva, A. A.; Ejegbavwo, O. A.; Stephenson, K. S.; Kittikhunnatham, P.; Karakalos, S. G.; Smith, M. D.; Greytak, A. B.; Garashchuk, S.; Shustova, N. B. *J. Am. Chem. Soc.* **2019**, *141*, 5350–5358.

[66] Seiler, V. K.; Robeyns, K.; Tumanov, N.; Cinčić, D.; Wouters, J.; Champagne, B.; Leyssens, T. A *CrystEngComm* **2019**, *21*, 4925–4933.

[67] Feuerstein, T. J.; Müller, R.; Barner-Kowollik, B.; Roesky, P. W. *Inorg. Chem.* **2019**, *58*, 15479–15486.

[68] Rostovtseva, I. A.; Chernyshev, A. V.; Tkachev, V. V.; Dorogan, I. V.; Voloshin, N. A.; Solov'eva, E. V.; Metelitsa, A. V.; Gaeva, E. B.; Aldoshin, S. M.; Minkin, V. I. *J. Mol. Struct.* **2017**, *1145*, 55–64.

[69] Remacle, F.; Speiser, S.; Levine, R. D. *J. Phys. Chem. B* **2001**, *105*, 5589–5591.

[70] Nordin, R.; Lazim, A. M.; Hasbullah, S. A. *AIP Conf. Proc.* **2013**, *1571*, 817.

[71] Natali, M.; Giordani, S. *Org. Biomol. Chem.* **2012**, *10*, 1162–1171.

[72] Martin, C. R.; Leith, G. A.; Kittikhunnatham, P.; Park, K. C.; Ejegbavwo, O. A.; Mathur, A.; Callahan, C. R.; Desmond, S. L.; Keener, M. R.; Ahmed, F.; Pandey, S.; Smith, M. D.; Phillpot, S. R.; Greytak, A. B.; Shustova, N. B. *Angew. Chem. Int. Ed.* **2021**, *60*, 8072–8080.

[73] Wudl, F.; Bryce, M. R. *J. Chem. Educ*. **1990**, *67*, 717.

[74] Sun, L.; Park, S. S.; Sheberla, D.; Dincă, M. *J. Am. Chem. Soc* **2016**, *138*, 14772–14782.

[75] Šimenas, M.; Kobalz, M.; Mendt, M.; Eckold, P.; Krautscheid, H.; Banys, J.; Pöppl, A. *J. Phys. Chem. C* **2015**, *119*, 4898–4907.

[76] Del Sesto, R. E.; Arif, A. M.; Miller, J. S. *Inorg. Chem.* **2000**, *39*, 4894–4902.

[77] Swiatkowski, M.; Lanka, S.; Czylkowska, A.; Gas, K.; Sawicki, M. *Materials* **2021**, *14*, 2148.

[78] Yurtaeva, S. V.; Gilmutdinov, I. F.; Rodionov, A. A.; Zaripov, R. B.; Kutyreva, M. P.; Bondar, O. V.; Nedopekin, O. V.; Khafizov, N. R.; Kadkin, O. N. *ACS Omega* **2019**, *4*, 16450–16461.

[79] Gautier-Luneau, I.; Phanon, D.; Duboc, C.; Luneau, D.; Pierre, J. L. *Dalt. Trans.* **2005**, 3795–3799.

[80] Paredes-García, V.; Santana, R. C.; Madrid, R.; Vega, A.; Spodine, E.; Venegas-Yazigi, D. *Inorg. Chem.* **2013**, *52*, 8369–8377.

[81] Ozarowski, A. *Inorg. Chem.* **2008**, *47*, 9760–9762.

[82] Alter, M.; Binet, L.; Touati, N.; Lubin-Germain, N.; Le Hô, A. S.; Mirambet, F.; Gourier, D. *Inorg. Chem.* **2019**. *58*, 13115–13128.

[83] Dolgopolova, E. A.; Brandt, A. J.; Ejegbavwo, O. A.; Duke, A. S.; Maddumapatabandi, T. D.; Galhenage, R. P.; Larson, B. W.; Reid, O. G.; Ammal, S. C.; Heyden, A.; Chandrashekhar, M.; Stavila, V.; Chen, D. A.; Shustova, N. B. *J. Am. Chem. Soc.* **2017**, *139*, 5201–5209.

[84] Biesinger, M. C. *Surf. Interface Anal.* **2017**, *49*, 1325–1334.

[85] Ilton, E. S.; Post, J. E.; Heaney, P. J.; Ling, F. T.; Kerisit, S. N. *Appl. Surf. Sci.* **2016**, *366*, 475–485.

[86] Duke, A. S.; Dolgopolova, E. A.; Galhenage, R. P.; Ammal, S. C.; Heyden, A.; Smith, M. D.; Chen, D. A.; Shustova, N. B. *J. Phys. Chem. C* **2015**, *119*, 27457–27466.

[87] Ilton, E. S.; Du, Y.; Stubbs, J. E.; Eng, P. J.; Chaka, A. M.; Bargar, J. R.; Nelin, C. J.; Bagus, P. S. *Phys. Chem. Chem. Phys.* **2017**, *19*, 30473–30480.

[88] Armendáriz-Vidales, G.; Martínez-González, E.; Hernández-Melo, D.; Tiburcio, J.; Frontana, C. *Procedia Chem.* **2014**, *12*, 41–46.

[89] Bobo, M. V.; Arcidiacono, A. M.; Ayare, P. J.; Reed, J. C.; Helton, M. R.; Ngo, T.; Hanson, K.; Vannucci, A. K. *ChemPhotoChem* **2021**, *5*, 51–57.

[90] Joshi-Pangu, A.; Lévesque, F.; Roth, H. G.; Oliver, S. F.; Campeau, L. C.; Nicewicz,

D.; DiRocco, D. A. *J. Org. Chem.* **2016**, *81*, 7244–7249.

[91] Singha, N. K.; German, A. L. *J. Appl. Polym. Sci.* **2005**, *98*, 1418–1426.

[92] Scott, M. J.; Billiar, T. R.; Stoyanovsky, D. A. *Sci. Reports* **2016**, *6*, 38773.

[93] Ranguelova, K.; Mason, R. P. *Magn. Reson. Chem.* **2011**, *49*, 152.

[94] Buettner, G. R. *Free Radic. Res. Commun.* **1993**, *19*, S79–87.

[95] Karoui, H.; Hogg, N.; Fréjaville, C.; Tordo, P.; Kalyanaraman, B. *J. Biol. Chem.* **1996**, *271*, 6000–6009.

[96] Zamora, P. L.; Villamena, F. A. *J. Phys. Chem. A* **2012**, *116*, 7210–7218.

[97] Li, L.; Abe, Y.; Kanagawa, K.; Usui, N.; Imai, K.; Mashino, T.; Mochizuki, M.; Miyata, N. *Anal. Chim. Acta* **2004**, *512*, 121–124.

[98] Singh, R. J.; Karoui, H.; Gunther, M. R.; Beckman, J. S.; Mason, R. P.; Kalyanaraman, B. *Proc. Natl. Acad. Sci.* **1998**, *95*, 6675–6680.

[99] Jones, C. M.; Burkitt, M. J. *J. Chem. Soc. Perkin Trans. 2* **2002**, *2*, 2044–2051.

[100] Clément, J. L.; Ferré, N.; Siri, D.; Karoui, H.; Rockenbauer, A.; Tordo, P. *J. Org. Chem.* **2005**, *70*, 1198–1203.

[101] Zhang, Z.-X.; Wei, W.; Bai, F.-Q.; Bibi, S.; Zhang, H.-X. *Org. Chem. Front.* **2017**, *4*, 2191–2201.

[102] Stranius, K.; Börjesson, K. *Sci. Rep.* **2017**, *7*, 41145.

[103] Samai, S.; Bradley, D. J.; Choi, T. L. Y.; Yan, Y.; Ginger, D. S. *J. Phys. Chem. C* **2017**, *121*, 6997–7004.

[104] Shinoda, K.; Yokojima, S.; Fukaminato, T.; Nakamura, S. *J. Phys. Chem. A* **2021**, *125*, 5895–5902.

[105] Morimitsu, K.; Kobatake, S.; Irie, M. *Mol. Cryst. Liq. Cryst.* **2005**, *431*, 451–454.

[106] Shibata, K.; Muto, K.; Kobatake, S.; Irie, M. *J. Phys. Chem. A* **2002**, *106*, 209–214.

[107] Li, W.; Li, X.; Xie, Y.; Wu, Y.; Li, M.; Wu, X. Y.; Zhu, W. H.; Tian, H. *Sci. Reports* **2015**, *5*, 9186.

[108] Qin, Y.; Wang, Y.-T.; Yang, H.-B.; Zhu, W. *Chem. Synth.* **2021**, *1*, 2.

[109] Frigoli, M.; Mehl, G. H. *Chem. Commun.* **2004**, *4*, 818–819.

[110] Cox, J. M.; Walton, I. M.; Benedict, J. B. *J. Mater. Chem. C* **2016**, *4*, 4028–4033.

[111] Kingo, U.; Yasuhide. N.; Masahiro. I. *Bull. Chem. Soc. Jpn.* **1990**, *63*, 1311–1315.

[112] Irie, M.; Miyatake, O.; Uchida, K. *J. Am. Chem. Soc.* **2002**, *114*, 8715–8716.

[113] Takeshita, M.; Tanaka, C.; Miyazaki, T.; Fukushima, Y.; Nagai, M. *New J. Chem.* **2009**, *33*, 1433–1438.

[114] Takeshita. M.; Kato, N.; Kawauchi, S.; Imase, T.; Watanabe, J.; Irie, M. *J. Org. Chem.* **1998**, *63*, 9306–9313.

[115] Kaieda, T.; Kobatake, S.; Miyasaka, H.; Murakami, M.; Iwai, N.; Nagata, Y.; Itaya, A.; Irie, M. *J. Am. Chem. Soc.* **2002**, *124*, 2015–2024.

[116] Irie, M. *Chem. Rev.* **2000**, *100*, 1685–1716.

[117] Zhang, Y.-H.; Sun, X.-W.; Zhang, T.-S.; Liu, X.-Y.; Cui, G. *J. Phys. Chem. A* **2020**, *124*, 2547–2559.

[118] Fidder, H.; Rini, M.; Nibbering, E. T. J. *J. Am. Chem. Soc.* **2004**, *126*, 3789–3794.

[119] Vázquez, A.; Nudelman, N. S. *Int. J. Chem. Kinet.* **2012**, *44*, 736–744.

[120] Cuia, S.; Yanga, Y.; Pu, S. *Adv. Mater. Res.* **2012**, *583*, 105–108.

[121] Li, M.; Pu, S.; Zheng, C.; Luo, M.; Le, Z. *Surface Review and Letters* **2008**, *15*, 145–151.

[122] Zanoni, M.; Coleman, S.; Fraser, K. J.; Byrne, R.; Wagner, K.; Gambhir, S.; Officer, D. L.; Wallace, G. G.; Diamond, D. *Phys. Chem. Chem. Phys.* **2012**, *14*, 9112–9120.

[123] Stafforst, T.; Hilvert, D. *Chem. Commun.* **2009**, 287–288.

[124] Rini, M.; Holm, A. K.; Nibbering, E. T. J.; Fidder, H. *J. Am. Chem. Soc.* **2003**, *125*, 3028–3034.

[125] Buback, J.; Kullmann, M.; Langhojer, F.; Nuernberger, P.; Schmidt, R.; Würthner, F.; Brixner, T. *J. Am. Chem. Soc.* **2010**, *132*, 16510–16519.

[126] Kortekaas, L.; Chen, J.; Jacquemin, D.; Browne, W. R. *J. Phys. Chem. B* **2018**, *122*, 6423–6430.

[137] Williams, D. E.; Martin, C. R.; Dolgopolova, E. A.; Swifton, A.; Godfrey, D. C.; Ejegbavwo, O. A.; Pellechia, P. J.; Smith, M. D.; Shustova, N. B. *J. Am. Chem. Soc.* **2018**, *140*, 7611–7622.

[138] Tam, E. S.; Parks, J. J.; Shum, W. W.; Zhong, Y. W.; Santiago-Berríos, M. B.; Zheng, X.; Yang, W.; Chan, G. K. L.; Abruña, H. D.; Ralph, D. C. *ACS Nano* **2011**, *5*, 5115–5123.

[139] Lucas, L. N.; de Jong, J. J. D.; van Esch, J. H.; Kellogg, R. M.; Feringa, B. L. *Eur. J. Org. Chem.* **2003**, *2003*, 155–166.

[140] Farha, O. K.; Malliakas, C. D.; Kanatzidis, M. G.; Hupp, J. T. *J. Am. Chem. Soc.* **2010**, *132*, 950–952.

[141] Dolgopolova, E. A.; Williams, D. E.; Greytak, A. B.; Rice, A. M.; Smith, M. D.; Krause, J. A.; Shustova, N. B. *Angew. Chem. Int. Ed.* **2015**, *54*, 13639–13643.

[142] Chui, S. S. Y.; Lo, S. M. F.; Charmant, J. P. H.; Orpen, A. G.; Williams, I. D. *Science* **1999**, *283*, 1148–1150.

[143] Song, X.; Jeong, S.; Kim, D.; Lah, M. S. *CrystEngComm* **2012**, *14*, 5753–5756.

[144] Park, J.; Feng, D.; Yuan, S.; Zhou, H.-C. *Angew. Chem. Int. Ed.* **2015**, *54*, 430–435.

[145] Dolgopolova, E. A.; Galitskiy, V. A.; Martin, C. R.; Gregory, H. N.; Yarbrough, B. J.; Rice, A. M.; Berseneva, A. A.; Ejegbavwo, O. A.; Stephenson, K. S.; Kittikhunnatham, P.; Karakalos, S. G.; Smith, M. D.; Greytak, A. B.; Garashchuk, S.; Shustova, N. B. *J. Am. Chem. Soc.* **2019**, *141*, 5350–5358.

[146] Batool, S. S.; Gilani, S. R.; Tahir, M. N.; Siddique, A.; Harrison, W. T. *J. Struct. Chem.* **2016**, *57*, 1176–1181.

[147] Ejegbavwo, O. A.; Berseneva, A. A.; Martin, C. R.; Leith, G. A.; Pandey, S.; Brandt, A. J.; Park, K. C.; Mathur, A.; Farzandh, S.; Klepov, V. V.; Heiser, B. J.; Chandrashekhar, M.; Karakalos, S. G.; Smith, M. D.; Phillpot, S. R.; Garashchuk, S.; Chen, D. A.; Shustova, N. B. *Chem. Sci.* **2020**, *11*, 7379–7389.

[148] Dolgopolova, E. A.; Brandt, A. J.; Ejegbavwo, O. A.; Duke, A. S.; Maddumapatabandi, T. D.; Galhenage, R. P.; Larson, B. W.; Reid, O. G.; Ammal, S. C.; Heyden, A.; Chandrashekhar, M.; Stavila, V.; Chen, D. A.; Shustova, N. B. *J. Am. Chem. Soc.* **2017**, *139*, 5201–5209.

[149] Wudl, F.; Bryce, M. R. *J. Chem. Educ*. **1990**, *67*, 717–718.

[150] Sun, L.; Park, S. S.; Sheberla, D.; Dincă, M. Measuring and Reporting Electrical Conductivity in Metal−Organic Frameworks: Cd_2(TTFTB) as a Case Study. *J. Am. Chem. Soc* **2016**, *138*, 14772–14782.

[151] Bobo, M. V.; Arcidiacono, A. M.; Ayare, P. J.; Reed, J. C.; Helton, M. R.; Ngo, T.; Hanson, K.; Vannucci, A. K. *ChemPhotoChem* **2021**, *5*, 51–57.

[152] Joshi-Pangu, A.; Lévesque, F.; Roth, H. G.; Oliver, S. F.; Campeau, L. C.; Nicewicz, D.; DiRocco, D. A. *J. Org. Chem.* **2016**, *81*, 7244–7249.

[153] Stoll, S.; Schweiger, A. *J. Magn. Reson.* **2006**, *178*, 42–55.

[154] Shibata, K.; Muto, K.; Kobatake, S.; Irie, M. *J. Phys. Chem. A* **2002**, *106*, 209–214.

[155] Stranius, K.; Börjesson, K. *Sci. Rep.* **2017**, *7*, 41145.

[156] Duke, A. S.; Dolgopolova, E. A.; Galhenage, R. P.; Ammal, S. C.; Heyden, A.; Smith, M. D.; Chen, D. A.; Shustova, N. B. *J. Phys. Chem. C,* **2015**, *119*, 27457–27466.

[157] Krausa, L.; Herbst-Irmer, R.; Sheldrick, G. M.; Stalke, D. *J. Appl. Cryst.* **2015**, *48*, 3–10.

[158] APEX3 Version 2019.11-0 and SAINT+ Version 8.40B. Bruker AXS, Inc., Madison, Wisconsin, USA, **2019**.

[159] Sheldrick, G. M. *Acta Cryst.* **2015**, *A71*, 3–8.

[160] Sheldrick, G. M. *Acta Cryst.* **2015**, *C71*, 3–8.

[161] Dolomanov, O. V.; Bourhis, L. J.; Gildea, R. J.; Howard, J. A. K.; Puschmann, H. *J. Appl. Cryst.* **2009**, *42*, 339–341.

[162] Liu, J.; Wang, Y.; Benin, A. I.; Jakubczak, P.; Willis, R. R.; LeVan, M. D. *Langmuir* **2010**, *26*, 14301–14307.

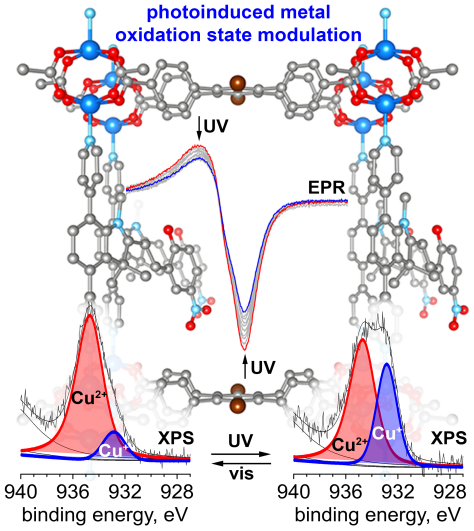

Scheme 4.1. Photoswitch-directed oxidation state modulation in photochromic MOFs is brought into the spotlight. Changes in EPR and XPS spectra were monitored as a function of an excitation wavelength. The gray, red, aqua, brown, and blue spheres represent C, O, N, Br, and Cu atoms, respectively.

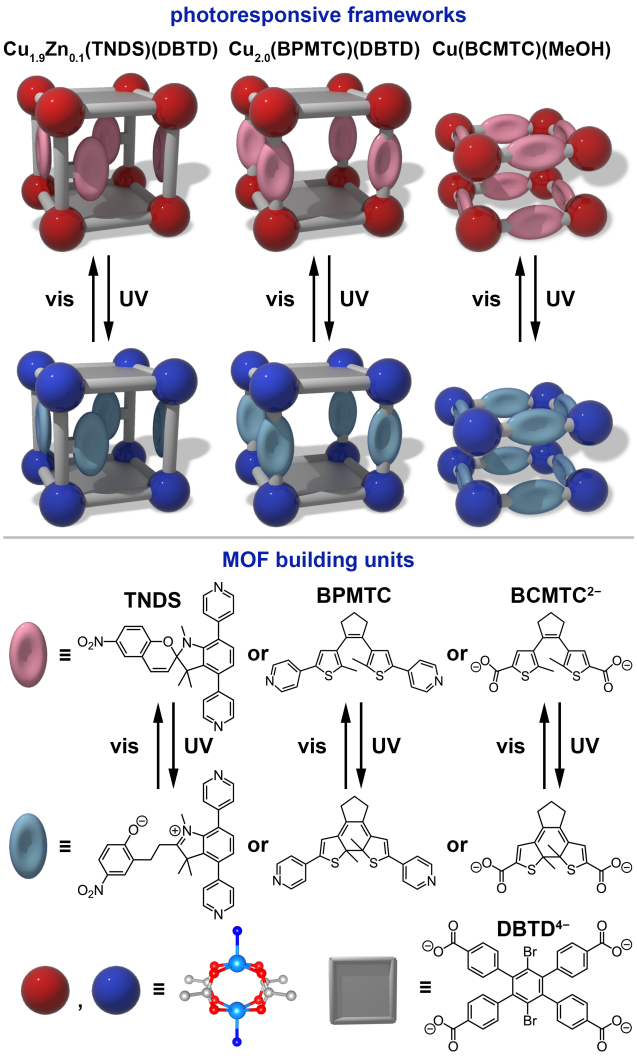

Figure 4.1. (*top*) Schematic representation of photochromic MOFs prepared in the current work. (*bottom*) The building blocks used for MOF preparation. The photochromic behavior of TNDS, BPMTC, and $BCMTC^{2-}$ as a function of UV and visible excitation is shown. The gray, red, dark blue, and light blue spheres represent C, O, N, and Cu atoms, respectively.

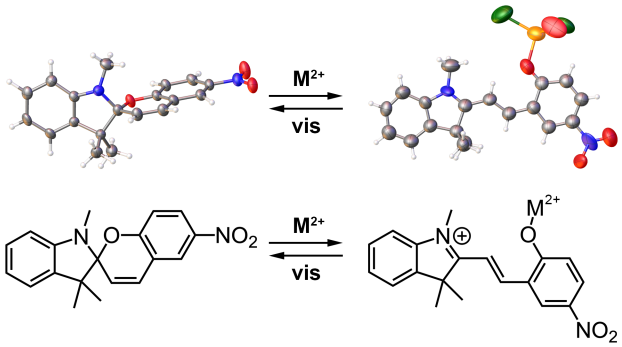

Figure 4.2. (*top*) Single-crystal X-ray structure of spiropyran and merocyanine showing the reversible binding of M^{2+} (e.g., M = Cu or Zn).[66–69] Thermal displacement parameters are drawn at the 40% probability level. Gray, blue, orange, red, green, and white spheres represent C, N, Zn, O, Cl, and H atoms, respectively. (*bottom*) The molecular representations of the crystal structures above.

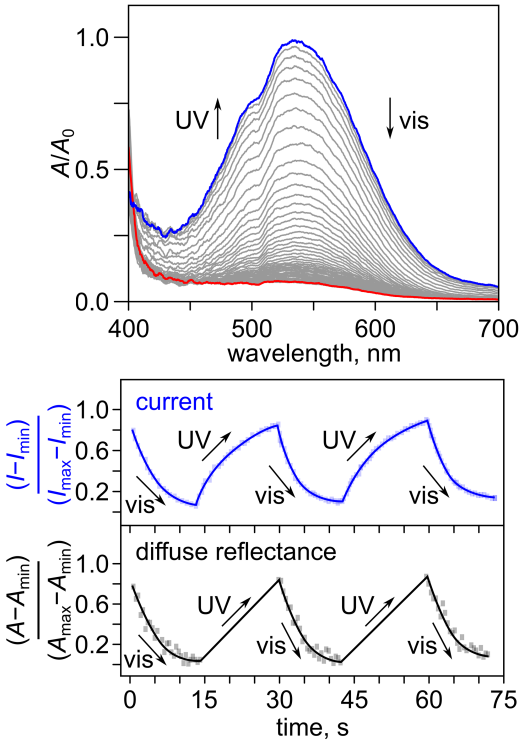

Figure 4.3. (*top*) Normalized diffuse reflectance profile of diarylethene attenuation in $Cu_{2.0}$(BPMTC)(DBTD) after 30 seconds of UV (λ_{ex} = 365 nm) excitation and attenuation under visible light. (*bottom*) Normalized current and optical cycling of photochromic $Cu_{2.0}$(BPMTC)(DBTD) through alternation of UV (λ_{ex} = 365 nm) and visible (λ_{ex} = 590 nm) irradiation. I_{max} and I_{min} = the maximum and minimum current values, respectively; A_{max} and A_{min} = the maximum and minimum absorbance values (converted from reflectance via the Kubelka–Munk function), respectively.

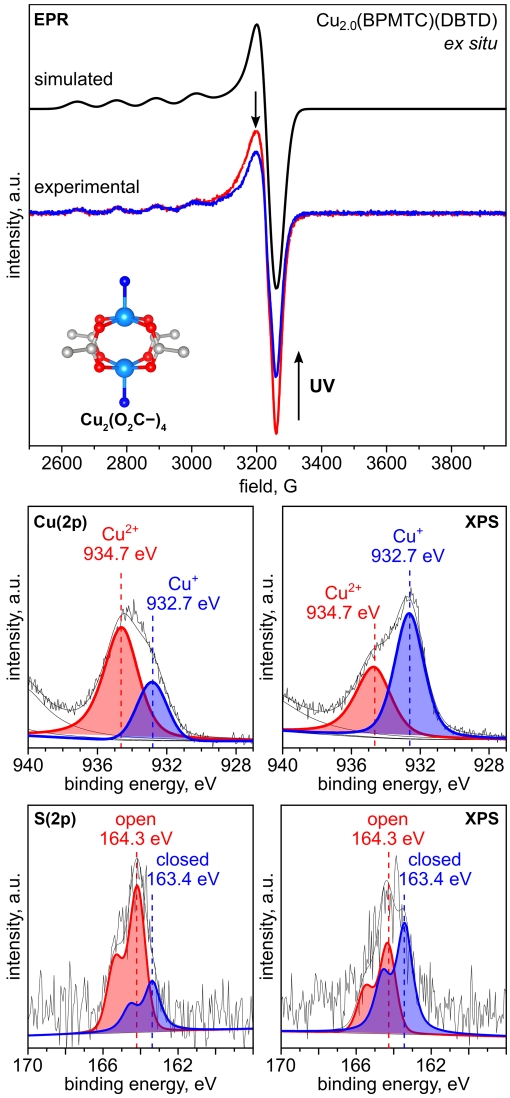

Figure 4.4. (*top*) EPR spectra of $Cu_{2.0}$(BPMTC)(DBTD) before (red) and after (blue) 365 nm *ex situ* irradiation. The inset shows a paddlewheel metal node. The gray, red, dark blue, and light blue spheres represent C, O, N, and Cu atoms, respectively. The simulated spectrum is shown in black. (*middle*) XPS data for the Cu(2p) region for $Cu_{2.0}$(BPMTC)(DBTD) in the dark (*middle left*) and under continuous UV irradiation (*middle right*). (*bottom*) XPS data for the S(2p) region for $Cu_{2.0}$(BPMTC)(DBTD) in the dark (*bottom left*) and under continuous UV irradiation (*bottom right*).

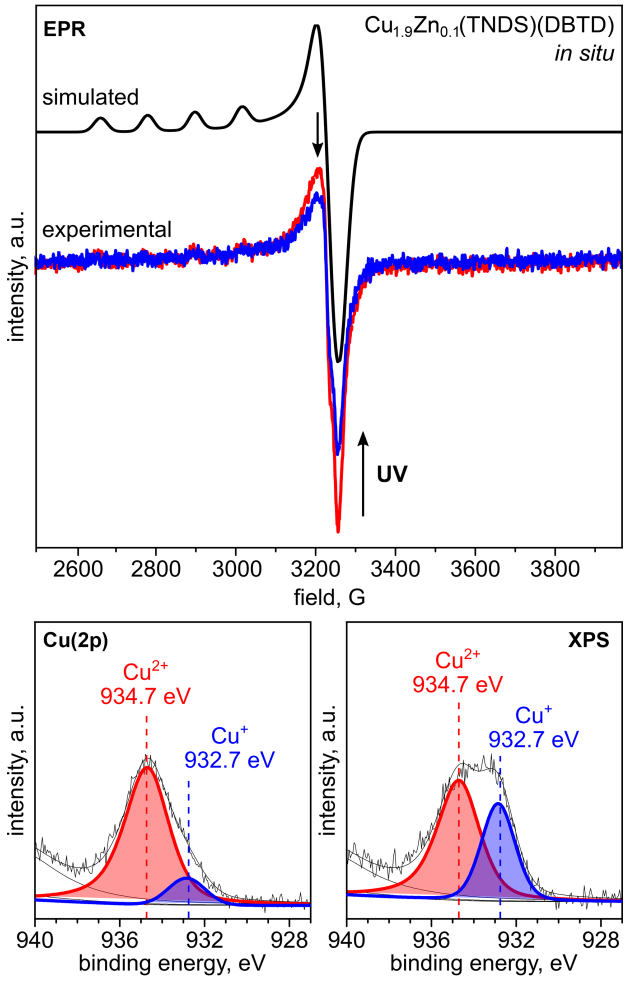

Figure 4.5. (*top*) EPR spectra of $Cu_{1.9}Zn_{0.1}$(TNDS)(DBTD) before (red) and after (blue) 365 nm *ex situ* irradiation. The simulated spectrum is shown in black. XPS data for the Cu(2p) region for $Cu_{1.9}Zn_{0.1}$(TNDS)(DBTD) in the dark (*bottom left*) and under continuous UV irradiation (*bottom right*).

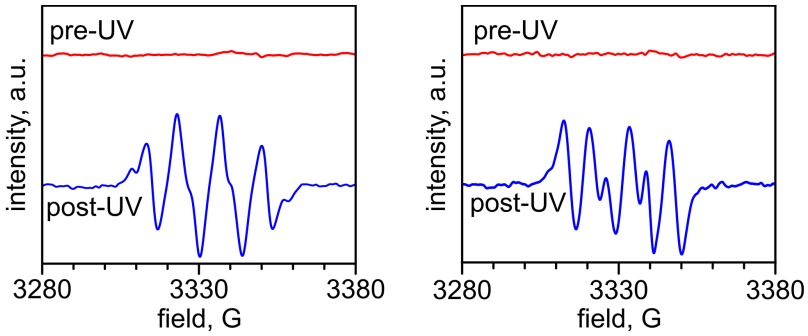

Figure 4.6. EPR spectra of a SP and DMPO solution in THF before (*top left*) and after (*bottom left*) UV irradiation (λ_{ex} = 365 nm). EPR spectra of a BPMTC and DMPO solution in THF before (*top right*) and after (*bottom right*) UV irradiation (λ_{ex} = 365 nm).

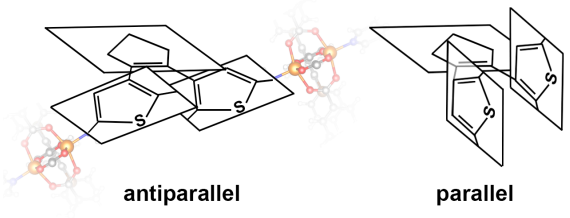

compound	$k_{forward}$, ms^{-1}	*T*, %	φ_{PI}, %
$Cu_{1.9}Zn_{0.1}$(TNDS)(DBTD)	3.6	27 ± 0.3	8 ± 0.9
$Cu_{2.0}$(BPMTC)(DBTD)	9.7	14 ± 1.3	79 ± 1.5
Aberchrome 670	6.2	96 ± 0.5	27[a]

[a] value obtained from *Sci. Rep.*, **2017**, *7*, 41145.

Figure 4.7. Schematic representation of the (*top left*) antiparallel and (*top right*) parallel confirmations of diarylethene. In the case of the antiparallel confirmation, coordination to the MOF metal node is outlined. (*bottom*) The forward photoisomerization rates ($k_{forward}$), transmission (*T*, %) at λ_{ex} = 365 nm, and photoisomerization quantum yields (φ_{PI}) for diarylethene and spiropyran-containing MOFs.

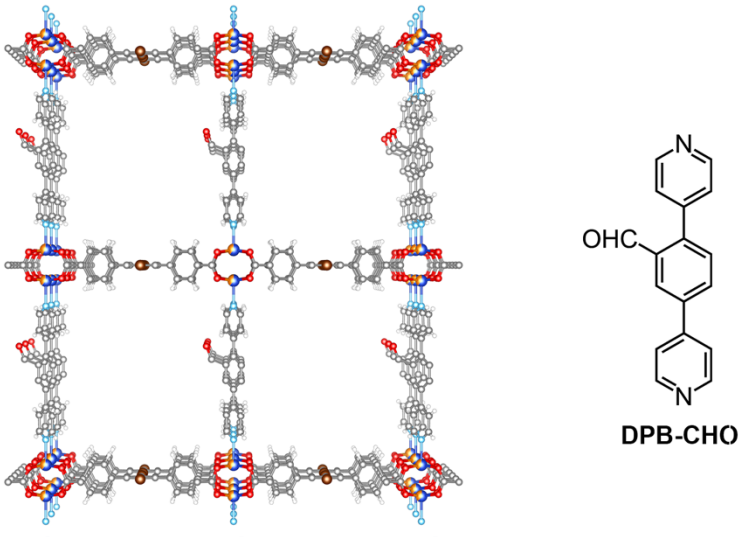

Figure 4.8. Single-crystal X-ray structure of (*left*) $Cu_{1.2}Zn_{0.8}$(DPB-CHO)(DBTD). The -CHO substituents on the central phenyl rings of the pillaring linkers were simulated for improved visualization. The gray, light blue, red, white, dark blue, and orange spheres represent carbon, nitrogen, oxygen, hydrogen, copper, and zinc atoms, respectively. (*right*) The molecular structure of the DPB-CHO linker.

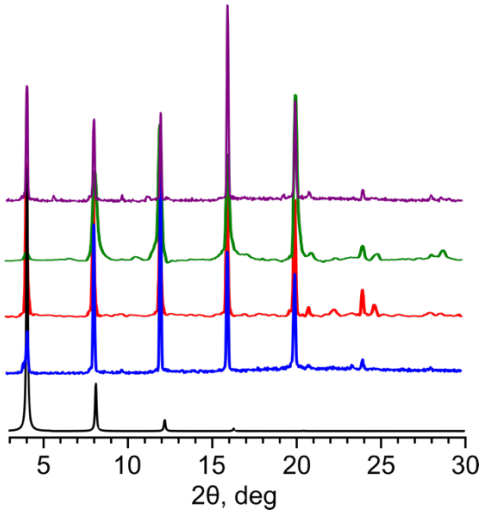

Figure 4.9. PXRD patterns of simulated $Zn_{2.0}$(BPMTC)(DBTD) (black),[134] as-synthesized $Zn_{2.0}$(BPMTC)(DBTD) (blue), and as-synthesized $Cu_{2.0}$(BPMTC)(DBTD) before (red) and after (green) three hours of *in situ* and 30 minutes of *ex situ* UV irradiation (purple; λ_{ex} = 365 nm).

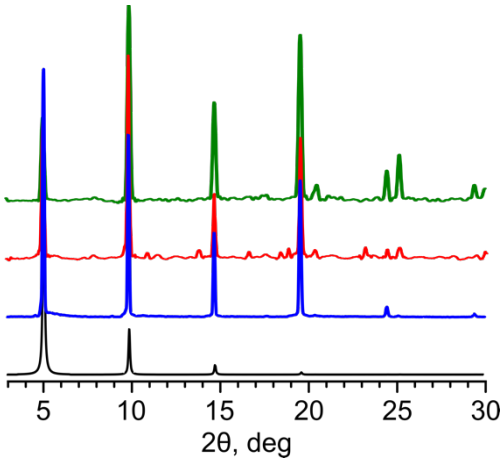

Figure 4.10. PXRD patterns of simulated $Zn_{2.0}$(TNDS)(DBTD) (black),[128] as-synthesized $Zn_{2.0}$(TNDS)(DBTD) (blue), and as-synthesized $Cu_{1.9}Zn_{0.1}$(TNDS)(DBTD) before (red) and after (green) 30 minutes of *in situ* UV irradiation (λ_{ex} = 365 nm).

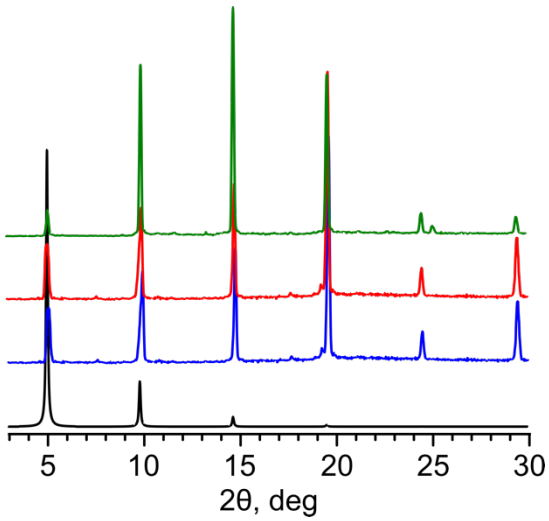

Figure 4.11. PXRD patterns of simulated $Zn_{2.0}$(DPB-CHO)(DBTD) (black),[135] as-synthesized $Zn_{2.0}$(DPB-CHO)(DBTD) (blue), and as-synthesized $Cu_{1.2}Zn_{0.8}$(DPB-CHO)(DBTD) before (red) and after (green) 30 minutes of *in situ* UV irradiation (λ_{ex} = 365 nm).

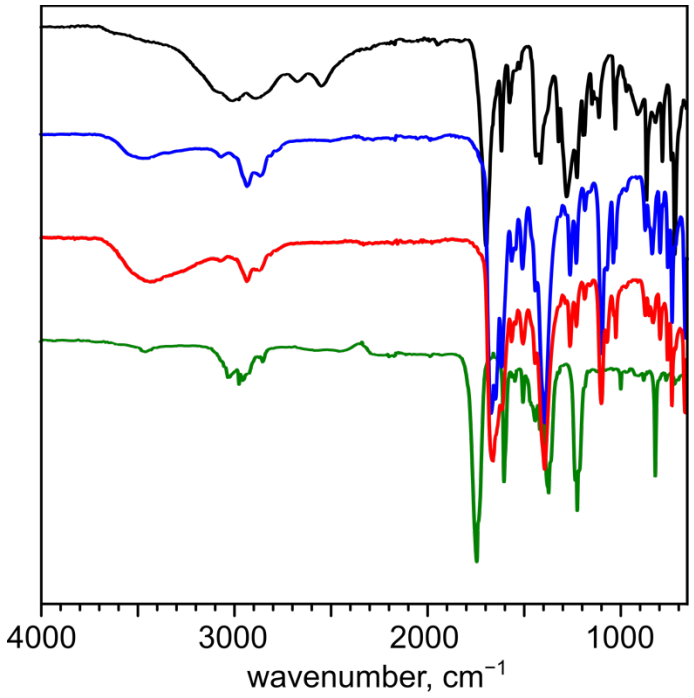

Figure 4.12. FTIR spectra of H_4DBTD (black), $Zn_{2.0}$(BPMTC)(DBTD) (blue), $Cu_{2.0}$(BPMTC)(DBTD) (red), and BPMTC (green).

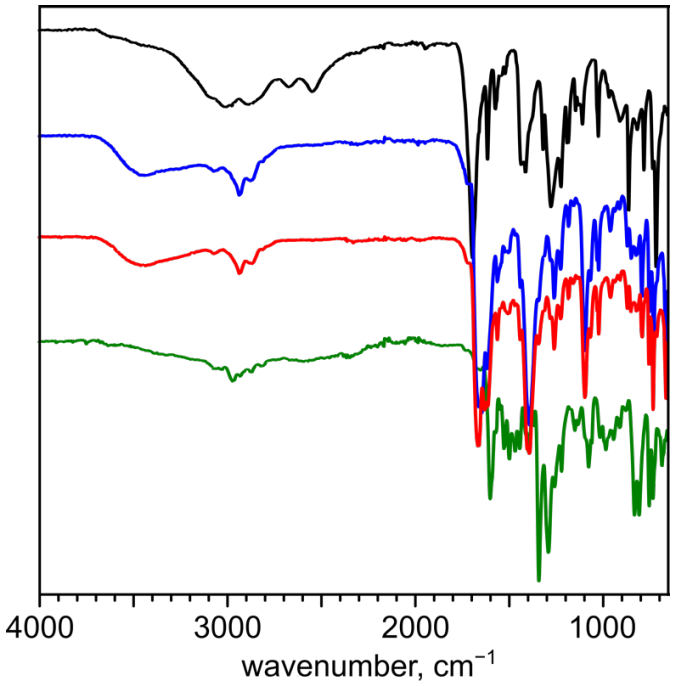

Figure 4.13. FTIR spectra of H_4DBTD (black), $Zn_{2.0}$(TNDS)(DBTD) (blue), $Cu_{2.0}$(TNDS)(DBTD) (red), and TNDS (green).

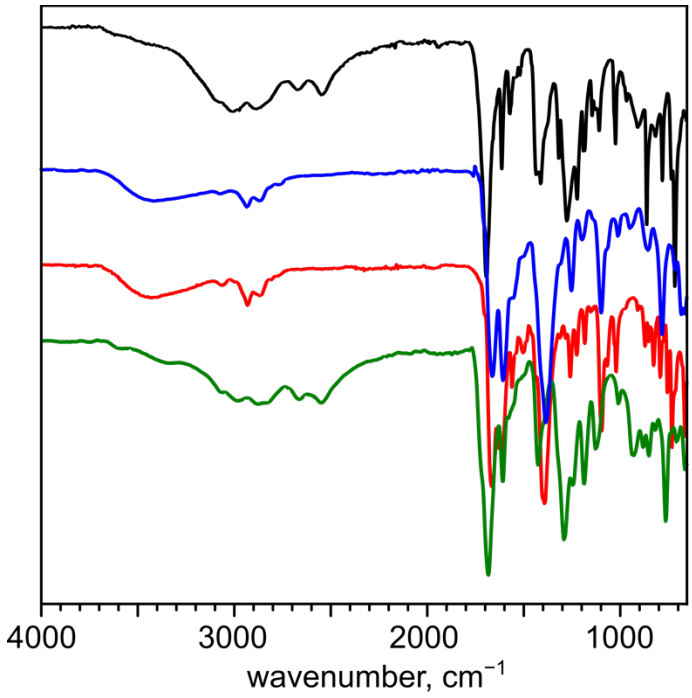

Figure 4.14. FTIR spectra of H_4DBTD (black), $Zn_{2.0}$(DPB-CHO)(DBTD) (blue), $Cu_{1.2}Zn_{0.8}$(DPB-CHO)(DBTD) (red), and DPB-CHO (green).

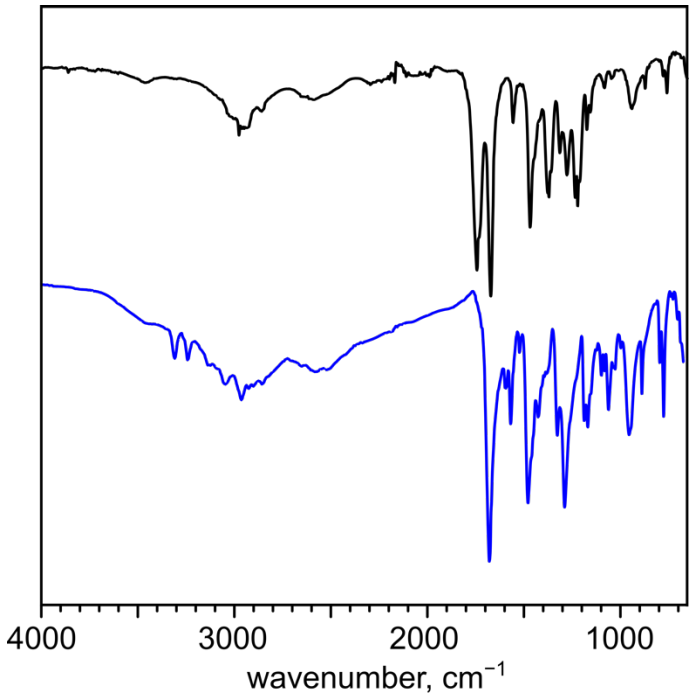

Figure 4.15. FTIR spectra of H_2BCMTC (black) and Cu(BCMTC)(MeOH) (blue).

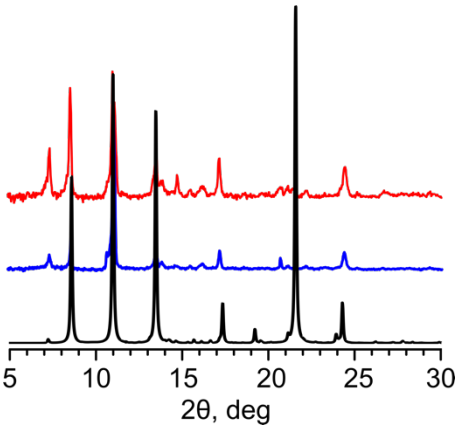

Figure 4.16. PXRD patterns of simulated Cu(BCMTC)(MeOH) (black) and as-synthesized Cu(BCMTC)(MeOH) before (blue) and after (red) one hour of *in situ* UV irradiation (λ_{ex} = 365 nm).

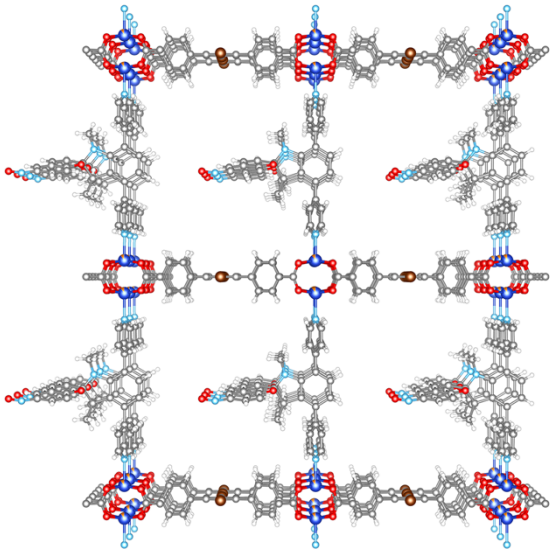

Figure 4.17. Single-crystal X-ray structure of $Cu_{1.9}Zn_{0.1}$(TNDS)(DBTD). The -$C_{13}H_{14}N_2O_3$ substituents on the central phenyl rings of the pillaring linkers for $Cu_{1.9}Zn_{0.1}$(TNDS)(DBTD) were simulated for improved visualization. The gray, light blue, red, white, dark blue, and orange spheres represent carbon, nitrogen, oxygen, hydrogen, copper, and zinc atoms, respectively.

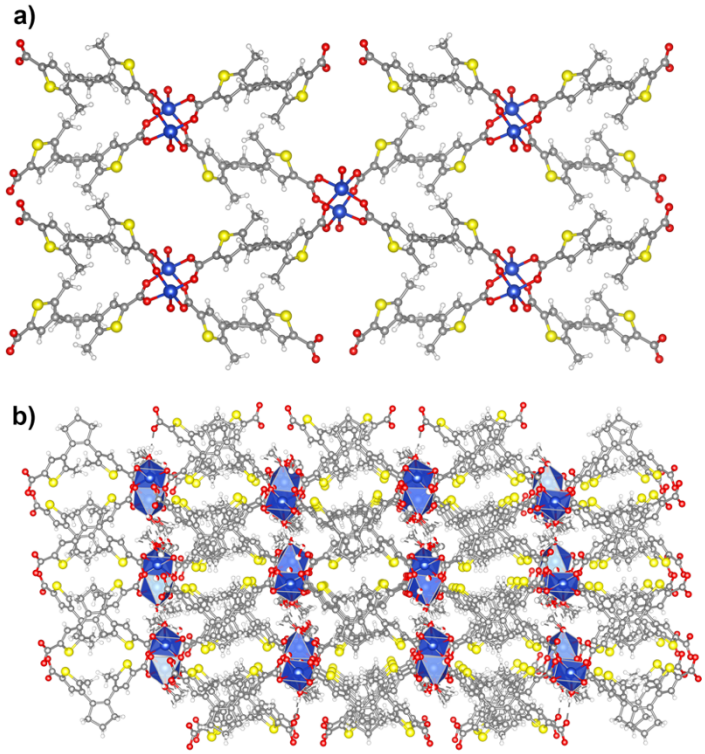

Figure 4.18. Single-crystal X-ray structure of Cu(BCMTC)(MeOH) (a) truncated to show two-dimensional connectivity, viewed down the *a*-axis, and (b) the extended structure viewed down the *b*-axis. The gray, red, yellow, white, and dark blue spheres represent carbon, oxygen, sulfur, hydrogen, and copper atoms, respectively.

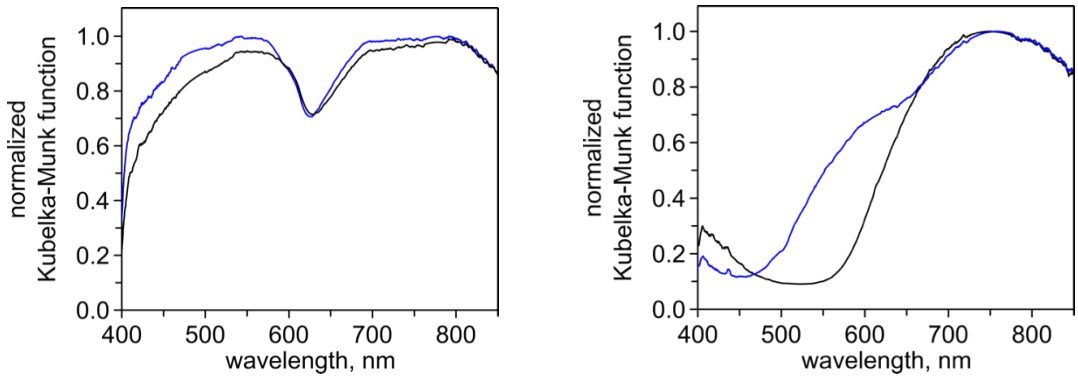

Figure 4.19. Diffuse reflectance spectra of (*left*) $Cu_{1.9}Zn_{0.1}$(TNDS)(DBTD) and (*right*) $Cu_{2.0}$(BPMTC)(DBTD) before (black) and after (blue) one minute of UV irradiation (λ_{ex} = 365 nm). Notably, there is no background subtraction corresponding to the MOFs absorption (in contrast to the spectra in Figures 4.3, 4.22, and 4.23).

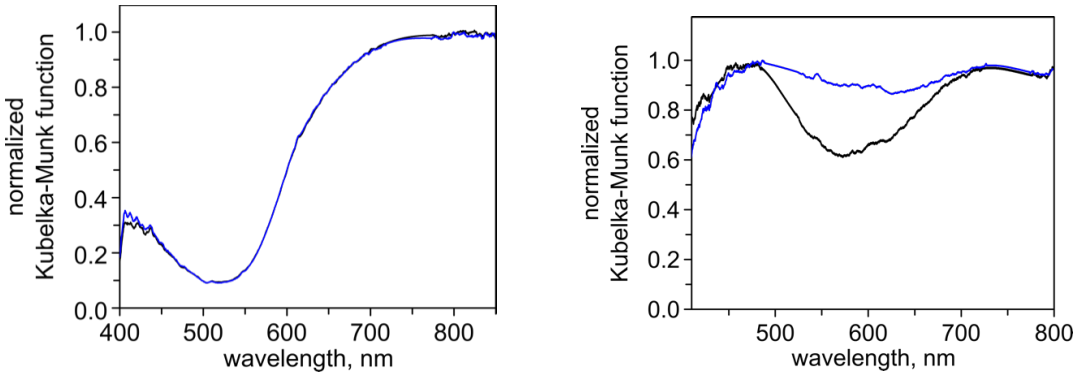

Figure 4.20. Diffuse reflectance spectra of (*left*) $Cu_{1.2}Zn_{0.8}$(DPB-CHO)(DBTD) and (*right*) Cu (BCMTC)(MeOH) before (black) and after (blue) one minute of UV irradiation (λ_{ex} = 365 nm). Notably, there is no background subtraction corresponding to the MOFs absorption (in contrast to the spectra in Figures 4.3, 4.22, and 4.23).

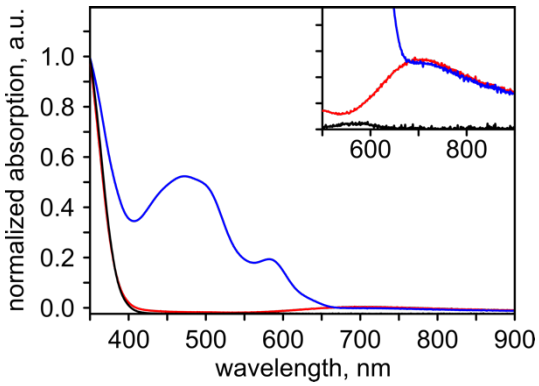

Figure 4.21. Absorption spectra of 1′,3′-dihydro-1′,3′,3′-trimethyl-6-nitrospiro[2*H*-1-benzopyran-2,2′-(2*H*)-indole] (SP) in THF (40 μM; black), a mixture of SP and $Cu(NO_3)_2$ in THF (40 μM each) after storing for four days in the dark (blue), and irradiating for five minutes with visible light (red; λ_{ex} = 590 nm).

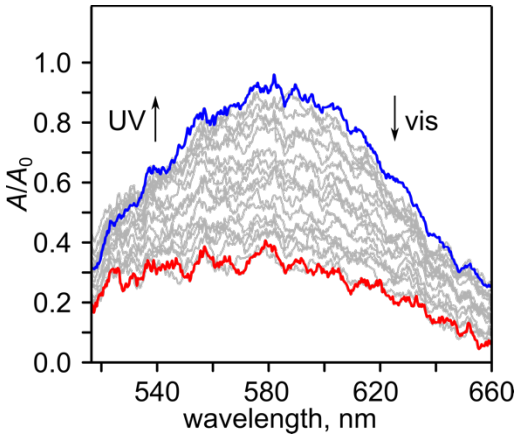

Figure 4.22. Normalized diffuse reflectance profile of diarylethene attenuation in Cu(BCMTC)(MeOH) after 30 seconds of UV (λ_{ex} = 365 nm) excitation and attenuation under visible light.

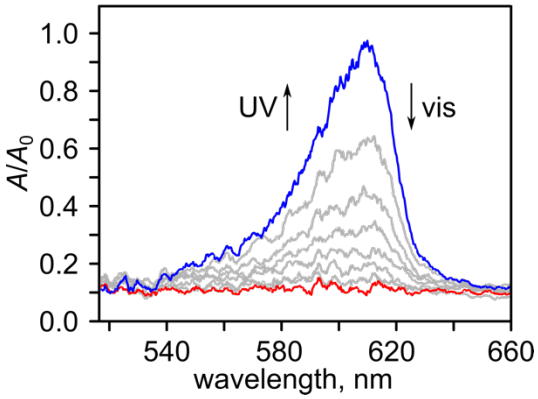

Figure 4.23. Normalized diffuse reflectance profile of spiropyran attenuation in $Cu_{1.9}Zn_{0.1}$(TNDS)(DBTD) after 30 seconds of UV (λ_{ex} = 365 nm) excitation and attenuation under visible light.

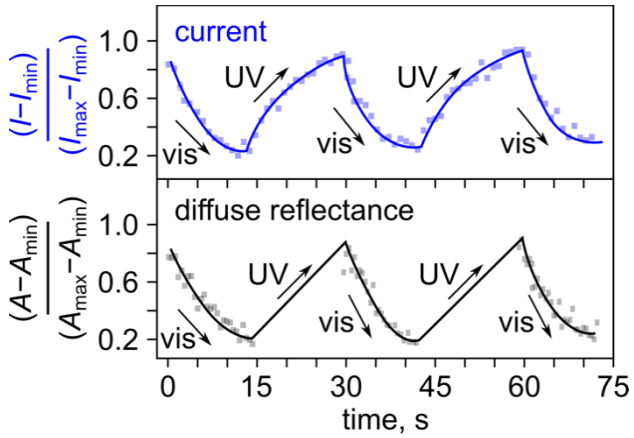

Figure 4.24. Current (*top*) and optical (*bottom*) cycling of $Cu_{1.9}Zn_{0.1}$(TNDS)(DBTD) monitored through alternation of UV (λ_{ex} = 365 nm) and visible (λ_{ex} = 590 nm) irradiation.

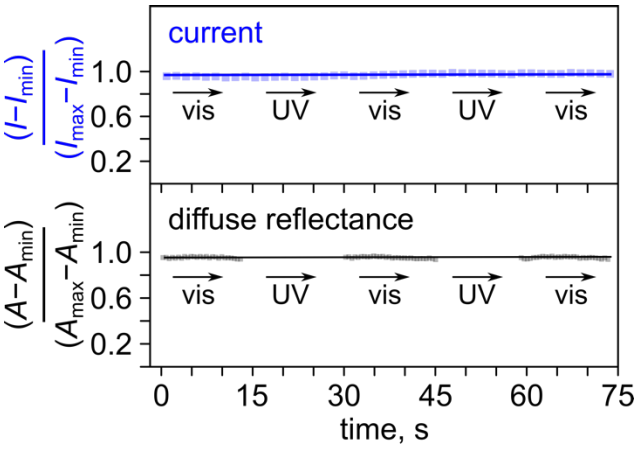

Figure 4.25. Current (*top*) and optical (*bottom*) cycling of $Cu_{1.2}Zn_{0.8}$(DPB-CHO)(DBTD) monitored through alternation of UV (λ_{ex} = 365 nm) and visible (λ_{ex} = 590 nm) irradiation.

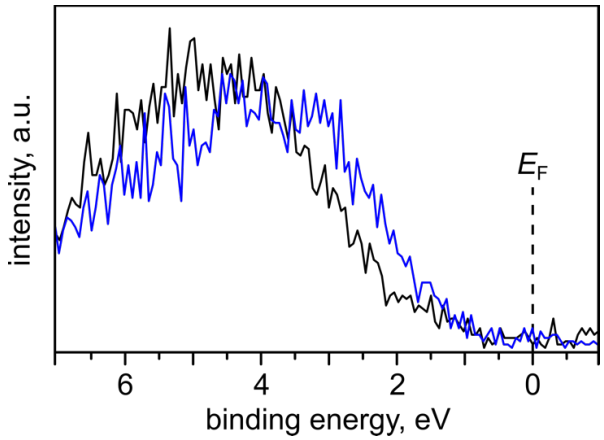

Figure 4.26. XPS data showing the valance band region of $Cu_{2.0}$(BPMTC)(DBTD) before (black) and after (blue) UV irradiation (λ_{ex} = 365 nm).

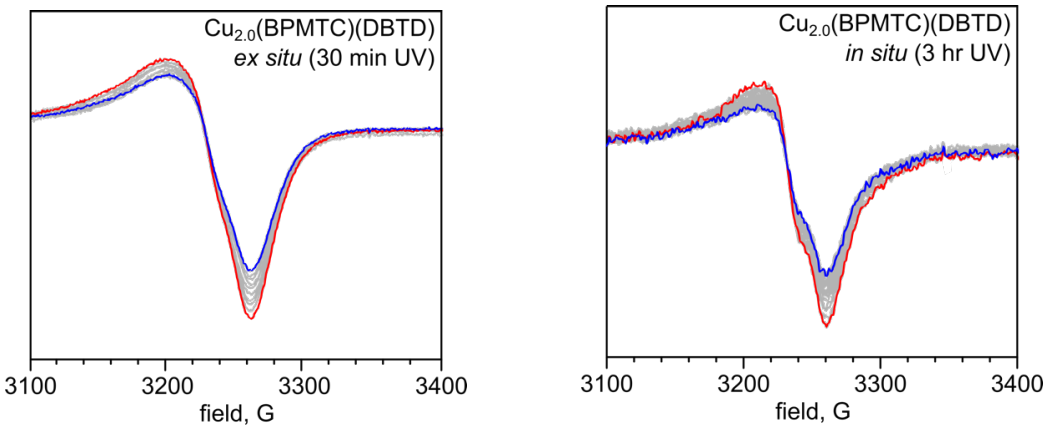

Figure 4.27. EPR spectra of $Cu_{2.0}$(BPMTC)(DBTD) before (blue) and after (red) 30 minutes of *ex situ* (*left*) and 3 hours of *in situ* (*right*) irradiation (λ_{ex} = 365 nm). Measurement conditions: center of field = 3220 G, sweep width = 2000 G, sweep time = 30 seconds (2 scans averaged), and microwave power = 1.262 mW.

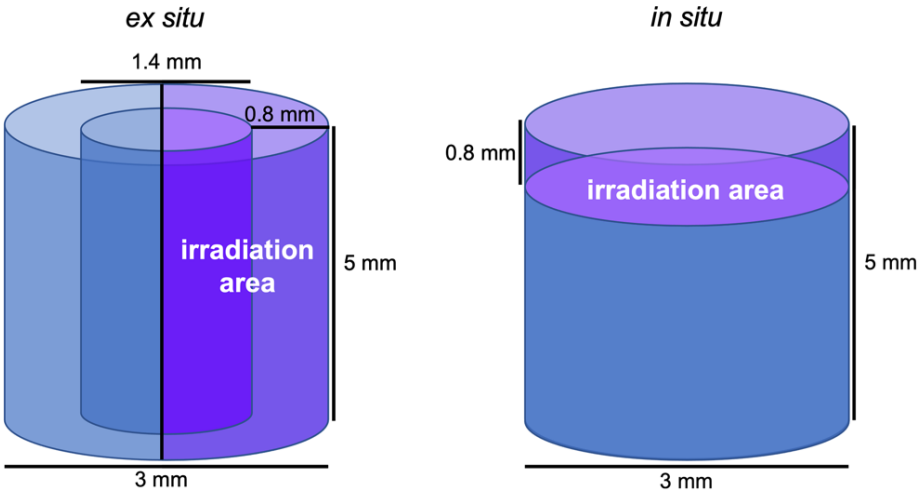

Figure 4.28. Schematic representation of the irradiated areas in (*left*) *ex situ* and (*right*) *in situ* irradiation EPR experiments.

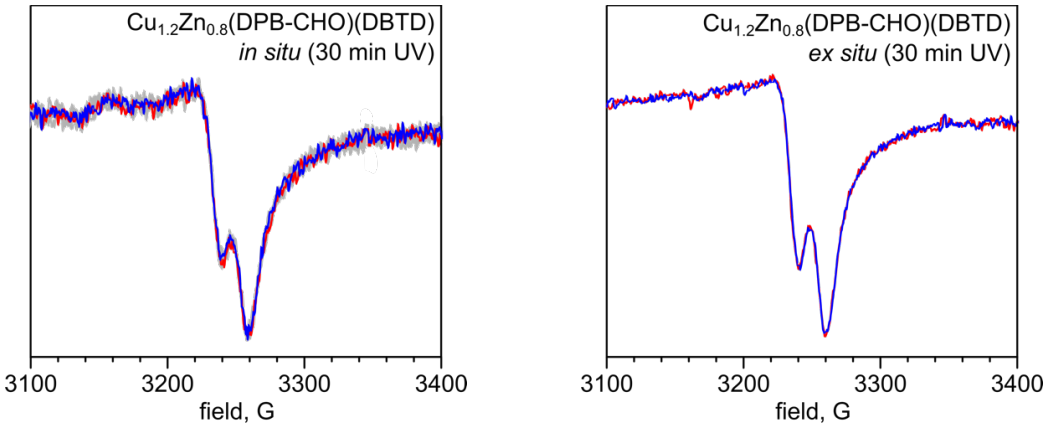

Figure 4.29. EPR spectra of $Cu_{1.2}Zn_{0.8}$(DPB-CHO)(DBTD) before (blue) and after (red) 30 minutes of *in situ* (*left*) and 30 minutes of *ex situ* (*right*) irradiation (λ_{ex} = 365 nm). Measurement conditions: center of field = 3220 G, sweep width = 1500 G, sweep time = 60 seconds (10 scans averaged for *ex situ* and 2 scans averaged for *in situ*), and microwave power = 1.589 mW.

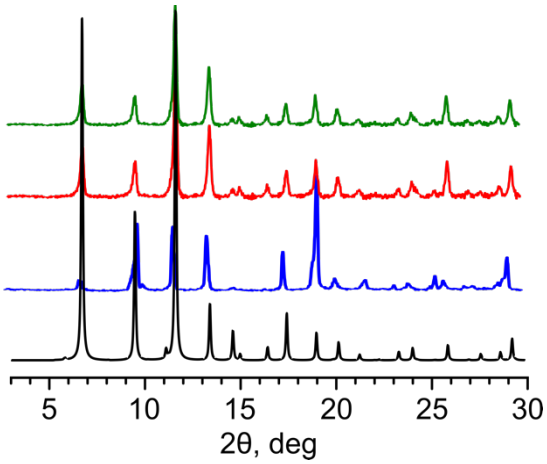

Figure 4.30. PXRD patterns of simulated $Zn_3(BTC)_2$ (black),[133] experimental $Zn_3(BTC)_2$ (blue), as-synthesized $Zn_{1.95}Cu_{1.05}(BTC)_2$ (red), and as-synthesized $Zn_{1.40}Cu_{1.60}(BTC)_2$ (green).

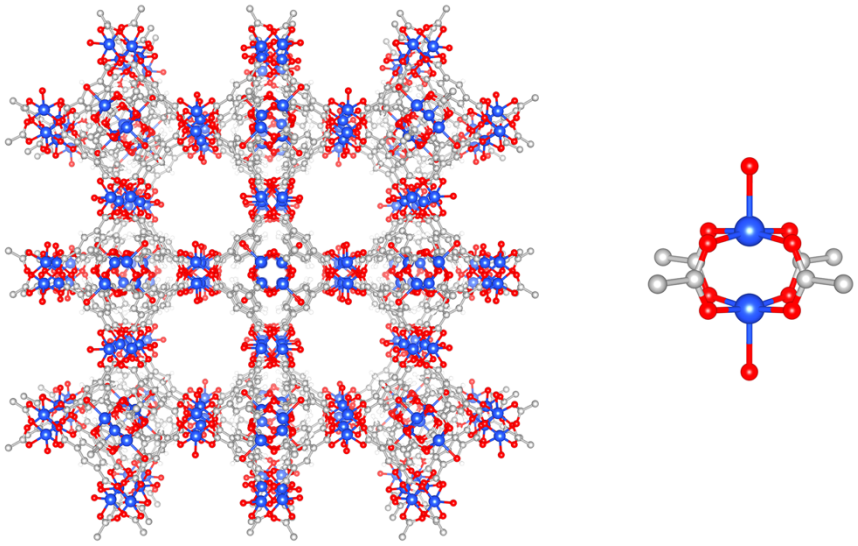

Figure 4.31. Single-crystal X-ray structure of (*left*) $Cu_3(BTC)_2$[162] that is isostructural to $Zn_3(BTC)_2$, $Zn_{1.40}Cu_{1.60}(BTC)_2$, and $Zn_{1.95}Cu_{1.05}(BTC)_2$. (*right*) A paddlewheel metal node of the copper-based MOFs in this manuscript. The gray, red, and dark blue spheres represent carbon, oxygen, and copper atoms, respectively.

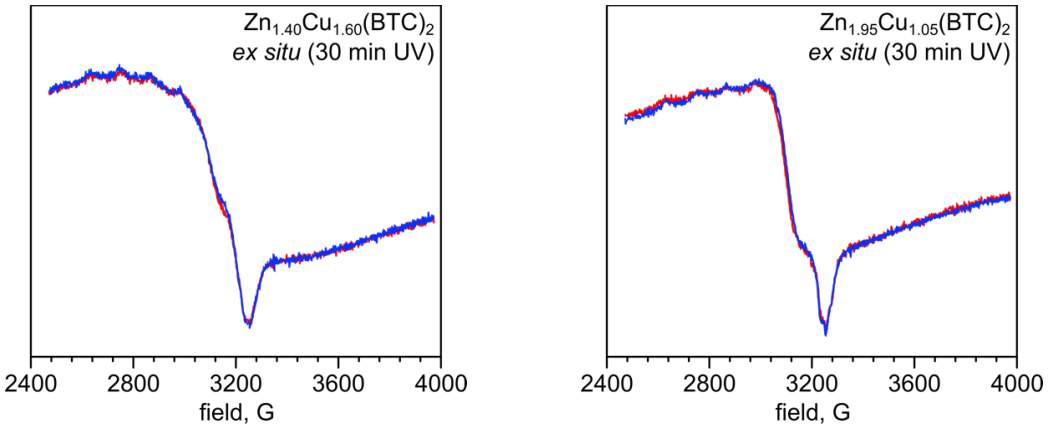

Figure 4.32. EPR spectra $Zn_{1.40}Cu_{1.60}(BTC)_2$ (*left*) and of $Zn_{1.95}Cu_{1.05}(BTC)_2$ (*right*) (control experiments) before (blue) and after (red) 30 minutes of *ex situ* irradiation (λ_{ex} = 365 nm). Measurement conditions: center of field = 3220 G, sweep width = 3220 G, sweep time = 60 seconds (5 scans averaged), and microwave power = 1.589 mW.

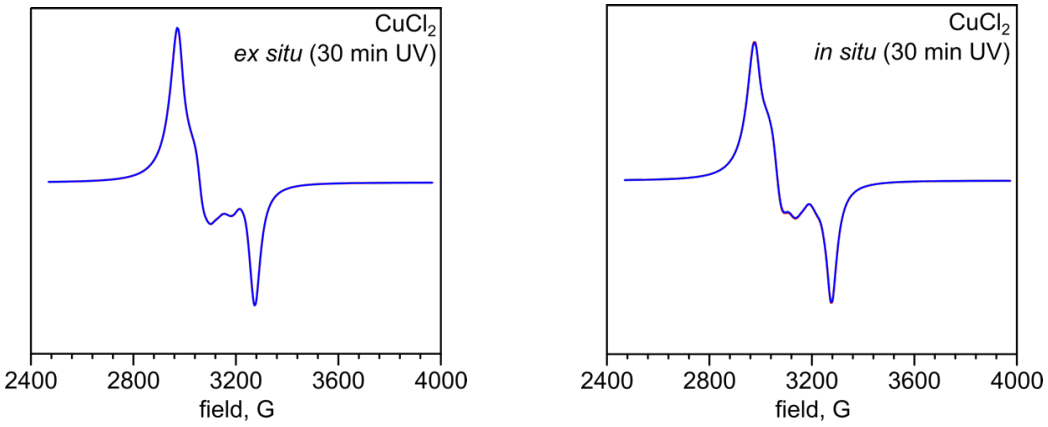

Figure 4.33. EPR spectra of $CuCl_2 \cdot 2H_2O$ (control experiments) before (blue) and after (red) 30 minutes of *ex situ* (*left*) and 30 minutes of *in situ* (*right*) irradiation (λ_{ex} = 365 nm). Measurement conditions: center of field = 3220 G, sweep width = 1500 G, sweep time = 64.5 seconds (2 scans averaged), and microwave power = 0.7962 mW.

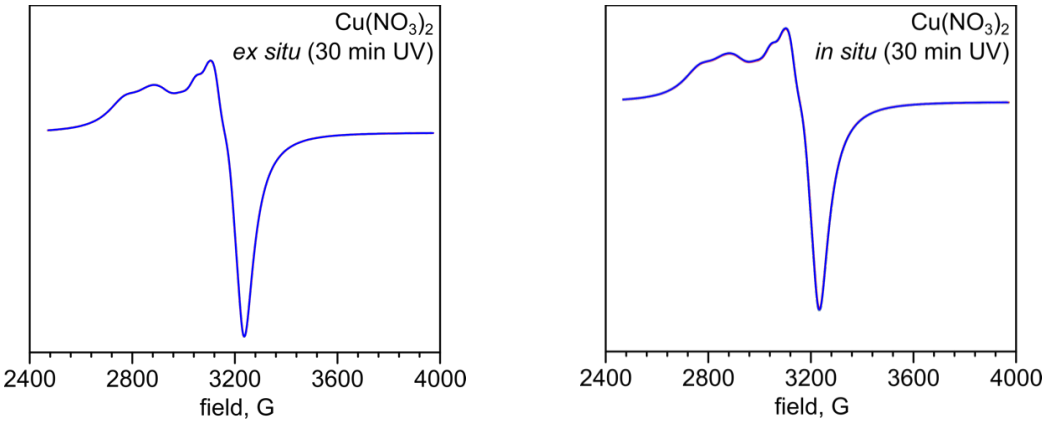

Figure 4.34. EPR spectra of $Cu(NO_3)_2 \cdot 2.5H_2O$ (control experiments) before (blue) and after (red) 30 minutes of *ex situ* (*left*) and 30 minutes of *in situ* (*right*) irradiation (λ_{ex} = 365 nm). Measurement conditions: center of field = 3230 G, sweep width = 1500 G, sweep time = 64.5 seconds (2 scans averaged), and microwave power = 0.6325 mW.

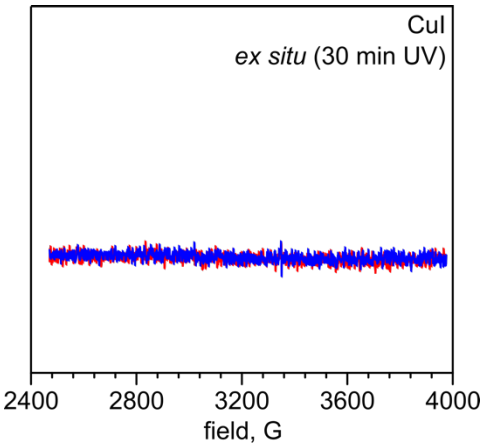

Figure 4.35. EPR spectra of CuI as a control experiment before (blue) and after (red) 30 minutes of *ex situ* irradiation (λ_{ex} = 365 nm). Measurement conditions: center of field = 3220 G, sweep width = 1500 G, sweep time = 60 seconds (10 scans averaged), and microwave power = 2.000 mW.

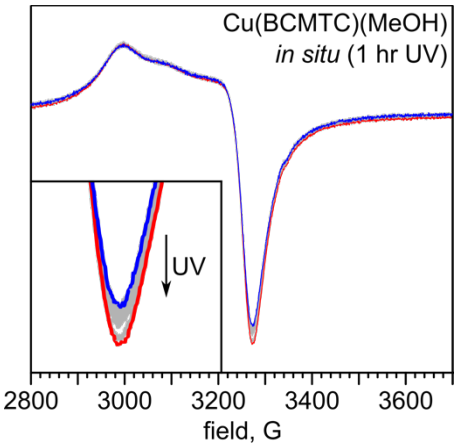

Figure 4.36. EPR spectra of Cu(BCMTC)(MeOH) before (blue) and after (red) one hour of *in situ* irradiation (λ_{ex} = 365 nm). The inset shows the expanded changes in the EPR signal. Measurement conditions: center of field = 3300 G, sweep width = 1000 G, sweep time = 60 seconds (2 scans averaged), and microwave power = 1.589 mW.

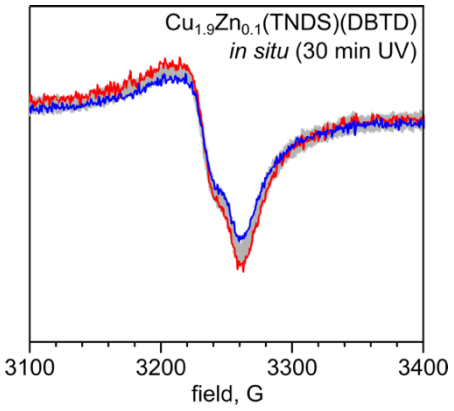

Figure 4.37. EPR spectra of $Cu_{1.9}Zn_{0.1}$(TNDS)(DBTD) before (blue) and after (red) 30 minutes of *in situ* irradiation (λ_{ex} = 365 nm). Measurement conditions: center of field = 3220 G, sweep width = 2000 G, sweep time = 30 seconds (2 scans averaged), and microwave power = 1.262 mW.

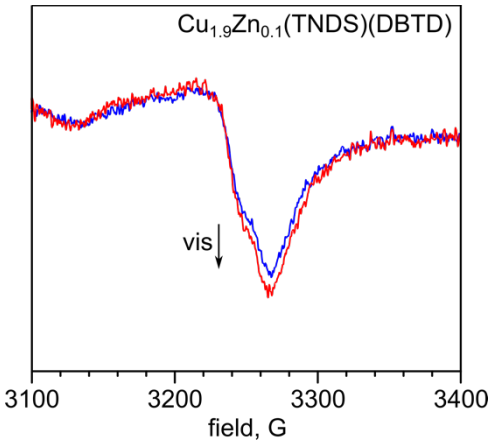

Figure 4.38. EPR spectra of $Cu_{1.9}Zn_{0.1}$(TNDS)(DBTD) after (blue) 30 minutes of 365 nm *in situ* irradiation, followed by (red) 30 minutes of 590 nm *in* situ irradiation. Measurement conditions: center of field = 3220 G, sweep width = 2000 G, sweep time = 30 seconds (2 scans averaged), and microwave power = 1.262 mW.

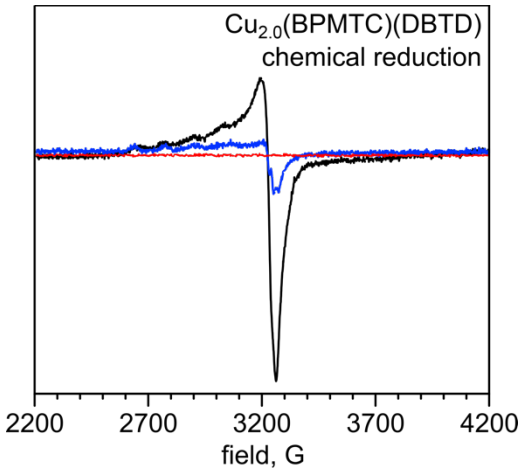

Figure 4.39. EPR spectra of $Cu_{2.0}$(BPMTC)(DBTD) before treatment (black), after treatment with 10 µL (1.0 M) hydrazine (blue), and after treatment with 10 µL (99%) hydrazine (red). Measurement conditions: center of field = 3220 G, sweep width = 2000 G, sweep time = 20 seconds (10 scans averaged), and microwave power = 1.262 mW.

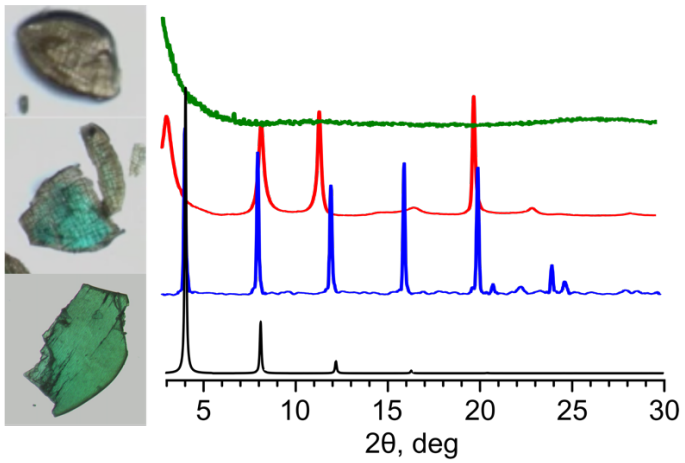

Figure 4.40. Crystals of as-synthesized $Cu_{2.0}$(BPMTC)(DBTD) (*bottom left*), after the addition of 10 µL (1.0 M) hydrazine monohydrate in tetrahydrofuran (*middle left*), and after the addition of 10 µL (99%) hydrazine monohydrate (*top left*). PXRD patterns of simulated $Zn_{2.0}$(BPMTC)(DBTD) (black),[134] as-synthesized $Cu_{2.0}$(BPMTC)(DBTD) (blue), $Cu_{2.0}$(BPMTC)(DBTD) after the addition of 10 µL (1.0 M) hydrazine monohydrate in tetrahydrofuran (red) and after the addition of 10 µL (99%) hydrazine monohydrate (green).

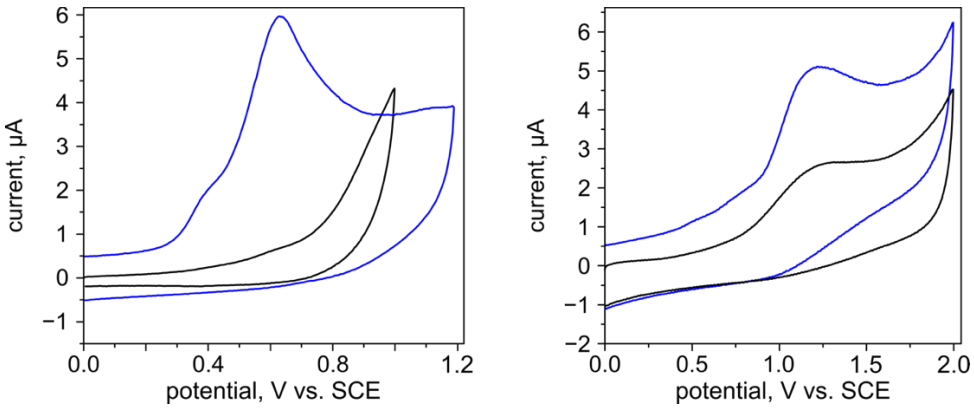

Figure 4.41. Cyclic voltammograms of (*left*) BPMTC in THF (5.0 mM) and (*right*) 5.0 mM TNDS in THF. All solutions contained 0.1 M tetrabutylammonium hexafluorophosphate. Measurements were performed in a glass solution reservoir equipped with SCE reference, platinum wire counter, and glassy carbon working electrodes. CV scans were collected at 100 mV s^{-1}. CV scans were initially collected of the samples in the dark (black), followed by exposure to 365 nm irradiation for five minutes and simultaneous voltammogram acquisition (blue).

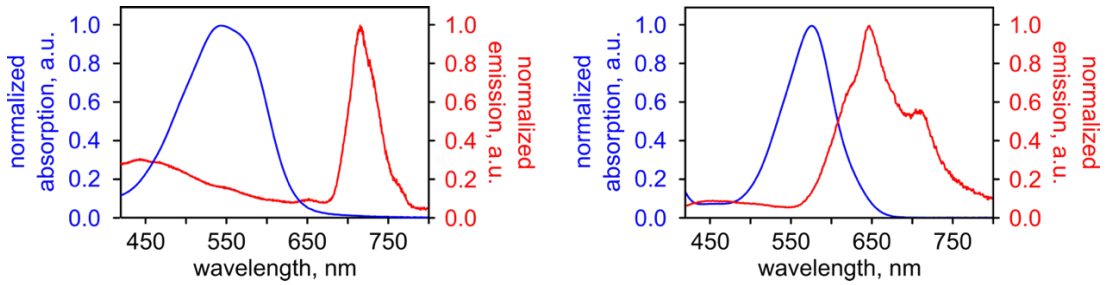

Figure 4.42. (*left*) The absorption spectrum (blue) of BPMTC (60 μM in DMF) and the emission spectrum (red) of $Cu_{2.0}$(BPMTC)(DBTD). (*right*) The absorption spectrum (blue) of TNDS (50 μM in DMF) and the emission spectrum (red) of $Cu_{1.9}Zn_{0.1}$(TNDS)(DBTD). The energy of the lowest vibrational transition, E_{0-0}, was determined to be 1.92 V for BPMTC and 2.04 V for TNDS.

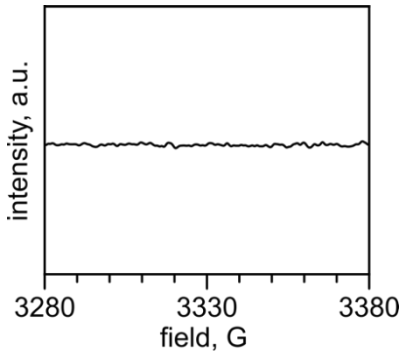

Figure 4.43. EPR spectrum of DMPO after five minutes of *ex situ* irradiation (λ_{ex} = 365 nm) in the absence of photochromic molecules. Measurement conditions: center of field = 3333 G, sweep width = 200 G, sweep time = 60 seconds (5 scans averaged), and microwave power = 1.589 mW.

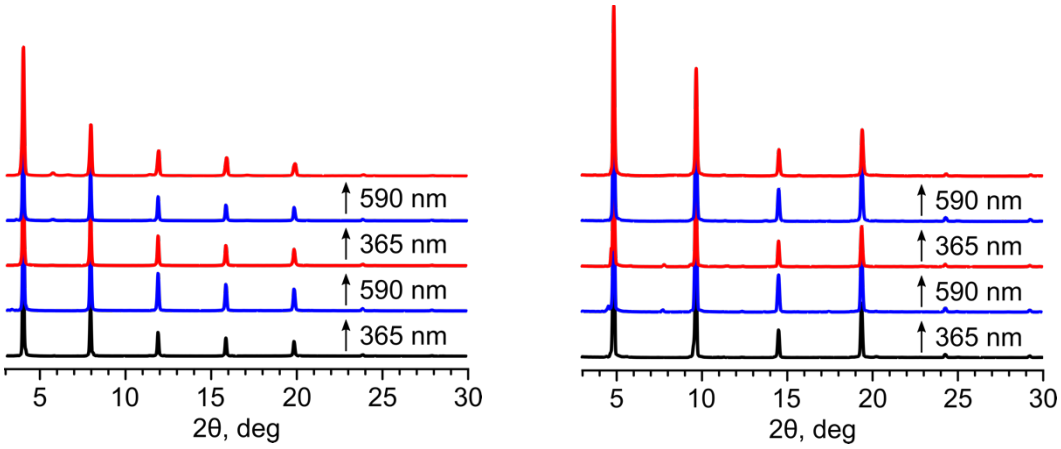

Figure 4.44. (*left*) PXRD patterns of as-synthesized $Cu_{2.0}$(BPMTC)(DBTD) (black) and after alternating 30-second cycles of UV (λ_{ex} = 365 nm; blue) and visible (λ_{ex} = 590 nm; red) irradiation. (*right*) PXRD patterns of as-synthesized $Cu_{1.9}Zn_{0.1}$(TNDS)(DBTD) (black) and after alternating 30-second cycles of UV (λ_{ex} = 365 nm; blue) and visible (λ_{ex} = 590 nm; red) irradiation.

Table 4.1. X-Ray structure refinement data for Cu(BCMTC)(MeOH).[a]

compound	**Cu(BCMTC)(MeOH)**
formula	$C_{36.77}H_{36}Cu_2O_{11.98}S_4$[b]
FW	924.82
T, K	100(2)
crystal system	monoclinic
space group	$P2_1/n$
Z	4
a, Å	15.4986(6)
b, Å	11.4389(4)
c, Å	24.6126(10
α, °	90
β, °	95.3132(14)

γ, °	90
V, Å^3	4344.7(3)
d_{calc} g/cm^3	1.414
μ, mm^{-1}	1.227
F(000)	1898.0
crystal size, mm^3	0.06 × 0.04 × 0.02
theta range	4.432 to 52.796
index ranges	−19 ≤ h ≤ 19 −14 ≤ k ≤ 14 −30 ≤ l ≤ 30
refl. collected	71075
data/restraints/parameters	8880/20/523
GOF on F^2	1.051
largest peak/hole e/Å^3	1.19/−0.81
R_1 (wR_2), %, [$I \geq 2$sigma(I)][c]	0.0649/0.1520

[a]Mo-Kα (λ = 0.71073 Å) radiation

[b]Formula is given based on single-crystal X-ray data and does not include disordered solvent molecules

[c]$R_1 = \Sigma||F_o| - |F_c||/ \Sigma |F_o|$, $wR_2 = \{\Sigma [w(F_o^2 - F_c^2)^2]/ \Sigma [w(F_o^2)^2]\}^{1/2}$

Table 4.2. X-ray structure refinement data for $Cu_{1.9}Zn_{0.1}$(TNDS)(DBTD) and $Cu_{1.2}Zn_{0.8}$(DPB-CHO)(DBTD).[a]

compound	**$Cu_{1.9}Zn_{0.1}$(TNDS)(DBTD)**	**$Cu_{1.2}Zn_{0.8}$(DPB-CHO)(DBTD)**
formula	$C_{50}H_{24}Br_2Cu_{1.9}N_2O_8Zn_{0.1}$[b]	$C_{51}H_{28}Br_2Cu_{1.2}Zn_{0.8}N_8O_9$[b]
FW	1316.07	1101.16
T, K	100(2)	100(2)
crystal system	orthorhombic	orthorhombic
space group	*Pmmm*	*Pmmm*
Z	1	1
a, Å	11.5411(13)	10.9157(12)
b, Å	15.5499(17)	15.9337(18)
c, Å	18.310(2)	18.246(2)
α, °	90	90
β, °	90	90
γ, °	90	90
V, Å^3	3286.0(6)	3175.3(6)
d_{calc} g/cm^3	0.504	0.599
μ, mm^{-1}	0.953	1.001
F(000)	530.0	531.0
crystal size, mm^3	0.42 × 0.12 × 0.08	0.4 × 0.34 × 0.1
theta range	4.926 to 55.298	4.348 to 50.322
index ranges	$-15 \le h \le 15$	$-13 \le h \le 12$

	$-20 \leq k \leq 20$ $-23 \leq l \leq 23$	$-18 \leq k \leq 19$ $-21 \leq l \leq 20$
refl. collected	183650	32759
data/restraints/parameters	4254/82/103	3201/82/103
GOF on F^2	1.066	1.077
largest peak/hole e/Å^3	0.49/−0.92	1.13/−0.93
R_1 (wR_2), %, [$I \geq 2$sigma(I)][c]	0.0389/0.1197	0.0690/0.2136

[a]Mo-Kα (λ = 0.71073 Å) radiation

[b]Formula is given based on single-crystal X-ray data and does not include disordered solvent molecules

[c]$R_1 = \Sigma||F_o| - |F_c||/ \Sigma |F_o|$, $wR_2 = \{\Sigma [w(F_o^2 - F_c^2)^2]/ \Sigma [w(F_o^2)^2]\}^{1/2}$

CHAPTER 5

BEYOND STRUCTURAL MOTIFS: THE FRONTIER OF ACTINIDE-CONTAINING METAL-ORGANIC FRAMEWORKS

Martin, C. R.; Leith, G. A.; Shustova, N. B. *Chem. Sci.* **2021**, *12*, 7214–7230.

Chapter abstract. In this chapter, we feature recent advances in the field of actinide-containing metal-organic frameworks (An-MOFs) with a main focus on their electronic, catalytic, photophysical, and sorption properties. This discussion deviates from a strictly crystallographic analysis of An-MOFs, reported in several reviews, or synthesis of novel structural motifs, and instead delves into the remarkable potential of An-MOFs for evolving the nuclear waste administration sector. Currently, the An-MOF field is dominated by thorium- and uranium-containing structures, with only one or two reports on transuranic frameworks. However, some of the reported properties in the field of An-MOFs foreshadow potential implementation of these materials and are the main focus of this report. Thus, this chapter intends to provide a glimpse into the challenges, triumphs, and future directions of An-MOFs in sectors ranging from the traditional realm of gas sorption and separation to recently emerging areas such as electronics and photophysics.

INTRODUCTION

The fundamental understanding of properties of actinide (An)-containing materials[1,2] is paramount for nuclear waste storage, separation, and efficient reprocessing, especially taking into account the abundance of nuclear weapons decommissioning programs and associated challenges with nuclear energy utilization and production.[3,4] As a response to the ever-increasing stockpiles of radionuclide waste, the interest in An-containing systems for gaining fundamental understanding and improving waste repurposing programs has only grown over time.[5–24] In this direction, studies of the physicochemical properties of An-based materials are necessary first steps to build a foundation for beginning to address the current challenges in waste reprocessing by revealing potential applications that have not yet been realized (Scheme 5.1).

High-temperature solid-state reactions have been predominantly used as an experimental approach for preparation of actinide- or transuranic-based materials for systematic studies of material properties.[16,25–29] However, metal-organic frameworks (MOFs) have recently emerged as materials of interest to advance actinide chemistry due to MOF's diverse structural topologies, porosity, and modularity.[30–34] As expected, the first steps in a relatively novel field of An-MOFs started with the development of synthetic approaches for framework preparation and establishment of methods for their structural characterization. The inclusion of actinides in MOFs can promote unique properties in comparison with those of well-studied transition metal-based MOFs. For actinides, in general, relativistic effects are substantially more prominent in comparison with transition metals or lanthanides, that can lead to profound spin-orbit coupling.[35–37]

The photophysical properties of An-based materials can be affected by relativistic effects of actinides through mixing of excited and ground states or the relativistic *f*–*f* transitions in crystal fields.[38–41] In many cases, theoretical calculations are used to rationalize the structural preferences of the 5*f*-orbitals in An-based complexes (e.g., $[ThH_6]^{2-}$) relative to the *d*-orbitals of transition metal-based compounds (e.g., $[HfH_6]^{2-}$).[42] For instance, it was determined that the nature of the *ungerade f*-orbitals found in actinide-containing motifs opens an avenue for structure-bonding that is typically not possible with only *gerade d*-orbitals found in transition metal systems.[42]

Another area of interest is the exceptional stability of actinide-based materials in the presence of ionizing radiation (i.e., high attenuation efficiencies).[43] For example, uranyl-coordination cages, $Li_{12}K_{48}[\{(UO_2)(O_2)\}_{60}(C_2O_4)_{30}]\cdot nH_2O$ and $Li_{24}Na_{24}[(UO_2)_{24}(O_2)_{24}(P_2O_7)_{12}]\cdot 120H_2O$, exhibited stability to both γ- and simulated α-

irradiation.[43] In contrast to purely-inorganic compounds that could possess long-term stability to ionizing radiation, it is important to investigate the advantages offered by hybrid systems such as An-MOFs, that could be used for short-term manipulation with radionuclides.[44–46]

Since MOFs can be considered as "bulky linkers" for stabilization of elusive oxidation states as it was shown on the example of transition metal-based MOFs,[47–49] it is also important to pursue this direction for actinide-containing frameworks. For example, the coordination of actinides in molecular complexes can lead to the stabilization of less-common oxidation states (e.g., Th^{2+}, U^{2+}, and Pu^{2+}).[50–52] Therefore, it is plausible to expect that a framework could allow for isolation of elusive oxidation states that enriches actinide chemistry. Furthermore, high coordination numbers (>14) observed in several examples of An-based organometallic complexes (e.g., $U(BH_4)_4$ and $[Th(H_3BNMe_2BH_3)_4]$)[53–57] could also be achieved through integration of actinides in a MOF. Currently, high coordination numbers (>10) for actinides have already been observed in An-MOFs, suggesting that there is more to be discovered upon further detailed investigations.[53–57]

To summarize, in comparison with the well-explored M-MOF field (M = a transition metal), the instantaneous development of An-MOFs and understanding of their properties (that is the main focus of this chapter, Scheme 5.1) is mainly impeded by careful implementation of safety protocols. Primarily due to this fact, the first transuranic MOFs have only recently been synthesized.[3,58–60] In general, analysis of reported An-MOF structures has demonstrated that connectivity of the secondary building units (metal nodes) could replicate structural motifs typically observed in natural minerals.[38] At the same time, the An-MOF lattice could support a metal coordination environment that is primarily

observed in organometallic complexes.[61–67] For example, the $[U_6O_8]^{8+}$ structural motif found in MOF metal nodes replicates the structure typically observed in actinide-based molecular complexes.[68–75] Similarly, the natural mineral, adolfpateraite, and the $UO_2(OH)(PYCA)$ (HPYCA = pyrazine-2-carboxylic acid) framework both contain similar vertex-sharing pentagonal bipyramidal uranyl metal nodes.[76,77] From this point of view, An-frameworks can be considered a versatile "bridge" between solution and solid-state actinide chemistry.[61] However, actinides integrated within the MOF lattice can also exhibit significantly different behavior in comparison with discrete metal complexes, as demonstrated on the example of cationic exchange reactions.[78] Furthermore, porosity and modularity of MOFs have showcased novel actinide integration methods that are unavailable in other solid-state systems. For instance, a radionuclide can be integrated as a part of a metal node or an organic linker (e.g., capping linkers; Figure 5.1) through several approaches such as transmetallation, chelation, or metal-node extension.[78] Due to an almost unlimited possibility of combinations of metals and organic linkers, a wide range of structural motifs can be achieved (Figure 5.2). Remarkably, some crystalline structures possess exceptionally large unit cell parameters, similar to natural proteins.[79–82] Another unique phenomenon, such as solvent-dependent structural dynamism, was recently reported for Th-MOFs in which the presence of dynamic structural behavior strongly correlated with the coordination number of organic linkers per thorium metal node and was not exhibited by non-radioactive isostructural Zr-containing analogs.[83]

The presented chapter will deviate from outlining exclusively structural aspects, and instead will focus on the remarkable potential of An-MOFs as innovative materials with an emphasis on their physicochemical properties. In particular, we focus on electronic

and photophysical properties of An-frameworks as well as their applications in heterogeneous catalysis and separation (Scheme 5.1).

ELECTRONIC PROPERTIES OF AN-MOFS

The first section of this chapter on the electronic properties of An-MOFs. Although only a few reports highlight the electronic properties of porous An-based hybrid materials, it has been demonstrated that the role of actinides can make a profound impact on the electronic structures of purely inorganic materials.[84–87] Specifically, unique electronic properties in actinide-containing materials (as opposed to transition metals) arise from relativistic effects resulting in: (1) mixing of electronic ground and excited states and (2) strong spin-orbit coupling.[35]

As previously demonstrated, the electronic properties of MOFs could be controlled "statically" (i.e., through structure modification with metals, linkers, or guests) or "dynamically" (i.e., through application of an external stimulus such as light).[78,83,88,89] The same approaches can be applied towards tailoring the electronic profiles of An-MOFs. Indeed, integration of a thorium cation inside uranium-containing MOFs through cationic exchange can significantly affect the framework's electronic behavior (Figure 5.1).[78,83,88] On the example of heterometallic U/Th-MOFs, it was shown that the band gap, estimated from a Tauc plot analysis, decreased from 3.3 eV ($Th_6O_4(OH)_8(Me_2BPDC)_4$; H_2Me_2BPDC = 2,2′-dimethylbiphenyl-4,4′-dicarboxylic acid) to 2.5 eV ($U_{1.23}Th_{4.77}O_4(OH)_8(Me_2BPDC)_4$).[83] The theoretical calculations supported the observed experimental data revealing that uranium integration resulted in changes in the density of states (DOS) near the Fermi edge (E_F). The orbital-projected DOS suggested that orbitals near E_F originated mainly from the uranium 5*f*- orbitals. Modularity of the frameworks

allowed for further tailoring of the Th/U-MOF electronic properties through integration of a transition metal, cobalt, using the metal node extension approach (Figure 5.1).[83] Integration of cobalt led to a further decrease of the band gap to 1.9 eV that was also reflected in changes in the calculated DOS of the Th/U/Co-MOF that were primarily dominated by the cobalt 3*d*-orbitals and oxygen 2*p*-orbitals.[83] The observed changes in the electronic structures were in-line with conductivity measurements that revealed a three-orders-of-magnitude enhancement from 7.0×10^{-10} S cm^{-1} (Th/U-MOF) to 1.4×10^{-7} S cm^{-1} (Th/U/Co-MOF).[78] Thus, these examples demonstrated that integration of actinides or transition metals can significantly affect the electronic profiles of actinide-containing materials. However, to build a correlation between electronic properties and metal node nuclearity, similar to that reported for transition metal-based MOFs,[90] large samples of data with application of a systematic approach is necessary.

In addition to metal integration, changes in electronic properties of An-frameworks could be made through incorporation of redox-active guests such as 7,7,8,8-tetracyanoquinodimethane (TCNQ) or I_2.[88] For instance, a 50-fold conductivity enhancement was detected for the iodine-doped Th-MOF, I_2@Th-MOF, in comparison with the parent Th-framework.[88]

A next step in tailoring of An-MOF properties is utilizing "dynamic" control through application of an external stimuli (Figure 5.3).[89,91–96] To engineer these An-materials, stimuli-responsive components were integrated inside a framework matrix. This approach has been successfully employed on the examples of monometallic Th-MOFs and heterometallic Th/U-MOFs containing spiropyran-based photochromic units (Figure 5.3).[88] Spiropyran derivatives are known to exhibit fast and reversible photoisomerization

upon alternation of an excitation wavelength in solution.[94] Upon integration into porous An-MOFs, for instance, as a capping linker (Figure 5.1), they preserve their photochromic behavior, and as a result, could significantly affect properties of the framework.[95,96] Indeed, integration of $TNDA^{2-}$ (H_2TNDA = 4,4'-(1',3',3'-trimethyl-6-nitrospiro[chromene-2,2'-indoline]-4',7'-diyl)dibenzoic acid) inside Th- or Th/U-MOFs resulted in significant changes in the DOS of the framework, as demonstrated by theoretical calculations.[88] Indeed, the DOS near E_F of non-photoresponsive monometallic and heterometallic Th- or Th/U-MOFs mainly originated from the 5*f* orbitals of the metals while upon photochromic unit integration, the frontier orbitals were localized on the photochromic linker.[88] Experimental detection of electronic property modulation upon alternating irradiation with UV and visible light was monitored by changes in conductivity. In addition to optical cycling, alternation of current was observed as shown in Figure 5.3.

As an alternative avenue for tailoring electronic properties of An-MOFs, one can rely on a combination of the aforementioned "static" and "dynamic" approaches.[83,88] For instance, redox-active guest molecules such as TCNQ and I_2 could be integrated inside photochromic An-MOFs.[88] Indeed, modulation of electronic properties upon excitation wavelength alternation was achieved in photochromic Th- and Th/U-MOFs containing TCNQ and I_2 guests, respectively.

As an expansion on actinide-based frameworks with a focus on electronic properties, proton conductivity was measured on the example of a uranyl-containing MOF, $K_2(UO_2)(\mu_3\text{-}O)(BPDSDC)_{0.5}(H_2O)_2$ ($K_2H_2BPDSDC$ = biphenyl-3,3′-disulfonyl-4,4′-dicarboxylic acid dipotassium salt), that exhibited high proton conductivity values due to the decoration of the pores with hydrophilic sulfonate groups (Figure 5.4).[97] The highest

conductivity value obtained for $K_2(UO_2)(\mu_3\text{-}O)(BPDSDC)_{0.5}(H_2O)_2$ was 1.07×10^{-3} S cm^{-1} at 85 °C (enhanced from 1.27×10^{-5} S cm^{-1} at 45 °C). The origin of such behavior was attributed to vehicle-like proton transfer: presence of the sulfonate groups can affect the dynamics of the absorbed water molecules that act as carriers for H^+.[98–101]

As clearly shown based on the reports highlighted in this chapter, studies of An-MOF electronic properties are in their infancy. In contrast to MOFs made of transition metals, where major breakthroughs have already been reported,[102–109] An-MOFs require significant attention from the scientific community. Complimentary to a plethora of crystallographic investigations,[61] computational methods can serve as a reliable and powerful screening tool for the selection of the object of interest, especially taking into account safety protocols required for comprehensive studies of An-MOFs. Currently, theoretical investigations on the electronic properties of An-MOFs are limited to very few reports;[110–112] however, they already provided several pathways for future investigations that can be crucial for expanding the studies on transuranic MOFs.

AN-MOFS FOR SORPTION AND SEPARATION

MOFs are renowned for their sorption and separation capabilities ranging from the removal of harmful biotoxins, long-term storage of energy-relevant gases, charged and neutral organic species separation, and radionuclide sequestration.[113–124] Over the last several decades, trends for designing efficient absorbents based on transition metal-containing MOFs have been preliminarily identified and are still being developed (e.g., high framework flexibility for inert gas capture and separation).[125–131] Large An cations available for MOF synthesis could potentially bring a new flavor to the landscape of MOF-based absorbents and membranes (Figure 5.5). For example, adsorption of carbon dioxide

in NU-1302 (NU = Northwestern University) resulted in a phase transition.[132] This section will present An-MOFs that have been employed to separate ions (e.g., perrhenate, dichromate, perfluorooctane sulfonate (PFOS), and cesium),[65,133–135] molecular species (e.g., iodine and organic dyes),[136–138] and gases (e.g., carbon dioxide, hydrogen, methane, ethylene, and xenon),[132,139–141] taking into account the possibility of radiation-induced damage in MOFs.[137,142–147]

The interest in MOF-based sorption materials arises from their highly porous nature and the ability to alter a MOFs pore environment through linker functionalization and framework topology.[148–154] Through strategic design of a MOFs metal node and organic linker, metal cations can be exchanged via an ion metathesis reaction.[155–158] For instance, Shi and coworkers prepared a bipyridinium-based U-containing MOF that was applied for selective removal of perrhenate anions, ReO_4^- (as a non-radioactive surrogate for TcO_4^-).[133] Using $[(UO_2)(BCBP)(OH)(H_2O)]\cdot Cl$ ($[H_2BCBP]Cl_2$ = 1,1'-bis(4-carboxyphenyl)-4,4'-bipyridnium bis(chloride)), the authors were able to achieve a high degree of ReO_4^- sequestration at acidic conditions (86.2% from a 10 mg L^{-1} solution, pH = 4.0). A decrease in pH to 2.0 still resulted in substantial removal of perrhenate anions (63%), foreshadowing practical utilization of the prepared framework for TcO_4^- removal from highly acidic radioactive waste mixtures.[135,164–167]

The first cationic thorium-based framework was recently surveyed for its ability to trap several different types of ions (e.g., polyoxoanions and persistent organic pollutants).[134] The $[Th_3(BPTC)_3O(H_2O)_{3.78}]Cl\cdot(C_5H_{14}N_3Cl)\cdot 8H_2O$ (H_3BPTC = [1,1'-biphenyl]-3,4',5-tricarboxylic acid) framework was prepared via ionothermal synthesis (synthesis in an ionic liquid medium) in tetramethylguanidine chloride at 140 °C.[134] The

cationic nature and hydrolytic stability of the Th-based MOF enabled the authors to test its anion-exchange capabilities for perrhenate, dichromate, methyl blue, and PFOS (a persistent organic pollutant). Employment of the Th-MOF resulted in efficient and rapid removal of all of the aforementioned anions. For instance, 80% of ReO_4^- anions and 96% of PFOS were extracted from solution using the Th-MOF in 2 minutes. The authors attributed such high sorption capacity to the cationic nature of the $[Th_3(COO)_9O(H_2O)_3]^+$ metal nodes.[134]

Hierarchical tunability of MOF structures allowed Wang and coworkers to develop a Th-MOF containing a very high void space (76%) and a large surface area (3396.5 m^2 g^{-1}) for radioactive iodine (I^{129} and I^{131}) sequestration[138] as a highly volatile, radiotoxic substance that is detrimental to the human metabolic processes.[168,169] One focus of their report also includes the use of modulating acids[170] for efficient control of the MOF growth. The mass uptake of I_2 (gas-phase studies) in the prepared $Th_6(O)_4(OH)_4(H_2O)_6(SBDC)_6$ (H_2SBDC = 4,4'-stilbenedicarboxylic acid) was found to be 1.5 I_2 molecules per Th atom, that is comparable with other MOF-based systems (e.g., 5.4 I_2 molecules per cage in Cu_3BTC_2 (H_3BTC = 1,3,5-benzenetricarboxylic acid)).[171,172] Notably, solution-based sorption studies of iodine in cyclohexane (200 mg L^{-1}) revealed that nearly quantitative iodine removal, using the Th-framework, could be achieved.[138]

As mentioned above, due to high surface areas and the presence of unsaturated metal sites, gas-based sorption and separation are widely studied in MOFs consisting of transition metals.[173–184] Similar studies have also been probed on An-containing frameworks (Figure 5.5). By utilizing the pore space of An-MOFs, selective separation of C_2H_4 from a mixture of C_2H_4, C_2H_2, and C_2H_6 was achieved using a Th-based MOF,

$Th_6O_4(OH)_4(H_2O)_6(TBA)_6$ (HTBA = 4-(1*H*-tetrazol-5-yl) benzoic acid).[139] This Th-based MOF showed a high adsorption capacity for C_2H_6 (>100.2 $cm^3\ g^{-1}$ at room temperature and 100 kPa), that surpassed the values reported for several other leading transition metal-based porous adsorbents such as $Fe_2(O_2)$(DOBDC) (H_2DOBDC = 2,5-dioxido-1,4-benzenedicarboxylic acid), Zn(BATZ) (H_2BATZ = bis(5-amino-1*H*-1,2,4-triazol-3-yl)methane), ZIF-7 (ZIF = zeolitic imidazolate framework), ZIF-8, PCN-245 (PCN = porous coordination network), MIL-142A (MIL = Materials Institute Lavoisier), $Cu(Qc)_2$ (HQc = quinoline-5-carboxylic acid), or $Zn_2(ATZ)_2(IPA)$ (HATZ = 3-amino-1,2,4-triazole; H_2IPA = isophthalic acid).[185–192] Compared to C_2H_6, the Th-based MOF had a lower adsorption capacity for C_2H_4 (81.1 $cm^3\ g^{-1}$ at room temperature and 100 kPa) as well as a high adsorption heat enthalpy (25.4 kJ mol^{-1} for C_2H_6) compared to C_2H_2 (26.1 kJ mol^{-1}), that could promote studies for selective C_2H_4 separation from ternary $C_2H_6/C_2H_4/C_2H_2$ mixtures. Along these lines, the authors were also able to purify C_2H_4 (>99.9%) using the Th-based MOF. The proposed mechanism of such behavior in the framework relied on strong van der Waals interactions between C_2H_6 and the MOF skeleton according to DFT calculations.[139]

An important aspect of An-MOFs, that is crucial for a number of the aforementioned applications but especially pertaining to storage/separations, is the stability of frameworks in the presence of ionizing radiation.[137,142–146] Farha and coworkers recently studied radiation-induced damage on the example of two Zr-based MOFs as well as factors that could potentially affect the radiolytic stability such as ligand aromaticity and connectivity, metal node density and connectivity, as well as interligand distance.[146] The authors proposed that differences in the MOF's radiolytic stability could be applied for

specific radiological applications (e.g., long-term storage versus scintillation sensors). Similarly, Loiseau and coworkers studied the resistance of several MOFs to γ-irradiation.[143] In their study, γ-irradiation (up to 175 Mrad) was applied towards frameworks, followed by extensive characterization using powder X-ray diffraction (PXRD), gas sorption analysis, and nuclear magnetic resonance and Fourier-transform infrared spectroscopies. Comprehensive analysis confirmed structural stability after significant γ dosages. In a similar vein, Shustova and coworkers studied γ-irradiation of a Zr-based MOF, $Zr_6O_4(OH)_8(Me_2BPDC)_4$, for a total dose of 19.7 Mrad (209 hours at a dose rate of 94.3 krad/hour), and the MOF still maintained its structural integrity according to crystallographic data.[147]

As clearly demonstrated, these reports have only grazed the surface of storage/separations that could be performed on An-MOFs. More in-depth studies are necessary to highlight the unique role of actinides in sorption processes in which unusual coordination numbers and environments of actinides integrated into a framework lattice could play a significant role (substantially different from ones observed for transition metals).[53–57] High removal capacities of radioactive species in aqueous media using An-frameworks may compete or even surpass other transition metal- or lanthanide-based materials. However, material radioactivity should be taken into account for employment of these materials beyond fundamental studies. For instance, employment of An-MOFs as sorbents for efficient gas separation could be limited due to the required safety protocols. At the same time, the use of radioactive MOFs for targeted sequestration of radioactive species could be a prospective direction for future studies.

PHOTOPHYSICS OF AN-MOFS

A variety of photophysical studies, which describe Stokes shifts, quantum yields (QYs), lifetimes, effects of external stimuli, and local environment, have been reported for a number of MOF-based systems and is primarily driven by their implementation in programmable sensors, X-ray scintillators, solar cells, photocatalysts, or light-harvesting systems.[89,193–202] A main focus in these studies has been on either specific chromophores (e.g., porphyrin- or boron dipyrromethene-(BODIPY) based linkers)[203–209] integrated inside a MOF matrix or antenna chromophores coupled to lanthanide-containing metal nodes.[210–214] The ability of actinides to support high coordination numbers and a large range of oxidation states (that are different from the properties of transition metals or lanthanides),[12,61,63,215] could result in unique pathways for tailoring photophysical properties. This section of the chapter will highlight the current progress of photophysical studies on An-MOFs, emphasizing the distinct benefits of MOFs with integrated actinides and pose future possible pathways for material development.

One particular facet of MOF-based photophysics, in which actinide-based MOFs have the capability to stand above the large pool of photoluminescent frameworks, is X-ray scintillation.[199–201] Coupling the porosity, modularity, and luminescent properties of MOFs facilitates their ability to be applied as highly efficient X-ray sensors, as discussed in several reviews.[193,202] For preparing X-ray scintillating materials, in general, a crystalline matrix is typically doped with guest ions that endow the material with luminescent properties to achieve X-ray-to-visible-light conversion.[216–219] Uranium can be considered as a desirable choice for preparation of MOF-based X-ray scintillating materials due to its high atomic number (correlating to a high X-ray attenuation efficiency) in comparison with

other natural heavy element currently used in X-ray scintillators (e.g., lead, tungsten, or thallium).[220] In general, the green emission of uranyl species has been well-documented as a vibrationally-coupled charge-transfer mechanism and has been observed in many systems.[221–223] Owing to these considerations, Wang and coworkers studied X-ray scintillation properties of a uranyl-based MOF as the first MOF-based scintillator with actinide-centered emission.[224] In their report, $UO_2(HBTA)(H_2O)$ (H_3BTA = 1,3,5-benzenetricarboxylic acid) was shown to exhibit an X-ray excited luminescence (XEL) spectrum nearly identical to that of the UV-excited emission spectrum (Figure 5.6). The QY of $UO_2(HBTA)(H_2O)$ was determined to be 58%, that was the highest value among other reported uranyl-containing hybrid materials at that time,[61,65,78,160,161,225–227] including uranyl nitrate (QY = 36%). The observed high QY was attributed to the rigid and dense structure of the U-MOF that restricts non-radiative decay pathways. Moreover, the prepared frameworks demonstrated stability against radiation damage (up to 20 Mrad of radiation; ^{60}Co γ source). The attenuation efficiency of $UO_2(HBTA)(H_2O)$ was notably greater than that of the commercial thallium-doped cesium iodide (CsI:Tl) scintillator, above a photon energy of 20 keV (Figure 5.6). The MOF-based material also maintained a substantially lower structural density (2.88 g cm^{-3} for $UO_2(HBTA)(H_2O)$ and 4.51 g cm^{-3} for CsI:Tl), implying that there is room for improvement as a higher concentration of uranyl units within the lattice may further increase X-ray attenuation efficiency. Thus, given the large attenuation efficiency, high QY, radiation-damage resistance, and lower structural density, these studies highlight the "yet-to-be-revealed" potential for An-MOF-based scintillators that could facilitate changes in the current technological sector.

In a similar vein, Wang and coworkers highlighted the use of a uranyl-based MOF, $(TMA)_2[(UO_2)_4(ox)_4suc]$ (TMA^+ = tetramethylammonium cation; ox = oxalate; and H_2suc = succinic acid) as efficient X-ray and γ-irradiation detectors.[227] As a starting point for their studies, they noticed that UV-irradiation of the U-MOF caused emission attenuation, i.e., decreased the emission response over time. Indeed, after only 20 minutes of material irradiation at 365 nm, the emission intensity decreased by 50%, and it was completely quenched after five hours of 365-nm exposure. For emission restoration, the irradiated U-MOF underwent heating at 200 °C for 12 hours. Photoluminescence intensity cycling could also be achieved through alternation of 6 krad γ-irradiation followed by heating. Moreover, exposure of the MOF to only 12 rad of γ-irradiation resulted in a nearly 20% decrease in emission that was four-fold more sensitive than a previously reported solvent-assisted photoluminescence quenching dosimeter.[228–230] Furthermore, exposing the MOF to 10 rad of X-ray led to a 12% decrease in emission intensity.[227]

As mentioned in the first section of this chapter, modulation in photophysical properties of An-MOFs could result in tailoring their electronic properties. To probe this phenomenon, the Shustova research group studied the photochromic properties of An-MOFs with embedded photoresponsive moieties.[88] In particular, one of the focuses of their studies was testing the suitability of different scaffolds to achieve efficient photoisomerization of integrated photochromic diarylethene- and spiropyran units.[96] The latter exhibited limited photoisomerization in the solid state due to constraints imposed by necessary structural rearrangements associated with isomerization processes.[89] However, integration of the abovementioned photoresponsive units inside a porous scaffold resulted in restoration of their photochromic behavior.[96] The monometallic Th- and heterometallic

Th/U-based MOFs were chosen as the platform for tuning of photophysical properties as a function of an excitation wavelength.[88] In particular, diffuse reflectance (DR) measurements showed modulation of absorption profiles upon alternation of UV- and visible light irradiation. Optical cycling showcased the reversibility of photoisomerization processes (Figure 5.3). Studies of photoisomerization kinetics allowed for estimation of the attenuation rate of a Th-based spiropyran-containing MOF (3.9×10^{-1} s^{-1}), that is similar to that of a Zr analog (1.5×10^{-1} s^{-1}), and is in line with a previously reported value for a Zn-based spiropyran-containing frameworks (1.6×10^{-1} s^{-1}).[96]

Luminescent MOFs have been readily employed for the creation of sensors and light-emitting diodes;[231–236] however, only recently have they resulted in the preparation of a self-induced radioluminescent system[237] on the example of a Th-MOF, $Th(NDC)_2$ (H_2NDC = 2,6-naphthalenedicarboxylic acid). The $Th(NDC)_2$ framework contains scintillating naphthalene-based struts that are capable of radiation-induced autoluminescence.[237] In the prepared framework, autoluminescence arose from the interactions of the radioemitted ionizing alpha emission from Th^{4+} and the scintillating moiety, NDC^{2-} (Figure 5.7). Despite alpha emission, the framework retained crystallinity, even after one year. This noteworthy development emphasizes that harnessing the inherent properties of actinides (e.g., radioactivity) could lead to unconventional avenues for the development of futuristic materials.[231–236]

Another possible pathway for gaining information of An-MOF photophysics, that is worth mentioning in this chapter, is obtaining knowledge from similar actinide-based discrete systems such as metal-coordination cages (MCCs) and then applying that information to extended structures such as MOFs. For example, photoreactivity of UO_2^{2+}

was explored on the example of a MCC.[238] An initial uranyl-based cage (tripodal), formed upon reaction of *cis*-calix[4]pyrrole dibenzoic acid with uranyl nitrate and pyridine, underwent conversion to a tetrapodal cage through uranyl-assisted activation of molecular oxygen in the presence of light.[238] Photoreactivity of UO_2^{2+}-based metal nodes coordinated to benzoate groups could be a transformative concept for replication in MOFs possessing similar architectures. In fact, there are a number MOFs with uranyl-containing metal nodes[61,67] and an in-depth photophysical analysis could assist in unveiling their potential.

To summarize, MOF-based photophysics has been reviewed on several occasions,[193–198,239] yet still only a small fraction of reports have focused on the photophysics of An-MOFs beyond recording solely the framework emission spectra. Given the remarkable properties of actinides (e.g., high atomic numbers, high X-ray attenuation, and unique metal coordination environments), photoluminescent An-based MOFs undoubtedly have the capability to cultivate the technological sector. Moreover, fostering a diverse array of investigations is necessary to gain a more comprehensive overview of the An-MOF capabilities.

HETEROGENOUS AN-MOF CATALYSIS

Heterogenous catalysis is one of the most widely studied directions for MOFs, as outlined by over a dozen reviews within the last several years.[203–220] The excitement surrounding MOF-based catalysis comes from the intrinsic properties of the frameworks such as the high density of evenly-distributed catalytic active sites, the inherent porous nature, as well as the ability for facile separation of catalyst from products, e.g., *in-situ* enantiomeric separations.[240–257] Despite the aforementioned advantages[258] and the potential for small molecule activation using actinide organometallic compounds,[259–272] reports on

An-MOF-based catalysis are very limited. For example, there are very few types of reactions (e.g., cycloaddition, dehydrogenation, and photocatalytic oxidation)[57,273–276] that have been probed so far on An-MOFs as heterogeneous catalysts. As a result, there are even fewer reports focused on mechanistic studies of catalytic transformations occurring in An-based MOFs. This section of the chapter features current An-MOF-based catalysts as well as speculates on the forthcoming discoveries in this promising direction.

In an approach employed by the Farha group, a Th-based MOF, Th-NU-1008 (Figure 5.8), was applied as a Lewis acid catalyst, and catalytic activity was examined in comparison with isostructural hexanuclear frameworks containing transition metals, Zr and Hf, and a lanthanide, Ce.[273] The CO_2 cyclization into styrene oxide was selected as a model reaction. A 65% conversion of styrene oxide to styrene carbonate after 72 hours was achieved by utilization of Th-NU-1008, while it was surpassed by the Ce-based analog (nearly full conversion in 20 hours). To rationalize the observed catalytic activity (Ce > Zr > Hf > Th for 20 hour reactions), the authors estimated the Lewis acidity of the catalysts by temperature-programmed desorption of ammonia (TPD-NH_3) measurements.[277] However, the established trend Th > Zr > Hf > Ce deviates from the one determined for the catalytic performance that allowed the authors to speculate that other factors rather than Lewis acidity contributed to the reaction progress. One factor that could be responsible for such deviation is terminal water dissociation. For example, dissociation of a water molecule from the cerium-based Lewis sites occurred more rapidly at a lower temperature in comparison with the Th-containing metal nodes.[273] This conclusion was supported by mechanistic studies previously performed for transition metal-containing MOFs.[278] In a similar vein, a mixed-metal Th/Ni-based MOF, $[Ni_3Th_6(\mu_3\text{-}O)_4(\mu_3\text{-}OH)_4(IN)_{12}]\cdot(OH)_6$,[276]

was explored for Lewis acid catalysis (Figure 5.8). Specifically, a MOF constructed of $Th_{48}Ni_6$ clusters was examined for the photocatalytic CO_2 cycloaddition of styrene oxide to styrene carbonate (Figure 5.8). For catalytic activity, yields range from 89% to 99% (12 hour reaction) using 2-methyloxirane, 2-(chloromethyl)oxirane, 2-(phenoxymethyl)oxirane, 2-((benzyloxy)methyl)oxirane, and 2-phenyloxirane as starting materials. The mechanism of this catalytic reaction was proposed to be mediated by the terminal oxygen atoms of a Th-based metal node with the metal node stabilizing an alkyl-carbonate salt intermediate.[276] The framework also exhibited stability under β-irradiation up to 40 Mrad. As shown in these examples, the unique binding environment of Th- (or U-)[134] containing MOFs could potentially assist in expanding Lewis acid catalysis.[215,279–281]

One of the common organic reactions for testing catalytic properties is photodegradation of organic dyes (e.g., methyl orange (MO), methyl blue (MB), or rhodamine B (RhB)) which was also explored on several An-MOFs.[282–286] For example, a three-dimensional MOF, $[Na(H_2O)_4][(UO_2)_2Na(FDA)_3(H_2O)_2]$ (H_2FDA = 2,5-furandicarboxylic acid), was capable of decomposing 21.5% of MO after 1.5 hours of UV-irradiation.[247] Similarly, a heterometallic framework, $Ni_2(H_2O)_2(QA)_2(BPy)_2U_5O_{14}(H_2O)_2(OAc)_2$ (H_2QA = quinolinic acid; HOAc = acetic acid), constructed from polyoxouranium ribbons and nickel-based layers bridged by QA^{2-} ligands was employed for photocatalytic degradation of MB.[283] The Chen group synthesized heterometallic MOFs, $Ag(Bipy)(UO_2)(BDC)_{1.5}$ (Bipy= 2,2'-bipyridyl; H_2BDC = 1,4-benzenedicarboxylic acid) and $Ag_2(phen)_2UO_2(BTEC)$ (phen= 1,10-phenanthroline; H_4BTEC = 1,2,4,5-benzenetetracarboxylic acid) and probed them for the photocatalytic degradation of RhB.[287] The authors evaluated the performance of their MOFs against

commercial TiO_2 (Degussa P-25) and found that the frameworks displayed photocatalytic activities higher than TiO_2 under UV-irradiation. In particular, a decrease in total organic carbon was 34% and 40% for $Ag(Bipy)(UO_2)(BDC)_{1.5}$ and $Ag_2(phen)_2UO_2(BTEC)$, respectively. The difference in catalytic activity between the two frameworks was mainly attributed to steric hindrance and therefore, ability for the dye substrate to access the uranium center where catalytic conversion occurred. In addition, $Ag(Bipy)(UO_2)(BDC)_{1.5}$ has a more spacious interlayer area compared to $Ag_2(phen)_2UO_2(BTEC)$, thus making it easier for the dye molecule to diffuse and access the uranium-containing nodes. Interestingly, $Ag(Bipy)(UO_2)(BDC)_{1.5}$ also showed photocatalytic activity under visible light irradiation; however, $Ag_2(phen)_2UO_2(BTEC)$ did not, which was explained by the differences in the absorption profiles of the two MOFs.[287] The reaction was proposed to be catalyzed through photoexcitation of uranium, followed by proton abstraction from RhB. Specifically, a proton is abstracted from the methylene group of RhB, resulting in C–N bond cleavage, and a stepwise *N*-deethylation of RhB.[287] As a follow-up study, the same group designed novel U-based MOFs and probed whether the presence of a transition metal would improve the photocatalytic reaction rate.[285] Irradiation with UV light revealed that two U-based MOFs, $(UO_2)_8(1,4\text{-NDC})_{12}(4,4'\text{-BipyH}_2)_3(4,4'\text{-BipyH})_3$ (1,4-H_2NDC = 1,4-naphthalenedicarboxylic acid) and $(UO_2)_3O[Ag(Bipy)_2]_2(NDC)_3$, would almost quantitatively degrade RhB after 80 minutes, and the use of visible light resulted in degradation of RhB after 10 hours of irradiation. The presence of silver in one of these frameworks, containing a similar amount of uranium (~30%), did not affect the photocatalytic performance, allowing the authors to surmise that the presence of silver was inconsequential in the photocatalytic reactions.

A more recent report utilized MOF modularity to create four U-polycarboxylates frameworks with honeycomb (6,3) nets containing transition metal/phenanthroline complexes or viologen guest molecules to enhance the photodegradation of RhB.[286] The authors discovered that (MV)[$(UO_2)_2(TDC)_3$] (MV^{2+} = methyl viologen; H_2TDC = thiophene-2,5-dicarboxylic acid) outperformed the other U-based MOFs in this study with almost complete degradation of RhB under visible light irradiation after 60 minutes. The observed photocatalytic performance is suspected to be due to the electron accepting nature of MV^{2+} that can stabilize active peroxide anions that are responsible for the oxidation of RhB. Overall, this work demonstrated that uranium-based photocatalysts could outperform benchmark materials and showcased An-based MOFs as stable photodegradation catalysts for UV- and visible-irradiation.

The photocatalytic activity of porphyrin-containing An-frameworks was recently reported as a stable and heterogenous alternative to porphyrin-based homogeneous catalysts.[274–275] For example, a U-MOF with integrated porphyrin-based linkers, Co-TCPP (Co-TCPP = Co(II) tetra(4-carboxyphenyl) porphyrin) was used for catalyzing N-heterocycle dehydrogenation reactions.[57] Specifically, dehydration of nine different N-heterocyclic compounds (e.g., 1,2,3,4-tetrahydroquinoline to quinoline) occurred at yields ranging from 61–98%. The authors compared their findings to the activity of a well-known (and structurally similar) homogenous catalyst, Co-TPP (Co-TPP = Co(II) tetraphenyl porphyrin), and determined that the catalytic activity of the Co-based porphyrin MOF was substantially higher (e.g., a 64% yield for Co-TPP and a 93% yield for the MOF). In a similar vein, two porphyrin-based Th-MOFs were probed for the photocatalytic oxidation of 2-chloroethyl ethyl sulfide or the CO_2 fixation to styrene oxide.[274] These Th-MOFs were

constructed from tetrakis(4-carboxyphenyl)porphyrin ($TCPP^{4-}$) ligands and either 2,2′-bipyridyl-5,5′-dicarboxylate ($BPYDC^{2-}$) or 4,4′-biphenyldicarboxylate ($BPDC^{2-}$) linkers.[274] The $BPYDC^{2-}$-containing Th-MOF, (Th-IHEP-5; Figure 5.8), showed 71% photocatalytic conversion of styrene oxide to styrene carbonate after 48 hours; whereas, the $BPDC^{2-}$-containing MOF showed no catalytic activity. Moreover, control experiments performed for each individual organic linker resulted in no product formation. The authors suspect that the bipyridine core of the $BPYDC^{2-}$ linker acted as a photosensitizer and improved the photocatalytic activity of the Th-based porphyrin MOF in the visible region. Since this type of catalytic reaction is influenced by the organic linker, there is uncertainty regarding the role of integrated actinide moieties in comparison with, for instance, well-studied transition metal-based frameworks.[288–290]

The aforementioned results demonstrate the current limitations of the field of heterogeneous catalysis involving An-MOFs. Overall, most reports of An-MOF-based catalysts focused on either the metal site Lewis acidity (that does not surpass the existing MOF-based catalysts) or catalytically-active centers coordinated to the organic linkers rather than the actinide nodes. In contrast, actinide-centered catalysis in organometallic complexes have foreshadowed novel avenues for hydrocarbon photooxidation and photoinduced hydrogen atom abstraction.[259–272] Overall, actinide integration inside a framework lattice could expand the realm of catalytic transformations currently dominated by transition metal-based MOFs and lead to new reactive pathways (through stabilization of unique oxidation states of actinides) or lower activation energy barriers.[47–49,259–272] However, as clearly seen from this section, none of these benefits, as a result of integration of actinides in the MOF lattice, have been demonstrated extensively yet. Therefore,

expanding the currently explored routes, that traditionally rely on lanthanides or transition metals, is crucial since it could lead to unexpected results that arise from the unique electronic behavior and possibly reveal cooperative reactivity of actinide-based catalytically active metal nodes and surrounding organic ligands.

SUMMARY

As featured in this chapter, the field of An-containing MOFs has grown significantly in the past five years, and yet there remains a significant amount of knowledge to discover by preparing unique An-containing motifs. Currently, the An-MOF field has been dominated by thorium- and uranium-containing structures, with only a few reports on transuranic scaffolds.[3,58–60] One of the main challenges that largely impedes the development of the designated field is limited access to actinide-based precursors as well as rigorous safety protocols that are implemented for not only synthetic research groups but also for national facilities where the majority of materials characterization occurs. One could anticipate that the development of stringent safety protocols could facilitate access to transuranic elements beyond national laboratories, leading to the discovery of novel chemical principles or actinide-based materials possessing unprecedented properties. These developments could elevate investigations on transuranic frameworks by addressing fundamental questions regarding their chemical behavior and physicochemical properties. To some extent, this statement is also applicable for the more thoroughly examined uranium- and thorium-containing MOFs. As shown above, each section of this chapter contains only a few examples. For instance, less than five reports discuss the electronic behavior of An-frameworks. Only recently the first photochromic actinide-based frameworks have been synthesized.[88] Along these lines, photophysical studies of actinide-

containing MOFs mainly include reports of emission profiles that are essential, but insufficient for the advancement of An-MOF photophysics. Alternatively, a more promising situation is observed in the area related to An-MOF-based sequestration. There are a number of studies demonstrating the suitability of An-MOFs for radionuclide immobilization. Partially, it is due to the enormous previous success achieved for transition metal-based MOFs in the areas of gas storage and separation, that allowed for the research teams to apply similar methods for material analysis of An-containing frameworks. However, it is important to note that the practicality of An-MOF employment as sorbent materials could be very limited due to their radioactive nature. At the same time, sequestration of radioactive species performed on An-MOFs could be one of the areas that will be boosted during the next decade. In terms of catalyst development, An-MOFs have only made their first steps. As expected, only simple transformations have been probed that did not provide a comprehensive overview of possible future directions. Currently, a deficiency of property investigations is due to the relative youth of An-based MOF catalysts that will change as new materials emerge. In particular, small-molecule activation was explored on actinide-based molecular complexes[259–272] and could be probed in An-based MOFs that will translate to the overall success of actinides in the sector of heterogeneous catalysis. Development in this area could also result in the concept proposed above: utilization of radioactive materials for nuclear waste reprocessing.

An area that has barely been explored is the utilization of actinide-containing MOFs for medical applications. Similarly to transition metal-containing MOFs, An-MOFs could be used as targeted drug delivery systems for delivering drugs to tumor tissues.[291] In a similar vein, radioactive transition metals (e.g., ^{99}Tc) have proved successful as

metalloradiopharmaceuticals, specifically therapeutic radionuclides that are β- or α-emitters.[292] In particular, a MOF that acted as an α-emitter could potentially be applied in radioactive therapy of, for instance, a malignant tumor.[292] Furthermore, an interesting direction towards radiation-induced autoluminescence of An-MOFs has only been demonstrated on one example.[237]

Another avenue toward the development of An-based radioisotope thermoelectric generators for fueling planetary exploration, currently represented by purely inorganic systems (e.g., US, US_2, U_2S_3, and UN),[293–296] can be expanded through application of recent advances achieved in the MOF field.

Thus, this field of An-MOFs, much like an iceberg where only the surface is exposed, is ripe with opportunity. Especially, taking into account that a MOF is a versatile platform for harnessing the unique properties of these captivating elements. Finding the niche for actinide-containing frameworks is essential for putting An-MOFs on the broad material landscape map.

REFERENCES

[1] Chen, Z.; Li, P.; Zhang, X.; Mian, M. R.; Wang, X.; Li, P.; Liu, Z.; O'Keeffe, M.; Stoddart, J. F.; Farha, O. K. *Nano Res.* **2021**, *14*, 376–380.

[2] Li, P.; Wang, X.; Otake, K. I.; Lyu, J.; Hanna, S. L.; Islamoglu, T.; Farha, O. K. *ACS Appl. Nano Mater.* **2019**, *2*, 2260–2265.

[3] Hastings, A. M.; Ray, D.; Jeong, W.; Gagliardi, L.; Farha, O. K.; Hixon, A. E. *J. Am. Chem. Soc.* **2020**, *142*, 9363–9371.

[4] Li, Y. L.; Zeidman, B. D.; Hu, S. Y.; Henager, C. H.; Besmann, T. M.; Grandjean, A. *Comput. Mater. Sci.* **2019**, *159*, 103–109.

[5] Lv, X.-L.; Feng, L.; Wang, K.-Y.; Xie, L.-H.; He, T.; Wu, W.; Li, J.-R.; Zhou, H.-C. *Angew. Chem., Int. Ed.* **2021**, *60*, 2053–2057.

[6] Yang, S.; Streater, D.; Fiankor, C.; Zhang, J.; Huang, J.; *J. Am. Chem. Soc.* **2021**, *143*, 1061–1068.

[7] Zhang, J.; Bu, X.; Feng, P.; Wu, T. *Acc. Chem. Res.* **2020**, *53*, 2261–2272.

[8] Zheng, M.; Wang, Y.; Feng, P. *Catalysts* **2020**, *10*, 309.

[9] Wang, H.; Liu, Y.; Li, J. *Adv. Mater.* **2020**, *32*, 2002603.

[10] Pattengale, B.; Santalucia, D. J.; Yang, S.; Hu, W.; Liu, C.; Zhang, X.; Berry, J. F.; Huang, J. *J. Am. Chem. Soc.* **2018**, *140*, 11573–11576.

[11] Murphy, G. L.; Wang, Y.; Kegler, P.; Wang, Y.; Wang, S.; Alekseev, E. V. *Chem. Commun.* **2021**, *57*, 496–499.

[12] Burns, P. C.; Nyman, M. *Dalt. Trans.* **2018**, *47*, 5916–5927.

[13] Sperling, J. M.; Warzecha, E. J.; Celis-Barros, C.; Sergentu, D.-C.; Wang, X.; Klamm, B. E.; Windorff, C. J.; Gaiser, A. N.; White, F. D.; Beery, D. A.; Chemey, A. T.; Whitefoot, M. A.; Long, B. N.; Hanson, K.; Kögerler, P.; Speldrich, M.; Zurek, E.; Autschbach, J.; Albrecht-Schönzart, T. E. *Nature* **2020**, *583*, 396–399.

[14] Hinz, K.; Fellhauer, D.; Gaona, X.; Vespa, M.; Dardenne, K.; Schild, D.; Yokosawa, T.; Silver, M. A.; Reed, D. T.; Albrecht-Schmitt, T. E.; Altmaier, M.; Geckeis, H. *Dalt. Trans.* **2020**, *49*, 1570–1581.

[15] Windorff, C. J.; Celis-Barros, C.; Sperling, J. M.; McKinnon, N. C.; Albrecht-Schmitt, T. E. *Chem. Sci.* **2020**, *11*, 2770–2782.

[16] Kocevski, V.; Juillerat, C. A.; Moore, E. E.; zur Loye, H.-C.; Besmann, T. M. *Cryst. Growth Des.* **2019**, *19*, 966–975.

[17] Cheng, L.; Liang, C.; Liu, W.; Wang, Y.; Chen, B.; Zhang, H.; Wang, Y.; Chai, Z.; Wang, S. *J. Am. Chem. Soc.* **2020**, *142*, 16218–16222.

[18] Hong, A. N.; Yang, H.; Zhou, A.; Bu, X.; Feng, P. *Cryst. Growth Des.* **2020**, *20*, 6668–6676.

[19] Tian, S.; Xu, S.; Liu, J.; He, C.; Xiong, Y.; Feng, P. *J. Clean. Prod.* **2019**, *239*, 117767.

[20] Cohen, S. M. *Chem. Rev.* **2012**, *112*, 970–1000.

[21] Kalaj, M.; Cohen, S. M. *ACS Cent. Sci.* **2020**, *6*, 1046–1057.

[22] Hu, Z.; Deibert, B. J.; Li, J. *Chem. Soc. Rev.* **2014**, *43*, 5815–5840.

[23] Gilson, S. E.; Fairley, M.; Julien, P.; Oliver, A. G.; Hanna, S. L.; Arntz, G.; Farha, O. K.; Laverne, J. A.; Burns, P. C. *J. Am. Chem. Soc.* **2020**, *142*, 13299–13304.

[24] Wen, Y.; Zhang, P.; Sharma, V. K.; Ma, X.; Zhou, H.-C. *Cell Reports Phys. Sci.* **2021**, *2*, 100348.

[25] Hickam, S.; Ray, D.; Szymanowski, J. E. S.; Li, R. Y.; Dembowski, M.; Smith, P.; Gagliardi, L.; Burns, P. C. *Inorg. Chem.* **2019**, *58*, 12264–12271.

[26] Autillo, M.; Wilson, R. E. *Inorg. Chem.* **2019**, *58*, 3203–3210.

[27] Juillerat, C. A.; Klepov, V. V.; Morrison, G.; Pace, K. A.; zur Loye, H.-C. *Dalt. Trans.* **2019**, *48*, 3162–3181.

[28] Morrison, G.; Christian, M. S.; Besmann, T. M.; zur Loye, H.-C. *J. Phys. Chem. A* **2020**, *124*, 9487–9495.

[29] Colliard, I.; Morrison, G.; zur Loye, H.-C.; Nyman, M. *J. Am. Chem. Soc.* **2020**, *142*, 9039–9047.

[30] Furukawa, H.; Cordova, K. E.; O'Keeffe, M.; Yaghi, O. M. *Science* **2013**, *341*, 1230444.

[31] Yaghi, O. M.; O'Keeffe, M.; Ockwig, N. W.; Chae, H. K.; Eddaoudi, M.; Kim, J. *Nature* **2003**, *423*, 705–714.

[32] Kim, C. R.; Uemura, T.; Kitagawa, S. *Chem. Soc. Rev.* **2016**, *45*, 3828–3845.

[33] Dang, S.; Zhu, Q. L.; Xu, Q. *Nat. Rev. Mater.* **2017**, *3*, 17075.

[34] Kitagawa, S.; Kitaura, R.; Noro, S. I. *Angew. Chem., Int. Ed.* **2004**, *43*, 2334–2375.

[35] Marsh, M. L.; White, F. D.; Galley, S. S.; Albrecht-Schmitt, T. E. *Handb. Phys. Chem. Rare Earths* **2018**, *53*, 1–33.

[36] Zhang, P.; Liu, H.; Zou, W.; Zhang, P.; Hu, S.-X. *J. Phys. Chem. A* **2020**, *40*, 8173–8183.

[37] Berning, A.; Schweizer, M.; Werner, H.-J.; Knowles, P. J.; Palmieri, P. *Mol. Phys.* **2000**, *98*, 1823−1833.

[38] Wybourne, B. G.; Smentek, L. *J. Alloys Compd.* **2002**, *341*, 71–75.

[39] Natrajan, L. S. *Coord. Chem. Rev.* **2012**, *256*, 1583–1603.

[40] Tobin, J. G.; Moore, K. T.; Chung, B. W.; Wall, M. A.; Schwartz, A. J.; van der Laan, G.; Kutepov, A. L. *Phys. Rev. B* **2005**, *72*, 085109.

[41] Marsh, M. L.; White, F. D.; Galley, S. S.; Albrecht-Schmitt, T. E. *Handb. Phys. Chem. Rare Earths* **2018**, *53*, 1–33.

[42] Straka, M.; Hrobárik, P.; Kaupp, M. *J. Am. Chem. Soc.* **2005**, *127*, 2591–2599.

[43] Fairley, M.; Myers, N. M.; Szymanowski, J. E. S.; Sigmon, G. E.; Burns, P. C.; LaVerne, J. A. *Inorg. Chem*. **2019**, *58*, 14112–14119.

[44] Wang, Y.; Li, Y.; Bai, Z.; Xiao, C.; Liu, Z.; Liu, W.; Chen, L.; He, W.; Diwu, J.; Chai, Z.; Albrecht-Schmitt, T. E.; Wang, S. *Dalton Trans*. **2015**, *44*, 18810–18814.

[45] Volkringer, C.; Henry, N.; Grandjean, S.; Loiseau, T. *J. Am. Chem. Soc.* **2012**, *134*, 1275–1283.

[46] Hanna, S. L.; Rademacher, D. X.; Hanson, D. J.; Islamoglu, T.; Olszewski, A. K.; Nenoff, T. M.; Farha, O. K. *Ind. Eng. Chem. Res.* **2020**, *59*, 7520–7526.

[47] Grancha, T.; Carné-Sánchez, A.; Zarekarizi, F.; Hernández-López, L.; Albalad, J.; Khobotov, A.; Guillerm, V.; Morsali, A.; Juanhuix, J.; Gándara, F.; Imaz, I.; Maspoch, D. *Angew. Chem., Int. Ed.* **2021**, *60*, 5729–5733.

[48] Shakya, D. M.; Ejegbavwo, O. A.; Rajeshumar, T.; Senanayake, S. D.; Brandt, A. J.; Farzandh, S.; Acharya, N.; Ebrahim, A. M.; Fenkel, A. I.; Rui, N.; Tate, G. L.; Monnier, J. R.; Vogiatzis, K. D.; Shustova, N. B.; Chen. D. A. *Angew. Chem., Int. Ed.* **2019**, *58*, 16533–16537.

[49] Chan, W. T. K.; Wong, W.-T. *Polyhedron* **2013**, *52*, 43–61.

[50] MacDonald, M. R.; Fieser, M. E.; Bates, J. E.; Ziller, J. W.; Furche, F.; Evans, W. J. *J. Am. Chem. Soc.* **2013**, *135*, 13310–13313.

[51] Langeslay, R. R.; Fieser, M. E.; Ziller, J. W.; Furche, F.; Evans, W. J. *Chem. Sci.* **2015**, *6*, 517–521.

[52] Windorff, C. J.; Chen, G. P.; Cross, J. N.; Evans, W. J.; Furche, F.; Gaunt, A. J.; Janicke, M. T.; Kozimor, S. A.; Scott, B. L. *J. Am. Chem. Soc.* **2017**, *139*, 3970–3973.

[53] Arliguie, T.; Belkhiri, L.; Bouaoud, S.-E.; Thuéry, P.; Villiers, C.; Boucekkine, A.;

Ephritikhine, M. *Inorg. Chem.* **2009**, *48*, 221–230.

[54] Daley, S. R.; Piccoli, P. M. B.; Schultz, A. J.; Todorova, T. K.; Gagliardi, L.; Girolami, G. S. *Angew. Chem., Int. Ed.* **2010**, *49*, 3379–3381.

[55] Hu, S.-X.; Zhang, P.; Zou, W.; Zhang, P. *Nanoscale* **2020**, *12*, 15054–15065.

[56] Tutson, C. D.; Gorden, A. E. V. *Coord. Chem. Rev.* **2017**, *333*, 27–43.

[57] Hu, K.-Q.; Huang, Z.-W.; Zhang, Z.-H.; Mei, L.; Qian, B.-B.; Yu, J.-P.; Chai, Z.-F.; Shi, W.-Q. *Chem. Eur. J.* **2018**, *24*, 16766–16769.

[58] Gilson, S. E.; Li, P.; Szymanowski, J. E. S.; White, J.; Ray, D.; Gagliardi, L.; Farha, O. K.; Burns, P. C. *J. Am. Chem. Soc.* **2019**, *141*, 11842–11846.

[59] Martin, N. P.; März, J.; Feuchter, H.; Duval, S.; Roussel, P.; Henry, N.; Ikeda-Ohno, A.; Loiseau, T.; Volkringer, C. *Chem. Commun.* **2018**, *54*, 6979–6982.

[60] Ridenour, J. A.; Surbella, R. G.; Gelis, A. V.; Koury, D.; Poineau, F.; Czerwinski, K. R.; Cahill, C. L. *Angew. Chem., Int. Ed.* **2019**, *58*, 16508–16511.

[61] Dolgopolova, E. A.; Rice, A. M.; Shustova, N. B. *Chem. Commun.* **2018**, *54*, 6472–6483.

[62] Falaise, C.; Assen, A.; Mihalcea, I.; Volkringer, C.; Mesbah, A.; Dacheux, N.; Loiseau, T. *Dalt. Trans*. **2015**, *44*, 2639–2649.

[63] Wang, Y.; Li, Y.; Bai, Z.; Xiao, C.; Liu, Z.; Liu, W.; Chen, L.; He, W.; Diwu, J.; Chai, Z.; Albrecht-Schmitt, T. E.; Wang, S. *Dalt. Trans.* **2015**, *44*, 18810–18814.

[64] Li, Y.; Weng, Z.; Wang, Y.; Chen, L.; Sheng, D.; Diwu, J.; Chai, Z.; Albrecht-Schmitt, T. E.; Wang, S. *Dalt. Trans.* **2016**, *45*, 918–921.

[65] Wang, Y.; Liu, Z.; Li, Y.; Bai, Z.; Liu, W.; Wang, Y.; Xu, X.; Xiao, C.; Sheng, D.; Diwu, J.; Su, J.; Chai, Z.; Albrecht-Schmitt, T. E.; Wang, S. *J. Am. Chem. Soc.* **2015**, *137*, 6144–6147.

[66] Li, Y.; Weng, Z.; Wang, Y.; Chen, L.; Sheng, D.; Liu, Y.; Diwu, J.; Chai, Z.; Albrecht-Schmitt, T. E.; Wang, S. *Dalt. Trans.* **2015**, *44*, 20867–20873.

[67] Lussier, A. J.; Lopez, R. A. K.; Burns, P. C. *Can. Mineral.* **2016**, *54*, 177–283.

[68] Falaise, C.; Assen, A.; Mihalcea, I.; Volkringer, C.; Mesbah, A.; Dacheux, N.; Loiseau, T. *Dalton Trans.* **2015**, *44*, 2639−2649.

[69] Takao, S.; Takao, K.; Kraus, W.; Emmerlink, F.; Scheinost, A. C.; Bernhard, G.; Hennig, C. *Eur. J. Inorg. Chem.* **2009**, *2009*, 4771−4775.

[70] Mougel, V.; Biswas, B.; Pécaut, J.; Mazzanti, M. *Chem. Commun.* **2010**, *46*, 8648−8650.

[71] Nocton, G.; Burdet, F.; Pécaut, J.; Mazzanti, M. *Angew. Chem., Int. Ed.* **2007**, *46*, 7574−7578.

[72] Falaise, C.; Volkringer, C.; Loiseau, T. *Cryst. Growth Des.* **2013**, *13*, 3225−3231.

[73] Hennig, C.; Takao, S.; Takao, K.; Weiss, S.; Kraus, W.; Emmerling, F.; Scheinost, A. C. *Dalton Trans.* **2012**, *41*, 12818−12823.

[74] Takao, K.; Takao, S.; Scheinost, A. C.; Bernard, G.; Hennig, C. *Inorg. Chem.* **2012**, *51*, 1336−1344.

[75] Knope, K. E.; Soderholm, L. *Inorg. Chem.* **2013**, *52*, 6770−6772.

[76] Severance, R. C.; Vaughn, S. A.; Smith, M. D.; zur Loye, H.-C. *Solid State Sci.* **2011**, *13*, 1344–1353.

[77] Plasil, J.; Hlousek, J.; Veselovsky, F.; Fejfarova, K.; Dusek, M.; Skoda, R.; Novak, M.; Cejka, J.; Sejkora, J.; Ondrus, P. *Am. Mineral.* **2012**, *97*, 447–454.

[78] Dolgopolova, E. A.; Ejegbavwo, O. A.; Martin, C. R.; Smith, M. D.; Setyawan, W.; Karakalos, S. G.; Henager, C. H.; zur Loye, H.-C.; Shustova, N. B. *J. Am. Chem. Soc.* **2017**, *139*, 16852–16861.

[79] Kato, S.; Otake, K. I.; Chen, H.; Akpinar, I.; Buru, C. T.; Islamoglu, T.; Snurr, R. Q.; Farha, O. K. *J. Am. Chem. Soc.* **2019**, *141*, 2568–2576.

[80] Wang, S.; Chen, Y.; Wang, S.; Li, P.; Mirkin, C. A.; Farha, O. K. *J. Am. Chem. Soc.* **2019**, *141*, 2215–2219.

[81] Chen, Y.; Li, P.; Modica, J. A.; Drout, R. J.; Farha, O. K. *J. Am. Chem. Soc.* **2018**, *140*, 5678–5681.

[82] Wang, S.; Park, S. S.; Buru, C. T.; Lin, H.; Chen, P. C.; Roth, E. W.; Farha, O. K.; Mirkin, C. A. *Nat. Commun.* **2020**, *11*, 2495.

[83] Ejegbavwo, O. A.; Martin, C. R.; Olorunfemi, O. A.; Leith, G. A.; Ly, R. T.; Rice, A. M.; Dolgopolova, E. A.; Smith, M. D.; Karakalos, S. G.; Birkner, N.; Powell, B. A.; Pandey, S.; Koch, R. J.; Misture, S. T.; zur Loye, H.-C.; Phillpot, S. R.;

Brinkman, K. S.; Shustova, N. B. *J. Am. Chem. Soc.* **2019**, *141*, 11628–11640.

[84] Wen, X.-D.; Martin, R. L.; Henderson, T. M.; Scuseria, G. E. *Chem. Rev.* **2013**, *113*, 1063–1096.

[85] Bugaris, D. E.; Ibers, J. A. *Dalton Trans.* **2010**, *39*, 5949–5964.

[86] Epifano, E.; Naji, M.; Manara, D.; Scheinost, A. C.; Hennig, C.; Lechelle, J.; Konings, R. J. M.; Guéneau, C.; Prieur, D.; Vitova, T.; Dardenne, K.; Rothe, J.; Martin, P. M. *Commun. Chem.* **2019**, *2*, 59.

[87] Yao, J.; Wells, D. M.; Chan, G. H.; Zeng, H.-Y.; Ellis, D. E.; Van Duyne, R. P.; Ibers, J. A. *Inorg. Chem.* **2008**, *47*, 6873–6879.

[88] Martin, C. R.; Leith, G. A.; Kittikhunnatham, P.; Park, K. C.; Ejegbavwo, O. A.; Mathur, A.; Callahan, C. R.; Desmond, S. L.; Keener, M. R.; Ahmed, F.; Pandey, S.; Smith, M. D.; Phillpot, S. R.; Greytak, A. B.; Shustova, N. B. *Angew. Chem., Int. Ed.* **2021**, *60*, 8072–8080.

[89] Rice, A. M.; Martin, C. R.; Galitskiy, V. A.; Berseneva, A. A.; Leith, G. A.; Shustova, N. B. *Chem. Rev.* **2020**, *120*, 8790–8813.

[90] Ejegbavwo, O. A.; Berseneva, A. A.; Martin, C. R.; Leith, G. A.; Pandey, S.; Brandt, A. J.; Park, K. C.; Mathur, A.; Farzandh, S.; Klepov, V. V.; Heiser, B. J.; Chandrashekhar, M.; Karakalos, S. G.; Smith, M. D.; Phillpot, S. R.; Garashchuk, S.; Chen, D. A.; Shustova, N. B. *Chem. Sci.* **2020**, *11*, 7379–7389.

[91] Castellanos, S.; Kapteijn, F.; Gascon, J. *CrystEngComm*. **2016**, *18*, 4006–4012.

[92] Haldar, R.; Heinke, L.; Wöll, C. *Adv. Mater.* **2020**, *32*, 1905227.

[93] Kanj, A. B.; Müller, K.; Heinke, L. *Macromol. Rapid Commun.* **2018**, *39*, 1700239.

[94] Klajn, R. *Chem. Soc. Rev.* **2014**, *43*, 148–184.

[95] Dolgopolova, E. A.; Galitskiy, V. A.; Martin, C. R.; Gregory, H. N.; Yarbrough, B. J.; Rice, A. M.; Berseneva, A. A.; Ejegbavwo, O. A.; Stephenson, K. S.; Kittikhunnatham, P.; Karakalos, S. G.; Smith, M. D.; Greytak, A. B.; Garashchuk, S.; Shustova, N. B. *J. Am. Chem. Soc.* **2019**, *141*, 5350–5358.

[96] Williams, D. E.; Martin, C. R.; Dolgopolova, E. A.; Swifton, A.; Godfrey, D. C.; Ejegbavwo, O. A.; Pellechia, P. J.; Smith, M. D.; Shustova, N. B. *J. Am. Chem. Soc.* **2018**, *140*, 7611–7622.

[97] Liu, D.-D.; Wang, Y.-L.; Luo, F.; Liu, Q.-Y. *Inorg. Chem.* **2020**, *59*, 2952–2960.

[98] Kreuer, K.-D.; Rabenau, A.; Weppner, W. *Angew. Chem., Int. Ed.* **1982**, *21*, 208–209.

[99] Suarez, S. N.; Jayakody, J. R. P.; Greenbaum, S. G.; Zawodzinski, T.; Fontanella, J. J. *J. Phys. Chem. B* **2010**, *114*, 8941–8947.

[100] Lim, D.-W.; Sadakiyo, M.; Kitagawa, H. *Chem. Sci.* **2019**, *10*, 16–33.

[101] Ludueña, G. A.; Kühne, T. D.; Sebastiani, D. *Chem. Mater.* **2011**, *23*, 1424–1429.

[102] Chen, T.; Dou, J.-H.; Yang, L.; Sun, C.; Libretto, N. J.; Skorupskii, G.; Miller, J. T.; Dincă, M. *J. Am. Chem. Soc.* **2020**, *142*, 12367–12373.

[103] Byun, Y.; Xie, L. S.; Fritz, P.; Ashirov, T.; Dincă, M.; Coskun, A. *Angew. Chem., Int. Ed.* **2020**, *59*, 15166–15170.

[104] Stolz, R. M.; Mahdavi-Shakib, A.; Frederick, B. G.; Mirica, K. A. *Chem. Mater.* **2020**, *32*, 7639–7652.

[105] Mendecki, L.; Mirica, K. A. *ACS Appl. Mater. Interfaces* **2018**, *10*, 19248–19257.

[106] Banda, H.; Dou, J.-H.; Chen, T.; Libretto, N. J.; Chaudhary, M.; Bernard, G. M.; Miller, J. T.; Michaelis, V. K.; Dincă, M. *J. Am. Chem. Soc.* **2021**, *143*, 2285–2292.

[107] Ko, M.; Mendecki, L.; Mirica, K. A. *Chem. Commun.* **2018**, *54*, 7873–7891.

[108] Dou, J.-H.; Arguilla, M. Q.; Luo, Y.; Li, J.; Zhang, W.; Sun, L.; Mancuso, J. L.; Yang, L.; Chen, T.; Parent, L. R.; Skorupskii, G.; Libretto, N. J.; Sun, C.; Yang, M. C.; Dip, P. V.; Brignole, E. J.; Miller, J. T.; Kong, J.; Hendon, C. H.; Sun, J.; Dincă, M. *Nat. Mater.* **2021**, *20*, 222–228.

[109] Meng, Z.; Stolz, R. M.; Mirica, K. A. *J. Am. Chem. Soc.* **2019**, *141*, 11929–11937.

[110] Pandey, S.; Jia, Z.; Demaske, B.; Ejegbavwo, O. A.; Setyawan, W.; Henager, C. H.; Shustova, N. B.; Phillpot, S. R. *J. Phys. Chem. C* **2019**, *123*, 26842–26855.

[111] Pandey, S.; Demaske, B.; Ejegbavwo, O. A.; Berseneva, A. A.; Setyawan, W.; Shustova, N. B.; Phillpot, S. R. *Comput. Mater. Sci.* **2020**, *184*, 109903.

[112] Li, L.; Ma, W.; Shen, S.; Huang, H.; Bai, Y.; Liu, H. *ACS Appl. Mater. Interfaces* **2016**, *8*, 31032–31041.

[113] Wu, Y.; Pang, H.; Yao, W.; Wang, X.; Yu, S.; Yu, Z.; Wang, X. *Sci. Bull.* **2018**, *63*, 831–839.

[114] Xiao, C.; Silver, M. A.; Wang, S. *Dalton Trans.* **2017**, *46*, 16381–16386.

[115] Belmabkhout, Y.; Bhatt, P. M.; Adil, K.; Pillai, R. S.; Cadiau, A.; Shkurenko, A.; Maurin, G.; Liu, G.; Koros, W. J.; Eddaoudi, M. *Nat. Energy* **2018**, *3*, 1059–1066.

[116] Chen, Y.; Zhang, X.; Mian, M. R.; Son, F. A.; Zhang, K.; Cao, R.; Chen, Z.; Lee, S.-J.; Idrees, K. B.; Goetjen, T. A.; Lyu, J.; Li, P.; Xia, Q.; Li, Z.; Hupp, J. T.; Islamoglu, T.; Napolitano, A.; Peterson, G. W.; Farha, O. K. *J. Am. Chem. Soc.* **2020**, *142*, 21428–21438.

[117] Santoso, S. P.; Angkawijaya, A. E.; Bundjaja, V.; Soetaredjo, F. E.; Ismadji, S. *Applications of Metal–Organic Frameworks and Their Derived Materials*, Wiley, **2020**, 313–355.

[118] Chen, R.; Yao, Z.; Han, N.; Ma, X.; Li, L.; Liu, S.; Sun, H.; Wang, S. *ACS Omega* **2020**, *5*, 15402–15408.

[119] Vellingiri, K.; Szulejko, J. E.; Kumar, P.; Kwon, E. E.; Kim, K.-H.; Deep, A.; Boukhvalov, D. W.; Brown, R. J. C. *Sci. Rep.* **2016**, *6*, 27813.

[120] Chen, Z.; Li, P.; Anderson, R.; Wang, X.; Zhang, X. Robison, L.; Redfern, L. R.; Moribe, S.; Islamoglu, T.; Gómez-Gualdrón, D. A.; Yildirim, T.; Stoddart, J. F.; Farha, O. K. *Science* **2020**, *368*, 297–303.

[121] Bobbitt, N. S.; Mendonca, M. L.; Howarth, A. J.; Islamoglu, T.; Hupp, J. T.; Farha, O. K.; Snurr, R. Q. *Chem. Soc. Rev.* **2017**, *46*, 3357–3385.

[122] Woellner, M.; Hausdorf, S.; Klein, N.; Mueller, P.; Smith, M. W.; Kaskel, S. *Adv. Mater.* **2018**, *30*, 1704679.

[123] Islamoglu, T.; Chen, Z.; Wasson, M. C.; Buru, C. T.; Kirlikovali, K. O.; Afrin, U.; Mian, M. R.; Farha, O. K. *Chem. Rev.* **2020**, *120*, 8130–8160.

[124] Li, H.; Wang, K.; Sun, Y.; Lollar, C. T.; Li, J.; Zhou, H.-C. *Mater. Today* **2018**, *21*, 108–121.

[125] Torrisi, A.; Mellot-Draznieks, C.; Bell, R. G. *J. Chem. Phys.* **2010**, *132*, 044705.

[126] Li, Z.; Liu, P.; Ou, C.; Dong, X. *ACS Sustain. Chem. Eng.* **2020**, *8*, 15378–15404.

[127] Banerjee, D.; Simon, C. M.; Elsaidi, S. K.; Haranczyk, M.; Thallapally, P. K. *Chem*

2018, *4*, 466–494.

[128] Hiraide, S.; Sakanaka, Y.; Kajiro, H.; Kawaguchi, S.; Miyahara, M. T.; Tanaka, H. *Nat. Commun.* **2020**, *11*, 3867.

[129] Parkes, M. V.; Staiger, C. L.; Perry IV, J. J.; Allendorf, M. D.; Greathouse, J. A. *Phys. Chem. Chem. Phys.* **2013**, *15*, 9093–9106.

[130] Perry, J. J.; Teich-Mcgoldrick, S. L.; Meek, S. T.; Greathouse, J. A.; Haranczyk, M.; Allendorf, M. D. *J. Phys. Chem. C* **2014**, *118*, 11685–11698.

[131] Feng, G.; Peng, Y.; Liu, W.; Chang, F.; Dai, Y.; Huang, W. *Inorg. Chem.* **2017**, *56*, 2363–2366.

[132] Hanna, S. L.; Zhang, X.; Otake, K.-I.; Drout, R. J.; Li, P.; Islamoglu, T.; Farha, O. K.; *Cryst. Growth Des*. **2019**, *19*, 506–512.

[133] Zeng, L.-W.; Hu, K.-Q.; Mei, L.; Li, F.-Z.; Huang, Z.-W.; An, S.-W.; Chai, Z.-F.; Shi, W.-Q. *Inorg. Chem.* **2019**, *58*, 14075–14084.

[134] Li, Y.; Yang, Z.; Wang, Y.; Bai, Z.; Zheng, T.; Dai, X.; Liu, S.; Gui, D.; Liu, W.; Chen, M.; Chen, L.; Diwu, J.; Zhu, L.; Zhou, R.; Chai, Z.; Albrecht-Schmitt, T. E.; Wang, S. *Nat. Commun.* **2017**, *8*, 1354.

[135] Bai, Z.; Wang, Y.; Li, Y.; Liu, W.; Chen, L.; Sheng, D.; Diwu, J.; Chai, Z.; Albrecht-Schmitt, T. E.; Wang, S. *Inorg. Chem.* **2016**, *55*, 6358–6360.

[136] Zhang, N.; Xing, Y.-H.; Bai, F.-Y. *Inorg. Chem.* **2019**, *58*, 6866–6876.

[137] Li, Z.-J.; Yue, Z.; Ju, Y.; Wu, X.; Ren, Y.; Wang, S.; Li, Y.; Zhang, Z.-H.; Guo, X.; Lin, J.; Wang, J.-Q. *Inorg. Chem.* **2020**, *59*, 4435–4442.

[138] Li, Z.-J.; Ju, Y.; Yu, B.; Wu, X.; Lu, H.; Li, Y.; Zhou, J.; Guo, X.; Zhang, Z.-H.; Lin, J.; Wang, J.-Q.; Wang, S. *Chem. Commun.* **2020**, *56*, 6715–6718.

[139] Xu, Z.; Xiong, X.; Xiong, J.; Krishna, R.; Li, L.; Fan, Y.; Luo, F.; Chen, B. *Nat. Commun.* **2020**, *11*, 3163.

[140] Wang, Y.; Liu, W.; Bai, Z.; Zheng, T.; Silver, M. A.; Li, Y.; Wang, Y.; Wang, X.; Diwu, J.; Chai, Z.; Wang, S. *Angew. Chem., Int. Ed.* **2018**, *57*, 5783–5787.

[141] Halter, D. P.; Klein, R. A.; Boreen, M. A.; Trump, B. A.; Brown, C. M.; Long, J. R. *Chem. Sci.* **2020**, *11*, 6709–6716.

[142] Widmer, R. N.;. Lampronti, G. I; Casati, N.; Farsang, S.; Bennett, T. D.; Redfern, S. A. T. *Phys. Chem. Chem. Phys.* **2019**, *21*, 12389–12395.

[143] Volkringer, C.; Falaise, C.; Devaux, P.; Giovine, R.; Stevenson, V.; Pourpoint, F.; Lafon, O.; Osmond, M.; Jeanjacques, C.; Marcillaud, B.; Sabroux, J. C.; Loiseau, T. *Chem. Commun.* **2016**, *52*, 12502–12505.

[144] Elsaidi, S. K.; Mohamed, M. H.; Helal, A. S.; Galanek, M.; Pham, T.; Suepaul, S. ; Space, B.; Hopkinson, D.; Thallapally, P. K.; Li, J. *Nat. Commun.* **2020**, *11*, 3103.

[145] Dorhout, J. M.; Wilkerson, M. P.; Czerwinski, K. R. *J. Radioanal. Nucl. Chem.* **2019**, *320*, 415–424.

[146] Hanna, S. L.; Rademacher, D. X.; Hanson, D. J.; Islamoglu, T.; Olszewski, A. K.; Nenoff, T. M.; Farha, O. K. *Ind. Eng. Chem. Res.* **2020**, *59*, 7520–7526.

[147] Berseneva, A. A.; Martin, C. R.; Galitskiy, V. A.; Ejegbavwo, O. A.; Leith, G. A.; Ly, R. T.; Rice, A. M.; Dolgopolova, E. A.; Smith, M. D.; zur Loye, H.-C.; DiPrete, D. P.; Amoroso, J. W.; Shustova, N. B. *Inorg. Chem.* **2020**, *59*, 179–183.

[148] Yang, H.; Wang, Y.; Krishna, R.; Jia, X.; Wang, Y.; Hong, A. N.; Dang, C.; Castillo, H. E.; Bu, X.; Feng, P. *J. Am. Chem. Soc.* **2020**, *142*, 2222–2227.

[149] Dinh, A.; Yang, H.; Peng, F.; Nguyen, T. C.; Hong, A.; Feng, P.; Bu, X. *Cryst. Growth Des.* **2020**, *20*, 3523–3530.

[150] Zhang, Y.-B.; Furukawa, H.; Ko, N.; Nie, W.; Park, H. J.; Okajima, S.; Cordova, K. E.; Deng, H.; Kim, J.; Yaghi, O. M. *J. Am. Chem. Soc.* **2015**, *137*, 2641–2650.

[151] Chen, H.; Chen, Z.; Zhang, L.; Li, P.; Liu, J.; Redfern, L. R.; Moribe, S.; Cui, Q.; Snurr, R. Q.; Farha, O. K. *Chem. Mater.* **2019**, *31*, 2702–2706.

[152] Fan, W.; Yuan, S.; Wang, W.; Feng, L.; Liu, X.; Zhang, X.; Wang, X.; Kang, Z.; Dai, F.; Yuan, D.; Sun, D.; Zhou, H.-C. *J. Am. Chem. Soc.* **2020**, *142*, 8728–8737.

[153] Wang, Y.; Jia, X.; Yang, H.; Wang, Y.; Chen, X.; Hong, A. N.; Li, J.; Bu, X.; Feng, P. *Angew. Chem., Int. Ed.* **2020**, *59*, 19027–19030.

[154] Lei, X.-W.; Yang, H.; Wang, Y.; Wang, Y.; Chen, X.; Xiao, Y.; Bu, X.; Feng, P. *Small* **2020**, 2003167.

[155] Zhao, X.; Bu, X.; Wu, T.; Zheng, S.-T.; Wang, L.; Feng, P. *Nat. Commun.* **2013**, *4*, 2344.

[156] Brozek, C. K.; Bellarosa, L.; Soejima, T.; Clark, T. V.; López, N.; Dincă, M. *Chem. Eur. J.* **2014**, *20*, 6871–6874.

[157] Chołuj, A.; Zieliński, A.; Grela, K.; Chmielewski, M. J. *ACS Catal.* **2016**, *6*, 6343–6349.

[158] He, P.; Haw, K.-G.; Ren, J.; Fang, Q.; Qiu, S.; Valtchev, V. *Inorg. Chem. Front.* **2018**, *5*, 2784–2791.

[159] Falaise, C.; Charles, J.-S.; Volkringer, C.; Loiseau, T. *Inorg. Chem.* **2015**, *54*, 2235–2242.

[160] Li, P.; Vermeulen, N. A.; Gong, X.; Malliakas, C. D.; Stoddart, J. F.; Hupp, J. T.; Farha, O. K. *Angew. Chem., Int. Ed.* **2016**, *55*, 10358–10362.

[161] Li, P.; Vermeulen, N. A.; Malliakas, C. D.; Gómez-Gualdrón, D. A.; Howarth, A. J.; Mehdi, B. L.; Dohnalkova, A.; Browning, N. D.; O'Keeffe M.; Farha, O. K. *Science* **2017**, *356*, 624–627.

[162] Falaise, C.; Volkringer, C.; Vigier, J.-F.; Henry, N.; Beaurain, A.; Loiseau, T. *Chem. Eur. J.* **2013**, *19*, 5324–5331.

[163] Ok, K. M.; Sung, J.; Hu, G.; Jacobs, R. M. J.; O'Hare, D. *J. Am. Chem. Soc.* **2008**, ***130***, 3762–3763.

[164] Garai, M.; Yavuz, C. T. *Chem* **2019**, *5*, 750–752.

[165] Zha, M.; Liu, J.; Wong Y.-L.; Xu, Z. *J. Mater. Chem. A* **2015**, *3*, 3928–3934.

[166] Zhang, J.; Chen, L.; Dai, X.; Zhu, L.; Xiao, C.; Xu, L.; Zhang, Z.; Alekseev, E. V.; Wang, Y.; Zhang, C.; Zhang, H.; Wang, Y.; Diwu, J.; Chai, Z.; Wang, S. *Chem* **2019**, *5*, 977–994.

[167] Huang, Z.-W.; Li, Z.-J.; Wu, Q.-Y.; Zheng, L.-R.; Zhou, L.-M.; Chai, Z.-F.; Wang, X.-L.; Shi, W.-Q. *Environ. Sci. Nano* **2018**, *5*, 2077–2087.

[168] Riley, B. J.; Vienna, J. D.; Strachan, D. M.; McCloy, J. S.; Jerden, J. L. *J. Nucl. Mater.* **2016**, *470*, 307–326.

[169] Huve, J.; Ryzhikov, A.; Nouali, H.; Lalia, V.; Augé, G.; Daou, T. J. *RSC Adv.* **2018**, *8*, 29248–29273.

[170] Schaate, A.; Roy, P.; Godt, A.; Lippke, J.; Waltz, F.; Wiebcke, M.; Behrens, P. *Chem. Eur. J.* **2011**, *17*, 6643–6651.

[171] Sava, D. F.; Chapman, K. W.; Rodriguez, M. A.; Greathouse, J. A.; Crozier, P. S.; Zhao, H.; Chupas, P. J.; Nenoff, T. M. *Chem. Mater.* **2013**, *25*, 2591–2596.

[172] Sava, D. F.; Rodriguez, M. A.; Chapman, K. W.; Chupas, P. J.; Greathouse, J. A.; Crozier, P. S.; Nenoff, T. M. *J. Am. Chem. Soc.* **2011**, *133*, 12398–12401.

[173] Bien, C. E.; Chen, K. K.; Chien, S-C.; Reiner, B. R.; Lin, L.-C.; Wade, C. R.; Ho, W. S. W. *J. Am. Chem. Soc.* **2018**, *140*, 12662–12666.

[174] Cai, Z.; Bien, C. E.; Liu, Q.; Wade, C. R. *Chem. Mater.* **2020**, *32*, 4257–4264.

[175] Connolly, B. M.; Madden, D. G.; Wheatley, A. E. H.; Fairen-Jimenez, D. *J. Am. Chem. Soc.* **2020**, *142*, 8541–8549.

[176] Xiao, Y.; Yang, H.; Bu, X.; Feng, P. *Carbon N. Y.* **2021**, *176*, 421–430.

[177] Gu, Y.; Zheng, J.-J.; Otake, K.-I.; Shivanna, M.; Sakaki, S.; Yoshino, H.; Ohba, M.; Kawaguchi, S.; Wang, Y.; Li, F.; Kitagawa, S. *Angew. Chem., Int. Ed*. **2021**, *60*, 11688–11694.

[178] Wu, P.; Li, Y.; Zheng, J.-J.; Hosono, N.; Otake, K.-I.; Wang, J.; Liu, Y.; Xia, L.; Jiang, M.; Sakaki, S.; Kitagawa, S. *Nat. Commun.* **2019**, *10*, 4362.

[179] Barman, S.; Furukawa, H.; Blacque, O.; Venkatesan, K.; Yaghi, O. M.; Berke, H. *Chem. Commun.* **2010**, *46*, 7981–7983.

[180] Britt, D.; Tranchemontagne, D.; Yaghi, O. M. *Proc. Natl. Acad. Sci. U. S. A.* **2008**, *105*, 11623–11627.

[181] Mao, V. Y.; Milner, P. J.; Lee, J.-H.; Forse, A. C.; Kim, E. J.; Siegelman, R. L.; McGuirk, C. M.; Porter-Zasada, L. B.; Neaton, J. B.; Reimer, J. A.; Long, J. R. *Angew. Chem., Int. Ed.* **2020**, *59*, 19468–19477.

[182] Jaffe, A.; Ziebel, M. E.; Halat, D. M.; Biggins, N.; Murphy, R. A.; Chakarawet, K.; Reimer, J. A.; Long, J. R. *J. Am. Chem. Soc.* **2020**, *142*, 14627–14637.

[183] Kałuża, A. M.; Mukherjee, S.; Wang, S.-Q.; O'Hearn, D. J.; Zaworotko, M. J. *Chem. Commun.* **2020**, *56*, 1940–1943.

[184] Li, H.; Li, L.; Lin, R.-B.; Zhou, W.; Zhang, Z.; Xiang, S.; Chen, B. *EnergyChem* **2019**, ***1***, 100006.

[185] Chen, K.-J.; Madden, D. G.; Mukherjee, S.; Pham, T.; Forrest, K. A.; Kumar, A.; Space, B.; Kong, J.; Zhang, Q.-Y.; Zaworotko, M. J. *Science* **2019**, *366*, 241–246.

[186] Lin, R.-B.; Wu, H.; Li, L.; Tang, X.-L.; Li, Z.; Gao, J.; Cui, H.; Zhou, W.; Chen, B. *J. Am. Chem. Soc.* **2018**, *140*, 12940–12946.

[187] Li, L.; Lin, R.-B.; Krishna, R.; Li, H.; Xiang, S.; Wu, H.; Li, J.; Zhou, W.; Chen, B. *Science* **2018**, *362*, 443–446.

[188] Wu, Y.; Chen, H.; Liu, D.; Qian, Y.; Xi, H. *Chem. Eng. Sci.* **2015**, *124*, 144–153.

[189] Chen, D.-L.; Wang, N.; Xu, C.; Tu, G.; Zhu, W.; Krishna, R. *Microporous Mesoporous Mater.* **2015**, *208*, 55–65.

[190] Lv, D.; Shi, R.; Chen, Y.; Wu, Y.; Wu, H.; Xi, H.; Xia, Q.; Li, Z. *ACS Appl. Mater. Interfaces* **2018**, *10*, 8366–8373.

[191] Chen, Y.; Wu, H.; Lv, D.; Shi, R.; Chen, Y.; Xia, Q.; Li, Z. *Ind. Eng. Chem. Res.* **2018**, *57*, 4063–4069.

[192] Liao, P.-Q.; Zhang, W.-X.; Zhang, J.-P.; Chen, X.-M. *Nat. Commun.* **2015**, *6*, 8697.

[193] Dolgopolova, E. A.; Rice, A. M.; Martin, C. R.; Shustova, N. B. *Chem. Soc. Rev.* **2018**, *47*, 4710–4728.

[194] Wang, Q.; Gao, Q.; Al-Enizi, A. M.; Nafady, A.; Ma, S. *Inorg. Chem. Front.* **2020**, *7*, 300–339.

[195] Martin, C. R.; Kittikhunnatham, P.; Leith, G. A.; Berseneva, A. A.; Park, K. C.; Greytak, A. B.; Shustova, N. B. *Nano Res.* **2021**, *14*, 338–354.

[196] Nguyen, T. N.; Ebrahim, F. M.; Stylianou, K. C. *Coord. Chem. Rev.* **2018**, *377*, 259–306.

[197] Leith, G. A.; Martin, C. R.; Mayers, J. M.; Kittikhunnatham, P.; Larsen, R. W.; Shustova, N. B. *Chem. Soc. Rev.* **2021**, *50*, 4382–4410.

[198] Zhuang, Z.; Liu, D. *Nano-Micro Lett.* **2020**, *12*, 132.

[199] Lu, J.; Xin, X.-H.; Lin, Y.-J.; Wang, S.-H.; Xu, J.-G.; Zheng, F.-K. Guo, G.-C. *Dalton Trans.* **2019**, *48*, 1722–1731.

[200] Wang, X.; Wang, Y.; Wang, Y.; Liu, H.; Zhang, Y.; Liu, W.; Wang, X.; Wang, S. *Chem. Commun.* **2020**, *56*, 233–236.

[201] Doty, F. P.; Bauer, C. A.; Skulan, A. J.; Grant, P. G.; Allendorf, M. D. *Adv. Mater.* **2009**, *21*, 95–101.

[202] Wang, C.; Volotskova, O.; Lu, K.; Ahmad, M. Sun, C.; Xing, L.; Lin, W. *J. Am. Chem. Soc.* **2014**, *136*, 6171–6174.

[203] Aziz, A.; Ruiz-Salvador, A. R.; Hernández, N. C.; Calero, S.; Hamad, S.; Grau-Crespo, R. *J. Mater. Chem. A* **2017**, *5*, 11894–11904.

[204] Zhou, Z.; Mukherjee, S.; Warnan, J.; Li, W.; Wannapaiboon, S.; Hou, S.; Rodewald, K.; Rieger, B.; Weidler, P. G.; Wöll, C.; Fischer, R. A. *J. Mater. Chem. A* **2020**, *8*, 25941–25950.

[205] Pratik, S. M.; Gagliardi, L.; Cramer, C. J. *J. Phys. Chem. C*, **2020**, *124*, 1878–1887.

[206] Yang, H.; Wang, J.; Ma, J.; Yang, H.; Zhang, J.; Lv, K.; Wen, L.; Peng, T. *J. Mater. Chem. A*, **2019**, *7*, 10439–10445.

[207] Yang, H.; Zhao, M.; Zhang, J.; Ma, J.; Wu, P.; Liu, W.; Wen, L. *J. Mater. Chem. A* **2019**, *7*, 20742–20749.

[208] Lee, C. Y.; Farha, O. K.; Hong, B. J.; Sarjeant, A. A.; Nguyen, S. T.; Hupp, J. T. *J. Am. Chem. Soc.* **2011**, *133*, 15858–15861.

[209] Chen, J.; Zhu, Y.; Kaskel, S. *Angew. Chem., Int. Ed.* **2021**, *60*, 5010–5035.

[210] Sun, T.; Gao, Y.; Du, Y.; Zhou, L.; Chen, X. *Front. Chem.* **2021**, *8*, 624592.

[211] Yan, B. *Acc. Chem. Res.* **2017**, *50*, 2789–2798.

[212] Meyer, L. V.; Schönfeld, F.; Müller-Buschbaum, K. *Chem. Commun.* **2014**, *50*, 8093–8108.

[213] Foucault-Collet, A.; Gogick, K. A.; White, K. A.; Villette, S.; Pallier, A.; Collet, G.; Kieda, C.; Li, T.; Geib, S. J.; Rosi, N. L.; Petoud, S. *Proc. Natl. Acad. Sci. U. S. A.* **2013**, *110*, 17199–17204.

[214] Wu, N.; Guo, H.; Wang, X.; Sun, L.; Zhang, T.; Peng, L.; Yang, W. *Colloids Surfaces A Physicochem. Eng. Asp.* **2020**, *616*, 126093.

[215] Islamoglu, T.; Atilgan, A.; Moon, S.-Y.; Peterson, G. W.; DeCoste, J. B.; Hall, M.; Hupp, J. T.; Farha, O. K. *Chem. Mater.* **2017**, *29*, 2672–2675.

[216] Lecoq, P. *Nucl. Instruments Methods Phys. Res. Sect. A Accel. Spectrometers, Detect. Assoc. Equip.* **2016**, *809*, 130–139.

[217] Birowosuto, M. D.; Cortecchia, D.; Drozdowski, W.; Brylew, K.; Lachmanski, W.;

Bruno, A.; Soci, C. *Sci. Rep.* **2016**, *6*, 37254.

[218] Zhu, W.; Ma, W.; Su, Y.; Chen, Z.; Chen, X.; Ma, Y.; Bai, L.; Xiao, W.; Liu, T.; Zhu, H.; Liu, X.; Liu, H.; Liu, X.; Yang, Y. *Light Sci. Appl.* **2020**, *9*, 112.

[219] Zhou, F.; Li, Z.; Lan, W.; Wang, Q.; Ding, L.; Jin, Z. *Small Methods* **2020**, *4*, 2000506.

[220] Liu, G.; Beitz, J. V. *The Chemistry of the Actinide and Transactinide Elements*, Springer, Heidelberg, **2006**.

[221] Liu, G.; Deifel, N. P.; Cahill, C. L.; Zhurov, V. V.; Pinkerton, A. A. *J. Phys. Chem. A*, **2012**, *116*, 855–864.

[222] Tsushima, S.; Götz, C.; Fahmy, K. *Chem. Eur. J.* **2010**, *16*, 8029–8033.

[223] Phillips, M. C.; Brumfield, B. E.; LaHaye, N.; Harilal, S. S.; Hartig, K. C.; Jovanovic, I. *Sci. Rep.* **2017**, *7*, 3784.

[224] Wang, Y.; Yin, X.; Liu, W.; Xie, J.; Chen, J.; Silver, M. A.; Sheng, D.; Chen, L.; Diwu, J.; Liu, N.; Chai, Z.; Albrecht-Schmitt, T. E.; Wang, S. *Angew. Chem., Int. Ed.* **2018**, *57*, 7883–7887.

[225] Wang, K.-X.; Chen, J.-S. *Acc. Chem. Res.* **2011**, *44*, 531–540.

[226] Volkringer, C.; Henry, N.; Grandjean, S.; Loiseau, T. *J. Am. Chem. Soc.* **2012**, *134*, 1275–1283.

[227] Xie, J.; Wang, Y.; Liu, W.; Yin, X.; Chen, L.; Zou, Y.; Diwu, J.; Chai, Z.; Albrecht-Schmitt, T. E.; Liu, G.; Wang, S. *Angew. Chem., Int. Ed.* **2017**, *56*, 7500–7504.

[228] Han, J.-M.; Xu, M.; Wang, B.; Wu, N.; Yang, X.; Yang, H.; Salter, B. J.; Zang, L. *J. Am. Chem. Soc.* **2014**, *136*, 5090–5096.

[229] Dong, X.; Hu, F.; Liu, Z.; Zhang, G.; Zhang, D. *Chem. Commun.* **2015**, *51*, 3892–3895.

[230] Han, J.-M.; Wu, N.; Wang, B.; Wang, C.; Xu, M.; Yang, X.; Yang, H.; Zang, L. *J. Mater. Chem. C* **2015**, *3*, 4345–4351.

[231] Liu, X.-Y.; Lustig, W. P.; Li, J. *ACS Energy Lett.* **2020**, *5*, 2671–2680.

[232] Lustig, W. P.; Wang, F.; Teat, S. J.; Hu, Z.; Gong, Q.; Li, J. *Inorg. Chem.* **2016**, *55*, 7250–7256.

[233] Gomez, G. E.; Marin, R.; Carneiro Neto, A. N.; Botas, A. M. P.; Ovens, J.; Kitos, A. A.; Bernini, M. C.; Carlos, L. D.; Soler-Illia, G. J. A. A.; Murugesu, M. *Chem. Mater.* **2020**, *32*, 7458–7468.

[234] Mondal, T.; Mondal, S.; Bose, S.; Sengupta, D.; Ghorai, U. K.; Saha, S. K. *J. Mater. Chem. C* **2018**, *6*, 614–621.

[235] Khatun, A.; Panda, D. K.; Sayresmith, N.; Walter, M. G.; Saha, S. *Inorg. Chem.* **2019**, *58*, 12707–12715.

[236] Shu, Y.; Ye, Q.; Dai, T.; Xu, Q.; Hu, X. *ACS Sens*. **2021**, *6*, 641–658.

[237] Andreo, J.; Priola, E.; Alberto, G.; Benzi, P.; Marabello, D.; Proserpio, D. M.; Lamberti, C.; Diana, E. *J. Am. Chem. Soc.* **2018**, *140*, 14144–14149.

[238] Lee, J.; Brewster, J. T.; Song, B.; Lynch, V. M.; Hwang, I.; Li, X.; Sessler, J. L. *Chem. Commun.* **2018**, *54*, 9422–9425.

[239] So, M. C.; Wiederrecht, G. P.; Mondloch, J. E.; Hupp, J. T.; Farha, O. K. *Chem. Commun.* **2015**, *51*, 3501–3510.

[240] Lee, J.; Farha, O. K.; Roberts, J.; Scheidt, K. A.; Nguyen, S. T.; Hupp, J. T. *Chem. Soc. Rev.* **2009**, *38*, 1450–1459.

[241] Shen, K.; Chen, X.; Chen, J.; Li, Y. *ACS Catal.* **2016**, *6*, 5887–5903.

[242] Huang, Y.-B.; Liang, J.; Wang, X.-S.; Cao, R. *Chem. Soc. Rev.* **2017**, *46*, 126–157.

[243] Chen, Y.-Z.; Zhang, R.; Jiao, L.; Jiang, H.-L. *Coord. Chem. Rev.* **2018**, *362*, 1–23.

[244] Liu, J.; Chen, L.; Cui, H.; Zhang, J.; Zhang, L.; Su, C.-Y. *Chem. Soc. Rev.* **2014**, *43*, 6011–6061.

[245] Li, B.; Chrzanowski, M.; Zhang, Y.; Ma, S. *Coord. Chem. Rev.* **2016**, *307*, 106–129.

[246] Dhakshinamoorthy, A.; Alvaro, M.; Garcia, H. *Chem. Commun.* **2012**, *48*, 11275–11288.

[247] García-García, P.; Müller, M.; Corma, A. *Chem. Sci.* **2014**, *5*, 2979–3007.

[248] Bernales, V.; Ortuño, M. A.; Truhlar, D. G.; Cramer, C. J.; Gagliardi, L. *ACS Cent. Sci.* **2018**, *4*, 5–19.

[249] Gascon, J.; Corma, A.; Kapteijn, F.; Llabrés i Xamena, F. X. *ACS Catal.* **2014**, *4*,

361–378.

[250] Farrusseng, D.; Aguado, S.; Pinel, C. *Angew. Chem., Int. Ed.* **2009**, *48*, 7502–7513.

[251] Dhakshinamoorthy, A.; Alvaro, M.; Corma, A.; Garcia, H. *Dalton Trans.* **2011**, *40*, 6344–6360.

[252] Corma, A.; García, H.; Llabrés i Xamena, F. X. *Chem. Rev.* **2010**, *110*, 4606–4655.

[253] Chughtai, A. H.; Ahmad, N.; Younus, H. A.; Laypkov, A.; Verpoort, F. *Chem. Soc. Rev.* **2015**, *44*, 6804–6849.

[254] Yang, Q.; Xu, Q.; Jiang, H.-L. *Chem. Soc. Rev.* **2017**, *46*, 4774–4808.

[255] Zhu, L.; Liu, X.-Q.; Jiang, H.-L.; Sun, L.-B. *Chem. Rev.* **2017**, *117*, 8129–8176.

[256] Ma, L.; Abney, C.; Lin, W. *Chem. Soc. Rev.* **2009**, *38*, 1248–1256.

[257] Zhao, S.-N.; Song, X.-Z.; Song, S.-Y.; Zhang, H.-J. *Coord. Chem. Rev.* **2017**, *337*, 80–96.

[258] Fujita, M.; Kwon, Y. J.; Washizu, S.; Ogura, K. *J. Am. Chem. Soc.* **1994**, *116*, 1151–1152.

[259] Wang, W.-D.; Bakac, A.; Espenson, J. H. *Inorg. Chem.* **1995**, *34*, 6034–6039.

[260] Mao, Y.; Bakac, A. *J. Phys. Chem.* **1996**, *100*, 4219–4223.

[261] Burrows, H. D.; Kemp, T. J. *Chem. Soc. Rev.* **1974**, *3*, 139–165.

[262] Thangavelu, S. G.; Cahill, C. L. *Inorg. Chem.* **2015**, *54*, 4208–4221.

[263] August Ridenour, J.; Cahill, C. L. *New J. Chem.* **2018**, *42*, 1816–1831.

[264] Leduc, J.; Frank, M.; Jürgensen, L.; Graf, D.; Raauf, A.; Mathur, S. *ACS Catal.* **2019**, *9*, 4719–4741.

[265] West, J. G.; Bedell, T. A.; Sorensen, E. J. *Angew. Chem., Int. Ed.* **2016**, *55*, 8923–8927.

[266] McGrail, B. T.; Pianowski, L. S.; Burns, P. C. *J. Am. Chem. Soc*. **2014**, *136*, 4797–4800.

[267] Mao, Y.; Bakac, A. *Inorg. Chem.* **1996**, *35*, 3925–3930.

[268] McCleskey, T. M.; Burns, C. J.; Tumas, W. *Inorg. Chem.* **1999**, *38*, 5924–5925.

[269] Nagaishi, R.; Katsumura, Y.; Ishigure, K.; Aoyagi, H.; Yoshida, Z.; Kimura, T.; Kato, Y. *J. Photochem. Photobiol. A Chem.* **2002**, *146*, 157–161.

[270] Kramer, G. M.; Dines, M. B.; Kaldor, A.; Hall, R.; McClure, D. *Inorg. Chem.* **1981**, *20*, 1421–1426.

[271] Miyake, C.; Yamana, Y.; Imoto, S.; Ohya-Nishiguchi, H. *Inorganica Chim. Acta*, **1984**, *95*, 17–21.

[272] Rofer-DePoorter, C. K.; DePoorter, G. L. *J. Inorg. Nucl. Chem.* **1977**, *39*, 631–634.

[273] Lyu, J.; Zhang, X.; Li, P.; Wang, X.; Buru, C. T.; Bai, P.; Guo, X.; Farha, O. K. *Chem. Mater.* **2019**, *31*, 4166–4172.

[274] Huang, Z.-W.; Hu, K.-Q.; Mei, L.; Kong, X.-H.; Yu, J.-P.; Liu, K.; Zeng, L.-W.; Chai, Z.-F.; Shi, W.-Q. *Dalton. Trans.* **2020**, *49*, 983–987.

[275] Li, P.; Goswami, S.; Otake, K.-I.; Wang, X.; Chen, Z.; Hanna, S. L.; Farha, O. K. *Inorg. Chem.* **2019**, *58*, 3586–3590.

[276] Xu, H.; Cao, C.-S.; Hu, H.-S.; Wang, S.-B.; Liu, J.-C.; Cheng, P.; Kaltsoyannis, N.; Li, J.; Zhao, B. *Angew. Chem., Int. Ed.* **2019**, *58*, 6022–6027.

[277] Shannon, R. D.; Prewitt, C. T. *Acta Crystallogr. Sect. B Struct. Crystallogr. Cryst. Chem.* **1969**, *25*, 925–946.

[278] Kim, J.; Kimg, S.-N.; Jang, H.-G.; Seo, G.; Ahn, W.-S. *Appl. Catal., A* **2013**, *453*, 175−180.

[279] Beyzavi, M. H.; Stephenson, C. J.; Liu, Y.; Karagiaridi, O.; Hupp, J. T.; Farha, O. K. *Front. Energy Res.* **2015**, *2*, 1–10.

[280] Mondloch, J. E.; Katz, M. J.; Isley, W. C.; Ghosh, P.; Liao, P.; Bury, W.; Wagner, G. W.; Hall, M. G.; DeCoste, J. B.; Peterson, G. W.; Snurr, R. Q.; Cramer, C. J.; Hupp, J. T.; Farha, O. K. *Nat. Mater.* **2015**, *14*, 512–516.

[281] Beyzavi, M. H.; Klet, R. C.; Tussupbayev, S.; Borycz, J.; Vermeulen, N. A.; Cramer, C. J.; Stoddart, J. F.; Hupp, J. T.; Farha, O. K. *J. Am. Chem. Soc.* **2014**, *136*, 15861–15864.

[282] Jennifer, S. J.; Jana, A. K. *Cryst. Growth Des.* **2017**, *17*, 5318–5329.

[283] Yu, Z.-T.; Liao, Z.-L.; Jiang, Y.-S.; Li, G.-H.; Li, G.-D.; Chen, J.-S. *Chem. Commun.* **2004**, 1814–1815.

[284] Wang, H.; Chang, Z.; Li, Y.; Wen, R.-M.; Bu, X.-H. *Chem. Commun.* **2013**, *49*, 6659–6661.

[285] Liao, Z.-L.; Li, G.-D.; Bi, M.-H.; Chen, J.-S. *Inorg. Chem.* **2008**, *47*, 4844–4853.

[286] Li, H.-H.; Zeng, X.-H.; Wu, H.-Y.; Jie, X.; Zheng, S.-T.; Chen, Z.-R. *Cryst. Growth Des.* **2015**, *15*, 10–13.

[287] Yu, Z.-T.; Liao, Z.-L.; Jiang, Y.-S.; Li, G.-H.; Chen, J.-S. *Chem. Eur. J.* **2005**, *11*, 2642–2650.

[288] Ji, P.; Feng, X.; Oliveres, P.; Li, Z.; Murakami, A.; Wang, C.; Lin, W. *J. Am. Chem. Soc.* **2019**, *141*, 14878–14888.

[289] Epp, K.; Semrau, A. L.; Cokoja, M.; Fischer, R. A. *ChemCatChem*, **2018**, *10*, 3506–3512.

[290] Hu, Z.; Zhao, D. *CrystEngComm*. **2017**, *19*, 4066–4081.

[291] Cai, M.; Chen, G.; Qin, L.; Qu, C.; Dong, X.; Ni, J.; Yin, X. *Pharmaceutics* **2020**, *12*, 232.

[292] Boros, E.; Packard, A. B. *Chem. Rev.* **2019**, *119*, 870–901.

[293] Warren, I. H.; Price, C. E. *Can. Met. Quart.* **1964**, *3*, 183–196.

[294] Kamimoto, M.; Takahashi, Y.; Mukaibo, T. *J. Nucl. Mater.* **1976**, *59*, 149–157.

[295] Didchenko, R.; Gortsema, F. P. *Inorg. Chem.* **1963**, *2*, 1079–1080.

[296] Warren, I. H.; Price, C. E. *Can. Met. Quart.*, **1964**, *3*, 245–256.

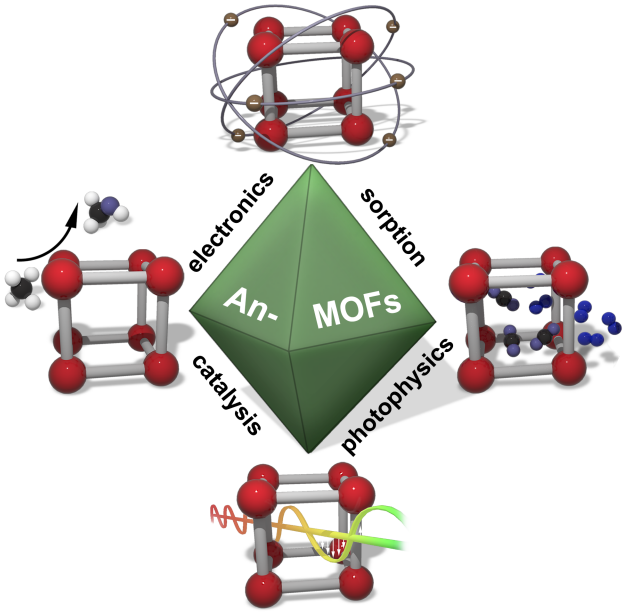

Scheme 5.1. An overview of the sections related to actinide-containing MOFs discussed in this chapter.

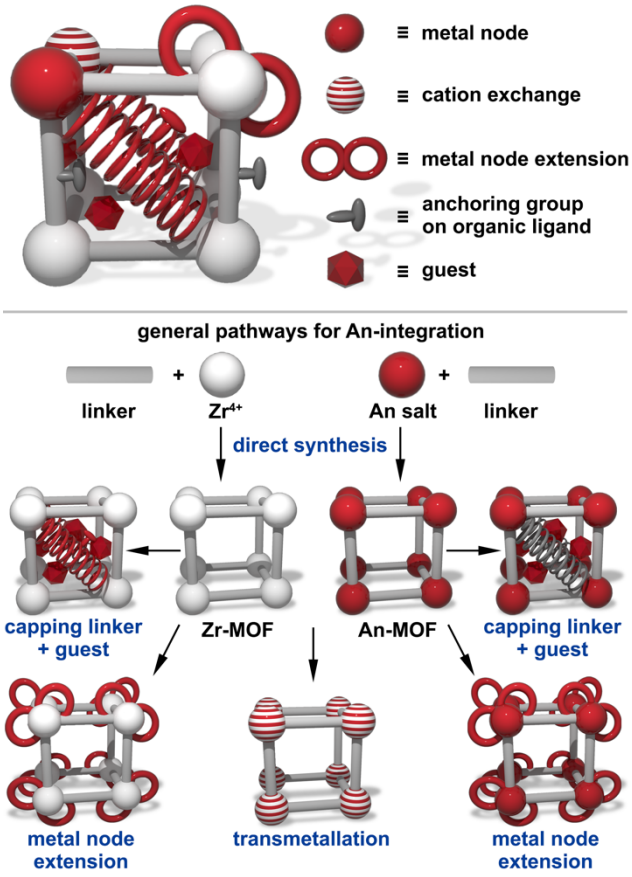

Figure 5.1. (*top*) A schematic representation of a MOF with pathways for actinide integration highlighted in red. (*bottom*) A schematic representation of framework modularity for actinide integration utilizing Zr- and An-based MOFs as precursors. The integrated actinides are displayed in red. Reproduced from ref. 78 with permission from American Chemical Society, Copyright 2017.

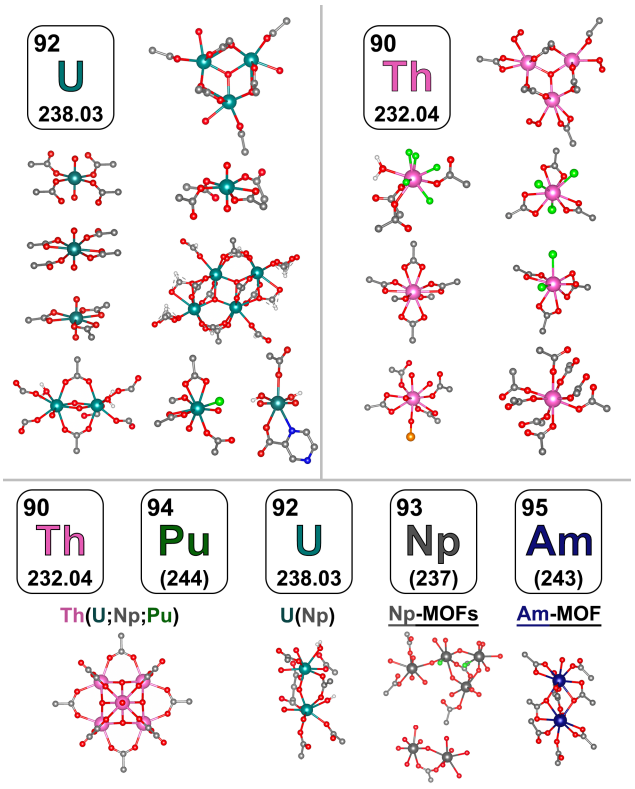

Figure 5.2. Secondary building units of several examples of Th, U, Np, Pu, and Am-based MOFs. The teal, pink, dark gray, dark blue, light gray, red, blue, white, and green spheres correspond to uranium, thorium, neptunium, americium, carbon, oxygen, nitrogen, hydrogen, and halogen atoms, respectively.

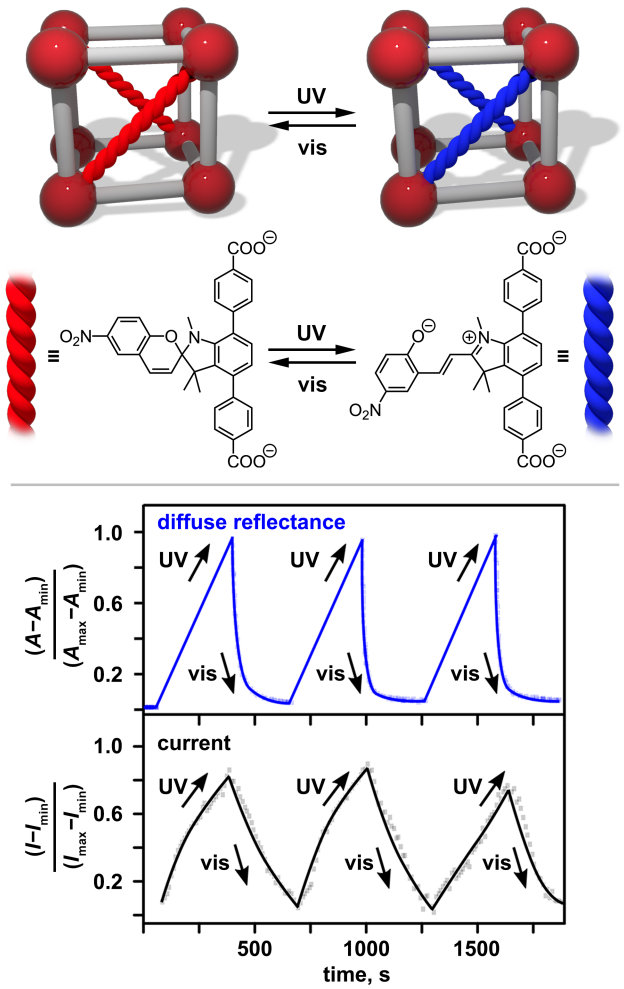

Figure 5.3. (*top*) Schematic representation of spiropyran photoswitching in Th-based MOFs. (*bottom*) Normalized optical and current cycling of photochromic Th-MOF through alternation of UV- (λ_{ex} = 365 nm) and visible- (λ_{ex} = 590 nm) irradiation. I_{max} and I_{min} = the maximum and minimum current values, respectively; A_{max} and A_{min} = the maximum and minimum absorption values (converted from reflectance via the Kubelka-Munk function), respectively. Reproduced from ref. 88 with permission from John Wiley and Sons, Copyright 2021.

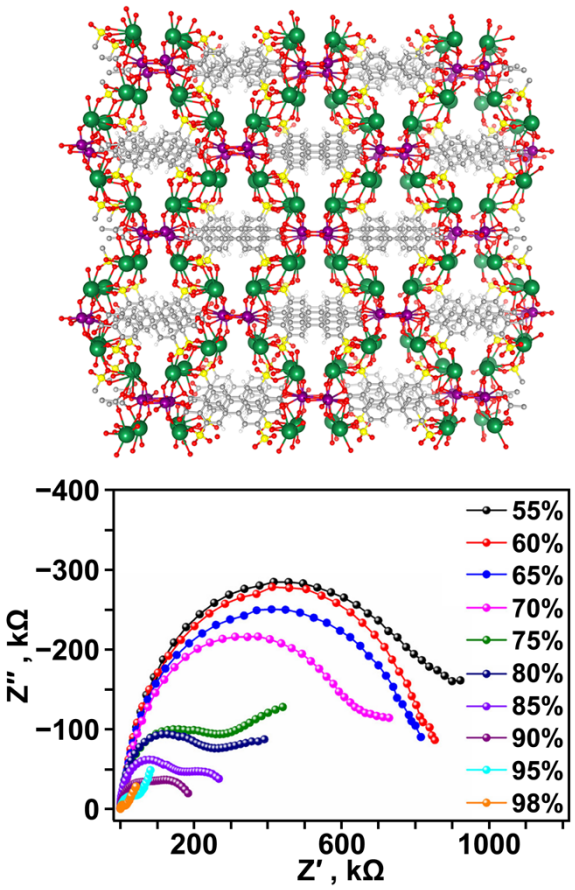

Figure 5.4. (*top*) X-ray crystal structure of $K_2(UO_2)(\mu_3\text{-}O)(BPDSDC)_{0.5}(H_2O)_2$ and (*bottom*) Nyquist plots of $K_2(UO_2)(\mu_3\text{-}O)(BPDSDC)_{0.5}(H_2O)_2$ collected under varied relative humidity percentages at 85 °C. The gray, white, yellow, red, purple, and green spheres represent carbon, hydrogen, sulfur, oxygen, uranium, and potassium, respectively. Reproduced from ref. 97 with permission from American Chemical Society, Copyright 2020.

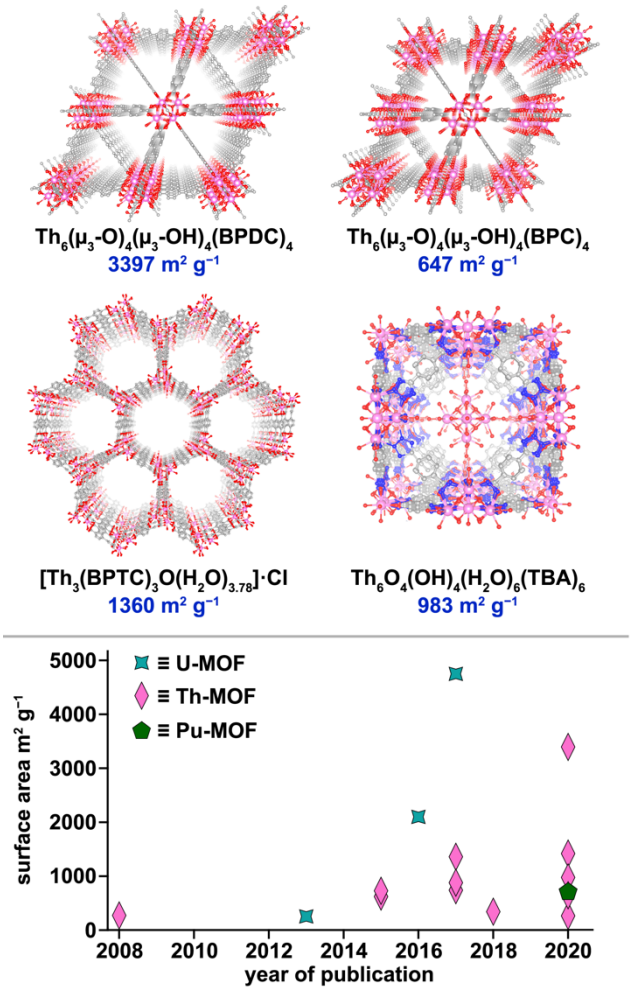

Figure 5.5. (*top*) X-ray crystal structures of $Th_6(\mu_3\text{-}O)_4(\mu_3\text{-}OH)_4(BPDC)_6$, $Th_6(\mu_3\text{-}O)_4(\mu_3\text{-}OH)_4(BDC)_6$, $[Th_3(BPTC)_3O(H_2O)_{3.78}]\cdot Cl$, and $Th_6O_4(OH)_4(H_2O)_6(TBA)_6$. The pink, blue, gray, and red, spheres represent thorium, nitrogen, carbon, and oxygen atoms, respectively. (*bottom*) Literature analysis of the surface areas of several reported An-MOFs over time.[3,59,66,78,134,138,159–163]

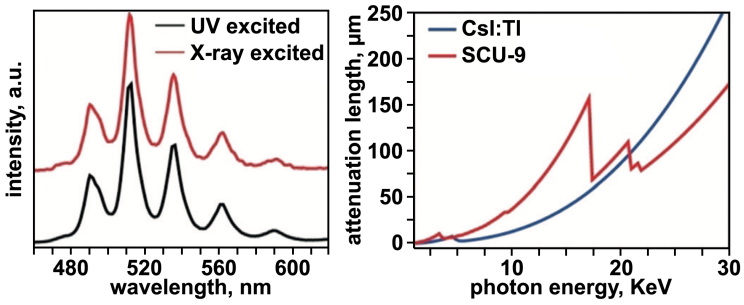

Figure 5.6. (*left*) Emission profile of $UO_2(HBTA)(H_2O)$ under UV (black) and X-ray (red) excitation. (*right*) X-ray attenuation lengths for $UO_2(HBTA)(H_2O)$ (red) and CsI:Tl (dark blue) in the X-ray energy region ranging from 30 eV to 30 keV. Reproduced from ref. 224 with permission from John Wiley and Sons, Copyright 2018.

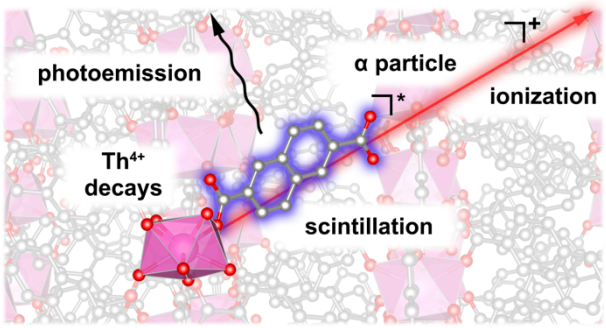

Figure 5.7. Autoluminescence in $Th_2(NDC)$ occurring through emission of an alpha particle from a thorium cation, subsequent ionization of the scintillator (NDC^{2-}), followed by core-hole recombination that leaves the system in an electronic excited state, and then visible light photoemission. Reproduced from ref. 237 with permission from American Chemical Society, Copyright 2018.

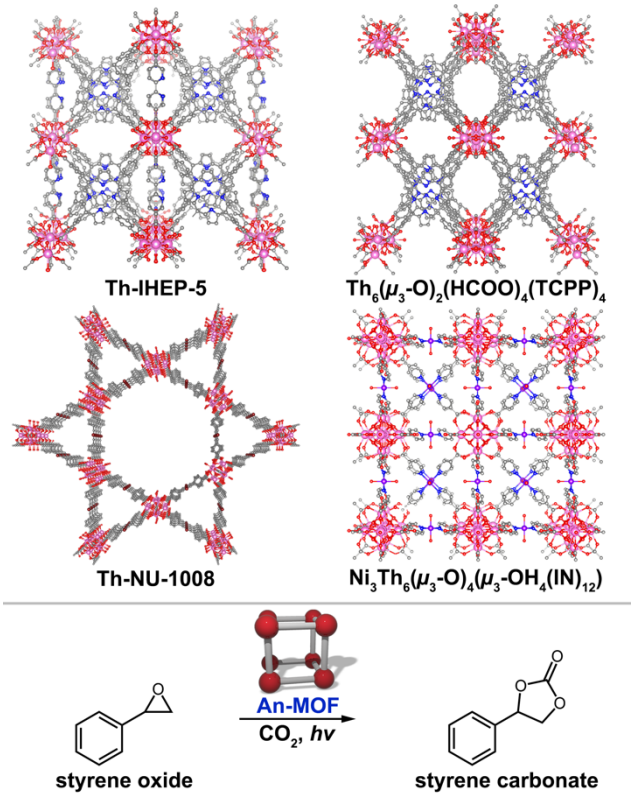

Figure 5.8. (*top*) X-ray crystal structures of Th-IHEP-5, $Th_6(\mu_3\text{-}O)_2(HCOO)_4(TCPP)_4$, Th-NU-1008, and $Ni_3Th_6(\mu_3\text{-}O)_4(\mu_3\text{-}OH)_4(IN)_{12}\cdot(OH)_6$. The pink, purple, dark red, blue, gray, and red, spheres represent thorium, nickel, bromine, nitrogen, carbon, and oxygen atoms, respectively. (*bottom*) A model photocatalytic CO_2 cycloaddition reaction that has been performed with An-MOFs as a catalyst.[273,274,275,276]

CHAPTER 6

HETEROMETALLIC ACTINIDE-CONTAINING PHOTORESPONSIVE METAL-ORGANIC FRAMEWORKS: DYNAMIC AND STATIC TUNING OF ELECTRONIC PROPERTIES

Martin, C. R.; Leith, G. A.; Kittikhunnatham, P.; Park, K. C.; Ejegbavwo, O. A.; Mathur, A.; Callahan, C. R.; Desmond, S. L.; Keener, M. R.; Ahmed, F.; Pandey, S.; Smith, M. D.; Phillpot, S. R.; Greytak, A. B.; Shustova N. B. *Angew. Chem. Int. Ed.* **2021**, *60*, 8072–8080.

Chapter abstract. Acquiring fundamental knowledge of properties of actinide-based materials is a necessary step to create new possibilities for addressing the current challenges in the nuclear energy and nuclear waste sectors. In this report, we established a photophysics–electronics correlation for actinide-containing metal-organic frameworks (An-MOFs) as a function of excitation wavelength, for the first time. A stepwise approach for dynamically modulating electronic properties was applied for the first time towards actinide-based heterometallic MOFs through integration of photochromic linkers. Optical cycling, modeling of density of states near the Fermi edge, conductivity measurements, and photoisomerization kinetics were employed to shed light on the process of tailoring optoelectronic properties of An-MOFs. Furthermore, the first photochromic MOF-based field-effect transistor, in which the field-effect response could be changed through light exposure, was constructed. As a demonstration, the change in current upon light exposure was sufficient to operate a two-LED fail-safe indicator circuit.

INTRODUCTION

Exploring optical, catalytic, and electronic properties of actinide-containing metal-organic frameworks (An-MOFs) is paramount to addressing the growing challenge of radioactive waste accumulation.[1–10] However, unlocking the full potential of An-MOFs for future applications requires acquiring extensive fundamental knowledge relative to their behavior, which is an imperative first step, and thus, is the primary focus of the presented studies.[11–22] Hierarchical hybrids, such as metal-organic frameworks (MOFs), allow for performing studies of material properties in a stepwise manner by varying one parameter at a time (Scheme 6.1a). For instance, they serve as a multifaceted platform for the integration of a second or third metal, guests, or organic linkers through various pathways

(e.g., backbone, side group, or capping linker) with the possibility for complete replacement of one linker by another.[23–26] Merging the distinct advantages of MOFs (e.g., ultra-high porosity, crystallinity, robustness, and modularity) with the characteristics of actinides (e.g., large cations and *f*-electrons) could be the key to repurposing radionuclide waste or even extend future applications of actinide-based hybrids to the practical realm. Although there are clear benefits to this approach, the majority of literature reports focus on crystallographic aspects as the first step for understanding the structure of actinide-hybrids, and only very recently have studies providing a more fundamental glimpse into material properties emerged.[27–30] This aspect highlights that the field of actinide-containing metal-organic materials is a relatively new direction that will grow substantially during the next decade. This sector faces challenges such as the development of safety protocols and material instability, but foreshadows the possibility of solving challenges related to radioactive waste accumulation through new directions focused on practical applications.[31]

Herein, we tailor optoelectronic properties of heterometallic An-MOFs, M^{IV}-MOFs (M = U and Th), through the design of heterometallic nodes, integration of stimuli-responsive organic moieties, and inclusion of redox-active guests (Scheme 6.1). Two types of guest molecules, iodine and 7,7,8,8-tetracyanoquinodimethane (TCNQ), have been selected for tuning MOF electronic structures due to two different reasons: synthetic limitations imposed by scaffold stability and redox activity as discussed below.[32–38]

We consider static and dynamic tailoring of electronic properties through second metal integration ("irreversible" modifications, i.e., static) and photochromic linker installation allowing alternation of an electronic profile as a function of an excitation wavelength (i.e., dynamic). To the best of our knowledge, there are no previous reports on

dynamically controlled electronic behavior of photoresponsive An-MOFs, as well as no reports on the preparation of heterometallic photochromic MOFs in general; therefore, it is a pressing goal to address this gap in knowledge through a systematic approach that is presented in this work. In particular, we harnessed the dynamic control of electronic properties and established a photophysics–electronic structure relationship for photoresponsive An-MOFs by analyzing changes in the electronic and absorption profiles as a function of an excitation wavelength. We delved further into tuning the electronic properties of photochromic MOFs by comparing *d*- and *f*-block elements (Zr^{4+} versus Th^{4+} and U^{4+}) for the first time. Furthermore, we gained insight into the density of states (DOS) near the Fermi edge using theoretical modeling that supports our experimental findings. The presented studies also provide the first insight into photo- isomerization rates within An-MOFs containing photoresponsive units. Lastly, we visualized our findings through engineering the first photochromic MOF-based field-effect transistor (FET) as well as its integration into a two-LED fail- safe circuit.

RESULTS AND DISCUSSION

Due to safety specifications required for working with radionuclides such as uranium and thorium, we performed preliminary studies to determine reliable experimental conditions using isostructural, but nonradioactive, Zr^{IV}-based frameworks. Overall, coordinative immobilization of photo- chromic moieties inside a framework requires: (i) accommodation of structural rearrangements of the photoresponsive unit accompanied with the photoisomerization process, (ii) preservation of framework structural integrity upon irradiation with light after several optical cycles, and (iii) a synthetically feasible pathway for integration of a photochromic unit into a scaffold (e.g., through postsynthetic

modification). Moreover, the selected photochromic moiety should be capable of fast photoisomerization inside a scaffold allowing for dynamic control of photophysical behavior with the possibility of a pronounced effect on material properties.[39,40] Therefore, prior to working with heterometallic An-MOFs, we initiated our studies using a topologically analogous Zr- MOF, $Zr_6(OH)_8O_4(Me_2BPDC)_4$ (Zr-MOF; H_2Me_2BPDC = 2,2'-dimethylbiphenyl-4,4'dicarboxylic acid),[23] that satisfies the aforementioned criteria. In particular, Zr-MOF possesses ≈ 16 Å pores that can accommodate photoisomerization of the photoresponsive fragments. In addition, the metal nodes of $Zr_6(OH)_8O_4(Me_2BPDC)_4$ are unsaturated (i.e., containing less than 12 linkers per metal node), allowing for postsynthetic installation of the selected photochromic linker. As a photoresponsive component, we have chosen a spiropyran- based linker, 4,4'-(1',3',3'-trimethyl-6-nitrospiro[chromene-2,2'-indoline]-4',7'-diyl)dibenzoic acid (H_2TNDA, Figure 6.1), that has a backbone consisting of three phenyl rings to match the size of the installation pocket in the MOF matrix[41,42] and terminal carboxylate groups that are necessary for coordination to the metal nodes. Selection of spiropyran-based building blocks as a class of photochromic molecule for our studies was due to the fact that they can undergo rapid photoisomerization inside of porous frameworks (otherwise inaccessible in the solid state),[41,43] leading to significant dynamic changes in material performance.[39, 40] Spiropyran → merocyanine conversion can be induced by applying UV-irradiation, and the reversible transformation occurs under visible light.[44, 45]

The mechanism of spiropyran photoisomerization is based on a heterocyclic C−O bond cleavage followed by a *cis-trans* isomerization to form a highly colored photoisomer, merocyanine (Figure 6.1).[44, 45] Substantial differences in properties of photoisomers arise

from alternation of a neutral charge and orthogonal geometry (spiropyran) and a charge-separated planar zwitterion (merocyanine).[44, 45]

The photoresponsive H_2TNDA molecule was prepared using a seven-step procedure (see the experimental section for synthetic details, Scheme 6.2). The spiropyran linker, H_2TNDA, and all its precursors were characterized by ^{13}C and ^{1}H nuclear magnetic resonance (NMR) and Fourier- transform infrared (FTIR) spectroscopies, and high-resolution mass spectrometry (Figures 6.5–6.7). Crystals of H_2TNDA and the ester precursor (Me_2TNDA) were analyzed using single crystal X-ray diffraction (Table 6.1 and Figures 6.8 and 6.9). To probe the possibility for integration of the prepared H_2TNDA linker, a postsynthetic installation procedure[23,26,30] was carried out: Zr-MOF was heated in a H_2TNDA solution for three days (see experimental section for details). Installation was possible due to the fact that Zr-MOF meets the structural criteria: possessing unsaturated metal nodes that are necessary for coordinative ligand installation and having a suitable pocket size of 15.1 Å[30] which correlates with the length of the H_2TNDA linker (15.6 Å, the distance between the centroids of the oxygen atoms of the terminal carboxylate groups). As a result, two compositions with the general formula M-L% (M = the metal and L = the amount of $TNDA^{2-}$ linker installed), Zr-33 % and Zr-65 %, were prepared (Figure 6.10). Our PXRD studies demonstrated that both frameworks maintain structural integrity upon UV-irradiation (Figures 6.11 and 6.12). Iodine and TCNQ were selected as guest molecules to further tune the electronic properties of the prepared MOFs. The rationale behind the guest choice and experimental details are described below.

The selected actinide-containing framework, $Th_6(OH)_8O_4(Me_2BPDC)_4$ (Th-MOF), was prepared by heating a solution of $Th(NO_3)_4$ and H_2Me_2BPDC in DMF (with the

addition of trifluoroacetic acid at 120 °C for 3 days). Heterometallic $Th_{4.77}U_{1.23}(OH)_8O_4(Me_2BPDC)_4$ (Th_5U-MOF) was prepared by transmetallation of $U_6(OH)_8O_4(Me_2BPDC)_4$ (U-MOF) in a solution of $Th(NO_3)_4$ in DMF. X-ray photoelectron spectroscopy (XPS) studies demonstrated that uranium has a +4 oxidation state in the parent monometallic U-MOF that was preserved upon integration of Th^{IV} (Figures 6.13 and 6.14), and the ratio of uranium to thorium was determined by inductively coupled plasma mass spectrometry (ICP-MS).[24] Interestingly, the reverse transmetallation process (Th-to-U) did not occur, allowing us to hypothesize that one of the driving forces for solid-state metathesis to occur is the oxidation of uranium (from +4 to +6), forcing its removal from the metal node.

Both monometallic and heterometallic actinide-based frameworks satisfy the aforementioned criteria for installation of a photochromic unit. Similar to the zirconium analog, metal nodes in Th-MOF and Th_5U-MOF are unsaturated, providing a pathway for H_2TNDA integration (Figure 6.2). The pore size in the monometallic and heterometallic actinide- based frameworks are close to 16 Å that is sufficient for spiropyran → merocyanine photoisomerization.[41] Initially, we focused on installation of the photoresponsive H_2TNDA moiety into Th-MOF due to its higher stability in comparison with heterometallic Th_5U-MOF. The integration of a photochromic linker, H_2TNDA, inside a framework was performed through heating of Th-MOF in a solution of H_2TNDA in DMF at 75 °C and 85 °C for three days, resulting in formation of Th-34% and Th-65%, respectively. Using the established experimental conditions for monometallic Zr- and Th-frame- work preparation, while also considering the difference in framework stability, we were able to synthesize Th_5U-50%. Our PXRD studies demonstrated that all An-MOFs

maintain structural integrity upon UV-irradiation (Figures 6.17–6.20). The amount of the installed linker was determined from frameworks that underwent a digestion procedure using an acidic treatment[41] and then we subsequently performed ^{1}H NMR spectroscopy to calculate the ratio of H_2TNDA to H_2Me_2BPDC (see experimental section for details; Figures 6.21 and 6.22).

For spectroscopic characterization of the photoisomerization process of the photoresponsive spiropyran moiety coordinatively immobilized inside a framework, we used diffuse reflectance (DR) spectroscopy.[43] The spiropyran → merocyanine conversion inside a framework upon 365-nm excitation resulted in a bathochromic shift (λ_{max} = 570 nm) detected in the DR profile as shown in Figures 6.23–6.27. The observed changes are in line with previous reports for spiropyran-based materials.[44–49] Using the collected DR data, we also performed a Tauc plot analysis for evaluation of changes in the optical band gap under the assumption of direct allowed transitions.[30,50–52] As a result, by fitting the linear region of the Tauc plots to the onset of the photon energy, we revealed that the optical band gap narrows upon exposure to one minute of UV-irradiation for photoresponsive frameworks (Figure 6.3, Figures 6.23–6.27, and Table 6.2). For instance, a reduction of the optical band gap from 2.1 eV to 2.0 eV was detected for Th-65% upon in situ UV-irradiation (Figure 6.3c). Evaluation of PXRD patterns of Th-34%, Th-65%, and Th_5U-50% before and after UV-irradiation revealed preservation of framework crystallinity (Figures 6.17–6.20). To provide further insight into changes in the electronic structure of photoresponsive An-MOFs, theoretical calculations of the DOS[43,53] near the Fermi edge were employed. Using the Vienna ab initio Simulation Package (VASP) and GGA-PBE level of theory (+U corrections for U), DOS calculations were performed for frameworks

containing spiropyran and merocyanine linkers including simulation of the truncated MOF models for M'-MOF, M'-MOF(spiropyran), and M'- MOF(merocyanine), where M' = Zr, Th, and Th/U (Figures 6.30–6.34 and Table 6.3). Initially, we evaluated models of spiropyran and merocyanine linkers themselves (Figure 6.28) and then extended the DOS calculations to truncated models of photochromic MOFs (Figures 6.29–6.34). The electronic structure calculations revealed that the frontier orbitals nearest to the Fermi level for spiropyran- and merocyanine-containing MOFs were localized on the spiropyran or merocyanine linkers, respectively (Figure 6.3a). In particular, the highest occupied molecular orbital (HOMO) was formed by C($2p_z$) orbitals and hybridized by N($2p_z$) orbitals, and the lowest unoccupied molecular orbital (LUMO) was mostly contributed by O($2p_y$) orbitals and hybridized by N($2p_y$) and C($2p_y$) orbitals. The dominating character of the DOS of frameworks containing *d*- or *f*-block elements was associated with the integrated photochromic linkers. Indeed, in the case of Th_5U-MOF with spiropyran or merocyanine linkers, even with varying positions of the uranium cation in the metal node (Figure 6.34), the frontier orbitals were identical to the ones found in photochromic Th- and Zr-MOFs (Figure 6.3a). In contrast to the photochromic actinide frameworks, the DOS near the Fermi edge of non-photo- responsive heterometallic Th/U-MOFs originate mainly from the uranium 5*f*-orbitals, whereas the DOS above and near the Fermi edge (associated with the conduction band) are composed of uranium and thorium 5*f*-orbitals. Thus, for the first time, theoretical modeling allowed us to reveal a fundamental difference in electronic structures of non-photoresponsive and photochromic actinide-based MOFs.

To establish a photophysics-electronics correlation, we combined time-resolved DR spectroscopic studies with conductivity measurements. For the latter, we used a home-

built in situ 2-contact probe pressed-pellet setup (2C3PS) that allowed for simultaneous irradiation of An-MOFs while measuring the flow of current at a sweep of applied voltages (details in the experimental section).[43] For DR measurements in this instance, the sample background was initially subtracted in order to visualize only the changes resulting from the spiropyran photoisomerization process. A mounted high-powered LED (λ_{ex} = 365 nm) was used to irradiate the samples in situ for five minutes prior to measurements, and then the sample underwent photoinduced attenuation for five minutes (see the experimental section for more details). Similarly, for electronic measurements, a sample was loaded into the 2C3PS, and a constant voltage of 1 V was applied. Alternating in situ irradiation with 365-nm and 590-nm light (irradiation time for both wavelengths was five minutes) was used to induce reversible photoisomerization of a photochromic moiety. This procedure was performed for several optical cycles, and the rates were extrapolated by fitting the data with a first-order rate equation (Figures 6.3b and 6.35).[54] The rate of optical attenuation for Th-34 % (i.e., merocyanine → spiropyran conversion inside the MOF) was estimated to be 3.9×10^{-1} s $^{-1}$ which is in line with the measured rate of the spiropyran moiety integrated inside Zr-33 % (1.53×10^{-1} s $^{-1}$). Modulation of electronic properties upon alternation of 365-nm and 590-nm excitation wavelengths was explored by monitoring changes in conductivity. Indeed, for both mono- metallic and heterometallic frameworks containing *d*- or *f*-block elements, integration of a photoresponsive unit allowed us to study conductivity as a function of an excitation wavelength. As a control experiment, we performed studies on the parent scaffolds (i.e., non-photochromic MOFs) and, as expected, no changes in electronic properties were detected. Although integration of spiropyran moieties inside frameworks allowed us to dynamically control electronic behavior of the

material, a significant "static" conductivity enhancement was achieved through integration of a second actinide metal, U^{4+} inside Th-MOF. Indeed, a 31-fold increase in conductivity value was measured for Th_5U-MOF in comparison with the parent Th-MOF. The measurements of the U-MOF were challenging due to instability of the sample, even under anaerobic conditions. Integration of spiropyran units inside Th_5U-MOF also allowed us to observe conductivity modulation (Figure 6.2 and Table 6.4). An additional avenue for tailoring electronic behavior of actinide-containing scaffolds relies on guest integration inside a scaffold. As mentioned in the introduction, two types of guest molecules, iodine and TCNQ, were selected to tune MOF electronic structures due to two different reasons: synthetic limitations imposed by scaffold stability and redox activity.[32,33] Iodine doping in porous materials typically exploits a charge transfer (CT) mechanism that introduces a labile charge transport material that is affected by the microenvironment and redox activity (I2 and TCNQ).[55–60] For instance, it has been reported that iodine doping in porous materials resulted in enhanced conductivity due to I_2-ligand interactions (e.g., CT complex formation),[61,62] a Grotthuss-like charge transport mechanism,[63–65] or through metal oxidation in framework nodes.[55,66] In the presented studies, Th^{4+} and Zr^{4+} in metal nodes cannot be further oxidized, and therefore, conductivity enhancement likely originates from I_2-ligand interactions.[61,62] In a similar vein, TCNQ is a well-studied electron acceptor and introduction of which commonly results in the formation of CT complexes.[67–69] A number of literature reports have demonstrated that incorporation of TCNQ in MOFs can enhance conductivity.[56,57,67] In our report, we used TCNQ as a guest in MOFs with Th^{4+} and Zr^{4+} metal nodes that are resistant to further oxidation and as such, the guest-guest or ligand-guest interactions would likely be the primary mode of conductivity enhancement.

Experimental measurements for TCNQ-integrated Th-MOF (2.4 TCNQ molecules per pore determined using the digestion procedure followed by ^{1}H NMR spectroscopic analysis) revealed a 66-fold increase in conductivity compared to the parent Th-MOF, which is in line with the data obtained for TCNQ-integrated Zr-MOF and expected based on literature reports.[70] We also anticipated that changes between photoisomers with vastly different dipole moments upon irradiation could also affect CT processes,[41,44] and changes in conductivity could reveal it. Therefore, we carried out experiments to measure the conductivity of photochromic actinide frameworks containing redox-active guest moieties (TCNQ@Th-65%). As a result, we were able to modulate the conductivity value by 55% upon alternating excitation wavelength. Expansion of our trials on TCNQ inclusion into the heterometallic actinide framework was limited by the framework stability. Therefore, we had to select an alternative synthetic route that required less rigorous conditions for guest inclusion. We chose iodine since its incorporation could be performed through iodine vapor exposure, in contrast to rigorous heating (75 °C) for three days required for TCNQ immobilization. Specifically, an uncapped 0.5-dram vial (containing 8.0 mg of washed MOF) was placed inside a 20-mL vial that was charged with iodine crystals, sealed, and left undisturbed for 72 hours. The quantity of iodine adsorbed was determined by ICP-MS after an extensive washing procedure (Table 6.5). Conductivity measurements on an iodine-doped framework, I_2@Th-MOF, showed a significant enhancement in conductivity: 50-fold for I_2@Th-MOF compared to that of Th-MOF. Dynamic modulation of the electronic properties could also be achieved through spiropyran-linker integration (Table 6.4). Notably, all measurements were performed on bulk powders. Similar to the monometallic Th-containing framework, integration of iodine into heterometallic Th_5U-

50% led to changes in electronic properties that were detected through conductivity enhancement of I_2@Th_5U-50 % versus Th_5U-MOF (Table 6.4).

To visualize the differences in electronic behavior of photoresponsive MOFs (from $TNDA^{2-}$ isomerization), we built a FET (Scheme 6.1b) using our MOF as the semiconducting layer. To prepare the FET, the MOF was deposited between the electrodes on a home-built chip (Scheme 6.1b, see the experimental section for details) by drop-casting a DMF suspension of MOF crystals. Due to the safety protocols and limitations associated with Th- and U-containing frameworks, we utilized a Zr-MOF as a model to illustrate the optoelectronic behavior of photochromic frameworks. A p-type gate voltage response was observed for the FET prepared with TCNQ@Zr-65 % (drain voltage = 5 V). Interestingly, the drain current could be modulated with applied gate voltages and by UV excitation. Specifically, sweeps of gate voltage (−10 V to −5 V) were measured in the dark, and after five minutes of UV excitation, we observed a shift to a less negative threshold voltage and increased transconductance following UV exposure (Figure 6.4).

We exploited the concept of tunable conductivity observed in photochromic MOFs and facilitated a guest-induced field-effect response, each of which has previously been considered independently in other MOFs,[43,70] to build a “fail- safe” circuit powered by our TCNQ@Zr-65%-FET (Scheme 6.1c). As a model system to detect and report hazardous conditions, the circuit has a constantly illuminated red LED (indicating flow of current to a target device) and a “switchable” green LED that toggles as a function of UV stimulus (Figures 6.4a and b). Specifically, for a low total drain current, most of the current flows through the red LED due to its smaller forward threshold voltage. As the drain current increases, the voltage drop across the red LED and its series resistor causes the green LED

to come into forward conduction, so that the ratio of the light intensity varies sharply with the total current. We verified the operation of the circuit by separately measuring the current–voltage curves of the two LEDs (Figures 6.4a and 6.50) and then connected it in series with the TCNQ@Zr-65%-FET. The circuit showed constant illumination of a lower biased red LED under a set gate voltage (−5 V); however, upon 365-nm irradiation, the green LED lit up, indicating electronic property modulation under 365-nm irradiation. Importantly, the change in drain current was sufficiently large to drive noticeable changes in the output of the LED circuit with no further amplification required. This proof-of-concept study portends the possibility for orthogonal control of electronic devices by using photochromic MOFs as their active elements, responding both to an applied electric field and light.

To confirm that the observed changes were due to the photoresponsive moieties ($TNDA^{2-}$), we performed control experiments with Zr-MOF, Zr-65%, and TCNQ@Zr-MOF. As expected, utilization of Zr-MOF did not result in any changes to the current during modulation of the gate voltage (− 10 V to 5 V) in the dark or under UV-irradiation (Figure 6.4c). On the other hand, Zr-65% showed changes in current as a function of UV excitation, but there was no field effect observed, regardless of applied gate voltage. The TCNQ-containing framework, TCNQ@Zr-MOF, showed a discernible field effect upon applying a range of gate voltages; however, the gate-dependence behavior was restricted exclusively to applied gate voltage and not to UV-irradiation. Thus, these experiments demonstrated that cur- rent could only be simultaneously controlled via light and an applied gate voltage using photochromic frameworks.

SUMMARY

The aforementioned results demonstrated the first preparation of photochromic monometallic and heterometallic actinide-containing crystalline scaffolds. Tunability of their electronic properties can be realized by harnessing framework modularity through a stepwise approach (e.g., integration of photoswitches, secondary metal integration, and guest incorporation). Notably, the relationship between photochromic An-MOFs photophysical properties and electronic structure as a function of excitation wavelength was revealed for the first time. Furthermore, the presented studies provide the first insight into photoisomerization rates within An-MOFs containing photoresponsive units. This work also sheds light on the distinct effect that *d*- and *f*-block elements have on the electronic structure of crystalline scaffolds. Theoretical analysis probing DOS near the Fermi edge of photoresponsive An-MOFs indicated that the photochromic linker contribution dominated in contrast to non-photochromic actinide- based frameworks, in which DOS near the Fermi edge originate mainly from the actinide 5*f*-orbitals. To visualize the observed dynamic control of electronic properties, we designed a FET device for orthogonal control of drain current due to incorporation of photochromic scaffolds. Thus, this proof-of-concept study showcases a novel way to utilize a photochromic MOF to control the FET drain current. Furthermore, we were able to design a two-LED fail-safe circuit utilizing photochromic MOFs as the FETs' semiconducting layer. To summarize, only the surface of synthetic methodologies, photophysics, and theoretical modeling of An-MOFs has been recently grazed,[31] and this work showcases the tunability and tailoring of optoelectronic behavior of An-MOFs as a first step toward understanding their fundamental properties.

EXPERIMENTAL SECTION

Materials. *Caution! Uranium tetrachloride and thorium nitrate are radioactive and chemically toxic reactants; suitable precautions, care, and protection for the handling of such substances must be followed.*

Uranium tetrachloride (>95%, International Bio-Analytical Industries Inc.), thorium nitrate hydrate (>95%, International Bio-Analytical Industries Inc.), zirconium chloride (99.5%, Alfa Aesar), cesium fluoride (99%, Oakwood Chemical), tin(II) chloride anhydrous (98%, BeanTown Chemical), copper(I) chloride anhydrous (97%, Strem Chemicals), bis(triphenylphosphine)palladium(II) dichloride (96%, Oakwood Chemical), sodium carbonate (ACS grade, Ameresco), magnesium sulfate anhydrous (USP, Chem-Impex, International Inc.), sodium sulfate anhydrous (99.5%, Oakwood Chemical), sodium hydroxide (ACS grade, Oakwood Chemical), potassium hydroxide (ACS grade, Fisher Chemical), 2,5-dibromonitrobezene (99%, Oakwood Chemical), sodium nitrite (98%, Oakwood Chemical), 3-methyl-2-butanone (98%, BeanTown Chemical), methyl trifluoromethanesulfonate (97%, Matrix Scientific), 2-hydroxy-5- nitrobenzaldehyde (98%, Oakwood Chemical), 4-methoxycarbonylphenylboronic acid (>97%, Boronic Molecular), methyl-4-iodo-3-methylbenzoate (98%, BeanTown Chemical), 4,4,4′,4′,5,5,5′,5′-octamethyl-2,2′-bi(1,3,2-dioxaborolane) (>98%, Ark Pharm), 7,7,8,8-tetracyanoquinodimethane (>98%, TCI), iodine (ACS grade, Fisher Scientific), celite 545 (filter aid, VWR), hydrochloric acid (ACS, Fisher Chemical), sulfuric acid (ACS grade, Fisher Chemical), nitric acid (ACS reagent, Sigma-Aldrich), fluoroboric acid (48%, Oakwood Chemical), ethanol (200 proof, Decon Laboratories, Inc.), methanol (ACS grade, Fisher Scientific), methylene chloride (99.9%, Fisher Chemical), acetone (ACS grade,

Sigma-Aldrich), ethyl acetate (99.9%, Fisher Chemical), chloroform (99.9%, Fisher Chemical), diethyl ether (ACS grade, J. T. Baker Chemicals), hexanes (ACS, BDH), N,N-dimethylformamide (ACS grade, Oakwood Chemical), piperidine (99%, Sigma-Aldrich), carbon tetrachloride (99.9%, Sigma-Aldrich), bromine (99.8%, Acros Organics), tetrahydrofuran (HPLC grade, BeanTown Chemical), 100 mm boron-doped Si wafer with 285-nm thermally grown SiO_2 (prime grade, Addison Engineering, Inc.), titanium pellets (99.995%, Kurt J. Lesker), gold pellets (99.99%, Kurt J. Lesker), chloroform-*d* (99.8%, Cambridge Isotope Laboratories, Inc.), deuterium chloride (99%, Cambridge Isotope Laboratories, Inc.), acetone-d_6 (99.9%, Cambridge Isotope Laboratories, Inc.), and dimethyl sulfoxide-d_6 (99.9%, Cambridge Isotope Laboratories, Inc.) were used as received.

The compounds 2,5-dibromoaniline (**II**, Scheme 6.2),[71] (2,5-dibromophenyl)hydrazine (**III**, Scheme 6.2),[72] 4,7-dibromo-2,3,3-trimethyl-3*H*-indole (**IV**, Scheme 6.2),[72] [4,7-dibromo-1,2,3,3-tetramethyl-3*H*-indol-1-ium][trifluoromethanesulfonate] (**V**, Scheme 6.2),[73] 4',7'-dibromo-1',3',3'-trimethyl-6-nitrospiro-[chromene-2,2'-indoline] (**VI,** Scheme 6.2), 2,2'-dimethyl-[1,1'-biphenyl]-4,4'-dicarboxylic acid (H_2Me_2BPDC),[74] $Th_6O_4(OH)_8(Me_2BPDC)_4$ (Th-MOF),[75] $Zr_6O_4(OH)_8(Me_2BPDC)_4$ (Zr-MOF),[74] $U_6O_4(OH)_8(Me_2BPDC)_4$ (U-MOF),[75] and $Th_5UO_4(OH)_8(Me_2BPDC)_4$ (Th_5U-MOF)[75] were synthesized based on modified literature procedures.

Synthesis of dimethyl 4,4'-(1',3',3'-trimethyl-6-nitrospiro[chromene-2,2'-indoline]-4',7'- diyl)dibenzoate ($C_{35}H_{30}N_2O_7$, Me_2TNDA, Scheme 6.2). Using a Schlenk technique, 25 mL of anhydrous DMF was transferred into a flask containing VI (0.30 g,

0.62 mmol, Scheme 6.2), Na_2CO_3 (0.24 g, 2.3 mmol), $Pd(PPh_3)_4$ (0.15 g, 0.13 mmol), CuCl (0.13 g, 1.4 mmol), and 4-methoxycarbonylphenylboronic acid (0.67 g, 3.7 mmol). The mixture was stirred for 4 hours at 120 °C. After cooling to room temperature, the reaction mixture was transferred into a 1-L separatory funnel followed by dilution with deionized water (500 mL). The product was then extracted with methylene chloride (3 × 200 mL). The organic layers were combined, washed with deionized water (5 × 500 mL), brine (2 × 100 mL), and dried over sodium sulfate, followed by filtration and solvent removal under vacuum. The resulting red/brown oil was then diluted with 10 mL of methylene chloride and filtered through a silica plug with an excess of methylene chloride. The resulting filtrate was reduced under vacuum until ca 10 mL remained. The filtrate was then combined with silica gel and dried under vacuum until the powder was free flowing. Lastly, the product was purified using a silica gel column (l = 10 cm, d = 4.0 cm, 2:3:15 ethyl acetate/methylene chloride/hexanes by volume). Fractions were left to sit for 24 hours until yellow block-shaped crystals formed. The crystals were collected via filtration and washed with a minimal amount of ethyl acetate. After drying, Me_2TNDA (0.10 g, 0.17 mmol) was isolated in 27% yield. The detailed description for the crystallographic data collection and refinement details are given in Table 6.1 and the X-ray structure of Me_2TNDA is shown in Figure 6.8. ^{1}H NMR (chloroform-*d*, 400 MHz): δ = 0.74 (3H, s), 1.26 (3H, s), 2.32 (3H, s), 3.94 (6H, s), 5.79-5.81 (1H, d, J = 10.5 Hz), 6.69–6.71 (1H, d, J = 7.8 Hz), 6.78–6.80 (1H, d, J = 9.0 Hz), 6.86–6.89 (1H, d, J = 10.5 Hz), 7.07–7.09 (1H, d, J = 7.8 Hz), 7.44–7.46 (2H, d, J = 8.1 Hz) 7.50–7.52 (2H, d, J = 7.0 Hz), 7.92–7.93 (1H, d, J = 2.7 Hz), 7.97–8.00 (1H, dd, J = 2.7 Hz and 9.0 Hz), and 8.06–8.08 (4H, d, J = 8.5 Hz) ppm (Figure 6.5). ^{13}C NMR (chloroform-d, 400 MHz): δ = 21.00, 25.69, 33.47, 52.20, 52.69, 107.69, 115.31,

118.26, 121.34, 121.90, 122.70, 122.76, 125.90, 128.79, 128.86, 128.98, 129.16, 129.51, 129.65, 130.17, 133.50, 137.66, 140.94, 145.21, 145.37, 145.68, 159.70, 166.92, and 166.94 ppm (Figure 6.5). FTIR (neat, cm^{-1}): 656, 681, 707, 735, 748, 769, 778, 805, 837, 858, 911, 917, 949, 1016, 1050, 1069, 1089, 1098, 1112, 1129, 1155, 1175, 1188, 1228, 1271, 1306, 1335, 1365, 1380, 1186, 1388, 1401, 1434, 1466, 1469, 1510, 1555, 1573, 1606, 1646, 1717, 2837, 1870, 2903, 2951, 2972, 2998, 3052, and 3108. HRMS (ESI, *m*/*z*) calculated for $C_{35}H_{30}N_2O_7$ $[M-H]^-$ 591.2126, found 591.2125.

Synthesis of dimethyl 4,4'-(1',3',3'-trimethyl-6-nitrospiro[chromene-2,2'-indoline]-4',7'-diyl)dibenzoic acid ($C_{33}H_{26}N_2O_7$, H_2TNDA, Scheme 6.2). A 50-mL round-bottom flask was wrapped in aluminum foil, Me_2TNDA (20.0 mg, 34.0 μmol) was added to the flask, followed by the addition of 10.0 mL of tetrahydrofuran, 5.00 mL of methanol, and 5.00 mL of KOH (2.00 M). The bright yellow solution was then stirred at room temperature in the dark for 24 hours. The solution was dried under vacuum, and then 5.00 mL of deionized water was added. The solution was acidified with HCl (3.00 M) while stirring until a pH of 1 was reached. A dark red precipitate formed, followed by a slow color change from red to yellow. After the suspension was stirred for 8 hours in the dark, the precipitate was filtered and washed with water (50.0 mL) and methylene chloride (50.0 mL). The powder was then collected and dried under vacuum to yield H_2TNDA (18.0 mg, 32.0 μmol) in 95% yield. Crystals of H_2TNDA were obtained by slow evaporation of dimethyl sulfoxide-d_6 (0.500 mL) in an open 20-mL scintillation vial. The detailed description for the crystallographic data collection and refinement details are given in Table 6.1. The X-ray structure of H_2TNDA is shown in Figure 6.9. ^{1}H NMR (dimethyl sulfoxide-d_6, 400 MHz): δ = 0.64 (3H, s), 1.25 (3H, s), 2.28 (3H, s), 5.96-5.99 (1H, d, J =

10.4 Hz), 6.66–6.68 (1H, d, J = 8.2 Hz), 6.92–6.94 (1H, d, J = 8.9 Hz), 7.06–7.08 (1H, d, J = 7.9 Hz), 7.18–7.21 (1H, d, J = 10.6 Hz), 7.48–7.50 (2H, d, J = 8.2 Hz), 7.53–7.55 (2H, d, J = 7.41 Hz), 7.96–8.01 (5H, m) 8.15–8.16 (1H, d, J = 2.8 Hz), and 13.02 (2H, s) ppm (Figure 6.6). 13C NMR (dimethyl sulfoxide-d_6, 400 MHz): δ = 21.03, 25.97, 33.64, 52.72, 108.01, 115.80, 118.96, 121.64, 122.04, 122.57, 123.33, 126.21, 129.24, 129.40, 129.45, 129.82, 129.89, 129.94, 130.24, 130.48, 133.74, 137.69, 140.98, 144.91, 145.38, 145.41, 159.74, and 167.58 ppm (Figure 6.6). FTIR (neat, cm^{-1}): 657, 668, 701, 748, 770, 794, 806, 820, 847, 859, 910, 917, 949, 996, 1020, 1046, 1068, 1087, 1099, 1118, 1128, 1150, 1175, 1227, 1251, 1266, 1305, 1333, 1361, 1390, 1405, 1438, 1465, 1477, 1508, 1558, 1572, 1607, 1645, 1699, 2483, 2585, 2752, 2869, 2905, 2929, 2971, 2993, 3041, 3053, 3103, and 3410 (Figure 6.7). HRMS (ESI, m/z) calculated for $C_{33}H_{26}N_2O_7$ $[M-H]^-$ 561.1667, found 561.1668.

Preparation of Th_5U-MOF. The framework of composition Th_5U-MOF was synthesized based on a modified literature procedure.[75] Freshly synthesized U-MOF (36.0 mg) was washed with DMF and then placed into a 20-mL scintillation vial. To this vial, 1.00 mL of 0.170 M $Th(NO_3)_4{\cdot}H_2O$ was added, and the vial was undisturbed for 48 hours at room temperature. The freshly prepared MOF was immediately washed with DMF (5.0 mL) and characterized by powder X-ray diffraction (PXRD) and Fourier-transform infrared spectroscopy (FTIR). A portion of the MOF powder was subjected to vigorous washing via a Soxhlet apparatus for 3 days in DMF, then the powder was analyzed by inductively-coupled plasma mass spectrometry (ICP-MS) to determine the remaining uranium percentage.

Linker installation procedure. In order to postsynthetically install $TNDA^{2-}$ into a parent framework, freshly synthesized Th-MOF, Zr-MOF, or Th_5U-MOF was washed with DMF (1.0 mL) and then dried in air for 10 minutes. The MOF (8.0 mg) was then placed into a 1-dram vial and 1.0 mL of a DMF solution of H_2TNDA (0.030 M, 0.030 mmol) was added. The vial was then heated in a preheated oven (75 °C for Zr-33% and Th-34%; and 85 °C for Zr-65%, Th-65%, and Th5U-50%) for 72 hours, cooled to room temperature, filtered, and washed with DMF (5.0 mL). The samples were analyzed by using PXRD and FTIR, and the linker installation was confirmed by ^1H nuclear magnetic resonance (NMR) spectroscopy as described below.

Preparation of iodine-loaded frameworks. Preparation of iodine loaded frameworks, I_2@Zr-MOF, I_2@Th-MOF, I_2@Th-65%, and I_2@Th5U-50%, was performed based on a modified literature procedure.[76] An uncapped 0.5-dram vial containing 8.0 mg of filtered MOF was placed inside a 20-mL vial that was charged with iodine crystals (0.10 g, 0.39 mmol), sealed, and were undisturbed for 72 hours at room temperature. The iodine-loaded material was then filtered and washed with 2.0 mL of DMF to remove iodine from the surface. The samples were analyzed by using PXRD and FTIR. Iodine incorporation was quantified via ICP-MS (Table 6.5). The iodine-loaded materials were then subjected to in-situ pressed-pellet conductivity measurements (see the section *conductivity measurements*).

Preparation of tetracyanoquinodimethane-loaded frameworks. Preparation of tetracyanoquinodimethane (TCNQ) loaded frameworks, TCNQ@Zr-MOF, TCNQ@Zr-65%, TCNQ@Th-MOF, and TCNQ@Th-65%, was performed based on a modified literature procedure.[77] A 20-mL vial containing 8.0 mg of filtered MOF was loaded with a

1.0 mL solution of 100 mM TCNQ in DMF. The vial was then sealed and heated for 72 hours at 75 °C. The TCNQ-loaded material was filtered and washed with 2.0 mL of DMF to remove residual TCNQ from the surface. The amount of TCNQ loaded in the samples was determined by ^{1}H NMR on digested samples. There were 3.95 TCNQ molecules per pore in Zr-65%. The samples were analyzed by using PXRD and FTIR. The TCNQ-loaded materials were then subjected to in-situ pressed-pellet conductivity measurements (see the section *conductivity measurements*).

General digestion procedure. In order to study the prepared MOFs by ^{1}H NMR spectroscopy, a solution of 5.0 μL of deuterium chloride in 500 μL of acetone-d_6 was added to 5.0 mg of washed MOF, followed by sonication for 5 minutes and heating until complete sample dissolution. The percent linker installation was calculated based on linker ratios found in the ^{1}H NMR spectra of the digested samples. The highest amount of linker installation can be calculated from geometrical analysis of the parent MOF structure and the length of the installed linker as shown by Zhou and co-workers.[74]

Diffuse reflectance and photoluminescence spectroscopy. Diffuse reflectance spectra were collected on an Ocean Optics JAZ spectrometer. An Ocean Optics ISP-REF integrating sphere was connected to the spectrometer using a 450-μm SMA fiber optic cable. Samples were loaded in a 4.0-mm quartz sample cell, which was referenced to as an Ocean Optics WS-1 Spectralon® standard. A mounted high-powered LED (M365L2, Thorlabs, λ_{ex} = 365 nm, distance = 1 cm, and LEDD1B power supply set at 700 mA) was used for in situ irradiation of the samples.

Steady-state emission spectra were acquired on an Edinburgh FS5 fluorescence spectrometer equipped with a 150-W Continuous Wave Xenon Lamp source for excitation.

Emission measurements on solid samples were collected from the powders of the desired materials placed inside a 0.5-mm quartz sample holder using the front-facing module.

Conductivity measurements. A two-point method was employed to measure conductance σ (S/cm) of pressed pellets according to following equation:

$$\sigma = Il/VA,$$

where I = current, l = thickness of the pellets, V = voltage, and A = surface area of the prepared pellets. A home-built two-contact probe pressed pellet setup (2C3PS)[78–80] made it possible to fabricate the pressed pellets and perform measurements in situ while also allowing for simultaneous MOF irradiation and monitoring changes in electrical current flow under the applied voltage. The MOF crystalline powder (10 mg), that was pre-dried for 20 minutes in air (unless otherwise noted), was pressed between two stainless steel rods inside an insulating quartz tube. The diameter of the resulting pellet is the same as the inner diameter of the quartz tube (d = 2 mm). The thickness of the pellets was kept consistent (l = 1 mm) by using the same amount of material. After forming a small pellet, the stainless steel rods were connected to a Keithley 2636A sourcemeter using a 3-slot Triax to alligator clip (Keithley 237-ALG-2 Triax cable) to perform conductivity measurements. For all measurements, the number of power line cycles (NPLC) was set to 5.

To measure the electrical conductivity for photochromic MOFs before and after irradiation with UV light, the sample was first dried in air for 20 minutes and then placed into the 2C3PS. The sample was measured in the dark initially and then again after irradiation with a mounted high- powered LED (M365L2, Thorlabs, λ_{ex} = 365 nm, distance = 6 cm, and LEDD1B power supply set at 700 mA) for 5 minutes. The measurements were

performed using the 2C3PS connected to a Keithley 2636A sourcemeter. The *I*−*V* curve was collected by supplying a voltage in the range from −1 V to +1 V. The electrical conductance in the prepared materials follows Ohm's law and was estimated by fitting the obtained linear *I*−*V* curves. Standard errors were calculated by dividing the standard deviation by the square root of the number of samples measured (5).

MOF-based field-effect transistor preparation. Field-effect transistors (FETs) were fabricated on a heavily boron-doped Si wafer with a 285-nm thermally grown SiO_2 insulating layer, as obtained from Addison Engineering, Inc. First, the Si wafer was rinsed thoroughly with isopropyl alcohol, and deionized water before immediately drying with a stream of nitrogen and heating at 180 °C for 5 minutes. After that, titanium/gold (30 nm/70 nm, respectively) electrodes were fabricated using an electron-beam evaporation technique on the Si wafer substrate. The dimensions of the electrodes were defined by photolithography (the gap between electrodes was 2 μm and the width of the edge was 1.0 mm). MOF crystals were then deposited between the electrodes by drop casting a suspension of the MOF (in DMF) to produce MOF-based FETs. The contact between the MOF crystals and the electrodes was confirmed via optical microscopy.

Transfer characteristic measurements of MOF-based FETs. All measurements were performed in the dark or under constant UV-irradiation using a high-powered LED (M365L2, Thorlabs, λ_{ex} = 365 nm, distance = 2 cm, and LEDD1B power supply set at 700 mA). A Keithley 2636A sourcemeter was used to supply a constant drain voltage (5 V) and collect drain current-gate voltage curves (i.e., transfer characteristics).

Electronic structure as a function of external stimuli. Dependence of the current values on an excitation wavelength was measured using the 2C3PS,[78–80] which was

connected to a Keithley 2636A sourcemeter. Constant voltage (1 V) was applied, while current was measured every 1 second. Before data collection, an equilibration time (t = 90 seconds) was applied in the dark. Then, the sample was irradiated (t = 5 minutes) using a high-powered LED (M365L2, Thorlabs, λ_{ex} = 365 nm, distance = 2 cm, and LEDD1B power supply set at 700 mA), followed by relaxation by irradiating with a high-powered LED (M590L3, Thorlabs, λ_{ex} = 590 nm, distance = 2 cm, and LEDD1B power supply set at 1000 mA). The procedure was repeated for 3 consecutive irradiation cycles (Figure 6.2 and 6.35).

The DFT calculations were performed using the Vienna ab initio simulation package (VASP)[81,82] with plane wave basis sets, and employing the Projector-augmented wave (PAW)[83,84] pseudopotentials. We have considered the following valence electrons for each atomic species: C $2s^2 2p^2$, H $1s^1$, O $2s^2 2p^2$, N $2s^2 2p^3$, Zr $4s^2 5s^2\ 4p^6 4d^2$, Th $6s^2 7s^2\ 6p^6 6d^1\ 5f^1$ U $6s^2 7s^2 6p^6 6d^1 5f^3$. The geometries were optimized using the GGA-PBE exchange correlation functionals. The van der Waals interactions were taken into account using the dispersion correction formula in the PBE-D3 functionals by Grimme et al.[86] with Becke−Johnson damping. In addition, an on-site Coulomb interaction was added to the uranium f-electrons within the DFT+U formalism[87] to attenuate the electron delocalization due to the self-interaction of electrons. Based on previous studies,[88,89] a U–J = 4 eV was used for uranium. No DFT+U corrections were needed for Th, based on previous works[90,91] and was again confirmed in this work. The planewave energy cutoff was set to 520 eV and spin-polarized calculations were performed at the Γ-only k-point. Structural optimization was performed until the forces on each ion were less than 25 meV/Å, using 0.0001 eV as the energy tolerance criteria for the electronic step. Gaussian smearing with a width of 0.05

eV was applied to all optimizations. A conjugate-gradient algorithm[92,93] was used to relax all of the ions. The calculations were performed on SBUs isolated in a 30 Å cubic box. The total and partial DOS were calculated by single point calculations following the geometry optimizations.

Other physical measurements. FTIR spectra were obtained on a Perkin-Elmer Spectrum 100. ^{13}C and ^{1}H NMR spectra were collected on a Bruker Avance III-HD 400 MHz NMR spectrometer. ^{13}C and ^{1}H NMR spectra were referenced to natural abundance ^{13}C peaks and residual ^{1}H peaks of deuterated solvents, respectively. PXRD patterns were recorded on a Rigaku Miniflex II diffractometer at a scan rate of 1 °/min with accelerating voltage and current of 30 kV and 15 mA, respectively. ICP-MS analysis was conducted using a Finnigan ELEMENT XR double focusing magnetic sector field inductively coupled plasma mass spectrometer with Ir, Rh, or both as internal standards. A Micromist U-series nebulizer (0.2 mL/min, GE, Australia), quartz torch, and injector (Thermo Fisher Scientific, USA) were used for sample introduction. Sample gas flow was 1.08 mL/min and the forwarding power was 1250 W. The samples that do not contain iodine were digested in Teflon vessels with nitric and hydrochloric acids and then heated at 180 °C for 4 hours. Iodine-containing samples were digested in Teflon vessels with nitric and hydrochloric acids at room temperature. X-ray photoelectron spectroscopy (XPS) measurements were performed using a Kratos AXIS Ultra DLD XPS system with a monochromatic Al Kα source operated at 15 keV and 150 W and a hemispherical energy analyzer. Samples were placed in small powder pockets on the holder, and analysis was performed at pressures below 1×10^{-9} mbar. High-resolution core level spectra were measured with a pass energy of 40 eV, and analysis of the data was carried out using

XPSPEAK41 software. The Water QTOF-I quadrupole time-of-flight and Thermo Scientific Orbitrap Velos Pro mass spectrometers were used to record the mass spectra of the prepared compounds.

X-ray crystal structure determination for Me_2TNDA ($C_{35}H_{30}N_2O_7$). X-ray intensity data from a colorless needle crystal were collected at 100(2) K using a Bruker D8 QUEST diffractometer equipped with a PHOTON-100 CMOS area detector and an Incoatec microfocus source (Mo Kα radiation, λ = 0.71073 Å). The raw area detector data frames were reduced and corrected for absorption effects using the Bruker APEX3, SAINT+ and SADABS programs.[94,95] Final unit cell parameters were determined by least-squares refinement of 9805 reflections taken from the data set. The structure was solved with SHELXT.[96,97] Subsequent difference Fourier calculations and full-matrix least-squares refinement against F^2 were performed with SHELXL-2018[96,97] using OLEX2.[98]

The compound crystallizes in the triclinic system. The space group *P*-1 was confirmed by structure solution. The asymmetric unit consists of one molecule. Minor disorder of the nitro group (atoms N2/O2/O3) was modeled with two components. The major disorder population fraction refined to 0.66(1). N-C and N-O distances for disordered atoms were each restrained to be similar to those of the same kind (SHELX SADI). All non-hydrogen atoms were refined with anisotropic displacement parameters. Hydrogen atoms bonded to carbon were located in difference Fourier maps before being placed in geometrically idealized positions and included as riding atoms with d(C–H) = 0.95 Å and U_{iso}(H) = 1.2U_{eq}(C) for aromatic hydrogen atoms and d(C–H) = 0.98 Å and U_{iso}(H) = 1.5U_{eq}(C) for methyl hydrogens. The methyl hydrogens were allowed to rotate as a rigid group to the orientation of maximum observed electron density. The largest

residual electron density peak in the final difference map is 0.33 e/Å^3, located 0.70 Å from C31.

X-ray crystal structure determination for H_2TNDA ($C_{33}H_{26}N_2O_7$). X-ray intensity data from a light brown plate were collected at 100(2) K using a Bruker D8 QUEST diffractometer equipped with a PHOTON-100 CMOS area detector and an Incoatec microfocus source (Mo Kα radiation, λ = 0.71073 Å). The raw area detector data frames were reduced and corrected for absorption effects using the Bruker APEX3, SAINT+ and SADABS programs.[95,99] The structure was solved with SHELXT.[96,97] Subsequent difference Fourier calculations and full-matrix least-squares refinement against F^2 were performed with SHELXL-2018[96,97] using OLEX2.[98]

The compound crystallizes in the triclinic system. The space group *P*-1 (No. 2) was confirmed by structure solution. The asymmetric unit consists of one $C_{33}H_{26}N_2O_7$ molecule and two independent dimethyl sulfoxide-d_6 molecules. All non-hydrogen atoms were refined with anisotropic displacement parameters. Hydrogen and deuterium atoms bonded to carbon were located in difference Fourier maps before being placed in geometrically idealized positions and included as riding atoms with d(C–H) = 0.95 Å and U_{iso}(H) = 1.2U_{eq}(C) for aromatic hydrogen atoms and d(C–H/D) = 0.98 Å and U_{iso}(H/D) = 1.5U_{eq}(C) for methyl hydrogen and deuterium atoms. The methyl hydrogen and deuterium atoms were allowed to rotate as a rigid group to the orientation of maximum observed electron density. The two carboxylic hydrogen atoms were located and refined freely. The largest residual electron density peak in the final difference map was 0.62 e/Å^3, located 0.94 Å from O4.

REFERENCES

[1] Chen, Z.; Li, P.; Zhang, X.; Mian, M. R.; Wang, X.; Li, P.; Liu, Z.; O'Keeffe, M.; Stoddart, J. F.; Farha, O. K. *Nano Res*. **2021**, *14*, 376–380.

[2] Zhu, L.; Sheng, D.; Xu, C.; Dai, X.; Silver, M. A.; Li, J.; Li, P.; Wang, Y.; Wang, Y.; Chen, L.; Xiao, C.; Chen, J.; Zhou, R.; Zhang, C.; Farha, O. K.; Chai, Z.; Albrecht-Schmitt, T. E.; Wang, S. *J. Am. Chem. Soc.* **2017**, *139*, 14873–14876.

[3] Amoroso, J.; Marra, J.; Conradson, S. D.; Tang, M.; Brinkman, K. *J. Alloys Compd.* **2014**, *584*, 590–599.

[4] Li, D.; Shustova, N. B.; Martin, C. R.; Taylor-Pashow, K.; Seaman, J. C.; Kaplan, D. I.; Amoroso, J. W.; Chernikov, R. *J. Environ. Radioact.* **2020**, *222*, 106372.

[5] Delchet, C.; Tokarev, A.; Dumail, X.; Toquer, G.; Barré, Y.; Guari, Y.; Guerin, C.; Larionova, J.; Grandjean, A. *RSC Adv.* **2012**, *2*, 5707–5716.

[6] Yang, H.; Luo, M.; Luo, L.; Wang, H.; Hu, D.; Lin, J.; Wang, X.; Wang, Y.; Wang, S.; Bu, X.; Feng, P.; Wu, T. *Chem. Mater.* **2016**, *28*, 8774–8780.

[7] Sheng, D.; Zhu, L.; Dai, X.; Xu, C.; Li, P.; Pearce, C. I.; Xiao, C.; Chen, J.; Zhou, R.; Duan, T.; Farha, O. K.; Chai, Z.; Wang, S. *Angew. Chem. Int. Ed.* **2019**, *58*, 4968–4972.; *Angew. Chem.* **2019**, *131*, 5022–5026

[8] zur Loye, H.-C.; Besmann, T.; Amoroso, J.; Brinkman, K.; Grandjean, A.; Henager, C. H.; Hu, S.; Misture, S. T.; Phillpot, S. R.; Shustova, N. B.; Wang, H.; Koch, R. J.; Morrison, G.; Dolgopolova, E. *Chem. Mater.* **2018**, *30*, 4475–4488.

[9] Li, D.; Seaman, J. C.; Hunyadi Murph, S. E.; Kaplan, D. I.; Taylor-Pashow, K.; Feng, R.; Chang, H.; Tandukar, M. *J. Hazard. Mater.* **2019**, *374*, 177–185.

[10] Makowski, P.; Deschanels, X.; Grandjean, A.; Meyer, D.; Toquer, G.; Goettmann, F. *New J. Chem.* **2012**, *36*, 531–541.

[11] Li, W.; Watzele, S.; El-Sayed, H. A.; Liang, Y.; Kieslich, G.; Bandarenka, A. S.; Rodewald, K.; Rieger, B.; Fischer, R. A. *J. Am. Chem. Soc.* **2019**, *141*, 5926–5933.

[12] Choi, H.; Peters, A. W.; Noh, H.; Gallington, L. C.; Platero-Prats, A. E.; DeStefano, M. R.; Rimoldi, M.; Goswami, S.; Chapman, K. W. ; Farha, O. K.; Hupp, J. T. *ACS Appl. Energy Mater.* **2019**, *2*, 8695–8700.

[13] Mao, C.; Wang, Y.; Jiao, W.; Chen, X.; Lin, Q.; Deng, M.; Ling, Y.; Zhou, Y.; Bu,

X.; Feng, P. *Langmuir* **2017**, *33*, 13634–13639.

[14] Wu, Y.-P.; Xu, G.-W.; Dong, W.-W.; Zhao, J.; Li, D.-S.; Zhang, J.; Bu, X. *Inorg. Chem.* **2017**, *56*, 1402–1411.

[15] Wang, Y.; Jia, X.; Yang, H.; Wang, Y.; Chen, X.; Hong, A. N.; Li, J.; Bu, X.; Feng, P. *Angew. Chem. Int. Ed.* **2020**, *59*, 19027–19030.; *Angew. Chem.* **2020**, *132*, 19189–19192

[16] Kalaj, M.; Palomba, J. M.; Bentz, K. C.; Cohen, S. M. *Chem. Commun.* **2019**, *55*, 5367–5370.

[17] Gonzalez, A.; Kengmana, E. S.; Fonseca, M. V.; Han, G. G. D. *Mater. Today Adv.* **2020**, *6*, 100058.

[18] Bohaty, A. K.; Newton, M. R.; Zharov, I. *J. Porous Mater.* **2010**, *17*, 465–473.

[19] Newsome, W. J.; Ayad, S.; Cordova, J.; Reinheimer, E. W.; Campiglia, A. D.; Harper, J. K.; Hanson, K.; Uribe-Romo, F. J. *J. Am. Chem. Soc.* **2019**, *141*, 11298–11303.

[20] Wu, Y.-P.; Tian, J.-W.; Liu, S.; Li, B.; Zhao, J.; Ma, L.-F.; Li, D.-S.; Lan, Y.-Q.; Bu, X. *Angew. Chem. Int. Ed.* **2019**, *58*, 12185–12189.; *Angew. Chem.* **2019**, *131*, 12313–12317

[21] Zhou, Z.; Mukherjee, S.; Warnan, J.; Li, W.-J.; Wannapaiboon, S.; Hou, S.; Rodewald, K.; Rieger, B.; Weidler, P. G.; Wöll, C.; Fischer, R. A. *J. Mater. Chem. A* **2020**, *8*, 25941–25950.

[22] Kung, C.-W.; Platero-Prats, A. E.; Drout, R. J.; Kang, J.; Wang, T. C.; Audu, C. O.; Hersam, M. C.; Chapman, K. W.; Farha, O. K.; Hupp, J. T. *ACS Appl. Mater. Interfaces* **2018**, *10*, 30532–30540.

[23] Yuan, S.; Lu, W.; Chen, Y.-P.; Zhang, Q.; Liu, T.-F.; Feng, D.; Wang, X.; Qin, J.; Zhou, H.-C. *J. Am. Chem. Soc.* **2015**, *137*, 3177–3180.

[24] Dolgopolova, E. A.; Ejegbavwo, O. A.; Martin, C. R.; Smith, M. D.; Setyawan, W.; Karakalos, S. G.; Henager, C. H.; zur Loye, H.-C.; Shustova, N. B. *J. Am. Chem. Soc.* **2017**, *139*, 16852–16861.

[25] Berseneva, A. A.; Martin, C. R.; Galitskiy, V. A.; Ejegbavwo, O. A.; Leith, G. A.; Ly, R. T.; Rice, A. M.; Dolgopolova, E. A.; Smith, M. D.; zur Loye, H.-C.; DiPrete, D. P.; Amoroso, J. W.; Shustova, N. B. *Inorg. Chem.* **2020**, *59*, 179–183.

[26] Yuan, S.; Chen, Y.-P.; Qin, J.-S.; Lu, W.; Zou, L.; Zhang, Q.; Wang, X.; Sun, X.; Zhou, H.-C. *J. Am. Chem. Soc.* **2016**, *138*, 8912–8919.

[27] Dolgopolova, E. A.; Brandt, A. J.; Ejegbavwo, O. A.; Duke, A. S.; Maddumapatabandi, T. D.; Galhenage, R. P.; Larson, B. W.; Reid, O. G.; Ammal, S. C.; Heyden, A.; Chandrashekhar, M.; Stavila, V.; Chen, D. A.; Shustova, N. B. *J. Am. Chem. Soc.* **2017**, *139*, 5201–5209.

[28] Ejegbavwo, O. A.; Berseneva, A. A.; Martin, C. R.; Leith, G. A.; Pandey, S.; Brandt, A. J.; Park, K. C.; Mathur, A.; Farzandh, S.; Klepov, V. V.; Heiser, B. J.; Chandrashekhar, M.; Karakalos, S. G.; Smith, M. D.; Phillpot, S. R.; Garashchuk, S.; Chen, D. A.; Shustova, N. B. *Chem. Sci.* **2020**, *11*, 7379–7389.

[29] Pandey, S.; Demaske, B.; Ejegbavwo, O. A.; Berseneva, A. A.; Setyawan, W.; Shustova, N. B.; Phillpot, S. R. *Comput. Mater. Sci.* **2020**, *184*, 109903.

[30] Ejegbavwo, O. A.; Martin, C. R.; Olorunfemi, O. A.; Leith, G. A.; Ly, R. T.; Rice, A. M.; Dolgopolova, E. A.; Smith, M. D. Karakalos, S. G.; Birkner, N.; Powell, B. A.; Pandey, S.; Koch, R. J.; Misture, S. T.; zur Loye, H.-C.; Phillpot, S. R.; Brinkman, K. S.; Shustova, N. B. *J. Am. Chem. Soc.* **2019**, *141*, 11628–11640.

[31] Rice, A. M.; Leith, G. A.; Ejegbavwo, O. A.; Dolgopolova, E. A.; Shustova, N. B. *ACS Energy Lett.* **2019**, *4*, 1938–1946.

[32] Falaise, C.; Volkringer, C.; Facqueur, J.; Bousquet, T.; Gasnot, L.; Loiseau, T. *Chem. Commun.* **2013**, *49*, 10320–10322.

[33] Leith, G. A.; Rice, A. M.; Yarbrough, B. J.; Berseneva, A. A.; Ly, R. T.; Buck III, C. N.; Chusov, D.; Brandt, A. J.; Chen, D. A.; Lamm, B. W.; Stefik, M.; Stephenson, K. S.; Smith, M. D.; Vannucci, A. K.; Pellechia, P. J.; Garashchuk, S.; Shustova, N. B. *Angew. Chem. Int. Ed.* **2020**, *59*, 6000–6006.; *Angew. Chem.* **2020**, *132*, 6056–6062

[34] Sutton, A. L.; Abrahams, B. F.; D'Alessandro, D. M.; Hudson, T. A.; Robson, R.; Usov, P. M. *CrystEngComm* **2016**, *18*, 8906–8914.

[35] Schneider, C.; Mendt, M.; Pöppl, A.; Crocellà, V.; Fischer, R. A. *ACS Appl. Mater. Interfaces* **2020**, *12*, 1024–1035.

[36] Erickson, K. J.; Léonard, F.; Stavila, V.; Foster, M. E.; Spataru, C. D.; Jones, R. E.; Foley, B. M.; Hopkins, P. E.; Allendorf, M. D.; Talin, A. A. *Adv. Mater.* **2015**, *27*, 3453–3459.

[37] Allendorf, M. D.; Foster, M. E.; Léonard, F.; Stavila, V.; Feng, P. L.; Doty, F. P.; Leong, K.; Ma, E. Y.; Johnston, S. R.; Talin, A. A. *J. Phys. Chem. Lett.* **2015**, *6*, 1182–1195.

[38] Hendon, C. H.; Walsh, A. *Chem. Sci.* **2015**, *6*, 3674–3683.

[39] Mehlana, G.; Bourne, S. A. *CrystEngComm* **2017**, *19*, 4238–4259.

[40] Castellanos, S.; Kapteijn, F.; Gascon, J. *CrystEngComm* **2016**, *18*, 4006–4012.

[41] Williams, D. E.; Martin, C. R.; Dolgopolova, E. A.; Swifton, A.; Godfrey, D. C.; Ejegbavwo, O. A.; Pellechia, P. J.; Smith, M. D.; Shustova, N. B. *J. Am. Chem. Soc.* **2018**, *140*, 7611–7622.

[42] Yuan, S.; Huang, L.; Huang, Z.; Sun, D.; Qin, J.-S.; Feng, L.; Li, J.; Zou, X.; Cagin, T.; Zhou, H.-C. *J. Am. Chem. Soc.* **2020**, *142*, 4732–4738.

[43] Dolgopolova, E. A.; Galitskiy, V. A.; Martin, C. R.; Gregory, H. N.; Yarbrough, B. J.; Rice, A. M.; Berseneva, A. A.; Ejegbavwo, O. A.; Stephenson, K. S.; Kittikhunnatham, P.; Karakalos, S. G.; Smith, M. D.; Greytak, A. B.; Garashchuk, S.; Shustova, N. B. *J. Am. Chem. Soc.* **2019**, *141*, 5350–5358.

[44] Klajn, R. *Chem. Soc. Rev.* **2014**, *43*, 148–184.

[45] Rice, A. M.; Martin, C. R.; Galitskiy, V. A.; Berseneva, A. A.; Leith, G. A.; Shustova, N. B. *Chem. Rev.* **2020**, *120*, 8790–8813.

[46] Healey, K.; Liang, W.; Southon, P. D.; Church, T. L.; D'Alessandro, D. M. *J. Mater. Chem. A* **2016**, *4*, 10816–10819.

[47] Ou, R.; Zhang, H.; Truong, V. X.; Zhang, L.; Hegab, H. M.; Han, L.; Hou, J.; Zhang, X.; Deletic, A.; Jiang, L.; Simon, G. P.; Wang, H. *Nat. Sustain.* **2020**, *3*, 1052–1058.

[48] Zhu, M.-Q.; Zhu, L.; Han, J. J.; Wu, W.; Hurst, J. K.; Li, A. D. Q. *J. Am. Chem. Soc.* **2006**, *128*, 4303–4309.

[49] Starikov, A. G.; Butova, V. V.; Ozhogin, I. V.; Soldatov, A. V. *J. Mol. Model.* **2020**, *26*, 212.

[50] Nguyen, H. L.; Vu, T. T.; Le, D.; Doan, T. L. H.; Nguyen, V. Q.; Phan, N. T. S. *ACS Catal.* **2017**, *7*, 338–342.

[51] Leong, C. F.; Wang, C.-H.; Ling, C. D.; D'Alessandro, D. M. *Polyhedron* **2018**, *154*, 334–342.

[52] Xie, L. S.; Alexandrov, E. V.; Skorupskii, G.; Proserpio, D. M.; Dincă, M. *Chem. Sci.* **2019**, *10*, 8558–8565.

[53] Grimme, S.; Antony, J.; Ehrlich, S.; Krieg, H. *J. Chem. Phys.* **2010**, *132*, 154104.

[54] Görner, H. *Phys. Chem. Chem. Phys.*, **2001**, *3*, 416–423.

[55] Zhang, X.; da Silva, I.; Fazzi, R.; Sheveleva, A. M.; Han, X.; Spencer, B. F.; Sapchenko, S. A.; Tuna, F.; McInnes, E. J. L.; Li, M.; Yang, S.; Schröder, M. *Inorg. Chem.* **2019**, *58*, 14145–14150.

[56] Schneider, C.; Ukaj, D.; Koerver, R.; Talin, A. A.; Kieslich, G.; Pujari, S. P.; Zuilhof, H.; Janek, J.; Allendorf, M. D.; Fischer, R. A. *Chem. Sci.* **2018**, *9*, 7405–7412.

[57] Zhang, X.; Saber, M. R.; Prosvirin, A. P.; Reibenspies, J. H.; Sun, L.; Ballesteros-Rivas, M.; Zhao, H.; Dunbar, K. R. *Inorg. Chem. Front.* **2015**, *2*, 904–911.

[58] Mahajan, M.; Bhargava, S. K.; O'Mullane, A. P. *RSC Adv.* **2013**, *3*, 4440–4446.

[59] Shimomura, S.; Matsuda, R.; Tsujino, T.; Kawamura, T.; Kitagawa, S. *J. Am. Chem. Soc.* **2006**, *128*, 16416–16417.

[60] Pham, T. C. T.; Docao, S.; Hwang, I. C.; Song, M. K.; Choi, D. Y.; Moon, D.; Oleynikov, P.; Yoon, K. B. *Energy Environ. Sci.* **2016**, *9*, 1050–1062

[61] Hu, Y.-Q.; Li, M.-Q.; Wang, Y.; Zhang, T.; Liao, P.-Q.; Zheng, Z.; Chen, X.-M.; Zheng, Y.-Z. *Chem. Eur. J.* **2017**, *23*, 8409–8413.

[62] Li, G.-P.; Zhang, K.; Zhao, H.-Y.; Hou, L.; Wang, Y.-Y. *Chempluschem* **2017**, *82*, 716–720.

[63] Lin, J.-X.; Liang, J.; Feng, J.-F.; Karadeniz, B.; Lü, J.; Cao, R. *Inorg. Chem. Front.* **2016**, *3*, 1393–1397.

[64] Lim, D.-W.; Sadakiyo, M.; Kitagawa, H. *Chem. Sci.* **2019**, *10*, 16–33.

[65] Wang, H.; Liu, X.; Wang, Z.; Li, H.; Li, D.; Meng, Q.; Chen, L. *J. Phys. Chem. B* **2006**, *110*, 5970–5974.

[66] Kobayashi, Y.; Jacobs, B.; Allendorf, M. D.; Long, J. R. *Chem. Mater.* **2010**, *22*, 4120–4122.

[67] Sengupta, A.; Datta, S.; Su, C.; Herng, T. S.; Ding, J.; Vittal, J. J.; Loh, K. P. *ACS*

Appl. Mater. Interfaces **2016**, *8*, 16154–16159.

[68] Washino, Y.; Murata, K.; Ashizawa, M.; Kawauchi, S.; Michinobu, T. *Polym. J.* **2011**, *43*, 364–369.

[69] O'Mullane, A. P.; Fay, N.; Nafady, A.; Bond, A. M. *J. Am. Chem. Soc.* **2007**, *129*, 2066–2073.

[70] Bodkhe, G. A.; Deshmukh, M. A.; Patil, H. K.; Shirsat, S. M.; Srihari, V.; Pandey, K. K.; Panchal, G.; Phase, D. M.; Mulchandani, A.; Shirsat, M. D. *J. Phys. D. Appl. Phys.* **2019**, *52*, 335105.

[71] Maya, F.; Tour, J. M. *Tetrahedron* **2004**, *60*, 81–92.

[72] Benniston, A. C.; Harriman, A.; Howell, S. L.; Li, P.; Lydon, D. P. *J. Org. Chem.* **2007**, *72*, 888–897.

[73] Williams, D. E.; Martin, C. R.; Dolgopolova, E. A.; Swifton, A.; Godfrey, D. C.; Ejegbavwo, O. A.; Pellechia, P. J.; Smith, M. D.; Shustova, N. B. *J. Am. Chem. Soc.* **2018**, *140*, 7611–7622.

[74] Yuan, S.; Lu, W.; Chen, Y.-P.; Zhang, Q.; Liu, T.-F.; Feng, D.; Wang, X.; Qin, J.; Zhou, H.-C. *J. Am. Chem. Soc.* **2015**, *137*, 3177–3180.

[75] Dolgopolova, E. A.; Ejegbavwo, O. A.; Martin, C. R.; Smith, M. D.; Setyawan, W.; Karakalos, S. G.; Henager, C. H.; zur Loye, H.-C.; Shustova, N. B. *J. Am. Chem. Soc.* **2017**, *139*, 16852–16861.

[76] Chapman, K. W.; Sava, D. F.; Halder, G. J.; Chupas, P. J.; Nenoff, T. M. *J. Am. Chem. Soc* **2011**, *133*, 18583–18585.

[77] Talin, A. A.; Centrone, A.; Ford, A. C.; Foster, M. E.; Stavila, V.; Haney, P.; Kinney, R. A.; Szalai, V.; Gabaly, F. E.; Yoon, H. P.; Léonard, F.; Allendorf, M. D. *Science* **2014**, *343*, 66–69.

[78] Sun, L.; Park, S. S.; Sheberla, D.; Dincă, M. *J. Am. Chem. Soc* **2016**, *138*, 14772–14782.

[79] Wudl, F.; Bryce, M. R. *J. Chem. Educ.* **1990**, *67*, 717–718.

[80] Dolgopolova, E. A.; Galitskiy, V. A.; Martin, C. R.; Gregory, H. N.; Yarbrough, B. J.; Rice, A. M.; Berseneva, A. A.; Ejegbavwo, O. A.; Stephenson, K. S.; Kittikhunnatham, P.; Karakalos, S. G.; Smith, M. D.; Greytak, A. B.; Garashchuk,

S.; Shustova, N. B. *J. Am. Chem. Soc.* **2019**, *141*, 5350–5358.

[81] Kresse, G.; Hafner, J. *Phys. Rev. B: Condens. Matter Mater. Phys.* **1993**, *47*, 558–561.

[82] Kresse, G.; Furthmüller, J. *Phys. Rev. B: Condens. Matter Mater. Phys.* **1996**, *54*, 11169–11186.

[83] Blöchl, P. E. *Phys. Rev. B: Condens. Matter Mater. Phys.* **1994**, *50*, 17953–17979.

[84] Kresse, G.; Joubert, D. *Phys. Rev. B: Condens. Matter Mater. Phys.* **1999**, *59*, 1758–1775.

[85] Perdew, J. P.; Burke, K.; Ernzerhof, M. *Phys. Rev. Lett*, **1996**, *77*, 3865–3868.

[86] Grimme, S.; Antony, J.; Ehrlich, S.; Krieg, H. *J. Chem. Phys.* **2010**, *132*, 154104.

[87] Dudarev, S. L.; Botton, G. A.; Savrasov, S. Y.; Humphreys, C. J.; Sutton, A. P. *Phys. Rev. B: Condens. Matter Mater. Phys.* **1998**, *57*, 1505–1509.

[88] Dorado, B.; Amadon, B.; Freyss, M.; Bertolus, M. *Phys. Rev. B: Condens. Matter Mater. Phys.* **2009**, *79*, 235125.

[89] Dudarev, S. L.; Castell, M. R.; Botton, G. A.; Savrasov, S. Y.; Muggelberg, C.; Briggs, G. A. D.; Sutton, A. P.; Goddard, D. T. *Micron* **2000**, *31*, 363–372.

[90] Shields, A. E.; Santos-Carballal, D.; de Leeuw, N. H. *J. Nucl. Mater.* **2016**, *473*, 99–111.

[91] Pegg, J. T.; Aparicio-Anglès, X.; Storr, M.; de Leeuw, N. H. *J. Nucl. Mater.* **2017**, *492*, 269–278.

[92] Bylander, D. M.; Kleinman, L.; Lee, S. *Phys. Rev. B: Condens. Matter Mater. Phys.* **1990**, *42*, 1394–1403.

[93] Teter, M. P.; Payne, M. C.; Allan, D. C. *Phys. Rev. B: Condens. Matter Mater. Phys.* **1989**, *40*, 12255–12263.

[94] APEX III Version 2016.5-0 and SAINT+ Version 8.38A. **2016**, Bruker AXS, Inc., Madison, Wisconsin, USA.

[95] Krause, L.; Herbst-Irmer, R.; Sheldrick, G. M.; Stalke, D. *J. Appl. Cryst.* **2015**, *48*, 3–10.

[96] Sheldrick, G. M. *Acta Cryst.* **2015**, *A71*, 3–8.

[97] Sheldrick, G. M. *Acta Cryst.* **2015**, *C71*, 3–8.

[98] Dolomanov, O. V.; Bourhis, L. J.; Gildea, R. J.; Howard, J. A. K.; Puschmann, H.

J. Appl. Cryst. **2009**, *42*, 339–341.

[99] APEX III Version 2018.1-0 and SAINT+ Version 8.38A. **2016**, Bruker AXS, Inc., Madison, Wisconsin, USA.

[100] Barroso-Bogeat, A.; Alexandre-Franco, M.; Fernández-González, C.; Gómez-Serrano, V. *Energy Fuels* **2014**, *28*, 4096–4103.

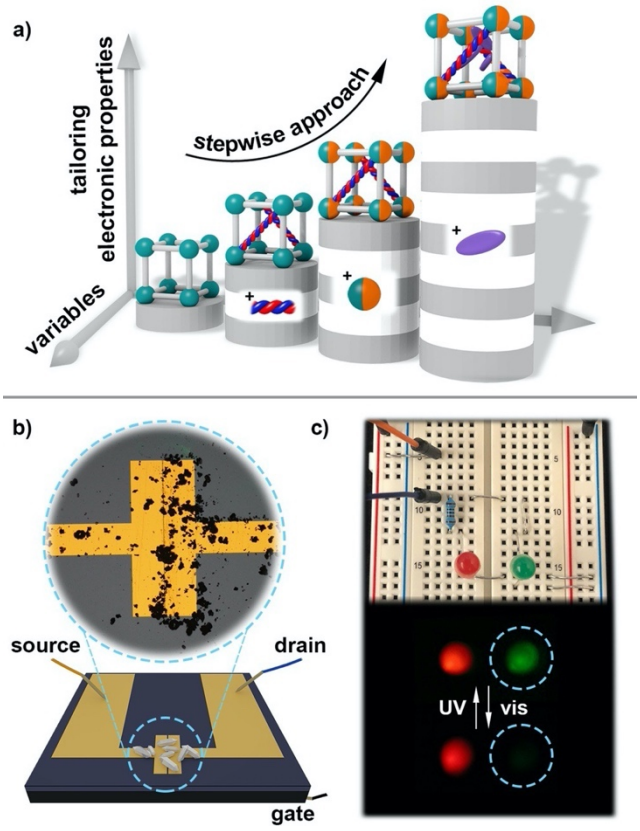

Scheme 6.1. a) A schematic representation of the tunability of MOF electronic properties as a function of stimuli-responsive capping linker integration (blue and red spirals), *f*-block elements (teal and/or orange spheres), and guest molecules (purple ovals). b) A schematic representation of the MOF-based field-effect transistor. The inset shows an optical image of drop-cast crystals between the electrodes. c) Two-LED fail-safe circuit designed for visualization of electronic property control.

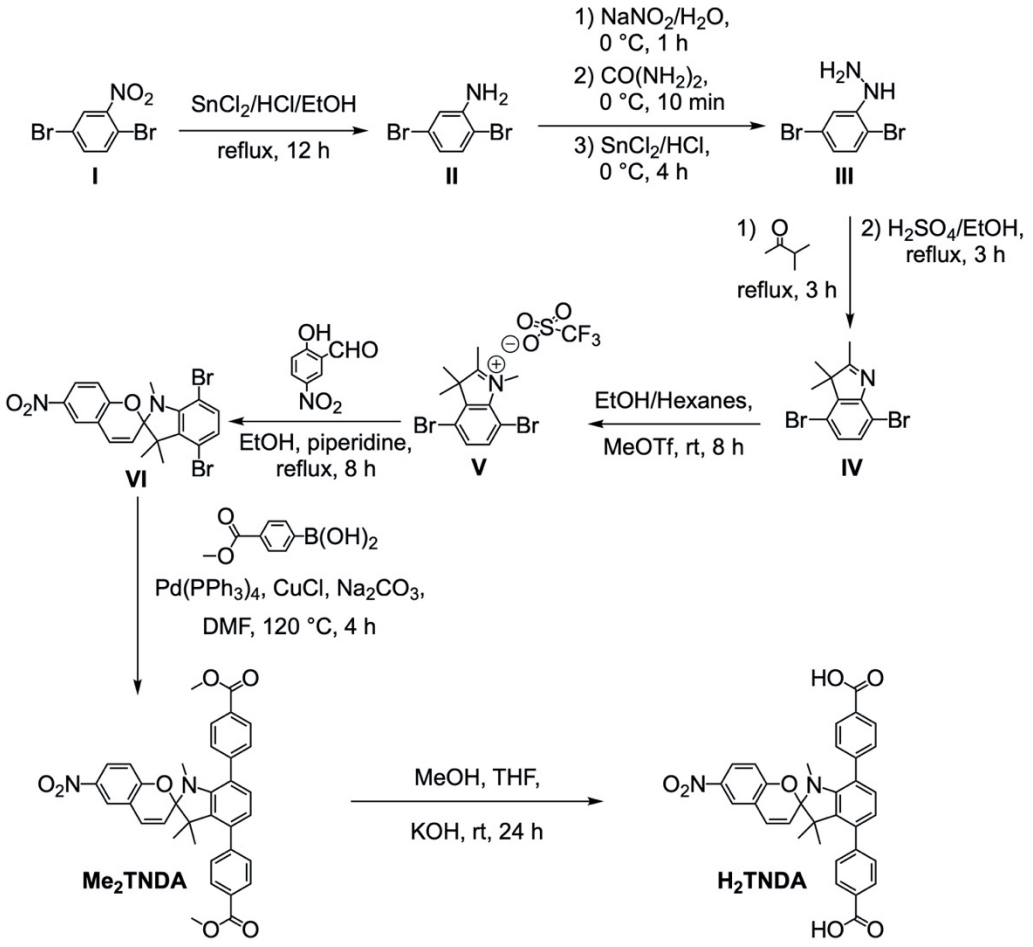

Scheme 6.2. Synthesis of H_2TNDA

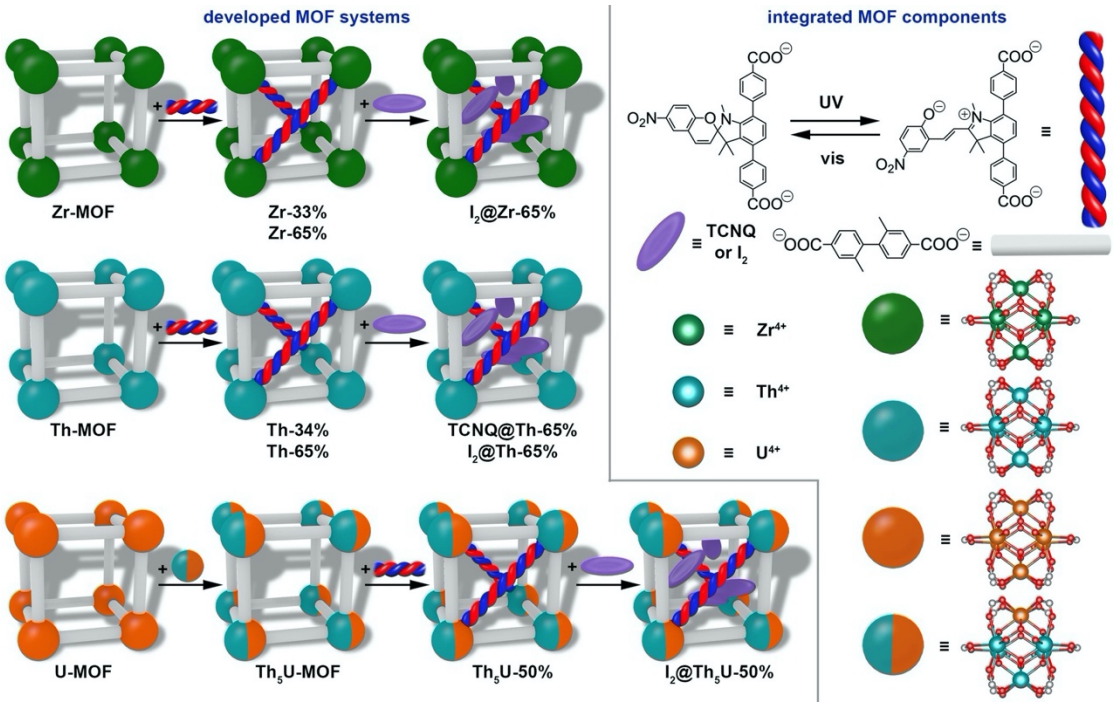

Figure 6.1. (*left*) Schematic representation of the synthetic pathways for development of photoresponsive monometallic and heterometallic frameworks containing *d*- and *f*-elements pursued in the current work. (*right*) Building blocks used for construction or modification of photochromic MOFs. The red and gray spheres in the metal nodes represent oxygen and carbon atoms, respectively.

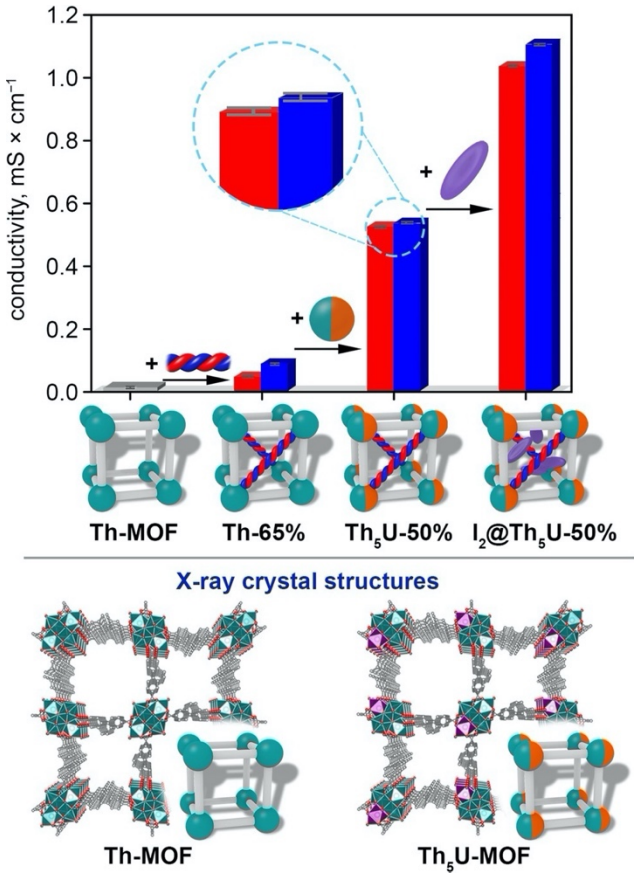

Figure 6.2. (*top*) A bar graph of conductivity data for Th-MOF, Th-65%, Th_5U-50%, and I_2@Th_5U-50%. The gray bar correlates with conductivity values measured for the photoinactive framework (Th-MOF) and red and blue bars represent pre- and post-UV irradiation (λ_{ex} = 365 nm) of photochromic frameworks, respectively. (*bottom*) Single crystal X-ray structures of Th-MOF and Th_5U-MOF.[24]

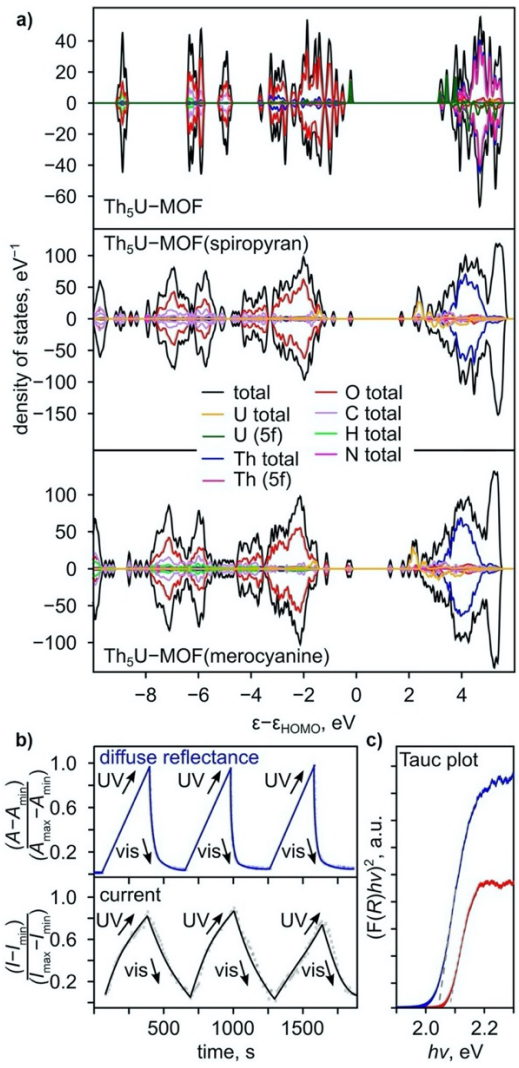

Figure 6.3. a) Total and partial DOS calculations of Th_5U-MOF and photochromic Th_5U-MOF (spiropyran/merocyanine linkers). b) Normalized optical and current cycling of photochromic Th-65% through alternation of UV- (λ_{ex} = 365 nm) and visible- (λ_{ex} = 590 nm) irradiation. I_{max} and I_{min} = the maximum and minimum current values, respectively; A_{max} and A_{min} = the maximum and minimum absorption values (converted from reflectance via the Kubelka–Munk function), respectively. c) A Tauc analysis of the reflectance data for Th-65% before (red) and after (blue) conversion to the merocyanine photoisomer by five minutes of UV-irradiation (λ_{ex} = 365 nm) showing a shift in the apparent band edge.

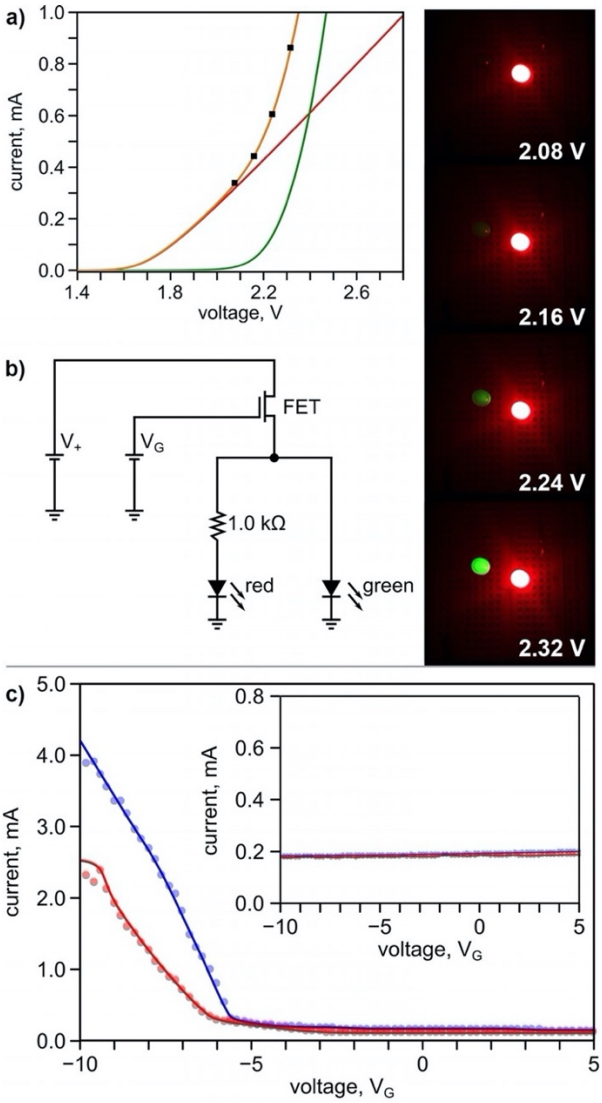

Figure 6.4. a) Current-voltage curves of green and red (with 1.0 kW resistor) LEDs used to construct our two-LED fail-safe circuit and color-coded accordingly. The orange curve is the sum of the green and red curves. The black squares correspond to the data of the optical images (*right*) of the LED dyad powered at varying applied voltages. b) Circuit diagram for our two-LED fail-safe circuit with integrated MOF-based FET. c) Plots of drain current against gate voltage for TCNQ@Zr-65 % in the dark (red) and under constant UV irradiation (blue, λ_{ex} = 365 nm). The inset shows Zr-MOF in the dark (red) and under constant UV irradiation (blue, λ_{ex} = 365 nm).

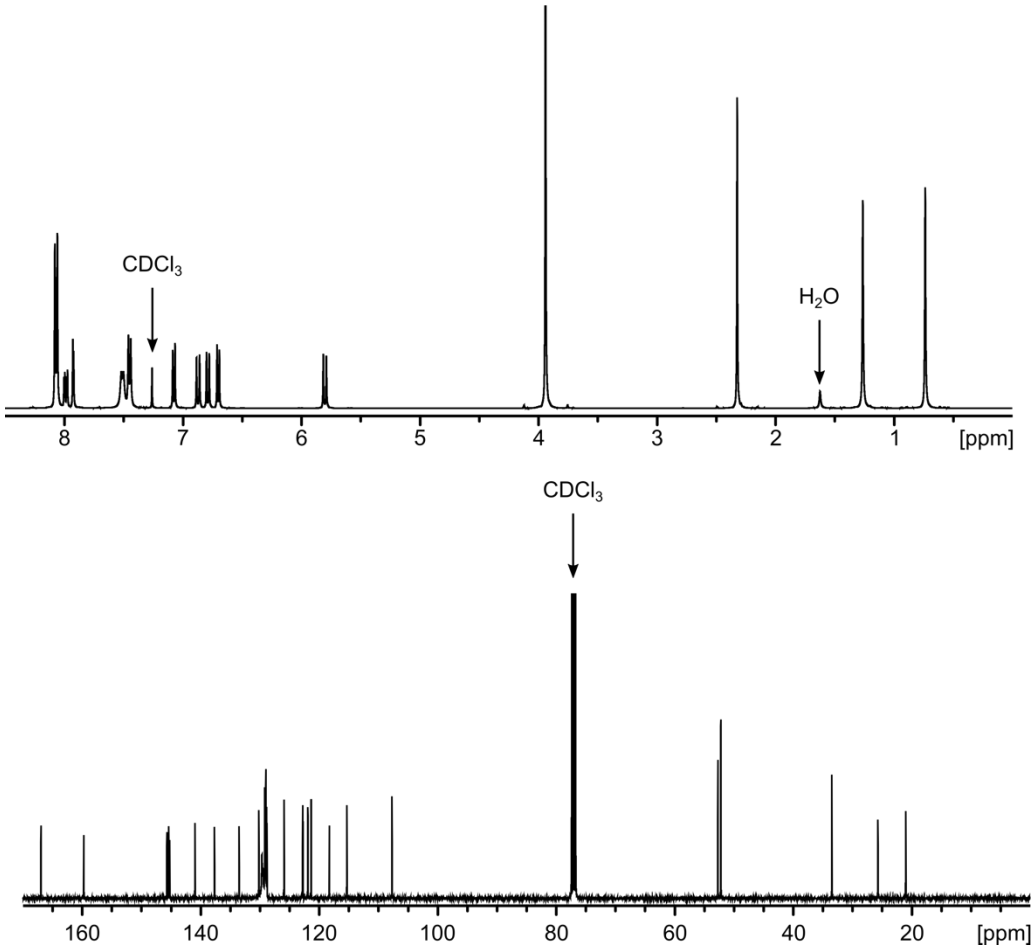

Figure 6.5. ^{1}H NMR (*top*) and ^{13}C NMR (*bottom*) spectra of Me_2TNDA in chloroform-*d*.

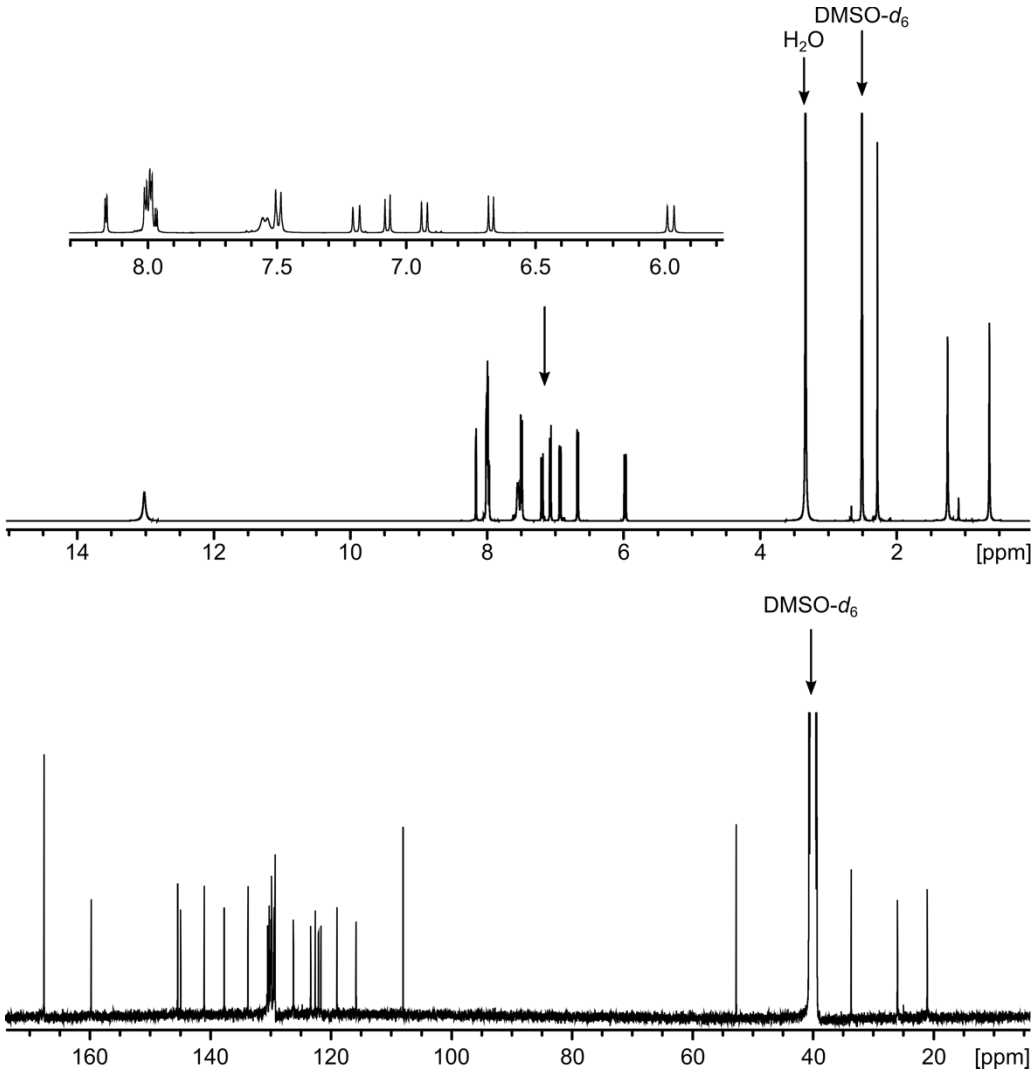

Figure 6.6. ^{1}H NMR (*top*) and ^{13}C NMR (*bottom*) spectra of H2TNDA in dimethyl sulfoxide-d_6.

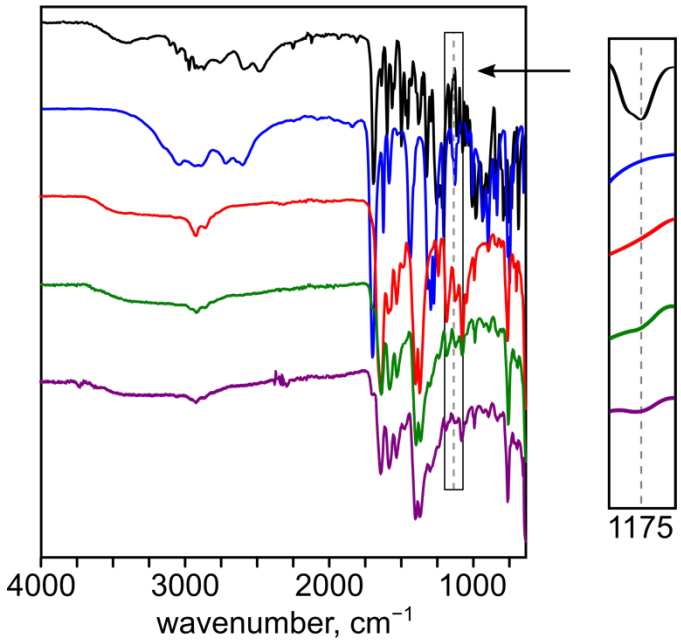

Figure 6.7. FTIR spectra of H_2TNDA (black), H_2Me_2BPDC (blue), Zr-MOF (red), Zr-33% (green), and Zr-65% (purple). The gray dashed line highlights the appearance of ν(C−O−C) at 1175 cm^{-1} in spiropyran-containing samples.[100]

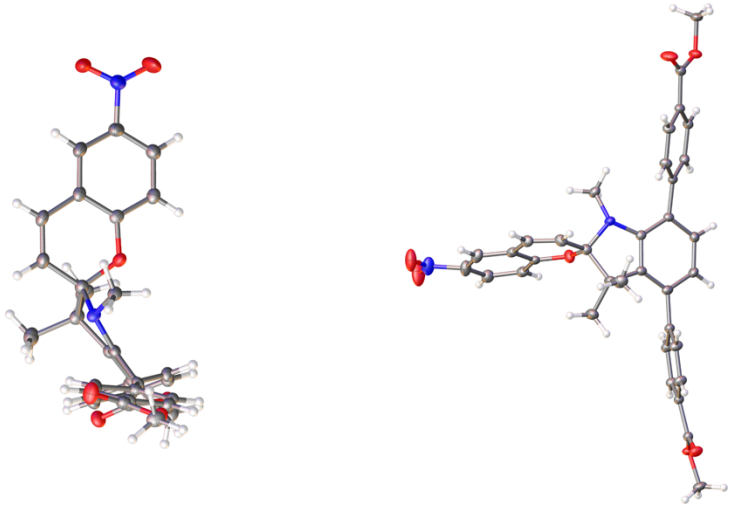

Figure 6.8. The single crystal X-ray structure of Me_2TNDA (Scheme 6.2). Displacement ellipsoids are drawn at the 50% probability level. Blue, red, gray, and white spheres represent N, O, C, and H atoms, respectively.

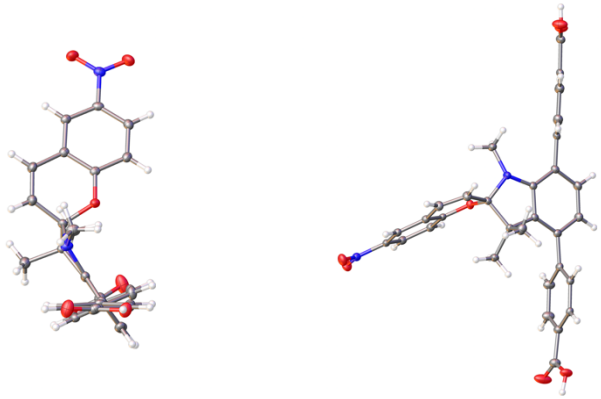

Figure 6.9. The single crystal X-ray structure of H_2TNDA (Scheme 6.2). Displacement ellipsoids are drawn at the 50% probability level. Blue, red, gray, and white spheres represent N, O, C, and H atoms, respectively.

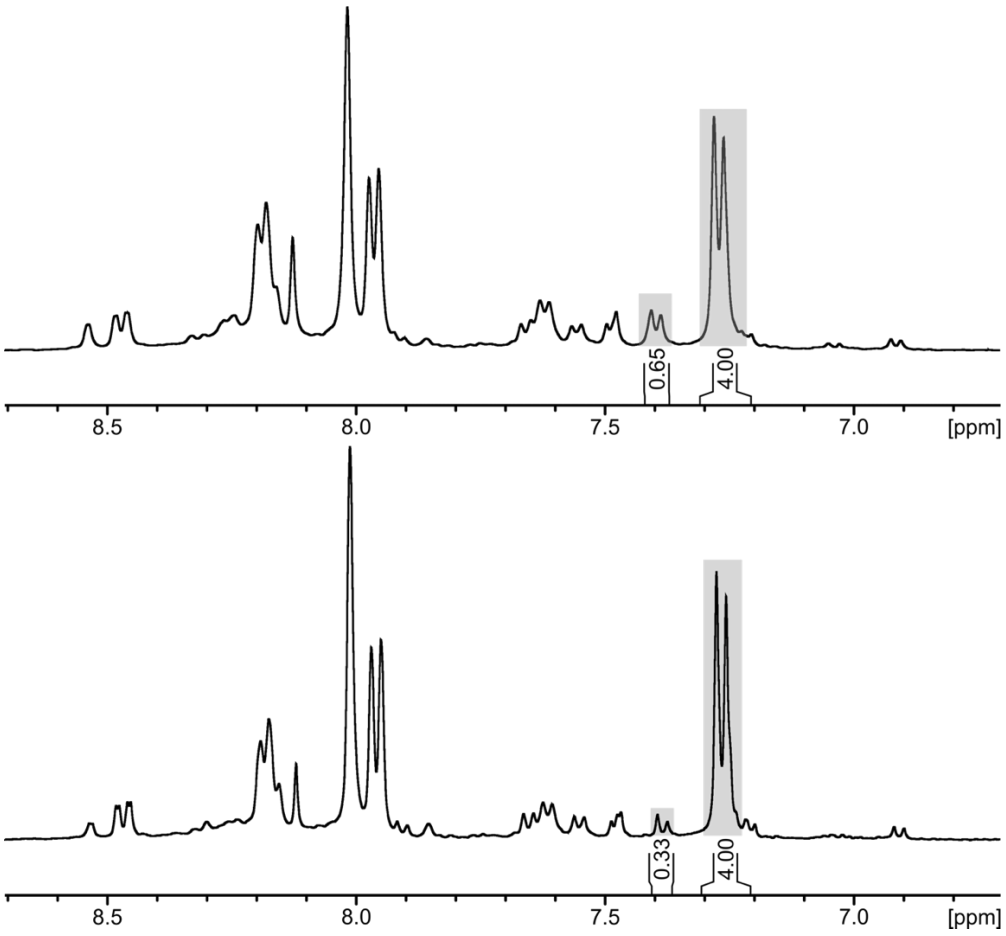

Figure 6.10. ^{1}H NMR spectra of (*top*) digested Zr-65% and (*bottom*) digested Zr-33% in acetone-d_6.

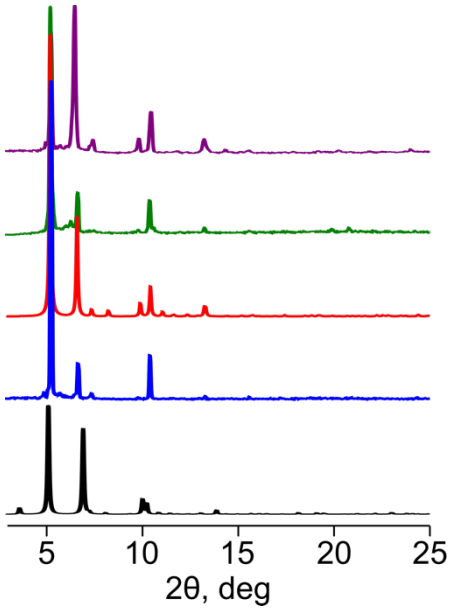

Figure 6.11. PXRD patterns of simulated[74] (black) and experimental Zr-MOF (blue), simulated $Zr_6O_4(OH)_6(Me_2BPDC)_4(Me_2TPDC)$ (H_2Me_2TPDC = 2',5'-dimethyl-[1,1':4',1''-terphenyl]-4,4''-dicarboxylic acid)[74] (red), Zr-33% (green), and Zr-65% (purple).

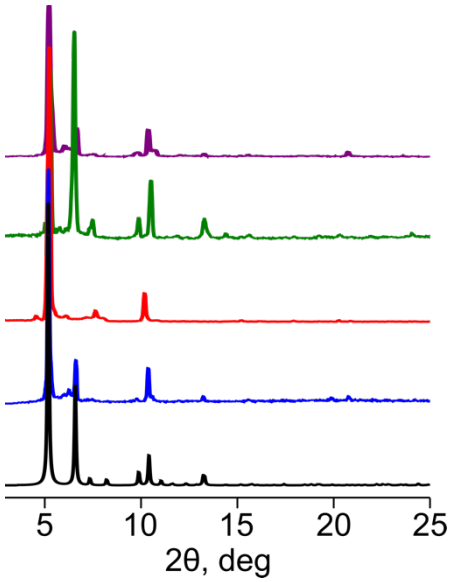

Figure 6.12. PXRD patterns of simulated $Zr_6O_4(OH)_6(Me_2BPDC)_4(Me_2TPDC)$[74] (black), Zr-33% before (blue) and after (red) 10-minutes UV-irradiation, and Zr-65% before (green) and after (purple) 10-minutes UV-irradiation.

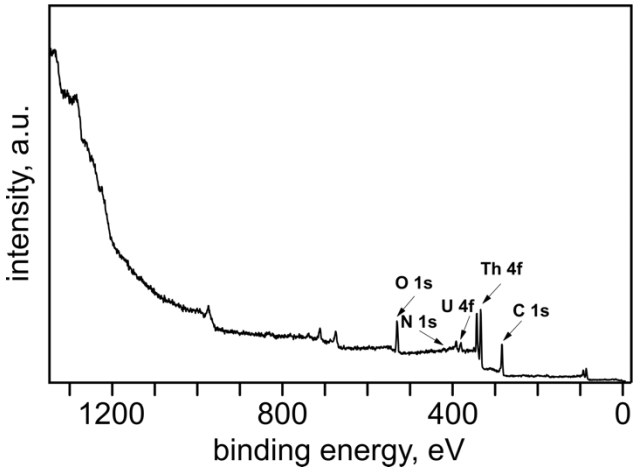

Figure 6.13. XPS survey scan of Th_5U-MOF.

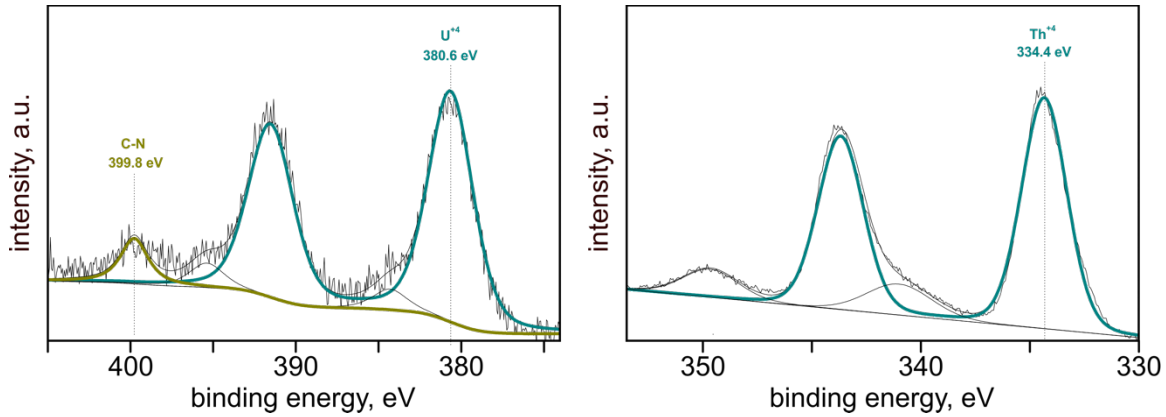

Figure 6.14. XPS data showing the U(4f) (*left*) and Th(4f) (*right*) regions for Th_5U-MOF.

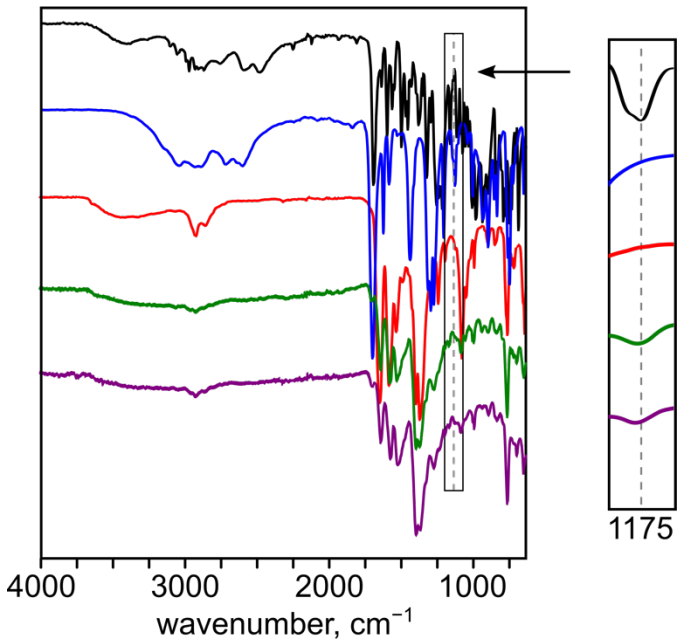

Figure 6.15. FTIR spectra of H_2TNDA (black), H_2Me_2BPDC (blue), Th-MOF (red), Th-34% (green), and Th-65% (purple). The gray dashed line highlights the appearance of ν(C−O−C) at 1175 cm^{-1} in spiropyran-containing samples.[100]

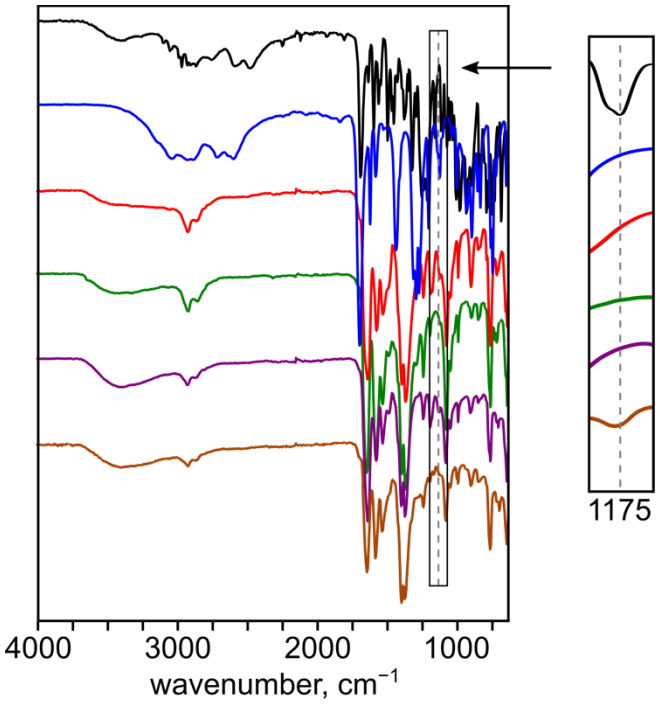

Figure 6.16. FTIR spectra of H_2TNDA (black), H_2Me_2BPDC (blue), U-MOF (red), Th-MOF (green), Th_5U-MOF (purple), and Th_5U-50% (brown). The gray dashed line highlights the appearance of ν(C−O−C) at 1175 cm^{-1} in spiropyran-containing samples.[100]

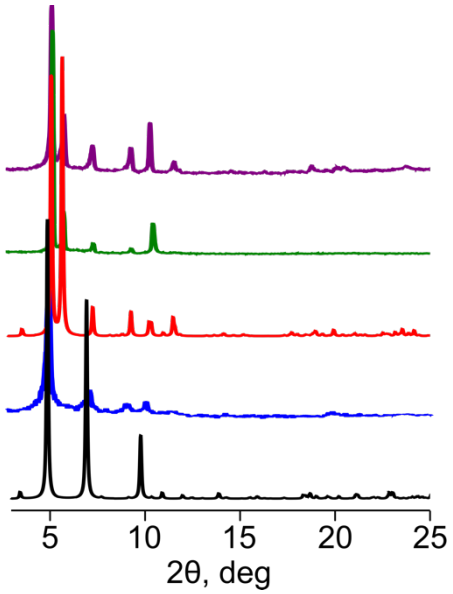

Figure 6.17. PXRD patterns of simulated[75] (black) and experimental Th-MOF (blue), simulated $Zr_6O_4(OH)_6(Me_2BPDC)_4$(TPDC-DEPU) ($H_2$TPDC-DEPU = 2'-(3-(diethoxyphosphoryl)ureido)-[1,1':4',1''-terphenyl]-4,4''-dicarboxylic acid)[75] (red), Th-34% (green), and Th-65% (purple).

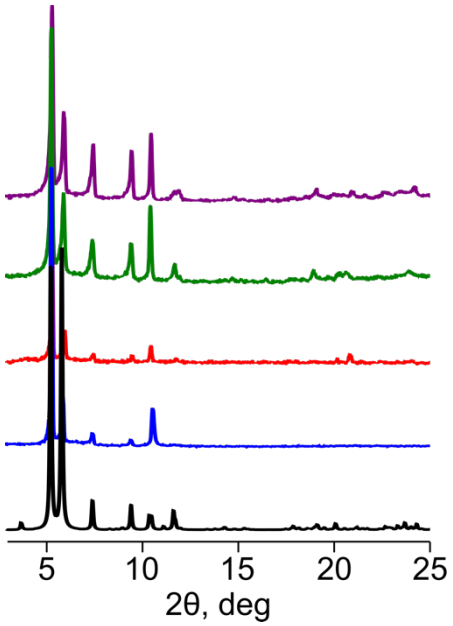

Figure 6.18. PXRD patterns of simulated $Zr_6O_4(OH)_6(Me_2BPDC)_4$(TPDC-DEPU)[75] (black), Th- 34% before (blue) and after (red) 10-minutes of UV-irradiation, and Th-65% before (green) and after (purple) 10-minutes of UV-irradiation.

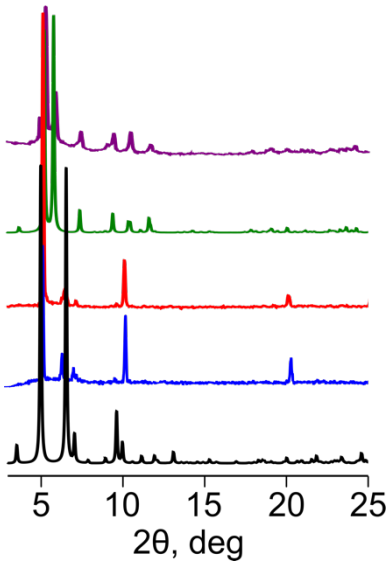

Figure 6.19. PXRD patterns of simulated (black) and experimental U-MOF[75] (blue), Th_5U-MOF (red), simulated $Zr_6O_4(OH)_6(Me_2BPDC)_4$(TPDC-DEPU)[75] (green), and Th_5U-50% (purple).

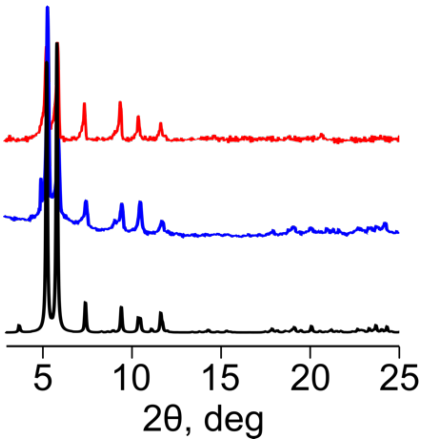

Figure 6.20. PXRD patterns of simulated $Zr_6O_4(OH)_6(Me_2BPDC)_4$(TPDC-DEPU)[75] (black) and Th_5U-50% before (blue) and after (red) 10-minutes of UV-irradiation.

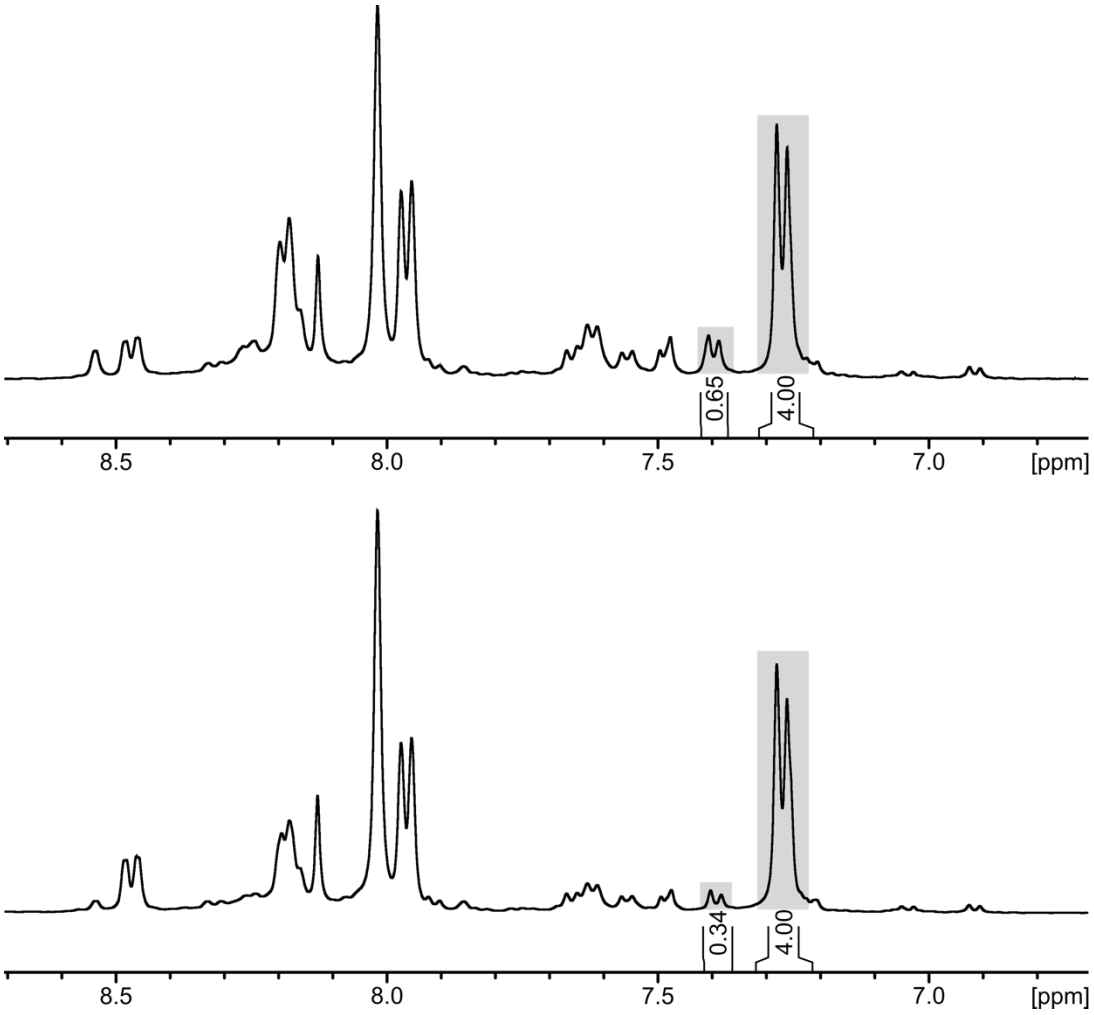

Figure 6.21. ^{1}H NMR spectra of (*top*) digested Th-65% and (*bottom*) digested Th-34% in acetone-d_6.

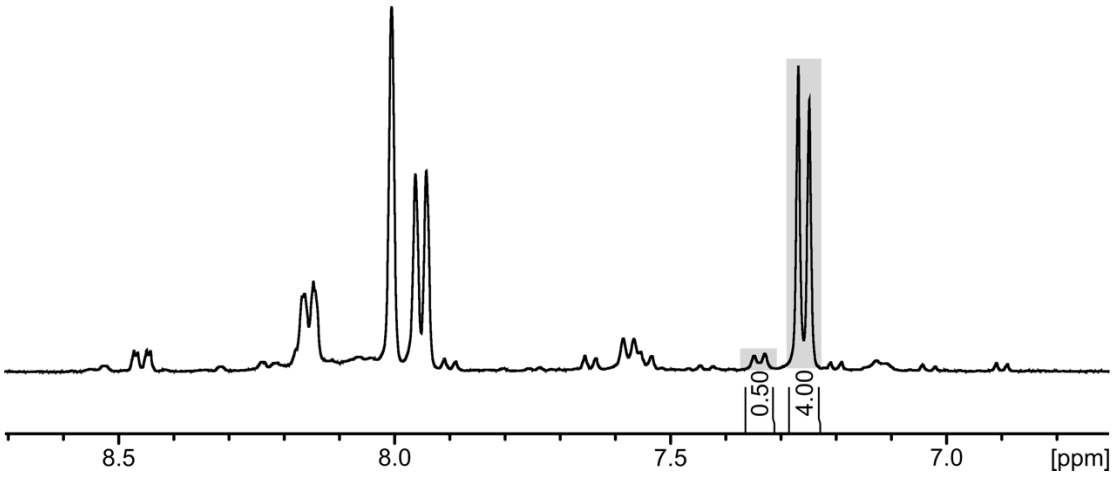

Figure 6.22. ^{1}H NMR spectrum of digested Th_5U-50% in acetone-d_6.

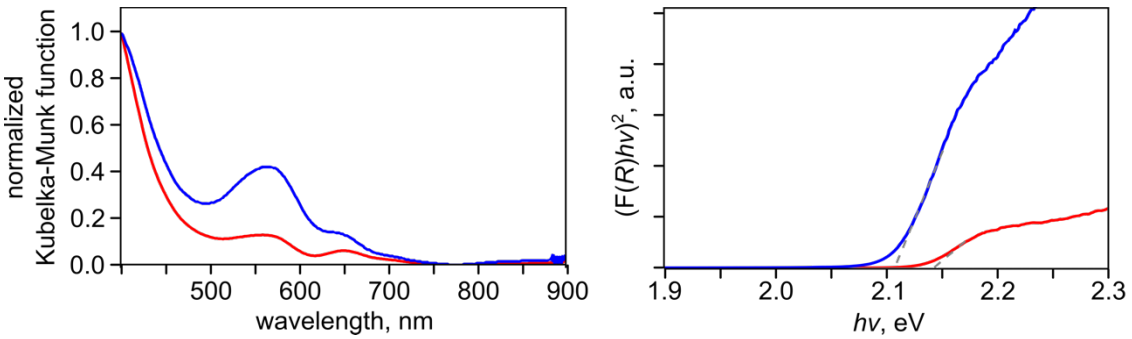

Figure 6.23. Diffuse reflectance spectra (*left*) and Tauc plot ([F(*R*) × *hv*]^2 vs *hv*) for band gap transitions (*right*) of Zr-33% before (red) and after 1-minute of UV-irradiation (λ_{ex} = 365 nm, blue).

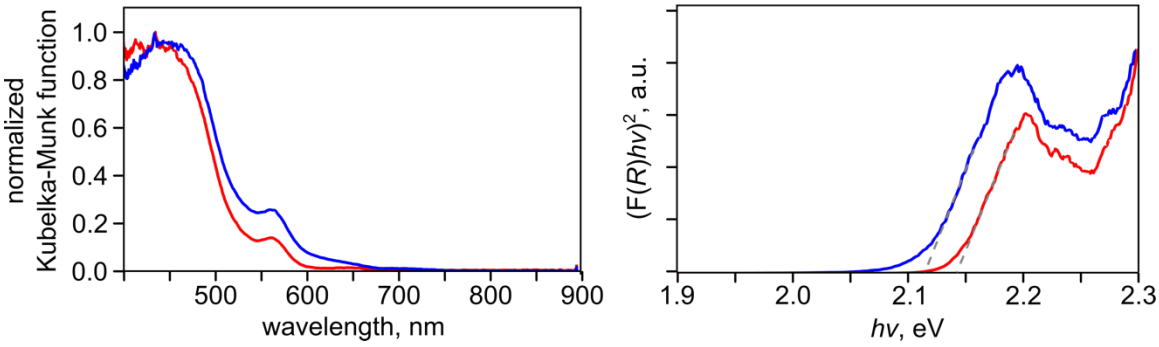

Figure 6.24. Diffuse reflectance spectra (*left*) and Tauc plot ([F(*R*) × *hv*]^2 vs *hv*) for band gap transitions (*right*) of Zr-65% before (red) and after 1-minute of UV-irradiation (λ_{ex} = 365 nm, blue).

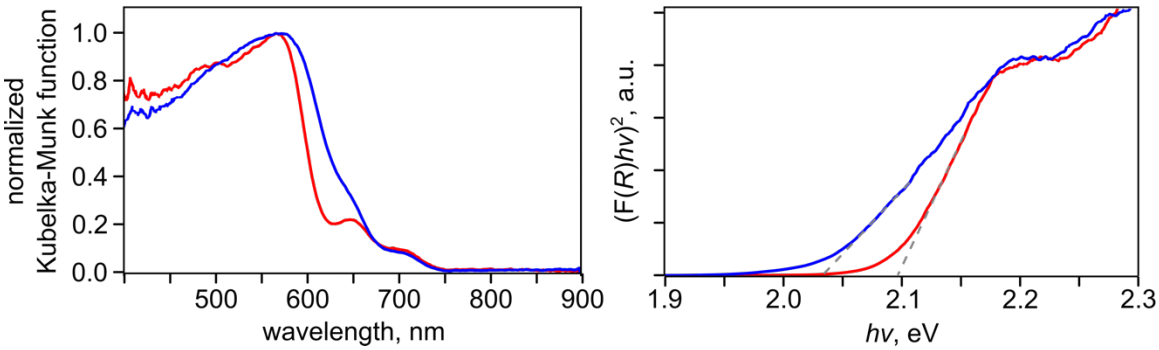

Figure 6.25. Diffuse reflectance spectra (*left*) and Tauc plot ([F(*R*) × *hv*]^2 vs *hv*) for band gap transitions (*right*) of Th-34% before (red) and after 1-minute of UV-irradiation (λ_{ex} = 365 nm, blue).

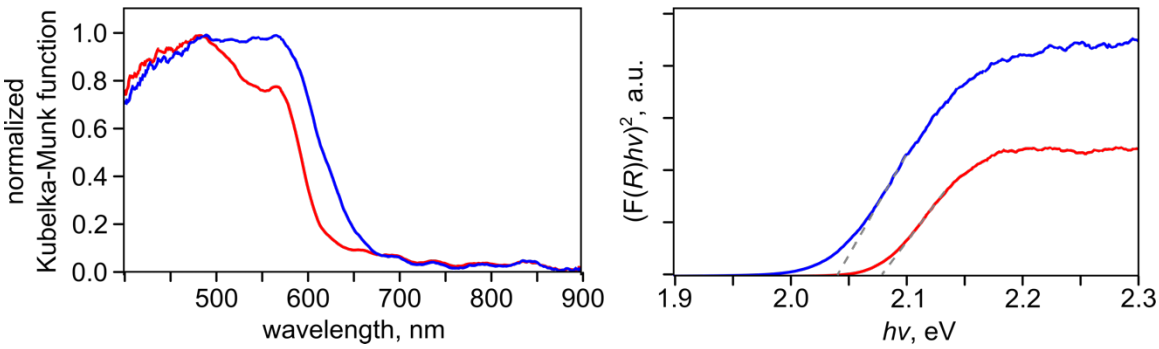

Figure 6.26. Diffuse reflectance spectra (*left*) and Tauc plot ([F(*R*) × *hv*]^2 vs *hv*) for band gap transitions (*right*) of Th-65% before (red) and after 1-minute of UV-irradiation (λ_{ex} = 365 nm, blue).

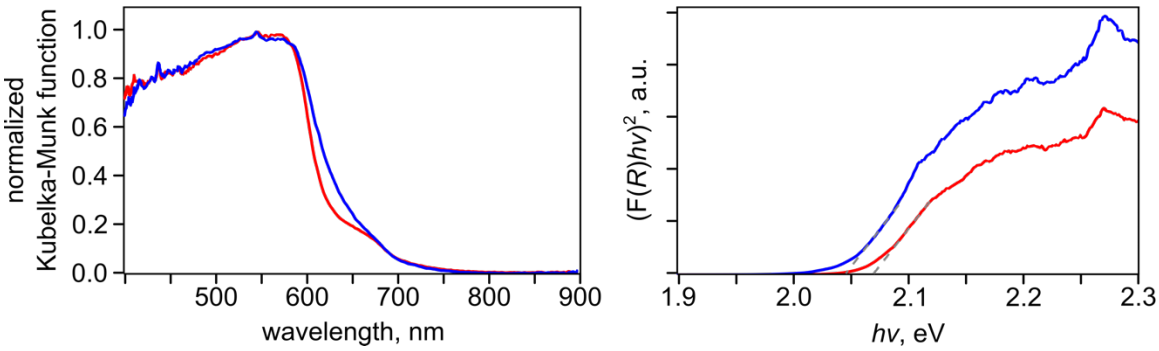

Figure 6.27. Diffuse reflectance spectra (*left*) and Tauc plot ([F(*R*) × *hv*]^2 vs *hv*) for band gap transitions (*right*) of Th_5U-50% before (red) and after 1-minutes of UV-irradiation (λ_{ex} = 365 nm, blue).

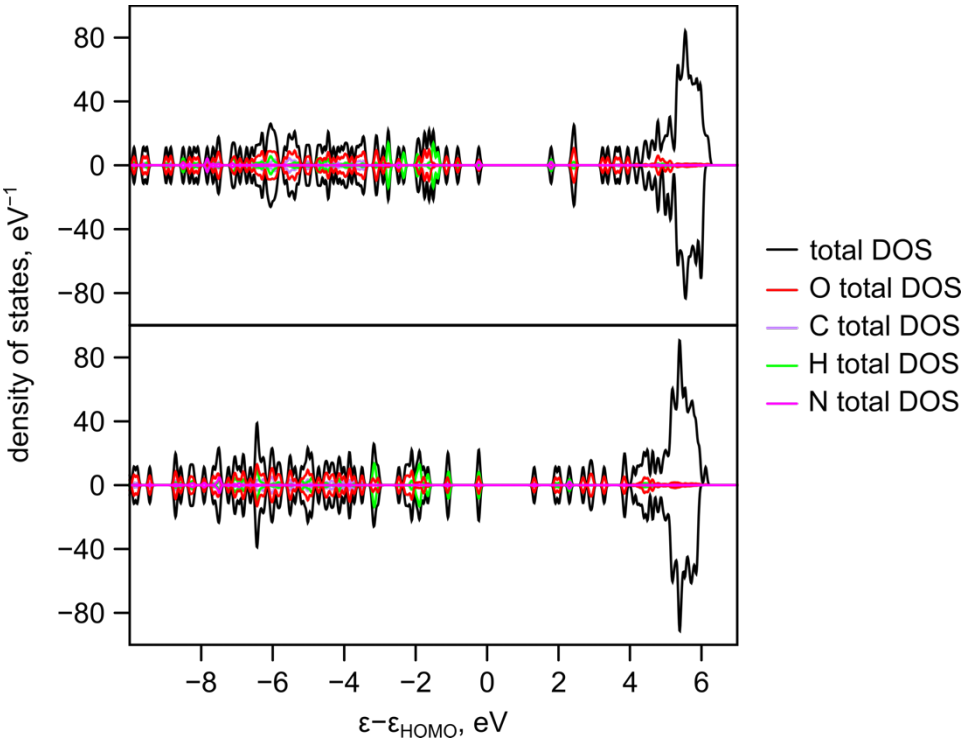

Figure 6.28. Total and partial DOS computed using the GGA-PBE level of theory. The optimized structures of (*top*) spiropyran (band gap = 1.95 eV) and (*bottom*) merocyanine (band gap = 1.55 eV).

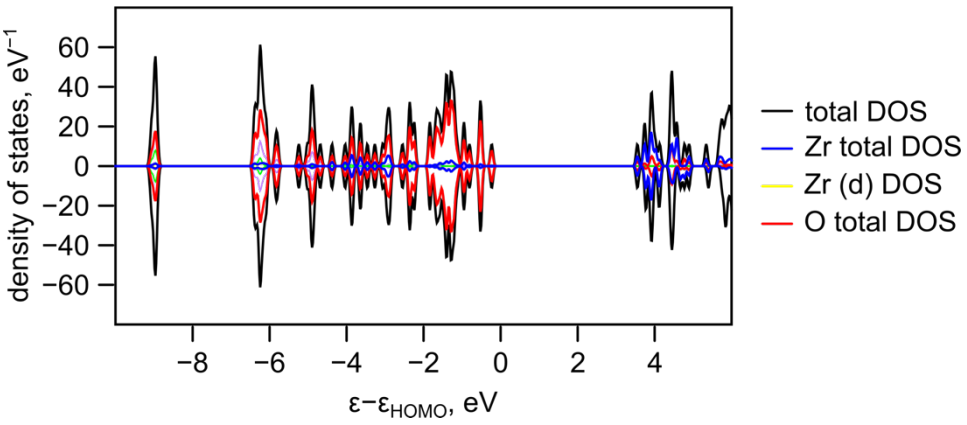

Figure 6.29. Total and partial DOS computed using the GGA-PBE level of theory. The optimized structures of Zr-MOFs SBU (band gap = 3.60 eV).

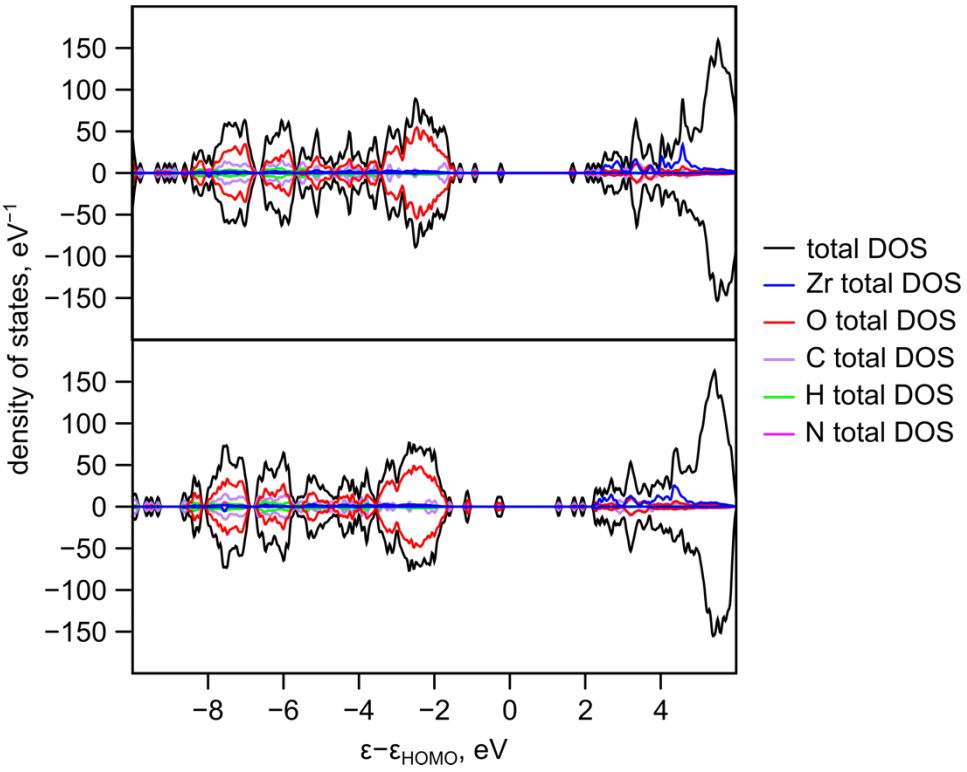

Figure 6.30. Total and partial DOS computed using the GGA-PBE level of theory. The optimized structures of (*top*) Zr(spiropyran) (band gap = 1.95 eV) and (*bottom*) Zr(merocyanine) (band gap = 1.55 eV).

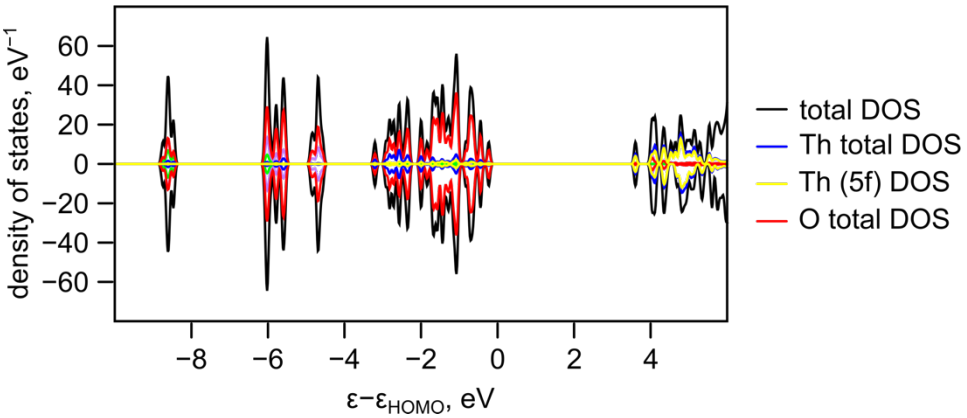

Figure 6.31. Total and partial DOS computed using the GGA-PBE level of theory. The optimized structures of Th-MOFs SBU (band gap = 3.50 eV).

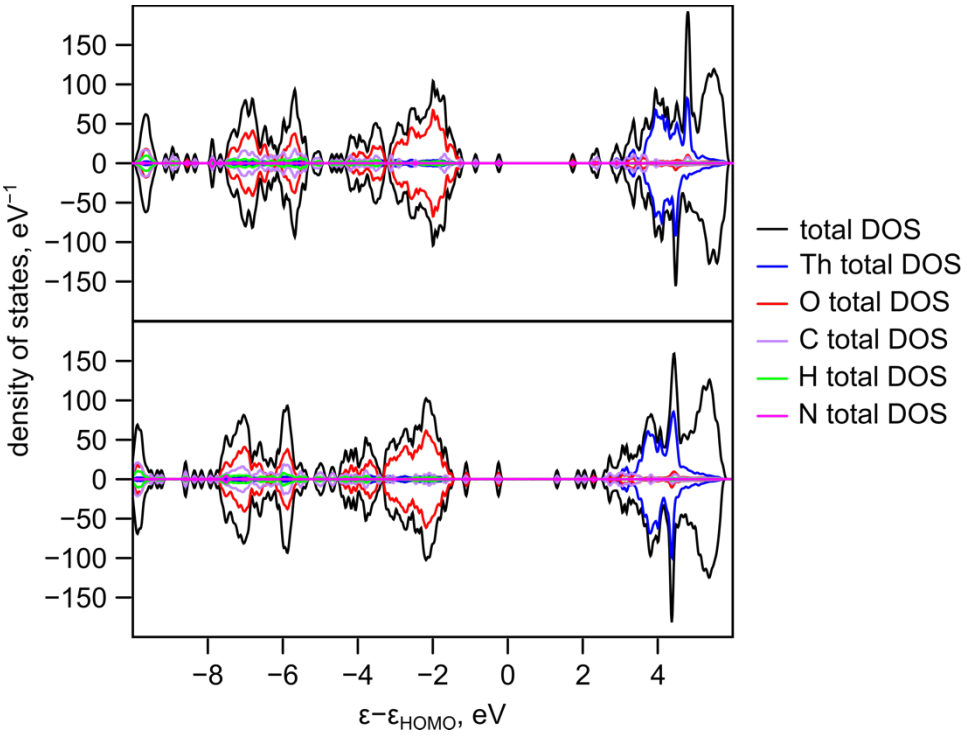

Figure 6.32. Total and partial DOS computed using the GGA-PBE level of theory. The optimized structures of (*top*) Th(spiropyran) (band gap = 1.95 eV) and (*bottom*) Th(merocyanine) (band gap = 1.55 eV).

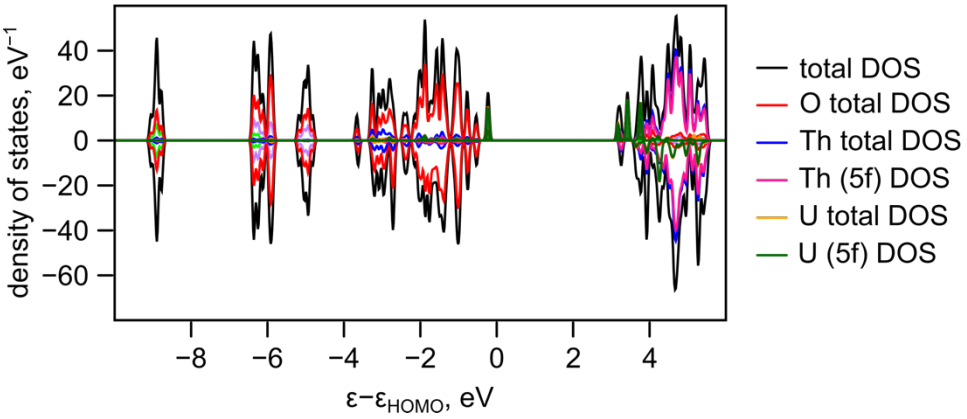

Figure 6.33. Total and partial DOS computed using the GGA-PBE level of theory. The optimized structures of Th_5U-MOFs SBU (band gap = 3.50 eV).

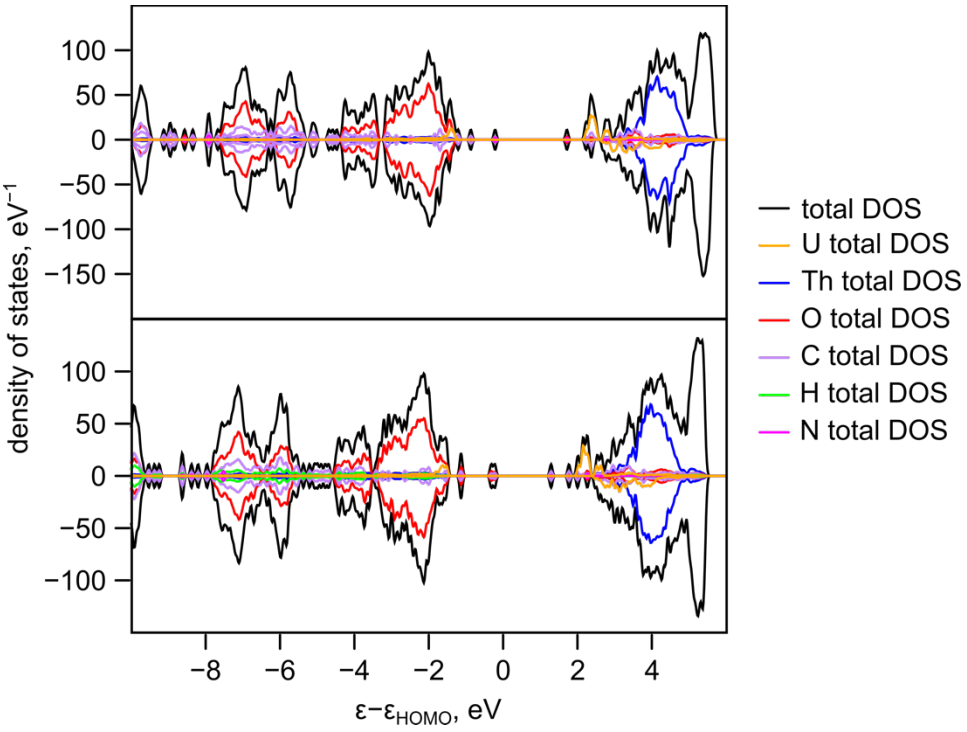

Figure 6.34. Total and partial DOS computed using the GGA-PBE level of theory. The optimized structures of (*top*) Th_5U(spiropyran) (band gap = 1.95 eV) and (*bottom*) Th_5U(merocyanine) (band gap = 1.55 eV).

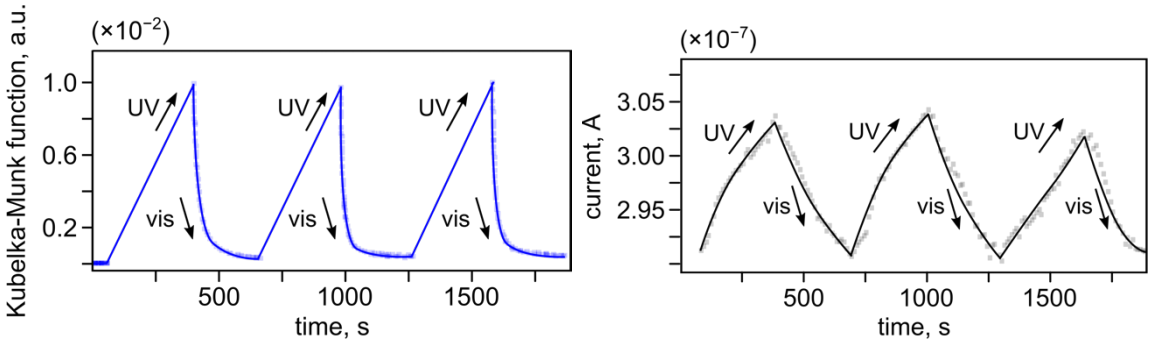

Figure 6.35. Optical (*left*) and current (*right*) cycling of photochromic Th-65% through alternation of UV- (λ_{ex} = 365 nm) and visible- (λ_{ex} = 590 nm) irradiation.

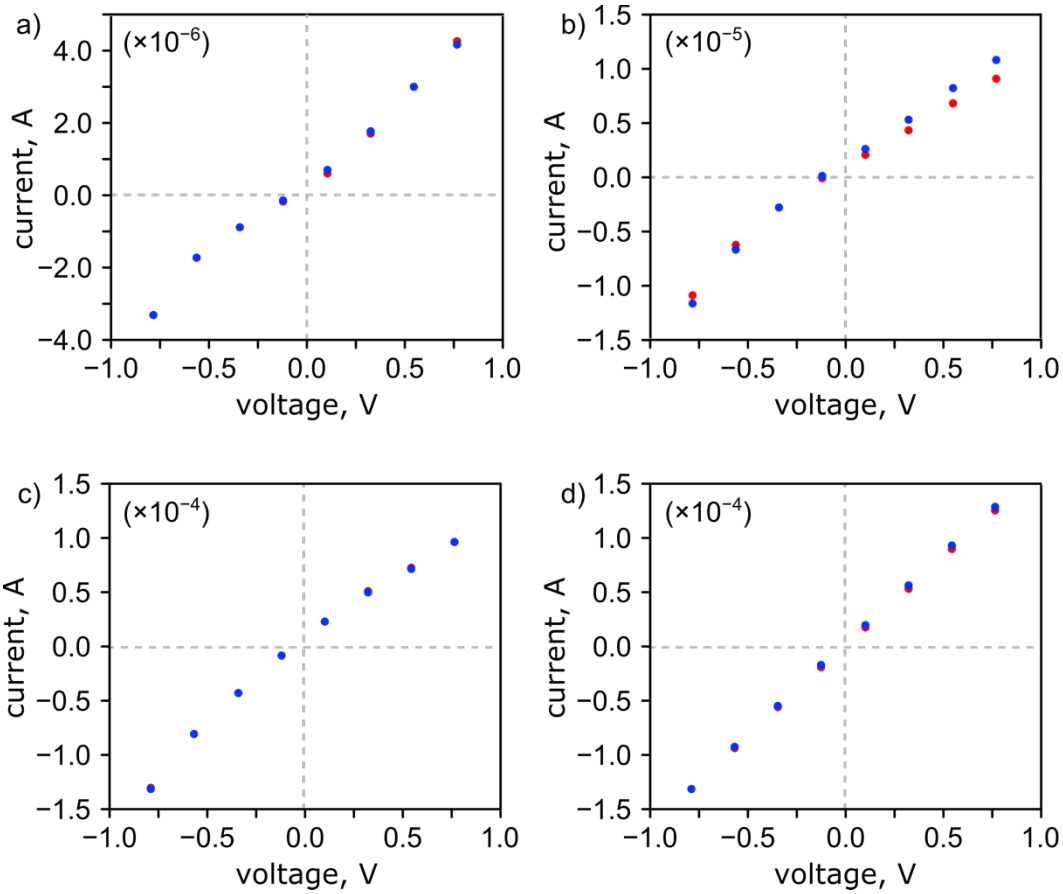

Figure 6.36. Current-voltage curves of (a) Th-MOF, (b) Th-34%, (c) Th_5U-MOF, and (d) Th_5U-50% before (red) and after (blue) UV-irradiation (λ_{ex} = 365 nm).

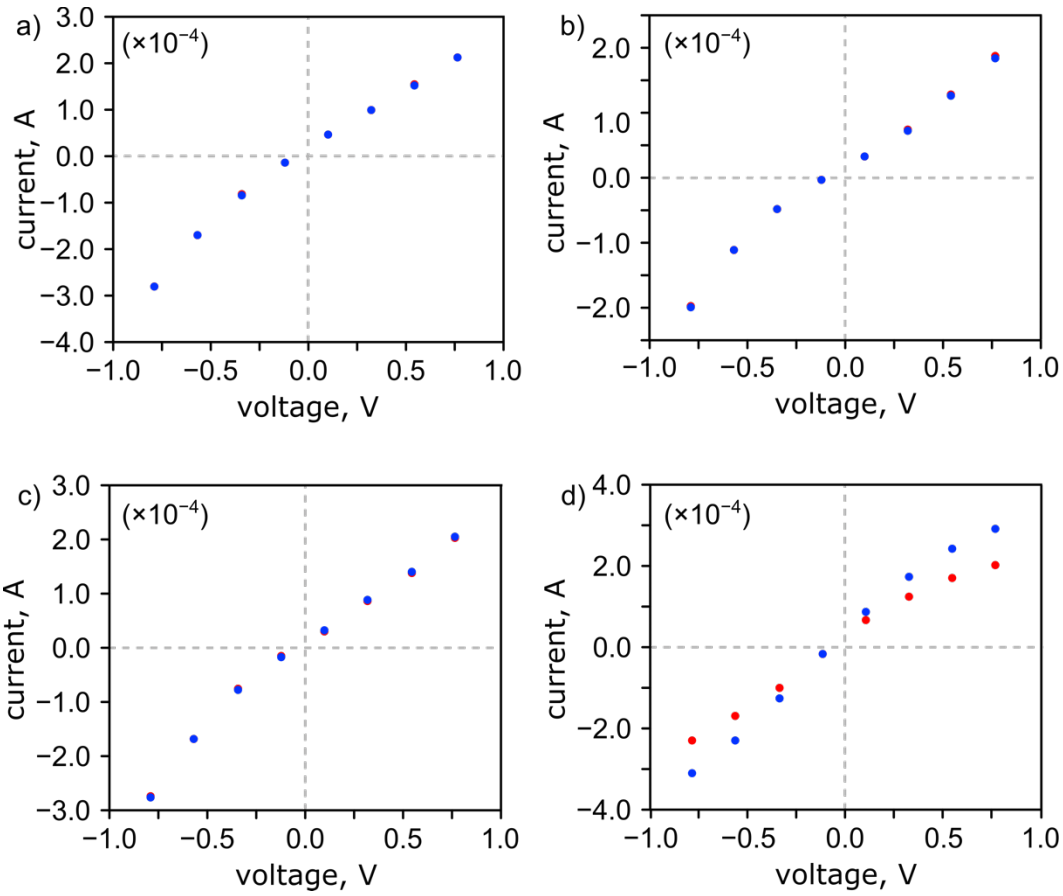

Figure 6.37. Current-voltage curves of (a) TCNQ@Zr-MOF, (b) I_2@Th-MOF, (c) TCNQ@Th-MOF, and (d) I_2@Th-65% before (red) and after (blue) UV-irradiation (λ_{ex} = 365 nm).

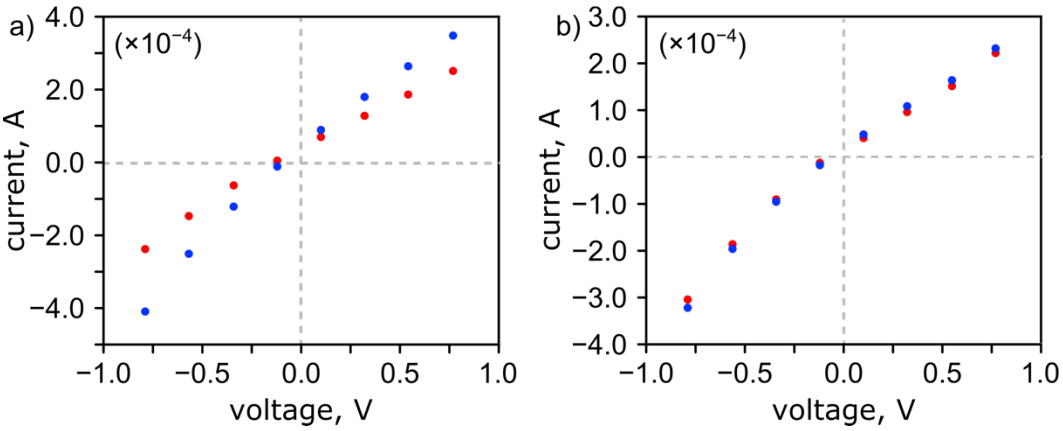

Figure 6.38. Current-voltage curves of (a) TCNQ@Th-65% and (b) I_2@Th_5U-50% before (red) and after (blue) UV-irradiation (λ_{ex} = 355 nm).

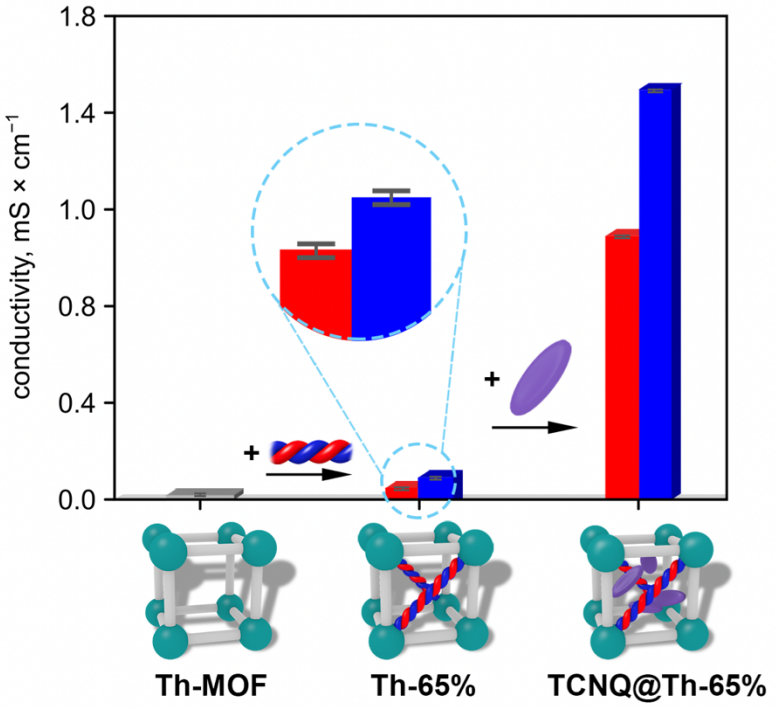

Figure 6.39. A bar graph of conductivity data for Th-MOF, Th-65%, and TCNQ@Th-65%. The gray bar correlates with conductivity values measured for the photoinactive framework (Th-MOF) and red and blue bars represent pre- and post-UV irradiation (λ_{ex} = 365 nm) of photochromic frameworks, respectively.

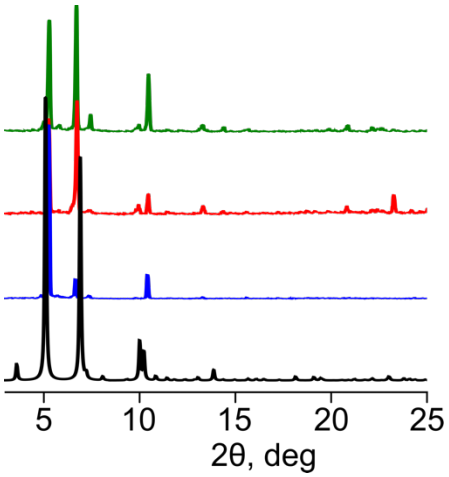

Figure 6.40. PXRD patterns of simulated[74] (black) and experimental Zr-MOF (blue), I_2@Zr-MOF (red), and TCNQ@Zr-MOF (green).

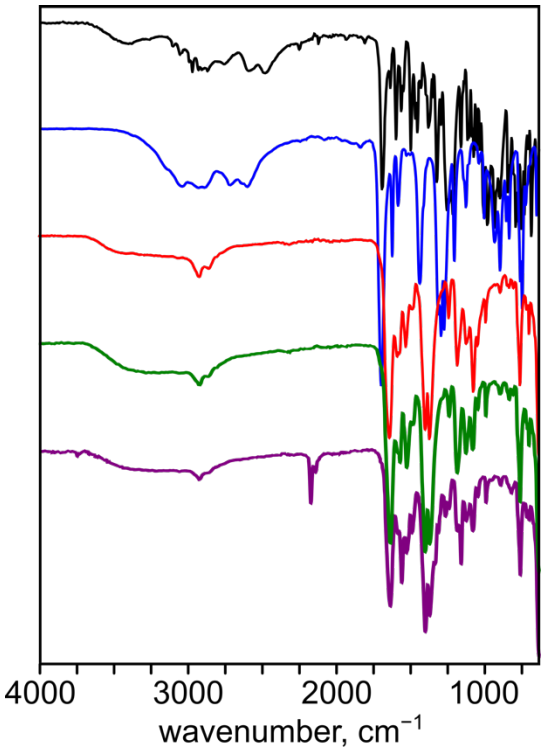

Figure 6.41. FTIR spectra of H_2TNDA (black), H_2Me_2BPDC (blue), Zr-MOF (red), I_2@Zr-MOF (green), and TCNQ@Zr-MOF (purple).

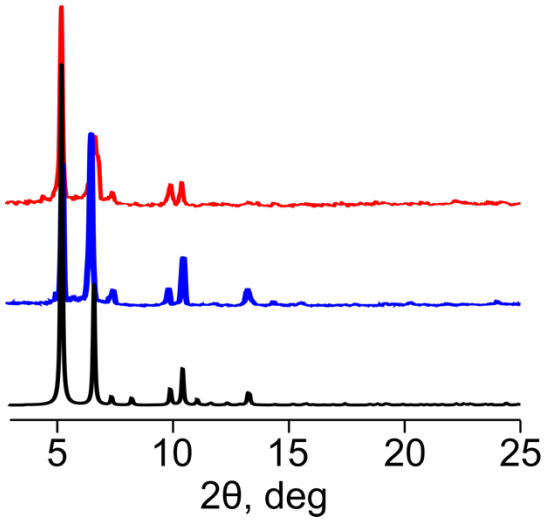

Figure 6.42. PXRD patterns of simulated $Zr_6O_4(OH)_6(Me_2BPDC)_4(Me_2TPDC)$[74] (black), Zr-65% (blue), and TCNQ@Zr-65% (red).

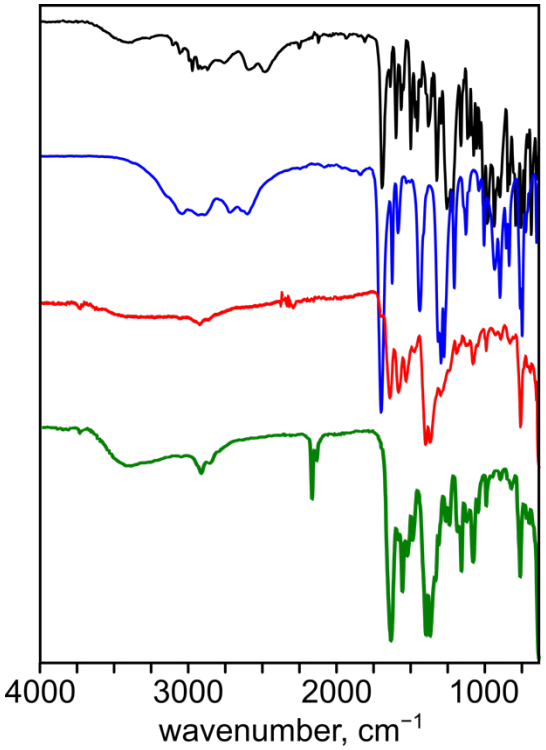

Figure 6.43. FTIR spectra of H_2TNDA (black), H_2Me_2BPDC (blue), Zr-65% (red), and TCNQ@Zr-65% (green).

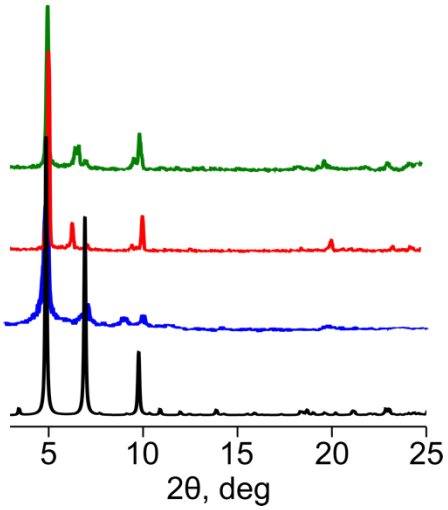

Figure 6.44. PXRD patterns of simulated[75] (black) and experimental Th-MOF (blue), I_2@Th-MOF (red), and TCNQ@Th-MOF (green).

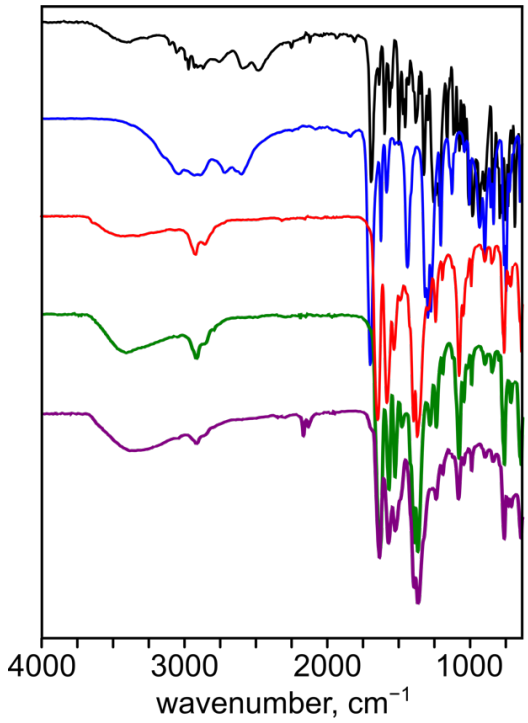

Figure 6.45. FTIR spectra of H_2TNDA (black), H_2Me_2BPDC (blue), Th-MOF (red), I_2@Th-MOF (green), and TCNQ@Th-MOF (purple).

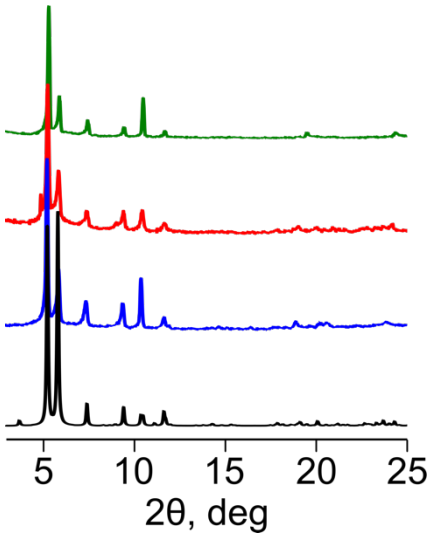

Figure 6.46. PXRD patterns of simulated $Zr_6O_4(OH)_6(Me_2BPDC)_4$(TPDC-DEPU)[75] (black), Th- 65% (blue), I_2@Th-65% (red), and TCNQ@Th-65% (green).

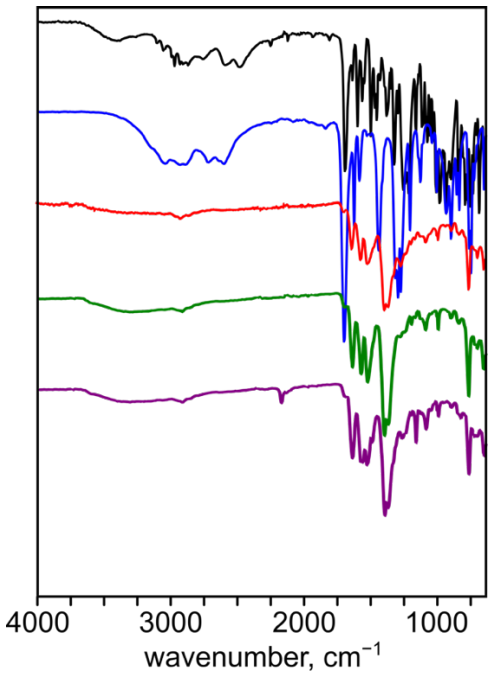

Figure 6.47. FTIR spectra of H_2TNDA (black), H_2Me_2BPDC (blue), Th-65% (red), I_2@Th-65% (green), and TCNQ@Th-65% (purple).

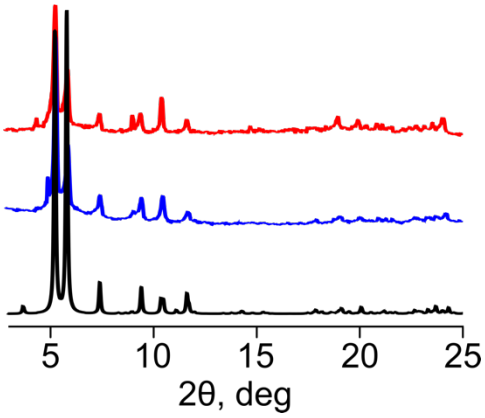

Figure 6.48. PXRD patterns of simulated $Zr_6O_4(OH)_6(Me_2BPDC)_4$(TPDC-DEPU)[75] (black), Th_5U-50% (blue), and I_2@Th_5U-50% (red).

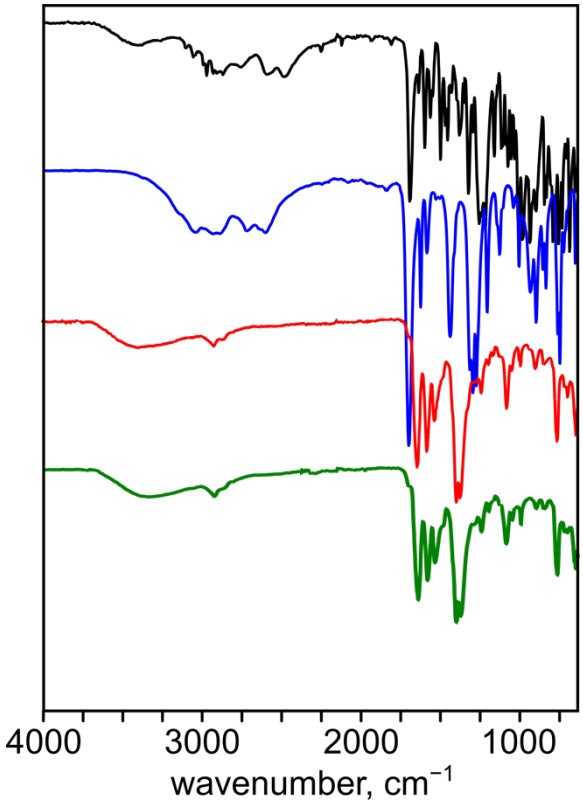

Figure 6.49. FTIR spectra of H_2TNDA (black), H_2Me_2BPDC (blue), Th_5U-50% (red), I_2@Th_5U-50% (green).

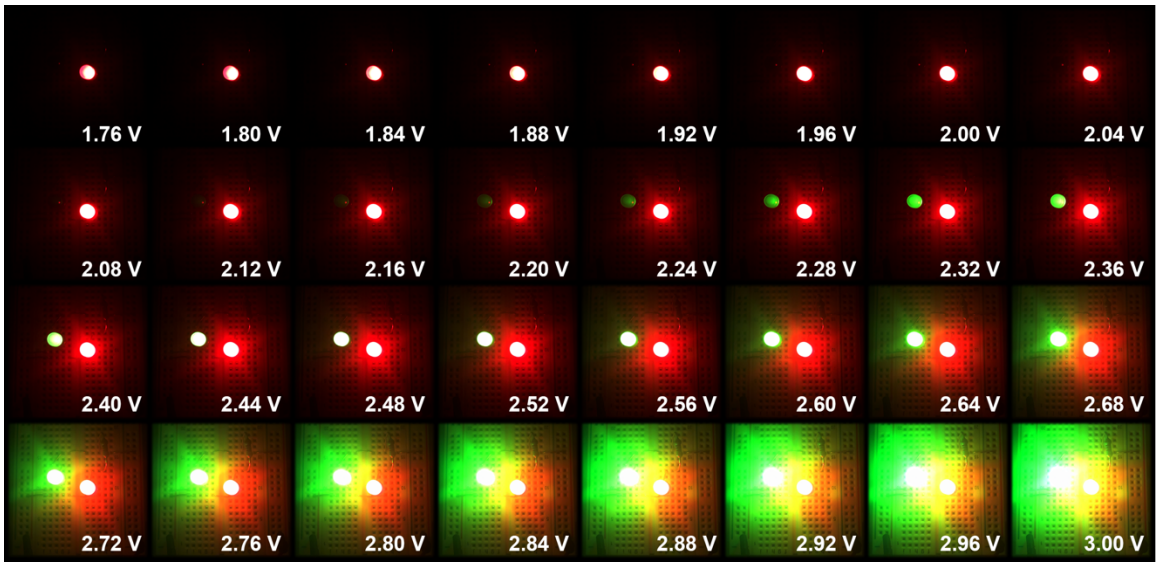

Figure 6.50. Two-LED circuit calibration of a red (+ 1 kΩ resistor) and green LED under a range of applied voltages. The IV curves of each LED can be found in Figure 6.4.

Table 6.1. X-ray structure refinement data for compound **VI**[a] and TNDS.[a]

compound	**Me_2TNDA**	**H_2TNDA**
formula	$C_{35}H_{30}N_2O_7$[b]	$C_{37}H_{26}N_2O_9S_2$[b]
FW	590.61	730.89
T, K	100(2)	100(2)
crystal system	triclinic	triclinic
space group	*P*-1	*P*-1
Z	2	2
a, Å	6.9366(3)	10.7471(6)
b, Å	12.6004(5)	11.9431(7)
c, Å	16.5294(7)	14.8938(8)
α, °	100.089(2)	97.395(3)
β, °	91.122(2)	98.994(3)

γ, °	97.741(2)	111.979(2)
V, Å^3	1408.05(10)	1713.97(17)
d_{calc} g/cm^3	1.393	1.416
μ, mm^{-1}	0.098	0.215
F(000)	620	756
crystal size, mm^3	0.44 × 0.06 × 0.03	0.48 × 0.16 × 0.04
theta range	4.5 to 55.178	4.192 to 56.754
index ranges	$-9 \leq h \leq 9$ $-16 \leq k \leq 16$ $-21 \leq l \leq 21$	$-14 \leq h \leq 14$ $-15 \leq k \leq 15$ $-19 \leq l \leq 19$
refl. collected	64270	78045
data/restraints/parameters	6504/9/419	467
GOF on F^2	1.018	1.025
largest peak/hole e/Å^3	0.33/−0.22	0.62/−0.41
R_1 (wR_2), %, $[I \geq 2\text{sigma}(I)]$[c]	0.0442/0.0977	0.0388/0.0960

[a]Mo-Kα (λ = 0.71073 Å) radiation

[b]Formula is given based on single-crystal X-ray data and does not include disordered solvent molecules

[c]$R_1 = \Sigma||F_o| - |F_c||/ \Sigma |F_o|$, $wR_2 = \{\Sigma [w(F_o^2 - F_c^2)^2]/ \Sigma [w(F_o^2)^2]\}^{1/2}$

Table 6.2. Estimated optical band gaps of reported MOFs.

MOF	optical band gap (ΔE_g, eV) dark	optical band gap (ΔE_g, eV) under UV
Zr-MOF	3.35	3.35
Zr-33%	2.15	2.11
Zr-65%	2.15	2.11
Th-MOF	3.31	3.31
Th-34%	2.10	2.04
Th-64%	2.08	2.04
Th_5U-MOF	2.50	2.50
Th_5U-50%	2.06	2.04

Table 6.3. Calculated band gaps of reported MOFs.

MOF	theoretical band gap (ΔE_g, eV) dark	theoretical band gap (ΔE_g, eV) under UV
Zr-MOF	3.60	n/a
Zr-photoswitch	1.95	1.55
Th-MOF	3.50	n/a
Th-photoswitch	1.95	1.55
Th_5U-MOF	3.00	n/a
Th_5U-photoswitch	1.95	1.55

Table 6.4. Conductivity results and standard error for reported MOFs.

MOF	conductivity value ($S \times cm^{-1}$) dark	standard error ($S \times cm^{-1}$) dark	conductivity value ($S \times cm^{-1}$) under UV	standard error ($S \times cm^{-1}$) under UV
Th-MOF	1.46×10^{-5}	9.17×10^{-8}	1.45×10^{-5}	7.21×10^{-8}
Th-34%	3.97×10^{-5}	1.87×10^{-7}	4.46×10^{-5}	8.85×10^{-8}
Th_5U-MOF	4.61×10^{-4}	3.05×10^{-6}	4.62×10^{-4}	1.01×10^{-6}
Th_5U-50%	5.21×10^{-4}	6.22×10^{-6}	5.31×10^{-4}	4.11×10^{-6}
TCNQ@Zr-MOF	9.21×10^{-4}	8.30×10^{-6}	9.21×10^{-4}	7.76×10^{-6}
I_2@Th-MOF	7.41×10^{-4}	3.70×10^{-6}	7.42×10^{-4}	6.28×10^{-6}
TCNQ@Th-MOF	9.66×10^{-4}	2.33×10^{-5}	9.66×10^{-4}	4.72×10^{-5}
I_2@Th-65%	9.55×10^{-4}	4.48×10^{-6}	1.12×10^{-3}	3.06×10^{-6}
TCNQ@Th-65%	9.85×10^{-4}	6.98×10^{-6}	1.53×10^{-3}	5.58×10^{-5}
I_2@Th_5U-50%	1.04×10^{-3}	3.51×10^{-5}	1.11×10^{-3}	1.64×10^{-5}

Table 6.5. ICP-MS results for iodine-doped frameworks.

MOF	iodine atoms per pore
I_2@Zr-MOF	8.7
I_2@Zr-33%	7.7
I_2@Th-34%	7.1

APPENDIX A: COPYRIGHT PERMISSIONS

Chapter 1.

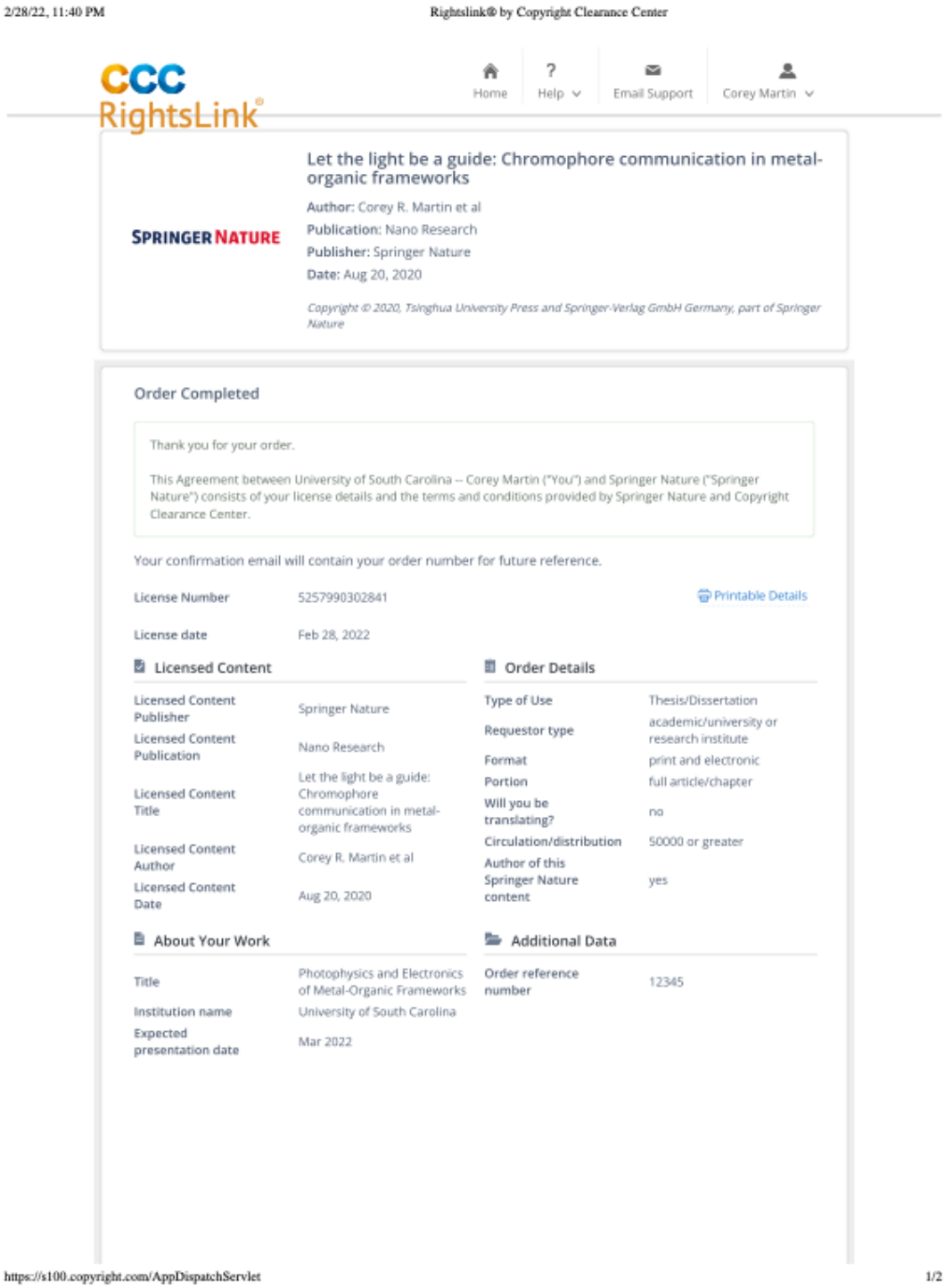

2/28/22, 11:40 PM Rightslink® by Copyright Clearance Center

CCC RightsLink

Home | Help | Email Support | Corey Martin

SPRINGER NATURE

Let the light be a guide: Chromophore communication in metal-organic frameworks

Author: Corey R. Martin et al
Publication: Nano Research
Publisher: Springer Nature
Date: Aug 20, 2020

Copyright © 2020, Tsinghua University Press and Springer-Verlag GmbH Germany, part of Springer Nature

Order Completed

Thank you for your order.

This Agreement between University of South Carolina -- Corey Martin ("You") and Springer Nature ("Springer Nature") consists of your license details and the terms and conditions provided by Springer Nature and Copyright Clearance Center.

Your confirmation email will contain your order number for future reference.

Printable Details

License Number	5257990302841
License date	Feb 28, 2022

Licensed Content

Licensed Content Publisher	Springer Nature
Licensed Content Publication	Nano Research
Licensed Content Title	Let the light be a guide: Chromophore communication in metal-organic frameworks
Licensed Content Author	Corey R. Martin et al
Licensed Content Date	Aug 20, 2020

Order Details

Type of Use	Thesis/Dissertation
Requestor type	academic/university or research institute
Format	print and electronic
Portion	full article/chapter
Will you be translating?	no
Circulation/distribution	50000 or greater
Author of this Springer Nature content	yes

About Your Work

Title	Photophysics and Electronics of Metal-Organic Frameworks
Institution name	University of South Carolina
Expected presentation date	Mar 2022

Additional Data

Order reference number	12345

https://s100.copyright.com/AppDispatchServlet 1/2

Chapter 2.


2/28/22, 11:38 PM
Rightslink® by Copyright Clearance Center
RightsLink
Home
Help
Email Support
Corey Martin
Flipping the Switch: Fast Photoisomerization in a Confined Environment
Author: Derek E. Williams, Corey R. Martin, Ekaterina A. Dolgopolova, et al
Publication: Journal of the American Chemical Society
Publisher: American Chemical Society
Date: Jun 1, 2018
Copyright © 2018, American Chemical Society
PERMISSION/LICENSE IS GRANTED FOR YOUR ORDER AT NO CHARGE
This type of permission/license, instead of the standard Terms and Conditions, is sent to you because no fee is being charged for your order. Please note the following:
- Permission is granted for your request in both print and electronic formats, and translations.
- If figures and/or tables were requested, they may be adapted or used in part.
- Please print this page for your records and send a copy of it to your publisher/graduate school.
- Appropriate credit for the requested material should be given as follows: "Reprinted (adapted) with permission from {COMPLETE REFERENCE CITATION}. Copyright {YEAR} American Chemical Society." Insert appropriate information in place of the capitalized words.
- One-time permission is granted only for the use specified in your RightsLink request. No additional uses are granted (such as derivative works or other editions). For any uses, please submit a new request.
If credit is given to another source for the material you requested from RightsLink, permission must be obtained from that source.
BACK
CLOSE WINDOW
© 2022 Copyright - All Rights Reserved | Copyright Clearance Center, Inc. | Privacy statement | Terms and Conditions
Comments? We would like to hear from you. E-mail us at customercare@copyright.com
https://s100.copyright.com/AppDispatchServlet
1/1

Chapter 3.

Photoresponsive frameworks: energy transfer in the spotlight

C. R. Martin, K. C. Park, R. E. Corkill, P. Kittikhunnatham, G. A. Leith, A. Mathur, Sakiru L. Abiodun, A. B. Greytak and N. B. Shustova, *Faraday Discuss.*, 2021, **231**, 266 **DOI:** 10.1039/D1FD00013F

Chapter 4.

2/28/22, 11:44 PM Rightslink® by Copyright Clearance Center

CCC RightsLink

Home | Help | Email Support | Corey Martin

ACS Publications

Stimuli-Modulated Metal Oxidation States in Photochromic MOFs

Author: Corey R. Martin, Kyoung Chul Park, Gabrielle A. Leith, et al
Publication: Journal of the American Chemical Society
Publisher: American Chemical Society
Date: Feb 1, 2022

Copyright © 2022, American Chemical Society

PERMISSION/LICENSE IS GRANTED FOR YOUR ORDER AT NO CHARGE

This type of permission/license, instead of the standard Terms and Conditions, is sent to you because no fee is being charged for your order. Please note the following:

- Permission is granted for your request in both print and electronic formats, and translations.
- If figures and/or tables were requested, they may be adapted or used in part.
- Please print this page for your records and send a copy of it to your publisher/graduate school.
- Appropriate credit for the requested material should be given as follows: "Reprinted (adapted) with permission from {COMPLETE REFERENCE CITATION}. Copyright {YEAR} American Chemical Society." Insert appropriate information in place of the capitalized words.
- One-time permission is granted only for the use specified in your RightsLink request. No additional uses are granted (such as derivative works or other editions). For any uses, please submit a new request.

If credit is given to another source for the material you requested from RightsLink, permission must be obtained from that source.

BACK CLOSE WINDOW

© 2022 Copyright - All Rights Reserved | Copyright Clearance Center, Inc. | Privacy statement | Terms and Conditions
Comments? We would like to hear from you. E-mail us at customercare@copyright.com

https://s100.copyright.com/AppDispatchServlet 1/1

Chapter 5.

Beyond structural motifs: the frontier of actinide-containing metal–organic frameworks

C. R. Martin, G. A. Leith and N. B. Shustova, *Chem. Sci.*, 2021, **12**, 7214 **DOI:** 10.1039/D1SC01827B

Chapter 6.

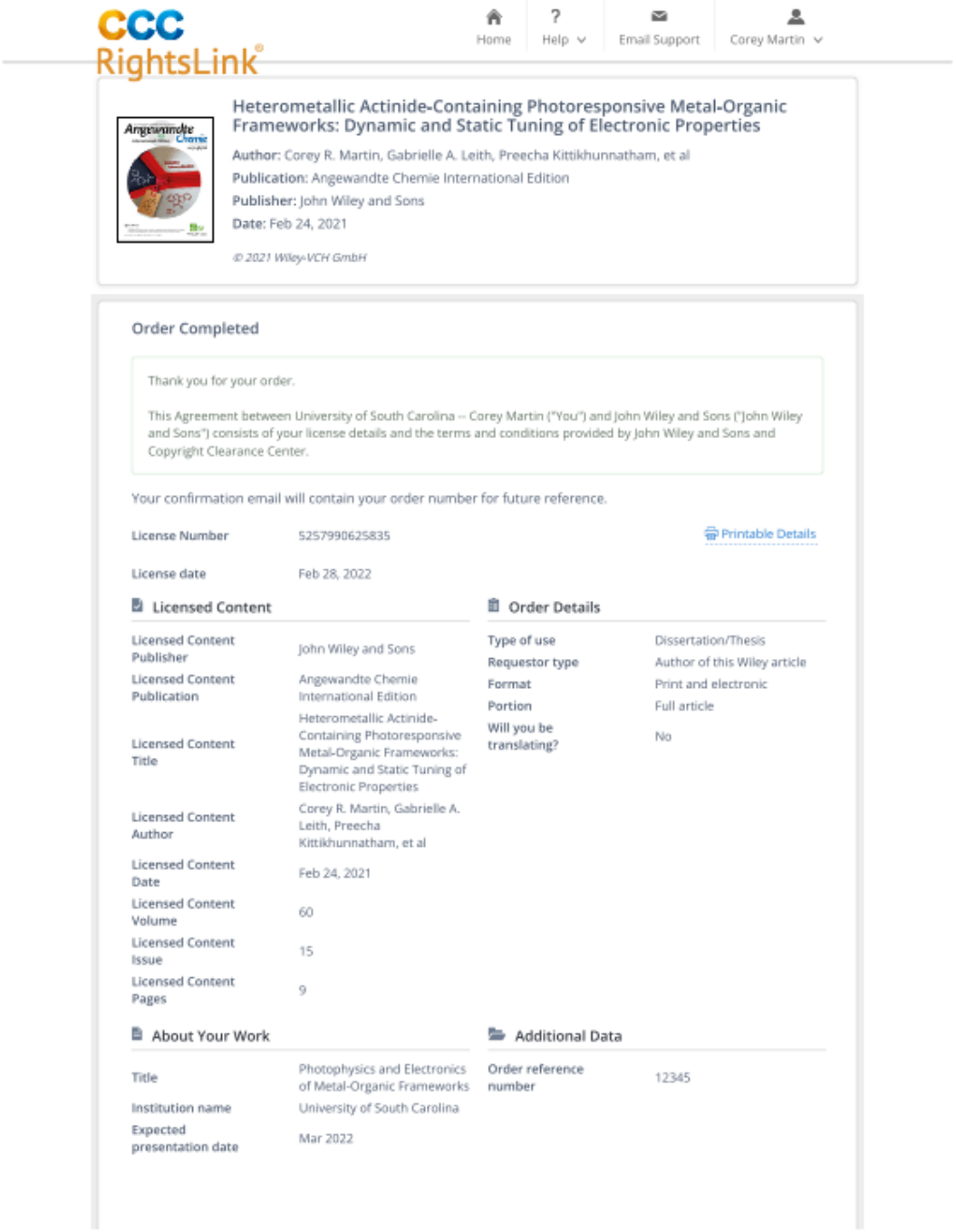

CCC RightsLink

Home | Help | Email Support | Corey Martin

Heterometallic Actinide-Containing Photoresponsive Metal-Organic Frameworks: Dynamic and Static Tuning of Electronic Properties

Author: Corey R. Martin, Gabrielle A. Leith, Preecha Kittikhunnatham, et al
Publication: Angewandte Chemie International Edition
Publisher: John Wiley and Sons
Date: Feb 24, 2021

Order Completed

Thank you for your order.

This Agreement between University of South Carolina -- Corey Martin ("You") and John Wiley and Sons ("John Wiley and Sons") consists of your license details and the terms and conditions provided by John Wiley and Sons and Copyright Clearance Center.

Your confirmation email will contain your order number for future reference.

Printable Details

License Number	5257990625835
License date	Feb 28, 2022

Licensed Content

Licensed Content Publisher	John Wiley and Sons
Licensed Content Publication	Angewandte Chemie International Edition
Licensed Content Title	Heterometallic Actinide-Containing Photoresponsive Metal-Organic Frameworks: Dynamic and Static Tuning of Electronic Properties
Licensed Content Author	Corey R. Martin, Gabrielle A. Leith, Preecha Kittikhunnatham, et al
Licensed Content Date	Feb 24, 2021
Licensed Content Volume	60
Licensed Content Issue	15
Licensed Content Pages	9

Order Details

Type of use	Dissertation/Thesis
Requestor type	Author of this Wiley article
Format	Print and electronic
Portion	Full article
Will you be translating?	No

About Your Work

Title	Photophysics and Electronics of Metal-Organic Frameworks
Institution name	University of South Carolina
Expected presentation date	Mar 2022

Additional Data

Order reference number	12345